Green Chemistry and Sustainable Technology

Taicheng An
Huijun Zhao
Po Keung Wong *Editors*

Advances in Photocatalytic Disinfection

Springer

Green Chemistry and Sustainable Technology

Aims and Scope

The series *Green Chemistry and Sustainable Technology* aims to present cutting-edge research and important advances in green chemistry, green chemical engineering and sustainable industrial technology. The scope of coverage includes (but is not limited to):

- Environmentally benign chemical synthesis and processes (green catalysis, green solvents and reagents, atom-economy synthetic methods etc.)
- Green chemicals and energy produced from renewable resources (biomass, carbon dioxide etc.)
- Novel materials and technologies for energy production and storage (bio-fuels and bioenergies, hydrogen, fuel cells, solar cells, lithium-ion batteries etc.)
- Green chemical engineering processes (process integration, materials diversity, energy saving, waste minimization, efficient separation processes etc.)
- Green technologies for environmental sustainability (carbon dioxide capture, waste and harmful chemicals treatment, pollution prevention, environmental redemption etc.)

The series *Green Chemistry and Sustainable Technology* is intended to provide an accessible reference resource for postgraduate students, academic researchers and industrial professionals who are interested in green chemistry and technologies for sustainable development.

More information about this series at http://www.springer.com/series/11661

Taicheng An • Huijun Zhao • Po Keung Wong
Editors

Advances in Photocatalytic Disinfection

Springer

Editors
Taicheng An
Institute of Environmental Health and Pollution Control, School of Environmental Science and Engineering
Guangdong University of Technology
Guangzhou, Guangdong, China

Huijun Zhao
Centre for Clean Environment and Energy
Griffith University
Gold Coast, QLD, Australia

Po Keung Wong
School of Life Science
The Chinese University of Hong Kong
Hong Kong SAR, China

ISSN 2196-6982 ISSN 2196-6990 (electronic)
Green Chemistry and Sustainable Technology
ISBN 978-3-662-53494-6 ISBN 978-3-662-53496-0 (eBook)
DOI 10.1007/978-3-662-53496-0

Library of Congress Control Number: 2016959267

Printed on acid-free paper

This Springer imprint is published by Springer Nature
The registered company is Springer-Verlag GmbH Germany
The registered company address is: Heidelberger Platz 3, 14197 Berlin, Germany

Preface

Due to the increasing demand of clean and safe drinking water, numerous alternative technologies for water purification have been developed. Recently, photocatalysis has been widely considered as a promising alternative for water purification due to its potential to use sunlight-driven heterogeneous catalytic disinfection processes with less or even no disinfection by-product (DBP) formation. Under specific light irradiation on the photocatalyst, reactive charged and reactive oxygen species (ROSs) are generated and can cause fatal damages to microorganisms. However, the large-scale photocatalytic disinfection application has not been established. One of the reasons is that the inactivation of microorganisms by the ROSs generated by photocatalysis is not so effective as other disinfectants such as chlorine even though the chlorination is well-known to produce toxic and mutagenic DPBs. Another reason is that the photocatalytic inactivation mechanism of microbial has still not been well clarified and this poses a great challenge to scale-up of the disinfection device and incorporation of photocatalytic disinfection unit into conventional water or wastewater treatment facilities. Furthermore, the complicate processes to fabricate highly effective visible-light-driven (VLD) photocatalysts lead to produce a small-quantity and comparatively high-cost product which also render the large-scale application of photocatalytic disinfection in water purification or wastewater treatment. This book intends to provide the most updated potential solution to the abovementioned problems of applying photocatalytic disinfection in large-scale use.

Chapters 2 and 3 present the feasibility of photocatalytic application of natural minerals such as natural sphalerite and natural pyrrhotite in organic degradation and bacterial disinfection under visible light. Although the photocatalytic efficiencies of these natural minerals are lower than those of synthetic VLD photocatalysts, the availability in a large quantity at low cost makes these natural minerals become cost effective for water purification. Chapter 2 focuses on the photocatalytic disinfection by natural sphalerite, while Chap. 3 focuses on the development of natural minerals (with or without magnetic property) collected from various mining sites in China as visible-light-driven (VLD) photocatalysts for microbial inactivation. The natural

magnetic minerals (NMMs) such as natural magnetic sphalerite and natural pyrrhotite etc. can be obtained in a large quantity at low cost, and the experimental results found that they can be separated very well and recycled for reuse; hence, the treatment can be easily achieved by the aid of electromagnetic field. Although the efficiency and property of individual NMM samples from different mining sites may slightly vary, the results indicate that such variations can be minimized by magnetic separation at the mining site. Or the quick and economical pretreatment of the NMM samples such as natural pyrrhotite can eliminate the efficiency and property variation between different batches of samples collected from different mining sites.

Chapter 4 first introduces bismuth-based photocatalysts for VLD photocatalytic disinfection. The author describes synthesis, characterization, and photocatalytic inactivation efficiencies of the bismuth-based photocatalysts into the following sections: (1) bismuth oxides and bismuth oxyhalides; (2) bismuth metallates; (3) plasmonic bismuth compounds; and (4) other bismuth-based composites such as $Bi_2O_2CO_3/Bi_3NbO_7$, β-Bi_2O_3/Bi_2MoO_6, etc. Then, the detailed mechanism(s) of photocatalytic disinfection including the reactive species (RSs) involved in disinfection by these bismuth-based photocatalysts is presented. Finally, the authors prepare a comprehensive table to summarize all recent studies on bismuth-based photocatalysts for photocatalytic disinfection.

Chapters 5 and 6 describe the development of silver (Chap. 5) or silver (Ag)-containing photocatalysts or silver halogens (e.g., silver bromide, AgBr) (Chap. 6) as photocatalysts in VLD photocatalytic disinfection. In Chap. 5, the author first describes the principles of water disinfection by silver nanoparticle (AgNP) and its photocatalytic application in bacterial inactivation process. The detailed synthesis, characterization, and mechanisms of photocatalytic inactivation of bacteria by AgNP and Ag-based photocatalysts such as Ag-TiO_2, Ag-AgX (X=halogens), and Ag-ZnO were discussed. Comprehensive comparison of photocatalytic disinfection using Ag-TiO_2, Ag-AgX, and Ag-ZnO was compiled and presented in tables. In Chap. 6, the authors describe the doping of Ag onto TiO_2 significantly enhanced photocatalytic bacterial inactivation activity by the composite. They also study the major RSs (oxidative and charged) involved in photocatalytic inactivation of bacteria by Ag-containing composites. Finally, they studied the interaction between bacterial cell and Ag-containing photocatalysts. They found that pH of the reaction solution imposed great influence on the surface charge of the bacterial cells and Ag-containing photocatalysts and concluded that the electrostatic force interaction plays a crucial role in effective photocatalytic bacterial inactivation by Ag-containing photocatalysts. Also plasmonic effect was the major driving force to produce reactive species for silver halogen composite such as Ag-AgI/Al_2O_3 to inactivate bacterial cells.

Chapter 7 focuses on the photocatalytic disinfection by metal-free photocatalysts. The unique features of these photocatalysts are earth-abundant, low cost, and environmentally friendly. The chapter lists the recent studies on the use carbon nitride (g-C_3N_4)- and graphene-based photocatalysts. These photocatalysts have excellent photocatalytic bacterial disinfection efficiency and

their simple structures make their synthesis much easier. The chapter also provides new information on the use of element such as phosphorous in photocatalytic bacterial inactivation. The studies on how to improve the photocatalytic bacterial inactivation by simple modification of the element are discussed.

Chapter 8 shows a practical use of photocatalytic disinfection under solar irradiation. The chapter first reviews the use of various types of catalysts in photocatalytic disinfection. Then the authors describe the structural changes of bacterial cells, protozoa, and viruses during photocatalytic disinfection, followed by a detailed discussion of the kinetics of photocatalytic inactivation. The final part focuses on the updated cases on the large-scale application of photocatalytic disinfection.

Chapters 9, 10, 11, and 12 introduce the great application of the modified process of photocatalysis (PC) and photoelectrocatalysis (PEC), in which a small bias is applied to quickly and efficiently remove photogenerated electrons (e^-) to prevent the recombination of photogenerated e^- and holes (h^+), thus leaving the h^+ with much long life span to directly react with or further producing RSs to react with and inactivate microbial cells. The inactivation efficiency is 10–100 times faster than that of photocatalysis. Chapter 9 first introduces the principle of PEC. Then the authors compared the bacterial inactivation efficiency between PC and PEC and found that PEC was far more effective and faster than PC for bacterial inactivation. The major cause for the great difference in bacterial inactivation was due to a large amount of h^+ and its derived RSs were available to react with and inactivate bacterial cells. Then, they focused on the development of highly efficient photoelectrode, especially anode with TiO_2 and non-TiO_2-based materials to significantly enhance the treatment efficiency of the PEC system.

In Chap. 10, these authors used a bottom-up approach to study the PC and PEC treatment of the building block of macro-biomolecules such as DNAs, RNAs, proteins, lipids, and carbohydrates. They used nucleosides and amino acids as model compounds and found that PC and PEC could easily decompose these building blocks and their degradation efficiencies were higher under PEC treatment. These building blocks could also completely mineralize (degradation into CO_2 and water) with proper treatment time by PEC. They also found that same trend for the selected macro-biomolecules. Finally, the authors compare the PC and PEC inactivation of two selected microorganisms, a bacterium (*E. coli*) and an animal virus (adenovirus). Surprisingly, results indicated that the virus was more resistant to PC and PEC treatment than the bacterium. In addition, they found that the presence of halogens, especially chloride (Cl^-) and bromide (Br^-), would lead to much faster and long-lasting inactivation of the microorganisms by PC and PEC. They proposed the production of single and bi-halogen radicals, leading to the quick and long-lasting microbial inactivation since the halogen radicals are more powerful and stable in the reaction solution.

Chapter 11 focused on the identification of the major RSs, the targets RSs of the bacterial cells and the inactivation mechanism of PC and PEC in bacterial inactivation. Using various scavengers for respective RSs, the authors identified the subtle difference between the RSs involved in bacterial inactivation in PC and PEC processes. They also use a "partition system" to address the issue of the

requirement of direct contact between the photocatalyst(s) and bacterial cells which are prerequisite for effective bacterial inactivation in both PC and PEC. For the targets of RS attack in the bacterial cells, there were cell envelopes such as extracellular polymeric substances, cell wall and cell membrane, enzymes, other structural proteins, and DNA and RNA which were reported in numerous studies, and there was no generalization of the "hot spot" target in bacterial cells for the attack by RSs. If either PC or PEC is proceeded for appropriate time, the mineralization of all microbial compounds could be observed. In Chap. 12, based on the studies of Chaps. 10 and 11, the cellular responses and damages of the bacterial cell under PEC treatment were being explored, and the chapter also proposes a more detailed mechanism for the PEC disinfection of bacteria.

Chapter 13 shows the mechanistic modelling of photocatalytic disinfection. The model includes several interactions such as the initial contact between the photocatalysts and microbial cells, and this step was extremely important for efficient inactivation of microorganisms since the RSs, either diffusible or surface, or oxidative or charged, would have much high inactivation efficiency to get direct contact, once produced, with the microbial cells. The authors proposed a model for the kinetics of interaction between the photocatalyst and microbial cell, as well as the microbial inactivation. Based on the experimental results, the authors proposed that the sequence for the photocatalytic microbial inactivation by UV-TiO_2 system was the following: the attachment of TiO_2 to the surface of bacterial cell, light propagation through the suspension, the quantum yield of hydroxyl radical generation, and bacterial cell surface oxidation. Based on the verified model, they proposed that the better inactivation can be achieved by maintaining a relatively low photocatalyst-to-microorganism ratio while maximizing the light intensity at low to moderate ionic strength. The availability of the model can be beneficial for predicting the capability and treatment efficiency of the photocatalytic disinfection system.

The 12 chapters (Chaps. 2, 3, 4, 5, 6, 7, 8, 9, 10, 11, 12 and 13) of this book can be categorized into four parts: The first part has two chapters (i.e. Chaps. 2 and 3) which cover the use of naturally occurring visible-light active minerals for microbial disinfection, while Chaps. 4, 5, 6, 7, and 8 are the second part which describes the use of various synthetic visible-light active catalysts for photocatalytic disinfection. Part III consists of Chaps. 9, 10, 11, and 12 and focuses on photoelectrocatalytic disinfection its disinfection efficiency is greatly enhanced by applying an external bias. Part IV (Chap. 13) focuses on the modeling of photocatalytic disinfection. The data, technology and information presented in this book are the major advances in photocatalytic disinfection in the last decade, which provides a useful resource for people working in academic, engineering, and technical sectors.

Guangzhou, Guangdong, China — Taicheng An
Nathan, QLD, Australia — Huijun Zhao
Hong Kong SAR, China — Po Keung Wong

Contents

Contributors

Taicheng An The State Key Laboratory of Organic Geochemistry, Guangzhou Institute of Geochemistry, Chinese Academy of Sciences, Guangzhou, China

Institute of Environmental Health and Pollution Control, School of Environmental Science and Engineering, Guangdong University of Technology, Guangzhou, Guangdong, China

O. Kofi Dalrymple Algenol Biotech, Fort Myers, FL, USA

Cong Ding The Key Laboratory of Orogenic Belts and Crustal Evolution, School of Earth and Space Science, Peking University, Beijing, China

Hongrui Ding The Key Laboratory of Orogenic Belts and Crustal Evolution, School of Earth and Space Science, Peking University, Beijing, China

D. Yogi Goswami Clean Energy Research Center, University of South Florida, Tampa, FL, USA

Sheng Guo School of Resources and Environmental Engineering, Wuhan University of Technology, Wuhan, People's Republic of China

School of Chemistry and Environmental Engineering, Wuhan Institute of Technology, Wuhan, People's Republic of China

Xuesen Hong School of Civil Engineering and Transportation, South China University of Technology, Guangzhou, China

Chun Hu Research Center for Eco-Environmental Sciences, Chinese Academy of Sciences, Beijing, China

Yongyou Hu School of Environment and Energy, South China University of Technology, Guangzhou, China

Guiying Li Institute of Environmental Health and Pollution Control, School of Environmental Science and Engineering, Guangdong University of Technology, Guangzhou, Guangdong, China

Centre for Clean Environment and Energy, Griffith University, Gold Coast, QLD, Australia

Yan Li The Key Laboratory of Orogenic Belts and Crustal Evolution, School of Earth and Space Science, Peking University, Beijing, China

Yanzhang Li The Key Laboratory of Orogenic Belts and Crustal Evolution, School of Earth and Space Science, Peking University, Beijing, China

Yi Liu The Key Laboratory of Orogenic Belts and Crustal Evolution, School of Earth and Space Science, Peking University, Beijing, China

Anhuai Lu The Key Laboratory of Orogenic Belts and Crustal Evolution, School of Earth and Space Science, Peking University, Beijing, China

Dionissios Mantzavinos Department of Chemical Engineering, University of Patras, Patras, Greece

Hongwei Sun The State Key Laboratory of Organic Geochemistry, Guangzhou Institute of Geochemistry, Chinese Academy of Sciences, Guangzhou, China

Key Laboratory of Aquatic Botany and Watershed Ecology, Wuhan Botanical Garden and Sino-Africa Joint Research Center, Chinese Academy of Sciences, Wuhan, China

Danae Venieri School of Environmental Engineering, Technical University of Crete, Chania, Greece

Changqiu Wang The Key Laboratory of Orogenic Belts and Crustal Evolution, School of Earth and Space Science, Peking University, Beijing, China

Wanjun Wang School of Life Sciences, The Chinese University of Hong Kong, Hong Kong SAR, China

Department of Chemistry, The Chinese University of Hong Kong, Hong Kong SAR, China

Po Keung Wong School of Life Sciences, The Chinese University of Hong Kong, Hong Kong SAR, China

Dehua Xia School of Life Sciences, The Chinese University of Hong Kong, Hong Kong SAR, China

Gaoke Zhang School of Resources and Environmental Engineering, Wuhan University of Technology, Wuhan, People's Republic of China

Haimin Zhang Key Laboratory of Materials Physics, Centre for Environmental and Energy Nanomaterials, Anhui Key Laboratory of Nanomaterials and Nanotechnology, Institute of Solid State Physics, Chinese Academy of Sciences, Hefei, China

Huijun Zhao Centre for Clean Environment and Energy, Griffith University, Gold Coast, QLD, Australia

Chapter 1
Introduction

Taicheng An, Huijun Zhao, and Po Keung Wong

1.1 Water Disinfection

The last 50 years have witnessed a growing awareness of the fragile state of most of the planets' drinking water resources. Access to freshwater will become even more important in the near future, as the world's population rises from 7 billion today to 9 billion by 2050. The World Health Organization (WHO) has estimated that 80 % of illnesses in the developing world are water related, resulting from poor water quality and lack of sanitation [1]. There are 3.3 million deaths each year from diarrheal diseases caused by bacteria such as *Escherichia coli*, *Salmonella* sp. and *Cholera* sp., parasites and viral pathogens. In the 1990s, the number of children who died of diarrhoea was greater than the sum of people killed in conflicts since World War II [2]. It is also estimated that around 4 billion people worldwide experience to have no or little access to clean and sanitized water supply, and millions of people died of severe waterborne diseases annually [3, 4].

Waterborne diseases are caused by pathogenic microorganisms that most commonly are transmitted in contaminated freshwater. The pathogenic microorganisms responsible for these diseases include a variety of helminthes, protozoa, fungi,

T. An
Institute of Environmental Health and Pollution Control, School of Environmental Science and Engineering, Guangdong University of Technology, Guangzhou 510006, Guangdong, China
e-mail: antc99@gdut.edu.cn; antc99@gig.ac.cn

H. Zhao
Centre for Clean Environment and Energy, Griffith University, Gold Coast Campus, Gold Coast, QLD 4222, Australia
e-mail: h.zhao@griffith.edu.au

P.K. Wong (✉)
School of Life Sciences, The Chinese University of Hong Kong, Shatin, N.T., Hong Kong SAR, China
e-mail: pkwong@cuhk.edu.hk

T. An et al. (eds.), *Advances in Photocatalytic Disinfection*, Green Chemistry and Sustainable Technology, DOI 10.1007/978-3-662-53496-0_1

bacteria, rickettsiae, viruses and prions [1, 5], many of which are intestinal parasites or invade the tissues or circulatory system through walls of the digestive tract. Water disinfection means the removal, deactivation or killing of pathogenic microorganisms, resulting in termination of growth and reproduction. Problems with waterborne diseases are expected to grow worse in the future, both in developing and industrialized nations. Therefore, effective and lower-cost methods to disinfect microorganism-contaminated waters are urgently needed, without further stressing the environment or endangering human health by the treatment itself [6].

1.2 Traditional Water Disinfection Methods

The existing drinking water pretreatment processes, such as coagulation, flocculation and sedimentation, can remove a maximum of 90 % of bacteria, 70 % of viruses and 90 % of protozoa [4]. Filtration for drinking water treatment (e.g. sand and membrane filtration), with proper design and adequate operation, can act as a consistent and effective barrier for microbial pathogens leading to about 90 % removal of bacteria. However, the remaining bacteria might still be able to cause disease, which makes filtration a good pretreatment, but not a completely safe disinfection technique [7]. The most commonly used drinking water disinfection techniques after pretreatment include chlorination (chlorine and derivates), ozonation and UVC irradiation.

1.2.1 Chlorination

Chlorine is a very effective disinfectant for most microorganisms. It is reported that 99 % of bacterial cells can be killed with chlorine of 0.08 mg/min/L at 1–2 °C under neutral pH condition. In addition, 99 % of viruses can be killed by 12 mg/min/L chlorine at 0–5 °C under neutral pH condition. However, the protozoa including *Cryptosporidium*, *Giardia* and *Acanthamoeba* are quite resistant to chlorination and cannot be effectively inactivated [7]. Another major disadvantage of chlorination is the formation of potentially mutagenic and carcinogenic disinfection byproducts (DBPs) during water chlorination, which can lead to the problems of recontamination and salting of freshwater sources [8, 9]. The DBPs are formed from the reaction of chlorine with natural organics in water and include trihalomethanes (THMs) and haloacetic acids (HAAs). US Environmental Protection Agency (USEPA) regulations have further limited THMs, HAAs and other DBPs (including chlorite and bromate) in drinking water [10]. As a result, many water systems now limit the use of chlorine to high-quality groundwater or reduce total organic carbon prior to disinfection.

1.2.2 Ozonation

The application of ozone is another widespread disinfection method for drinking water treatment throughout the world [11]. Similar to chlorination, ozone is unstable in water and undergoes reactions with some water matrix components. However, the unique feature of ozone is its decomposition into hydroxyl radicals (•OH), which are the strongest oxidants in water [12]. While disinfection occurs dominantly through ozone, oxidation processes may occur through both ozone and •OH [13], making the ozonation even more effective than Cl_2 in destroying bacterial cells and viruses [14, 15]. It is reported that 99 % of bacterial cells can be removed with 0.02 mg/min/L ozone at 5 °C under neutral pH condition. For the disinfection of protozoa *Cryptosporidium*, the required ozone concentration is suggested to be 40 mg/min/L at 1 °C [16]. Despite its highly efficient inactivation of all microorganisms, ozonation can also produce DBPs, such as aldehydes, carboxylic acids and ketones, in the presence of dissolved organic matter [17]. However, as ozonation is usually followed by biological filtration, some organic compounds can be mineralized microbiologically. Thus, the most important ozonation DBP regulated in drinking waters today is bromate, which is formed during ozonation of bromide-containing waters and cannot be degraded in biological filtration process [18, 19]. In addition, ozonation is a more complex technology than chlorination and is often associated with increased costs and process complexity [20].

1.2.3 UV Irradiation

Water disinfection utilizing germicidal UV irradiation has become more and more important in recent years, as the low-pressure UV produces almost no disinfection byproducts [21]. In addition, unlike chemical disinfectants, the biological stability of the water is not affected by low-pressure lamps. In Europe, UV has been widely applied for drinking water disinfection since the 1980s, for the control of incidental contamination of vulnerable groundwater and for the reduction of heterotrophic plate counts [22]. Depending on irradiation wavelengths, UV can be divided into UVA (315–400 nm), UVB (280–315 nm), UVC (200–280 nm) and vacuum UV (VUV) (100–200 nm). In particular, UVC is the most effective wavelength for microorganism inactivation, as UVC light will damage irradiated DNA, directly inducing pyrimidine and purine dimers and pyrimidine adducts. For water disinfection, 99 % inactivation of bacterial cells can be achieved at UVC intensity of 7 mJ/cm^2. The susceptibility of protozoa to UVC damage is very similar to that of bacteria; thus, the 99 % inactivation for *Cryptosporidium* can be achieved at 5 mJ/cm^2 [23]. However, due to the weak penetration power, UV disinfection can only inactivate bacterial cells on the surface of the wastewater [24], and the treated cells can often regrowth after removal of UV irradiation [25]. General application of UV

disinfection was further hampered because of high costs, poor equipment reliability and maintenance problems [26, 27].

Therefore, although traditional disinfection methods can be effectively applied in water disinfection, the disadvantages of these methods must be considered when selecting suitable disinfection methods for water treatment, and alternative technologies are needed.

1.3 Advanced Oxidation Process

Advanced oxidation processes (AOPs) are defined as the processes that generate hydroxyl radicals (•OH) in sufficient quantities to be able to oxidize the majority of the complex chemicals present in the effluent water [28]. AOPs have been receiving increasing attention to be effectively applied in the near-ambient total degradation of soluble organic contaminants from waters and soils, as the produced •OH would be able to oxidize almost all organic compounds to carbon dioxide and water because of its powerful redox potential (2.8 V vs. NHE) [29]. These processes include cavitation [30, 31], photo-Fenton [32, 33], photocatalytic oxidation [34] and other combination methods, such as H_2O_2/UV, O_3/UV and H_2O_2/O_3/UV, which utilize the photolysis of H_2O_2 and O_3 to produce •OH [35]. In particular, heterogeneous photocatalysis based on the use of a semiconductor with suitable energy band gap (Eg) is the most interesting and promising advanced oxidation technology that has received much attention in the past few decades for a variety of photochemical applications, including water splitting, organic compounds degradation and CO_2 reduction, as well as water disinfection.

1.4 Photocatalysis

With respect to the generally accepted definition of thermal catalysis, photocatalysis can be defined as "acceleration of a photoreaction by the presence of a catalyst", which indicates both light and a catalyst are necessary to bring about or to accelerate a chemical transformation [36]. As the photoreaction takes place in more than one homogeneous medium, it is usually called "heterogeneous photocatalysis" [37, 38].

Fujishima and Honda (1972) [39] discovered the photocatalytic splitting of water on TiO_2 electrodes, which has marked the beginning of heterogeneous photocatalysis [40]. Since then, tremendous research efforts have been devoted into understanding the fundamental process of heterogeneous photocatalysis, thus enhancing the photocatalytic efficiencies [41–44]. Photocatalysis was initially applied in hydrogen evolution by splitting water, with intention to address the energy crisis [45–48]. Research activities were soon extended to photocatalytic oxidation of organic pollutants [49, 50], CO_2 reduction [51] and the disinfection of microorganisms in contaminated water [52, 53]. Although an early study

demonstrated that there was no improved antimicrobial activity of TiO_2 for the disinfection of primary wastewater effluent [54], a number of subsequent studies have shown the effectiveness of TiO_2 photocatalysis for water disinfection [55, 56], including inactivation of bacterial cells [57] and viruses from contaminated water [58], tertiary treatment of wastewater [59], purifying drinking water [60], treatment of wash waters from vegetable preparation [61] and in bioreactor design to prevent biofilm formation [62].

1.4.1 Fundamental Mechanism for TiO_2 Photocatalysis

Semiconductors acting as the photocatalysts for the light-reduced redox processes, such as TiO_2, ZnO, Fe_2O_3, CdS and ZnS, are characterized by a filled valence band and an empty conduction band [63]. When the valence band receives a photon with energy bigger than the band gap, an electron (e^-) will be excited and promoted into the conduction band, leaving a hole (h^+) in the valence band. The photo-generated e^--h^+ pairs will subsequently migrate onto the surface of photocatalyst and undergo a variety of complicated reactions to produce reactive oxidative species (ROSs), which are potentially involved in the photocatalytic oxidation process. The most widely used photocatalyst is TiO_2, as it is nontoxic, low cost and highly efficient and has long-term photostability [64, 65]. The fundamental mechanism for TiO_2 photocatalysis under UV irradiation has been well established for photocatalytic oxidation process towards organic compounds degradation as well as microorganism inactivation (Fig. 1.1) [38, 66].

The primary photocatalytic oxidation mechanism includes the following four steps (Eqs. 1.1, 1.2, 1.3, 1.4, 1.5, 1.6, 1.7, 1.8, 1.9, 1.10, 1.11 and 1.12):

1. Irradiation
   The first step is the light irradiation process for harvesting and conversion of light energy to chemical energy, thus leading to the generation of e^--h^+ pairs.

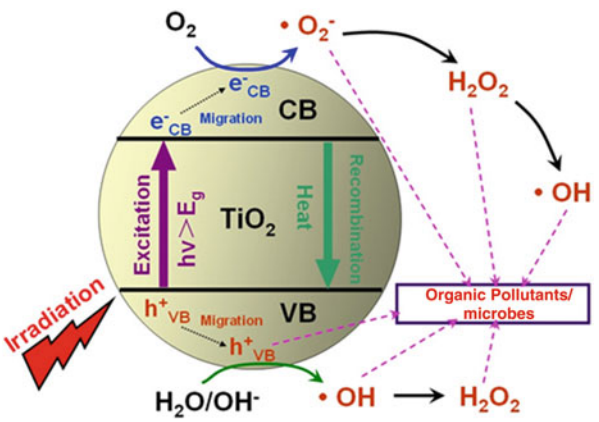

Fig. 1.1 A schematic diagram showing the photocatalytic oxidation mechanism of TiO_2 photocatalysis under UV irradiation

The requirement of this step is the incoming photon should have an energy of $h\nu$ that matches or exceeds the semiconductor band gap energy. For TiO_2, the light wavelength for fulfilment of the excitation process is restricted to the UV region because of its wide band gap (3.2 eV) [67].

2. Separation and recombination of e^--h^+ pairs
The photoexcited e^- is injected into the conduction band, leading to the separation of e^--h^+ pairs. However, the photo-generated e^- and h^+ can recombine in bulk or on surface of the semiconductor within extremely short time, releasing energy in the form of heat or photons (Eqs. 1.1 and 1.2) [68, 69].

$$TiO_2 + h\nu \rightarrow h_{vb}{}^+ + e_{cb}{}^- \tag{1.1}$$

$$h_{vb}{}^+ + e_{cb}{}^- \rightarrow \text{recombination} + \text{energy (heat/photons)} \tag{1.2}$$

The separated e^- and h^+ without recombination are migrated to the surface of TiO_2 and trigger photochemical reactions to produce secondary reactive species (i.e. ROSs) or directly oxidize/reduce the substrates adsorbed by the TiO_2.

3. h^+ trapping reactions
In the valence band, the separated h^+ is migrated to the surface and trapped by surface-adsorbed hydroxyl groups or water to produce trapped holes $\left(\equiv Ti^{IV}O\bullet\right)$ (Eq. 1.3), which is usually described as a surface-bound or surface-adsorbed hydroxyl radical ($\bullet OH_{ads}$) [70–72]. When electron donors (Red) (i.e. reductants) are available on the TiO_2 surface, the photocatalytic oxidation process thus happens by electron transferring from Red to trapped holes (Eq. 1.4). The subsequent release of $\bullet OH_{ads}$ to bulk solution, thus leading to the formation of bulk hydroxyl radical ($\bullet OH_{bulk}$), is suggested to contribute to the oxidation process (Eqs. 1.5, 1.6 and 1.7) [73]. On the other hand, h^+ can also be directly involved in oxidation of Red [74] and indirectly involved in production of H_2O_2 by coupling of two •OH (Eqs. 1.8 and 1.9) [75–77].

$$h_{vb}{}^+ + \equiv Ti^{IV}OH \rightarrow \left[\equiv Ti^{IV}OH\bullet\right]^+ \rightarrow \equiv Ti^{IV}O\bullet + H^+ \tag{1.3}$$

$$\equiv Ti^{IV}O\bullet + \text{Red} + H^+ \rightarrow \equiv Ti^{IV}OH + \bullet Red^+ \tag{1.4}$$

$$h_{vb}{}^+ + H_2O \rightarrow \bullet OH_2{}^+ \rightarrow \bullet OH + H^+ \tag{1.5}$$

$$h_{vb}{}^+ + OH^- \rightarrow \bullet OH \tag{1.6}$$

$$\bullet OH + \text{Red} + H^+ \rightarrow \bullet Red^+ \tag{1.7}$$

$$h_{vb}{}^+ + \text{Red} \rightarrow \bullet Red^+ \tag{1.8}$$

$$\bullet OH + \bullet OH \rightarrow H_2O_2 \tag{1.9}$$

4. e^- trapping reactions
In the conduction band, O_2 often acts as the electron acceptor to trap the photoexcited $e_{cb}{}^-$ in aerated systems, thus preventing the e^--h^+ recombination. In this process, $\bullet O_2{}^-$ is formed and undergoes a variety of reactions to produce H_2O_2 (Eqs. 1.10, 1.11, 1.12 and 1.13) [78, 79]. Meanwhile, the as-generated

H_2O_2 can also produce the highly reactive •OH by reduction or cleaving (Eqs. 1.14 and 1.15) [80–82].

$$O_2 + e_{cb}^- \rightarrow \bullet O_2^- \quad (1.10)$$

$$H_2O + \bullet O_2^- \rightarrow \bullet OOH + OH^- \quad (1.11)$$

$$2 \bullet OOH \rightarrow O_2 + H_2O_2 \quad (1.12)$$

$$\bullet OOH + H_2O + e_{cb}^- \rightarrow H_2O_2 + OH^- \quad (1.13)$$

$$H_2O_2 + e^- \rightarrow \bullet OH + OH^- \quad (1.14)$$

$$H_2O_2 \rightarrow \bullet OH + \bullet OH \quad (1.15)$$

During the overall photochemical process, the photo-generated e^-/h^+ and the produced ROSs such as •OH, $\bullet O_2^-$, •OOH and H_2O_2 are suggested to be responsible for the oxidation of organic pollutants, including synthetic dyes and pathogenic microorganisms in aqueous media. The importance of •OH as the oxidation agent was particularly attended by researchers in this typical mechanism model of photocatalytic oxidation in UV irradiation TiO_2 systems [38, 83, 84].

1.4.2 Photocatalytic Water Disinfection

Photocatalysis was first shown to be an effective disinfection process by Matsunaga et al. (1985) [53], who reported on the inactivation of *Lactobacillus acidophilus*, *Saccharomyces cerevisiae* and *Escherichia coli* by Pt-loaded TiO_2. Since then, a concerted range of research has been conducted on the development of photocatalysis for water disinfection. Photocatalytic disinfection of a wide range of bacteria and yeasts including *Escherichia coli* [85, 86], *Candida albicans* [87], *Enterococcus faecium*, *Pseudomonas aeruginosa*, *Staphylococcus aureus* [24], *Streptococcus faecalis* [88], *Streptococcus mutans* [89], *Salmonella choleraesuis*, *Vibrio parahaemolyticus* and *Listeria monocytogenes* [90] as well as poliovirus [91] has been reported. The inactivation of the protozoan of *Cryptosporidium* and *Giardia*, known for their resistance to many chemical disinfectants, including chlorine, was also reported in recent years [92–94].

As the archetypical photocatalyst for water splitting and organic compounds degradation, TiO_2 also holds the preponderant position in water disinfection for destruction of various microorganism including bacteria (both Gram-negative and Gram-positive), fungi, algae, protozoa and viruses as well as microbial toxins [56]. Table 1.1 shows the typical examples of TiO_2 photocatalysis for microorganism inactivation. For all the inactivation of microorganism reported so far, only *Acanthamoeba* cysts and *Trichoderma asperellum* conidiospores were found to be resistant to photocatalysis [95, 96]. There are three crystal phases of TiO_2: anatase, rutile and brookite, in which anatase shows the highest photocatalytic activity [97].

Table 1.1 Typical examples of microorganism inactivation caused by TiO_2 photocatalysis [56]

Microorganism	Photocatalysts	References
Bacteria (Gram-negative)		
Escherichia coli	Degussa P25 suspension	[98]
Escherichia coli	TiO_2-impregnated cloth filter	[99]
Enterobacter aerogenes	Degussa P25 suspension	[100]
Flavobacterium sp.	TiO_2-coated glass beads	[101]
Fusobacterium nucleatum	Anatase TiO_2 thin film	[102]
Pseudomonas aeruginosa	TiO_2-coated soda lime glass and silica tubing	[103, 104]
Legionella pneumophila	Degussa P25 suspension	[105]
Porphyromonas gingivalis	TiO_2 sol/gel-coated orthodontic wires	[106]
Vibrio vulnificus	TiO_2-impregnated steel fibres	[107]
Bacteria (Gram-positive)		
Actinobacillus actinomycetemcomitans	TiO_2 coated on Ti substrates	[102]
Bacillus cereus	TiO_2 suspension	[108]
Streptococcus cricetus	Kobe Steel TiO_2	[109]
Streptococcus mutans	TiO_2 thin film	[110]
Clostridium difficile	Evonik Aeroxide P25 thin film	[111]
Clostridium perfringens spores	Degussa P25 suspension	[112]
Bacillus subtilis endospore	TiO_2 coated on Al foil	[113]
Fungi		
Aspergillus niger	TiO_2 coated on wood	[114]
Aspergillus niger spores	Degussa P25 film on quartz discs	[62]
Candida famata	TiO_2-coated catheters	[115]
Candida albicans	TiO_2 thin film	[24]
Penicillium citrinum	TiO_2-coated air filter	[116]
Trichoderma asperellum	TiO_2-coated concrete	[96]
Protozoa		
Cryptosporidium parvum	Nanostructured TiO_2 films	[117]
Giardia sp.	Fibrous ceramic TiO_2 filter	[94]
Giardia lamblia	TiO_2 thin film	[118]
Acanthamoeba castellanii	Degussa P25 suspension	[95]
Algae		
Cladophora sp.	TiO_2-coated glass	[119]
Chroococcus sp.	Anatase TiO_2	[120]
Oedogonium sp.	TiO_2-coated concrete	[121]
Melosira sp.	TiO_2-coated glass	[122]
Virus		
Influenza A/H5N2	Degussa P25/TiO_2 Millennium PC500	[123]
E. coli coliphage	Degussa P25 suspension	[112]
E. coli MS2	TiO_2 suspension	[124]
E. coli λ vi	Degussa P25 suspension	[125]
Influenza A/H1N1	TiO_2 suspension	[126]

(continued)

Table 1.1 (continued)

Microorganism	Photocatalysts	References
Influenza A/H3N2	TiO_2/Pt-TiO_2	[127]
SARS coronavirus	Titanium apatite filter	[128]
Toxins		
Brevetoxins	Degussa P25 suspension	[129]
Microcystins LR, YR and YA	Degussa P25 suspension	[130]
Nodularin	Degussa P25 suspension	[131]

However, the most active and commercially available TiO_2 is P25 (Degussa Ltd., Germany), consisting of 80 % anatase and 20 % rutile. The improved activity of mixed crystal phases is generally ascribed to interactions between the two forms, thus preventing bulk recombination. For catalyst immobilization, TiO_2 is often coated on various supports, including glass plate, cloth filter, steel substrates, silica, wood, catheter, concrete, etc.

Although exciting progress has been made in TiO_2 photocatalysis for microorganism disinfection, challenges still pose in achieving photocatalytic water disinfection utilizing solar energy. Unfortunately, the most widely used TiO_2 is only active under UV irradiation which accounts for only 4 % of the sunlight spectrum, while 45 % of the sunlight spectrum is visible light. TiO_2 modification techniques have been attempted to shift its light absorption capacity towards visible wavelengths, while considerable scientific interests have been devoted to the development of new types of photocatalyst that is active under visible light irradiation. This opens avenue for designing and fabricating nanostructured materials that can be used in photocatalytic water disinfection by employing material science and nanotechnology [132–134].

1.4.3 Advances in Photocatalytic Disinfection

In this book, some of the key development of photocatalytic disinfection in the last decade will be presented and discussed. The use of naturally occurring minerals or novel synthetic catalysts for effective microbial disinfection will be compiled. In addition, the mechanism, catalysts and performance of microbial disinfection by photoelectrocatalytic process will be presented and discussed. Finally, how to apply modelling approaching to study the kinetics of the photocatalytic disinfection will be included in this book. With all these updated information, the useful information and data will be provided to the people in academic, engineering and technical sectors.

References

1. World Health Organization (2003) Emerging issues in water and infectious disease 1–22. World Health Organization, Geneva
2. Smith A (2009) Nanotechnology: an answer to the world's water crisis. Chem Int 31:12–14
3. Montgomery MA, Elimelech M (2007) Water and sanitation in developing countries: including health in the equation. Environ Sci Technol 41:17–24
4. Malato S, Fernandez-Ibanez P, Maldonado MI, Blanco J, Gernjak W (2009) Decontamination and disinfection of water by solar photocatalysis: recent overview and trends. Catal Today 147:1–59
5. Pitman GK (2002) Bridging troubled waters – assessing the World Bank water resources strategy. World Bank Publications, Washington, DC
6. Shannon MA, Bohn PW, Elimelech M, Georgiadis JG, Marinas BJ, Mayes AM (2008) Science and technology for water purification in the coming decades. Nature 452:301–310
7. World Health Organization (2006) Guidelines for drinking-water quality first addendum to third edition 1 recommendations. World Health Organization, Library Cataloguing-in-Publication Data
8. Bryant EA, Fulton GP, Budd GC (1992) Disinfection alternatives for safe drinking water. van Nostrand Reinhold, New York
9. Nieuwenhuijsen MJ, Toledano MB, Eaton NE, Fawell J, Elliott P (2000) Chlorination disinfection byproducts in water and their association with adverse reproductive outcomes: a review. Occup Environ Med 57:73–85
10. Public Law (1996) Safe drinking water act amendments of 1996, 104–182, 1620–1621
11. Camel V, Bermond A (1998) The use of ozone and associated oxidation processes in drinking water treatment. Water Res 32:3208–3222
12. Staehelin J, Hoigné J (1985) Decomposition of ozone in water in the presence of organic solutes acting as promoters and inhibitors of radical chain reactions. Environ Sci Technol 19:1206–1213
13. Hoigné J (1998) Chemistry of aqueous ozone, and transformation of pollutants by ozonation and advanced oxidation processes. In: Hubrec J (ed) The handbook of environmental chemistry quality and treatment of drinking water. Springer, Berlin, pp 341–368
14. United States Environmental Protection Agency (1991) Guidance manual for compliance with the filtration and disinfection requirements for public water systems using surface water sources. Office of Drinking Water, United States Environmental Protection Agency, Washington, DC
15. United States Environmental Protection Agency (2003) Long term 2 enhanced surface water treatment rule toolbox guidance manual (DRAFT). Office of Drinking Water, United States Environmental Protection Agency, Washington, DC
16. World Health Organization, International Programme on Chemical Safety (IPCS) (1999) Disinfectants and disinfectant by-products, international program on chemical safety (Environmental Health Criteria 216), Geneva
17. Huang WJ, Fang GC, Wang CC (2005) The determination and fate of disinfection by-products from ozonation of polluted raw water. Sci Total Environ 345:261–272
18. Richardson SD, Thruston AD, Caughran TV, Chen PH, Collette TW, Floyd TL, Schenck KM, Lykins BW, Sun GR, Majetich G (1999) Identification of new ozone disinfection byproducts in drinking water. Environ Sci Technol 33:3368–3377
19. von Gunten U (2003) Ozonation of drinking water: Part I. Oxidation kinetics and product formation. Water Res 37:1443–1467
20. Sichel C, Blanco J, Malato S, Fernández-Ibáñez P (2007) Effects of experimental conditions on *E. coli* survival during solar photocatalytic water disinfection. J Photochem Photobiol A Chem 189:239–246
21. Hijnen WAM, Beerendonk EF, Medema GJ (2006) Inactivation credit of UV radiation for viruses, bacteria and protozoan (oo)cysts in water: a review. Water Res 40:3–22

22. Kruithof JC, Van der Leer RC, Hijnen WAM (1992) Practical experiences with UV disinfection in The Netherlands. J Water Supply Res Technol Aqua 41:88–94
23. Masschelin WJ, Rice RG (2002) Ultraviolet light in water and wastewater sanitation. Lewis Publishers, Boca Raton
24. Kühn KP, Chaberny IF, Massholder K, Stickler M, Benz VW, Sonntag HG, Erdinger L (2003) Disinfection of surfaces by photocatalytic oxidation with titanium dioxide and UVA light. Chemosphere 53:71–77
25. Hancock GG, Davis EM (1999) Regrowth potential of coliforms after UV disinfection of municipal wastewater. J Environ Sci Health, Part A: Tox Hazard Subst Environ Eng 34:1737–1743
26. Wolfe RL (1990) Ultraviolet disinfection of potable water – current technology and research needs. Environ Sci Technol 24:768–772
27. Hoyer O (2004) Water disinfection with UV radiation – requirements and realization. In: Proceedings of the European conference UV Karlsruhe, UV radiation. Effects and technologies, September 2003, Karlsruhe
28. Gogate PR, Pandit AB (2004) A review of imperative technologies for wastewater treatment I: oxidation technologies at ambient conditions. Adv Environ Res 8:501–551
29. Pera-Titus M, Garcia-Molina V, Banos MA, Gimenez J, Esplugas S (2004) Degradation of chlorophenols by means of advanced oxidation processes: a general review. Appl Catal B Environ 47:219–256
30. Adewuyi YG (2001) Sonochemistry: environmental science and engineering applications. Ind Eng Chem Res 40:4681–4715
31. Gogate PR (2002) Cavitation: an auxiliary technique in wastewater treatment schemes. Adv Environ Res 6:335–358
32. Venkatadri R, Peters RW (1993) Chemical oxidation technologies – ultraviolet-light hydrogen-peroxide, fenton reagent, and titanium dioxide-assisted photocatalysis. Hazard Waste Hazard Mater 10:107–149
33. Nesheiwat FK, Swanson AG (2000) Clean contaminated sites using Fenton's reagent. Chem Eng Prog 96:61–66
34. Bhatkhande DS, Pangarkar VG, Beenackers A (2002) Photocatalytic degradation for environmental applications – a review. J Chem Technol Biotechnol 77:102–116
35. Trapido M, Hirvonen A, Veressinina Y, Hentunen J, Munter R (1997) Ozonation, ozone/UV and UV/H_2O_2 degradation of chlorophenols. Ozone Sci Eng 19:75–96
36. Kisch H (1989) What is photocatalysis? In: Serpone N, Pelizzetti E (eds) Photocatalysis: fundamentals and applications. Wiley, New York
37. Fox MA, Dulay MT (1993) Heterogeneous photocatalysis. Chem Rev 93:341–357
38. Hoffmann MR, Martin ST, Choi WY, Bahnemann DW (1995) Environmental applications of semiconductor photocatalysis. Chem Rev 95:69–96
39. Fujishima A, Honda K (1972) Electrochemical photolysis of water at a semiconductor electrode. Nature 37:238
40. Linsebigler AL, Lu GQ, Yates JT (1995) Photocatalysis on TiO_2 surfaces – principles, mechanisms, and selected results. Chem Rev 95:735–758
41. Mills A, LeHunte S (1997) An overview of semiconductor photocatalysis. J Photochem Photobiol A Chem 108:1–35
42. Sakthivel S, Kisch H (2003) Daylight photocatalysis by carbon-modified titanium dioxide. Angew Chem Int Ed 42:4908–4911
43. Kamat PV (2007) Meeting the clean energy demand: nanostructure architectures for solar energy conversion. J Phys Chem C 111:2834–2860
44. Chen XB, Liu L, Yu PY, Mao SS (2011) Increasing solar absorption for photocatalysis with black hydrogenated titanium dioxide nanocrystals. Science 331:746–750
45. Bard AJ (1979) Photoelectrochemistry and heterogeneous photocatalysis at semiconductors. J Photochem 10:59–75
46. Bard AJ (1980) Photoelectrochemistry. Science 207:139–144

47. Bard AJ (1982) Design of semiconductor photo-electrochemical systems for solar-energy conversion. J Phys Chem 86:172–177
48. Kalyanasundaram K, Gratzel M, Pelizzetti E (1986) Interfacial electron-transfer in colloidal metal and semiconductor dispersions and photodecomposition of water. Coord Chem Rev 69:57–125
49. Carey JH, Lawrence J, Tosine HM (1976) Photo-dechlorination of PCBs in presence of titanium-dioxide in aqueous suspensions. Bull Environ Contam Toxicol 16:697–701
50. Frank SN, Bard AJ (1977) Heterogeneous photocatalytic oxidation of cyanide ion in aqueous-solutions at TiO_2 powder. J Am Chem Soc 99:303–304
51. Inoue T, Fujishima A, Konishi S, Honda K (1979) Photoelectrocatalytic reduction of carbon-dioxide in aqueous suspensions of semiconductor powders. Nature 277:637–638
52. Matusunga T (1985) Sterilization with particulate photosemiconductor. J Antibact Antifung Agents 13:211–220
53. Matsunaga T, Tomoda R, Nakajima T, Wake H (1985) Photoelectrochemical sterilization of microbial-cells by semiconductor powders. FEMS Microbiol Lett 29:211–214
54. Carey JH, Oliver BG (1980) The photochemical treatment of waste water by ultraviolet irradiation of semiconductors. Water Pollut Res J Can 15:157–185
55. Baram N, Starosvetsky D, Starosvetsky J, Epshtein M, Armon R, Ein-Eli Y (2011) Photocatalytic inactivation of microorganisms using nanotubular TiO_2. Appl Catal B Environ 101:212–219
56. Foster HA, Ditta IB, Varghese S, Steele A (2011) Photocatalytic disinfection using titanium dioxide: spectrum and mechanism of antimicrobial activity. Appl Microbiol Biotechnol 90:1847–1868
57. Chung CJ, Lin HI, Chou CM, Hsieh PY, Hsiao CH, Shi ZY, He JL (2009) Inactivation of *Staphylococcus aureus* and *Escherichia coli* under various light sources on photocatalytic titanium dioxide thin film. Surf Coat Technol 203:1081–1085
58. Li QL, Mahendra S, Lyon DY, Brunet L, Liga MV, Li D, Alvarez PJJ (2008) Antimicrobial nanomaterials for water disinfection and microbial control: potential applications and implications. Water Res 42:4591–4602
59. Arana J, Melian JAH, Rodriguez JMD, Diaz OG, Viera A, Pena JP, Sosa PMM, Jimenez VE (2002) TiO_2-photocatalysis as a tertiary treatment of naturally treated wastewater. Catal Today 76:279–289
60. Lonnen J, Kilvington S, Kehoe SC, Al-Touati F, McGuigan KG (2005) Solar and photocatalytic disinfection of protozoan, fungal and bacterial microbes in drinking water. Water Res 39:877–883
61. Selma MV, Allende A, Lopez-Galvez F, Conesa MA, Gil MI (2008) Heterogeneous photocatalytic disinfection of wash waters from the fresh-cut vegetable industry. J Food Prot 71:286–292
62. Wolfrum EJ, Huang J, Blake DM, Maness PC, Huang Z, Fiest J, Jacoby WA (2002) Photocatalytic oxidation of bacteria, bacterial and fungal spores, and model biofilm components to carbon dioxide on titanium dioxide-coated surfaces. Environ Sci Technol 36:3412–3419
63. Boer KW (1990) Survey of semiconductor physics. van Nostrand Reinhold, New York
64. McLoughlin OA, Ibanez PF, Gernjak W, Rodriguez SM, Gill LW (2004) Photocatalytic disinfection of water using low cost compound parabolic collectors. Sol Energy 77:625–633
65. Chong MN, Jin B, Chow CWK, Saint C (2010) Recent developments in photocatalytic water treatment technology: a review. Water Res 44:2997–3027
66. Brillas E, Mur E, Sauleda R, Sanchez L, Peral J, Domenech X, Casado J (1998) Aniline mineralization by AOP's: anodic oxidation, photocatalysis, electro-Fenton and photoelectro-Fenton processes. Appl Catal B Environ 16:31–42
67. Serpone N (2006) Is the band gap of pristine TiO_2 narrowed by anion- and cation-doping of titanium dioxide in second-generation photocatalysts? J Phys Chem B 110:24287–24293

68. Li FB, Li XZ (2002) The enhancement of photodegradation efficiency using Pt-TiO_2 catalyst. Chemosphere 48:1103–1111
69. Ni M, Leung MKH, Leung DYC, Sumathy K (2007) A review and recent developments in photocatalytic water-splitting using TiO_2 for hydrogen production. Renew Sustain Energy Rev 11:401–425
70. Sun YF, Pignatello JJ (1995) Evidence for a surface dual hole – radical mechanism in the TiO_2 photocatalytic oxidation of 2,4-dichlorophenoxyacetic acid. Environ Sci Technol 29:2065–2072
71. Rabani J, Yamashita K, Ushida K, Stark J, Kira A (1998) Fundamental reactions in illuminated titanium dioxide nanocrystallite layers studied by pulsed laser. J Phys Chem B 102:1689–1695
72. Chen YX, Yang SY, Wang K, Lou LP (2005) Role of primary active species and TiO_2 surface characteristic in UV-illuminated photodegradation of acid orange 7. J Photochem Photobiol A Chem 172:47–54
73. Turchi CS, Ollis DF (1990) Photocatalytic degradation of organic-water contaminants – mechanisms involving hydroxyl radical attack. J Catal 122:178–192
74. Palominos R, Freer J, Mondaca MA, Mansilla HD (2008) Evidence for hole participation during the photocatalytic oxidation of the antibiotic flumequine. J Photochem Photobiol A Chem 193:139–145
75. Sakai H, Baba R, Hashimoto K, Fujishima A, Heller A (1995) Local detection of photoelectrochemically produced H_2O_2 with a wired horseradish-peroxidase microsensor. J Phys Chem 99:11896–11900
76. Kikuchi Y, Sunada K, Iyoda T, Hashimoto K, Fujishima A (1997) Photocatalytic bactericidal effect of TiO_2 thin films: Dynamic view of the active oxygen species responsible for the effect. J Photochem Photobiol A Chem 106:51–56
77. Ranjit KT, Willner I, Bossmann SH, Braun AM (2001) Lanthanide oxide-doped titanium dioxide photocatalysts: novel photocatalysts for the enhanced degradation of p-chlorophenoxyacetic acid. Environ Sci Technol 35:1544–1549
78. Cho M, Chung H, Choi W, Yoon J (2004) Linear correlation between inactivation of *E. coli* and •OH radical concentration in TiO_2 photocatalytic disinfection. Water Res 38:1069–1077
79. Rincón AG, Pulgarin C (2004) Effect of pH, inorganic ions, organic matter and H_2O_2 on *E. coli* K12 photocatalytic inactivation by TiO_2 – implications in solar water disinfection. Appl Catal B Environ 51:283–302
80. Wang YB, Hong CS (1999) Effect of hydrogen peroxide, periodate and persulfate on photocatalysis of 2-chlorobiphenyl in aqueous TiO_2 suspensions. Water Res 33:2031–2036
81. Rincón AG, Pulgarin C (2003) Photocatalytical inactivation of *E. coli*: effect of (continuous-intermittent) light intensity and of (suspended-fixed) TiO_2 concentration. Appl Catal B Environ 44:263–284
82. Kositzi M, Poulios I, Malato S, Caceres J, Campos A (2004) Solar photocatalytic treatment of synthetic municipal wastewater. Water Res 38:1147–1154
83. Bahnemann D (2004) Photocatalytic water treatment: solar energy applications. Sol Energy 77:445–459
84. Kilic M, Cinar Z (2009) A quantum mechanical approach to TiO_2 photocatalysis. J Adv Oxidation Technol 12:37–46
85. Christensen PA, Curtis TP, Egerton TA, Kosa SAM, Tinlin JR (2003) Photoelectrocatalytic and photocatalytic disinfection of *E. coli* suspensions by titanium dioxide. Appl Catal B Environ 41:371–386
86. Dunlop PSM, Ciavola M, Rizzo L, Byrne JA (2011) Inactivation and injury assessment of *Escherichia coli* during solar and photocatalytic disinfection in LDPE bags. Chemosphere 85:1160–1166
87. Tatlidil I, Sokmen M, Breen C, Clegg F, Buruk CK, Bacaksiz E (2011) Degradation of candida albicans on TiO_2 and Ag-TiO_2 thin films prepared by sol-gel and nanosuspensions. J Sol-Gel Sci Technol 60:23–32

88. Melián JAH, Rodríguez JMD, Suárez AV, Rendón ET, do Campo CV, Arana J, Peña JP (2000) The photocatalytic disinfection of urban waste waters. Chemosphere 41:323–327
89. Saito T, Iwase T, Horie J, Morioka T (1992) Mode of photocatalytic bactericidal action of powdered semiconductor TiO_2 on *mutans streptococci*. J Photochem Photobiol B 14:369–379
90. Kim B, Kim D, Cho D, Cho S (2003) Bactericidal effect of TiO_2 photocatalyst on selected food-borne pathogenic bacteria. Chemosphere 52:277–281
91. Watts RJ, Kong SH, Orr MP, Miller GC, Henry BE (1995) Photocatalytic inactivation of coliform bacteria and viruses in secondary waste-water effluent. Water Res 29:95–100
92. Cho M, Yoon J (2008) Measurement of •OH radical CT for inactivating C*ryptosporidium parvum* using photo/ferrioxalate and photo/TiO_2 systems. J Appl Microbiol 104:759–766
93. Ryu H, Gerrity D, Crittenden JC, Abbaszadegan M (2008) Photocatalytic inactivation of *Cryptosporidium parvum* with TiO_2 and low-pressure ultraviolet irradiation. Water Res 42:1523–1530
94. Navalon S, Alvaro M, Garcia H, Escrig D, Costa V (2009) Photocatalytic water disinfection of *Cryptosporidium parvum* and *Giardia lamblia* using a fibrous ceramic TiO_2 photocatalyst. Water Sci Technol 59(4):639–645
95. Sökmen M, Degerli S, Aslan A (2008) Photocatalytic disinfection of *Giardia intestinalis* and *Acanthamoeba castellani* cysts in water. Exp Parasitol 119:44–48
96. Giannantonio DJ, Kurth JC, Kurtis KE, Sobecky PA (2009) Effects of concrete properties and nutrients on fungal colonization and fouling. Int Biodeterior Biodegrad 63:252–259
97. Wang H, Wu Y, Xu BQ (2005) Preparation and characterization of nanosized anatase TiO_2 cuboids for photocatalysis. Appl Catal B Environ 59:139–146
98. Benabbou AK, Derriche Z, Felix C, Lejeune P, Guillard C (2007) Photocatalytic inactivation of *Escherichia coli* – effect of concentration of TiO_2 and microorganism, nature, and intensity of UV irradiation. Appl Catal B Environ 76:257–263
99. Vohra A, Goswami DY, Deshpande DA, Block SS (2006) Enhanced photocatalytic disinfection of indoor air. Appl Catal B Environ 64:57–65
100. Ibáñez JA, Litter MI, Pizarro RA (2003) Photocatalytic bactericidal effect of TiO_2 on enterobacter cloacae: comparative study with other Gram(−) bacteria. J Photochem Photobiol A Chem 157:81–85
101. Cohen-Yaniv V, Narkis N, Armon R (2008) Photocatalytic inactivation of flavobacterium and *E. coli* in water by a continuous stirred tank reactor (CSTR) fed with suspended/immobilised TiO_2 medium. Water Sci Technol 58(1):247–252
102. Suketa N, Sawase T, Kitaura H, Naito M, Baba K, Nakayama K, Wennerberg A, Atsuta M (2005) An antibacterial surface on dental implants, based on the photocatalytic bactericidal effect. Clin Implant Dent Relat Res 7:105–111
103. Amezaga-Madrid P, Nevarez-Moorillon GV, Orrantia-Borunda E, Miki-Yoshida M (2002) Photoinduced bactericidal activity against *pseudomonas aeruginosa* by TiO_2 based thin films. FEMS Microbiol Lett 211:183–188
104. Amezaga-Madrid P, Silveyra-Morales R, Cordoba-Fierro L, Nevarez-Moorillon GV, Miki-Yoshida M, Orrantia-Borunda E, Solis FJ (2003) TEM evidence of ultrastructural alteration on *pseudomonas aeruginosa* by photocatalytic TiO_2 thin films. J Photochem Photobiol B Biol 70:45–50
105. Cheng YW, Chan RCY, Wong PK (2007) Disinfection of *Legionella pneumophila* by photocatalytic oxidation. Water Res 41:842–852
106. Chun MJ, Shim E, Kho EH, Park KJ, Jung J, Kim JM, Kim B, Lee KH, Cho DL, Bai DH, Lee SI, Hwang HS, Ohk SH (2007) Surface modification of orthodontic wires with photocatalytic titanium oxide for its antiadherent and antibacterial properties. Angle Orthod 77:483–488
107. Song SJ, Kim KS, Kim KH, Li HJ, Cho DL, Kim JB, Park HJ, Shon H, Kim JH (2008) Fabrication of TiO_2 impregnated stainless steel fiber photocatalysts and evaluation of photocatalytic activity. J Kor Ind Eng Chem 19:674–679
108. Cho M, Choi Y, Park H, Kim K, Woo GJ, Park J (2007) Titanium dioxide/UV photocatalytic disinfection in fresh carrots. J Food Prot 70:97–101

109. Nagame S, Oku T, Kambara M, Konishi K (1989) Antibacterial effect of the powdered semiconductor TiO_2 on the viability of oral microorganisms. J Dent Res 68:1696–1697
110. Kim BH, Kim D, Cho DL, Lim SH, Yoo SY, Kook JK, Cho YI, Ohk SH, Ko YM (2007) Sterilization effects of a TiO_2 photocatalytic film against a *streptococcus mutans* culture. Biotechnol Bioprocess Eng 12:136–139
111. Dunlop PSM, Sheeran CP, Byrne JA, McMahon MAS, Boyle MA, McGuigan KG (2010) Inactivation of clinically relevant pathogens by photocatalytic coatings. J Photochem Photobiol A Chem 216:303–310
112. Guimarães JR, Barretto AS (2003) Photocatalytic inactivation of *Clostridium perfringens* and coliphages in water. Braz J Chem Eng 20:403–411
113. Greist HT, Hingorani SK, Kelly K, Goswami DY (2002) Using scanning electron microscopy to visualize photocatalytic mineralization of airborne microorganisms. In: Proceedings of the 9th international conference on indoor air quality and climate, July 2002, Monterey, California., pp 712–717
114. Chen FN, Yang XD, Wu Q (2009) Antifungal capability of TiO_2 coated film on moist wood. Build Environ 44:1088–1093
115. Yao Y, Ohko Y, Sekiguchi Y, Fujishima A, Kubota Y (2008) Self-sterilization using silicone catheters coated with Ag and TiO_2 nanocomposite thin film. J Biomed Mater Res B Appl Biomater 85B:453–460
116. Lin CY, Li CS (2003) Effectiveness of titanium dioxide photocatalyst filters for controlling bioaerosols. Aerosol Sci Technol 37:162–170
117. Sunnotel O, Verdoold R, Dunlop PSM, Snelling WJ, Lowery CJ, Dooley JSG, Moore JE, Byrne JA (2010) Photocatalytic inactivation of *Cryptosporidium parvum* on nanostructured titanium dioxide films. J Water Health 8:83–91
118. Lee JH, Kang M, Choung SJ, Ogino K, Miyata S, Kim MS, Park JY, Kim JB (2004) The preparation of TiO_2 nanometer photocatalyst film by a hydrothermal method and its sterilization performance for *Giardia lamblia*. Water Res 38:713–719
119. Peller JR, Whitman RL, Griffith S, Harris P, Peller C, Scalzitti J (2007) TiO_2 as a photocatalyst for control of the aquatic invasive alga, cladophora, under natural and artificial light. J Photochem Photobiol A Chem 186:212–217
120. Hong JL, Ma H, Otaki M (2005) Controlling algal growth in photo-dependent decolorant sludge by photocatalysis. J Biosci Bioeng 99:592–597
121. Linkous CA, Carter GJ, Locuson DB, Ouellette AJ, Slattery DK, Smitha LA (2000) Photocatalytic inhibition of algae growth using TiO_2, WO_3, and cocatalyst modifications. Environ Sci Technol 34:4754–4758
122. Kim SC, Lee DK (2005) Inactivation of algal blooms in eutrophic water of drinking water supplies with the photocatalysis of TiO_2 thin film on hollow glass beads. Water Sci Technol 52(9):145–152
123. Guillard C, Bui TH, Felix C, Moules V, Lina B, Lejeune P (2008) Microbiological disinfection of water and air by photocatalysis. C R Chim 11:107–113
124. Cho M, Chung HM, Choi WY, Yoon JY (2005) Different inactivation behaviors of MS-2 phage and *Escherichia coli* in TiO_2 photocatalytic disinfection. Appl Environ Microbiol 71:270–275
125. Yu KP, Lee GWM, Lin ZY, Huang CP (2008) Removal of bioaerosols by the combination of a photocatalytic filter and negative air ions. J Aerosol Sci 39:377–392
126. Lin ZX, Li ZH, Wang XX, Fu XZ, Yang GQ, Lin HX, Meng C (2006) Inactivation efficiency of TiO_2 on H1N1 influenza virus. Chem J Chin Univ 27:721–725
127. Kozlova EA, Safatov AS, Kiselev SA, Marchenko VY, Sergeev AA, Skarnovich MO, Emelyanova EK, Smetannikova MA, Buryak GA, Vorontsov AV (2010) Inactivation and mineralization of aerosol deposited model pathogenic microorganisms over TiO_2 and Pt/TiO_2. Environ Sci Technol 44:5121–5126

128. Han W, Zhang PH, Cao WC, Yang DL, Taira S, Okamoto Y, Ara JI, Yan XY (2004) The inactivation effect of photocatalytic titanium apatite filter on SARS virus. Prog Biochem Biophys 31:982–985
129. Khan U, Benabderrazik N, Bourdelais AJ, Baden DG, Rein K, Gardinali PR, Arroyo L, O'Shea KE (2010) UV and solar TiO_2 photocatalysis of brevetoxins (PbTxs). Toxicon 55:1008–1016
130. Shephard GS, Stockenstrom S, De Villiers D, Engelbrecht WJ, Sydenham EW, Wessels GFS (1998) Photocatalytic degradation of cyanobacterial microcystin toxins in water. Toxicon 36:1895–1901
131. Liu I, Lawton LA, Bahnemann DW, Robertson PKJ (2005) The photocatalytic destruction of the cyanotoxin, nodularin using TiO_2. Appl Catal B Environ 60:245–252
132. Theron J, Walker JA, Cloete TE (2008) Nanotechnology and water treatment: applications and emerging opportunities. Crit Rev Microbiol 34:43–69
133. Likodimos V, Dionysiou DD, Falaras P (2010) Clean water: water detoxification using innovative photocatalysts. Rev Environ Sci Bio-Technol 9:87–94
134. Zhang DQ, Li GS, Yu JC (2010) Inorganic materials for photocatalytic water disinfection. J Mater Chem 20:4529–4536

Chapter 2
Visible Light Photocatalysis of Natural Semiconducting Minerals

Yan Li, Cong Ding, Yi Liu, Yanzhang Li, Anhuai Lu, Changqiu Wang, and Hongrui Ding

Abstract Semiconducting minerals of rutile (TiO_2) and sphalerite (ZnS) are visible light (VL)-responsive photocatalysts in nature. The substitutions of metal ions for Ti^{IV} and Zn^{II} make their electronic structure differ from their "pure" counterparts and result in the broad absorption of VL. The conduction band of sphalerite is negative enough to photoreduce many organics. While, the valence band potential of rutile is more positive than sphalerite, which enables it with stronger oxidation ability. Their good VL photocatalytic activities are therefore verified by the photooxidation of methyl orange (MO) by rutile's valence band holes and photoreduction of carbon tetrachloride (CT) by sphalerite's conduction band electrons, respectively. The abundant deposition and low cost make natural rutile and sphalerite, along with other semiconducting minerals, promising candidates for developing green photocatalytic technologies.

Keywords Visible light • Semiconducting minerals • Photocatalyst • Rutile • Sphalerite

2.1 Introduction

Semiconducting minerals are a unique but widely distributed class of minerals in nature. They play critical roles in near surface geological processes, including the formation of prebiotic organic molecules [1], controlling and affecting redox-based geochemical and biogeochemical processes in nature [2, 3].

There are hundreds of semiconducting minerals on Earth, most of which are common mineral phases near the Earth's surface: oxides [e.g., rutile (TiO_2), limonite ($FeTiO_3$), hematite (Fe_2O_3), goethite (FeOOH)] and sulfides [e.g., sphalerite (ZnS), greenockite (CdS), pyrite (FeS_2)]. The band structure, structural defects, and other physical characteristics of natural semiconducting minerals

Y. Li • C. Ding • Y. Liu • Y. Li • A. Lu (✉) • C. Wang • H. Ding
The Key Laboratory of Orogenic Belts and Crustal Evolution, School of Earth and Space Science, Peking University, Beijing 100871, China
e-mail: ahlu@pku.edu.cn

T. An et al. (eds.), *Advances in Photocatalytic Disinfection*, Green Chemistry and Sustainable Technology, DOI 10.1007/978-3-662-53496-0_2

Table 2.1 Bandgap of natural semiconductors and the corresponding maximal wavelength for inducing photoelectron-hole pairs [5, 6]

Minerals	Formula	E_g/eV	λ/nm	Minerals	Formula	E_g/eV	λ/nm
Baddeleyite	ZrO_2	5.00	249	Sphalerite	ZnS	3.60	345
Romarchite	SnO	4.20	296	Alabandite	MnS	3.00	414
Geikielite	$MgTiO_3$	3.70	336	Orpiment	As_2S_3	2.50	497
Manganosite	MnO	3.60	345	Greenockite	CdS	2.40	518
Bunsenite	NiO	3.50	355	Berndtite	SnS_2	2.10	592
Cassiterite	SnO_2	3.50	355	Cinnabar	HgS	2.00	622
Eskolaite	Cr_2O_3	3.50	355	Lorandite	$TlAsS_2$	1.80	691
Zincite	ZnO	3.20	388	Stibnite	Sb_2S_3	1.72	723
Anatase	TiO_2	3.20	388	Livingstonite	$HgSb_4S_8$	1.68	740
Pyrophanite	$MnTiO_3$	3.10	401	Tungstenite	WS_2	1.35	921
Rutile	TiO_2	3.00	414	Enargite	Cu_3AsS_4	1.28	971
Senarmontite	Sb_2O_3	3.00	414	Molybdenite	MoS_2	1.17	1062
Massicot	PbO	2.80	444	Chalcocite	Cu_2S	1.10	1130
Bismite	Bi_2O_3	2.80	444	Herzenbergite	SnS	1.01	1231
Shcherbinaite	V_2O_5	2.80	444	Bornite	Cu_5FeS_4	1.00	1243
Ilmenite	$FeTiO_3$	2.80	444	Pyrite	FeS_2	0.95	1309
Goethite	FeOOH	2.60	478	Argentite	Ag_2S	0.92	1351
Wuestite	FeO	2.40	518	Cobaltite	CoAsS	0.50	2486
Monteponite	CdO	2.20	565	Hauerite	MnS_2	0.50	2486
Hematite	Fe_2O_3	2.20	565	Polydymite	NiS	0.40	3108
Cuprite	Cu_2O	2.20	565	Galena	PbS	0.37	3360
Montroydite	HgO	1.90	654	Chalcopyrite	$CuFeS_2$	0.35	3552
Tenorite	CuO	1.70	731	Vaesite	NiS_2	0.30	4144
Avicennite	Tl_2O_3	1.60	777	Arsenopyrite	FeAsS	0.20	6216
Pyrolusite	MnO_2	0.25	4972	Pyrrhotite	FeS	0.10	12,431
Magnetite	Fe_3O_4	0.10	12,431	Covellite	CuS	0.00	

were systematically studied in the 1970s [4]. Xu and Schoonen (2000) compiled the absolute energy positions of conduction band (CB) and valence band (VB) edges for about 50 semiconducting metal oxide and metal sulfide minerals [5]. Based on their work, we know that impurities and defects, such as substituting ions, interstitial ions or atoms, and vacancies, result in major changes in the electronic structures of semiconducting minerals. In most cases, the bandgap of a natural semiconducting mineral is narrower than its synthetic "pure" counterpart, which makes it more susceptible to excitation when exposed to visible light (VL), thereby generating electron-hole pairs. The bandgap of 56 natural semiconducting minerals and their corresponding maximal wavelength for inducing photoelectron-hole pairs are listed in Table 2.1. Most of them are very abundant on Earth and widely used as an important source of metal elements in industrial production and life.

However, compared with synthesized photocatalysts, there are few reports about natural semiconducting minerals used as photocatalysts and applied for

environmental treatment. In the 1990s, a few scholars have studied on this subject and put forward some tentative ideas [7–10], but no systematic research has been carried out. Whether the natural semiconducting minerals can be used as efficient photocatalysts and be applied to environmental treatments is worth being studied.

Among the popular semiconductor photocatalysts, TiO_2 is the most promising one due to its strong oxidability, nontoxicity, cost-effectiveness, and long-term photostability [11–13]. Also, ZnS was chosen as a suitable photocatalytic reducing reagent for the reduction of pollutants [14] because of its much negative conduction band potential (−1.4 V vs. SCE) [5]. However, the bandgap of pure TiO_2 and ZnS is about 3.0 eV and 3.6 eV, respectively. Only a small part of solar light with wavelength shorter than ultraviolet light can excite them [15, 16]. Previous researches indicated that incorporation of transition metal ions into the crystal lattice could significantly extend the light absorption into the VL region [17–19]. Moreover, many studies have reported that V- or Fe-doped TiO_2 and Fe-doped ZnS absorbed VL and exhibited effective photoactivity under VL irradiation [20–23]. It is interesting to note that the natural rutile (TiO_2) and sphalerite (ZnS) always contain minor elements of V and/or Fe, so it probably can function well in VL [24–26]. In addition, compared with synthesized photocatalysts, the natural rutile and sphalerite samples are cheaper and easier to obtain. If it can be used to photodegrade organic pollutants under VL, it may be a novel and cost-effective photocatalyst with potential applications in environmental remediation.

This chapter mainly discusses about the mineralogical and semiconducting characteristics of natural rutile (TiO_2) and sphalerite (ZnS), aiming to explore the possibility of using them as VL-responsive photocatalysts. Since methyl orange (MO) and carbon tetrachloride (CCl_4) were selected as model compounds in many studies [27], the photocatalytic oxidation of MO and the reduction of CCl_4 were employed here to study the photoactivity of the catalysts. The photocatalytic ability of the natural rutile and sphalerite sample was evaluated by comparing with P25 TiO_2 and synthesized ZnS, respectively, and the mechanisms of the VL-induced photoactivity were investigated.

2.2 Mineralogical Characterization of Natural Rutile (TiO_2) and Sphalerite (ZnS)

2.2.1 Occurrence

2.2.1.1 Natural Rutile (TiO_2)

The principal occurrences of rutile in nature are (1) as primary deposit that occurs in high-temperature quartz veins and pegmatite veins and (2) as placer deposit formed by weathering and sedimentation. The major commercial deposits of rutile are placer deposits distributed in Australia, Sierra Leone, India, South Africa, Sri Lanka, and the United States. Besides, rutile also occurs fairly commonly in

Table 2.2 The occurrence characteristics of three rutile deposits in China

Location	Deposit type	Color	Particle size
Daixian, Shanxi Province	Magmatic-type primary deposit	Maroon	Coarse, 0.1–1.0 mm
Zaoyang, Hubei Province	Metamorphic-type primary deposit	Maroon	Coarse, 0.1–1.0 mm
Hainan Province	Depositional-type placer deposit	Field gray	Fine, under 0.1 mm

Table 2.3 The occurrence characteristics of four sphalerite deposits in China

Location	Deposit type	Composition character	Color
Huangshaping, Hunan Province	Skarn	Rich in Fe, Mn, Cu	Dark gray and black
Dongpo, Hunan Province	Middle-temperature hydrothermal	Rich in Cd; poor in Fe	Light gray
Dachang, Guangxi Province	High-temperature hydrothermal	Rich in Fe, Mn	Dark gray
Huize, Yunnan Province	Carbonatite	Rich in Fe; less impurity elements	Gray

many provinces in China, such as Shanxi, Hubei, Hainan, and so on. Characteristics of samples collected from these places are listed in Table 2.2. The natural rutile sample used in this study was from Daixian, Shanxi Province.

2.2.1.2 Natural Sphalerite (ZnS)

Natural sphalerite occurs most commonly in the ocean bottom and thermal hydro vent, mainly as middle-high temperature carbonate-hosted lead-zinc deposits and hydrothermal-type deposits. Therefore, sphalerite is often found to be associated with galena (PbS). Table 2.3 shows four typical natural sphalerite deposits in China. Iron and zinc are common in these deposits as major elements. But the type and content of the trace elements are quite different, leading to the differences in crystal chemistry, electronic structure, and surface chemistry among different sphalerite samples. The natural sphalerite used in this work was from Huize, Yunnan Province.

2.2.1.3 Crystal Chemical Characteristics

Generally, the rutile TiO_2 crystallizes in a tetragonal cell (a =4.594 Å, c = 2.959 Å, space group $P4_2/mnm$). Its structure is built up by hexagonal close packing of oxide atoms, wherein TiO_6 octahedra share edges along (001) or c axis [28]; the sphalerite ZnS crystallizes in a cubic cell ($a = b = c = 5.417$ Å, space group $F43m$). The sulfur atoms are in cubic close packing, with half the tetrahedron occupied by a zinc atom.

Mineral Phase

Natural Rutile (TiO_2)

The XRD pattern (Fig. 2.1) shows strong reflections at 27.5°, 36.1°, and 54.4°, corresponding to (110), (101), and (211) of rutile, respectively (JCPDF 77-0442 data). The result indicates that the natural sample is dominated by rutile TiO_2.

Natural Sphalerite (ZnS)

The XRD pattern of natural sphalerite is shown in Fig. 2.2. As compared with JCPDF 05-0566 data files, the strong reflections at 28.5°, 47.5°, and 56.4°

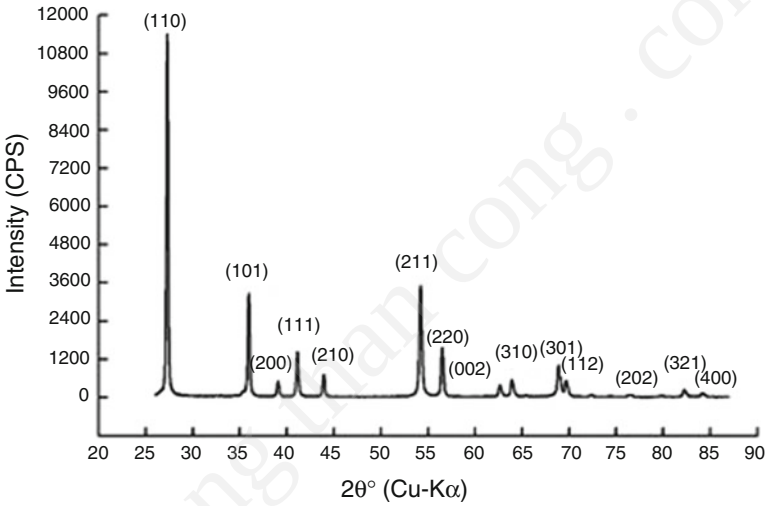

Fig. 2.1 Powder X-ray diffraction pattern of natural rutile sample

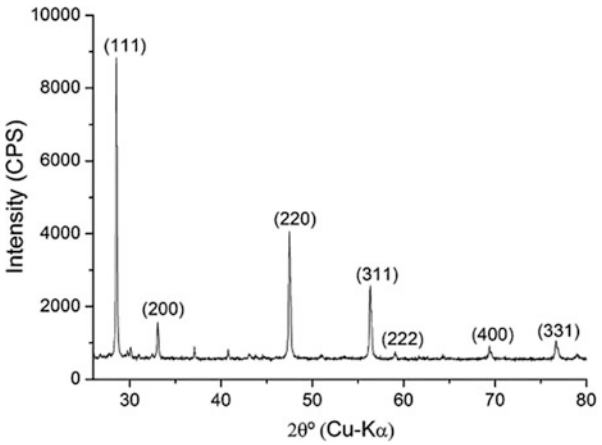

Fig. 2.2 Powder X-ray diffraction pattern of natural sphalerite sample (Reprinted from Ref. [29], Copyright 2008, with permission from Elsevier)

correspond to (111), (220), and (311) of sphalerite, respectively, indicating that the sample is in cubic sphalerite phase.

Chemical Compositions

Natural Rutile (TiO_2)

Compared with the ideal crystal, the ratio of metal atoms and oxygen atoms in natural rutile is greater than 1/2, indicating that there are some oxygen vacancy and lattice defects. The average crystal chemical formula of the rutile sample used in this study can be given as $(Ti_{0.988}V_{0.01}Fe_{0.004})_{\Sigma 1.002}O_2$, based on two oxygen atoms. Table 2.4 shows EMPA (electron microprobe analyzer) point analysis on eight randomly selected rutile particles.

Natural Sphalerite (ZnS)

Stoichiometric sphalerite is cubically packed in sulfur with half the tetrahedral sites occupied by zinc. Due to the complex geological environment, the natural sphalerite samples do not form the perfect crystal, but always contain minor and trace elements embedded in the crystal structure, presenting a variable stoichiometry. The element analyses of ten measurement spots were investigated by EMPA (Table 2.5). The EMPA data shows that Fe comprises the vast majority of the impurities of natural sphalerite. The Fe-rich sphalerite contains variable amounts of Fe, which is specific due to the complicated forming process in nature. Derived from the data shown in Table 2.5, the nonstoichiometric chemical formula of the natural sphalerite samples is $(Zn_{0.936}Fe_{0.045}Cd_{0.001})_{\Sigma 0.982}S$.

Surface Charge

Natural Rutile (TiO_2)

The surface charge of natural rutile is characterized by zeta potential, which is a function of pH, reflecting the stability of colloidal dispersions. The point of zero potential is called isoelectric point or point of zero charge (PZC), which varies with functional groups or defects of mineral surface. The isoelectric point of the natural rutile sample is pH 2.7 (Fig. 2.3), while that of P25 TiO_2 (synthetic sample) is pH 5.3 [30], indicating that there are more hydroxyl groups adsorbed on the surface of the natural rutile sample than on the surface of P25 TiO_2 at the same pH in aqueous solution.

Natural Sphalerite (ZnS)

The zeta potential of the natural sphalerite sample changing with the pH values of the solution is shown in Fig. 2.4. As shown in Fig. 2.4, the PZC (point of zero charge) of the natural sample is about 3.6 pH units. This suggests the surface of the sphalerite sample is positively charged when $pH < 3.6$ and is negatively charged when $pH > 3.6$. The reported PZC of synthetic sphalerite is 6.7 pH units [32], higher than that of the natural samples. The inconsistency of the PZC between them could be ultimately related to the impurity of natural samples. The presence of foreign atoms

Table 2.4 Chemical compositions of the natural rutile sample (all concentrations in wt%)

rutile	TiO_2	V_2O_5	Fe_2O_3	Nb_2O_5	ZnO	CaO	SiO_2	MgO	NiO	As_2O_5	Al_2O_3	CuO	MnO	Total
No.1	97.77	1.16	0.69	0.06	0.04	0.04	0.05	0.04	bdl	bdl	0.01	bdl	0.06	99.92
No.2	98.67	1.41	0.87	0.04	bdl	0.04	0.03	bdl	0.01	0.03	0.15	bdl	bdl	101.25
No.3	97.87	1.20	1.11	0.23	0.06	0.03	0.03	bdl	bdl	bdl	0.03	bdl	bdl	100.56
No.4	99.07	0.84	0.76	0.04	bdl	0.01	0.04	bdl	0.05	bdl	bdl	bdl	0.03	100.84
No.5	99.17	0.73	0.67	bdl	bdl	0.08	0.01	bdl	0.06	0.01	0.03	bdl	0.03	100.79
No.6	97.31	1.66	0.96	0.14	0.08	0.03	0.03	bdl	bdl	bdl	bdl	0.01	bdl	100.22
No.7	99.17	0.73	0.58	0.06	bdl	0.03	0.01	bdl	0.05	0.01	0.03	0.08	bdl	100.75
No.8	98.72	1.21	1.18	0.07	0.11	0.03	0.03	0.04	0.05	bdl	0.02	bdl	bdl	101.46
Average	98.47	1.12	0.85	0.08	0.036	0.036	0.025	0.01	0.028	0.006	0.034	0.011	0.015	100.72

bdl not detected, or average below detection limit

Table 2.5 Chemical compositions of the natural sphalerite sample

Spots	S	Zn	Fe	Cd	Mn	Ge	Se	Ga	Cu	Total
1	33.30	62.27	3.84	0.12	0.03	0.01	0.05	0.08	0.00	99.69
2	32.73	62.16	4.21	0.17	0.01	0.00	0.02	0.00	0.00	99.30
3	33.76	64.72	0.27	0.23	0.01	0.05	0.06	0.03	0.00	99.14
4	33.18	63.66	2.57	0.17	0.00	0.01	0.20	0.00	0.03	99.83
5	33.24	62.64	3.33	0.13	0.01	0.00	0.00	0.01	0.00	99.40
6	33.11	64.17	2.06	0.10	0.02	0.04	0.00	0.09	0.00	99.59
7	32.73	62.87	3.27	0.19	0.03	0.05	0.00	0.00	0.02	99.17
8	33.50	63.82	2.61	0.17	0.01	0.00	0.00	0.00	0.10	100.23
9	34.00	62.83	3.04	0.11	0.06	0.10	0.01	0.03	0.02	100.22
10	32.88	65.12	1.01	0.15	0.01	0.06	0.07	0.00	0.02	99.33

All concentrations in wt%

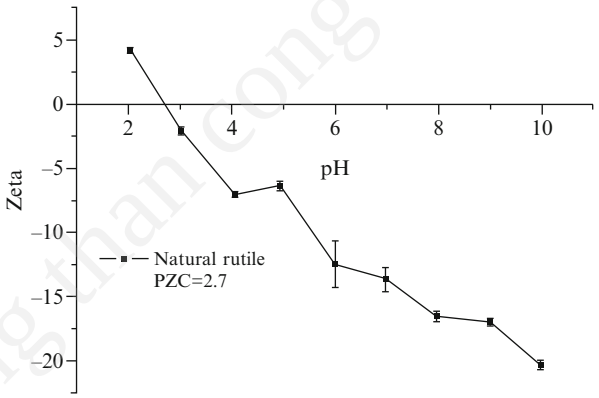

Fig. 2.3 Plots of the zeta potential as a function of pH for natural rutile suspension (0.5 g/L) in the presence of NaCl (0.1 M) (Reprinted from Ref. [31], Copyright 2007, with permission from Elsevier)

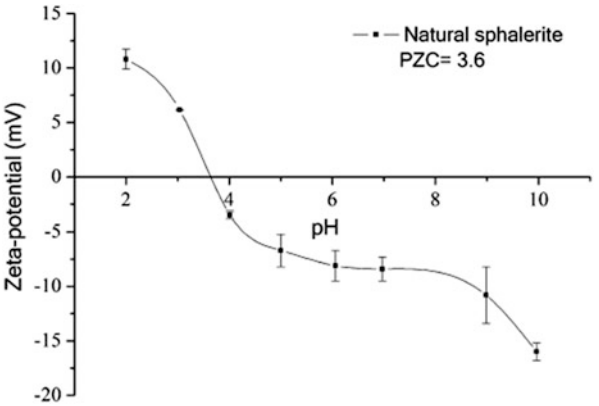

Fig. 2.4 Plots of the zeta potential as a function of pH for natural sphalerite suspension (0.5 g/L) in the presence of NaCl (0.1 M) (Reprinted from Ref. [29], Copyright 2008, with permission from Elsevier)

and the surface defects in the natural sample resulted in the change of the surface property, including surface electronic states. The changes in the surface electronic states then result in the change in surface charge and finally change in the PZC.

2.3 Semiconductor Characteristics of Natural Rutile (TiO_2) and Sphalerite (ZnS)

2.3.1 Optical Absorption

2.3.1.1 Natural Rutile (TiO_2)

Because of its superior physicochemical properties, P25 TiO_2 is a most widely used photocatalyst. Therefore, it is a high benchmark to compare the photocatalytic activity of the natural rutile sample with P25 TiO_2 [33]. The UV-vis diffuse reflectance absorption spectra (DRS) of the natural rutile and P25 TiO_2 samples are shown in Fig. 2.5. The UV-vis absorption spectrum of P25 TiO_2 shows a steep absorption edge at about 402 nm, implying that only a small fraction of VL could be absorbed by P25 to induce electron-hole pairs. But the spectrum of the natural rutile sample shows both a steep absorption edge at about 410 nm and a wide absorption shoulder band in the vicinity of 400–600 nm, indicating that a larger fraction of VL could be absorbed to induce electron-hole pairs.

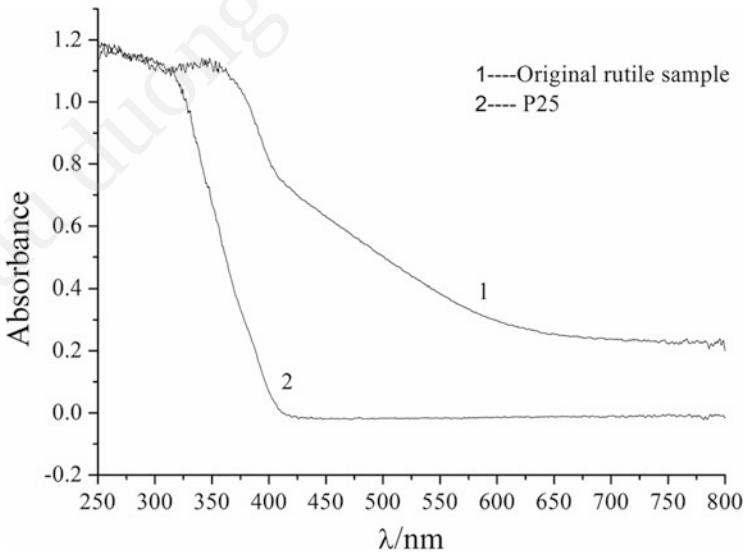

Fig. 2.5 The UV-vis diffuse reflectance absorption spectra of the natural rutile and P25 TiO_2 samples (Reprinted from Ref. [31], Copyright 2007, with permission from Elsevier)

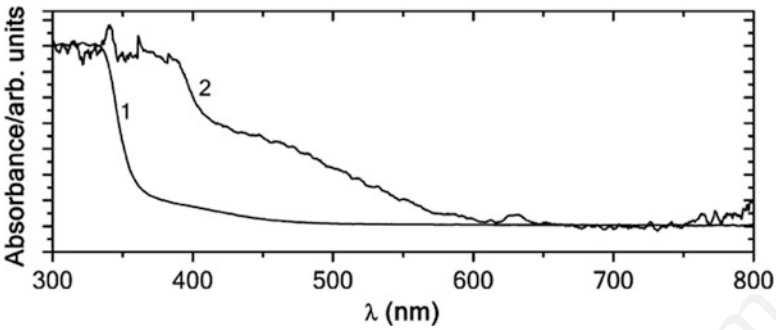

Fig. 2.6 UV-vis DRS of (*1*) pure and (*2*) natural sphalerite ZnS samples (Reprinted from Ref. [29], Copyright 2008, with permission from Elsevier)

2.3.1.2 Natural Sphalerite (ZnS)

Figure 2.6 shows the UV-vis DRS of the natural and pure sphalerite samples. The onset of the absorption edge of the pure ZnS sample is at 365 nm, corresponding to the bandgap of 3.4 eV. This implied the pure sphalerite sample could not utilize VL to induce electron-hole pairs. However, the UV-vis DRS of the natural sphalerite sample shows both a steep absorption edge at about 410 nm and a broad absorption shoulder band in the vicinity of 400–600 nm. The UV-vis diffuse reflectance absorption spectra of the natural sphalerite sample suggest it could be a potentially good candidate in a VL-driven photocatalytic reaction.

As is well known, the shape of the steep absorption edge reveals a bandgap transition between the valence and conduction bands in direct semiconductors [34]. And the adsorption shoulders indicate discontinuous energy levels formed by the dopants or defects in the forbidden band [35]. As a result, the red shift of the steep absorption edge suggests that the intrinsic bandgap of the catalyst narrows due to the substitution of transition metal ions (Fe^{2+} and Cu^{2+}) for Zn^{2+}.

2.3.2 Electronic Structure

2.3.2.1 Natural Rutile (TiO_2)

The density of states (DOS) of pure TiO_2 is shown in Fig. 2.7a. The calculated bandgap is 1.98 eV, lower than the experimental value (3.0 eV). According to the crystal field theory, Ti (3d) orbitals should split into t_{2g} and e_g levels separated by ~1.0 eV due to Ti^{4+} located in the TiO_6 octahedron. Therefore, the conduction band splits into two parts as expected. The upper part of conduction band is mainly composed of O (2p) and Ti e_g state, and O (2p) and Ti t_{2g} state constitute the underpart. In addition, the upper and lower spins of DOS are completely symmetrical, so that the pure TiO_2 does not have any magnetic properties.

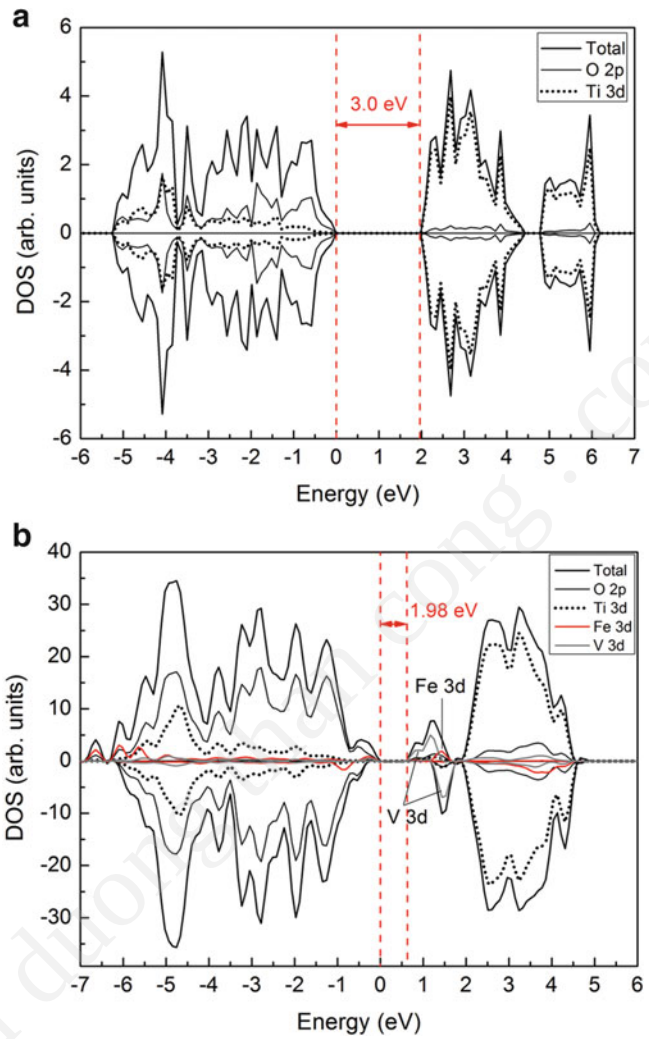

Fig. 2.7 Total and projected density of states (DOS): (**a**) pure TiO_2, (**b**) Fe and V co-doped TiO_2 ($Ti_{14}FeVO_{32}$)

Taking into consideration the chemical composition of the natural rutile sample (section "Chemical composition"), we calculated the DOS of Fe and V co-doped rutile TiO_2 (Fig. 2.7b), which was to simulate the electronic structure of natural rutile. As expected, a wide band with V (3d) and Fe (3d) states can be found in the bandgap. And two impurity energy levels introduced by Fe(3d) form in the middle of the forbidden band. The bandwidth is 0.54 eV and 0.51 eV, respectively. We can see from the partial-wave DOS that the impurity band is mainly composed of V (3d) and O (2p), Fe (3d) and O (2p), and a small part of orbital hybridization by O (2p) and Ti (3d). Consequently, the overall bandgap is further reduced to 1.73 eV as compared to pure TiO_2.

2.3.2.2 Natural Sphalerite (ZnS)

Figure 2.8a shows the total DOS of pure ZnS. We can see that the calculated theoretical bandgap is 2.85 eV, lower than the experimental value (3.60 eV) [36]. This is because the DFT overestimates the bandwidth and underestimates the bandgap, but this does not affect the theoretical analysis of the electronic structure [37].

In order to simulate the electronic structure of the natural sphalerite sample, we calculated the DOS of Fe and Cd co-doped sphalerite (shown in Fig. 2.8b). The bandgap of co-doped sphalerite is 2.49 eV, lower than 2.85 eV. The reason is that

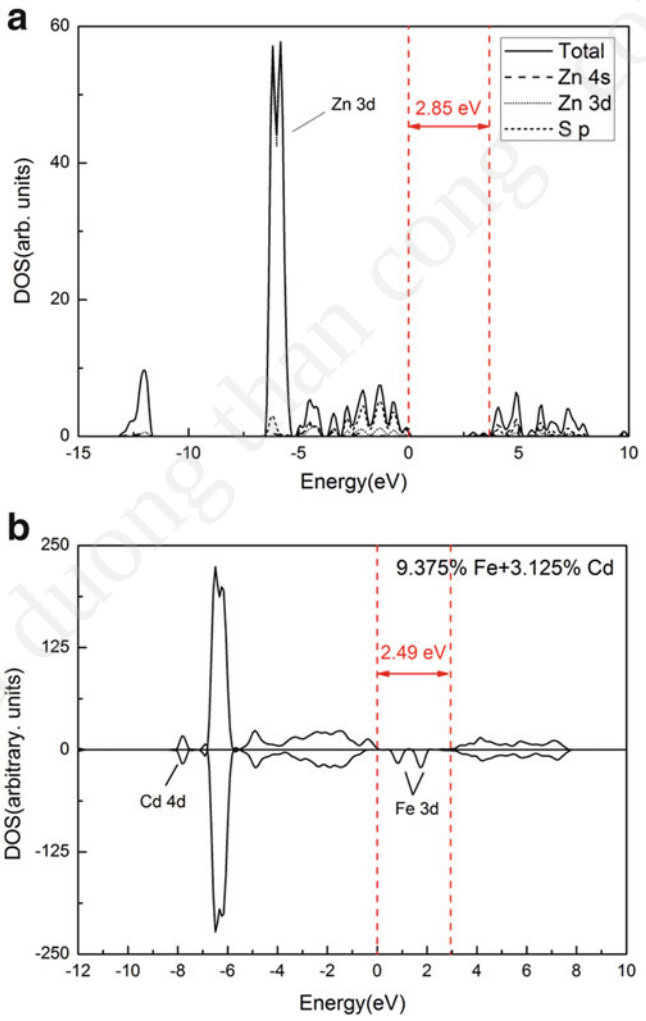

Fig. 2.8 (**a**) Total density of states (DOS) for pure ZnS, (**b**) Projected density of states for Fe and Cd co-doped sphalerite ZnS ($Zn_{28}Fe_3CdS_{32}$)

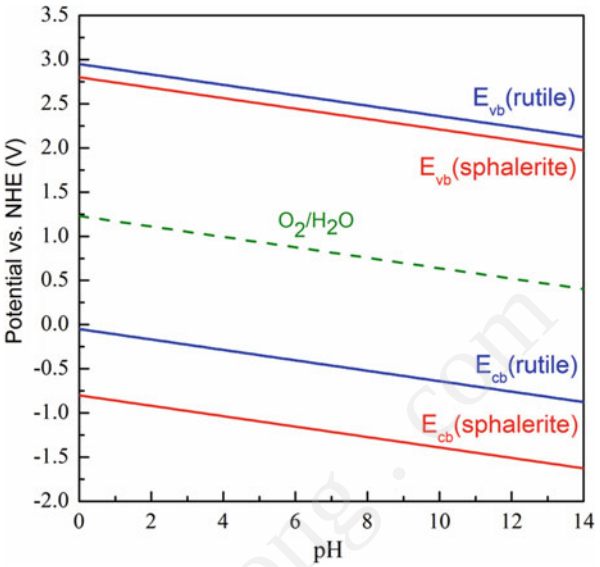

Fig. 2.9 pH dependence of conduction band edge and valence band edge of rutile and sphalerite in an aqueous electrolyte solution

the 3d electrons of Fe and Cd participate in bonding and cause the top of valence band to move up. Meanwhile, the hybridization of Fe (3d) and S (2p) orbital introduces two donor energy levels in the middle of the forbidden band, the band width is 0.65 eV and 0.71 eV each. According to the crystal field theory, Fe (3d) orbitals split into E_{t2g} and E_{eg} levels because Fe^{3+} locates in FeO_4 tetrahedron.

2.3.3 *Conduction and Valence Band Potentials*

The CB and VB potentials of rutile and sphalerite vary with pH (Fig. 2.9), both following a linear relation known as the Nernstian relation [5]. At each pH, sphalerite has a quite negative conduction band potential, varying from -0.8 V (vs. NHE) at pH 0 to -1.6 V (vs. NHE) at pH 14. Therefore, the conduction band of sphalerite is thermodynamically amenable for photoreduction of many organic pollutants, such as photoreductive dehalogenation of polyhalogenated benzenes and photoreductive decoloration of azo dyes [29]. In comparison, the valence band potential of rutile is more positive than sphalerite, ranging from 3.0 V (vs. NHE) at pH 0 to 2.1 (vs. NHE) at pH 14, which enables rutile with stronger oxidation ability in photocatalytic reactions. In the experiments described as follows, the photodegradation of methyl orange (MO) and carbon tetrachloride (CT) are achieved by the holes in rutile's valence band and the electrons in sphalerite's conduction band, respectively.

2.4 Visible Light Photocatalytic Oxidation of Organics by Natural Rutile

TiO_2 has been treated as a promising photocatalyst and widely used for industrial and environmental applications [20, 38]. However, with a bandgap of 3.2 eV, its poor absorption of solar light greatly weakens the practical use. Natural rutile, which contains substituting metal ions as V^{5+} and Fe^{3+}, has a smaller bandgap and exhibits good VL response as described in Figs. 2.5 and 2.7. Based on these theory studies, its VL photoactivity was studied.

2.4.1 Photooxidation of Methyl Orange (MO)

Since methyl orange (MO) was selected as a model compound in many studies [39], the photocatalytic oxidation of MO was employed here to study the photoactivity of the catalysts. The degradation experiment was conducted by adding 0.1 g of the catalyst into 100 mL of 11.307 mg/L MO solution. 3.8 mM H_2O_2 was added as the electron acceptor. Before illumination, each aqueous suspension was stirred for 2 h in the dark to reach the adsorption equilibrium. The concentration of MO was measured by spectrophotometry. The degradation percentage of MO was calculated by the equation $R\ (\%) = [(C_0 - C_t)/C_0] \times 100$, where R is the degradation ratio, C_0 is the initial concentration of MO, and C_t is the concentration of MO at time t.

Table 2.6 shows that there are three factors affecting the degradation of MO: self-degradation of MO in VL, oxidation of MO by H_2O_2, and photocatalytic oxidation of MO by rutile. These three factors have a synergetic effect on MO degradation. The result showed that after 1 h of VL irradiation, 60.59 % of MO was degraded in the presence of H_2O_2 and rutile. If the degradation of MO could be

Table 2.6 Photocatalytic and non-photocatalytic factors that affect the decoloration of MO by the natural rutile sample

Sample	Affecting factor	Decoloration (%)			
		0	20 min	40 min	60 min
1[a]	Self-degradation	0	0.99	2.10	4.09
2[b]	Self-degradation combines with oxidation by H_2O_2	0	3.86	12.18	22.16
3[c]	Self-degradation combines with oxidation by H_2O_2 and photocatalysis	0	31.16	49.58	60.59

Reprinted from Ref. [31], Copyright 2007, with permission from Elsevier

[a]System includes 11.307 mg/L MO under irradiation of a 500 W high-pressure tungsten halogen lamp: pH 7.1 for system

[b]System includes 11.307 mg/L MO and 3.8 mM H_2O_2 under irradiation of a 500 W high-pressure tungsten halogen lamp: pH 3.0 for system

[c]System includes 1 g/L rutile, 11.307 mg/L MO and 3.8 mM H_2O_2 under irradiation of 500 W high-pressure tungsten halogen lamp: pH 3.0 for system

Table 2.7 Photocatalytic degradation percentage of MO by natural rutile and P25 TiO_2 (%)

Agents	Rutile/%	Crystal size/nm	C_0 (MO)/ mg/L	C_0 (TiO_2)/ g/L	Light source	Degradation/%	
						1 h	2 h
Natural rutile	93	75×10^3	11.307	1.0	VL	60.59	82.33
P25 TiO_2	20	30	11.307	1.0	VL	69.26	94.85

Reprinted from Ref. [31], Copyright 2007, with permission from Elsevier

regarded as the additive contributions of the three factors, the contribution of photocatalysis (37.32 %) would be the largest.

To compare the photoactivity of the natural rutile sample with that of P25 TiO_2, two parallel experiments were conducted by using 1.0 g/L natural rutile sample and 1.0 g/L P25 TiO_2, respectively. Each experiment was carried out with two sets, one with 3.8 mM H_2O_2 as sacrificial oxidant, and the other without H_2O_2. The pH of each set was 3.0. The degradation experiments were conducted as described above.

As introduced in Fig. 2.5, natural rutile has a steep absorption edge at 410 nm and a wider adsorption shoulder band in VL region, which imply a better adsorption of VL compared to P25 TiO_2. However, experimental results showed that the photoactivity of the natural rutile sample was a little lower than that of P25 TiO_2. 82.33 % of MO was photooxidized by the natural rutile sample after 2 h of VL irradiation, while by P25 was 94.85 % (Table 2.7). One possible reason was that the particle size of P25 TiO_2 (30 nm) was significantly smaller than that of the natural rutile sample (70–80 μm), so P25 TiO_2 had a larger surface area to react with MO. Another potential reason was that the natural rutile sample had more oxygen defects in the crystal structure. It is probably attributed to the partial substitution of Ti^{4+} by Fe^{3+} in the natural rutile sample. As a result, oxygen defects form to keep the charge balance. These defects acted as electron-hole recombination centers, and consequently suppressed the photocatalytic reaction [40].

2.4.2 Photooxidation Mechanism

In the photocatalytic degradation of MO experiments, H_2O_2 serves as a sacrificial oxidant. In brief, H_2O_2 plays two important roles in the photocatalytic reactions: (1) enhancing the capture rate of photogenerated electrons, and consequently suppressing electron-hole recombination, and (2) generating more oxidizing radicals and species. H_2O_2 can capture photo-induced conduction band electrons (e^-_{cb}) to form hydroxyl radical (•OH) (Eq. (2.1)), which is a strong oxidizing species. In the absence of H_2O_2, dissolved oxygen molecules in the aqueous solution acted as an electron scavenger to react with e^-_{cb} and thus yielded superoxide radical anions ($O_2^{\bullet -}$) (Eq. (2.2)). H_2O_2 is a stronger electron acceptor than oxygen molecules [41]. When H_2O_2 was added, hydroxyl radicals (•OH) are generated, along with the superoxide radical anion ($O_2^{\bullet -}$), to oxidize MO.

$$H_2O_2 + e^-_{cb} \rightarrow OH^- + \bullet OH \quad (2.1)$$

$$O_2 + e^-_{cb} \rightarrow O_2^{\bullet -} \quad (2.2)$$

In addition, it is reported that H_2O_2 can be easily adsorbed onto the surface of TiO_2 to generate titanium (IV) hydrogen peroxide complexes $\left(\equiv Ti^{IV} - OOH\right)$ [42, 43] (Eq. (2.3)). These surface complexes could extend the photoresponse of TiO_2 into the VL region and result in the VL-induced electron transfer from the surface complexes to the conduction band [42, 43]. Thus, under VL irradiation, $\left(\equiv Ti^{IV} - OOH\right)$ could be excited to produce the surface complex $\left(\equiv Ti^{IV} - OOH\right)^*$ (Eq. (2.4)). Meanwhile, $\left(\equiv Ti^{IV} - OOH\right)^*$ injected an electron to the conduction band of TiO_2, resulting in the generation of the conduction band electron and $\left(\equiv Ti^{IV} - \bullet OOH\right)$ (Eq. (2.5)), which further gave rise to $\left(\equiv Ti^{IV} - OH\right)$ (Eq. (2.6)). Furthermore, the injected conduction band electrons could react with the adsorbed H_2O_2 to produce •OH radicals (Eq. (2.7)). Therefore, the formation of the surface complex $\left(\equiv Ti^{IV} - OOH\right)_{surf}$ assisted the production of •OH in VL, thus improving the VL-induced photocatalytic activity.

$$\left(\equiv Ti^{IV} - OH\right)_{surf} + \left(H_2O_2\right)_{ad} \rightarrow \left(\equiv Ti^{IV} - OOH\right)_{surf} + H_2O \quad (2.3)$$

$$\left(\equiv Ti^{IV} - OOH\right)_{surf} + h\upsilon \rightarrow \left(\equiv Ti^{IV} - OOH\right)_{surf^*} \quad (2.4)$$

$$\left(\equiv Ti^{IV} - OOH\right)_{surf^*} \rightarrow \left(e^-_{cb}\right)_{injected} + \left(\equiv Ti^{IV} - \bullet OOH\right)_{surf} \quad (2.5)$$

$$\left(\equiv Ti^{IV} - \bullet OOH\right)_{surf} + OH^- \rightarrow \left(\equiv Ti^{IV} - OH\right) + 1/2\, H_2O_2 + 1/2\, O_2 \quad (2.6)$$

$$H_2O_2 + \left(e^-_{cb}\right)_{injected} \rightarrow OH^- + \bullet OH \quad (2.7)$$

$$OH^- + h^+_{vb} \rightarrow \bullet OH \quad (2.8)$$

Surface hydroxyl groups are also thought to have an important influence on the photoactivity because these groups react with photogenerated valence band holes (h^+_{vb}) to form •OH (Eq. (2.8)). Meanwhile, the capture of photogenerated holes suppresses electron-hole recombination. As a result, it is expected that a greater number of hydroxyl groups yield higher reaction efficiency [30]. In aqueous solution, the number of surface hydroxyl groups is related to the isoelectric point of the catalyst. The isoelectric point of the natural rutile sample is pH 2.7 (Fig. 2.3), while that of P25 TiO_2 is pH 5.3 [30]. This means that there are more hydroxyl groups adsorbed on the surface of the natural rutile sample than on the surface of P25 TiO_2 at the same pH. However, our results showed that the photoactivity of P25 TiO_2 was higher than that of the natural rutile sample. The lower photoactivity of the natural rutile sample is likely to be related to its much larger particle size and more surface defects, which will affect the adsorption behavior of MO and the lifetime of the photogenerated electron-hole pairs.

Apart from the particle size and oxygen defects that restrain photoactivity, there are some factors that enhance natural rutile's VL response and photocatalytic

efficiency. One is the optical adsorption of the natural rutile sample. Aside from the steep band edge, absorption bands with shoulders in the VL region are also observed (Fig. 2.5). These absorption shoulders indicate that a discontinuous level is formed by dopants in the forbidden band [35]. Also, the calculated DOS of Fe and V co-doped TiO_2 indicates donor energy levels are formed in the forbidden band (Fig. 2.7b). Therefore, VL with energy lower than the bandgap could also be absorbed to excite electrons transition from the donor band to the conduction band, thereby leading to an improved visible light photocatalytic performance.

Another important factor is the dopants in natural rutile samples. Compared with Ti^{4+}, V^{5+} has a higher charge to radius ratio. As a result, the polarization ability of V^{5+} is greater than that of Ti^{4+}. The polarization not only makes the photogenerated electrons transfer more easily but also increases the odds of electrons being captured by electron scavengers, thereby prolonging the existing lifetime of photogenerated holes [44]. Besides, Fe^{3+} and V^{5+} in their high oxidation states (M^{n+}) could capture photo-induced electrons to form Fe^{2+} and V^{4+}, which are in low oxidation states (M^{n-1}). The substituting metal ions in their low oxidation states would then further react with surface-adsorbed oxygen (O_{ads}) to form surface oxidant radicals ($O_{ads}^{\bullet -}$). The reactions may be expressed by

$$M^{n+} + e_{cb}^{-} \rightarrow M^{n-1} \text{(capture photo-induced electrons)}$$

$$M^{n-1} + O_{ads} \rightarrow M^{n+} + O_{ads}^{\bullet -} \text{(react with absorbed O at the interface)}$$

Therefore, Fe^{3+} and V^{5+} in natural rutile could make contributions to capture electrons in the conduction band, leading to the effective separation of electron-hole pairs.

2.5 Visible Light Photocatalytic Reduction of Organics by Natural Sphalerite

Photocatalytic oxidation and photocatalytic reduction processes are popular ways for pollutants degradation. However, some organics like perhalogenated hydrocarbons were found to be hardly degraded by hole-initiated photooxidizing processes because they are often inert toward h^{+}_{VB} or •OH [45–47]. Alternatively, semiconductor photoreduction was proposed and proven as a good choice for the degradation of perhalogenated hydrocarbons, such as carbon tetrachloride (CT). Sphalerite, with a conduction band potential from −0.8 V (vs. NHE at pH 0) to −1.6 V (vs. NHE at pH 14) is a potential photocatalyst to reduce halohydrocarbons. Compared to the poor VL response of pure ZnS, natural sphalerite has a better VL adsorption (Fig. 2.6), and the dopants notably reduce its bandgap and change its electronic structure (Fig. 2.8). The visible light photoreduction activity of natural sphalerite is carried out by using CT as a degrading target.

2.5.1 Photoreduction of CT

The degradation experiments were conducted in 22 ml borosilicate glass vessels (20 mm internal diameter, 2 mm wall thickness) equipped with PTFE/silicone septum-lined screw-top cap, which guarantees the air tightness during the photocatalytic process. First, 1000 mg/L CT was prepared in the DMF solvent and diluted to the desired concentration of CT. Then, a certain amount of sphalerite was directly added into the reactor. Before illumination, the suspensions were allowed to equilibrate for 1–2 h in the dark. To keep the system homogeneous, the suspensions were continuously stirred during the whole experimental processes. After a certain period of irradiation, 1 ml of the suspensions was withdrawn for gas chromatography-mass spectrometry (GC-MS) analysis.

Under the optimum experimental conditions, HCOOH was chosen as an electron donor. As shown in Fig. 2.10, CT was degraded by 92 % in the presence of 1 g/L sphalerite and 0.5 mol/L formic acid in air-equilibrium environment after irradiation under VL (500 W-VL) for 8 h. However, in either the light-free or sphalerite-free controls, a very slight decrease in CT was observed, which was possibly attributed to the natural volatilization or adsorption of CT by the sphalerite sample during stirring and sampling processes. Therefore, CT could be effectively degraded only with the coexistence of VL and photocatalyst, which indicated that the VL-driven photocatalysis of natural sphalerite played the leading role in CT degradation.

The analysis of the degradation products was performed with a gas chromatograph coupled with an electron capture detector (Agilent 7890 GC-ECD). No other response signals except the signals of CT were detected. So, we can estimate that CT was completely degraded via a reductive degradation pathway in the VL-irradiated sphalerite suspension, thus producing inorganic chloride ion (Cl^-).

The quantification of CO_2 evolved from CT degradation was detected by gas chromatography-mass spectrometry (GC-MS). Taking the initial CO_2 content as

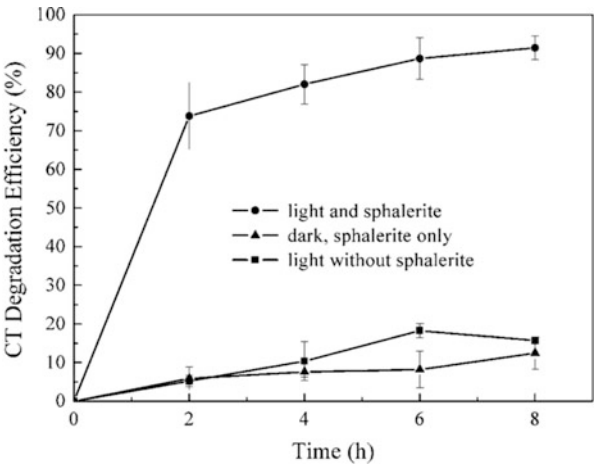

Fig. 2.10 CT degradation efficiency under optimized conditions and its parallel controlled trials: (●) light and sphalerite; (▲) dark, only sphalerite; and (■) only light, without sphalerite. Experimental conditions: sphalerite = 1.0 g/L, HCOOH = 0.5 mol/L, CCl_4 = 10 mg/L, light source, 500 W-VL (Reprinted from Ref. [48], Copyright 2011, with permission from Elsevier)

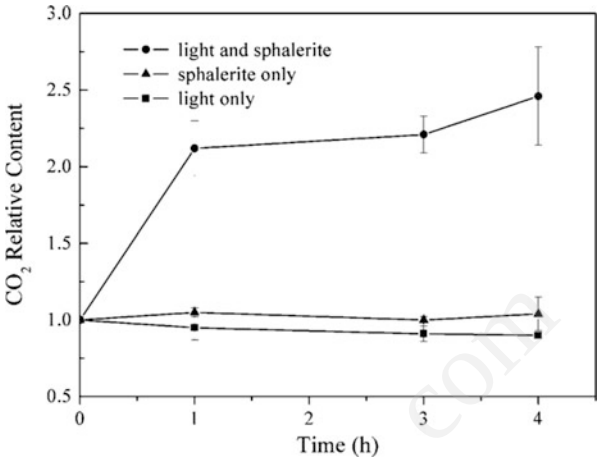

Fig. 2.11 The relative contents of CO_2 under different experimental treatments (Reprinted from Ref. [48], Copyright 2011, with permission from Elsevier)

unit 1.0, the relative contents of CO_2 under different experimental treatments are shown in Fig. 2.11. In the presence of both VL and sphalerite, significant generation of CO_2 was observed. By contrast, there was no CO_2 production in the experimental treatments with sphalerite only or with light only, which clearly demonstrated that most of the CO_2 came from CT degradation under the VL-induced photocatalysis of natural sphalerite.

2.5.2 *Degradation Mechanism*

Based on the above results, we proposed the following mechanism of CT degradation in the VL-irradiated sphalerite suspension. First, photoelectrons (e^-_{CB}) and holes (h^+_{VB}) are, respectively, generated in the conduction and valence bands of sphalerite under VL irradiation (Eq. (2.9)). Then, formic acid ($HCOO^-$) played as a suitable electron donor to react with h^+_{VB} and generate $\bullet COO^-$ (Eq. (2.10)). The redox potential of the conduction band of sphalerite (E_{CB}) is -0.9 V vs. NHE (pH 7), and the redox potential of CO_2/COO^- is -1.6 V vs. NHE, both of which are more negative than $E(CCl_4/\bullet CCl_3) = -0.51$ V vs. NHE [49, 50]. Therefore, e^-_{CB} works together with $\bullet COO^-$ to reduce CT (Eqs. 2.11 and 2.12), thus producing radical chlorinated intermediates as $\bullet CCl_3$ and $:CCl_2$, which further undergo secondary reduction reaction (Eqs. 2.13, 2.14, and 2.15) and cause the complete mineralization of CT [51].

$$ZnS + h\nu \xrightarrow{VL} e_{CB}^- + h_{VB}^+ \tag{2.9}$$

$$h_{VB}^+ + HCOO^- \rightarrow \bullet COO^- + H^+ \tag{2.10}$$

$$e_{CB}^{-} + CCl_4 \rightarrow \bullet CCl_3 + Cl^- \quad (2.11)$$

$$\bullet COO^- + CCl_4 \rightarrow \bullet CCl_3 + Cl^- + CO_2 \quad (2.12)$$

$$\bullet CCl_3 + e_{CB}^{-} \rightarrow :CCl_2 + Cl^- \quad (2.13)$$

$$\bullet CCl_3 + \bullet COO^- \rightarrow :CCl_2 + Cl^- + CO_2 \quad (2.14)$$

$$:CCl_2 + 2H_2O \rightarrow CO_2 + 2HCl + 2Cl^- \quad (2.15)$$

The dissolved O_2 is an alternative electron acceptor to compete with CT (Eqs. 2.16 and2.17), so it should be inhibited in the photocatalytic reduction process. However, the CT degradation efficiency in air-saturated suspension was much higher than those observed in O_2- and N_2-saturated suspensions, which indicates that moderate amount of O_2 promotes the photoreductive degradation rate of CT. Since no significant amounts of chlorinated byproducts were detected during the course of CT photodegradation, we estimate that $\bullet CCl_3$ and :CCl radicals rapidly react with dissolved O_2 to yield CO_2 and inorganic Cl^- as the final products (Eqs. 2.18 and 2.19). Therefore, higher CT degradation efficiency can be achieved in the presence of O_2. However, the presence of excess O_2 decreases the photoreductive degradation efficiency of CT, because the dissolved O_2 could compete with CT for accepting electrons from reducing species as e^- and $\bullet COO^-$ (Eqs. 2.16 and 2.17).

$$O_2 + e_{CB}^{-} \rightarrow O_2^- \quad (2.16)$$

$$O_2 + \bullet COO^- \rightarrow CO_2 + O_2^- \quad (2.17)$$

$$\bullet CCl_3 + O_2 \rightarrow \bullet OOCCl_3 \rightarrow CO_2 + 3Cl^- \quad (2.18)$$

$$:CCl_2 + O_2 \rightarrow \bullet OOCCl_2 \rightarrow CO_2 + 3Cl^- \quad (2.19)$$

Natural sphalerite was active under VL, thus producing sufficient photoelectrons and holes for further reactions. The optical absorption spectra (Fig. 2.6) and electronic structure calculation results (Fig. 2.8) indicate that the VL adsorption and the changes in electronic structure contribute to natural sphalerite's VL photocatalytic activity.

According to the chemical composition (section "Chemical composition"), the major substituting ions in natural sphalerite are Fe^{2+} and Cd^{2+}. The results of DOS simulation (Fig. 2.8b) indicate that the hybridization of Fe/Cd (3d) and S (2p) elevates the valence band and reduces the bandgap without any loss in reducing power of electrons in the conduction band. Meanwhile, the substitution of Fe for Zn introduces two donor states within the bandgap, as shown in Fig. 2.8b. So a large segment of solar light can be used to excite Fe 3d electrons to the conduction band of sphalerite. Moreover, the doped Fe^{2+} may simultaneously take part in the following reaction: $Fe^{2+} + h^+ \rightarrow Fe^{3+}$, so that leads to an effective separation between photo-induced electrons and holes. This process has proved to be very fast in heterogeneous reactions [52].

2.6 Conclusion

Natural semiconducting minerals such as rutile and sphalerite represent a new class of VL-responsive photocatalysts. They are unique as they absorb VL without modification, have a large supply, and are cheap to obtain. Through photodegradation experiments, natural rutile and sphalerite exhibit high efficiency of MO oxidation and CT reduction under VL, respectively. The DOS simulation results show that the substituting transition metal ions change the band structure and the surface states of natural semiconducting minerals, thereby resulting in VL response and good photoactivity. Therefore, natural rutile and sphalerite, along with other natural semiconducting minerals, could be suggested as a novel class of cost-effective and VL-induced photocatalyst.

Acknowledgments This work was supported by the National Basic Research Program of China (973 Program, Program No. 2014CB846001) and the National Natural Science Foundation of China (Grant No. 41230103 & 41272003 & 41522201).

References

1. Schoonen M, Smirnov A, Cohn C (2004) A perspective on the role of minerals in prebiotic synthesis. Ambio 33:539–551
2. Rosso KM (2001) Structure and reactivity of semiconducting mineral surfaces: convergence of molecular modeling and experiment. Rev Mineral Geochem 42:199–272
3. Lu A, Li Y, Jin S, Wang X, Wu XL, Zeng C, Li Y, Ding H, Hao R, Lv M, Wang C, Tang Y, Dong H (2012) Growth of nonphototrophic microorganisms on solar energy through mineral photocatalysis. Nat Commun 3:768–775
4. Shuey RT (1975) Semiconducting ore minerals. Elsevier, Amsterdam
5. Xu Y, Schoonen M (2000) The absolute energy positions of conduction and valence bands of selected semiconducting minerals. Am Mineral 85:543–556
6. Lu A (2013) Mineralogical photocatalysis in natural self-purification of inorganic minerals. Acta Petrologica Et Mineralogica 22:323–331
7. Schoonen M, Xu Y, Strongin DR (1998) An introduction to geocatalysis. J Geochem Explor 62:201–215
8. Selli E, Giorgi AD, Bidoglio G (1996) Humic acid-sensitized photoreduction of Cr(VI) on ZnO particles. Environ Sci Technol 30:598–604
9. Stumm W, Morgan JJ (1995) Aquatic chemistry: chemical equilibrium and rates in natural waters, P. imprenta. Wiley, New York, p 1022
10. Sulzberger B (1990) Aquatic chemical kinetics: reaction rates of processes in natural waters, Environmental Science and Technology Series. Wiley, New York, pp 401–429
11. Linsebigler AL, Lu GQ, Yates JT Jr (1995) Photocatalysis on TiO_2 surfaces: principles, mechanisms, and selected results. Chem Rev 95:735–758
12. Sun CC, Chou TC (2000) Electrochemically promoted photocatalytic oxidation of nitrite ion by using rutile form of TiO_2/Ti electrode. J Mol Catal A Chem 151:133–145
13. Fujishima A, Zhang XT (2006) Titanium dioxide photocatalysis: present situation and future approach. C R Chim 9:750–760

14. Yin H, Wada Y, Kitamura T, Yanagida S (2001) Photoreductive dehalogenation of halogenated benzene derivatives using ZnS or CdS nanocrystallites as photocatalysis. Environ Sci Technol 35:227–231
15. Fujishima A, Rao TN, Tryk DA (2000) Titanium dioxide photocatalysis. J Photochem Photobiol C: Photochem Rev 1:4
16. Benedix R, Dehn F, Quaas J, Orgass M (2000) Leipzig annual civil engineering report no. 5. Institut für Massivbau und Baustofftechnologie, Leipzig, p 161
17. Muraoka Y, Yamauchi T, Ueda Y, Hiroi Z (2002) Efficient photocarrier injection in a transition metal oxide heterostructure. J Phys Condens Matter 14:757
18. Ohno T, Tanigawa F, Fujihara K, Izumi S, Matsumura M (1999) J Photochem Photobiol A Chem 127:107
19. Ranjit KT, Cohen H, Willner I, Bossmann S, Braun AM (1999) J Mater Sci 34:5273
20. Depero LE (1993) Coordination geometry and catalytic activity of vanadium on Tio2 surfaces. J Solid State Chem 103:528–532
21. Yu JC, Lin J, Kwok RWM (1997) J Photochem Photobiol A Chem 111:199
22. Yu XB, Wang GH, Luo YQ, Chen XH, Zu J (2000) J Shanghai Norm Univ 29:75
23. Yu XY, Cheng JJ (2001) J Inorg Mater 16:742
24. Liu J, Lu AH, Guo YJ, Li N, Li QR, Zheng J (2003) Acta Petrol Mineral 22:339
25. Lu AH, Liu J, Zhao DG, Guo YJ, Li QR, Li N (2004) Catal Today 90:337
26. Lu AH, Guo YJ, Liu J, Liu F, Wang CQ, Li N, Li QR (2004) Chin Sci Bull 49:2284
27. Al-Qaradawi S, Salman SR (2002) J Photochem Photobiol A Chem 148:161
28. Ballirano P, Caminiti R (2001) Rietveld refinements on laboratory energy dispersive X-ray diffraction (EDXD) data. J Appl Crystallogr 34:757–762
29. Li Y, Lu AH, Wang CQ, Wu XL (2008) Characterization of natural sphalerite as a novel visible light-driven photocatalyst. Sol Energy Mater Sol Cells 92:953–959
30. Lin J, Yu JC, Lo D, Lam SK (1999) Photocatalytic activity of rutile Ti1-xSnxO2 solid solutions. J Catal 183:368–372
31. Lu AH, Li Y, Lv M, Wang CQ, Yang L, Liu J, Wang YH, Wong KH, Wong PK (2007) Photocatalytic oxidation of methyl orange by natural V-bearing rutile under visible light. Sol Energy Mater Sol Cells 91:1849–1855
32. Zang L, Liu CY, Ren XM (1995) Photochemistry of semiconductor particles 3. Effects of surface charge on reduction rate of methyl orange photosensitized by ZnS sols. J Photochem Photobiol A Chem 85:239
33. Piscopo A, Robert D, Weber JV (2001) J Photochem Photobiol A Chem 139:253
34. Kudo A, Tsuji I, Kato H (2002) AgInZn7S9 solid solution photocatalyst for H2 evolution from aqueous solutions under visible light irradiation. Chem Commun 1958
35. Lei ZB, Ma GJ, Liu MY, You WS, Yan HJ, Wu GP, Takata T, Hara M, Domen K, Li C (2006) Sulfur-substituted and zinc-doped In (OH) (3): a new class of catalyst for photocatalytic H2 production from water under visible light illumination. J Catal 237:322–329
36. Geng BY, Liu XW, Du QB, Wei XW, Zhang LD (2006) Structure and optical properties of periodically twinned ZnS nanowires. Appl Phys Lett 88:1631041–1631043
37. Godby RW, Schlüter M, Sham LJ (1986) Accurate exchange-correlation potential for silicon and its discontinuity on addition of an electron. Phys Rev Lett 56:2415–2418
38. Leung TY, Chan CY, Hu C, Yu JC, Wong PK (2008) Photocatalytic disinfection of marine bacteria using fluorescent light. Water Res 42:4827–4837
39. Al-Quadawi S, Salman SR (2002) Photocatalytic degradation of methyl orange as a model compound. J Photoch Photobio A 148:161–168
40. Miyauchi M, Takashio M, Tobimatsu H (2004) Photocatalytic activity of $SrTiO_3$ codoped with nitrogen and lanthanum under visible light illumination. Langmuir 20:232–236
41. Ohno T, Masaki Y, Hirayama S, Matsumura M (2001) TiO_2-photocatalyzed epoxidation of 1-decene by H2O2 under visible light. J Catal 204:163–168

42. Rincon AG, Pulgarin C (2004) Effect of pH, inorganic ions, organic matter and H_2O_2 on E. coli K12 photocatalytic inactivation by TiO_2 – implications in solar water disinfection. Appl Catal B Environ 51:283–302
43. Li XZ, Chen CC, Zhao JC (2001) Mechanism of photodecomposition of H_2O_2 on TiO_2 surfaces under visible light irradiation. Langmuir 17:4118–4122
44. Morris D, Dixon R, Jones FH, Dou Y, Egdell RG, Downes SW, Beamson G (1997) Nature of band-gap states in V-doped TiO_2 revealed by resonant photoemission. Phys Rev B 55:16083–16087
45. Choi WY, Hoffmann MR (1995) Photoreductive mechanism of CCl_4 degradation on TiO_2 particles and effects of electron-donors. Environ Sci Technol 29:1646–1654
46. Lal M, Schoneich C, Monig J, Asmus KD (1988) Rate constants for the reactions of halogenated organic radicals. Int J Radiat Biol 54:773–785
47. Ollis DF, Pelizzetti E, Serpone N (1991) Photocatalyzed destruction of water contaminants. Environ Sci Technol 25:1522–1529
48. Yang X, Li Y, Lu AH, Yan YH, Wang CQ, Wong PK (2011) Photocatalytic reduction of carbon tetrachloride by natural sphalerite under visible light irradiation. Sol Energy Mater Sol Cells 95:1915–1921
49. Winkelmann K, Calhoun RL, Mills G (2006) Chain photoreduction of CCl_3F in TiO_2 suspensions: enhancement induced by O-2. J Phys Chem A 110:13827–13835
50. Stanbury D (1989) Reduction potentials involving inorganic free radicals in aqueous solution. Adv Inorg Chem 33:69–138
51. Calhoun RL, Winkelmann K, Mills G (2001) Chain photoreduction of CCl_3F induced by TiO_2 particles. J Phys Chem B 105:9739–9746
52. Stumm W, Sulzberger B (1992) The cycling of iron in natural environments – considerations based on laboratory studies of heterogeneous redox processes. Geochim Cosmochim Acta 56:3233–3257

Chapter 3
Visible-Light-Driven Photocatalytic Treatment by Environmental Minerals

Dehua Xia, Wanjun Wang, and Po Keung Wong

Abstract Naturally occurring semiconductor minerals can perform visible-light-driven (VLD) photocatalysis for environmental remediation that have attracted particular attention. Compared with frequently reported VLD photocatalysts that are tedious in fabrication procedure and expensive for massive production, these materials are readily obtained in large quantity at lower cost. Specially, some minerals containing iron, which makes the minerals become visible light responsive and magnetic, possess great potential for materials recycle. The acceptable performance with regard to photocatalytic activity and its superior properties enable them to be good candidates for cost-effective VLD photocatalytic treatment of toxic organics and infectious microbes in water and wastewater samples. This chapter presents an overview of current research activities that center on utilizing natural semiconductor minerals for water disinfection under visible light irradiation. It is organized into two major parts. One is the development of natural and natural magnetic materials for environmental remediation. The other part is the development and modification of materials to elevate its photocatalytic activity for application. Finally, we conclude with a discussion of what major advancements are needed to move the field of photocatalytic water disinfection forward.

Keywords Minerals • Photocatalysis • Water disinfection • Antimicrobial • Visible-light-driven

D. Xia • P.K. Wong (✉)
School of Life Sciences, The Chinese University of Hong Kong, Shatin, N.T., Hong Kong SAR, China
e-mail: xiadehua2010@hotmail.com; pkwong@cuhk.edu.hk

W. Wang
School of Life Sciences, The Chinese University of Hong Kong, Shatin, N.T., Hong Kong SAR, China

Department of Chemistry, The Chinese University of Hong Kong, Shatin, N.T., Hong Kong SAR, China
e-mail: wanjun_w@163.com

T. An et al. (eds.), *Advances in Photocatalytic Disinfection*, Green Chemistry and Sustainable Technology, DOI 10.1007/978-3-662-53496-0_3

3.1 Introduction

As a green technology, photocatalysis takes advantage of directly converting the natural solar energy to chemical energy, thus driving all kinds of chemical transformations, including water splitting to generate H_2 [1], toxicant/pollutant degradation [2], CO_2 reduction to generate CH_4 and/or methanol [3], water disinfection [4], etc. At the heart of the photon-reaction process is a highly efficient photocatalyst functioning like an energy converter. Therefore, enormous efforts are devoted to the design, fabrication, and modification of various photocatalysts to achieve the requirements for practical use. Although exciting progress has been made on some of the photocatalysts, these photocatalysts are eventually artificially produced, which will consume additional energy and often require multifarious procedures for the fabrication. An ideal situation for the application of photocatalysis is that the functional photocatalyst could be obtained directly in nature, without any catalyst preparation process. Fortunately, nature always provides us with all kinds of exquisite materials in an infinite way.

Minerals are naturally occurring solid chemical substances, which have characteristic chemical composition, formed through biogeochemical processes. Naturally occurring semiconductor minerals consist of a main component and many other trace amounts of metal elements. The incorporation of various impurity elements and complicated crystal lattice defects in these materials could induce the promising visible-light-driven (VLD) photocatalytic activity [5–10]. Such elaborate system is almost impossible to be synthesized by conventional chemical process; however, nature has already carefully designed and fabricated it for us human beings. Lu et al. have reviewed 52 kinds of semiconducting metal oxides and metal sulfide minerals, as shown in Table 3.1 [6]. It is found that the maximal adsorption wavelength for most metal oxide minerals is located in the visible light region, whereas that of metal sulfide minerals is corresponding to the infrared light region. These results may indicate that most of these minerals could be excited by the visible light and photocatalytically generate reactive species. The photocatalysis function in minerals can play a unique role in self-cleaning of the environment on the Earth's surface.

Actually, only a limited number of minerals belong to intrinsic semiconductor, such as FeAsS, β-MnO_2, etc. [34, 35]. Most minerals are non-intrinsic semiconductors, whose electrons or holes are generated by impurity levels and formed by the isomorphism and point defects in minerals [34, 35]. Semiconductor minerals can be classified into n-type and p-type. For n-type, impurity level is located close to the conduction band (CB); the excited electrons from impurity levels would transfer to the conduction band, with the holes survived in the impurity level. The main carrier is the electron, and the impurities become a donor in this case, such as TiO_2, V_2O_5, $CuFeS_2$, and ZnO. For p-type, impurity level is located next to the valence band (VB); the electrons excited from the valence band would transfer into the impurity levels, with the holes survived in the valence band. The major carrier is the hole, and the impurities become an acceptor, such as Cu_2O, NiO, and Cr_2O_3. Actually, most semiconductor minerals are a mixture of n- and p-types, which

Table 3.1 Bandgap E_g and maximal wavelength of light deriving photoelectron λ

Name	Formula	E_g/eV[a]	λ/nm	Name	Formula	E_g/eV[a]	λ/nm
Baddeleyite	ZrO_2	5.00	249	Sphalerite	ZnS	3.60	345
Romarchite	SnO	4.20	296	Alabandite	MnS	3.00	414
Geikielite	$MgTiO_3$	3.70	336	Orpiment	As_2S_3	2.50	497
Manganosite	MnO	3.60	345	Greenockite	CdS	2.40	518
Bunsenite	NiO	3.50	355	Berndtite	SnS_2	2.10	592
Cassiterite	SnO_2	3.50	355	Cinnabar	HgS	2.00	622
Eskolaite	Cr_2O_3	3.50	355	Lorandite	$TlAsS_2$	1.80	691
Zincite	ZnO	3.20	388	Stibnite	Sb_2S_3	1.72	723
Anatase	TiO_2	3.20	388	Livingstonite	$HgSb_4S_8$	1.68	740
Pyrophanite	$MnTiO_3$	3.10	401	Tungstenite	WS_2	1.35	921
Rutile	TiO_2	3.00	414	Enargite	Cu_3AsS_4	1.28	971
Senarmontite	Sb_2O_3	3.00	414	Molybdenite	MoS_2	1.17	1062
Massicot	PbO	2.80	444	Chalcocite	Cu_2S	1.10	1130
Bismite	Bi_2O_3	2.80	444	Herzenbergite	SnS	1.01	1231
Shcherbinaite	V_2O_5	2.80	444	Bornite	Cu_5FeS_4	1.00	1243
Ilmenite	$FeTiO_3$	2.80	444	Pyrite	FeS_2	0.95	1309
Goethite	FeOOH	2.60	478	Argentite	Ag_2S	0.92	1351
Wuestite	FeO	2.40	518	Cobaltite	CoAsS	0.50	2486
Monteponite	CdO	2.20	565	Hauerite	MnS_2	0.50	2486
Hematite	Fe_2O_3	2.20	565	Polydymite	NiS	0.40	3108
Cuprite	Cu_2O	2.20	565	Galena	PbS	0.37	3360
Montroydite	HgO	1.90	654	Chalcopyrite	$CuFeS_2$	0.35	3552
Tenorite	CuO	1.70	731	Vaesite	NiS_2	0.30	4144
Avicennite	Tl_2O_3	1.60	777	Arsenopyrite	FeAsS	0.20	6216
Pyrolusite	MnO_2	0.25	4972	Pyrrhotite	FeS	0.10	12,431
Magnetite	Fe_3O_4	0.10	12,431	Covellite	CuS	0.00	

[a]The band energy of E_g were calculated based on these references: Boldish and White [11], Brezonik [12], Butler and Ginley [13], Dovgii and Bilen'kii [14], Efstathiou and Levin [15], Freidman and Gubanov [16], Halouani and Deschavres [17], Jaegermann and Tributsch [18], Kanemoto et al. [19], Mills et al. [20], Nozik [21], Oosawa et al. [22], Quarto et al. [23], Rodriguez et al. [24], Sakkopoulos et al. [25], Sculfort and Gautron [26], Shuey [27], Sugiura et al. [28], Temmerman et al. [29], Wang et al. [30], Wei and Osso-Asare [31], Xu et al. [32], Zhang and Satpathy [33]

depends on the concentration and transfer rate of carriers, such as α-Fe_2O_3 and FeS_2 [34, 35]. Taking pyrrhotite ($Fe_{1-x}S$) as an example, the substituting Co^{2+}, Ni^{2+}, and Cu^{2+} of Fe^{2+} are impurity donors and became n-type, while substituting As, Sb, and Te of S are impurity acceptors and became p-type [34, 35]. Till now, several kinds of natural semiconductor minerals like V-bearing rutile, sphalerite, and pyrite have been successfully utilized for environmental remediation, including degradation of persistent organic contaminants and reduction of toxic inorganic metals. As Earth's surface is mainly built up by these metal oxides and sulfides, these studies do not only provide many Earth-abundant photocatalysts but also opened a new venue to study the self-cleaning system of the Earth's surface.

3.2 Environmental Remediation by Natural Mineral

3.2.1 Natural V-bearing Rutile

Rutile is one of the crystal phases of titanium dioxide (TiO_2). Different from pure TiO_2 with bandgap of 3.2 eV, which cannot be activated by VL, natural V-bearing rutile could photodegrade 60.59 % of methyl orange (MO) after 1 h visible light irradiation [36]. The visible light response can be attributed to the substitution of Ti^{4+} by V^{5+} and Fe^{3+} elements and survived structural vacancies as well as microstrain through distorting polyhedral. The proposed band structure of the natural rutile sample is illustrated in Fig. 3.1, with a calculated bandgap of 2.65 eV. Moreover, Lu et al. [36] revealed that the substituting metal ions in their high oxidation states (V^{5+} and Fe^{3+}) could capture photogenerated electrons to suppress electron–hole combination. Then, the electrons further react with surface-adsorbed oxygen to form surface oxidant radicals, thereby leading to an improved photocatalytic performance. Similar results were found in Yang et al. study [37], which further confirms the photocatalytic activity of natural rutile.

The V-bearing rutile was further modified to enhance its photocatalytic activity through heating, quenching, and electron irradiation. Meanwhile, the photocatalytic activity of modified samples was evaluated through degradation of trichloroethylene and tetrachloroethylene [38]. The quenched rutile at 1273 and 1373°K has the highest photoactivity. The enhanced photoactivity is attributed to the highest concentrations of adsorbed water and V^{5+} on its surface, although the lattice volumes decrease by 0.01–0.07 %. On the contrary, heating distinctly increases the lattice volumes by 0.93–2.13 % at 973–1373°K. Combined with the increased concentration of adsorption water on the surface, the degradation rate is also improved accordingly. The author also revealed that heating also can segregate the V^{5+} ions outward to the surface and rehabilitate the lattice distortion by reconstruction in certain crystal faces, recrystallization, and release of the

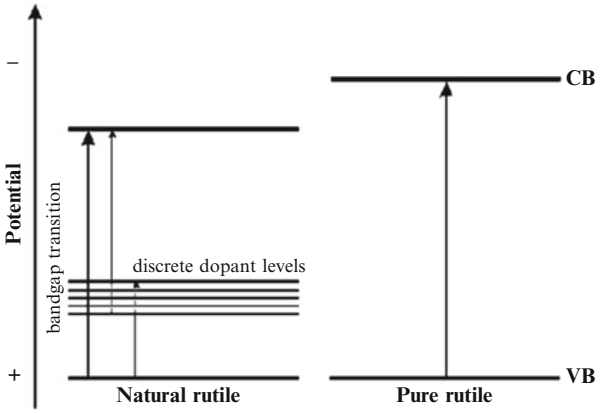

Fig. 3.1 Proposed band structure based on the UV-vis diffuse reflectance spectra of natural rutile (Reprinted from Ref. [36] Copyright © 2007 Elsevier)

microstrain. Moreover, grinding rutile samples into powder with the particle size of 70–80 μm also results in little increase of their lattice volumes, therewith higher degradation efficiency. Nevertheless, electron irradiation decreased the concentration of adsorbed water on the surface of rutile, which results in lower degradation rate for trichloroethylene.

Similarly, the visible light absorption of natural V-bearing rutile was also significantly enhanced simply through annealing under argon [39]. In the visible light region of 400–750 nm, the integral absorbance of rutile treated at 1173°K increased by around 63 % compared to untreated rutile. Electron paramagnetic resonance (EPR) measurements indicated that annealing of V-bearing rutile in argon atmosphere induced a substantial increase of V^{4+} as an active state of V-doping ions for the visible light absorption.

3.2.2 Natural Sphalerite

Natural sphalerite (NS, mainly ZnS) is another pioneering semiconductor mineral, which shows good photocatalytic activity for pollutant removal. Pure ZnS lacks visible-light-driven photocatalytic activity, due to its large bandgap of 3.6 eV. Unlike pure ZnS, NS samples collected from mineral deposits always incorporate with several foreign metal elements (e.g., Fe^{2+} and Cd^{2+}), which help to shift its adsorption edge to the visible light region. Specifically, the bandgap of NS samples is about 2.95 eV. The coexistence of impurity semiconductors could promote the separation of e^{-}-h^{+} pairs, and the cleavage planes as well as fracture surfaces could provide more active sites [40, 41].

Natural sphalerite was characterized and investigated for photoreduction of an azo dye methyl orange (MO) under visible light by Li et al. [42]. After 2 h of visible light irradiation, a complete decolorization of the MO solution was achieved. The degradation rate was related to the pH value of the solution. Spectra from Fourier transform infrared (FT-IR) spectroscopic analysis indicate an initial adsorption of MO to sphalerite via its sulfonate group. Further reduction of the adsorbed MO by sphalerite under visible light irradiation led to the destruction of the azo structure, as indicated by the results from UV-vis, FT-IR, and ESI-MS analyses. The visible-light-induced photocatalytic reductive activity of natural sphalerite is mainly attributed to the distribution of foreign metal atoms in its crystal lattice, which reduces the intrinsic bandgap of sphalerite and also broadens its spectra responding range. In addition, the high conduction band potential of natural sphalerite may also enhance the photoreduction of MO.

The photocatalytic reductive capability of natural sphalerite has been also studied for Cr^{6+} reduction, almost 91.95 % of the Cr^{6+} is reduced into Cr^{3+} under 9 h visible light irradiation, higher than the 70.58 % under 9.5 h UV light irradiation [43]. The highly reductive ability results from its super negative potential of electrons in the conduction band. Furthermore, Fe substitution for Zn introduces donor states, and the oxidation process of Fe^{2+} to Fe^{3+} makes it an

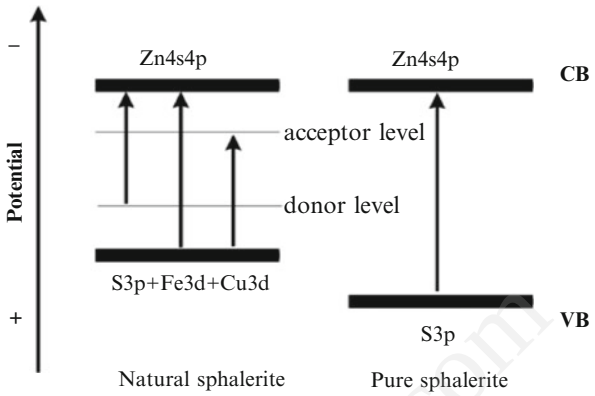

Fig. 3.2 The estimated band structure of natural sphalerite (Reprinted from Ref. [40] Copyright© 2008 Elsevier)

effective hole scavenger. Cd and Cu substitutes for Zn also reduce the bandgap and help broaden the absorbing edge toward the visible light (Fig. 3.2). These substituting metal ions in natural sphalerite make it a hyperactive photocatalyst and very attractive for solar energy utilization.

Later, natural sphalerite ((Zn, Fe)S mineral) was also utilized for photoreductive degradation of carbon tetrachloride (CT) under visible light irradiation [44]. About 92 % of CT was degraded in N,N-dimethylformamide (DMF) organic solvent system after 8 h of visible light irradiation. The effects of light source, natural sphalerite dosage, electron donors, dissolved oxygen, and carbon tetrachloride initial concentration on the efficiency of photocatalytic carbon tetrachloride degradation were discussed. The degradation products were analyzed by gas chromatography-mass spectrometry (GC-MS), and the photocatalytic degradation mechanism of carbon tetrachloride was then proposed.

To further improve its photocatalytic efficiency in visible light, the research team conducted the heat-treating experimental study of natural sphalerite at 500–1200 °C in static air [45]. The physical and chemical semiconductor properties of the original and modified samples were analyzed and characterized. The X-ray diffraction results showed that sphalerite was converted into $Zn_3O(SO_4)_2$ and then into zincite and franklinite with the increasing heat-treating temperature. Samples were totally converted into ZnO-$ZnFe_2O_4$ binary compound semiconductor at 1100–1200 °C. The UV-vis diffuse reflectance spectra (DRS) results show that the response of modified samples to visible light is stronger than that of the original sample and the absorption range of visible light of 900–1200 °C modified samples is larger than that of 500–800 °C modified samples. Then the original and modified samples were utilized to degrade methyl orange. Results show that the 1100–1200 °C heat modification of natural sphalerite significantly improves its degradation rate of methyl orange from 54.2 to 99.7 %, which indicates that the photocatalytic capability in visible light of 1100–1200 °C modified samples is the best. The results infer that the photocatalytic capability in visible light of ZnO-$ZnFe_2O_4$ binary compound semiconductor is higher than that of the single ZnS semiconductor and other types of compound semiconductor. The main reason

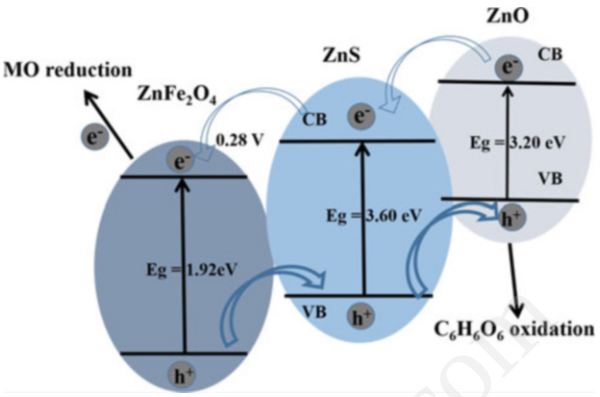

Fig. 3.3 Schematic diagram of charge transfer processes in $ZnFe_2O_4$/ZnS/ZnO hybrid photocatalysts

can be attributed to the acceleration of photoelectron transfer between the three semiconductors composite in Fig. 3.3.

Wang et al. [46] also studied the effect of heat treatment temperature on photocatalytic activity of natural zinc blendes and use Rhodamine B, a dyestuff in wastewater, to evaluate the photocatalytic activity of the materials. Results showed that the components of zinc blendes without heat treatment and that treated at 400 °C were both pure zinc sulfide (ZnS), while part of zinc blende converted to zinc oxide as heat treatment temperature rose above 600 °C. Zinc blendes without heat treatment are photocatalytically active, while zinc blendes after heat treatment at 400 °C had a higher photocatalytic activity than that of untreated zinc blende, and the photodecoloration rate to Rhodamine B reached 15.32 %, after 3 h sunlight irradiation. However, zinc blendes heat-treated above 600 °C nearly had no photocatalytic activity. Although both studies have different results, both still indicate that heat treatment could induce a variety of component and structure in ZnS and therewith higher photocatalytic activity.

Above studies show great potential in the harvesting and conversion of solar energy environmental remediation using natural mineral photocatalysts. However, solar photocatalytic water disinfection is still facing many challenges, since the most widely used TiO_2 photocatalyst requires UV irradiation which accounts for only 4 % of the sunlight spectrum. Although synthetic photocatalysts show promising disinfection performance under visible light (VL), the massive production of such synthetic photocatalysts at low cost has been a major limitation to its large-scale application. The acceptance efficiency in environmental remediation by utilizing natural semiconductors, combined with its advantages of readily accessible large quantities at low cost, opens an avenue for developing natural materials for photocatalytic water disinfection. It is envisaged that developing a natural mineral-based photocatalytic disinfection technique will be an economically viable solution for large-scale wastewater treatment. In this chapter, we present an overview of current research activities that center on the developing natural semiconductor photocatalysts for water disinfection under visible light (VL) irradiation.

3.3 Photocatalytic Inactivation by Natural Mineral

3.3.1 Natural Sphalerite

The application of natural materials for VLD photocatalytic water disinfection was first reported in 2011 [47]. We employed the natural sphalerite for the inactivation of *E. coli* under VL irradiation, and 7-log of *E. coli* could be completely inactivated within 6 h. The photocatalytic disinfection mechanism was investigated by using multiple scavengers. Results showed that the addition of Fe(II) as H_2O_2 scavenger would lead to a decrease of disinfection efficiency, indicating the involvement of H_2O_2 in the disinfection process. Most importantly, by conducting quadruple scavengers (KI, isopropanol, Fe(II), and TEMPOL) combined with a partition system, we experimentally proved that the photogenerated electrons could be injected into the bacterial cells and cause the cell inactivation by chemical reduction. The photocatalytic destruction process of bacterial cells began from cell wall and cell membrane to intracellular components (Fig. 3.4), exhibiting a similar process of bacterial inactivation caused by photocatalytic oxidation [48]. This emerging area of finding novel naturally occurring photocatalysts is of particular interest, because the fabrication costs of photocatalysts partially restrict the practical application. Natural materials are readily accessible and can be obtained in large quantity. Immediate research direction should be the search of more potential natural minerals for photocatalytic disinfection.

The selection of the light source is also very crucial for efficient VLD photocatalysis [49]. For UV irradiation, the inactivation efficiency is strongly dependent on the spectral distribution of the light source of photons: the disinfection effect of UVC is very fast, even in the absence of the photocatalyst. The results of Benabbou et al. [50] also showed that at equivalent intensity, the UVC/TiO_2 system was more effective to inactivate *E. coli* than the UVA/TiO_2 and UVB/TiO_2 systems. Although UV sources emit higher energy irradiation that leads to more effective bacterial disinfection, they are hazardous and only account for less 4 % of the sunlight. Thus, VL sources have greater potential applications in the water purification and wastewater treatment.

Compared with traditional VL sources such as easy-available fluorescent tube (FT) and high light intensity of xenon lamp, the advantages of light-emitting diode (LED) lamp are that it has long life expectancy and relatively low energy consumption, which are more applicable than for large-scale application. Therefore, Chen et al. [51] also studied the photocatalytic disinfection of *Escherichia coli* K-12 by the natural sphalerite (NS) under different spectra, wavelengths, and intensities of visible light (VL) emitted by LED lamp. The spectrum effect of VL on disinfection efficiency is studied by using white LED lamp, fluorescent tube (FT), and Xenon (XE) lamp, which indicates that the “discrete peak spectrum” of FT is more effective to inactivate bacteria than “continuous spectrum” of LED and XE lamps (Fig. 3.5a). It is hypothesized that the “discrete peak spectrum” supplies more photons to induce photoelectron–hole pairs.

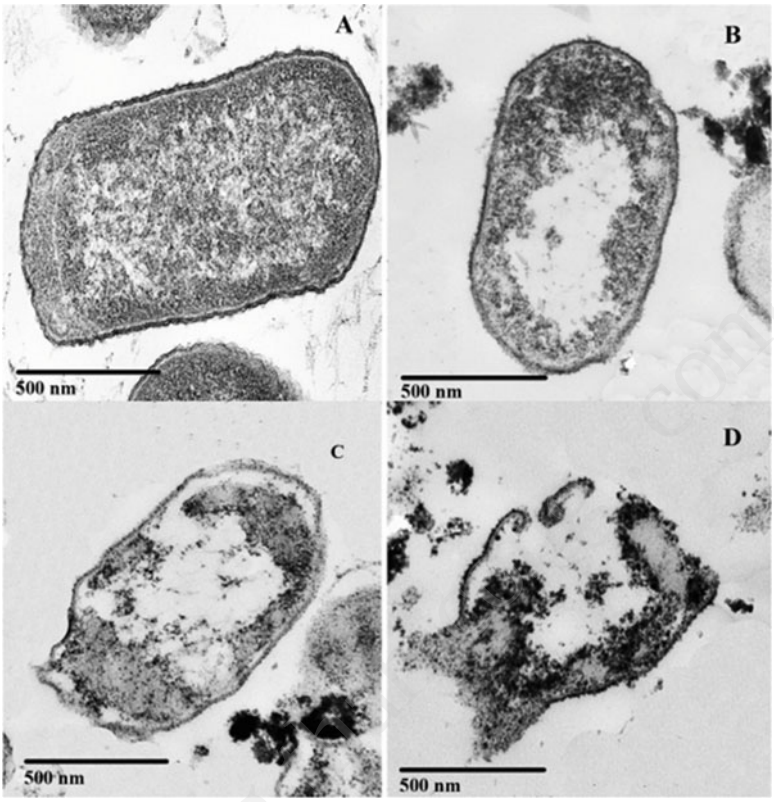

Fig. 3.4 TEM images of *E. coli* K-12 photocatalytically treated with the natural sphalerite under VL irradiation adding quadruple scavengers (KI, isopropanol, Fe(II) and TEMPOL). (**a**) 0 h, (**b**) 6 h, (**c**) 12 h, and (**d**) 30 h. The bacterial destruction process through photocatalytic reduction by conduction band electrons is shown to begin from cell wall cell membrane to intracellular components (Reprinted from Ref. [47] Copyright© 2011 American Chemical Society)

Besides, the photocatalytic disinfection of bacteria is compared under different single-spectrum (blue, green, yellow, and red color) LED lamps. The results show that the most effective wavelength ranges of VL for photocatalytic disinfection with the NS is 440–490 nm (blue), because the photon energy of blue LED lamp is higher than those of other colored LED lamps and the wavelength of blue LED lamp overlaps with the steep absorption edge of the NS. The disinfection efficiency under white LED lamp is lower than that under blue and yellow LED lamps (Fig. 3.5b); it is probably because the invalid red wavelength in white LED lamp occupies parts of the intensity of lamp. Furthermore, a positive relationship is obtained between the disinfection efficiency and the VL intensity. The results also showed the inactivation of bacteria is more sensitive at alkaline pH than at acidic and neutral pH, which is probably due to more oxidative species produced at more alkaline pH so that it exhibits higher disinfection efficiency at alkaline

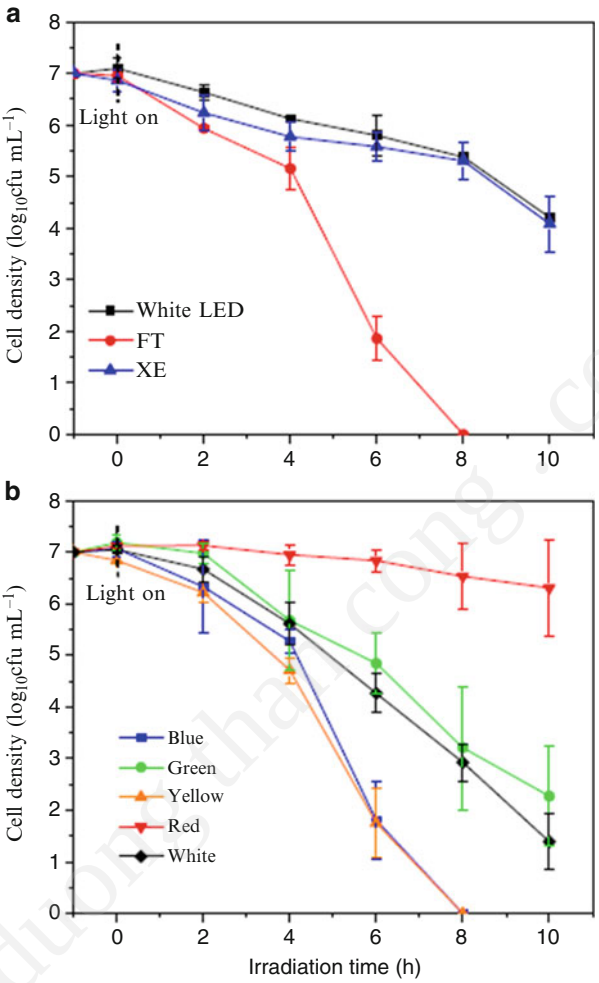

Fig. 3.5 Disinfection efficiency of *E. coli* K-12 (10^7 cfu mL^{-1}) by the NS at (**a**) different spectra of VL irradiation under VL intensity of 3 mW cm^{-2}, and (**b**) different wavelengths of VL irradiation under VL intensity of 87 mW cm^{-2} (Reprinted from Ref. [51] Copyright© 2011 Elsevier)

pH. The wide pH adaptability of NS is meaningful for the NS application. This work indicates that selecting an appropriate wavelength range of VL can improve the disinfection efficiency and save energy, giving good guidance for the application of NS in water disinfection.

Recently, controversial conclusions have been drawn from the photocatalytic inactivation of different kinds of bacteria, such as Gram-positive and Gram-negative bacteria, and the photocatalytic inactivation mechanism of different bacteria is still not clear. Cik et al. [52] reported that the photocatalytic

inactivation of a Gram-negative bacterium *E. coli* was more efficient than that of a Gram-positive bacterium *Staphylococcus aureus*. Pal et al. [53] found that two strains of *E. coli* (Gram-negative bacteria) were more effectively inactivated than four strains of *Bacillus subtilis* (Gram-positive bacteria). However, van Grieken et al. [54] reported that the Gram-negative bacterium *E. coli* and a Gram-positive bacterium *Enterococcus faecalis* had no significant difference in both TiO_2 suspension and immobilized TiO_2 photocatalytic systems. Therefore, Chen et al. [55] further compared the photocatalytic inactivation of a Gram-negative bacterium *Escherichia coli* with a Gram-positive bacterium *Microbacterium barkeri* to reveal the inactivation mechanism by using natural mineral photocatalysts [55].

The natural sphalerite was able to inactivate 10^5 cfu/mL of the Gram-positive bacterium *M. barkeri* within 10 h at neutral pH, while 10^7 cfu/mL of the Gram-negative bacterium *E. coli* was inactivated within 6 h. The difference in inactivation between the two bacteria is due to the structural differences of the two bacteria as the Gram-positive bacterium has a thicker cell wall than that of the Gram-negative bacterium [56], which will be more difficult to be attacked by photogenerated reactive oxidative species (ROS). This also agrees with the results from previous study which reported that Gram-positive bacteria are more resistant than Gram-negative bacteria in photocatalytic inactivation [52, 53].

In addition, the bacterial inactivation efficiency was enhanced with the increase of pH from 5 to 10, as H_2O_2 was the primary ROS and more H_2O_2 were produced under alkaline than acidic or neutral condition. The electrostatic interaction to the inactivation efficiencies at different pH values was excluded, since the zeta potentials of the samples were similar in the range of pH 5–10. As shown in Fig. 3.6, the point of zero charge (PZC) of NS was approximately 3.5 pH units. In the range of pH 3.5–10, both the surfaces of NS and *E. coli* were negatively charged, whereas that of *M. barkeri* was nearly neutral (Fig. 3.6); therewith there was no electrostatic attraction between the bacterial cell and NS.

The major reactive species for photocatalytic inactivation by the NS were determined using multiple scavengers, and H_2O_2 was found to be the major ROS in *M. barkeri* inactivation, while both H_2O_2 and e^- contributed to *E. coli* inactivation. The photocatalytic inactivation process is similar for the two bacteria, as indicated by direct observation of the cell wall and cell membrane by transmission electron microscopy and leakage detection of potassium ions, both of them are damaged from the cell wall. But the destructive process of *E. coli* is much faster than *M. barkeri*. Since the inactivation of both bacteria starts at the cell envelope (i.e., cell wall and cell membrane), this also suggests that the difference in major ROS involved between the two bacteria is related to their cell envelope structures, since the cell wall of Gram-positive is much thicker than Gram-negative bacteria. Results of this study will help optimize engineering parameters in future application of natural sphalerite in large-scale wastewater disinfection.

To date, the genetic functioning and role of bacterial cellular components in the photocatalytic inactivation of *E. coli* under visible light irradiation have not been well understood [57]. Therefore, Shi et al. firstly investigated how a natural

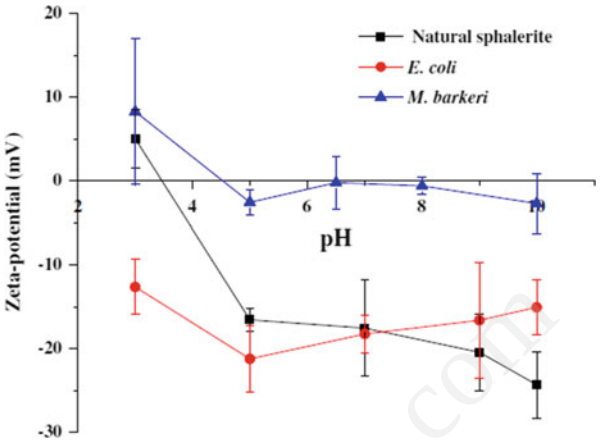

Fig. 3.6 Zeta potentials for suspensions of NS, *M. barkeri* and *E. coli* in the presence of NaCl (0.1 M) (Reprinted from Ref. [55] Copyright© 2013 Elsevier)

sphalerite (NS) photocatalyst, under visible light irradiation, supports the mechanism of photocatalytic bacterial inactivation. This was done by comparing parent *E. coli* BW25113 and its two isogenic single-gene knockout mutants, *E. coli* JW0797-1 (dps$^-$ mutant) and JW1721-1 (katE$^-$ mutant), where both dps and KatE genes are likely related to H_2O_2 production. NS could inactivate approximately 5-, 7-, and 7-log of *E. coli* BW25113, JW0797-1, and JW1721-1 within 6 h irradiation, respectively. The two isogenic mutants are more susceptible to photocatalysis than the parental strain because they are lacking a defense system against H_2O_2 oxidative stress. *E. coli* JW1721-1 is a catalase (CAT) gene defect mutant; its CAT production is much lower than the parental strain. Thus the CAT mutant is more easily attacked by in situ resultant H_2O_2 during the initial stage of photocatalytic inactivation. Similarly, the deletion of the dps gene in *E. coli* JW0797-1 reduced resistance to H_2O_2 attack and made it easier to be attacked by *in situ* H_2O_2 during the initial stage of the photocatalytic inactivation compared with the parental strain. Studying catalase activity further revealed that in situ H_2O_2 played an important role in these inactivation processes. The CAT activity trends across the three strains are very similar, but the CAT activity of *E. coli* BW25113 is higher than both mutants, particularly *E. coli* JW1721-1. This is because *E. coli* JW1721-1 is a catalase gene defect mutant; thus, CAT production amount is lower than the parental strain, leading to much higher photocatalytic inactivation of *E. coli* JW1721-1. As for *E. coli* JW0797-1, the CAT activity is lower than the parental strain during the photocatalytic process. This is because *E. coli* JW0797-1 is a dps gene defect mutant, making it easier to be attacked by H_2O_2. The enzyme activity was lost when the bacterial cells were attacked by H_2O_2. This method allows insight into the photocatalytic inactivation mechanism, with different bacteria encoded with different genes. Furthermore, these results reveal the photocatalytic inactivation mechanism of *E. coli* in water environments, pointing to a more practical cost-efficient water disinfection technology candidate.

3.4 Photocatalytic Inactivation with Natural Magnetic Minerals

Above studies have greatly confirmed the great bactericidal performance of natural sphalerite (NS), which could totally inactivate 7-$\log_{10}$ *Escherichia coli* K-12 within 6 h under irradiation of fluorescent tubes (FTs), owing to the major effect of conduction band e^-, and directly inject into bacteria and lead to the irreversible damage of the cell [48]. Compared with frequently reported VLD photocatalysts that are tedious in fabrication procedure, and expensive for massive production, natural VLD minerals readily are obtained with lower cost and have a great potential in cost-effective environmental applications. Nevertheless, difficulty in separation and recycling of these materials may still hinder their large-scale application in some content.

Magnetically separable photocatalysts have attracted increasing attention due to their efficient recycle effect in water treatment and purification system, because filtration and centrifuge are costly and tedious [58]. However, strategies to synthesize magnetically VLD photocatalysts tend to be limited for application, as most of which suffered dramatically decrease of photocatalytic activities and poor stability, such as $Fe_2O_3/SiO_2/TiO_2$, $TiO_2/ZnFe_2O_4$, etc. [59–62]. Therefore, to search and utilize the natural magnetic minerals will be more meaningful to solve this problem. A study of photocatalysis by natural magnetic sphalerite (NMS) is necessary for evaluating its practical applications such as development of a natural magnetic photocatalyst-based disinfection technique. The emphasis of this chapter is on the developments of natural magnetic minerals and its modification with enhanced activity.

3.4.1 Natural Magnetic Sphalerite

A novel natural magnetic sphalerite (NMS) was discovered from a lead–zinc mine in China and utilized directly for bacterial inactivation [63]. It is worthwhile to note the differences of NMS from the previously reported NS:

Firstly, Fig. 3.7 illustrates the representative magnetic hysteresis loops of NMS, with about 9.8 emu/g saturation magnetization, suggesting a typical ferromagnetic behavior and soft magnetic feature with less coercivity and remanence, while the saturation magnetism of NS could be negligible [64, 65]. Superior to NS, these typically soft magnetic NMS can be easily magnetically separated from water, which is desirable for their applications considering its dispersion and recycle (inset of Figure 3.7).

Secondly, unlike NS, chemical composition of NMS can be expressed as $(Zn_{0.856}Fe_{0.169}Cu_{0.0004})_{1.0254}S$ based on electron microprobe analysis (EMPA) results, revealing good coherence with doped ZnS and

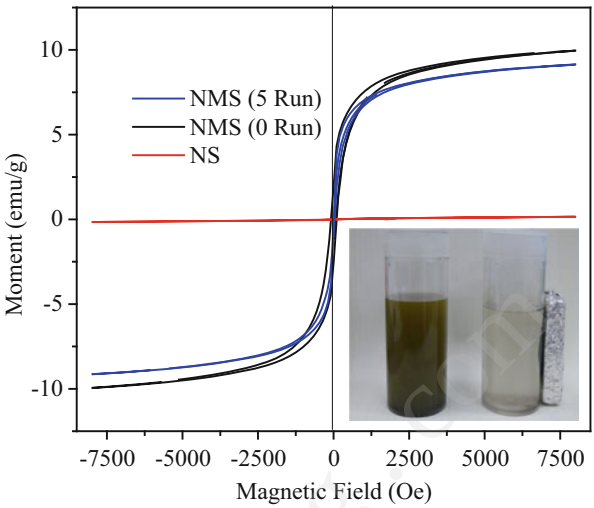

Fig. 3.7 Magnetic hysteresis loops of NS and NMS (Reprinted from Ref. [63] Copyright© 2013 American Chemical Society)

complicated crystal lattice defect of NMS, while NS is $(Zn_{0.732}Fe_{0.284}Cu_{0.043}Ni_{0.003}Ag_{0.003}Cd_{0.002}Mn_{0.002}Co_{0.001})_{1.070}S$.

Thirdly, UV-vis DRS test displayed narrower band structure (2.03 eV) for NMS than NS (2.24 eV), indicating better VL adsorption ability.

Natural magnetic sphalerite (NMS) was successfully utilized for VLD bacterial inactivation by Xia et al. [63]. Under the 6 h irradiation of fluorescent tubes, NMS could inactivate both Gram-positive *S. aureus* and Gram-negative *E. coli* without any regrowth. The cell destruction process starting from cell wall to intracellular components was verified by TEM, due to the critical role of direct contact between bacterial cell and NMS, the first attack site is expected to be the cell envelope.

About the primary reactive species, superoxide radical ($\bullet O_2^-$) rather than hydroxyl radical (•OH) was proposed to be the primary reactive oxidative species (ROS) responsible for *E. coli* inactivation by the use of specific probes and electron spin resonance. There was no occurrence of characteristic peaks corresponding to DMPO-•OH adducts, but the six characteristic peaks of the DMPO-$\bullet O_2^-$ adducts were observed under VL. Similarly, no fluorescence after •OH-trap agent (terephthalic acid) was added, while purple product formed after XTT ($\bullet O_2^-$ probe) was added. The results are consistent with the condition in theory that the VB holes of NMS, elevated by the substitution of Zn with transition metal of Fe and Cu (VB for pure sphalerite is 2.2 eV vs NHE; thus VB for NMS is less than 2.2 eV), could not oxidize the OH^-/H_2O to produce •OH (E_0 (OH^-/•OH)) = 2.38 eV vs NHE), while the CB electrons of NMS have more negative potential (−1.4 V vs NHE) to reduce the surface chemisorbed O_2 to produce $\bullet O_2^-$ ($E_0(O_2/\bullet O_2^-)$) = −0.33 eV vs NHE). Meanwhile, H_2O_2 determined by fluorescence method is also greatly involved in bacterial inactivation in both non-partition and partition systems. In CB, H_2O_2 is believed to be produced by the reduction or disproportionation of $\bullet O_2^-$, whereas in VB H_2O_2 is formed by the coupling of two •OH too [66–68]. As

mentioned, $\bullet O_2^-$ rather than •OH plays a more important role in the reaction; thus the primary origin of H_2O_2 should be from $\bullet O_2^-$ generated from CB. This result is different from NS, as e^- is the primary reactive species; this may attribute to the fact that the chemical components of these two materials are different.

A five-run experiment revealed excellent stability of recycled NMS without any significant loss of photocatalytic activity and change in magnetic property (Fig. 3.7). Although a little amount of elution of Zn^{2+} (0.17 mg/L) and Fe^{2+} (0.032 mg/L) can be detected by AAS when NMS was immersed in bacterial cell suspension within the 8 h experimental time scale, other metal impurities were undetectable; the photocorrosion-induced metal ion leakage with small quantity show no toxicity to cells in the control experiments. Li et al. [43] also found that after 9 h irradiation by a 500 W tungsten halogen lamp, the Zn atom percentage on the NS surface decreased from 27.5 to 24.4 %, corresponding to a loss of 3.1 % of the ZnS particles. As photocorrosion occurred to such a minor extent, the stability of NMS is considerable.

3.4.2 *Natural Pyrrhotite*

Motivated by the good bactericidal performance of natural magnetic sphalerite, the selection and the development of these kinds of more efficient alternative materials are urgently needed for cost-effective environmental remediation. However, utilization of these materials still comes across the problems of ion leakage and limited activity, making its application limited [63]. Thermal modification of natural minerals may be a good choice to address the above two problems simultaneously, because heating can repair the lattice defects and improve the crystalline degree [69], amplify the crystalline size [70], transform the mineral phase [71], and possibly remove the impurities [72].

A novel magnetic natural pyrrhotite (NP) mineral photocatalyst was developed and modified by thermal treatment [73]. Different from the pure material, natural pyrrhotite always occurred with impurity mineral phases. The most common associated mineral of pyrrhotite is pyrite (FeS_2), which is also a semiconductor mineral. A pristine NP sample is composed of mixed phases of pyrrhotite-6 T ($Fe_{1-x}S$, PDF 29-0725) and pyrite (FeS_2, PDF 42-1340). The chemical formula of NP can be expressed as $(Fe_{0.8656}Ni_{0.00045}Mn_{0.0018}Cu_{0.002}Pd_{0.0028}Zn_{0.0015}Cd_{0.0001}Co_{0.0002})_{0.875}S$. UV-vis spectrum shows a broad absorption band in the range of 300–800 nm, indicating both UV and visible light response of the natural mineral. Importantly, pristine NP showed a saturation magnetization of approximately 5 emu/g.

The photocatalytic activity of treated NP was evaluated by photocatalytic inactivation of *Escherichia coli* K-12 under visible light. As compared to NP, the annealed NP was found to exhibit a remarkable enhanced bactericidal activity. Among them, the NP treated at 600 °C in air (NP600) had the highest activity, and the inactivation rate was nearly three times higher than that of untreated NP. The X-ray diffraction (XRD) spectra indicated the mineral phase of NP600 transformed

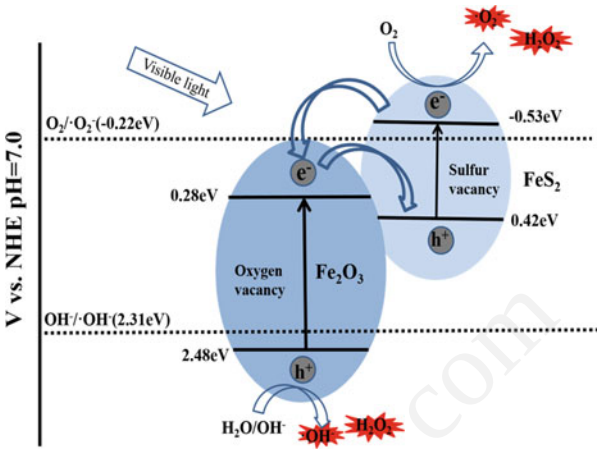

Fig. 3.8 Schematic diagram of the energy band configuration of FeS_2/Fe_2O_3 heterojunction and separation of electron–hole pairs at the interface under light irradiation (Reprinted from Ref. [73] Copyright© 2015 Elsevier)

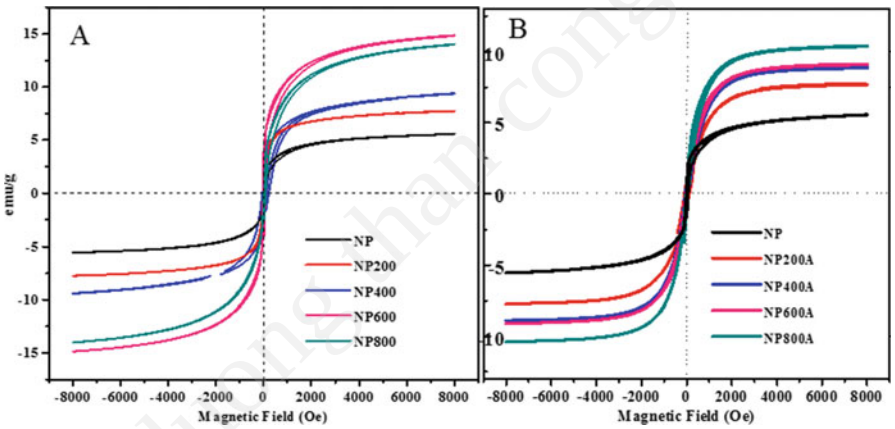

Fig. 3.9 Magnetic hysteresis curves of annealed NP in (**a**) air and (**b**) argon (Reprinted from Ref. [73] Copyright© 2015 Elsevier)

to mixed crystallite phases of hematite-pyrite (Fe_2O_3-FeS_2) composite. So, the enhanced photocatalytic performance was mainly attributed to the formation of Z-scheme photocatalysis system composed of hematite and pyrite (Fig. 3.8), which could improve the electron–hole separation efficiency and the bactericidal efficiency. This hypothesis was confirmed by scavenger study, as the dominant bactericidal agent changed from superoxide radical ($\cdot O_2^-$) for NP to hydroxyl radical ($\cdot OH$) for NP600. The Z-scheme is also effective for the illustration of NP annealed in argon.

Moreover, vibrating sample magnetometer (VSM) analysis revealed that the saturated magnetism of NP after thermal anneal was enhanced. The strong magnetic behavior of thermally treated NP enabled the magnetic recovery of photocatalysts after liquid phase reaction. Hysteresis loops in Fig. 3.9 revealed how the curves change with the formation of new phases after NP was annealed. For NP200, the

increased phase proportion of pyrrhotite induced a slight increase of the magnetization to 7.5 emu/g. The saturated magnetization value rapidly increased to 9.5 emu/g for NP400 and to 15 emu/g for NP600, mainly due to the appearance of magnetite and maghemite [74–76]. As for NP800, the ferromagnetic property slightly decreased to 14 emu/g because magnetite was further oxidized into antiferromagnetic hematite with a negligible saturation magnetization of 0.57 emu/g [77, 78]. While in argon atmosphere, the saturation magnetization of thermally treated samples increased from 5 to 10 emu/g with the rising temperature, mainly due to the continuing production of pyrrhotite.

In addition, NP600 was much stable than untreated NP and with lower metal ion leakage even after four reaction cycles. The elution amount of Fe ion from NP600 was almost undetectable with a value of 0.084 mg/L, while a little amount of Fe^{3+} (2.6 mg/L is nontoxic to cells) can be detected when pristine NP was added within 4 h experimental duration, indicating the photostability was greatly enhanced after thermal treatment. This work supplied a cost-effective natural mineral-based photocatalyst and an efficient modification strategy to extend the application field of natural minerals in water disinfection.

3.5 Conclusions and Outlook

Solar photocatalysis undoubtedly represents the most promising alternative water disinfection technology. This chapter reviews recent progress on the development of VLD natural mineral semiconductor-based photocatalytic disinfection technology. To make these photocatalytic disinfection technology practical, major advancements are needed in the search for more efficient magnetic minerals and modification processes. The purpose of modification is to elevate the limited photocatalytic activity and photostability of pristine minerals, and this has been traditionally reached by post-thermal treatment. However, these processes face problems such as higher energy cost. One of the obstacles to overcome before industry application of these materials is the search of more efficient alternative minerals. However, specific photocatalysts are required with the ability to produce high amounts of diffusible reactive species with long lifetime, such as H_2O_2. While these issues still pose challenges, it is reasonable to expect that the next few years will bring major advancements in both basic and applied research on solar-induced photocatalytic water disinfection.

References

1. Wang XC, Maeda K, Thomas A, Takanabe K, Xin G, Carlsson JM, Domen K, Antonietti M (2009) A metal-free polymeric photocatalyst for hydrogen production from water under visible light. Nat Mater 8:76–80
2. Asahi R, Morikawa T, Ohwaki T, Aoki K, Taga Y (2001) Visible light photocatalysis in nitrogen-doped titanium oxides. Science 293:269–271

3. He YM, Zhang LH, Teng BT, Fan MH (2015) New application of Z-scheme Ag_3PO_4/g-C_3N_4 composite in converting CO_2 to fuel. Environ Sci Technol 49:649–656
4. Yu JC, Ho WK, Yu JG, Yip H, Wong PK, Zhao JC (2005) Efficient visible-light-induced photocatalytic disinfection on sulfur doped nanocrystalline titania. Environ Sci Technol 39:1175–1179
5. Lu AH (1997) A new survey of environmental mineralogical materials. Acta Petrol Mineral 16:184–187 (in Chinese with English abstract)
6. Lu AH (2003) Mineralogical photocatalysis in natural self-purification of inorganic minerals. Acta Petrol Sin 22:323–331 (in Chinese with English abstract)
7. Lu AH (2002) Environmental properties of minerals and natural self-purification of inorganic minerals. Bull Mineral Petrol Geochem 21:192–197 (in Chinese with English abstract)
8. Lu AH (1999) The application of environmental mineral materials to the treatment of contaminated soil, water and air. Acta Petrol Sin 18:292–300 (in Chinese with English abstract)
9. Lu AH (2000) Development of properties of mineralogy from resource to environmental. Geol J China Univ 6:245–251 (in Chinese with English abstract)
10. Lu AH (2001) Basic properties of environmental mineral materials: natural self-purification of inorganic minerals. Acta Petrol Mineral 20:371–381 (in Chinese with English abstract)
11. Boldish SI, White BE (1998) Optical band gaps of selected ternary sulfide minerals. Am Mineral 83:865–871
12. Brezonik P (1993) Chemical kinetics and process dynamics in aquatic systems. Lewis Publishers, Chelsea, 754
13. Bulter MA, Ginley DS (1978) Prediction of flatband potentials at semiconductor-electrolyte interfaces from atomic electronegativities. J Electrochem Soc 125:228–232
14. Dovgii YO, Bilen' kii BF (1966) Investigation of the fundamental absorption edges of α-Hg single crystals. Sov Phys Solid State 8:1280–1282
15. Efstathiou A, Levin ER (1968) Optical properties of As_2Se_3, $(As_xSb_{1-x})_2Se_3$ and Sb_2S_3. J Opt Soc Am 58:373–377
16. Freidman SP, Gubanov VA (1983) Electronic structure of 3d metal monosulfides by the Xα discrete variational method. J Phys Chem Solids 44:187–194
17. Halouani FE, Deschavres A (1982) Interfaces semiconducteur electrolyte: correlations entre le potentiel de bande plate et les echelles d'electronegativite. Mater Res Bull 17:1045–1052
18. Jaegermann W, Tributsch W (1988) Interfacial properties of semiconducting transition metal chalcogenides. Prog Surf Sci 29:1–167
19. Kanemoto M, Shiragami T, Pac C, Yanagida S (1992) Semiconductor catalysis. Effective photoreduction of carbon dioxide catalyzed by zinc sulfide quantum crystallites with low density of surface defects. J Phys Chem 96:3521–3526
20. Mills G, Li Z, Meisel D (1988) Photochemistry and spectroscopy of colloidal As_2S_3. J Phys Chem 92:822–828
21. Nozik AJ (1978) Photoelectrochemistry: applications to solar energy conversion. Annu Rev Phys Chem 29:189–222
22. Oosaw Y, Takahashi R, Younemura M, Sekine T, Goto Y (1989) Photocatalytic hydrogen evolution and oxygen evolution over ternary titanate and relationship between physical properties and kinetic properties. New J Chem 13:435–440
23. Quarto F, Sunseri PS, Romano M (1997) Semiempirical correlation between optical band gap values of oxides and the differences of electronegativity of the elements. Its importances for a quanti use of photocurrent spectroscopy in corrosion studies. J Phys Chem 101:2519–2525
24. Rodriguez JA, Chaturvedi S, Kuhn M, Hrbek J (1998) Reaction of H_2S and S_2 with metal/oxide surface: bandgap size and chemical reactivity. J Phys Chem B 102:5511–5519
25. Sakkopoulos S, Vitoratos E, Argyreas T (1984) Energy band diagram for pyrrhotite. J Phys Chem Solids 45:923–928
26. Sculfort J, Gautron J (1984) The role of the anion electronegativity in semiconductor-electrolyte and semiconductor-metal junctions. J Chem Phys 80:3767–3773
27. Shuey RT (1975) Semiconducting ore minerals. Amsterdam, Elsevier

28. Sugiura C, Gohshi Y, Suzuki I (1974) Sulfur kβ x-ray emission spectra and electronic structures of some metal sulfides. Phys Rev B 10:338–343
29. Temmerman WM, Durham PJ, Vaughan DJ (1993) The electronic structures of the pyrite type disulphides (MS_2, where M = Mn, Fe, Co, Ni, Cu, Zn) and the bulk properties of pyrite from local density approximation (LDA) band structure calculations. Phys Chem Miner 20:248–254
30. Wang P, Pan Z, Weng L (1982) System of mineralogy. Geological Press, Beijing (in Chinese)
31. Wei D, Osseo-Asare K (1997) Semiconductor electrochemistry of particulate pyrite. J Electrochem Soc 145:544–563
32. Xu Y, Schoonen MAA (2000) The absolute energy positions of conduction and valence bands of selected semiconducting minerals. Am Mineral 85:543–556
33. Zhang Z, Satpathy S (1991) Electron states, magnetism, and the Verwey transition in magnetite. Phys Rev B 44:13319–13331
34. Waite TD (1990) Photo redox processes at the mineral water interface. In: Hochella MF Jr, White AF (eds) Mineral-water interface geochemistry, Review in mineralogy. Mineralogical Society of America, Washington, DC, 559–597
35. Shuey RT (1975) Semiconducting ore minerals. Elsevier, Amsterdam
36. Lu AH, Li Y, Lv M, Wang CQ, Yang L, Liu J, Wang YH, Wong KH, Wong PK (2007) Photocatalytic oxidation of methyl orange by natural V-bearing rutile under visible light. Sol Energy Mater Sol Cells 91:1849–1855
37. Yang L, Wang Q, Lu A, Guo Y, Liu F, Ma S (2005) Photo-catalysis oxidation of methylene-blue by V-bearing rutile under visible light. Earth Sci Front 12:184–188
38. Lu AH, Liu J, Zhao DG, Guo YJ, Li QR, Li N (2004) Photocatalysis of V-bearing rutile on degradation of halohydrocarbons. Catal Today 90:337–342
39. Luo ZM, Lu AH, Li Y, Zhuang W, Wu J, Qin S, Wang CQ (2012) Enhanced visible-light response of natural V-bearing by annealing under argon. Eur J Mineral 24:551–557
40. Li Y, Lu A, Wang C, Wu X (2008) Characterization of natural sphalerite as a novel visible light-driven photocatalyst. Sol Energy Mater Sol Cells 92:953–959
41. Li Y, Lu AH, Wang CQ (2009) Semiconducting mineralogical characteristics of natural sphalerite gestating visible-light photocatalysis. Acta Geol Sin 83:633–639
42. Li Y, Lu A, Song J, Wang C (2009) Photo-reductive decolorization of an azo-dye by natural sphalerite case study of a new type of visible-light-sensitized photocatalyst. J Hazard Mater 170:479–486
43. Li Y, Lu AH, Wang CQ (2006) Photocatalytic reduction of Cr(VI) by natural sphalerite suspensions under visible light irradiation. Acta Geol Sin 80:267–272
44. Yang XG, Li Y, Lu AH, Yan YH, Wang CQ, Wong PK (2007) Photocatalytic reduction of carbon tetrachloride by natural sphalerite under visible light irradiation. Sol Energy Mater Sol Cells 95:1915–1921
45. Yin YD, Li Y, Yan YH, Lu AH (2013) A study of the photocatalytic capability of heat-treated sphalerite in visible light. Acta Petrol Mineral 32:825–832 (in Chinese with English abstract)
46. Wang C, Shi HS, Zhang P, Li Y (2010) Effect of heat treatment temperature on photocatalytic activity of natural zinc blende. Inorg Chem Ind 42:15–16 (in Chinese with English abstract)
47. Chen YM, Lu AH, Li Y, Zhang LS, Yip HY, Zhao HJ, An TC, Wong PK (2011) Naturally occurring sphalerite as a novel cost-effective photocatalyst for bacterial disinfection under visible light. Environ Sci Technol 45:5689–5695
48. Zhang LS, Wong KH, Yip HY, Hu C, Yu JC, Chan CY, Wong PK (2010) Effective photocatalytic disinfection of *E. coli* K-12 using $AgBr - Ag - Bi_2WO_6$ nanojunction system irradiated by visible light: the role of diffusing hydroxyl radicals. Environ Sci Technol 44:1392–1398
49. Leung TY, Chan CY, Hu C, Yu JC, Wong PK (2008) Photocatalytic disinfection of marine bacteria using fluorescent light. Water Res 42:4827–4837
50. Benabbou AK, Derriche Z, Felix C, Lejeune P, Guillard C (2007) Photocatalytic inactivation of Escherichia coli: effect of concentration of TiO_2 and microorganism, nature, and intensity of UV irradiation. Appl Catal B Environ 76:257–263

51. Chen YM, Lu AH, Li Y, Yip HY, An TC, Li GY, Jin P, Wong PK (2011) Photocatalytic inactivation of *Escherichia coli* by natural sphalerite suspension: effect of spectrum, wavelength and intensity of visible light. Chemosphere 84:1276–1281
52. Cik GS, Priesolova H, Bujdakova F, Šeršen T, Potheoova JK (2006) Inactivation of bacteria G^+-*S. aureus* and G^--*E. coli* by phototoxic polythiophene incorporated in ZSM-5 zeolite. Chemosphere 63:1419–1426
53. Pal V, Pehkonen SO, Yu LE, Ray MB (2007) Photocatalytic inactivation of Gram-positive and Gram-negative bacteria using fluorescent light. J Photochem Photobiol A Chem 186:335–341
54. van Grieken R, Marugan J, Pablos C, Furones L, Lopez A (2010) Comparison between the photocatalytic inactivation of Gram-positive *E. faecalis* and Gram negative *E. coli* faecal contamination indicator microorganisms. Appl Catal B Environ 100:212–220
55. Chen YM, Ng TW, Lu AH, Li Y, Yip HY, An TC, Li GY, Zhao HJ, Gao MH, Wong PK (2013) Comparative study of visible-light-driven photocatalytic inactivation of two different wastewater bacteria by natural sphalerite. Chem Eng J 234:43–48
56. Slonczewski JL, Foster JW (2011) Microbiology: an evolving science. W.W. Norton & Company, Inc., New York
57. Shi HX, Huang GC, Xia DH, Ng TW, Yip HY, Li GY, An TC, Zhao HJ, Wong PK (2015) Role of in situ resultant H_2O_2 in the visible-light-driven photocatalytic inactivation of *E. coli* using natural sphalerite: a genetic study. J Phys Chem B 119:3104–3111
58. Polshettiwar V, Luque R, Fihri A, Zhu HB, Bouhrara M, Basset JM (2011) Magnetically recoverable nanocatalysts. Chem Rev 111:3036–3075
59. Kostedt WL, Drwiega J, Mazyck DW, Lee SW, Sigmund W, Wu CY, Chadik P (2005) Magnetically agitated photocatalytic reactor for photocatalytic oxidation of aqueous phase organic pollutants. Environ Sci Technol 39:8052–8056
60. Zhang L, Wang WZ, Zhou L, Shang M, Sun SM (2009) Fe_3O_4 coupled BiOCl: a highly efficient magnetic photocatalyst. Appl Catal B Environ 90:458–462
61. Barmatova MV, Ivanchikova ID, Kholdeeva OA, Shmakov AN, Zaikovskii VI, Mel'gunov MS (2009) Magnetically separable titanium-silicate mesoporous materials with core−shell morphology: synthesis, characterization and catalytic properties. J Mater Chem 19:7332–7339
62. Beydoun D, Amal R, Low G, McEvoy S (2000) Novel photocatalyst: titania-coated magnetite. Activity and photodissolution. J Phys Chem B 104:4387–4396
63. Xia DH, Ng TW, An TC, Li GY, Li Y, Yip HY, Zhao HJ, Lu AH, Wong PK (2013) A recyclable mineral catalyst for visible-light-driven photocatalytic inactivation of bacteria: natural magnetic sphalerite. Environ Sci Technol 47:11166–11173
64. Cullity BD, Graham CD (2009) Introduction to magnetic materials, 2nd edn. Wiley-IEEE Press, Hoboken
65. Rawat J, Rana S, Srivastava R, Misra RDK (2007) Antimicrobial activity of composite nanoparticles consisting of titania photocatalytic shell and nickel ferrite magnetic core. Mater Sci Eng C 27:540–545
66. Ranjit KT, Willner I, Bossmann SH, Braun AM (2001) Lanthanide oxide-doped titanium dioxide photocatalysts: novel photocatalysts for the enhanced degradation of *p*-chlorophenoxyacetic acid. Environ Sci Technol 35:1544–1549
67. Sakai H, Baba R, Hashimoto K, Fujishima A (1995) Local detection of photoelectrochemically produced H_2O_2 with a "wired" horseradish peroxidase microsensor. J Phys Chem 99:11896–11900
68. Kikuchi Y, Sunada K, Iyoda T, Hashimoto K, Fujishima A (1997) Photocatalytic bactericidal effect of TiO_2 thin films: dynamic view of the active oxygen species responsible for the effect. J Photochem Photobiol A Chem 106:51–56
69. Luan YB, Jing LQ, Wu J, Xie MZ, Feng YJ (2014) Long-lived photogenerated charge carriers of 001-facet-exposed TiO_2 with enhanced thermal stability as an efficient photocatalyst. Appl Catal B Environ 147:29–34
70. Le TK, Flahaut D, Martinez H, Nguyen HKH, Huynh TKX (2015) Study of the effects of surface modification by thermal shock method on photocatalytic activity of TiO_2 P25. Appl Catal B Environ 165:260–268

71. Aramendia MA, Borau V, Colmenares JC, Marinas A, Marinas JM, Navio JA, Urbano FJ (2008) Modification of the photocatalytic activity of Pd/TiO_2 and Zn/TiO_2 systems through different oxidative and reductive calcination treatments. Appl Catal B Environ 80:88–97
72. An TC, Liu JK, Li GY, Zhang SQ, Zhao HJ, Zeng XY, Sheng GY, Fu JM (2008) Structural and photocatalytic degradation characteristics of hydrothermally treated mesoporous TiO_2. Appl Catal A Gen 350:237–243
73. Xia DH, Li Y, Huang GH, Fong CC, An TC, Li GY, Yip HY, Zhao HJ, Lu AH, Wong PK (2015) Visible-light-driven inactivation of Escherichia coli K-12 over thermal treated natural pyrrhotite. Appl Catal B Environ 176:749–756
74. Nasrazadani S, Raman A (1993) The application of infrared spectroscopy to the study of rust systems-II. Study of cation deficiency in magnetite (Fe_3O_4) produced during its transformation to maghemite (γ-Fe_2O_3) and hematite (α-Fe_2O_3). Corros Sci 34:1355–1365
75. Ishikawa T, Matijevic E (1988) Formation of monodispersed pure and coated spindle-type iron particles. Langmuir 4:26–31
76. Wang L, Pan YX, Li JH, Qin HF (2008) Magnetic properties related to thermal treatment of pyrite. Sci China Ser D 51:1144–1153
77. Okada I, Ozaki M, Matijevic E (1991) Magnetic interactions between platelet-type colloidal particles. J Colloid Interface Sci 142:251–256
78. Baláž P, Aláčová A, Godočíková E, Kováč J, Škorvánek I, Jiang JZ (2004) Study of magnetic properties of nano-powders prepared by pyrite-troilite transformation via high energy milling. Czech J Phys 54:197–200

Chapter 4
Visible Light Photocatalytic Inactivation by Bi-based Photocatalysts

Sheng Guo and Gaoke Zhang

Abstract During the past decades, photocatalytic process has emerged as a promising alternative strategy for water treatment owning to its wide application in solar energy conversion and environmental remediation. Particularly, bismuth compounds have received remarkable attention as efficient photocatalysts for inactivation of bacteria due to their low cost, excellent photocatalytic activity, and chemical stability. This chapter summarizes the recent advances in the synthesis and photocatalytic inactivation activities of bismuth oxides and oxyhalides, bismuth metallates, plasmonic-bismuth compounds, and other bismuth composite photocatalysts. Emphasis is placed on the enhanced photocatalytic activity of the bismuth compounds which is affected by their crystallinity, microstructure, band gap, morphology, and particle size. Meanwhile, the bacterial inactivation process and mechanism are discussed in detail.

Keywords Photocatalytic • Water inactivation • Visible light • Bi-based photocatalysts • Inactivation mechanism

4.1 Introduction

The presence of pathogenic microorganisms in drinking water is a global concern since they may result in the risk of waterborne disease transmission such as typhoid, hepatitis, cholera, tuberculosis, and pneumonia [1, 2]. The World Health Organi-

S. Guo
School of Resources and Environmental Engineering, Wuhan University of Technology, 122 Luoshi Road, Wuhan 430070, People's Republic of China

School of Chemistry and Environmental Engineering, Wuhan Institute of Technology, 122 Luoshi Road, Wuhan 430070, People's Republic of China
e-mail: guosheng86@yahoo.com

G. Zhang (✉)
School of Resources and Environmental Engineering, Wuhan University of Technology, 122 Luoshi Road, Wuhan 430070, People's Republic of China
e-mail: gkzhang@whut.edu.cn

T. An et al. (eds.), *Advances in Photocatalytic Disinfection*, Green Chemistry and Sustainable Technology, DOI 10.1007/978-3-662-53496-0_4

zation (WHO) estimates that 884 million people lack access to improved water supplies, leading to millions of deaths and countless cases of disease and disability which is caused by microorganism-containing water [3]. Conventional inactivation methods are chlorination, ozonation, UV irradiation, and membrane technology. Of which, chlorination is the most widely used inactivation method because of its low cost, high efficiency, and residual effect. Unfortunately, chloro-organic by-products which are highly carcinogenic would be generated during the chlorination process [4]. Other frequently used processes are ozonation and UV irradiation, which also have drawbacks such as generation of toxic by-products, complicated and expensive equipment, and lack of residual effect [5, 6]. Membrane technology can only remove bacteria from water rather than kill them. Thus, alternative effective and low-cost methods of controlling pathogenic microorganisms with nontoxic by-products are urgently needed.

Since Fujishima and Honda discovered the photocatalytic splitting of water on TiO_2 electrodes [7], photocatalytic process has been widely used for the removal of various environmental pollutants and energy-related applications such as hydrogen production and solar cells of water treatment [8–11]. Photocatalytic process received even more attention when Matsunaga and coworkers first reported the inactivation of three microbial cells (*Lactobacillus acidophilus*, *Saccharomyces cerevisiae*, and *Escherichia coli*) through photoelectrochemical process in 1985 [12]. TiO_2 is considered as the most promising photocatalyst and has been intensively investigated owning to its nontoxicity, low cost, high efficiency, and long-term chemical and biological stability. However, due to the wide band (3.18 and 3.02 eV for anatase and rutile, respectively), TiO_2 can only be activated by wavelengths in the near ultraviolet (UV) region ($\lambda < 400$ nm), accounting for only a small potion (5 %) of the solar spectrum compared to visible light (45 %) [13]. Although the modification of TiO_2 such as impurity doping, metallization, sensitization, and coating could extend its application to the visible light region, it often leads to complex preparation processes and low stability. Moreover, the fast recombination rate of the photoexcited electrons and holes in TiO_2 leads to its limited quantum efficiency. Hence, from the viewpoint of efficient utilization of solar light, the development of efficient visible-light-driven photocatalysts for photocatalytic disinfection has been a crucial issue.

In recent years, a family of bismuth (Bi)-based compounds has been extensively studied due to their relatively high activity under visible light irradiation [14–22]. Bi is a kind of p-block metal with a d^{10} configuration, and the hybridized valence band by O 2p and Bi 6s can narrow the band gap as well as favor the mobility of photogenerated holes in the valence band (VB). The most commonly studied Bi compounds are Bi_2O_3, Bi_2S_3, BiOX (X = Cl, Br, I), Bi_2WO_6, Bi_2MoO_6, $BiFeO_3$, $Bi_2O_2CO_3$, $BiVO_4$, Bi_3NbO_7, and $BiPO_4$. To the best of our knowledge, most of the studies of Bi compounds are focused on photocatalytic evolution of O_2 and degradation of organic contaminants, and the work and review on bacteria inactivation is very limited.

In this chapter, we will address an overview of recent developments that center on the preparation, characterization, modification, and application of bismuth

oxides and oxyhalides, bismuth metallates, plasmonic-bismuth compounds, and other bismuth photocatalysts for water disinfection under visible light irradiation. Particular attention is given to the crystallinity, microstructures, band gap, morphology, and particle size of the Bi compounds with their enhanced inactivation activity under visible light irradiation. The antimicrobial processes and mechanisms are discussed. The current limitations, solutions, and future needs of research associated with the bacteria inactivation by Bi compounds are also highlighted. This chapter will involve the following sections: (1) water inactivation by bismuth oxides and sulfides, bismuth metallates, plasmonic-bismuth compounds, and other bismuth-based composites; (2) bacterial disinfection process; (3) role of reactive species; and (4) the summary and future outlook.

4.2 Photocatalytic Disinfection Using Bi Compounds

4.2.1 Bismuth Oxides and Oxyhalides

Among all the bismuth compounds, the simple bismuth oxides are much more promising for practical application owning to their unique advantages such as simple structure, low cost, facile synthesis, and easy to scale up for commercial applications. Particularly, as an important p-type semiconductor, bismuth oxide (Bi_2O_3) is of great interest and has been extensively applied in photovoltaic cells, gas sensing, fuel cells, and photocatalysis [23–26]. Qin et al. [27] synthesized size-tunable Bi_2O_3 porous nanospheres via a solvothermal method. The Bi_2O_3 nanospheres exhibit excellent size-dependent antibacterial activity toward Gram-positive *S. aureus* and Gram-negative *E. coli*, which is much better than commercial Bi_2O_3 (Fig. 4.1a). The growth inhibition of *E. coli* was not observed in the colloidal suspension containing Bi_2O_3, indicative of no toxic effect of Bi_2O_3 nanospheres to *E. coli*. Moreover, the obtained Bi_2O_3 nanospheres are multifunctional and also demonstrate outstanding performance in visible-light-driven photocatalysis for Cr(VI) and organic dye removal, as well as template synthesis for fabrication of bismuth-related hollow nanostructures (Bi_2S_3, Bi_2Se_3, Bi_2Te_3, $BiVO_4$, and Bi_2WO_6). Noticeably, their previous studies demonstrated no inhibition of Bi_2O_3 nanoparticles against *Helicobacter pylori*. Further work could be paid to investigate the selective inactivation of different bacteria by size-tunable Bi_2O_3 nanospheres.

Very recently, Wang et al. [28] discovered a new visible-light-driven photocatalyst, namely, monoclinic dibismuth tetraoxide (m-Bi_2O_4) through a simple hydrothermal method using $NaBiO_3$ as the sole starting material. This simple oxide with mixed valent states (Bi^{3+} and Bi^{5+}) has band gap energy of 2.0 eV and is responsive to wavelength up to 620 nm. The first-principle calculations within the hybrid density functional framework indicate that m-Bi_2O_4 is a typical indirect-gap semiconductor. Under visible light irradiation, the m-Bi_2O_4 exhibited remarkable photocatalytic activity for the inactivation of *E. coli* K-12, and total inactivation of

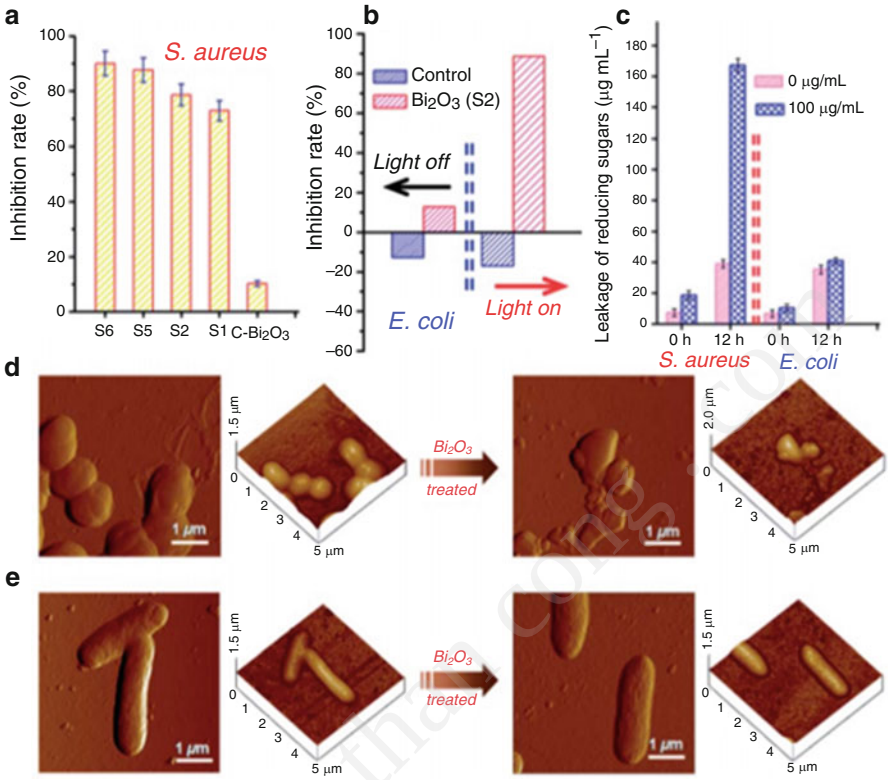

Fig. 4.1 (**a**) Inhibition rate of Bi_2O_3 nanospheres and C-Bi_2O_3 against *S. aureus*, (**b**) inhibition rate of Bi_2O_3 PNs (S2) against *E. coli* upon VL irradiation off (*left*) and on (*right*), (**c**) leakage of reducing sugars from bacteria cells of *S. aureus* (*left*) and *E. coli* (*right*) treated with Bi Bi_2O_3 PNs (S2), (**d** and **e**) topography images of *S. aureus* (**d**) and *E. coli* (**e**) cells before and after Bi_2O_3 PN (S2) treatment (Reprinted from Ref. [27] Copyright © 2014 Royal Society of Chemistry)

about 7 log of bacterial cells was achieved after 120 min of irradiation in the presence of 100-mg/L m-Bi_2O_4 (Fig. 4.2). This bacterial inactivation activity is much higher than many of the reported photocatalysts for disinfection, including B–Ni–TiO_2 [29], $CdIn_2S_4$ [30], natural sphalerite [31], and g-C_3N_4/graphene co-wrapped α-S_8 [32] under identical experimental conditions.

Recently, BiOX (X = F, Cl, Br, and I), as an important class of V–VI–VII ternary oxide semiconductors, have attracted much attention due to their unique structure and corresponding electronic and optical properties. The internal electric fields form between $[Bi_2O_2]^{2+}$, and the halogen atom layers are effective in accelerating the transport and improving the separation of photo-induced electron–hole pairs and thus have demonstrated excellent photocatalytic and photoelectrochemical performances in the field of water splitting, decomposition of toxic pollutants, as well as inactivation of bacteria [33–35]. Wu et al. [36] synthesized BiOBr nanosheets with fully exposed {001} and {010} facets via a

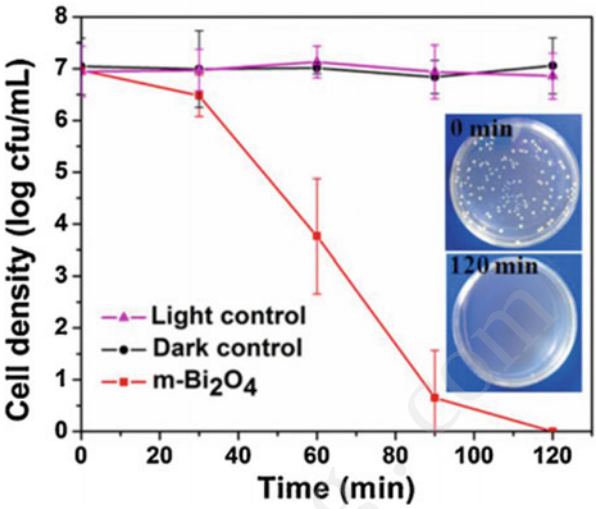

Fig. 4.2 Photocatalytic inactivation efficiency against *E. coli* K-12 (2×10^7 cfu/mL, 50 mL) in the presence of m-Bi_2O_4 (5 mg) under visible light irradiation (Reprinted from Ref. [28] Copyright © 2015 Elsevier)

facile hydrothermal method. In comparison with BiOBr with dominant {010}-facet (B010) nanosheets, BiOBr with dominant {001}-facet (B001) nanosheets exhibit remarkably higher photocatalytic activity in bacterial inactivation. The B001 nanosheets can completely inactivate 10^7 colony-forming unit (cfu)/mL^{-1} bacterial cells within 2 h, while only 1- and 6.5-log reduction of bacterial cells can be achieved within 2 and 6 h, respectively. The superior activity is ascribed to the more favorable separation and transfer of photogenerated electron–hole pairs as well as more oxygen vacancies of B001 nanosheets (Fig. 4.3).

Jamil et al. [37] prepared BiOI photocatalysts via solvothermal method using ethylene glycol (BiOI-EG) and hydrothermal method using distilled water (BiOI-DW). The experimental results showed that the photocatalytic inactivation efficiency of *Escherichia coli* strain (10^5 cfu/mL) using 0.75-g/L BiOI-EG was almost totally removed within 45 min under visible light, which was significantly higher than that of BiOI-DW. This can be ascribed to the high specific surface area of BiOI-EG (410 m^2/g) as compared to that of the BiOI-DW (296.6 m^2/g) and the difference in the morphology of both prepared catalysts. The enhanced larger surface area could absorb more light and increase active sites to improve the photocatalytic performance. Moreover, both of the catalyst exhibited excellent deactivation of *E. coli* under visible irradiation even after eight runs.

4.2.2 Bismuth Metallates

Bismuth metallates ($BiVO_4$, Bi_2WO_6, and Bi_2MoO_6) have gained much interest in the field of photocatalytic inactivation because of their high efficiency and visible light-responsive bacterial inactivation activity. $BiWO_6$ is the simplest member of

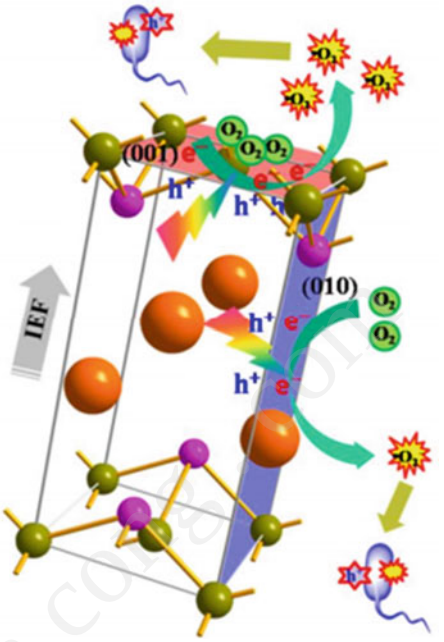

Fig. 4.3 Proposed mechanism of facet-dependent VLD bacterial inactivation of BiOBr nanosheets (Reprinted from Ref. [36] Copyright © 2009 Royal Society of Chemistry)

the *Aurivillius* family (when n = 1) with general formula $Bi_2A_{n-1}B_nO_{3n+3}$ (A = Ca, Sr, Ba, Pb, Bi, Na, K and B = Ti, Nb, Ta, Mo, W, Fe), which usually have the layer structures and unique properties [38]. It has been found that Bi_2WO_6 exhibits the highest photocatalytic activity among the above Bi^{3+}-based oxides under visible light irradiation [39]. Ren et al. [40] fabricated visible light-induced Bi_2WO_6 with the size of ca. 30 nm through a template-free hydrothermal method and investigated its photocatalytic bactericidal capability. The result showed that the inactivation efficiency of the as-prepared Bi_2WO_6 toward *E. coli* was up to 95 % after 2-h visible light irradiation with catalyst concentration of 0.5 mg/mL. The photocatalytic inactivation rate of *E. coli* with Bi_2WO_6 followed pseudo-first-order kinetics. And the Bi_2WO_6 photocatalyst also exhibited good stability in the photocatalytic process. The visible LED (Light Emitting Diode) has been widely used in outdoor and indoor lightings, and they provide different lights of varying monochromatic wavelengths. LED is far more efficient in converting electricity into light because the light emission by LED is induced by the recombination of excessive electrons and holes. Moreover, they have a long lifetime of more than 100,000 h and are much more rugged and compact than incandescent lamps. Thus, in order to harness the light emitted by visible LED, Wang et al. [41] prepared Bi_2MoO_6 photocatalyst and investigated its disinfection ability toward *E. coli* for the first time. The light source they used was a 3-W blue LED (λ = 465 nm). The main emission wavelength of the blue LED is within the absorption range of the Bi_2MoO_6 (500 nm), making Bi_2MoO_6 a good photocatalytic potential under the blue LED irradiation. The results demonstrated that *E. coli* inactivation efficiency of the Bi_2MoO_6

reached 95.3% after 6 h under LED illumination, while neither LED irradiation with photocatalyst nor Bi_2MoO_6 in the dark exhibited much bactericidal effects on *E. coli*, which proved that the inactivation of *E. coli* could be attributed to the photocatalytic reaction of the Bi_2MoO_6 under blue LED irradiation. $BiVO_4$ is also one of the visible-light-driven semiconductor photocatalysts that has been widely studied owning to their steep absorption edges in the visible light region. $BiVO_4$ has three main crystal structures, namely, tetragonal zircon, tetragonal scheelite, and monoclinic scheelite. The monoclinic scheelite phase of $BiVO_4$ has a band gap of 2.4 eV and has been demonstrated to exhibit much higher photocatalytic activity than the other two phases [42]. Monoclinic $BiVO_4$ nanotube was synthesized through a template-free solvothermal method by Wang et al. [43] and was used as a visible-light-driven photocatalyst for inactivation of *E. coli* K-12. The result showed that the photocatalytic efficiency was dependent on the concentration of $BiVO_4$ nanotube, the inactivation efficiency was proportionally increased, and the complete inactivation efficiency was achieved within 5 h when the catalyst concentration was 0.2 mg/ml. It is noticeable that no detectable bacterial count was observed after 96-h incubation period, indicating that the photocatalytic inactivation by the $BiVO_4$ nanotube leads to irreversible damage to *E. coli* K-12. Moreover, a partition system with pore size less than 5 nm was used to investigate whether the direct contact between photocatalyst and bacterial cell was required for an effective inactivation. The result showed the inactivation was mostly inhibited by the partition system, indicating the importance of direct contact between photocatalyst and bacterial cells. Adán et al. [44] prepared four $BiVO_4$ with different morphologies by using two different precipitating agents (NH_3 and triethylamine) following a hydrothermal treatment at different temperatures. The photocatalytic activity of the catalysts was investigated for the inactivation of *Escherichia coli* bacteria under both UV and visible light irradiation sources. Main results demonstrated that $BiVO_4$ were able to inactivate bacteria below the detection level. The photocatalytic activity of $BiVO_4$ was higher under UV light in comparison with the activity under visible light. The peanut-like $BiVO_4$ could favor higher visible light absorption and lower recombination process which presented better photocatalytic results under visible light (Fig. 4.4).

4.2.3 Plasmonic-Bismuth Compounds

Recently, various strategies have been explored to broaden photocatalyst response to visible light, including UV-activated elemental substitution [45], dye/nanocrystal-sensitized heterojunction [46], visible metal oxide composite, and noble metal depositing [47]. Of which, noble metal depositing on the surface of the semiconductor is considered as one of the most effective ways of improving photocatalytic performance. The surface plasmon resonance (SPR) of these noble metal nanocrystals has found to be excited and exhibits photocatalytic activity under visible light. This results from the fact that the noble metal can act as a sink for

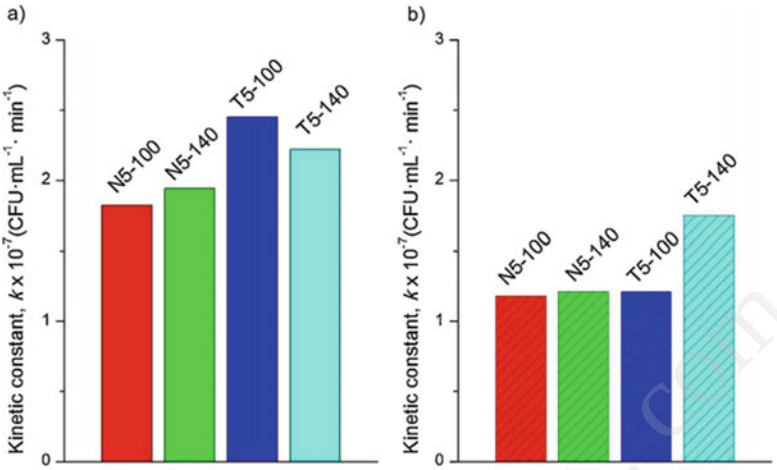

Fig. 4.4 Influence of $BiVO_4$ catalysts on the kinetic constants for inactivation of 10^6-cfu/mL^{-1} *E. coli* suspensions obtained under (**a**) UV–vis and (**b**) visible irradiation (Reprinted from Ref. [44] Copyright © 2015 Elsevier)

photo-induced electrons, thus promoting interfacial electron transfer process and enhancing the photocatalytic activity due to the high Schottky barriers at the metal–semiconductor interface. The SPR effect makes the transfer of energy to semiconductors easier in three ways: red shift of the absorption wavelength, increasing light scattering, and exciting electron–hole pairs by transferring plasmon energy from the metal to the semiconductor [48, 49]. Among all noble metals, silver is probably the most important material in plasmonics and has been widely used in the field of photocatalytic disinfection. For one reason, silver has the highest electrical and thermal conductivity among all metals, making it an ideal component for electrical interconnection; for another, silver can support a strong surface plasmon at a wide resonance wavelength from 300 to 1200 nm [50]. In addition, silver is relatively cost-effective and readily available , and Ag^+ itself exhibits bactericidal activity [51]. Considering the synergetic effect between the noble metal and semiconductor components, for the first time, Ag-loaded Bi_2WO_6 nanoparticles were prepared via a facile alcohol-thermal process by Ren et al. [52]. It is found that the metallic silver deposited on Bi_2WO_6 can significantly enhance the photocatalytic activity in the disinfection of *E. coli* when the Ag content is relatively lower, even eliminating the contribution of bactericidal effect brought by silver metal. However, higher Ag deposits conversely behave as recombinant centers, encouraging the recombination of charge carriers. *S. epidermidis*, a Gram-positive bacterium, was selected to confirm the photocatalytic inactivation ability of the Ag-loaded Bi_2WO_6. The Ag-loaded Bi_2WO_6 shows higher bactericidal activity for *E. coli* than *S. epidermidis*, which could be attributed to the different structures of Gram-positive (20–80-nm thick) and Gram-negative (10–15 nm) cell walls. The electrostatic interaction between bacteria and photocatalysts might be also used to

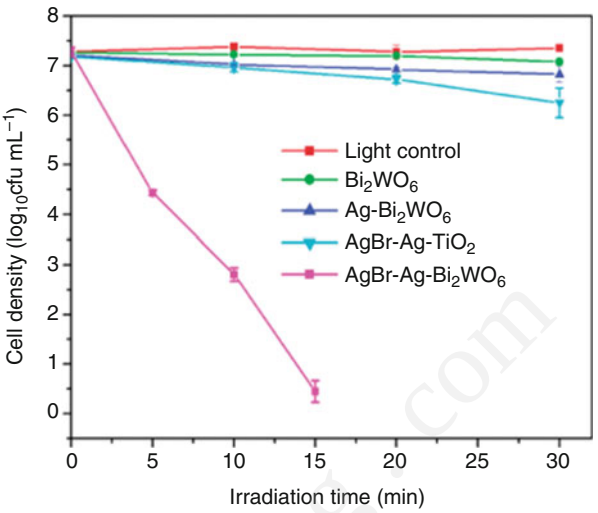

Fig. 4.5 Temporal course of the *E. coli* K-12 inactivation (~5×10^7 cfu/mL^{-1}, 50 mL) in aqueous dispersions containing different catalysts with the same weight of each VLD component under VL irradiation (Reprinted from Ref. [53] Copyright © 2010 American Chemical Society)

interpret this phenomenon. Zhang et al. [53] synthesized an AgBr–Ag–Bi_2WO_6 nanojunction through a hydrothermal method followed by a deposition–precipitation method. The AgBr–Ag–Bi_2WO_6 nanojunction has a Z-scheme structure, where a completely separated VB-hole (Bi_2WO_6) and CB-electron (AgBr) can be generated under visible light irradiation. Therefore, the visible-light-driven AgBr–Ag–Bi_2WO_6 nanojunction could completely inactivate 5×10^7-cfu/mL^{-1} *E. coli* K-12 within 15 min, which was superior to Bi_2WO_6 Ag–Bi_2WO_6 and AgBr–Ag–TiO_2 composite (Fig. 4.5). Noticeably, direct contact between the AgBr–Ag–Bi_2WO_6 nanojunction and bacterial cells was not necessary for the photocatalytic disinfection of *E. coli* K-12.

Ag/BiOI composites were prepared by a solvothermal process and subsequent photodeposition method and were used for photocatalytic disinfection of *E. coli* [54] and *E. coli* 8099 [55]. The deposited Ag can facilitate the surface-adsorbed O_2 to scavenge the photogenerated electrons from Ag/BiOI electrode, thus enhancing the photocatalytic disinfection efficiency of Ag/BiOI as compared to bare BiOI. The same conclusion was made by Booshehri et al. when using Ag/$BiVO_4$ for inactivation of *Escherichia coli* under visible light [56]. In their work, the rate of disinfection is almost doubled under natural sunlight compared to that under visible light ($\lambda > 420$ nm), which could be attributed to the UV content of the sunlight. Huang et al. [57] fabricated Ag/Ag_3PO_4 nanostructure-sensitized $BiPO_4$ photocatalyst using hydrothermal and impregnation processes. 15% Ag/Ag_3PO_4/$BiPO_4$ also exhibited excellent sunlight-induced photocatalytic disinfection activity toward *E. coli* cells. The enhanced photocatalytic performance and improved stability of Ag/Ag_3PO_4/$BiPO_4$ could be ascribed to the strong visible light absorption by Ag/Ag_3PO_4 nanostructures, a low electron–hole recombination rate as well as the highly efficient separation of photogenerated electron–hole pairs throughout Ag_3PO_4/$BiPO_4$heterostructures.

4.2.4 Other Bismuth-Based Composites

As previously mentioned, lots of bismuth oxides, oxyhalides, and metallates have been utilized for bacteria inactivation. However, the application of these materials is currently limited due to the low overall efficiency and rapid electron–hole recombination as well as the potentially poor surface chemistry. To overcome these problems, particular emphasis has been placed on complex/composite, hierarchical structure or heterojunction to facilitate the separation of photogenerated electron–hole pairs so as to improve the bactericidal performance. Semiconductor combination, which constructs a heterojunction interface between two types of semiconductors with matching energy band gaps, has been widely applied because it increases the lifetime of charge carriers, thus achieving better efficiency for the disinfection of bacteria in water [58]. Gan et al. [59] fabricated $Bi_2O_2CO_3/Bi_3NbO_7$ composite by a simple hydrothermal method. The conduction band of Bi_3NbO_7 is more negative than the corresponding band of $Bi_2O_2CO_3$, and the valence band of $Bi_2O_2CO_3$ is more positive than that of Bi_3NbO_7. The formation of $Bi_2O_2CO_3/Bi_3NbO_7$ heterostructures is advantageous for the separation and transportation of charge carriers (Fig. 4.6) and thus exhibited an enhanced visible-light-driven bactericidal property as compared to Bi_3NbO_7 and P25.

Xu et al. [60] synthesized hierarchical β-Bi_2O_3/Bi_2MoO_6 heterostructured flower-like microspheres through one-step template-free solvothermal route. The Bi_2O_3/Bi_2MoO_6 displayed enhanced visible light photocatalytic activity (99.90 %) for the destruction of *E. coli* as compared to Bi_2O_3 (81.67 %) and Bi_2MoO_6 (84.17 %), respectively. In addition, the β-Bi_2O_3 endowed good stability of the microspheres, and the composite can be easily recycled by a simple filtration step; thus the second

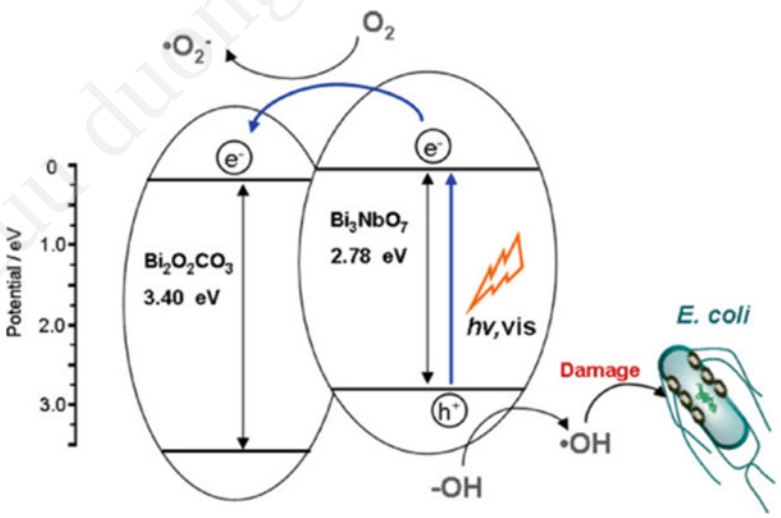

Fig. 4.6 Schematic illustration for energy bands structure, electron–hole separation, and transportation for the BiCO/BiNbO composite (Reprinted from Ref. [59] Copyright © 2013 Elsevier)

pollution can be effectively avoided. Similar hierarchical $Bi_2O_2CO_3/Bi_2MoO_6$ heterostructured photocatalysts were prepared and used for the destruction of *E. coli* by Xu et al. [61]. The composite semiconductor photocatalysts have also proven an effective way to expand the photoabsorption range and facilitate the separation of the photo-induced carriers. Hu et al. [62] prepared a monoclinic structure $SrBi_2O_4$ and $NiO/SrBi_2O_4$ composite by coprecipitation method. The results indicated that monoclinic structure $SrBi_2O_4$ showed visible light activity, and its bactericidal activity was greatly enhanced when further loaded with NiO, which would be ascribed to NiO promoting the electron–hole separation and interfacial charge transfer. The photocatalytic inactivation of pathogenic bacteria in water was investigated systematically with $NiO/SrBi_2O_4$ under visible light irradiation by Xu et al. [63]. Based on the investigation of experimental work such as pH, methanol, and inorganic ion study, they concluded that the electrostatic force interaction of bacteria–catalyst is crucial for high bactericidal efficiency. Some other bismuth-based composites such as $Cu_2O–CuO/Sr_3BiO_{5.4}$ [64] and Ag_2S/Bi_2S_3 [65] have also proven to be efficient for the photocatalytic inactivation against *E. coli* under visible light irradiation. Graphene, as a single layer of graphite, has gained tremendous attention recently, owning to its unique high specific surface area, two-dimensional structure, and extraordinary electronic properties. These unique physicochemical properties endow graphene great potential in environmental and energy applications [66–68]. Zhang et al. [69] synthesized Bi_2MoO_6–RGO composite nanoplates with good uniformity and highly oriented growth of the active lattice by a simple hydrothermal process. Interestingly, the presence of graphene could lead to the growth of Bi_2MoO_6 along the planary direction of graphene, forming a crystal with a highly ordered orientation, and the fine preferential growth of the Bi_2MoO_6–RGO nanoplates in the (020) and (002) directions is realized. Moreover, the photocatalytic disinfection property of the Bi_2MoO_6–RGO nanocomposite was enhanced greatly, which could be ascribed to the high orientation of Bi2MoO6, which effectively enhanced the separation of the photogenerated electrons and holes, as well as enabled the longer electron lifetime on the excited materials, because the electrons are injected into the graphene instantly at the site of generation, leading to a minimized charge recombination.

4.3 Bacterial Disinfection Process

It is generally believed that the bactericidal activity consists of two steps: first, disordering of the outer membrane in the cell envelope occurs, followed by the disordering of the inner membrane [70]. Transmission electron microscopy (TEM), atomic force microscopy (AFM), and BacLight kit fluorescent microscopy are frequently used to record the morphology and structure of bacteria before and after bactericidal experiment. In the bismuth vanadate nanotube (BV-NT) photocatalytic system under visible light irradiation [43], as can be seen from the

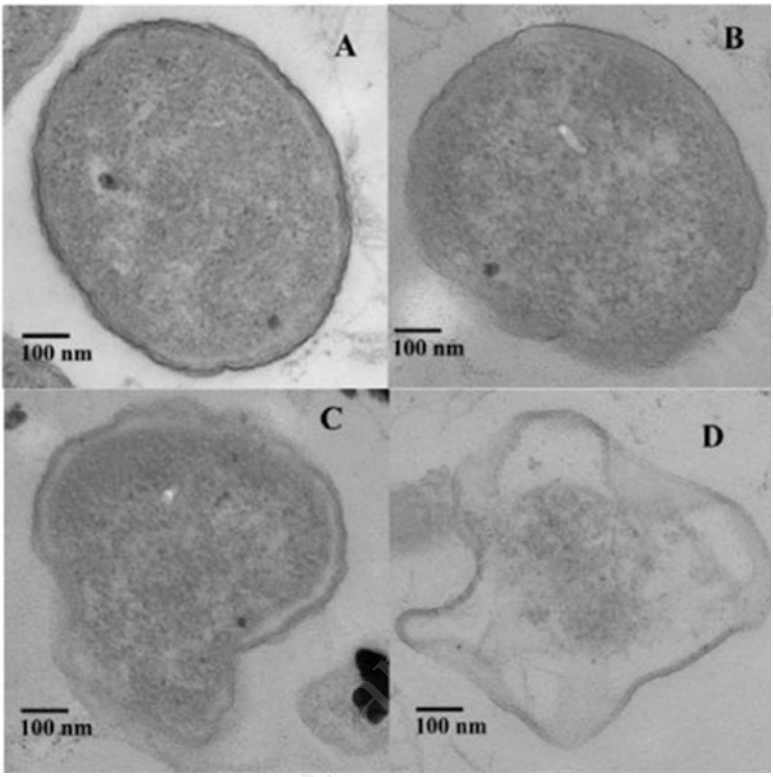

Fig. 4.7 TEM images of *E. coli* K-12 (2×10^7 cfu/mL, 50 mL) photocatalytically treated with BV-NT (100 mg/L) under VL irradiation. (**a**) 0 h, (**b**) 10 h, (**c**) 20 h, and (**d**) 32 h (Reprinted from Ref. [43] Copyright © 2012 American Chemical Society)

TEM images (Fig. 4.7), the cell of *E. coli* K-12 exhibits a well-defined cell wall and evenly colored interior, after 10-h irradiation; the central portion (cytoplasm) of the cell is still intact, but part of the cell wall structure appears obscure, indicating initial damage to the cell wall and cytoplasmic membrane. When further increasing the irradiation time to 20 h, part of the cell wall and cytoplasmic membrane is completely destroyed with an even more severe leakage of the intracellular components. Finally, after 32 h of irradiation, the cell becomes almost translucent, leaving only a distortional shape of the cell wall with little cytoplasmic components inside the cell. Based on these observations, they come to the conclusion that the destruction process of the cell is to begin from the cell wall to other cellular components, and due to the crucial role of direct contact between bacterial cell and BV-NT, the first attack site of bacterial cell is expected to be the cell wall and cytoplasmic membrane.

To understand the different antibacterial effects of Bi_2O_3 nanospheres toward *S. aureus* and *E. coli*, Qin et al. [27] used AFM to observe the topography changes of bacterial cell walls of *S. aureus* treated with Bi_2O_3. *S. aureus* cells show obvious

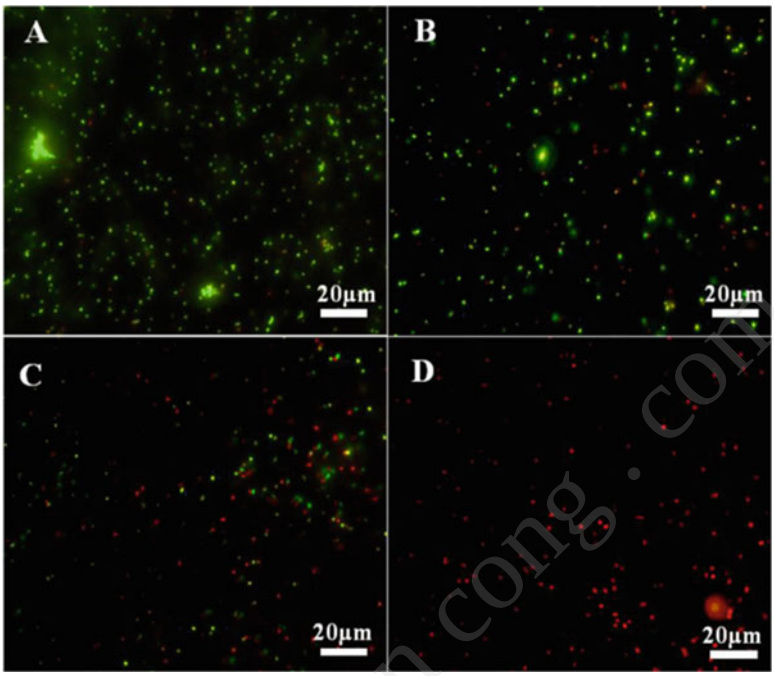

Fig. 4.8 Fluorescence microscopic images of *E. Coli* K-12 (2×10^7 cfu/mL, 50 mL) photocatalytically treated by m-Bi_2O_4 (5 mg) under visible light irradiation for (**a**) 0, (**b**) 30, (**c**) 60, and (**d**) 120 min (Reprinted from Ref. [28] Copyright © 2012 Elsevier)

bacterial membrane destruction and intracellular content leakage after 2-h incubation with Bi_2O_3 porous nanospheres (Fig. 4.1). Wang et al. [28] applied the BacLight kit fluorescent microscopic method to investigate the photocatalytic bacterial disinfection process of the monoclinic m-Bi_2O_4 toward *E. coli* K-12. The untreated and treated cells were stained with the mixtures of SYTO 9 green-fluorescent nucleic acid stain and the red-fluorescent nucleic acid stain, propidium iodide, which are typical cell-labeling dyes, respectively, for the detection of living and dead bacteria. As can be seen from Fig. 4.8, some bacterial cells exhibited red fluorescence after 30-min irradiation, which suggested partial amounts of the cells were inactivated. With prolonged irradiation time, rare and no green fluorescence could be observed after 60 and 120 min, respectively, indicating the excellent photocatalytic disinfection performance of m-Bi_2O_4 toward *E. coli* K-12.

The damage of bacteria can also be observed through FT-IR measurements on the bacterial cells before and after photocatalytic process, which is confirmed by Ren et al. [40] during the photocatalytic inactivation process of *E. coli* by Bi_2WO_6.

As we know, the cell membrane is of great importance to maintain the viability of cells. The K^+ ion leakage is usually monitored during the inactivation process because K^+ as a component in bacteria cells universally plays a role in the regulation of polysome content and protein synthesis [71]. To investigate the

permeability of the cell membrane, the K^+ leakage during different inactivation process was recorded by Gan et al. [59]. There was nearly the same K^+ leakage from *E. coli* cells without the catalyst under visible light irradiation and with the catalyst in dark. However, with the catalyst under visible light irradiation, the K^+ concentration was promptly increased with increasing the irradiation time, which indicates that the cell membrane permeability had been disrupted with the inactivation of *E. coli*. The damage in the membrane structure would also result in the leakage of reducing sugars. As investigated by Qin et al. [27], the leakage amount of reducing sugars from *S. aureus* cells treated with Bi_2O_3 is up to 167.1 μg mL^{-1}, but only 39 μg mL^{-1} in the control experiment (Fig. 4.1b, c), suggesting that Bi_2O_3 porous nanospheres may accelerate the reducing sugar leakage from *S. aureus* bacterial cytoplasm.

4.4 Bacterial Disinfection Mechanism

Defining the mechanism which results in bacteria inactivation has been the preoccupation of many researchers. There is still much debate over how or which process leads to death of an organism exposed to photocatalytic action. Till now, most of the bacterial disinfection processes by Bi-based photocatalysts were explained using the fundamental mechanism of photocatalytic oxidation process for the case of TiO_2 photocatalyst activated by UV light [72–74], which can be divided into three steps:

1. Electron–hole pairs would be generated when a semiconductor absorbs the energy of incident light having equivalent or excess energy to the band gap. This means that an electron in the valance band could only overcome the band gap and reach the conduction band with the concomitant vacancy in the valance band (the hole) when it gains sufficient energy. For TiO_2, the band gap can be overcome with energy from near UV photons. Fortunately, most of Bi-based semiconductor can be activated under visible light irradiation. It was reported that the photocatalytic inactivation of *E. coli* K-12 by $BiVO_4$ was higher under UV light in comparison with the activity under visible light. As reported by Booshehri et al. [56], the rate of disinfection by the Ag/$BiVO_4$ is almost doubled under natural sunlight compared to that under visible light ($\lambda > 420$ nm), which could be attributed to the UV content of the sunlight. However, it is worth noting that some of the bismuth compounds possess antimicrobial property even without light irradiation.
2. Once excited, the electrons (e^-) in the valence band will jump into the conduction band leaving holes (h^+) in the valence band simultaneously, then superoxide anions ($\bullet O_2^-$) would be generated when e^- is trapped by dissolved O_2 in water, and •OH (hydroxyl radicals) would be generated when h^+ reacts with surface water or OH^-. One problem that should be highlighted is that the electronic potential of conduction band should be more negative than the redox potentials

for $O_2/•O_2^-$, while the electronic potential of valence band should be more positive than the redox potentials for $•OH/OH^-$. Another problem which should be taken into consideration is that the photogenerated e^- and h^+ would recombine easily before they arrived at the surface of the semiconductor. Various methods such as facet/morphology control, metal/nonmetal doping, heterojunction/hierarchical structure formation, and creating oxygen vacancies are generally used to promote the separation of electrons and holes. Photoluminescence (PL) spectra, electrochemical impedance spectra (EIS), electron paramagnetic resonance (EPR) spectra, and transient photocurrent response are used to confirm the promoted separation of electrons and holes. A weaker intensity of PL peak represents a lower recombination probability of free charges. It was reported by Ren et al. [52] that there was a significant decrease in the intensity of PL spectra of Ag-loaded Bi_2WO_6 compared to that of pure Bi_2WO_6, indicating that Ag depositing could effectively inhibit the recombination of photogenerated charge carriers. To investigate the facet-dependent photocatalytic inactivation of *E. coli* by BiOBr, Wu et al. [36] analyzed the transient photocurrent responses of {001}- (B001) and {010} (B010)-facet exposed BiOBr. The result showed that B001 nanosheets present a distinctly higher current density, about four times than that of B010 nanosheets, manifesting an enhancement of the separation efficiency of electrons and holes. The EIS measurements were also employed to confirm the result. Compared with B010 nanosheets, B001 nanosheets displayed a smaller arc radius, which means a more effective interfacial charge transfer and separation of photogenerated electrons and holes. Moreover, from EPR result, a remarkable broad resonance signal can be observed for B001, which can be ascribed to the trapped electrons from oxygen vacancies. The oxygen vacancy could affect the charge transfer and separation process and thus would play a very important role in the photocatalytic inactivation activity.

3. The oxidative species attack the objects, resulting in the degradation of organic compounds and the inactivation of microorganisms. Sunada et al. [70] concluded that the first step of the photocatalytic inactivation process was the disordering of the outer membrane. This process is necessary for the inner membrane penetration of reactive species produced by photocatalysis. The second step was the disordering of the inner membrane (the cytoplasmic membrane). It is generally believed that $•OH$, $•O_2^-$, and H_2O_2 are responsible for the destruction of bacteria. The inactivation of bacteria may also occur via h^+ before it is trapped either within the semiconductor or at the semiconductor's surface. Booshehri [56] used fluorescence intensity of hydroxyterephthalate and UV–vis spectra of the solutions with nitroblue tetrazolium to confirm the generation of $•OH$ and $•O_2^-$, respectively. The detection of $•OH$ and $•O_2^-$ was carried out using 5,5-dimethylpyrroline N-oxide by Hu et al. [63]. To identify which reactive species play a major role in the bacterial inactivation by $BiVO_4$ nanotubes, the scavenging study was systematically performed by Wang et al. [43]. Table 4.1 summarizes some of the representative Bi-based photocatalysts with their synthesis methods, photocatalytic inactivation activities, and mechanisms.

Table 4.1 Representative Bi-based photocatalysts with their synthesis methods, photocatalytic inactivation activities, and mechanisms

Photocatalysts	Preparation method	Target bacteria	Efficiency	Catalyst dosage (mg/ml)	Reactive species	Light source	References
Ag/BiOI	Solvothermal + photodeposition	*E. coli*	$5*10^7$ cfu/ml in 60 min	0.5	–	Gallium iodine lamp (400 W)	[54]
Ag/$BiVO_4$	Precipitation + photodeposition	*E. coli*	10^7 cfu/ml in 3h	2	•OH $•O_2$	Xenon lamp (300 W)	[56]
AgBr–Ag–Bi_2WO_6	Hydrothermal + precipitation	*E. coli* K-12	$5*10^7$ cfu/ml in 15 min	0.1	•OH	Xenon lamp (300 W)	[53]
NiO/$SrBi_2O_4$	Precipitation	*E. coli*	$8*10^7$ cfu/ml in 50 min	0.2	•OH $•O_2$	Xenon lamp (350 W)	[63]
Ag–Bi_2WO_6	Alcohol–thermal	*E. coli*, *S. epidermidis*	$2*10^7$ cfu/ml in 15 min	0.5	•OH	Xenon lamp (500 W)	[52]
Ag/BiOI	Solvothermal + photodeposition	*E. coli* 8099	$5*10^7$ cfu/ml in 10 min	0.5	h^+/•OH O_2	Gallium iodine lamp (400 W)	[55]
Bi_2MoO_6–RGO	Hydrothermal	*E. coli* K-12	$5*10^5$ cfu/ml in 3 h	–	•OH	Xenon lamp	[69]
Bi_2O_3/Bi_2MoO_6	Solvothermal	*E. coli*	10^7 cfu/ml in 60 min	0.5	h^+/$•O_2$	Tungsten halide lamp (300 W)	[60]
$Bi_2O_2CO_3$/Bi_3NbO_7	Hydrothermal	*E. coli*	10^7 cfu/ml in 5 h	1	h^+/•OH	Xenon lamp (350 W)	[59]
Ag_2S/Bi_2S_3	Solvothermal	*E. coli*	$2.5*10^6$ cfu/ml in 100 min	1	•OH	Solar light	[65]
Bi_2MoO_6	Hydrothermal	*E. coli*	$2*10^7$ cfu/ml in 6 h	0.5	–	Blue LED (3 W)	[41]
m-Bi_2O_4	Hydrothermal	*E. coli* K-12	$2*10^7$ cfu/ml in 120 min	0.1	h^+/•OH	Xenon lamp (300 W)	[28]
$BiVO_4$	Hydrothermal	*E. coli*	$1*10^6$ cfu/ml in 4 h	0.5	h^+/•OH	Xenon car headlight lamp	[44]
NiO/$SrBi_2O_4$	Coprecipitation	*E. coli*	$5*10^6$ cfu/ml in 60 min	0.2	•OH $•O_2$	Xenon lamp (350 W)	[62]

Bi_2WO_6	Hydrothermal	*E. coli*	$2*10^7$ cfu/ml in 120 min	0.2–1	–	Xenon lamp (500 W)	[40]
BiOI	Hydrothermal	*E. coli*	10^5 cfu/ml in 45 min	0.75	h^+/•OH O_2	Metal halide lump (250 W)	[37]
Bi_2O_3	Solvothermal	*S. aureus*, *E. coli*	$5*10^4$ cfu/ml in 2h	$2*10^{-3}$	h^+/•OH O_2	Xenon lamp (500 W)	[27]
Ag/Ag_3PO_4/ $BiPO_4$	Hydrothermal + impregnation	*E. coli*	$1*10^3$ cfu/ml in 30 min	$2*10^{-6}$	h^+	Xenon lamp (150 W)	[57]
Cu_2O–CuO/ $Sr_3BiO_{5.4}$	Hydrothermal + precipitation	*E. coli* K-12	10^7 cfu/ml in 3 h	1	–	Fluorescent lamp (15 W)	[64]
BiOBr	Hydrothermal	*E. coli*	10^7 cfu/ml in 2 h	1	h^+/O_2	Fluorescent lamp (15 W)	[36]
$BiVO_4$ nanotube	Solvothermal	*E. coli* K-12	$2*10^5$ cfu/ml in 5h	0.1	h^+/•OH	Xenon lamp (300 W)	[43]
$Bi_2O_2CO_3$– Bi_2MoO_6	Template-free solvothermal	*E. coli*	10^7 cfu/ml in 60 min	0.5	–	Tungsten halide lamp (300 W)	[61]

4.5 The Summary and Future Outlook

Photocatalytic process has proven to be one of the most promising alternative water disinfection technologies. As has been stated in this chapter, a variety of Bi-based photocatalysts such as bismuth oxides and oxyhalides, bismuth metallates, plasmonic-bismuth compounds, and other bismuth composite photocatalysts have been adopted for photocatalytic inactivation of bacteria. The synthesis methods, modification technologies, and bacterial disinfection activities are reviewed. The bacterial disinfection process and mechanism have also been illustrated in detail. This progress has demonstrated that Bi-based photocatalysts are playing and will continue to play an important role in the bacterial disinfection field.

Although considerable progress has been achieved, the studies in this field are still at the primary stage, and further developments are required. Some of the important guidelines as established in the present work are as follows:

1. *E. coli* is used as the target bacteria in most of the studies; however, the photocatalytic disinfection mechanism is specific for different microorganisms. Thus, other bacteria should be applied to investigate the selectivity and general applicability of Bi-based photocatalysts.
2. To date, no specific study has explored to study the kinetics of photocatalytic inactivation process of Bi-based photocatalysts. Therefore, a robust mechanistic model is needed to determine the most efficient combination of different bacteria, contact time, catalyst dose, and light exposure.
3. Photocatalytic water inactivation technology will only be able to compete with conventional treatment if the cost of photocatalysts as well as the systems utilizing photocatalysts becomes comparable to the conventional methods. In this regard, economic analyses must take into consideration the benefit of lower photocatalysts cost as well as the cost associated with the potential environmental impacts in the event that photocatalysts escape from the treatment systems.
4. Bi-based materials provide a new promising class of photocatalysts that exhibit excellent bacterial disinfection activity. Many of the other Bi-based materials such as BiOCl, $BiFeO_3$, Ca-Bi_2O_4, $Bi_xTi_yO_z$, and metal (Cr, La, Ce) doped bismuth-composites, which exhibit good photocatalytic performance for the degradation of organic contaminants, may also possess bacterial disinfection activity under visible light irradiation.

References

1. Burch JD, Thomas KE (1998) Water disinfection for developing countries and potential for solar thermal pasteurization. Sol Energy 64:87–97
2. World Health Organization (2003) Emerging issues in water and infectious disease 1–22. World Health Organization, Geneva
3. Byrne JA, Fernandez-Ibanez PA, Dunlop PS, Alrousan D, Hamilton JW (2011) Photocatalytic enhancement for solar disinfection of water: a review. Int J Photoenergy 2011:1–12

4. Freuze I, Brosillon S, Laplanche A, Tozza D, Cavard J (2005) Effect of chlorination on the formation of odorous disinfection by-products. Water Res 39:2636–2642
5. Richardson SD (2003) Disinfection by-products and other emerging contaminants in drinking water. Trends Anal Chem 22:666–684
6. Huang WJ, Fang GC, Wang CC (2005) The determination and fate of disinfection by-products from ozonation of polluted raw water. Sci Total Environ 345:261–272
7. Fujishima A, Honda K (1972) Electrochemical photolysis of water at a semiconductor electrode. Nature 238:37–38
8. Kubacka A, Fernández MG, Colón G (2011) Advanced nanoarchitectures for solar photocatalytic applications. Chem Rev 112:1555–1614
9. Kudo A, Miseki Y (2009) Heterogeneous photocatalyst materials for water splitting. Chem Soc Rev 38:253–278
10. Meng N, Leung MKH, Leung DYC, Sumathy K (2007) A review and recent developments in photocatalytic water-splitting using TiO_2 for hydrogen production. Renew Sust Energ Rev 11:401–425
11. Mor GK, Shankar K, Paulose M, Varghese OK, Grimes CA (2006) Use of highly-ordered TiO_2 nanotube arrays in dye-sensitized solar cells. Nano Lett 6:215–218
12. Matsunaga T, Tomoda R, Nakajima T, Wake H (1985) Photo-electrochemical sterilization of microbial cells by semiconductor powders. FEMS Microbiol Lett 29:211–214
13. Zhang L, Kanki T, Sano N, Toyoda A (2003) Development of TiO_2 photocatalyst reaction for water purification. Sep Purif Technol 31:105–110
14. Jiang L, Wang LZ, Zhang JL (2010) A direct route for the synthesis of nanometer-sized Bi_2WO_6 particles loaded on a spherical MCM-48 mesoporous molecular sieve. Chem Commun 46:8067–8069
15. Zhang X, Ai ZH, Jia FL, Zhang LZ (2008) Generalized one-pot synthesis characterization, and photocatalytic activity of hierarchical BiOX (X = Cl, Br, I) nanoplate microspheres. J Phys Chem C 112:747–753
16. Yin WZ, Wang WZ, Zhou L, Sun SM, Zhang L (2010) CTAB-assisted synthesis of monoclinic $BiVO_4$ photocatalyst and its highly efficient degradation of organic dye under visible-light irradiation. J Hazard Mater 173:194–199
17. Chen XF, Dai JF, Shi GF, Li L, Wang GY, Yang H (2015) Visible light photocatalytic degradation of dyes by beta-Bi_2O_3/graphene nanocomposites. J Alloys Compd 649:872–877
18. Ding X, Ho W, Shang J, Zhang LZ (2016) Self doping promoted photocatalytic removal of NO under visible light with Bi_2MoO6: indispensable role of superoxide ions. Appl Catal B Environ 182:316–325
19. Zhang YL, Schultz AM, Salvador PA, Rohrer GS (2011) Spatially selective visible light photocatalytic activity of TiO_2/$BiFeO_3$ heterostructures. J Mater Chem 21:4168–4174
20. Manna G, Bose R, Pradhan N (2014) Photocatalytic Au-Bi_2S_3 heteronanostructures. Angew Chem Int Ed 53:6743–6746
21. Wang Y, Huang HW, Quan CM, Tian N, Zhang YH (2016) Hydrothermal fabrication of multi-functional Eu^{3+} and Tb^{3+} co-doped $BiPO_4$: photocatalytic activity and tunable luminescence properties. J Cryst Growth 433:1–6
22. Madhusudan P, Zhang J, Cheng B, Liu G (2013) Photocatalytic degradation of organic dyes with hierarchical $Bi_2O_2CO_3$ microstructures under visible-light. CrystEngComm 15:231–240
23. Hussain AM, Neppolian B, Shim HS, Kim SH, Kim SK, Choi HC et al (2010) Efficiency enhancement in bulk heterojunction polymer photovoltaic cells using $ZrTiO_4$/Bi_2O_3 metal-oxide nanocomposites. Jpn J Appl Phys 49:4R
24. Park S, Kim S, Sun GJ, Lee C (2015) Synthesis, structure, and ethanol gas sensing properties of In_2O_3 nanorods decorated with Bi_2O_3 nanoparticles. ACS Appl Mater Interfaces 7:8138–8146
25. Guan LL, He SF, Zhu XD, Liu T, Sun K (2015) Densification behavior and space charge blocking effect of Bi_2O_3 and Gd_2O_3 Co-doped CeO_2 as electrolyte for solid oxide fuel cells. Electrochim Acta 161:129–136

26. Sanchez MD, Juarez RI, Torres MLM, de Leon AI (2016) Photocatalytic properties of Bi_2O_3 powders obtained by an ultrasound-assisted precipitation method. Ceram Int 42:2013–2020
27. Qin F, Zhao HP, Li GF, Yang H, Li J, Wang RM et al (2014) Size-tunable fabrication of multifunctional Bi_2O_3 porous nanospheres for photocatalysis, bacteria inactivation and template-synthesis. Nanoscale 6:5402–5409
28. Wang WJ, Chen XQ, Liu G, Shen ZR, Xia DH, Wong PK et al (2015) Monoclinic dibismuth tetraoxide: a new visible-light-driven photocatalyst for environmental remediation. Appl Catal B Environ 176:444–453
29. Wang WJ, Zhang LS, An TC, Li GY, Yip HY, Wong PK (2011) Comparative study of visible-light-driven photocatalytic mechanisms of dye decolorization and bacterial disinfection by B–Ni-codoped TiO_2 microspheres: the role of different reactive species. Appl Catal B Environ 108–109:108–116
30. Wang WJ, Ng TW, Ho WK, Huang JH, Liang SJ, An TC et al (2013) $CdIn_2S_4$ microsphere as an efficient visible-light-driven photocatalyst for bacterial inactivation: synthesis, characterizations and photocatalytic inactivation mechanisms. Appl Catal B Environ 129:482–490
31. Chen YM, Lu AH, Li Y, Zhang LS, Yip HY, Zhao HJ et al (2011) Naturally occurring sphalerite as a novel cost-effective photocatalyst for bacterial disinfection under visible light. Environ Sci Technol 45:5689–5695
32. Wang WJ, Yu JC, Xia DH, Wong PK, Li YC (2013) Graphene and g-C_3N_4 nanosheets cowrapped elemental α-sulfur as a novel metal-free heterojunction photocatalyst for bacterial inactivation under visible-light. Environ Sci Technol 47:8724–8732
33. Zou SJ, Teng F, Chang C, Liu ZL, Wang SR (2015) Controllable synthesis of uniform BiOF nanosheets and their improved photocatalytic activity by an exposed high-energy (002) facet and internal electric field. RSC Adv 5:88936–88942
34. Dong F, Sun YJ, Fu M, Wu ZB, Lee SC (2012) Room temperature synthesis and highly enhanced visible light photocatalytic activity of porous BiOI/BiOCl composites nanoplates microflowers. J Hazard Mater 219:26–34
35. Fu J, Tian YL, Chang BB, Xi FN, Dong XP (2012) BiOBr-carbon nitride heterojunctions: synthesis, enhanced activity and photocatalytic mechanism. J Mater Chem 22:21159–21166
36. Wu D, Wang B, Wang W, An TC, Li GY, Ng TW et al (2009) Visible-light-driven BiOBr nanosheets for highly facet-dependent photocatalytic inactivation of Escherichia coli. J Mater Chem A 10:1940–1943
37. Jamil TS, Mansor ES, Liethy MAE (2015) Photocatalytic inactivation of E. coli using nano-size bismuth oxyiodide photocatalysts under visible light. J Environ Chem Eng 3:2463–2471
38. Li YY, Liu JP, Huang XT (2007) Synthesis and visible-light photocatalytic property of Bi_2WO_6 hierarchical octahedron-like structures. Nanoscale Res Lett 3:365–371
39. Finlayson AP, Tsaneva VN, Lyons L, Clark M, Glowacki BA (2006) Evaluation of Bi-W-oxides for visible light photocatalysis. Phys Status Solidi (a) 203:327–335
40. Ren J, Wang WZ, Zhang L, Chang J, Hu S (2009) Photocatalytic inactivation of bacteria by photocatalyst Bi_2WO_6 under visible light. Catal Commun 10:1940–1943
41. Zhang ZJ, Wang WZ, Ren J, Xu JH (2012) Highly efficient photocatalyst Bi_2MoO_6 induced by blue light-emitting diode. Appl Catal B Environ 123–124:89–93
42. Fan HM, Jiang TF, Li HY, Wang DJ, Wang LL, Zhai JL (2012) Effect of $BiVO_4$ crystalline phases on the photoinduced carriers behavior and photocatalytic activity. J Phys Chem C 116:2425–2430
43. Wang WJ, Yu Y, An TC, Li GY, Yip HY, Yu JC (2012) Visible-light-driven photocatalytic inactivation of E. coli K-12 by bismuth vanadate nanotubes bactericidal performance and mechanism. Environ Sci Technol 46:4599–4606
44. Adán C, Marugán J, Obregón S, Colón G (2015) Photocatalytic activity of bismuth vanadates under UV-A and visible light irradiation: inactivation of Escherichia coli vs oxidation of methanol. Catal Today 240:93–99
45. Asahi R, Morikawa T, Ohwaki T, Aoki K, Taga Y (2001) Visible-light photocatalysis in nitrogen-doped titanium oxides. Science 293:269–271

46. Lee YL, Lo YS (2009) Highly efficient quantum-dot-sensitized solar cell based on co-sensitization of CdS/CdSe. Adv Funct Mater 19:604–609
47. Amano F, Yamakata A, Nogami K, Osawa M, Ohtani B (2008) Visible light responsive pristine metal oxide photocatalyst: enhancement of activity by crystallization under hydrothermal treatment. J Am Chem Soc 130:17650–17651
48. Atwater HA, Polman A (2010) Plasmonics for improved photovoltaic devices. Nat Mater 9:205–213
49. Cushing SK, Li J, Meng F, Senty TR, Suri S, Zhi M et al (2012) Photocatalytic activity enhanced by plasmonic resonant energy transfer from metal to semiconductor. J Am Chem Soc 134:15033–15041
50. Rycenga M, Cobley CM, Zeng J, Li WY, Moran CH, Zhang Q et al (2011) Controlling the synthesis and assembly of silver nanostructures for plasmonic applications. Chem Rev 111:3669–3712
51. Copcoa VE, Luchian C, Dunca S, Bilba N, Hristodor CM (2011) Antibacterial activity of silver-modified natural clinoptilolite. J Mater Sci 46:7121–7128
52. Ren J, Wang WZ, Sun SM, Zhang L, Chang J (2009) Enhanced photocatalytic activity of Bi_2WO_6 loaded with Ag nanoparticles under visible light irradiation. Appl Catal B Environ 92:50–55
53. Zhang LS, Wong KH, Yip HY, Hu C, Yu JC, Chan CY et al (2010) Effective photocatalytic disinfection of E. coli K-12 using AgBr-Ag-Bi_2WO_6 nanojunction system irradiated by visible light: the role of diffusing hydroxyl radicals. Environ Sci Technol 44:1392–1398
54. Fang ZK, Yang JN, Cao Y, Zhu LF, Zhang Q, Shu D et al (2013) Disinfection of E. coli using visible-light-driven photocatalyst. Procedia Environ Sci 18:503–508
55. Zhu LF, Hu C, Huang YL, Chen ZH, Xia DH, Su MH et al (2012) Enhanced photocatalytic disinfection of E. coli 8099 using Ag/BiOI composite under visible light irradiation. Sep Purif Technol 91:59–66
56. Booshehri AY, Goh SCK, Hong JD, Jiang RR, Xu R (2014) Effect of depositing silver nanoparticles on $BiVO_4$ in enhancing visible light photocatalytic inactivation of bacteria in water. J Mater Chem A 2:6209–6217
57. Huang TY, Chen YJ, Lai CY, Lin YW (2015) Synthesis, characterization, enhanced sunlight photocatalytic properties, and stability of Ag/Ag_3PO_4 nanostructure-sensitized $BiPO_4$. RSC Adv 5:43854–43862
58. Chang XF, Yu G, Huang J, Li Z, Zhu SF, Yu PF et al (2010) Enhancement of photocatalytic activity over $NaBiO_3$/BiOCl composite prepared by an in situ formation strategy. Catal Today 153:193–199
59. Gan HH, Zhang GK, Huang HX (2013) Enhanced visible-light-driven photocatalytic inactivation of Escherichia coli by $Bi_2O_2CO_3$/Bi_3NbO_7 composites. J Hazard Mater 250–251:131–137
60. Xu YS, Zhang ZJ, Zhang WD (2013) Facile preparation of heterostructured Bi_2O_3/Bi_2MoO_6 hollow microspheres with enhanced visible-light-driven photocatalytic and antimicrobial activity. Mater Res Bull 48:1420–1427
61. Xu YS, Yu YX, Zhang WD (2014) Wide bandgap $Bi_2O_2CO_3$-Coupled Bi_2MoO_6 heterostructured hollow microspheres: one-pot synthesis and enhanced visible-light photocatalytic activity. J Nanosci Nanotechnol 14:6800–6808
62. Hu XX, Hu C, Qu JH (2006) Photocatalytic decomposition of acetaldehyde and Escherichia coli using NiO/$SrBi_2O_4$ under visible light irradiation. Appl Catal B Environ 69:17–23
63. Hu C, Hu XX, Guo J, Qu JH (2006) Efficient Destruction of pathogenic bacteria with NiO/$SrBi_2O_4$ under visible light irradiation. Environ Sci Technol 40:5508–5513
64. Zhao W, Wong KH, Hu C, Yu JC, Chan CY, Qi T et al (2012) Synthesize of Cu_2O-CuO/$Sr_3BiO_{5.4}$ and its photocatalytic activity. Appl Surf Sci 258:5955–5959
65. Sun B, Qiao Z, Shang K, Fan H, Ai SY (2013) Facile synthesis of silver sulfide/bismuth sulfide nanocomposites for photocatalytic inactivation of Escherichia coli under solar light irradiation. Mater Lett 91:142–145

66. Novoselov KS, Geim AK, Morozov SV, Jiang D, Zhang Y, Dubonos SV et al (2004) Electric field effect in atomically thin carbon films. Science 306:666–669
67. Geim AK, Novoselov KS (2007) The rise of graphene. Nat Mater 6:183–191
68. Ruoff R (2008) Graphene: calling all chemists. Nat Nanotechnol 3:10–11
69. Zhang Y, Zhu YK, Yu JQ, Yang DJ, Ng TW, Wong PK et al (2013) Enhanced photocatalytic water disinfection properties of Bi_2MoO_6–RGO nanocomposites under visible light irradiation. Nanoscale 5:6307–6310
70. Sunada K, Kikuchi Y, Hashimoto K, Fujishima A (1998) Bactericidal and detoxification effects of TiO_2 thin film photocatalysts. Environ Sci Technol 32:726–728
71. Wang WJ, Huang GC, Yu JC, Wong PK (2015) Advances in photocatalytic disinfection of bacteria development of photocatalysts and mechanisms. J Environ Sci 34:232–247
72. Linsebigler AL, Lu GQ, Yates JT (1995) Photocatalysis on TiO_2 surfaces-principles, mechanisms, and selected results. Chem Rev 95:735–758
73. Fujishima A, Zhang XT, Tryk DA (2008) TiO_2 photocatalysis and related surface phenomena. Surf Sci Rep 63:515–582
74. Yuan JX, Wang EJ, Chen YM, Yang WS, Yao JH, Cao YA (2011) Doping mode, band structure and photocatalytic mechanism of B-N-codoped TiO_2. Appl Surf Sci 257:7335–7342

Chapter 5
Synthesis and Performance of Silver Photocatalytic Nanomaterials for Water Disinfection

Yongyou Hu and Xuesen Hong

Abstract As a new generation of antimicrobial materials, silver nanoparticles have shown great potential in water disinfection due to its broad-spectrum antimicrobial activities. Besides, silver nanoparticles can prevent photogenerated electron-hole recombination by trapping electron and increase visible light absorption through the surface plasmon resonance enhancement, which exhibit excellent capability in enhancing photocatalytic efficiency of traditional photocatalysts, such as TiO_2, AgX (X = Cl, Br, I), and ZnO. And the photocatalysis has been widely demonstrated to inactivate microorganisms in water, which offers a low-cost, environmentally friendly, and sustainable method to achieve water disinfection. Therefore, many efforts have been made on the development and study of silver photocatalytic nanomaterials for water disinfection, and silver photocatalytic nanomaterials have shown effective antimicrobial activities through multiple mechanisms under both light and dark conditions. This chapter reviews the recent studies that are focused on the synthesis, disinfection performance, and mechanisms of silver-modified photocatalytic nanomaterials, including Ag-TiO_2, Ag-AgX (X = Cl, Br, I), and Ag-ZnO. The potential disinfection mechanisms of different types of photocatalytic nanomaterials are discussed, such as photocatalysis, antimicrobial effect of silver ions, and physical attack. And different synthesis methods of nanomaterials are also summarized, including reaction steps and parameters. Furthermore, the disinfection performance of different silver photocatalytic nanomaterials is compared. This chapter will offer useful scientific and technical information for the development and synthesis of new types of silver photocatalytic nanomaterials.

Keywords Silver nanoparticles • TiO_2 • Silver halides • ZnO • Photocatalytic nanomaterials • Photocatalysis • Antimicrobial • Water disinfection

Y. Hu (✉)
School of Environment and Energy, South China University of Technology, Guangzhou, China
e-mail: ppyyhu@scut.edu.cn

X. Hong
School of Civil Engineering and Transportation, South China University of Technology, Guangzhou, China
e-mail: scuthxs@outlook.com

T. An et al. (eds.), *Advances in Photocatalytic Disinfection*, Green Chemistry and Sustainable Technology, DOI 10.1007/978-3-662-53496-0_5

5.1 Introduction

5.1.1 The Antimicrobial Property of Silver Nanoparticles

Because of strong antimicrobial activity, broad antimicrobial spectrum, and low human toxicity, silver has been used as an effective bactericidal agent in the medical field for centuries. In the seventeenth and eighteenth centuries, silver nitrite was applied in the treatment of ulcers, venereal diseases, and fistulae from salivary glands [1, 2]. And 1 % silver nitrate eye drops were first used to prevent gonococcal conjunctivitis for newborn babies around 1884 [3]. In the first half of the twentieth century, silver was used as aqueous colloidal dispersion for oral consumption and the prevention of infection. But the antibiotics developed in the 1940s replaced the silver for the treatment of bacterial infections. Silver again came in picture when silver sulfadiazine cream was used in the treatment of burns in the 1960s, which contained silver nitrate and sulfonamide [1]. Recently, due to the emergence of antibiotic-resistant bacteria and limitations of the use of antibiotics, many researchers reconsider the potential application of silver in the antimicrobial treatment.

The development of nanotechnology realizes the controllable and reproducible synthesis of different types of silver nanoparticles (AgNPs). Meanwhile, the nanotechnology greatly changes and enhances the physicochemical properties of AgNPs. Among these physicochemical properties, the excellent antimicrobial activity against microorganism (including bacteria, fungi, and virus) has attracted the researchers' attention. Besides, in order to control the toxicity and enhance the antimicrobial efficiency, AgNPs successfully composite with many other materials, such as carbon fiber, porous ceramic, and polystyrene, which reduce the AgNP leakage, and improve their stability and diversity. Therefore, AgNPs have been widely used as antimicrobials in various consumer products including cosmetics, clothing, shoes, and water filters.

As shown in Fig. 5.1, the antimicrobial mechanisms of AgNPs are generally considered as a multi-factor, multi-way, and multi-target process, which are not yet fully understood [4–6]. However, there are three mainly acknowledged antimicrobial action modes of AgNPs:

1. Functional damage of free Ag^+ released by AgNPs. The released Ag^+ can interfere with the cell membrane permeability and disrupt the ATP production and DNA replication [7].
2. Oxidative stress of reactive oxygen species (ROS) produced by AgNPs and Ag^+. ROS plays an important role in many types of cellular injury, including breakdown of membrane, DNA damage, and apoptotic cell death [8, 9].
3. Direct damage to cell membranes by AgNPs. AgNPs interact with the cell membrane and are able to penetrate inside the cell, which cause the change in membrane permeability and leakage of intracellular contents [10, 11].

The physicochemical properties of AgNPs have been reported to influence the antimicrobial activity of AgNPs, including particle size, shape, crystalline, and capping agents. Smaller AgNPs exhibit stronger toxicity to bacteria because of

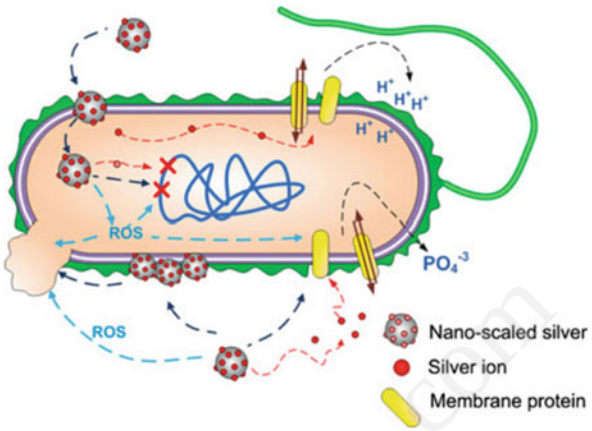

Fig. 5.1 Illustration of antibacterial mechanism of AgNPs (Reprinted from Ref. [10], with kind permission from Springer Science + Business Media)

larger specific surface area available for physicochemical interactions with cells [12, 13]. And {111} facets with higher reactivity enhance the antimicrobial activity of AgNPs, which make truncated triangular nanoplates exhibit stronger antimicrobial activity than spherical AgNPs [10]. In addition, the environment factors also make influence, such as irradiation, dissolved oxygen, pH, and ionic strength. Dissolved oxygen plays the important role in the oxidative dissolution of Ag^+ and production of ROS, both of which make a great influence on the antimicrobial activity [10]. And pH and ionic strength influence the surface potential of AgNPs and therefore dominate the aggregation of particles, which lead to the change of the antimicrobial activity [14, 15]. In order to synthesize high-performance AgNP antimicrobial materials, as well as make good use of these materials, it is necessary to understand the role of the above factors in the antimicrobial action of AgNPs.

5.1.2 The Photocatalytic Properties of Silver Nanoparticles

Since the discovery of the photocatalytic water splitting which occurred over TiO_2 during UV light irradiation in the 1970s [16], many researches have been carried out to exploit photocatalysis for promising applications ranging from environmental remediation and purification of contaminated air and water to self-cleaning applications. However, the conventional semiconductor photocatalysts, such as TiO_2 and ZnO, require high-energy UV radiation to accomplish photocatalytic process, which limits the wide application under visible light. The rise of noble metal nanoparticles fills the gaps, such as AgNPs. They are recognized as a new class of photocatalyst suitable for utilizing visible and ultraviolet light energy due to their high optical absorption over a wide range of the sunlight spectrum.

The localized surface plasmon resonance (LSPR) effect of noble metal nanoparticles causes the photocatalytic property of AgNPs. As shown in Fig. 5.2, LSPR is the resonant photon-induced coherent oscillation of charge at the metal-

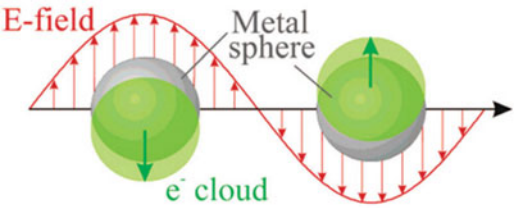

Fig. 5.2 Localized surface plasmon resonance due to coherent interaction of the electrons in the conduction band with light (Reproduced from Ref. [18] by permission of the Royal Society of Chemistry)

dielectric interface, established when the photon frequency matches the natural frequency of metal surface electrons oscillating against the restoring force of their positive nuclei. And the LSPR effect of AgNPs can couple the light flux to the conduction electrons of metal nanoparticles, and the excited electrons and enhanced electric fields nearby the nanoparticles can convert the solar energy to chemical energy by photon-driven photocatalytic reactions. This chemical energy results in high-energy electrons at the nanoparticle surface which is desirable for activating molecules for chemical reactions [17].

Several significant factors influence photocatalytic activity of AgNPs. The experiments of HCHO, benzyl alcohol, and SRB degradation have demonstrated that the photocatalytic activity of AgNPs is light intensity dependent, which can be enhanced with increasing light intensity [19]. Different from semiconductor photocatalysts, the photocatalytic ability of AgNPs can be tuned by changing the irradiation wavelength. The light with different wavelength makes different contribution to the photocatalytic ability [20]. And the effect of particle size on the photocatalytic activity of AgNPs is complicated because the LSPR effect is size dependent. Smaller nanoparticles have larger specific surface area but exhibit weaker LSPR effect, while bigger nanoparticles with less specific surface area have stronger LSPR effect [21]. Nanoparticle with appropriate particle size can both possess enough specific surface area for photocatalytic reaction and have suitable LSPR effect for harvesting light energy. The dependence of photocatalytic activity on light intensity, wavelength, and particle size indicates that the LSPR effect plays a key role in the photocatalysts of AgNPs.

5.1.3 The Potential of Silver Nanomaterials in the Photocatalytic Water Disinfection

Traditional water disinfection technologies such as chlorination, ozonization, and ultraviolet light can effectively inactivate the pathogens in water, which makes a great contribution to water quality. However, they have several disadvantages, such as the generation of potentially toxic disinfection by-products and ineffectiveness

against resistant microorganisms. The breakthrough work of the application of Pt-TiO_2 under irradiation for water disinfection offers photocatalysis an opportunity to address these shortcomings [22], because photocatalysis is a safe, nonhazardous, and eco-friendly process. However, the "bottleneck" of TiO_2 in the photocatalytic water disinfection is the inability to efficiently use solar light, which is composed of only 3–5 % UV. Additionally, slow reaction kinetics as a consequence of the recombination of photoexcited electrons and holes also limits the application of TiO_2 in the photocatalytic disinfection [23].

Modifying the traditional photocatalysts with noble metal nanoparticles is one strategy to improve the photocatalytic disinfection performance. Among the varieties of noble metal nanoparticles, the AgNPs are suitable for modified photocatalysts. The AgNPs on the surface of traditional photocatalysts cannot only act as traps to capture the photoinduced electrons and holes, which reduce the electron-hole recombination in the photocatalytic processes [24], but also increase the absorption of visible light due to the LSPR effect [25]. Furthermore, the intrinsic antimicrobial activity of AgNPs can improve the disinfection efficiency in the absence of irradiation. It is the photocatalytic and antimicrobial properties that make AgNPs particularly attractive in the development of metal-semiconductor composite photocatalysts, such as silver-titanium dioxide (Ag-TiO_2), silver-silver halides (Ag-AgX), and silver-zinc oxide (Ag-ZnO).

In this chapter, three major silver-semiconductor composites, Ag-TiO_2, Ag-AgX, and Ag-ZnO, are reviewed, highlighting their disinfection mechanism, synthesis, and photocatalytic disinfection performance. And the selected studies of photocatalytic disinfection using Ag-TiO_2, Ag-AgX, and Ag-ZnO are listed in Tables 5.1, 5.2, and 5.3, respectively. Through the systematic introduction of these silver-semiconductor composites, we attempt to provide assistance for researcher to design and synthesize new sunlight photocatalysts based on the comprehension of synergetic and individual role of silver and semiconductor in the photocatalytic disinfection.

5.2 Ag-TiO_2

5.2.1 Disinfection Mechanism of Ag-TiO_2

The exact antimicrobial mechanism of Ag-TiO_2 nanocomposites is still not known, but the possible mechanisms have been suggested, including disinfection action of photocatalysis and silver ions. Under light irradiation, a synergistic effect combining photocatalysis and Ag^+ is always exhibited. And the action of Ag^+ mainly causes antimicrobial activities in the dark. The direct contact with Ag-TiO_2 nanocomposites also contributes to the disinfection.

Table 5.1 Selected studies of photocatalytic disinfection using Ag-TiO_2 nanocomposites

Material	Synthesis	Photocatalytic performance	Disinfection test results	Disinfection mechanism	References
Ag-TiO_2 particles and Ag-TiO_2 films	Wet impregnation, UV photoreduction, and calcination	The deposition of AgNPs reduced the degradation of methylene blue	6 log removal of *E. coli* in 140 min by 0.8 wt% Ag-TiO_2 under irradiation, compared to 120 min in the dark	The bactericidal role of silver rather than the photocatalytic mechanism caused disinfection	[38]
Ag-TiO_2-anatase	Wet impregnation, calcination, and photodeposition	–	6 log removal of *E. coli* in 30 min by 1.0 wt% Ag-TiO_2 under irradiation; 1 log removal in the dark	The local-type modification of hydroxyl radicals formed upon light absorption by AgNPs governed photokilling activity	[28]
Nano-TiO_2@Ag/PVC film	Hydrothermal method, grafting, and doping	94 % of RhB was decomposed by 1.25 % nano-TiO_2@Ag/PVC film in 50 min, while 100 min for 0.63 % nano-TiO_2@Ag/PVC film	Nano-TiO_2@Ag/PVC film achieved 1.7 log removal of *E. coli* in the dark, while 3.3 log and 2.2 log under UV and solar irradiation, respectively	Ag^+ released from AgNPs and ROS photoinduced by TiO_2@Ag under irradiation caused the disinfection activity	[35]
Ag-TiO_2 film	Sol-gel spin-coating method, impregnation, and annealing	–	No *E. coli* survival after 20 min in the dark, compared with 15 min under irradiation	AgNPs improved the electron-hole separation, leading to the improvement of photocatalytic activity of TiO_2, which enhanced the bactericidal effect	[33]
Ag-TiO_2 nanofibers	Electrospinning process, calcination, and photochemical reaction	2 wt% and 10 wt% Ag-TiO_2 nanofibers resulted in the highest and lowest photocatalytic degradation of methylene blue	10 wt% Ag-TiO_2 nanofibers formed inhibition zone of 1.5 mm and 1.0 mm in the *S. aureus and E. coli*, respectively. TiO_2 nanofibers showed no inhibition zones against both bacteria	The antibacterial activity of AgNPs	[27]

Ag-TiO_2 nanoparticles	Wet impregnation, chemical reduction, and photoreduction	–	All Ag-TiO_2 nanoparticles exhibited stronger bactericidal activity than bare TiO_2 and AgNPs either in the dark or under UV irradiation	The inactivation mechanism under UV light was largely due to the ROS, while the inactivation mechanism was mainly due to direct contact with AgNPs and toxic Ag species in the dark	[39]
Ag-TiO_2/Ag/a-TiO_2 film	Sol-gel method, photoreduction, soak, and heat treatment	–	The antibacterial activity of Ag-TiO_2/Ag/a-TiO_2 film was 5.1 times greater than the a-TiO_2 film in the dark, and it was 1.35 and 6.90 times greater than the Ag/a-TiO_2 and a-TiO_2 films, respectively, under solar irradiation	Released Ag^+ controlled the antibacterial activity of the nanocomposite film	[29]
Ag/a-TiO_2 film	Sol-gel synthesis, dip-coating process, calcination, and annealing	The rate constant for the degradation of stearic acid was calculated at 4.05×10^{12} molecules cm^{-2} min^{-1} for TiO_2 and 5.85×10^{12} molecules cm^{-2} min^{-1} for Ag/a-TiO_2 film	The film achieved 99.997 %, 69 %, and 99.9 % bactericidal effectiveness against *S. aureus*, *E. coli*, and *B. cereus*, respectively	The synergic photocatalytic activity of AgNPs and TiO_2 killed the bacteria, not the Ag^+	[34]
Ag-TiO_2 film	Novel flame-assisted CVD process	All the samples had some UV photoactivity depending on the exact arrangement of the layers. The Ag layers gave comparable or improved photoactivity	TiO_2 layer on Ag film achieved 6 log reduction of *E. coli* in 60 min, compared with 250 min and 40 min for TiO_2 film and Ag film, respectively	–	[36]
Ag-TiO_2 film	Flame-assisted CVD process	The oxidation of stearic acid was 0.0107 cm min^{-1} for Ag-TiO_2 film, similar to 0.0109 cm min^{-1} for TiO_2 film	It costs 4 h, 2 h, and 1 h for Ag-TiO_2 film, TiO_2 film, and Ag film to achieve 6 log reductions of bacterial cells under irradiation	The release of Ag^+ was inhibited or Ag at the surface prevented binding of the bacterial cells to the titania	[37]

(continued)

Table 5.1 (continued)

Material	Synthesis	Photocatalytic performance	Disinfection test results	Disinfection mechanism	References
TiO_2/Ag film	Reactive co-sputtering followed by annealing	–	The TiO_2-10 % Ag film inactivated 85 % of *E. coli* cells in 25 min in the dark, compared with 90 % inactivation rate of bacterial cells in 12 min under visible light	Dissolved silver ions caused the damage to *E. coli*, and the doped Ag extended the effective light absorption of TiO_2, leading to the synergistic effect combining Ag and photocatalytic effect of TiO_2	[40]
TiO_2/Ag hybrid particles	Reverse micelle process, electrostatic layer-by-layer deposition together with a hydrophilic/hydrophobic interaction	Compared with pure TiO_2 particles, the photodegradation of methylene blue with increased efficiencies up to 63 % and 29 % for TiO_2/Ag particles with deposition cycles of 3 and 1, respectively	99 % reduction of bacteria in 24 h for TiO_2/Ag particles with 0.25 % Ag/Ti atomic ratio; 99 % bacterial reduction in 1 h for TiO_2/Ag particles with 0.53 % Ag/Ti atomic ratio	Ag^+ released from the hybrid particles influenced the antibacterial activity	[41]
Ag-TiO_2 particles	Photoreduction method	–	9 log inactivation of bacteria in 150 min and 230 min for TiO_2-Ag2% and TiO_2-Ag1%, respectively; 3 log inactivation of bacteria in 250 min for pure TiO_2; 4 log inactivation of bacteria in 250 min for TiO_2-Ag without UV irradiation	AgNPs not only inactivated *E. coli* cells directly but enhanced the generation of ROS of TiO_2 by preventing electron-hole pair recombination. The Ag^+ released form AgNPs also caused inactivation	[26]
Ag-TiO_2 film	Chemical reduction, spinning process, and calcination	–	The survival ratio of *E. coli* on the TiO_2 film was 60.1 % in the dark and 7.6 % under UV light for 5 min; the bacterial survival ratio on the Ag-TiO_2 film was 9.2 % in the dark and 0 % under UV light for 5 min	AgNPs not only inactivated bacterial cells themselves but also improved the photocatalytic disinfection of TiO_2 by reducing the recombination of electrons and holes	[30]

$Ag@TiO_2$ nanocomposites	Sol-gel method and photochemical reaction	–	The agar plates containing $Ag@TiO_2$ particles displayed nearly complete inhibition of bacterial growth. In the growth curve tests, the growth of *E. coli* was completely inhibited when the $Ag@TiO_2$ particle concentration was 10 μg/mL	The antibacterial activity of AgNPs caused the *E. coli* inactivation	[42]
Ag-TiO_2 particles	Photochemical reduction	–	Compared with pure TiO_2 particles, MS2 inactivation rate of Ag-TiO_2 particles was enhanced by more than fivefold, and the inactivation efficiency increased with increasing silver content	Silver doping enhanced photocatalytic inactivation of viruses primarily by increasing HO · production, and increased virus adsorption to silver sites and leaching of antimicrobial Ag^+ also contribute to virus removal	[31]
Hydroxyapatite-supported Ag-TiO_2	Precipitation method and impregnation	–	It took 65, 16, 20, and 2 min for TiO_2, Ag-TiO_2, Ag-HAP, and Ag-TiO_2/HAP to completely inactivate bacteria under irradiation, respectively	The photocatalytic bactericidal activity was achieved due to Ag effect, synergistic effect of Ag-TiO_2, and sense and shoot property of HAP	[43]
Ag-TiO_2 particles	Photoreduction	–	MIC values for Ag-TiO_2 on both *E. coli* and *S. aureus* were much lower than those for Ag metal	Released Ag^+ from AgNPs caused bacterial inactivation	[44]

Table 5.2 Selected studies of photocatalytic disinfection using Ag-AgX nanocomposites

Material	Synthesis	Photocatalytic performance	Disinfection test results	Disinfection mechanism	References
Ag-AgI/Al_2O_3	Deposition-precipitation and photoreduction method	–	The bactericidal efficiency was significantly enhanced by bicarbonate and sulfate, while phosphate had a slightly positive effect on the disinfection. And more inactivation of *E. coli* was observed at neutral and alkaline pH than at acid pH	The plasmon-induced electron holes on AgNPs and anionic radicals were involved in the bactericidal reaction. The enhanced electron transfer was more crucial than the electrostatic force interaction of bacteria and catalyst for the plasmon-induced inactivation of bacteria using Ag-AgI/Al_2O_3	[46]
AgBr-Ag-Bi_2WO_6	Deposition-precipitation method	–	AgBr-Ag-Bi_2WO_6 could completely inactivate 5×10^7 CFU/mL *E. coli* K-12 within 15 min	The diffusing hydroxyl radicals generated both by the oxidative pathway and the reductive pathway played an important role in the photocatalytic disinfection	[49]
Ag/AgBr/$WO_3 \cdot H_2O$	Light-induced chemical reduction	The decomposition of methylene orange by the Ag/AgBr/$WO_3 \cdot H_2O$ was completed in 20 min of visible light irradiation	Almost all of the *E. coli* were destroyed after 20 min of irradiation, while more than 95 % of the *E. coli* were still alive with $WO_3 \cdot H_2O$, N-TiO_2, and Ag/AgBr	AgNPs formed from AgBr did not play an important role in the antibacterial process, while the holes in the value band of $WO_3 \cdot H_2O$ oxidized the cell wall of the *E. coli* finally destroying it	[55]
Apatite-coated Ag/AgBr/TiO_2	Chemical reduction and calcination	–	7 log removal of *E. coli* was achieved within 2.5 h by apatite-coated Ag/AgBr/TiO_2, 5 log removal of *E. coli* within 3 h by Ag/AgBr/TiO_2, and no removal of *E. coli* by Ag-TiO_2	The inactivation was due to destruction of cell wall by various reactive species, and the photocatalyst could adhere to the outer cell of *E. coli* which enhanced the photocatalytic activity under visible light	[51]

Ag-AgBr/TiO_2	Sol-gel method, solvothermal method, and photoreduction	81 % of organic carbon could be mineralized along with decreased aromaticity and toxicity of the ibuprofen degradation products after 6 h of white LED irradiation, compared with 36 %, 23 %, and 26 % for Ag-AgBr, Ag-TiO_2, and TiO_2, respectively	Ag-AgBr/TiO_2 achieved 77 % and 6 log removal of *E. coli* within 1 h in the dark and under irradiation, respectively, compared with 10 % removal for TiO_2 in the dark and under irradiation	The coexistence of AgNPs and AgBr and the effective separation and transportation of charge carriers in the composite enhanced the photocatalytic inactivation	[47]
Ag-AgCl/TiO_2 xerogels	Modified single-step sol-gel methods	–	As the silver loading in the TiO_2 increases, the amount of xerogel required to inhibit the growth of bacteria decreased and pure TiO_2 was not bactericidal	Released Ag^+ controlled the inactivation of *E. coli*	[52]
Ag/AgBr/TiO_2	Deposition-precipitation method	More than 90 % of azo dyes could be degraded within 90 min for Ag/AgBr/TiO_2, while TiO_2 and Ag-TiO_2 showed no photodegradation	7.2 log removal of *E. coli* within 60 min for Ag/AgBr/TiO_2 under light, while neither pure TiO_2 nor Ag/AgBr/TiO_2 in the dark showed any bactericidal effects	The cell wall and the cell membrane were decomposed by ROS, leading to the leakage of intracellular molecules and causing the cell death	[50]
Ag/AgCl/$W_{18}O_{49}$ nanorods	Photoreduction	–	The inhibition zone in the dark was 0.9 cm and 0 cm for Ag/AgCl/$W_{18}O_{49}$ and $W_{18}O_{49}$, respectively, compared with 1.72 cm for Ag/AgCl/$W_{18}O_{49}$ under light irradiation	The coupling of $W_{18}O_{49}$ nanorods with Ag/AgCl plasmonic photocatalyst and the surface plasmon resonance of Ag contribute to the high efficient antibacterial properties of the Ag/AgCl/$W_{18}O_{49}$	[48]
Zeolite-based Ag/AgBr	Sol-gel and deposition method	Photodecolorization of azo dye was influenced by catalyst concentration, initial dye concentration, and temperature	5 log and 7 log removal of *E. coli* were achieved by zeolite-based Ag/AgBr in the dark and under light, respectively	ROS and released Ag^+ caused the cell death	[53]

Table 5.3 Selected studies of photocatalytic disinfection using Ag-ZnO nanocomposites

Material	Synthesis	Photocatalytic performance	Disinfection test results	Disinfection mechanism	References
Ag-ZnO thin film	Sol-gel dip-coating method	The degradation of methylene blue, rhodamine, and reactive orange by Ag-ZnO were all higher than those by ZnO by 10–20 %	Ag-ZnO showed antibacterial activity against *E. coli* under both UV blacklight irradiation and to a lesser extent in the dark. And the efficiency of killing the bacteria increased with the Ag loading on the ZnO thin film under UV black illumination	Photo-generated ROS produced by ZnO and Ag-ZnO led to the death of bacteria under irradiation, while the contact between bacterial cells and Ag-ZnO caused inactivation in the dark	[67]
Ag-ZnO	One-pot hydrothermal method	1.20 at.% Ag-ZnO degraded almost 100 % of orange G within 60 min, while pure ZnO degraded 80 % with 60 min	The MIC values of 1.2 at.% Ag-ZnO nanocomposites were 600 μg/mL for *E. coli* and 400 μg/mL for *S. aureus*, respectively. And the MIC values of pure ZnO were 3500 μg/mL for *E. coli* and 1000 μg/mL for *S. aureus*, respectively	The strong interaction between Ag and ZnO might enforce the electrostatic attraction between positively changed Ag and negatively charged bacteria, which would disturb the cell's power functions, increasing the bactericidal efficiency	[70]
AgNPs@ZnO paper	Papermaking technique, selective ion exchange, and photoreduction	–	Ag-free ZnO paper had no antibacterial activity. And the AgNPs@ZnO paper demonstrated the largest zone of inhibition	The elution of Ag^+ and the nanomorphology of AgNPs would synergistically contribute to the excellent antibacterial activity of AgNPs@ZnO paper	[76]
Ag-ZnO films	Solution combustion method and solution-casting method	100 % degradation of rhodamine B within 60 min was achieved by ZnO-Ag(1 %). And the photocatalytic activity was increased with the increasing silver content	The max inhibition zone against *E. coli* and *S. aureus* was 3.1 and 1.6 cm by ZnO-Ag(1 %). And pure ZnO showed no antibacterial activity	AgNPs were responsible for antimicrobial activity. And an increase in hydrophobicity of the Ag-doped ZnO nanoparticles was correlated to antimicrobial activity	[72]

Ag-ZnO nanoparticles	Oxalate decomposition method	–	The disk diffusion test against *P. aeruginosa*, *B. subtilis*, *S. gallinarum*, *E. coli*, and *S. aureus* was 12, 10, 12, 10, and 12 mm, respectively. And the MIC for *P. aeruginosa*, *B. subtilis*, *S. gallinarum*, *E. coli*, and *S. aureus* were 64, 128, 32, 32, and 128 μg/mL, respectively	The released Ag^+ contributed to the antibacterial activity. And the silver covered in the surface of Zn nanoparticles involved the electrons produced through photocatalytic reaction of Zn nanoparticles which increased electron isolation and made gaps in cell membrane, increasing its antimicrobial activity	[73]
Polystyrene (PS)/Ag-ZnO whiskers (ZnOw) composites	Photoreduction	–	The antibacterial rate against *E. coli* and *S. aureus* under light was both 99.99 % for PS/Ag-ZnOw (0.25 %). Compared with 88.33 % and 99.52 % against *E. coli* and *S. aureus* in the dark	The antibacterial mechanism of PS/Ag-ZnOw composites originated from both active oxygen and H_2O_2, with H_2O_2 being the primary factor. And incorporation of Ag onto the surface of ZnO improved the photocatalytic activity	[68]
Ag-ZnO hybrid nanorods (HNRs)	Two-step alcothermal seeding and hydrothermal growth process. And chemical reduction method	–	The Ag-ZnO HNRs achieved 100 % bactericidal activity in 30 min, the AgNPs achieved 100 % bactericidal activity in 90 min, and pure ZnO nanorods could not achieve complete bactericidal activity after 120 min	Direct contact killing upon contact of bacteria with Ag-ZnO HNRs and leaching of silver in a nanoparticle and ionic form	[71]

(continued)

Table 5.3 (continued)

Material	Synthesis	Photocatalytic performance	Disinfection test results	Disinfection mechanism	References
Ag-ZnO nanoparticles	Hydrothermal method	The maximum of bisphenol A and nonylphenol TOC conversion was 72.1 % and 81.08 %, respectively, by using 1 % Ag-ZnO photocatalytic	Almost 100 % disinfection was achieved by 1 % Ag-ZnO in 40 min	The antibacterial activities of Ag-ZnO were attributed to the generated species such as $OH\cdot$ and H_2O_2. And the Ag on the ZnO interacted with the cells and adhered to the cell walls, which enhanced the antibacterial activity	[74]

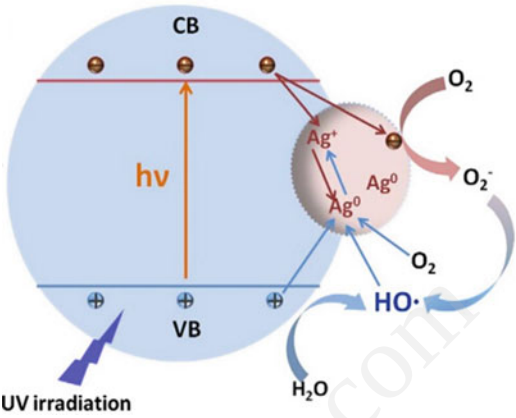

Fig. 5.3 Photocatalytic activity of Ag-TiO_2 (Reprinted from Ref. [26], Copyright 2011, with permission from Elsevier)

5.2.1.1 Photocatalysis

As shown in Fig. 5.3, the modification of Ag on the surface of TiO_2 improves the photocatalytic efficiency under irradiation by trapping the electrons, resulting in the interfacial charge transfer and the decrease in the recombination rate of the electron-hole pairs. And the electron-hole recombination rate can be indirectly monitored from photoluminescence. The higher the electron-hole recombination rate is, the higher the photoluminescence intensity is. Previous report found that the photoluminescence intensity decreased with the increasing nanosilver deposition in the Ag-TiO_2 nanofibers [27]. It confirmed that nanosilver acted as electron-trapping sites.

The reduction of electron-hole recombination is attributed to the LSPR effect of AgNPs. In the Ag-TiO_2 nanocomposites, where the plasmonic nanoparticles and semiconductor are in direct contact with each other, the LSPR excitation of conduction electrons of the AgNPs induced by the irradiation can result in rapid transfer of the energetic conduction electrons of the AgNPs to the TiO_2 conduction band, leaving positive charges on the AgNPs [17]. And the electrons can be transferred to molecular oxygen to form ROS, which can attack and inactivate microorganisms.

By using electron paramagnetic resonance (EPR) spectroscopies in the DMPO spin-trapping experiments, the generation of ROS can be studied. Previous study found that Ag-containing TiO_2 samples had OH radicals which apparently interacted with DMPO in a different way than those of titania with a faster formation of the DMPO-OH adduct [28]. And there was strong evidence that it occurred through hole-related radical attack, particularly involving OH-derived radicals. It indicated that modification of the hole properties could be the key effect of AgNPs. It also unveiled that local difference in the configuration of OH species near silver entities was at the heart of the enhanced *E. coli* inactivation rates.

5.2.1.2 Silver Ions

Silver ions play an important role in the antimicrobial activity of Ag-TiO_2 nanocomposites, especially in the dark. And the silver ions released are mainly produced by irreversible oxidation of AgNPs by reaction with O_2. However, the Ag^+ release behavior of Ag-TiO_2 nanocomposites exhibits distinct properties, which enhances the antimicrobial activity of Ag-TiO_2.

O. Akhavan found that the Ag/a-TiO_2 and Ag-TiO_2/Ag/a-TiO_2 thin films showed a saturation behavior at long times, which was completely different from the general ion release in silver-based bulk materials [29]. The results showed that the ion releasing process was mainly controlled by interdiffusion of water and AgNPs through the pores of the film, not by easy surface diffusion of water on the AgNPs. It indicated that the surface AgNPs in the Ag-TiO_2/Ag/a-TiO_2 film were protected by a nanometric TiO_2 barrier layer against easy ion release. This special Ag^+-releasing behavior made Ag-TiO_2/Ag/a-TiO_2 films to be long-lasting antimicrobial nanocomposites.

The released Ag^+ can react with thiol in cysteine by replacement of a hydrogen atom in the -SH group to form an -S-Ag complex, destroying the enzymatic function of the protein. Because the reaction of -S-Ag complexes can absorb UV irradiation up to 500 nm, the formation of -S-Ag complex was found to be enhanced under UVA irradiation (300–400 nm) and visible light [30], which led to the enhancement of antimicrobial activity of Ag^+. And the antimicrobial activities of silver ions in the disinfection of Ag-TiO_2 nanocomposites have been observed and demonstrated by many studies; some representative results are highlighted in Table 5.1.

5.2.1.3 Physical Damage

The modification of silver on the TiO_2 can change the bacterial adhesion properties, which affects the contact between the microorganisms and Ag-TiO_2 materials. Therefore, the Ag-TiO_2 nanocomposites can inactivate microorganisms by physical attack.

Mesoporous, large surface area, and rough texture make the Ag-TiO_2 nanocomposites favorable for bacterial adhesion in the inactivation. Liu et al. found that the outer membrane of cell was destroyed by mesoporous Ag-TiO_2 films [31]. Their results confirmed that the death of *E. coli* resulted from the destruction of outer membrane of bacteria. The interactions of amino acids with silver also contribute to the improvement of microbial adhesion. V. Liga et al. found that the MS2 adsorptive removal was increased by Ag-TiO_2 [32]. Because silver has a high affinity for sulfur moieties, there are 183 cysteine residues exposed on the MS2 capsid surface. It indicated that adsorption of MS2 to the Ag-TiO_2 played an important role in the inactivation of MS2.

Based on the investigation of FESEM and TEM (Fig. 5.4), Ma et al. found that Ag-TiO_2 particles absorbed on the surface of the bacteria damaged the cell wall and cell membrane under UVA irradiation, resulting in the leakage of intracellular substances and causing the cell death [26]. This result suggested that adsorption damage is an important inactivation mechanism for Ag-TiO_2 nanocomposites.

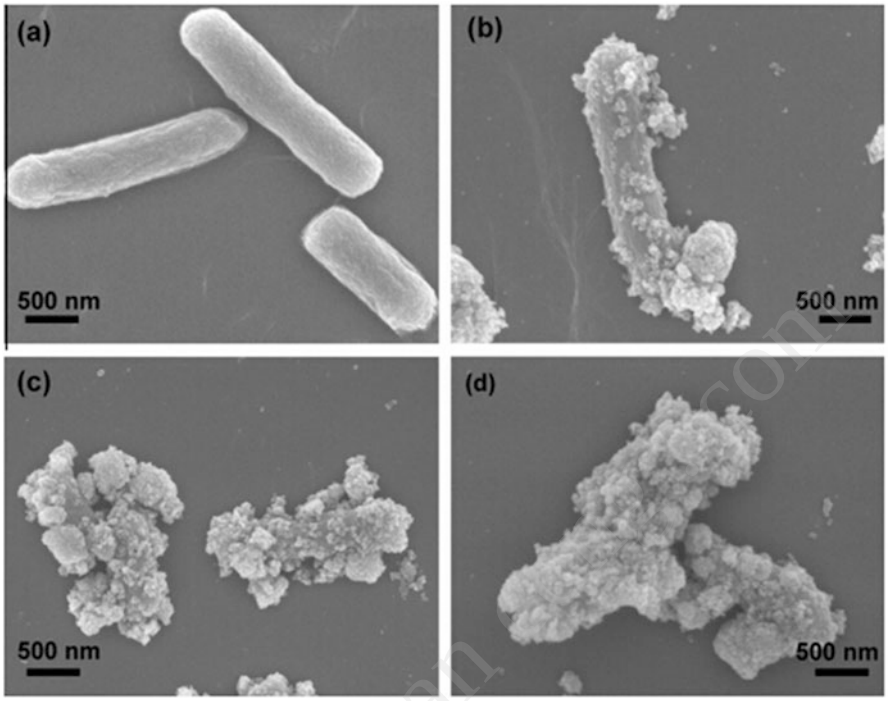

Fig. 5.4 FESEM images of *E. coli* before (**a**) and after photocatalytic reaction with TiO_2-Ag2.0 % under UVA irradiation for 30 min (**b**), 60 min (**c**), and 120 min (**d**), respectively (Reprinted from Ref. [26], Copyright 2011, with permission from Elsevier)

5.2.2 *Synthesis of Ag-TiO_2*

The synthesis of Ag-TiO_2 is a multi-step process. Generally speaking, it contains the synthesis of base material and modified material. As base material, TiO_2 is always prepared through sol-gel method, hydrothermal method, and hydrolysis method. CVD process is also used in some studies. And the modification of AgNPs on the TiO_2 is achieved by photocatalytic reduction, thermal reduction, and chemical reduction.

5.2.2.1 Sol-Gel Method

The precursors, including inorganic substance and metal alkoxide, are mixed in the liquid phase. And stable and transparent sol is formed via hydrolysis and condensation reaction in the solution. After aging, colloidal particles aggregate slowly and form gel with 3D structure, in which it is full of immobile solvent. After drying and calcination, nanomaterial can be obtained from gel. The sol-gel method is facile and simple, which is appropriate for research in the laboratory. By controlling parameter, small-scale and well-dispersive products can be synthesized in the sol-gel

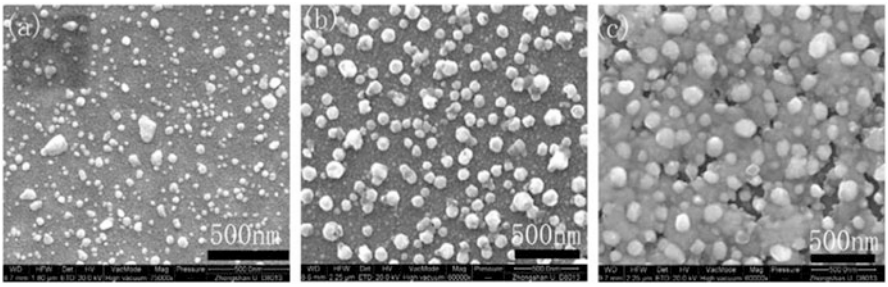

Fig. 5.5 SEM images of the Ag-TiO_2 samples annealed at different temperatures (Reprinted from Ref. [33], Copyright 2010, with permission from Elsevier)

method. However, shortcomings such as high-cost material and aggregation of nanoparticles should be overcome.

As shown in Fig. 5.5, L. Mai et al. synthesized TiO_2 thin films by sol-gel spin-coating method [33]. TiO_2 sol was prepared from the hydrolysis of tetrabutyl titanate ($Ti(OC_4H_9)_4$). Ethanol/H_2O/acetylacetone solution and $Ti(OC_4H_9)_4$/ethanol solution were prepared and mixed, and then the obtained $Ti(OC_4H_9)_4$/ethanol/H_2O/acetylacetone was stirred to get TiO_2 sol. After 48 h aging, the TiO_2 sol was used to coat on titanium plate by spin-coating method. In this synthesis, deionized water and acetylacetone were used for hydrolysis polycondensation reaction, and acetylacetone also acted as the chelating agent to decrease the reactivity of Ti $(OC_4H_9)_4$.

In the study of K. Page [34], they used titanium *n*-butoxide as precursor. First, titanium *n*-butoxide was chelated with a mixture of pentane-2,4-dione in butan-1-ol. Then distilled water was dissolved in the propan-2-ol and added to hydrolyze the titanium precursor. After stirring, the sol was used for dip coating.

5.2.2.2 Hydrothermal Method

Hydrothermal method uses aqueous solution as reaction medium in the autoclave. A high-temperature and high-pressure reaction environment is created by heating, which makes precursor dissolve, nucleate, grow, and form crystal particle. In this process, water acts as solvent, mineralizer, and pressure transmission medium. This method can synthesize and modify inorganic compound; it cannot only prepare one-component or multicomponent crystal but also overcome aggregation under high-temperature treatment. Because hydrothermal method is a low-temperature process, many characteristics can be achieved under 250 °C, including high purity, well dispersity, fine crystal form, no high-temperature treatment, and no aggregation. And particle size and crystal form can be manipulated by controlling technological parameter. Environmental friendship and low cost are also the advantages of hydrothermal method.

F. Liu et al. synthesized TiO_2 nanowires by hydrothermal method [35]. They added titanium dioxide powder and KOH aqueous solution into Teflon autoclave. After the hydrothermal reaction at 150 °C for 36 h, the long TiO_2 nanowires were collected and washed with distilled water.

5.2.2.3 Hydrolysis Method

In the hydrolysis method, inorganic salt, such as titanium tetrachloride and titanium sulfate, is added into water and diluted. With the help of surfactant, inorganic salt will hydrolyze by adding ammonia, and then products will be separated by precipitation. After filtration, drying, and calcination, final products can be obtained. In order to control particle size, acetic acid, citric acid, oxalic acid, and hydrogen peroxide can be added, which leads to the formation of complexes and thus controls the hydrolytic rate. Many advantages make hydrolysis method attractive, including simple technology, mild reaction conditions, well dispersity, and low cost. However, it needs repeated washing to remove inorganic ions. Therefore, product loss and liquid waste are the main problem of hydrolysis method.

5.2.2.4 Precipitation Method

Precipitation method uses titanium tetrachloride or titanium sulfate as precursor to get insoluble $Ti(OH)_4$. And the precipitation is calcined to obtain TiO_2 powder. Precipitation method includes direct precipitation method and uniform precipitation method.

In the direct precipitation method, precipitant is added into saline solution containing one or several ions, and then insoluble hydroxide is formed under special reaction condition. After washing, drying, and thermolysis, oxide powder can be obtained. This method is easy and low cost, but it is difficult to wash the precipitates, which can bring in impurity.

In the uniform precipitation method, crystalline ions can be slowly released from solution by some chemical reactions. And precipitation will form slowly. Therefore, by controlling the rate of precipitant formation, the nonuniform concentration can be avoided and the supersaturation can be controlled in appropriate range, which control the growth rate of particle and thus obtain uniform-size, dense, and high-purity nanoparticles.

5.2.2.5 CVD Process

CVD process uses evaporation of volatile compound, and target product formed in the reaction will condense rapidly in the protective gas, which synthesizes the final product. The nanomaterial made by this method is uniform in size, high-purity,

well-dispersity, and chemically active. The primary advantage of CVD process is high automaticity, but its evaporator is complicated.

L. A. Brook et al. and H. A. Foster et al. synthesized TiO_2 films by using atmospheric pressure CVD coater [36, 37]. They used either titanium tetrachloride and ethyl acetate or titanium tetraisopropoxide, which were transported through the reactor by a carrier gas of nitrogen. And the substrate temperature was 650 °C for $TiCl_4$ and 500 °C for titanium tetraisopropoxide.

5.2.2.6 Photoreduction

Under light irradiation of UV lamp or mercury lamp, Ag^+ in solution can be reduced to AgNPs on the base material.

R. Grieken et al. incorporated AgNPs to TiO_2 by photocatalytic reduction of silver nitrate, adding 2-propanol as hole/hydroxyl radical scavenger [38]. They used UVA lamp for irradiation that lasted for 2 h. In the study of C. Srisitthiratkul [27], they first dispersed TiO_2 nanofibers in deionized water containing $AgNO_3$. Then UV irradiation at 365 nm was applied onto the solution under stirring for 1 h.

5.2.2.7 Thermal Reduction

Thermal reduction reduces Ag^+ to AgNPs under high temperature. In the study of L. Mai et al. [33], they incorporated Ag by the reaction between TiO_2 thin films and $AgNO_3$ solution for 5 min. And the resulting composite films were subjected to heat treatment at 120 °C for 48 h, and then these films were annealed at 200 °C and 300 °C for 6 h to get Ag-TiO_2 film.

5.2.2.8 Chemical Reduction

In the chemical reduction, reductants, such as ethylene glycol, sodium borohydride, and sodium citrate, are used to reduce Ag^+ to metal Ag. In the study of M. Li [39], $NaBH_4$, at equivalent molar concentration of $AgNO_3$, was added as reducing agent.

5.2.3 Photocatalytic Disinfection Performance of Ag-TiO_2

Silver content makes a great influence on the photocatalytic disinfection performance of Ag-TiO_2 composites. In the study of C. Srisitthiratkul et al. [27], it showed that antimicrobial activities of Ag-TiO_2 nanofibers were enhanced with increasing nanosilver content. The inhibition zones of 10 wt% Ag-TiO_2 nanofibers were twice larger than those of 1 wt% Ag-TiO_2 nanofibers. The results of M. V. Liga et al. also supported that the inactivation efficiency of Ag-TiO_2 nanoparticles

increased with increasing silver content [32]. In their study, the inactivation rate was found to increase with the silver content on TiO_2, with rate constants of 0.089, 0.035, 0.017, and 0.013 s^{-1}, for the materials with 5.95, 4.36, 2.46, and 0 % silver, respectively.

However, too much deposition of silver on the TiO_2 will reduce the sites for irradiation adsorption, which may lead to the reduction of photocatalytic disinfection performance. J. Ma et al. studied the efficient antibacterial activity of Ag-TiO_2 with different silver contents [26]. And they found that 2.0 % Ag-TiO_2 showed superior antibacterial activity, which essentially inactivated all bacteria after 150 min, while both 1.0 % Ag-TiO_2 and 3.0 % Ag-TiO_2 inactivated all bacteria in more than 200 min. The results indicated that there existed an optimal amount which could improve the antibacterial activity of Ag-TiO_2 greatly.

The deposition way of silver on the TiO_2 also affects photocatalytic disinfection performance of Ag-TiO_2 composites. A. Kubacka investigated the antimicrobial activities of Ag-TiO_2 as a function of the preparation method [27]. In their study, Ag-TiO_2 composites were prepared by two different methods, thermal reduction and photoreduction. Both Ag-TiO_2 series of sample displayed maximum photokilling activity for 1 wt% silver loading. However, above this loading, photoreduction samples displayed improved performance. Because silver changed the adhesion properties of the bacteria to the Ag-TiO_2 surface and could work as an electron shrink, the latter would appear to significantly increase its importance for photoreduction samples with a silver content above 1 wt%.

The size of nanoparticles controls their toxicity. Nanoparticles with smaller size exhibit stronger antimicrobial activity than those with larger size. Size effect should be noticed in the photocatalytic disinfection.

L. Mai et al. found the size effect on the antimicrobial activity of Ag-TiO_2 films when treating the films at different annealed temperatures [33]. In their experiments, samples containing AgNPs with diameters of 20–30 nm killed 100 % bacteria within 20 min, samples containing AgNPs with diameters of 60–80 nm killed 86 % of bacteria within 20 min, and samples containing AgNPs with diameters over 100 nm killed 60 % of bacteria in the same time.

The deposition way and reactor configurations are another factor influencing the photocatalytic disinfection performance of Ag-TiO_2 composites.

Comparing suspending system with immobilized system, R. Grieken et al. regarded the latter one as an optimal system for photocatalytic disinfection, especially the immobilized system in wall reactor configuration (reactors shown in Fig. 5.6) [38]. Their points of view were as follows:

1. Silver incorporation increased the activity of the bare TiO_2 systems, as a result of reduction of the charge carrier recombination, an improvement of the bacterial adhesion and a parallel non-photocatalytic disinfection mechanism based on the toxicity of silver.
2. The time required to reach the bacterial detection limit was comparable to that of Ag-TiO_2 suspensions.

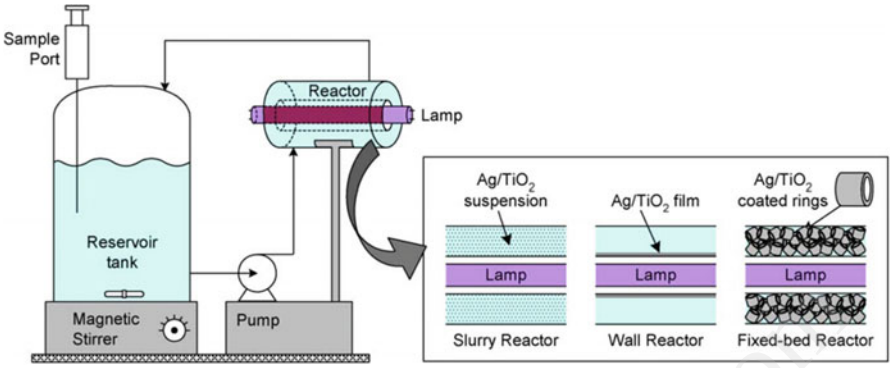

Fig. 5.6 Experimental setup used for the photocatalytic reactions (Reprinted from Ref. [38], Copyright 2009, with permission from Elsevier)

3. Their specific activity per gram of TiO_2 was higher than that of slurries or fixed-bed systems.
4. The reactor configuration, with irradiation from the opposite side to the silver-modified surface in contact with the solution, maximized the radiation absorption, reducing simultaneously the lixiviation of silver produced in the darker regions of fixed-bed and slurry systems.
5. The Ag-TiO_2 film was stable, showed no deactivation or lixiviation, and presented no inhibition by the organic residuals released after bacterial lysis, allowing the continuous treatment of water.

H^+ participates in the photocatalytic reaction of TiO_2. Therefore, the pH value is an important control factor during the photocatalytic disinfection. F. Liu et al. studied the influence of pH values on the antibacterial properties of nano-TiO_2@Ag/PVC film [35]. They found that the inhibitory rate of TiO_2@Ag/PVC film was increased from 89.2 to 91.9 % when the pH value was increased from 5.0 to 7.0, and the rate further increased to 97.2 % when the pH value reached 8.0. The catalytic antimicrobial activity was stronger in weak acidic conditions than that in strong acidic conditions, because of the more content of · OH with acutely oxidizing properties produced by nano-TiO_2@Ag/PVC film.

5.3 Ag-AgX

5.3.1 Disinfection Mechanism of Ag-AgX

Silver halides (AgX, X = Br, Cl, I) are photosensitive materials widely applied in photographic films. Silver halides can absorb photons to liberate electron-hole pairs, and the photoinduced electrons can reduce Ag^+ to metal silver in the AgX.

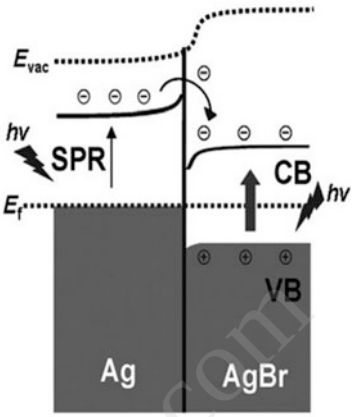

Fig. 5.7 Illustration of charge-separation process of Ag-AgBr under light irradiation (Reproduced from Ref. [45] by permission of John Wiley & Sons Ltd.)

Due to its instability under light, silver halides are not used as photocatalysts traditionally.

However, the synergistic effect of AgX and Ag makes Ag-AgX as an efficient and stable visible light photocatalyst. In the Ag-AgX system, AgNPs absorb visible light and produce electron-hole pairs. These can be effectively polarized by the surface plasmon resonance state of silver, causing efficient separation of the hole and electron, which is shown in Fig. 5.7. And the electrons transfer to molecular oxygen on the surface of AgNPs, generating ROS such as superoxide radical. In the same time, the holes transfer to the AgX surface and oxidize X^- into X^0, which is a powerful oxidizing agent; finally X^0 will be reduced back to X^-.

As a potential photocatalytic disinfection material, the disinfection mechanism of Ag-AgX is not fully understood. However, the photoinduced ROS and silver-silver ions are involved in the photocatalytic disinfection of Ag-AgX.

5.3.1.1 Photoinduced ROS

In the system of Ag-AgX, the synergistic effect of Ag and AgX makes great influence on the electron transfer process in the photocatalytic activities, enhancing the production of ROS.

Hu et al. investigated the plasmon-induced photocatalytic inactivation of enteric pathogenic microorganisms using Ag-AgI/Al_2O_3 under visible light irradiation [46]. They believed that the increased activity of Ag-AgI/Al_2O_3 was the result of the photoexcited AgI semiconductor and plasmon-induced AgNPs under visible light. In their study, two electron transfer processes occurred, from bacteria to AgNPs and from inorganic anions to AgNPs to form anionic radicals. These inorganic anions including OH^- in water not only enhanced electron transfer from plasmon-excited AgNPs to AgI and from *E. coli* to AgNPs, but their anion radicals also increased bactericidal efficiency due to their absorbability by cells. The plasmon-induced electron holes on AgNPs, superoxide anion, and anionic

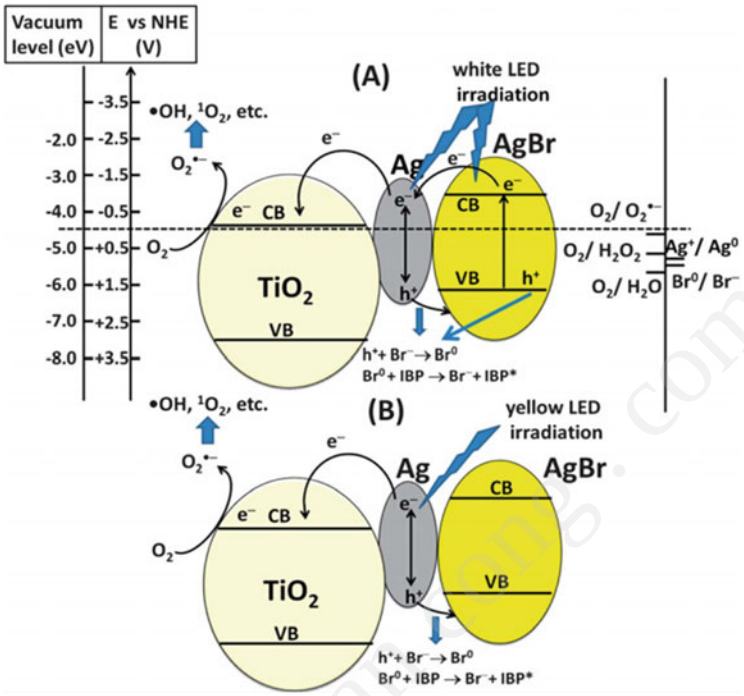

Fig. 5.8 Proposed photocatalytic mechanisms over the Ag-AgBr/TiO_2 under visible light LED irradiation (Reproduced from Ref. [47] by permission of the Royal Society of Chemistry)

radicals were involved in the reaction. The enhanced electron transfer was more crucial than the electrostatic force interaction of bacteria and catalyst for the plasmon-induced inactivation of bacteria using Ag-AgI/Al_2O_3.

In the study of Wang et al. [47], the electron transfer mechanism of Ag-AgBr/TiO_2 was also studied. They first used different colors of LED to elucidate the roles of AgNPs and AgBr in its visible light photocatalytic activity. As shown in Fig. 5.8, plasmon-excited AgNPs served as electron transfer media in the Ag-AgBr/TiO_2 composite, while TiO_2 also participated in the charge transfer besides serving as support for Ag-AgBr. The vectorial electron transfer of AgBr → Ag → TiO_2 occurring in the Ag-AgBr/TiO_2 composite could greatly enhance the interfacial charge transfer while ensuring the high stability of the composite. Among the various oxidative species (h^+, ·OH, O_2^-, and $^1O_2$), O_2^- was the predominant species involved in the photocatalytic disinfection of Ag-AgBr/TiO_2.

Chang et al. also confirmed the key role of Ag/AgCl in the photocatalytic system [48]. They synthesized Ag/AgCl/$W_{18}O_{49}$ nanorods and studied their antibacterial activities. In comparison with the $W_{18}O_{49}$ nanorods, the photocatalytic antibacterial activity of the Ag/AgCl/$W_{18}O_{49}$ nanorods was dramatically enhanced. They concluded that the plasmonic Ag/AgCl nanoparticles played crucial role in enhancing the antibacterial property of the $W_{18}O_{49}$ nanorods under light irradiation. Hybrid

plasmonic nanoparticles composed of Ag and AgCl had high absorption coefficients in a broad UV-visible-NIR spectral range due to the strong SPR of Ag. And the synergistic integration of the Ag/AgCl plasmonic photocatalyst and the $W_{18}O_{49}$ photocatalyst could prohibit the recombination of photoexcited electrons and holes in both AgCl and $W_{18}O_{49}$, enhancing the photocatalytic performance.

The role of ROS in the inactivation of bacterial cells has been reported in many studies. Similarly in the Ag-AgX system, the bactericidal effect of ROS is also confirmed.

Zhang et al. believed that the bactericidal action of ROS is the major mechanism of photocatalytic disinfection of Ag-AgX nanocomposites [49]. They studied the photocatalytic disinfection mechanism of AgBr-Ag-Bi_2WO_6 by using different scavengers, including sodium oxalate (a hole scavenger), Cr(VI) (an electron scavenger), and isopropanol (diffusing $\cdot$OH scavenger). It was found that the diffusing hydroxyl radicals generated both by the oxidative pathway and the reductive pathway played an important role in the photocatalysis. The electrostatic repulsion and the motility of bacteria resulted in that $\cdot$OH remaining bound to the surface had little chance to disinfect the major portion of bacterial cells. And the photocatalytic destruction of the bacterial cells was directly observed by TEM images and confirmed by the determination of potassium ion (K^+) leakage from the killed bacteria.

Hu et al. also confirmed that photoinduced ROS led to the death of bacterial cells [50]. In their study, Ag/AgBr/TiO_2 was prepared and showed high efficiency for the killing of *E. coli* under visible light irradiation. The characterization showed that the surface Ag species mainly existed as Ag^0 in the structure, and the Ag^0 species scavenged $h_{VB}{}^+$ and then trapped $e_{CB}{}^-$ in the process of photocatalytic reaction, inhibiting the decomposition of AgBr. And the studies of ESR and H_2O_2 formation revealed that $\cdot$OH and $O_2{}^-$ were formed in visible light-irradiated aqueous Ag/AgBr/TiO_2 suspension, while there was no ROS in the visible light-irradiated Ag^0/TiO_2 system. The results indicated that AgBr was the main photoactive species for the destruction of bacteria under visible light. In addition, the results of bactericidal experiments under visible light irradiation verified that the cell wall and the cell membrane were successively decomposed by ROS, leading to the leakage of intracellular molecules and causing the cell death.

The ability to adhere to the cell also makes influences on the photocatalytic activity of Ag-AgX composites. In the study of Elahifard et al. [51], they found that Ag/AgBr/TiO_2-covered apatite had a high ability to adsorb bacteria, which enhanced the photocatalytic activity under visible light.

5.3.1.2 Silver Ions

Besides AgNPs, the silver halides and soluble silver complexes (dissolved AgCl, $AgCl_x{}^-$) can also release Ag^+, which may contribute to the disinfection performance of Ag-AgX photocatalysts.

Tuncer et al. studied the antibacterial efficacies of silver/silver chloride-containing titania xerogels against *E. coli* [52]. And they focused on the effect of AgCl produced by the reaction of released Ag^+ ions with chloride present in the Mueller-Hinton (MH) medium. The local deposition of AgCl in the medium could be explained by the following chemical equation:

$$Ag^+_{(aq)} + Cl^-_{(aq)} \rightarrow AgCl_{(aq)} \tag{5.1}$$

In their study, high bacterial activities with both the Ag-TiO_2 and AgCl-TiO_2 xerogels were observed, but the Ag^+ release from the latter was lower due to Eq. (5.1). It indicated that the unnecessary release of silver occurred if silver was not in the form of AgCl crystallite phase, which contributed to the high antibacterial activities of Ag-AgCl/TiO_2 xerogels. More importantly, their results showed that without considering chloride ion present in the MH medium, the usage of antibacterial zone diameter and optical density measurements to assess real bactericidal performance of the materials could not be correct due to the possibility of the local precipitation of AgCl in the MH medium through the interaction between diffusing silver and chloride ion.

The bactericidal role of Ag^+ ions in the Ag-AgX system has also been investigated. In the study of Padervand et al. [53], the antibacterial zeolite-based Ag/AgBr composites were studied both in the dark and visible light. The results indicated that the antibacterial activity of the composites was attributed to the presence of Ag^+ ions. The dispersed silver ions at the compound surface or zeolite pores were released to the medium and inactivated the microorganism. According to the TEM analysis, a cell was observed without any wall and with a great amount of pervasively large granules adhered to it. The researchers concluded that there was a region containing a large amount of electron-dense granules and cytoplasm, which might be a characteristic form of the last life stage of the treated cell with composites containing Ag/AgBr. And the presence of Ag^+ ions in aqueous solution was confirmed by atomic absorption spectroscopy. These silver ions could interact with microorganisms' DNA and thiol group of cysteine, which led to the cell death.

5.3.2 Synthesis of Ag-AgX

Since Huang et al. synthesized Ag/AgCl by using ion exchange/photoreduction method [54], researchers have developed a variety of synthesis methods to improve the catalytic activity of Ag-AgX. In many studies, the synthesis of Ag-AgX contains two phases, including the synthesis of AgX and modification of Ag. Ion exchange, precipitation, oxidation, and hydrothermal methods can be used to synthesize AgX. And the deposition of silver on the AgX can be done by photoreduction and chemical reduction.

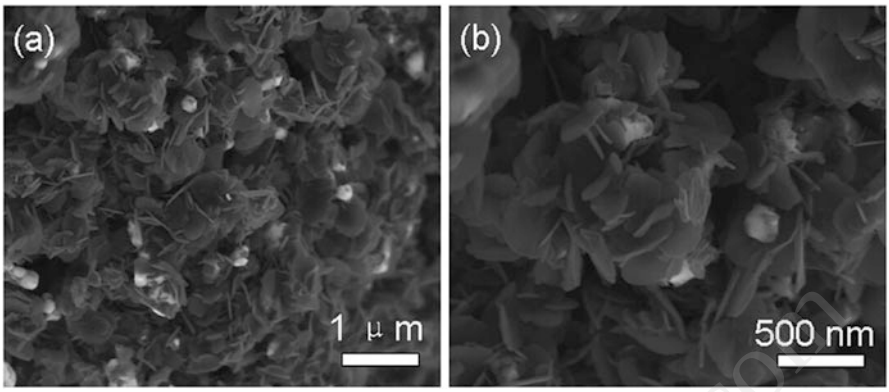

Fig. 5.9 SEM images of $Ag/AgBr/WO_3 \cdot H_2O$ (Reprinted with permission from Ref. [55]. Copyright 2009 American Chemical Society)

5.3.2.1 Ion Exchange Method

As precursor, inorganic compound containing Ag^+ or X^- is used to exchange with counterions, which can produce high-purity and well-crystallized AgX. As shown in Fig. 5.9, Wang et al. synthesized $Ag/AgBr/WO_3 \cdot H_2O$ by the ion exchange reaction [55]. First, $AgBr/WO_3 \cdot H_2O$ was synthesized by the hydrobromic acid treatment between $Ag_8W_4O_{16}$ and concentrated HBr while sonicating the solution until the completion of the hydrobromic acid treatment process. The precipitate was collected, washed, and dried, and then the $AgBr/WO_3 \cdot H_2O$ was obtained. Afterward, the $AgBr/WO_3 \cdot H_2O$ was put into a solution of MO dye, which was then irradiated with a 300 W Xe arc lamp equipped with an ultraviolet cutoff filter to provide visible light with $\lambda \geq 400$ nm. Then the resulting precipitate, $Ag/AgBr/WO_3 \cdot H_2O$, was washed and dried. Although this method makes great contribution to the synthesis of AgX, it is time consuming. Therefore, it is important to control parameters in the synthesis, which can realize the rapid response of ion exchange reaction.

5.3.2.2 Precipitation Method

In the precipitation method, silver nitrate or silver-ammonia solution directly reacts with solution containing halide ions and produces AgX precipitation. Because it is time-saving and facile, precipitation method is widely applied in the research. Hu et al. added silver-ammonia solution to the solution containing KI and mesoporous Al_2O_3 nanomaterial and hence synthesized AgI/Al_2O_3 nanostructure. Then $Ag\text{-}AgI/Al_2O_3$ was prepared via photocatalytic reduction method [56]. In the study of Yu et al., TiO_2 nanotube mesoporous nanofilm was used as support material and immersed in the HCl solution, deionized water, and $AgNO_3$ solution orderly [57]. Then they got $AgCl/TiO_2$ nanocomposites. Finally, the $AgCl/TiO_2$

nanocomposites were irradiated by a 300 W Xe lamp for 10 min to reduce Ag^+ ions in the AgCl particles to Ag^0 species by photochemical decomposition of AgCl or TiO_2 photocatalytic reduction, and then the Ag-AgCl/TiO_2 nanocomposites were obtained.

5.3.2.3 Surfactant- or Polymer-Assisted Method

Due to the unique dispersity in polar or nonpolar solvent, surfactant is always used as soft template and protective agent in the synthesis of nanomaterial. Hu et al. introduced poly(ethylene glycol)-block-poly(ethylene glycol) (P123) in the synthesis of AgBr/Al_2O_3, which enhanced the photocatalytic activity of AgBr/Al_2O_3 [58]. And then they found that the P123 improved and changed the dispersity and crystal structure of AgBr. Hu et al. also introduced cetyltrimethylammonium bromide (CTAB) in the synthesis of Ag/AgBr/TiO_2 [50]. In their synthesis process, CTAB could adsorb onto the surface of TiO_2 to limit the number of nucleation sites for AgBr island to grow, leading to homogeneously dispersed AgBr. Besides this, CTAB could supply Br^- to precipitate Ag^+ in solution. The amount of Br^- from CTAB was more than sufficient to precipitate AgBr from the added $AgNO_3$.

5.3.2.4 Hydrothermal Method

Due to the special reaction environment, hydrothermal method can synthesize high-purity, well-dispersity, and multi-morphology products. As shown in Fig. 5.10, Geng et al. synthesized AgBr nanosphere by the reaction of CTAB and silver-ammonium via hydrothermal method [59], and then the obtained AgBr was irradiated under sunlight to get Ag-AgBr. In the study of Li et al. [60], they synthesized Ag/AgCl nanomaterial by using $AgNO_3$ and ionic liquid containing Cl^- in the

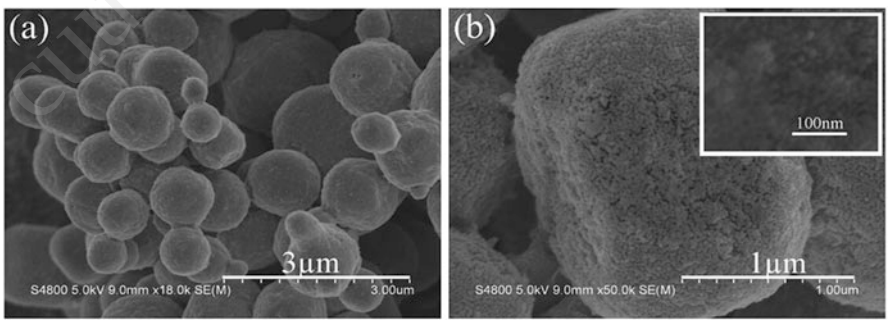

Fig. 5.10 SEM images of the as-prepared Ag-AgBr before photocatalytic reaction: (**a**) low resolution; (**b**) high resolution [59] (Reprinted with permission from Ref. [59]. Copyright 2010 American Chemical Society)

hydrothermal method. In the study of Wang et al. [47], Ag-AgBr/TiO_2 was synthesized via solvothermal route. The mixture of solution containing $AgNO_3$, titanium isopropoxide, and CTAB was heated to 150 °C for 4 h. The product was washed, dried, and calcined. Then the obtained AgBr/TiO_2 was irradiated under stirring and white LED, leading to the production of Ag-AgBr/TiO_2. Although hydrothermal method needs high temperature and pressure, sometimes long reaction time is also needed; studies above indicate that the controllable synthesis of AgX can be achieved by changing reaction parameters and different halide sources.

5.3.2.5 Oxidation Method

Many researchers selected $AgNO_3$ as silver source, but metal silver can also act as precursor of silver ions in the AgX synthesis for its weak reducibility. For example, Lei et al. deposited silver metal on the surface of polyacrylonitrile (PAN) nanofibers by electrochemical reduction [61] and then synthesized Ag/AgCl-grafted PAN nanofibers by in situ oxidation of $FeCl_3$. And the process of the preparation of Ag/AgCl-grafted PAN nanofibers is shown in Fig. 5.11. In addition, Ding et al. used $Ag_{20}Al_{80}$ as silver source, H_2O_2 as oxidant, and HCl as chlorine source [62]. And they synthesized AgCl/Ag with mesoporous sponge structure.

Although oxidation method is not widely used in the study of AgX synthesis, the well-developed study of silver nanostructure can offer opportunities to this method. Researchers can choose silver nanostructure with special shape and structure and synthesize shaped and structured AgX, which may have superior catalytic activity.

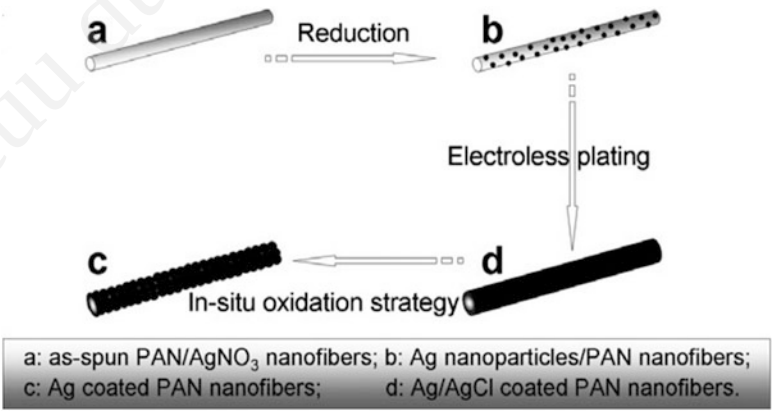

Fig. 5.11 Schematic illustration of the preparation of Ag-/AgCl-coated PAN nanofibers (Reprinted from Ref. [61], Copyright 2011, with permission from Elsevier)

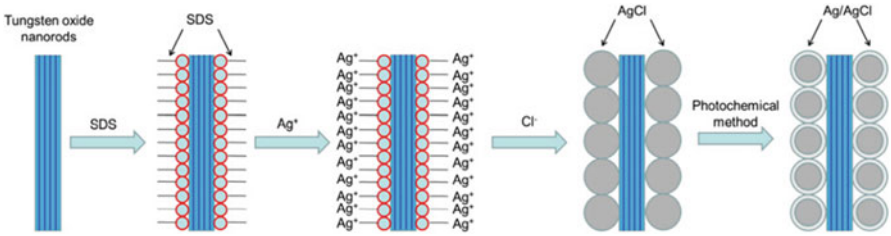

Fig. 5.12 Schematic illustration of the formation of the Ag/AgCl/$W_{18}O_{49}$ nanorods (Reprinted from Ref. [48], Copyright 2012, with permission from Elsevier)

5.3.2.6 Photoreduction

Because AgX can decompose and produce metal silver under light irradiation, photoreduction is an easy method to obtain Ag-AgX composites. In the photoreduction method, AgX is placed under irradiation of xenon or UV lamp, and then AgNPs will be produced from the decomposition of AgX. When the content of AgNPs reaches a certain level, the AgNPs will stop the further decomposition of AgX, and hence the stable Ag-AgX nanocomposite is obtained. In the study of Wang et al. [47], they put prepared AgBr/TiO_2 under vigorous stirring and white LED irradiation for 2 h and obtained gray Ag-AgBr/TiO_2 products finally. Chang et al. added $W_{18}O_{49}$ nanorods to the $AgNO_3$-ethanol solution, which was subsequently exposed to mimic daylight provided by a 300 W Xe lamp under magnetic stirring. During the irradiation processing, an excessive amount of dilute hydrochloric acid was dropwise added. After 30 min of irradiation, the Ag/AgCl/$W_{18}O_{49}$ nanorods were obtained [48]. The synthesis process of Ag/AgCl/$W_{18}O_{49}$ nanorods is shown in Fig. 5.12.

5.3.2.7 Chemical Reduction

Common reductant used in the modification of Ag on the AgX includes ethylene glycol and sodium borohydride. Sun et al. achieved partial reduction of AgCl by using ethylene glycol and obtained Ag/AgCl [63]. Moreover, they also realized the controllable synthesis of different shaped Ag/AgCl nanomaterials by controlling reaction temperature and ethylene glycol dosage. Zhang et al. also used ethylene glycol as reductant in the one-pot microwave synthesis of Ag/AgCl [64], and they found that the silver content could be controlled by reaction time. In the study of An et al. [65], they obtained Ag/AgCl by using sodium borohydride as reductant.

5.3.3 Photocatalytic Disinfection Performance of Ag-AgX

Like other silver nanocomposites, silver content greatly influences the disinfection performance of Ag-AgX composites. Tuncer et al. studied the effect of silver

content on the antibacterial activities of Ag-AgCl/TiO_2 xerogels [52]. The minimum amounts required for the inhibition of *E. coli* growth for 1.2 %, 12 %, and 29 % Ag-AgCl/TiO_2 xerogels were 5.6, 2.5, and 0.6 g/L, respectively. It showed that the antibacterial activities of Ag-AgCl/TiO_2 xerogels increased with the silver amount.

Light irradiation is a key factor in the photocatalytic disinfection, which greatly enhances the activities of Ag-AgX. Padervand et al. studied the antibacterial activity of zeolite-based Ag/AgBr composites [53]. The results showed that Ag/AgBr/zeolite and Ag/AgBr/TiO_2/zeolite achieved 7 log inactivation of *E. coli* after 3 h under visible light, while 5 log inactivation was achieved after 3 h in the dark. However, both zeolite and TiO_2/zeolite did not show any antibacterial activity in the dark and under visible light. It indicated that the photocatalytic activity of Ag/AgBr played an important role in the antibacterial activity of zeolite-based Ag/AgBr composites.

The pH and inorganic ions in the solution can affect the electron transfer process in the Ag-AgX system, which may influence the photocatalytic disinfection performance.

Hu et al. studied the effect of pH and inorganic ions on the photocatalytic disinfection of Ag-AgI/Al_2O_3 [46]. In their study, the bactericidal activity of Ag-AgI/Al_2O_3 increased significantly as the pH increased from 4.5 to 8.5, and both HCO_3^- and SO_4^{2-} ions significantly improved *E. coli* inactivation, while $H_2PO_4^-$ ions had a negative effect on the disinfection. By using cyclic voltammetry, they found that HCO_3^- could enhance electron transfer to AgNPs and lead to formation of inorganic anions, including O_2^- and OH. Similarly, pH had a similar effect on the electron transfer from AgNPs to donors. The reductive ability of $H_2PO_4^-$ was lower than that of HCO_3^-, which could not enhance electron transfer.

It seems that different synthesis methods also affect the disinfection performance. In the disinfection experiments of Wang et al. [47], they compared the disinfection performance of sol-gel synthesized Ag-AgBr/TiO_2 and solvothermal synthesized Ag-AgBr/TiO_2 (S-Ag-AgBr/TiO_2). In the dark, 77 % and 56 % of the bacterial cells were inactivated by Ag-AgBr/TiO_2 and S-Ag-AgBr/TiO_2 within 60 min, while both Ag-AgBr/TiO_2 and S-Ag-AgBr/TiO_2 achieved over 6 log inactivation of *E. coli* after 60 min of irradiation.

5.4 Ag-ZnO

5.4.1 Disinfection Mechanism of Ag-ZnO

As a wide bandage semiconductor, ZnO is considered as a suitable alternative photocatalyst due to its low cost and nontoxicity. Furthermore, ZnO has been found to be effective for the inactivation of *E. coli*, *B. subtilis*, and *S. aureus*.

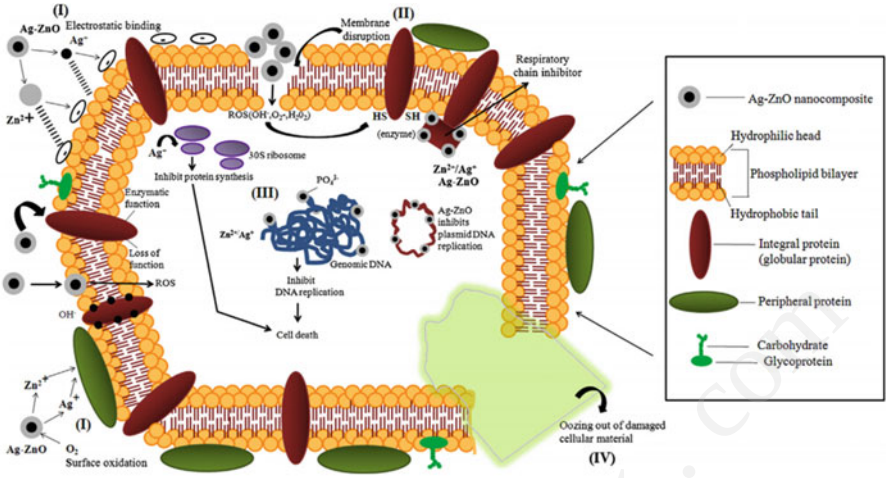

Fig. 5.13 Schematic representation of antibacterial mechanism of Ag-ZnO nanocomposite (Reprinted from Ref. [66], Copyright 2014, with permission from Elsevier)

And ZnO has good biocompatibility. Therefore, many attempts have been made to apply ZnO in the field of photocatalytic antimicrobial treatments. However, the low photocatalytic activity and easy photocorrosion limit the application of ZnO to photocatalysis. Efforts have been made to enhance the photocatalytic performance of ZnO. One strategy is combining ZnO with noble metal nanoparticles, such as Ag, Au, and Pt. The noble metal nanoparticles can prevent the recombination of charge carriers by acting as charge sinks for photoinduced electrons in the ZnO material. Due to its relatively low cost, silver is always used to modify ZnO photocatalysts. The synthesized Ag-ZnO nanocomposites show effectively photocatalytic and antibacterial activities, which are also photostable. Concerning the disinfection mechanism of Ag-ZnO nanocomposites, three mechanisms are considered to play a role, including photoinduced ROS inactivation, released metal ion inactivation, and physical attack inactivation. And their antibacterial actions are shown in Fig. 5.13.

5.4.1.1 Photoinduced ROS Inactivation

ZnO can generate ROS, such as hydrogen peroxide, superoxide anion radicals, and hydroxyl radicals, when ZnO absorbs photons with energy equal to or greater than its bandgap energy. These photoinduced ROS can react and destroy the outer membrane of bacteria and inhibit their growth. AgNPs on the surface of ZnO generate a new energy level that can receive the photoinduced electrons from the conduction band of ZnO, which limits the recombination of the opposite charges. Therefore, the modification of AgNPs to ZnO can improve the photocatalytic efficiency of ZnO, leading to the enhancement of antibacterial activities of Ag-ZnO nanocomposites.

In the study of Thongsuriwong et al. [67], the Ag-ZnO thin films showed antibacterial activity against *E. coli* under both UV blacklight irradiation and to a lesser extent in the dark. The researchers concluded that the antibacterial activity of Ag-ZnO thin films arisen from the ROS such as hydroxyl radical and superoxide anion, which were generated when the ZnO or Ag-doped ZnO absorbed the suitable energy photon. Furthermore, it was observed that the antibacterial activity of Ag-ZnO thin films increased with the Ag loading. And this enhancing effect of Ag on the antibacterial activity of the ZnO thin films might be due to its higher efficiency for generating the ROS.

Pan et al. also believed that the antibacterial mechanism of PS/Ag-ZnOw composites originated from both ROS and H_2O_2 [68], with H_2O_2 being the primary factor. By conducting experiment in the dark, the generation of active oxygen through photocatalytic process could be inhibited. Their result indicated that the ROS generated by photocatalytic activity played a less important role in antibacterial mechanism, and H_2O_2 was considered as the primary cause for antibacterial activity in the dark. However, ROS generated under light irradiation did function synergistically with H_2O_2 and further increased the antibacterial efficiency. And the incorporation of Ag onto the surface of ZnO contributed to the generation of ROS under light irradiation.

Zhang et al. monitored the intracellular ROS production induced by mixture of AgNPs and ZnO nanoparticles (AZNPs) and Ag-ZnO heterostructure nanoparticles (Ag-ZnO HNPs) [69]. In their experiments, significant increase in cellular ROS could be observed after the exposure of bacteria to all the tested materials, and Ag-ZnO HNPs could induce the increase of cellular ROS more efficiently than AZNPs of equal amount did in the same time. This increased ROS production was attributed to the interfacial interaction between Ag and ZnO in Ag-ZnO HNPs, which promoted the separation of charge carriers. They concluded that the enhancement of ROS might be the major cause for the enhanced activity of Ag-ZnO HNPs.

5.4.1.2 Released Metal Ion Inactivation

Matai et al. considered that released metal ions played a role in the antimicrobial activity of Ag-ZnO nanocomposite [66]. Their results showed that an increase in the Zn ion release was seen with increment in the incubation times from 6 to 24 h for both MIC and MKC concentration. Similarly, the rate of Ag ion release was found to increase from 6 to 12 h. They also analyzed the pDNA isolated from the untreated and treated *E. coli* cells and found that the intensity of pDNA band corresponding to *E. coli* treated with Ag-ZnO nanocomposites was significantly lower as compared to control pDNA, suggesting that Ag-ZnO exerted considerable effects on the plasmid DNA replication leading to cell death. In their conclusion, Ag-ZnO might interact directly with bacterial cell membrane by release of Ag^+ and Zn^{2+} upon surface oxidation or by electrostatic interactions between ions released and negatively charged bacterial cell wall. And Ag^+/Zn^{2+} could inhibit the DNA/plasmid replication and proteins/enzymes in cells.

5.4.1.3 Physical Attack Inactivation

The direct contact between nanoparticles and bacterial cells also contributes to the inactivation of Ag-ZnO nanomaterials. In this mode of inactivation action, the AgNPs play a key role due to its intrinsic antibacterial activity, while ZnO always acts as substrate, providing deposition sites for AgNPs.

Lu et al. synthesized Ag-ZnO nanocomposites by hydrothermal method with the assistance of tyrosine and studied their antibacterial activity [70]. In their conclusion, ZnO nanorods as a support decreased the aggregation of AgNPs, and then the AgNPs could have more opportunities to attach the cell membranes and interact with sulfur- and phosphorus-containing compounds in them. And this interaction between the AgNPs and cell membrane would disturb the cell's power functions, such as permeability and respiration, finally leading to cell death.

Agnihotri et al. described the enhanced antibacterial action of Ag-ZnO nanorods as a dual mode of bactericidal action, direct contact killing upon contact of bacteria with Ag-ZnO and leaching of silver in a nanoparticle and ionic form [71]. In contrast, the zinc nanoparticles and zinc ions did not play a role in antibacterial action, but contributed by providing a high surface area for the deposition of AgNPs. The direct contact was confirmed by the SEM and TEM images, and it was observed that AgNPs were located both at the periphery of the cell membrane and deep within the cells as aggregates with a peculiar pattern. These AgNPs could be translocated inside the bacterial machinery to carry out antibacterial action through multiple mechanisms, such as ROS generation, blocking cell respiration, and inhibiting DNA replication. Furthermore, the Ag-ZnO suppressed further growth of bacterial cells even after 24 h of incubation. It was concluded that release of silver was also responsible for the antimicrobial activity.

The presence of AgNPs can change the bacterial adhesion properties of Ag-ZnO nanomaterials, which enhances the antibacterial activity of Ag-ZnO.

Lu et al. found that AgNPs were very positively charged in Ag-ZnO nanocomposites compared to pure Ag [70]. They considered the transfer of electrons from AgNPs to ZnO nanorods as the main reason. And this strong interaction between Ag and ZnO might enforce the electrostatic attraction between positively charged Ag and negatively charged bacteria, increasing the bactericidal efficiency.

In the study of Michael et al. [72], they concluded that the AgNPs adhered to the surface of bacterial cell and altered the properties of membrane by degrading the lipopolysaccharide molecules and formation of pits which increased the membrane permeability. The AgNPs further penetrated into the bacterial cell wall resulting in the DNA damage; after the AgNPs entered the bacterial cell wall, the dissolution of silver occurred, creating silver ions which in turn increased the killing efficiency.

5.4.2 Synthesis of Ag-ZnO

The synthesis of Ag-ZnO nanocomposites involves the preparation of ZnO nanomaterials and the modification of AgNPs. According to the requirement of physicochemical properties, differently shaped ZnO nanostructures have been synthesized, such as nanoparticles, nano-ring, nano-belt, and nanowires. Generally speaking, the synthesis methods of Ag-ZnO nanomaterials mainly contain liquid-phase method and gas-phase method, including sol-gel method, hydrolysis method, precipitation method, hydrothermal method, chemical gas-phase oxidation method, and laser-induced CVD method.

5.4.2.1 Sol-Gel Method

Sol-gel method uses $Zn(OR)_2$ as raw material. The gel can be obtained from solution by hydrolysis reaction and condensation reaction. After dry and calcination, the gel will transform into powder. The product of sol-gel method processes uniform size and high purity. However, the cost is high for the sol-gel method.

Thongsuriwong et al. prepared Ag-doped ZnO thin film by a sol-gel dip-coating method [67]. In their study, required amounts of CH_3COOAg were added into Zn $(CH_3COO)_2 \cdot 2H_2O$ dissolved in isopropanol. Monoethanolamine (MEA), acting as a stabilizer, was added into the above solution. The homogenous solution was then stirred at 70 °C for 1 h to accelerate the hydrolysis reaction and to obtain a transparent sol, which was used as the coating sol. After being cooled and aged, Ag-doped ZnO thin films were deposited on soda lime glass substrates by a dip-coating method. They also studied the effect of silver concentration on the morphology of Ag-doped ZnO thin films. The results showed that the AgNP size was slightly decreased with the increasing Ag loading. The researchers concluded that if the Ag did not become incorporated into the ZnO structure, it would become segregated at the grain boundary. And the segregated Ag clusters at the grain boundary then acted as an obstacle that prevented the grain growth and recombination.

5.4.2.2 Hydrolysis Method

In the hydrolysis method, $Zn(OR)_2$ can hydrolyze rapidly in the solution and produce hydroxide precipitation. After washing, drying, and calcination, the ZnO nano-powder will be obtained from the precipitation. The reaction condition and operation of hydrolysis method are mild and easy, but the nucleation is not uniform.

In the study of Agnihotri et al. [71], arginine-assisted immobilization of AgNPs on ZnO nanorods was synthesized through a two-step alcothermal seeding and hydrothermal growth process. And the synthesis process is shown in Fig. 5.14. Ethanolic solution of zinc acetate dehydrate was refluxed with stirring and was

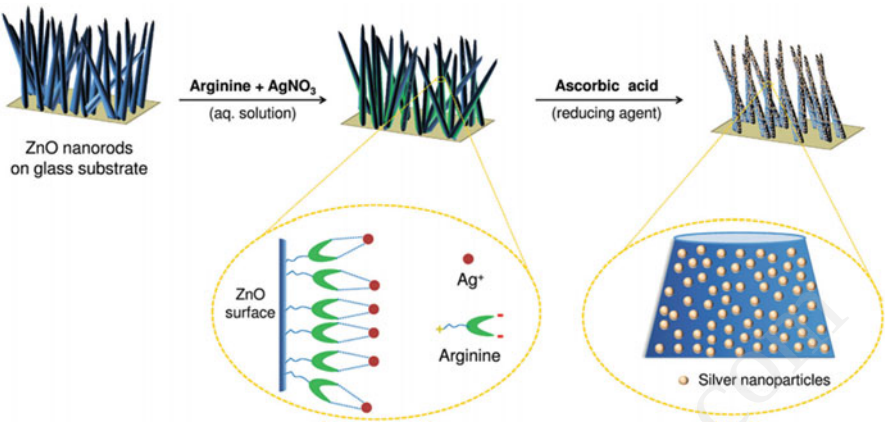

Fig. 5.14 Schematic representation of in situ synthesis and immobilization of silver nanoparticles on ZnO nanorods using arginine as a linker (Reproduced from Ref. [71] by permission of the Royal Society of Chemistry)

cooled down. The obtained zinc precursor was hydrolyzed using ethanolic solution of lithium hydroxide monohydrate, which produced precipitation of ZnO seeds. After the ZnO seeds were collected and washed, the ZnO seeds were drop coated on glass substrates and annealed. Then ZnO-deposited glass substrates were immersed in solution containing zinc nitrate and hexamethylenetetramine followed by heating. After resulting composites were washed and dried, ZnO substrates were immersed in a freshly prepared silver-arginine mixture. Subsequently, the substrates were washed and sonicated. Then AgNPs were deposited on ZnO substrates by chemical reduction, which produced Ag-ZnO composites. Different silver contents of Ag-ZnO composites were synthesized. Characterization showed that the presence of arginine not only facilitated a highly localized assembly of AgNPs but also enhanced the stability of ZnO deposition on the glass matrix and reduced the potential toxicity by limiting the release of zinc ions under alkaline conditions.

5.4.2.3 Precipitation Method

In the precipitation method, precipitant is added into the solution containing one or several ions, resulting in the precipitation away from the solution. According to the rate of precipitation, it includes direct precipitation method and uniform precipitation method. The formation of precipitation in the former is rapid, while the latter obtains precipitation by the slow release of precipitating ions. After washing and thermal decomposition, the nano-ZnO will be produced from the precipitation. Common precipitants include ammonia, ammonium carbonate, and ammonium oxalate. And different precipitants will lead to different products. Precipitation method does not require complex equipment and technical operation. And the

product is highly pure and low cost. However, the size range and dispersity of nanoparticles are wide and poor.

Jafari et al. synthesized Ag-ZnO nanocomposites by oxalate decomposition method [73]. In their study, zinc chloride and silver nitrate were added to ethanol. Then the mixture was heated to 50 °C. After 30 min of continuous stirring, oxalic acid was rapidly added to the mixture. And then the system was kept at 50 °C under reflux for 2 h and a gray precipitate was obtained. After dry and calcination, Ag-ZnO products were obtained from the precipitate.

5.4.2.4 Hydrothermal Method

Likes other nanomaterials, hydrothermal method is also widely used in the synthesis of Ag-ZnO nanostructures.

Lu et al. prepared Ag-ZnO metal-semiconductor nanocomposites through a facile one-plot hydrothermal method with the assistance of tyrosine [70]. In their synthesis method, a solution containing zinc nitrate, silver nitrate, and tyrosine was mixed with agitation. With the increasing addition of ammonia to the above mixture, initial white precipitates were formed at first and then the precipitates dissolved at last. The result solution was heated and then produced precipitates. After washing and drying, the Ag-ZnO products were obtained. The characterization of XRD showed that the added tyrosine served both as a shape conductor for the formation of ZnO faceted nanorods and as a reducing agent of Ag^+ ions. In the reaction process, the complexation of Ag^+ with NH_3 and OH^- decreased the redox potential of Ag^+/Ag, which prevented the formation of isolated AgNPs in solution.

In the study of Bechambi et al. [74], Ag-doped ZnO photocatalysts with different Ag molar contents were prepared via hydrothermal method. During the synthesis, zinc acetate dehydrate was added into water and stirred for 30 min, and then acetic acid was added in order to avoid the formation of the hydroxides. And silver nitrate was put into the above mixture with different molar concentration. Then NaOH solution was added to adjust pH until a white precipitate was produced. After stirring and heat treatment, a solid product which separated from solution was washed and dried. The characterization showed that the Ag doping did not change the average crystallite size with the low Ag content but slightly decreased with high Ag content. The specific surface area increased with the increase of the Ag content. The bandgap values of ZnO were decreased with the increase of Ag doping level.

5.4.2.5 Chemical Gas-Phase Oxidation Method

In the chemical gas-phase oxidation method, zinc powder reacts with oxygen under high temperature, which produces ZnO directly. The products obtained by this method have small size and good dispersity.

Pan et al. synthesized Ag/tetrapod-like ZnO whisker (T-ZnOw) photocatalysts by chemical gas-phase oxidation method and photoreduction method [68]. The

T-ZnOw was synthesized by preheating a boat of stainless steel-carrying pellets or pieces of sheet of metallic zinc in a furnace at 700 °C for 15 min. Silver nitrate was added into polyethylene glycol solution. Then T-ZnOw was poured into the obtained mixed solution and stirred in the dark. Subsequently, the suspension was subjected to UV irradiation from an 8 W UV lamp with main wavelength of 254 nm, while stirred at 50 °C for 4 h. Finally, the mixture was filtered, washed, and dried. XRD results showed that the intensity of the diffraction peaks of ZnO increased with the increasing Ag-ZnOw content.

5.4.2.6 Other Methods

Besides the above methods, more and more new methods are applied in the synthesis of Ag-ZnO nanocomposites.

Michael et al. synthesized silver-doped zinc oxide nanoparticles by a solution combustion method [72]. In their synthesis, zinc nitrate hexahydrate and silver nitrate were used as zinc and silver sources, respectively. And polyethylene glycol acted as fuel. These materials were mixed and then heated to 460 °C for ignition. After several minutes in the reaction, the synthesized materials were calcined at 550 °C for 30 min in order to remove the residual materials from the fuel. The characterization revealed the dispersion of silver presented as clusters and nanoparticles in ZnO matrix. And the silver clusters of an even number along with those of $(ZnO)_nAg_m$ were found at lower concentration of silver; however, on increasing the silver content in the composites, they were being replaced by odd-numbered clusters with a much smaller presence of even-numbered ones and total absence of ZnO-related clusters.

5.4.3 Photocatalytic Disinfection Performance of Ag-ZnO

Due to the antibacterial activity of Ag, the effect of Ag content greatly influences the disinfection performance of Ag-ZnO.

Das et al. investigated the effect of Ag content on the photocatalytic disinfection of Ag@ZnO core-shell nanocomposites [75]. In their experiments, the disinfection efficiency increased with an increase of Ag@ZnO loading up to optimum point (0.5 mg/L) and then decreased. Efficiency at 0.5 mg/L of Ag@ZnO loading was higher than that of other concentrations, as evident from the faster decrease in the cell viability and highest rate of the disinfection process. Lower concentration of catalyst was insufficient to form the required amount of ROS which was required to bring about disinfection of mass of cells and thus disinfection rate was poor. With increase in catalyst concentration, the ROS production increased and hence the disinfection rate developed promisingly. Expected declination in the killing rate with increasing the catalyst concentration was seen. This could be attributed to the

reduced percentage transmittance of sunlight through the slurry with an increase in catalyst concentration.

The bacterial adhesion property is another factor affecting the antibacterial activity of Ag-ZnO nanocomposites.

Michael et al. studied the effect of hydrophobicity on the antibacterial activity of Ag-ZnO nanocomposites [72]. The results showed that the hydrophobicity of Ag-ZnO nanocomposites increased with the increase in the concentration of Ag-ZnO. And the corresponding SEM images showed distinct reduction in the microbial attachment with increase in concentration of the Ag-ZnO in the polymer nanocomposites and also revealed that there was a major decrease in the bacterial colonization and count with respect to the concentration of Ag-ZnO nanocomposites. They concluded that hydrophobicity played a vital role in antimicrobial activity since the attachment of the organism to the polymer nanocomposites was hindered by hydrophobicity.

Some researchers also studied the effect of temperature on the disinfection performance of Ag-ZnO nanocomposites.

The impact of reaction temperature on the rate of disinfection process was studied by Das et al. [75]. In their experiments, the operational temperature was between 40 and 45 °C. And the rate of bacterial inactivation was increased with increase in the process temperature. However, drastic increase in the disinfection rate was not observed. At 65 °C, the highest rate of bacterial disinfection was noticed which might be attributed to accelerated cell death at higher temperature.

References

1. Klasen HJ (2000) Historical review of the use of silver in the treatment of burns. I. Early uses. Burns 26(2):117–130
2. Lansdown AB (2002) Silver. I: its antibacterial properties and mechanism of action. J Wound Care 11(4):125–130
3. Russell AD, Hugo WB (1994) 7 Antimicrobial activity and action of silver. Prog Med Chem 31 (31):351–370
4. Bae E, Park HJ, Lee J, Kim Y, Yoon J, Park K, Choi K, Yi J (2010) Bacterial cytotoxicity of the silver nanoparticle related to physicochemical metrics and agglomeration properties. Environ Toxicol Chem 29(10):2154–2160
5. Kahru A, Ivask A (2013) Mapping the dawn of nanoecotoxicological research. Acc Chem Res 46(3):823–833
6. Suresh AK, Pelletier DA, Doktycz MJ (2013) Relating nanomaterial properties and microbial toxicity. Nanoscale 5(2):463–474
7. Choi O, Hu ZQ (2008) Size dependent and reactive oxygen species related nanosilver toxicity to nitrifying bacteria. Environ Sci Technol 42(12):4583–4588
8. AshaRani PV, Mun GLK, Hande MP, Valiyaveettil S (2009) Cytotoxicity and genotoxicity of silver nanoparticles in human cells. ACS Nano 3(2):279–290
9. Hackenberg S, Scherzed A, Kessler M, Hummel S, Technau A, Froelich K, Ginzkey C, Koehler C, Hagen R, Kleinsasser N (2011) Silver nanoparticles: evaluation of DNA damage, toxicity and functional impairment in human mesenchymal stem cells. Toxicol Lett 201 (1):27–33

10. Marambio-Jones C, Hoek EM (2010) A review of the antibacterial effects of silver nanomaterials and potential implications for human health and the environment. J Nanopart Res 12(5):1531–1551
11. Sondi I, Salopek-Sondi B (2004) Silver nanoparticles as antimicrobial agent: a case study on *E-coli* as a model for Gram-negative bacteria. J Colloid Interface Sci 275(1):177–182
12. Park MV, Neigh AM, Vermeulen JP, de la Fonteyne LJ, Verharen HW, Briedé JJ, van Loveren H, de Jong WH (2011) The effect of particle size on the cytotoxicity, inflammation, developmental toxicity and genotoxicity of silver nanoparticles. Biomaterials 32 (36):9810–9817
13. Sharma VK, Yngard RA, Lin Y (2009) Silver nanoparticles: green synthesis and their antimicrobial activities. Adv Colloid Interface Sci 145(1–2):83–96
14. Yu SJ, Yin YG, Liu JF (2013) Silver nanoparticles in the environment. Environ Sci Processes Impacts 15(1):78–92
15. Zhang HY, Smith JA, Oyanedel-Craver V (2012) The effect of natural water conditions on the anti-bacterial performance and stability of silver nanoparticles capped with different polymers. Water Res 46(3):691–699
16. Fujishima A (1972) Electrochemical photolysis of water at a semiconductor electrode. Nature 238(5358):37–38
17. Sarina S, Waclawik ER, Zhu H (2013) Photocatalysis on supported gold and silver nanoparticles under ultraviolet and visible light irradiation. Green Chem 15(38):1814–1833
18. Kochuveedu ST, Jang YH, Kim DH (2013) A study on the mechanism for the interaction of light with noble metal-metal oxide semiconductor nanostructures for various photophysical applications. Chem Soc Rev 42(5):8467–8493
19. Chen X, Zheng Z, Ke X, Jaatinen E, Xie T, Wang D, Guo C, Zhao J, Zhu H (2010) Supported silver nanoparticles as photocatalysts under ultraviolet and visible light irradiation. Green Chem 12(3):414–419
20. Xi C, Zhu HY, Zhao JC, Zheng ZF, Gao XP (2008) Visible-light-driven oxidation of organic contaminants in air with gold nanoparticle catalysts on oxide supports. Angew Chem 47 (29):5433–5436
21. Bohren CF, Huffman DR (1983) Absorption and scattering of light by small particles. New York Wiley 307(1):290–291
22. Matsunaga T, Tomoda R, Nakajima T, Wake H (1985) Photoelectrochemical sterilization of microbial cells by semiconductor powders. FEMS Microbiol Lett 29(1–2):211–214
23. Hoffmann MR, Martin ST, Choi W, Bahnemann DW (1995) Environmental applications of semiconductor photocatalysis. Chem Rev 95(1):69–96
24. Herrmann J-M, Tahiri H, Ait-Ichou Y, Lassaletta G, Gonzalez-Elipe AR, Fernandez A (1997) Characterization and photocatalytic activity in aqueous medium of TiO2 and Ag-TiO2 coatings on quartz. Appl Catal B-Environ 13(96):219–228
25. Awazu K, Fujimaki M, Rockstuhl C, Tominaga J, Murakami H, Ohki Y, Yoshida N, Watanabe T (2008) A plasmonic photocatalyst consisting of silver nanoparticles embedded in titanium dioxide. J Am Chem Soc 130(5):1676–1680
26. Ma JZ, Xiong ZG, Waite TD, Ng WJ, Zhao XS (2011) Enhanced inactivation of bacteria with silver-modified mesoporous TiO_2 under weak ultraviolet: irradiation. Micropor Mesopor Mat 144(1–3):97–104
27. Srisitthiratkul C, Pongsorrarith V, Intasanta N (2011) The potential use of nanosilver-decorated titanium dioxide nanofibers for toxin decomposition with antimicrobial and self-cleaning properties. Appl Surf Sci 257(21):8850–8856
28. Kubacka A, Ferrer M, Martínez-Arias A, Fernández-García M (2008) Ag promotion of TiO_2-anatase disinfection capability: study of *Escherichia coli* inactivation. Appl Catal B Environ 84(1–2):87–93
29. Akhavan O (2009) Lasting antibacterial activities of Ag–TiO_2/Ag/a-TiO_2 nanocomposite thin film photocatalysts under solar light irradiation. J Colloid Interface Sci 336(1):117–124

30. Kim JY, Lee C, Cho M, Yoon J (2008) Enhanced inactivation of *E. coli* and MS2 phage by silver ions combined with UV-A and visible light irradiation. Water Res 42(1–2):356–362
31. Yang L, Wang X, Fan Y, Yang X (2008) Excellent antimicrobial properties of mesoporous anatase TiO_2 and Ag-TiO_2 composite films. Micropor Mesopor Mat 114(1–3):431–439
32. Liga MV, Bryant EL, Colvin VL, Li Q (2011) Virus inactivation by silver doped titanium dioxide nanoparticles for drinking water treatment. Water Res 45(2):535–544
33. Mai L, Wang D, Zhang S, Xie Y, Huang C, Zhang Z (2010) Synthesis and bactericidal ability of Ag-TiO_2 composite films deposited on titanium plate. Appl Surf Sci 257(3):974–978
34. Page K, Palgrave RG, Parkin IP, Wilson M, Savin SLP, Chadwick AV (2006) Titania and silver–titania composite films on glass-potent antimicrobial coatings. J Mater Chem 17 (1):95–104
35. Liu F, Liu H, Li X, Zhao H, Zhu D, Zheng Y, Li C (2012) Nano-TiO_2@Ag/PVC film with enhanced antibacterial activities and photocatalytic properties. Appl Surf Sci 258 (10):4667–4671
36. Foster HA, Pemble ME, Steele A (2007) Highly bioactive silver and silver/titania composite films grown by chemical vapour deposition. J Photoch Photobio A 187(1):53–63
37. Foster HA, Sheel DW, Sheel P, Evans P, Varghese S, Rutschke N, Yates HM (2010) Antimicrobial activity of titania/silver and titania/copper films prepared by CVD. J Photoch Photobio A 216(2–3):283–289
38. Grieken RV, Marugán J, Sordo C, Martínez P, Pablos C (2009) Photocatalytic inactivation of bacteria in water using suspended and immobilized silver-TiO_2. Appl Catal B Environ 93 (1–2):112–118
39. Li M, Noriega-Trevino ME, Nino-Martinez N, Marambio-Jones C, Wang J, Damoiseaux R, Ruiz F, Hoek EMV (2011) Synergistic bactericidal activity of Ag-TiO_2 nanoparticles in both light and dark conditions. Environ Sci Technol 45(20):8989–8995
40. Hsieh JH, Yu RB, Chang YK, Li C (2012) Structural analysis of TiO_2 and TiO_2-Ag thin films and their antibacterial behaviors. In: Journal of physics: conference series., p 2374
41. Lin WC, Chen CN, Tseng TT, Wei MH, Hsieh JH, Tseng WJ (2010) Micellar layer-by-layer synthesis of TiO_2/Ag hybrid particles for bactericidal and photocatalytic activities. J Eur Ceram Soc 30(14):2849–2857
42. Chen SF, Li JP, Qian K, Xu WP, Lu Y, Huang WX, Yu SH (2010) Large scale photochemical synthesis of M@TiO_2 nanocomposites (M = Ag, Pd, Au, Pt) and their optical properties, CO oxidation performance, and antibacterial effect. Nano Res 3(4):244–255
43. Reddy MP, Venugopal A, Subrahmanyam M (2007) Hydroxyapatite-supported Ag-TiO_2 as *Escherichia coli* disinfection photocatalyst. Water Res 41(2):379–386
44. Keleher J, Bashant J, Heldt N, Johnson L, Li Y (2002) Photo-catalytic preparation of silver-coated TiO_2 particles for antibacterial applications. World J Microbiol Biotechnol 18 (2):133–139
45. Jiang J, Li H, Zhang LZ (2012) New insight into daylight photocatalysis of AgBr@Ag: synergistic effect between semiconductor photocatalysis and plasmonic photocatalysis. Chem Eur J 18(20):6360–6369
46. Hu X, Hu C, Peng T, Zhou X, Qu J (2010) Plasmon-induced inactivation of enteric pathogenic microorganisms with Ag-AgI/Al_2O_3 under visible-light irradiation. Environ Sci Technol 44 (9):1425–1431
47. Wang XP, Tang YX, Chen Z, Lim TT (2012) Highly stable heterostructured Ag-AgBr/TiO_2 composite: a bifunctional visible-light active photocatalyst for destruction of ibuprofen and bacteria. J Mater Chem 22(43):23149–23158
48. Chang X, Sun S, Dong L, Yin Y (2012) Efficient synthesis of Ag/AgCl/$W_{18}O_{49}$ nanorods and their antibacterial activities. Mater Lett 83(12):133–135
49. Zhang LS, Wong KH, Yip HY, Hu C, Yu JC, Chan CY, Wong PK (2010) Effective photocatalytic disinfection of *E. coli* K-12 using AgBr-Ag-Bi_2WO_6 nanojunction system irradiated by visible light: the role of diffusing hydroxyl radicals. Environ Sci Technol 44 (4):1392–1398

50. Hu C, Lan Y, Qu J, Hu X, Wang A (2006) Ag/AgBr/TiO_2 visible light photocatalyst for destruction of azodyes and bacteria. J Phys Chem B 110(29):4066–4072
51. Elahifard MR, Rahimnejad S, Haghighi S, Gholami MR (2007) Apatite-coated Ag/AgBr/TiO_2 visible-light photocatalyst for destruction of bacteria. J Am Chem Soc 129(31):9552–9553
52. Tuncer M, Seker E (2011) Single step sol-gel made silver chloride on titania xerogels to inhibit *E. coli* bacteria growth: effect of preparation and chloride ion on bactericidal activity. J Sol-Gel Sci Techn 59(2):304–310(307)
53. Padervand M, Elahifard MR, Meidanshahi RV, Ghasemi S, Haghighi S, Gholami MR (2012) Investigation of the antibacterial and photocatalytic properties of the zeolitic nanosized AgBr/TiO_2 composites. Mater Sci Semicond Process 15(1):73–79
54. Peng W, Baibiao H, Qianqian Z, Xiaoyang Z, Xiaoyan Q, Ying D, Jie Z, Jiaoxian Y, Haixia L, Zaizhu L (2010) Highly efficient visible light plasmonic photocatalyst Ag@Ag(Br, I). Chem Eur J 16(33):10042–10047
55. Peng W, Huang B, Qin X, Zhang X, Ying D, Whangbo MH (2009) Ag/AgBr/$WO_3 \cdot H_2O$: visible-light photocatalyst for bacteria destruction. Inorg Chem 48(22):10697–10702
56. Hu C, Peng T, Hu X, Nie Y, Zhou X, Qu J, He H (2009) Plasmon-induced photodegradation of toxic pollutants with Ag-AgI/Al_2O_3 under visible-light irradiation. J Am Chem Soc 132 (9):1425–1431
57. Zhou J, Cheng Y, Yu J (2011) Preparation and characterization of visible-light-driven plasmonic photocatalyst Ag/AgCl/TiO_2 nanocomposite thin films. J Photoch Photobio A 223 (2):82–87
58. Zhou X, Hu C, Hu X, Peng T, Qu J (2010) Plasmon-assisted degradation of toxic pollutants with Ag−AgBr/Al_2O_3 under visible-light irradiation. J Phys Chem C 114(6):2746–2750
59. Long K, Baoyou G, Xiaoting C, Yanyan Z, Yinchan L (2010) Facile subsequently light-induced route to highly efficient and stable sunlight-driven Ag-AgBr plasmonic photocatalyst. Langmuir 26(24):18723–18727
60. Hui X, Li H, Xia J, Sheng Y, Luo Z, Ling L, Li X (2010) One-pot synthesis of visible-light-driven plasmonic photocatalyst Ag/AgCl in ionic liquid. Acs Appl Mater Inter 3(1):22–29
61. Lei J, Wang W, Song M, Dong B, Li Z, Wang C, Li L (2011) Ag/AgCl coated polyacrylonitrile nanofiber membranes: synthesis and photocatalytic properties. React Funct Polym 71 (11):1071–1076
62. Li Y, Ding Y (2010) Porous AgCl/Ag nanocomposites with enhanced visible light photocatalytic properties. J Phys Chem C 114(7):3175–3179
63. Peng S, Sun Y (2011) Ripening of bimodally distributed AgCl nanoparticles. J Mater Chem 21 (31):11644–11650
64. Jiang J, Zhang LZ (2011) Rapid microwave-assisted nonaqueous synthesis and growth mechanism of AgCl/Ag and its daylight-driven plasmonic photocatalysis. Chem Eur J 17 (13):3710–3717
65. An CH, Wang RP, Wang ST, Zhang XY (2011) Converting AgCl nanocubes to sunlight-driven plasmonic AgCl:Ag nanophotocatalyst with high activity and durability. J Mater Chem 21 (31):11532–11536
66. Matai I, Sachdev A, Dubey P, Kumar SU, Bhushan B, Gopinath P (2014) Antibacterial activity and mechanism of Ag–ZnO nanocomposite on *S. aureus* and GFP-expressing antibiotic resistant *E. coli*. Colloids Surf B: Biointerfaces 115(3):359–367
67. Thongsuriwong K, Amornpitoksuk P, Suwanboon S (2012) Photocatalytic and antibacterial activities of Ag-doped ZnO thin films prepared by a sol–gel dip-coating method. J Sol-Gel Sci Technol 62(3):304–312
68. Pan X, Peng L, Liu Y, Wang J (2014) Highly antibacterial and toughened polystyrene composites with silver nanoparticles modified tetrapod-like zinc oxide whiskers. J Appl Polym Sci 131(20):1366–1373
69. Yi Z, Gao X, Lei Z, Xin L, Wei J, Sun Y, Jie Y (2014) The synergetic antibacterial activity of Ag islands on ZnO (Ag-ZnO) heterostructure nanoparticles and its mode of action. J Inorg Biochem 130(1):74–83

70. Lu W, Liu G, Gao S, Xing S, Wang J (2008) Tyrosine-assisted preparation of Ag-ZnO nanocomposites with enhanced photocatalytic performance and synergistic antibacterial activities. Nanotechnology 19(44):17486
71. Shekhar A, Geetika B, Suparna M, Soumyo M (2015) Arginine-assisted immobilization of silver nanoparticles on ZnO nanorods: an enhanced and reusable antibacterial substrate without human cell cytotoxicity. Nanoscale 7:7415–7429
72. Michael RJV, Sambandam B, Muthukumar T, Umapathy MJ, Manoharan PT (2014) Spectroscopic dimensions of silver nanoparticles and clusters in ZnO matrix and their role in bioinspired antifouling and photocatalysis. Phys Chem Chem Phys 16(18):8541–8555
73. Jafari A, Ghane M, Arastoo S (2011) Synergistic antibacterial effects of nano zinc oxide combined with silver nanocrystales. Afr J Microbiol Res 5(30):5465–5473
74. Bechambi O, Chalbi M, Najjar W, Sayadi S (2015) Photocatalytic activity of ZnO doped with Ag on the degradation of endocrine disrupting under UV irradiation and the investigation of its antibacterial activity. Appl Surf Sci 347:414–420
75. Das S, Sinha S, Suar M, Yun SI, Mishra A, Tripathy SK (2015) Solar-photocatalytic disinfection of Vibrio cholerae by using Ag@ZnO core-shell structure nanocomposites. J Photochem Photobiol B 142:68–76
76. Koga H, Kitaoka T, Wariishi H (2009) In situ synthesis of silver nanoparticles on zinc oxide whiskers incorporated in a paper matrix for antibacterial applications. J Mater Chem 19:2135–2140

Chapter 6
Solar Photocatalytic Disinfection by Nano-Ag-Based Photocatalyst

Chun Hu

Abstract Numerous studies have suggested that photocatalytic disinfection is promising as a disinfection method due to its effectiveness against viral pathogens. Its application predominantly depends on the development of a new photocatalyst capable of inactivating viruses and other waterborne pathogens with much less energy used than UV and with sufficiently high throughput. Therefore, the development of visible-light photocatalysts or weak UV photocatalysts has become one of the most important topics in the photocatalysis field for using solar energy. Ag-based nanocomposites are one of the most promising photocatalysts. The photocatalysts, Ti(IV) and Ag co-substituted hydroxyapatite (HAPTiAg), supported silver halides (AgX/TiO_2), and plasmonic $Ag\text{-}AgI/Al_2O_3$, showed high efficiency for killing bacteria. Moreover, its bactericidal activities were much higher than that of P25-TiO_2 film. Reactive oxygen species ($^{\bullet}OH$, $O_2^{-\bullet}$, H_2O_2) and photogenerated holes (h+) were involved in the reaction. The process of destruction of the cell wall and the cell membrane was verified by TEM, potassium ion leakage, lipid peroxidation, and FTIR measurements. These results suggested that the photocatalytic degradation of the cell structure caused the cell death. The electrostatic force interaction of the bacteria-catalyst significantly affected the efficiency of disinfection on the basis of the *E. coli* inactivation under different conditions. The detailed study confirmed that the enhanced electron transfer was more crucial than the electrostatic force interaction of bacteria and catalyst for the plasmon-induced inactivation of bacteria using $Ag\text{-}AgI/Al_2O_3$.

Keywords Nano-Ag-based photocatalyst • Disinfection • Reactive oxygen species • Electrostatic force • Electron transfer

C. Hu (✉)
Research Center for Eco-Environmental Sciences, Chinese Academy of Sciences, Beijing, China
e-mail: huchun@rcees.ac.cn

T. An et al. (eds.), *Advances in Photocatalytic Disinfection*, Green Chemistry and Sustainable Technology, DOI 10.1007/978-3-662-53496-0_6

6.1 Destruction of Bacteria with Ti(IV) and Ag Co-substituted Hydroxyapatite Under Weak UVA Irradiation

6.1.1 Bactericidal Activity of Various Films

Calcium hydroxyapatite $Ca_{10}(PO_4)_6(OH)_2$ (HAP) is commonly used in the field of bioceramics and as an absorbent for liquid chromatography. It has thermal catalytic and photocatalytic properties [1]. Ca(II) of HAP can be exchanged with various metal ions in aqueous media [2, 3]. HAP was co-substituted with Ti(IV) and Ag^+ (HAPTiAg), by coprecipitation and ion-exchange methods. Then, the HAPTi and HAPTiAg were supported on spumous nickel meshwork (Fig. 6.1) [4]. Figure 6.2 shows the bactericidal activities of the various films in the inactivation of *E. coli* in water. Clearly, neither HAP film nor HAPTi film under weak UVA irradiation

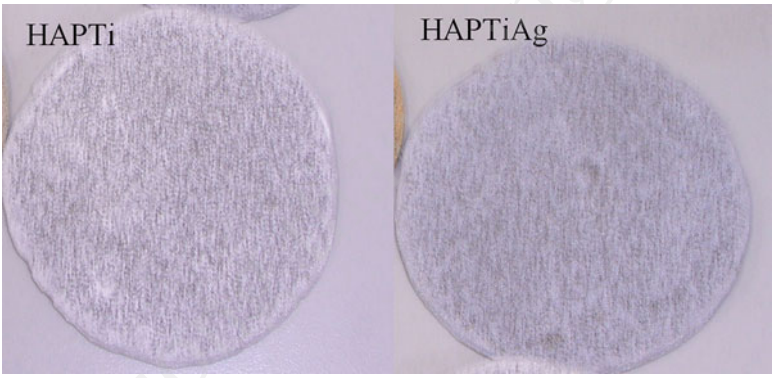

Fig. 6.1 The spumous nickel meshwork supported with HAPTi and HAPTiAg

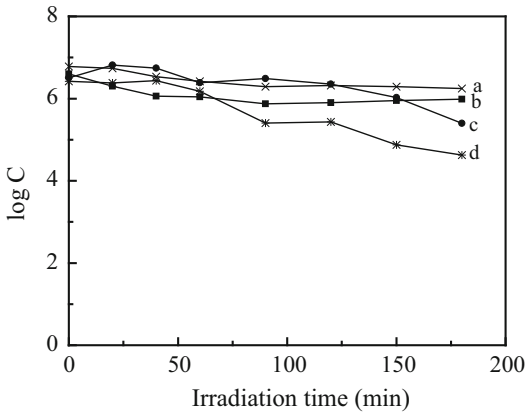

Fig. 6.2 Temporal course of the *E. coli* inactivation in aqueous solution under UVA irradiation: (**a**) only UVA irradiation, (**b**) HAP film, (**c**) HAPTi film, and (**d**) P25TiO_2 film (Reprinted from Ref. [4] Copyright © 2007 Elsevier)

showed any bactericidal effects on *E. coli*. Additionally, no significant inactivation of *E. coli* was observed under UVA irradiation with no catalyst. *E. coli* inactivation of 1.8 log occurred at 180 min of irradiation on P25-TiO_2 films. In contrast, *E. coli* was almost completely killed within 150 min on HAPTiAg films under weak UVA irradiation and in the dark (Fig. 6.3). Complete *E. coli* inactivation of 6.7 log occurred at 150 min with or without UVA irradiation. The maximum concentration of Ag^+ ions leached out into aqueous solution from the HAPTiAg film was about 0.6 mg/L, which did not show any bactericidal effects on *E. coli*. Compared with all the above results, the bactericidal activity of HAPTiAg film in both UVA and darkness was much higher than that of P25-TiO_2 film with UVA irradiation. Furthermore, *S. aureus* was also killed efficiently on HAPTiAg films, respectively, under UVA irradiation or in the dark (Fig. 6.4).

The above results indicated that it is quite possible that the *E. coli* was killed by the synergy of the decomposition role of ROS and the bacteriostatic action of these antibacterial ions. The involvement of $O_2^{-\bullet}$ radicals in different reaction systems

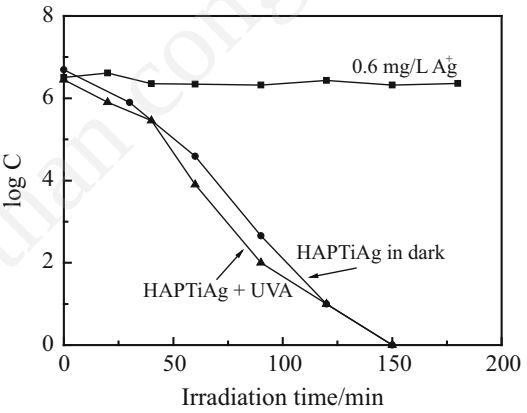

Fig. 6.3 Temporal course of the *E. coli* inactivation in HAPTiAg film (Reprinted from Ref. [4] Copyright © 2007 Elsevier)

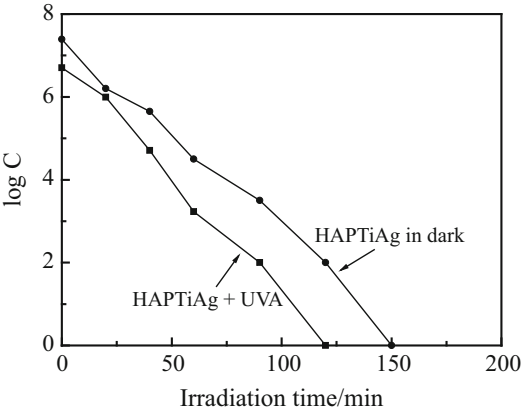

Fig. 6.4 Temporal course of the *S. aureus* inactivation in HAPTiAg film (Reprinted from Ref. [4] Copyright © 2007 Elsevier)

was examined in methanol with an Nd:YAG laser (355 nm) irradiation source or in the dark.

In HAPTiAg and HAPTi systems with and without UVA irradiation, six characteristic peaks of the DMPO- $O_2^{-\bullet}$ adducts were observed (Fig. 6.5), while in the control system, DMPO with methanol did not exhibit any signal. Furthermore, another control experiment was carried out. Superoxide dismutase (SOD) was added into HAPTiAg and HAPTi methanol suspensions in the dark under otherwise identical conditions. Obviously, the signal of DMPO- $O_2^{-\bullet}$ adducts was not observed in the control experiment since SOD scavenged $O_2^{-\bullet}$. The results confirmed that $O_2^{-\bullet}$ radicals were generated from HAPTiAg and HAPTi systems in the dark. For the P25-TiO_2, HAP systems (Fig. 6.6), six characteristic peaks of the DMPO- $O_2^{-\bullet}$ adducts were observed under UV irradiation, but no such signals were detected in the dark. The results verified that HAPTiAg and HAPTi can generate $O_2^{-\bullet}$ both under UVA irradiation and in the dark, while other materials have to be excited by UV light and then $O_2^{-\bullet}$ is generated. Therefore, in the dark, HAP and P25-TiO_2 films had no bactericidal activity, whereas HAPTi did not show any obvious effect either due to the little intensity of the DMPO- $O_2^{-\bullet}$. However, in HAPTiAg film systems, *E. coli* not only was decomposed by $O_2^{-\bullet}$ but also was inhibited by silver ions, causing faster inactivation in the dark.

Similarly, under UV irradiation, both HAPTiAg films had the same role as that in the dark, and the more $O_2^{-\bullet}$ was formed due to UV irradiation, the more

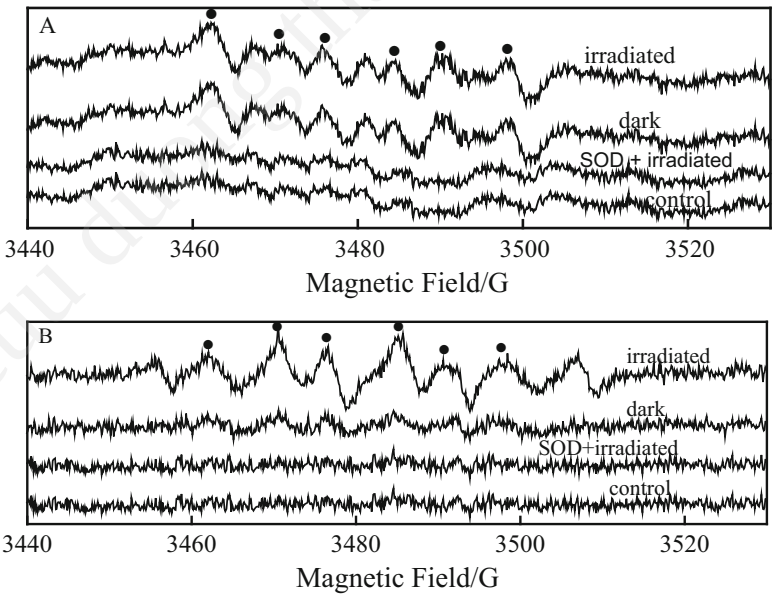

Fig. 6.5 DMPO spin-trapping ESR spectra recorded at ambient temperature in methanol dispersion under UVA irradiation or in dark, (**a**) HAPTiAg and (**b**) HAPTi (Reprinted from Ref. [4] Copyright © 2007 Elsevier)

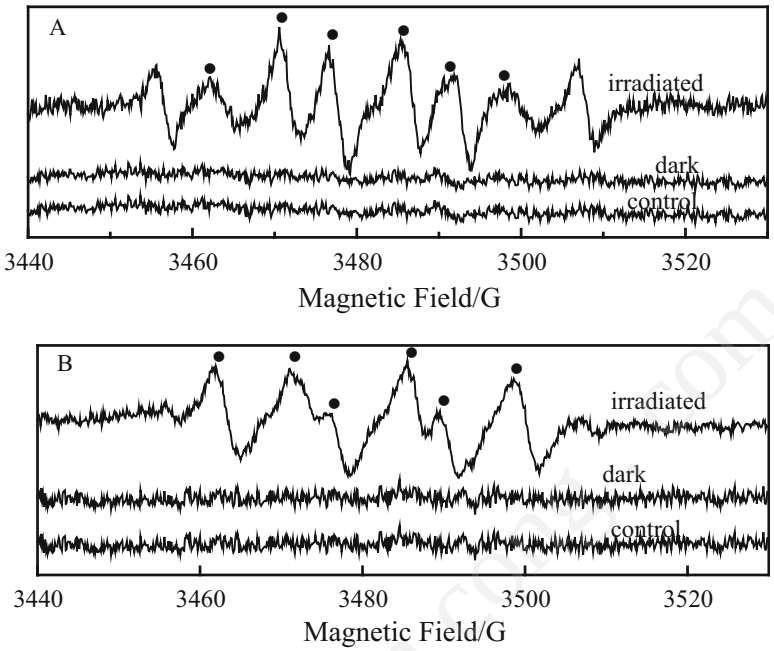

Fig. 6.6 DMPO spin-trapping ESR spectra in methanol dispersion under UVA irradiation or in dark, (**a**) P25-TiO_2 and (**b**) HAP (Reprinted from Ref. [4] Copyright © 2007 Elsevier)

inactivation of *E. coli* occurred. In contrast, HAP, HAPTi, and P25-TiO_2 only had the function of decomposing bacteria under UVA irradiation. Since the tested UVA intensity was relatively weak, the amount of $O_2^{-\bullet}$ formed from HAP and HAPTi was too small to lead to any obvious *E. coli* inactivation. However, the intensity of $O_2^{-\bullet}$ from P25-TiO_2 was stronger than that from HAP and HAPTi, and some *E. coli* inactivation was observed. Nevertheless, the bactericidal activity of P25-TiO_2 was still much lower than that of HAPTiAg. The results demonstrated that the synergistic effect of the oxidation reaction and antibacterial reaction was much greater than that of their sum.

The main mechanism for radical $O_2^{-\bullet}$ formation on HAP has been proposed. The radical $O_2^{-\bullet}$ could be formed on HAP by heat treatment or UV irradiation [5, 6]. The UV irradiation or heat treatment causes the changes of the surface PO_4 group, probably the formation of an oxygen vacancy, which traps the electrons, leading to the formation of the $O_2^{-\bullet}$ species [5]. HAPTi and HAPTiAg could generate $O_2^{-\bullet}$ species at room temperature without UV irradiation. Moreover, the intensity of $O_2^{-\bullet}$ signals formed in HAPTiAg was stronger than that in HAPTi. It is quite possible that the substitution of Ti(IV) caused the oxygen vacancy in the crystal of HAP because the valency of Ti(IV) is higher than that of Ca(II). The formation of the oxygen vacancy was attributed to the possible formation of $O_2^{-\bullet}$ at ambient temperature. Furthermore, HAPTiAg was characterized by XPS. The silver species mainly exists as Ag^0 (BE, 367.82 eV) and Ag^+ (BE, 367.55 eV).

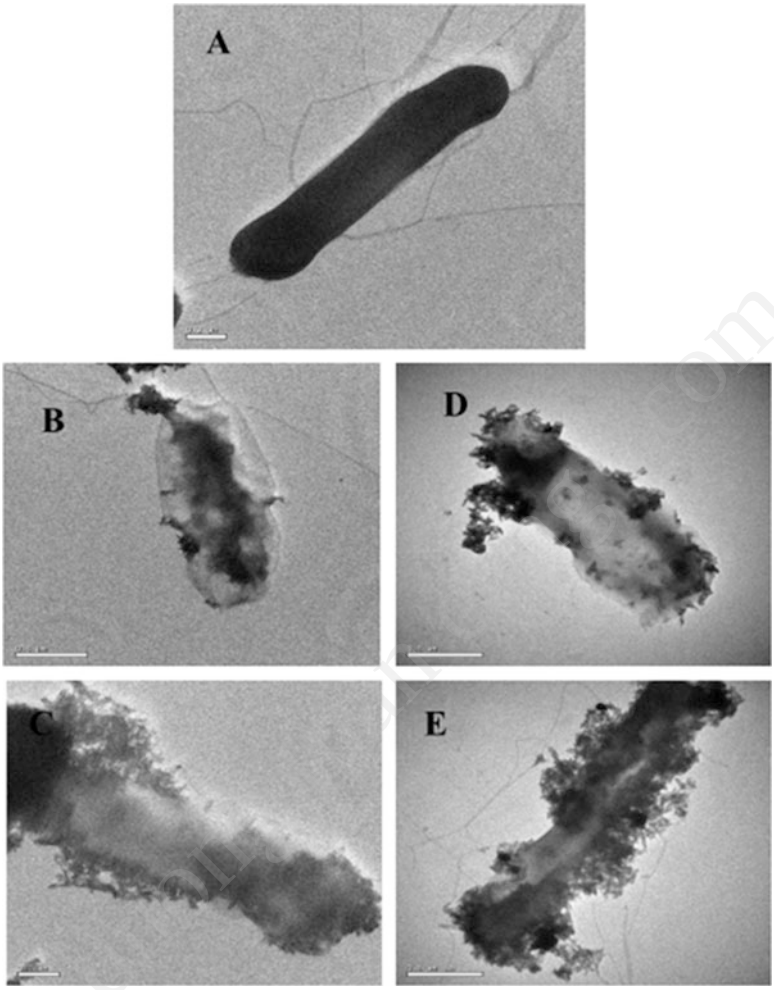

Fig. 6.7 (**a**) *E. coli* not treated, (**b**) and (**c**) TEM micrographs of *E. coli* in UVA-illuminated HAPTiAg suspension for 2 h, and (**d**) and (**e**) TEM micrographs in HAPTiAg suspension in the dark for 5 h (Reprinted from Ref. [4] Copyright © 2007 Elsevier)

Thus, the redox couple Ag^0/Ag^+ was formed in the structure of HAPTiAg. In the presence of oxygen, the $O_2^{-\bullet}$ could be generated by the electron transfer of the redox couple [7].

6.1.2 Cell Damage Mechanism

Figure 6.7 shows the appearance of *E. coli* after treatment of HAPTiAg films with or without UVA irradiation. Before the reaction, the *E. coli* are a well-defined cell

wall as well as the rendered interior of the cell, which corresponds to the presence of proteins and DNA (Fig. 6.7a). Great changes had taken place to the morphology of *E. coli* after 150 min illumination (Fig. 6.7b, c). The cell wall was decomposed and the rendered interior of the cell became white, indicating that the outer membrane of the cell was damaged leading to leakage of the interior component. Similarly, the cell wall of *E. coli* was also destructed resulting in leakage of the interior component (Fig. 6.7d, e) in the dark with HAPTiAg film. Based on the TEM investigation, the cell wall, the peptidoglycan layer, and the cell membrane of the bacteria were decomposed by $O_2^{-\bullet}$. K^+ exists universally in bacteria [8] and plays a role in the regulation of polysome content and protein synthesis. Therefore, K^+ leakage from the inactivated bacteria can examine the change in cell membrane permeability. As shown in Fig. 6.8, under only UVA irradiation or in the presence of 0.6 mg/L silver ions, the K^+ leakage was very slow. After the addition of HAPTiAg film with or without UVA irradiation, K^+ immediately started to leak from the *E. coli* cells, and the leakage gradually increased with reaction time, paralleling the loss of cell viability. The resultant K^+ concentrations were much higher than that of the control experiments. Moreover, the amount of the K^+ leakage was almost equal under the two conditions, indicating that the cell membrane was damaged to the same extent with or without UVA irradiation. These results demonstrate that the K^+ leakage was consistent with the disruption of the cell wall and the cell membrane by the oxidation and antibacterial action. In the bactericidal process of HAPTiAg, Ti (iV) and Ag^+ ions assist each other. On the one hand, the outer membrane of the cell is attacked by $O_2^{-\bullet}$ produced from HAPTiAg. Successively, Ag^+ ions are effectively taken into the cytoplasmic membrane by the partially decomposed outer membrane. Finally, the bacteria are inactivated by the bacteriostatic action of Ag^+. On the other hand, the bacteriostatic action of these ions enhances the efficiency of $O_2^{-\bullet}$ in killing bacteria. In a conclusion, the high bactericidal activity of HAPTiAg was due to the synergy of the oxidation role of the $O_2^{-\bullet}$ and the bacteriostatic action of antibacterial ions.

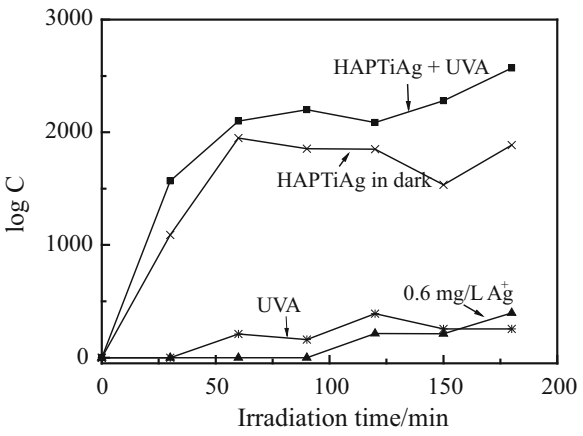

Fig. 6.8 Leakage of K^+ from *E. coli* cells in HAPTiAg film (Reprinted from Ref. [4] Copyright © 2007 Elsevier)

6.2 Visible-Light Photocatalytic Degradation of Pathogenic Bacteria Over Supported Silver Halides

Silver halides are well known as photosensitive materials and are widely employed as source materials in photographic films. AgI and AgBr were supported on P25-TiO_2 by the deposition-precipitation method in an aqueous solution of $AgNO_3$ and NH_4OH containing KI or KBr [9]. Silver halides could act as a good visible-light photocatalyst candidate for the removal of pollutants when suitable environmental conditions could be chosen to prevent their photodecomposition [10–12]. AgI/TiO_2 and AgBr/TiO_2 show high efficiency and photostability in the degradation of nonbiodegradable azo dyes under visible-light irradiation [9, 13]. These catalysts were also found to be highly effective in killing bacteria [13, 14].

6.2.1 Bacterial Inactivation Under Visible-Light Irradiation

The bactericidal activities of the samples were evaluated by the inactivation of *E. coli* and *S. aureus* in water under visible-light irradiation. *E. coli* is a Gram-negative bacteria and *S. aureus* is a Gram-positive bacteria. 6.8 log *E. coli* was completely inactivated within 60 min in the AgBr/TiO_2 suspension under visible-light irradiation (Fig. 6.9), whereas complete inactivation of 6.8 log *S. aureus* occurred at 40 min of irradiation. Neither pure TiO_2 with visible light nor AgBr/TiO_2 in the dark showed any bactericidal effects for the two bacteria (curves a and b). Similarly, 7.8 log *E. coli* and 7 log *S. aureus* were almost completely killed within 60 min and 100 min in the AgI/TiO_2 suspension under visible-light irradiation (Fig. 6.10). These results indicated that AgBr and AgI were the main active component of the catalyst under visible-light irradiation. Different times were

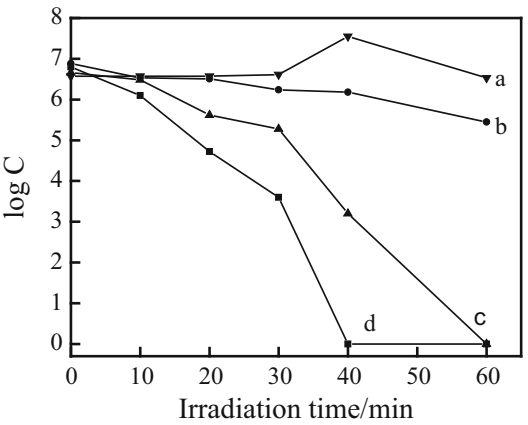

Fig. 6.9 Temporal course of the bacteria inactivation (2×10^7 cfu mL^{-1}, 30 mL) in aqueous dispersions containing 0.2 g L^{-1} of catalysts. (**a**) *S. aureus*/*E. coli* + AgBr/TiO_2 in dark, (**b**) *S. aureus*/*E. coli* + TiO_2, (**c**) *E. coli*, and (**d**) *S. aureus* in visible-light-illuminated AgBr/TiO_2 suspension (Reprinted from Ref. [13] Copyright © 2007 Elsevier)

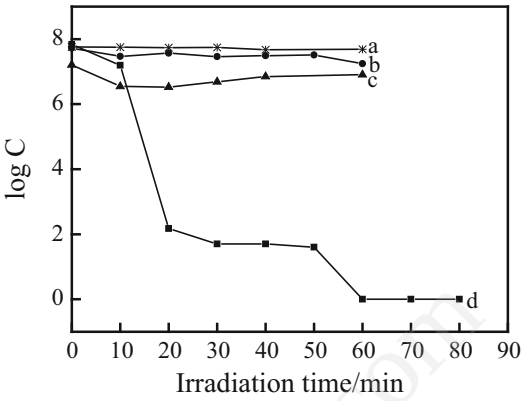

Fig. 6.10 Temporal course of the *E. coli* inactivation (~5×10^7 cfu/mL, 30 mL, pH = 4.04) in aqueous dispersions containing 0.2 g/L of catalysts under visible-light irradiation. (**a**) No catalyst, (**b**) TiO_2, (**c**) AgI/TiO_2 in dark, and (**d**) AgI/TiO_2 (Reprinted from Ref. [13] Copyright © 2007 Elsevier)

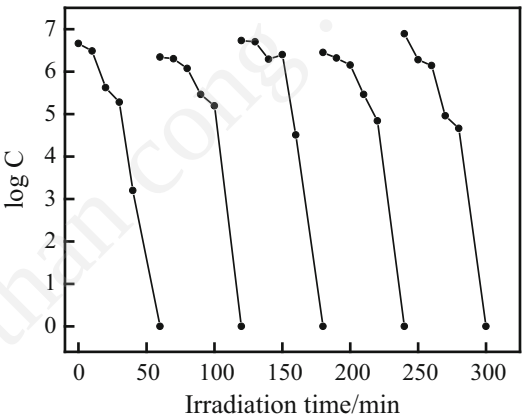

Fig. 6.11 Cycling runs in the photocatalytic inactivation of *E. coli* in the presence of $AgBr/TiO_2$ under visible-light irradiation. $AgBr/TiO_2$ (0.2 g L^{-1}); addition of *E. coli* cells (~2×10^7 cfu mL^{-1}/run) (Reprinted from Ref. [13] Copyright © 2007 Elsevier)

required for total cell inactivation of *E. coli* and *S. aureus* due to their dissimilar cell wall constituents. Gram-negative bacteria have a thin layer of peptidoglycan and a complex cell wall with two cell membranes: an outer membrane and a plasma membrane. Gram-positive bacteria have only one membrane with a relatively thick wall composed of many layers of peptidoglycan polymer. The addition of the outer membrane of Gram-negative bacteria influences the permeability of many molecules, and under certain conditions, Gram-negative bacteria are more resistant to many chemical agents than Gram-positive cells [15]. As shown in Fig. 6.11, the catalyst's activity did not significantly decrease in the inactivation of *E. coli* after five successive cycles under visible-light irradiation, confirming the stability of $AgBr/TiO_2$. These results indicated that the supported AgBr and AgI were highly effective at the killing of bacteria under visible light.

To illustrate the visible-light-induced bactericidal mechanism, the ESR spin-trap technique (with DMPO) was used to detect the nature of the reactive oxygen species generated on the surface of the catalysts under visible-light irradiation. As shown in Fig. 6.12, $^{\bullet}OH$ and $O_2^{-\bullet}$ radicals were formed in visible-light-irradiated

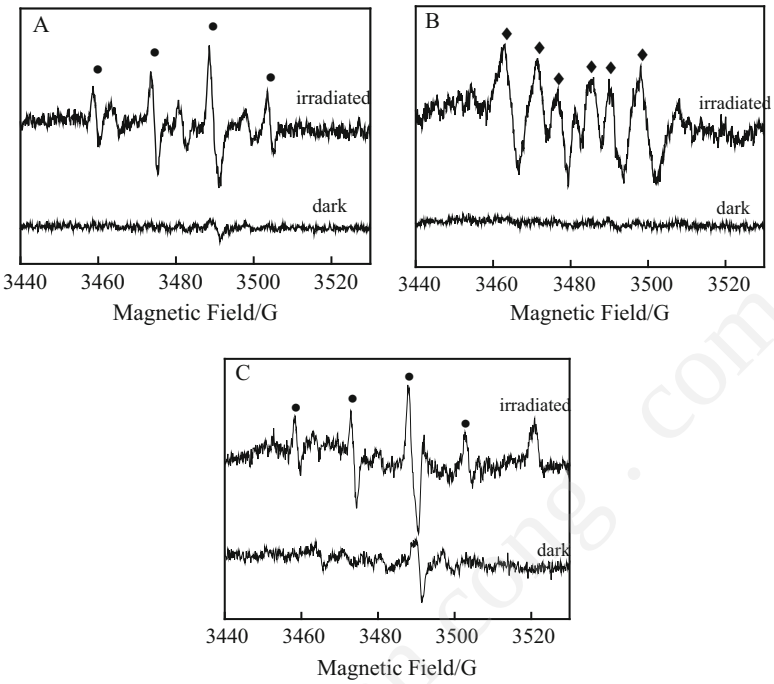

Fig. 6.12 DMPO spin-trapping ESR spectra recorded at ambient temperature with $AgBr/TiO_2$ as catalyst in aqueous (**a**) or methanol (**b**) dispersion and with AgI/TiO_2 as catalyst in aqueous dispersion (**c**) under visible-light irradiation ($\lambda > 420$ nm) (Reprinted from Ref. [13] Copyright © 2007 Elsevier)

$AgBr/TiO_2$ suspension. $^{\bullet}OH$ was also observed in the aqueous AgI/TiO_2 dispersion under visible-light irradiation. No $O_2^{-\bullet}$ radicals were detected in the AgI/TiO_2 dispersion in methanolic media. Furthermore, the formation of H_2O_2 was detected in the visible-light-irradiated $AgBr/TiO_2$ and AgI/TiO_2 system as shown in the previous work [9, 13]. These results indicated that $^{\bullet}OH$, $O_2^{-\bullet}$, and H_2O_2 reactive active species were involved in the photocatalytic bactericidal reaction.

6.2.2 *Interaction of Bacteria with Photocatalysts*

To clarify the interaction of bacteria-photocatalysts, the effects of pH and inorganic ions on bacterial photocatalytic inactivation were investigated. As shown in the previous work [13], the bactericidal activity of $AgBr/TiO_2$ decreased significantly with the pH increasing from 4.0 to 7.5. At pH 4 and pH 6.5, 7 log *E. coli* inactivation occurred at 60 min irradiation, while at pH 7.5, no significant inactivation of *E. coli* was observed. In the range of pH 4–8, the overall charges of the *E. coli* cells were negative, whereas the surface of the catalyst was positively charged at pH < 4.8,

and it was negatively charged at pH > 4.8. Electrostatic attraction existed between *E. coli* and the catalyst at pH 4, leading to more *E. coli* adsorption onto the surface of the catalyst. Thus, the catalyst exhibits more activity for the killing of *E. coli*. At pH 6.5 the surface of the catalyst was partly negatively charged because the pH was approaching the isoelectric point (pH 4.8). The repulsive electrostatic force between *E. coli* and the catalyst was weaker, so the inactivation of *E. coli* was not significantly depressed at pH 6.5. However, at pH 7.5, the surface charge of the catalyst became more negative, and the repulsive electrostatic force was stronger. *E. coli* was not easily adsorbed on the surface of the catalyst, and the *E. coli* inactivation was nearly inhibited. Only less than 1 log *E. coli* were inactivated at 60 min of irradiation. Similarly, in the AgI/TiO_2 system, the inactivation of *E. coli* was the highest at pH = 4.04, and 6.1 log *E. coli* inactivation occurred at 40 min irradiation, while at pH = 7.75, only 0.67 log *E. coli* inactivation was observed at the same irradiation time (Fig. 6.13).

The charges of the bacteria and AgI/TiO_2 under different pH conditions are shown in Fig. 6.14. In the range of pH 2–9, the overall charges of *E. coli* were negative, while the surface charge property of AgI/TiO_2 changed with the change of solution pH. The isoelectric point of AgI/TiO_2 was about 5.1. At pH < 5.1, the surface of the catalyst was positively charged, while it was negatively charged at

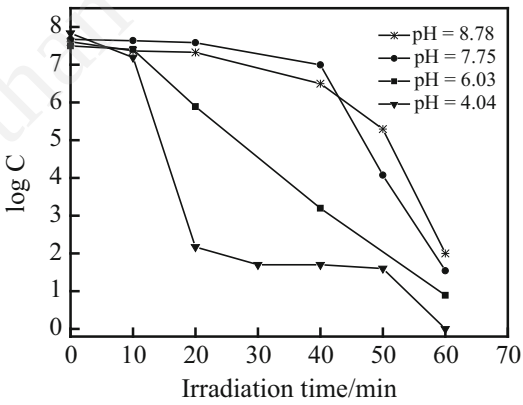

Fig. 6.13 The inactivation of *E. coli* (~5×10^7 cfu/mL) under different pH conditions with visible-light-illuminated AgI/TiO_2 (Reprinted from Ref. [14] Copyright © 2007 American Chemical Society)

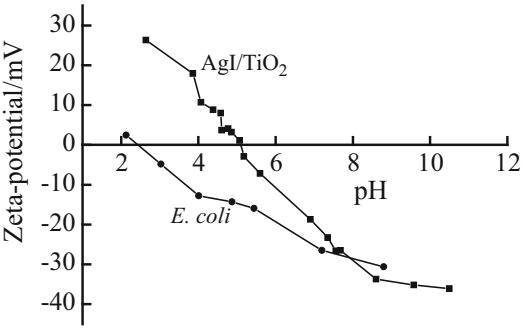

Fig. 6.14 Zeta potentials for a suspension of AgI/TiO_2 1.0 g/l in the presence of KNO_3 (10^{-3} M) (Reprinted from Ref. [14] Copyright © 2007 American Chemical Society)

pH > 5.1. Therefore, at pH = 4.04, electrostatic attraction existed between *E. coli* and catalyst, leading to *E. coli* being tightly bound with the catalyst surface. Thus, a higher inactivation rate was obtained. At pH > 5.1, the electrostatic repulsive force between the *E. coli* and the catalyst increased with the pH increasing due to the more negative zeta potential. This led to the reduction of the *E. coli* inactivation rate. The zeta potential of *E. coli* tended to be less negative at pH = 6.03. Thus, the inactivation of *E. coli* was inhibited to some extent. However, a stronger electrostatic repulsive force resulted in lower bactericidal efficiency at pH = 7.75. At pH = 8.78, the zeta potentials of the catalyst and *E. coli* did not change much as compared with the condition of pH = 7.75, so the inactivation rate of *E. coli* was similar to that at pH = 7.75. The results indicated that interaction of TiO_2 supported AgBr or AgI with bacteria played an important role in disinfection. Hamouda and Baker [16] also showed that if the antimicrobial composition had the same charge as the bacteria cells, this induced repulsion and prevented contact, while the addition of EDTA/Tris buffer to the formulation changed the charge and considerably improved the activity of the formulation. To further study the effects of the interaction between bacteria and catalyst, Ni^{2+} or Mg^{2+} was added into the reaction system. The inactivation rate of *E. coli* was greatly increased with the addition of Ni^{2+} and Mg^{2+} at pH 7.5 in AgBr/TiO_2 suspension and at pH 7.75 in AgI/TiO_2 suspension under visible-light irradiation (Fig. 6.15). The single inorganic ions with visible light did not show any bactericidal activity (Fig. 6.15, curves a and b), indicating that the tested concentration of inorganic ions did not inhibit the growth of bacteria. Furthermore, the zeta potential measurement showed that the zeta potential of AgBr/TiO_2 or AgI/TiO_2 (Fig. 6.16) was more positive in the presence of Ni^{2+}or Mg^{2+} than without the addition of ions. Thus, a weaker repulsive electrostatic force occurred between catalyst and bacteria at pH = 7.5, resulting in higher bactericidal activity. This result further confirmed the role of interaction for *E. coli*-AgX/TiO_2 in disinfection, although the addition of Ni^{2+} or Mg^{2+} may enhance the separation of photogenerated electrons and holes. All of the previous

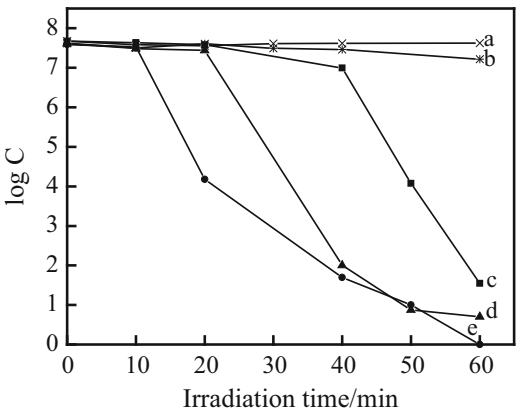

Fig. 6.15 Survival of *E. coli* with visible-light-illuminated AgI/TiO_2 dispersions (0.2 g/L, pH = 7) under otherwise different conditions: (**a**) Ni$(NO_3)_2$ with no catalyst, (**b**) $Mg(NO_3)_2$ with no catalyst, (**c**) without the addition of cations, (**d**) $Mg(NO_3)_2$, and (**e**) $Ni(NO_3)_2$. Cation concentration, 30 μM (Reprinted from Ref. [14] Copyright © 2007 American Chemical Society)

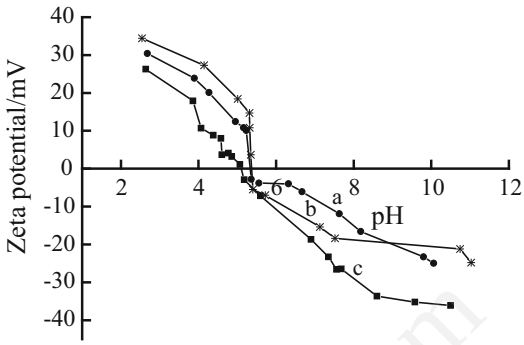

Fig. 6.16 Zeta potentials for different suspensions of AgI/TiO_2 1.0 g/L in the presence of KNO_3 (10^{-3} M): (**a**) 30 μM Ni $(NO_3)_2$, (**b**) 30 μM Mg $(NO_3)_2$, and (**c**) without the addition of ions (Reprinted from Ref. [14] Copyright © 2007 American Chemical Society)

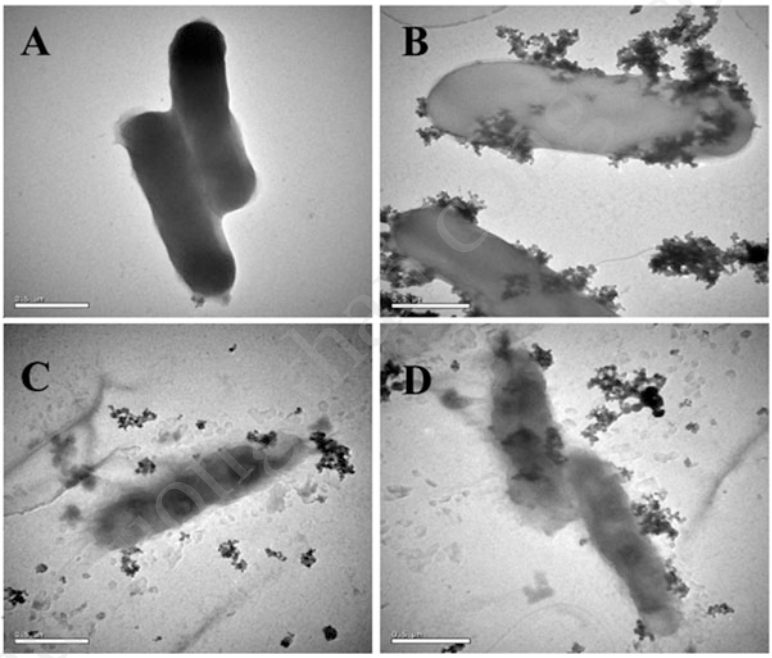

Fig. 6.17 TEM images of *E. coli* for different reaction times in visible-light-illuminated AgI/TiO_2 suspension: (**a**) *E. coli* before reaction, (**b**) *E. coli* treated for 30 min, and (**c**) and (**d**) *E. coli* treated for 120 min (Reprinted from Ref. [14] Copyright © 2007 American Chemical Society)

experimental results indicated that the electrostatic force interaction of the bacteria and catalyst is crucial for high bactericidal efficiency.

6.2.3 Destruction of Cell Structure

In Fig. 6.17, the morphology of bacteria at different stages during bactericidal experiments showed the bactericidal mechanism of various reactive species (e.g., $^{\bullet}$

OH, $O_2^{-\bullet}$, and H_2O_2). Figure 6.17a shows the TEM images of *E. coli*. The characteristics of the bacteria are a well-defined cell wall as well as the evenly rendered interior of the cell, which corresponds to the presence of proteins and DNA. Great changes had taken place to the morphology of *E. coli* that had been illuminated for 30 min (Fig. 6.17b). The cell wall was decomposed, and the rendered interior of the cell became white, indicating that the outer membrane of the cell was damaged, leading to a leakage of the interior component. This phenomenon was more significantly shown in the images of *E. coli* with 2 h irradiation (Fig. 6.17c, d). With irradiation time increasing, the catalyst nanoparticles penetrated inside the cells, resulting in more damage to the membranes of the cells. The lipopolysaccharide layer of the outer membrane plays an essential role in providing a barrier of selective permeability for *E. coli* Gram-negative bacteria. On the basis of the TEM investigation, the AgX/TiO_2 photocatalyst could decompose the cell wall and the cell membrane by reactive species, leading to a change in the cell membrane permeability and a resultant leakage of intracellular substances. K^+ exists universally in bacteria and plays a role in the regulation of polysome content and protein synthesis. Therefore, K^+ leakage from the inactivated bacteria was used in this work to examine the permeability of the cell membrane (Fig. 6.18). In both AgX/TiO_2 in the dark and with only visible-light irradiation (control experiments), there was nearly the same K^+ leakage from *E. coli* cells. The K^+ concentration gradually increased and became approximately steady with increasing reaction time. In the visible-light-illuminated AgX/TiO_2 suspensions, K^+ immediately leaked out, and the leakage increased in parallel with the inactivation of *E. coli* with irradiation time and the total K^+ content (2.66 ppm) from the tested *E. coli* was completely released when all the *E. coli* was completely killed at 60 min of irradiation. This result suggested that the cell membrane permeability had been disrupted with the inactivation of *E. coli*.

As reported before, malondialdehyde (MDA) is a lipid peroxidation product formed from the oxidation of *E. coli* membrane phosphatidylethanolamine [17]. To estimate membrane damage, the formation of MDA was examined in AgI/TiO_2 suspensions under different conditions. As shown in Fig. 6.19, when no AgI/TiO_2

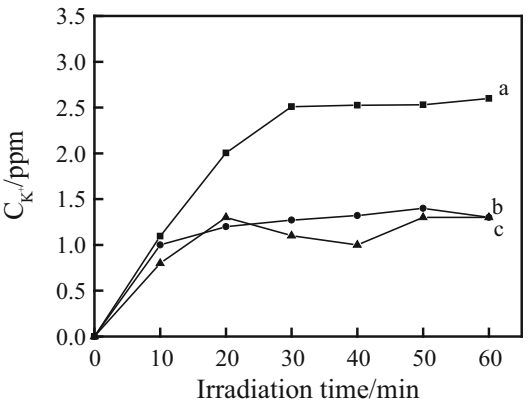

Fig. 6.18 Leakage of K^+ from *E. coli* cells under different conditions: (**a**) and (**b**) AgI/TiO_2 dispersions (0.2 g/L) with and without visible light and (**c**) visible light with no catalyst (Reprinted from Ref. [14] Copyright © 2007 American Chemical Society)

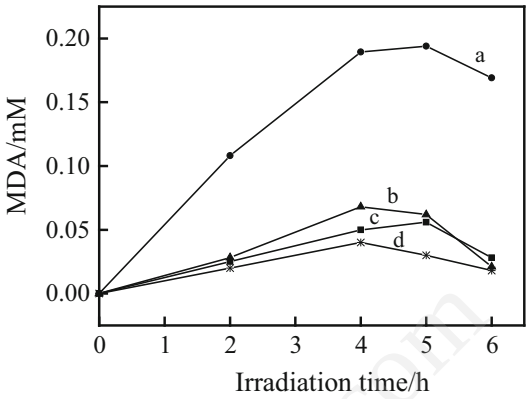

Fig. 6.19 The concentration of MDA from lipid peroxidation of *E. coli* changes with reaction time under different conditions: (**a**) and (**b**) AgI/TiO_2 dispersions (0.2 g/L) with and without visible light and (**c**) and (**d**) with and without visible light in the absence of AgI/TiO_2 (Reprinted from Ref. [14] Copyright © 2007 American Chemical Society)

was present, control cells with visible-light irradiation and in the dark produced comparable low levels of MDA, indicating that the amount of preexisting MDA was negligible and that visible light alone did not result in a significant level of lipid peroxidation. Moreover, when the catalyst was in the dark, the maximum MDA (0.06 μM) was detected at an *E. coli* concentration of 3.1×10^8 cfu/mL. Conversely, in the visible-light-irradiated AgI/TiO_2 suspension, the MDA concentration increased with irradiation time and reached a maximum of 0.19 μM at an *E. coli* concentration of 3.1×10^8 cfu/mL. Subsequently, the MDA concentration decreased with irradiation time. On the basis of all the previous experiments, it is confirmed that MDA was formed and then degraded only in a visible-light-irradiated AgI/TiO_2 system, indicating that the peroxidation reaction of an unsaturated lipid unit of the *E. coli* membrane was first caused by the reactive active species generated from the system, to yield hydroperoxide and dialkyl peroxides [18]. Furthermore, the breakdown of hydroperoxides and lipid endoperoxide radicals leads to the formation of various products including MDA [17, 19]. Continuously, MDA was further oxidized by reactive species. The results also indicated the process of the photodegradation of the cell membrane.

Figure 6.20 shows the FTIR spectra of *E. coli* as a function of time during AgI/TiO_2 visible-light photocatalysis. In the FTIR spectra of *E. coli*, the specific functional groups were obtained by referencing the reported values for biomolecules and bacteria cells [20]. In Fig. 6.20a, the characteristic peaks at 3295 and 3062 cm^{-1} were assigned to amide A and amide B, respectively, while the peaks at 2963, 2927, 2852, and 2872 cm^{-1} were attributed to $\nu a\ (CH_3)$, $\nu a\ (CH_2)$, $\nu s\ (CH_3)$, and $\nu s\ (CH_2)$, respectively. With irradiation time increasing, these characteristic peaks decreased. After 6 h, amide A at 3295 cm^{-1} and amide B at 3060 cm^{-1} disappeared, and also the peak intensity of the C–H bands at 2872 and 2852 cm^{-1} disappeared. The two peaks at 2963 and 2927 cm^{-1} were almost undetectable. Concomitantly, the wide band of the OH- vibrations is transformed in the skewed form with a maximum at around 3347 cm^{-1}. Figure 6.20b shows significant changes of the initial band shapes of the oligosaccharide bands around 1087 cm^{-1} and profile changes of the PO_2^- band near 1242 cm^{-1}, as well as the decay of the

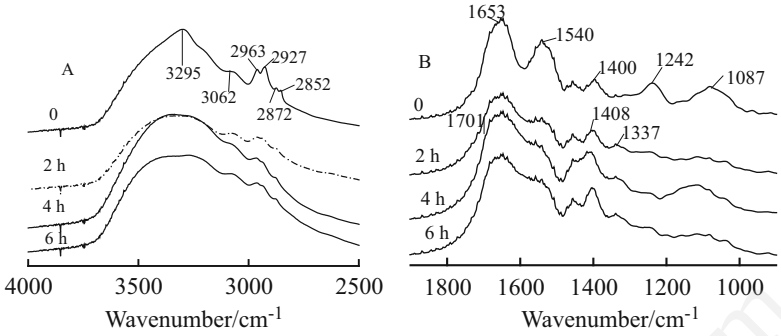

Fig. 6.20 Changes of FTIR spectra of *E. coli* during the photocatalytic inactivation of *E. coli* (Reprinted from Ref. [14] Copyright © 2007 American Chemical Society)

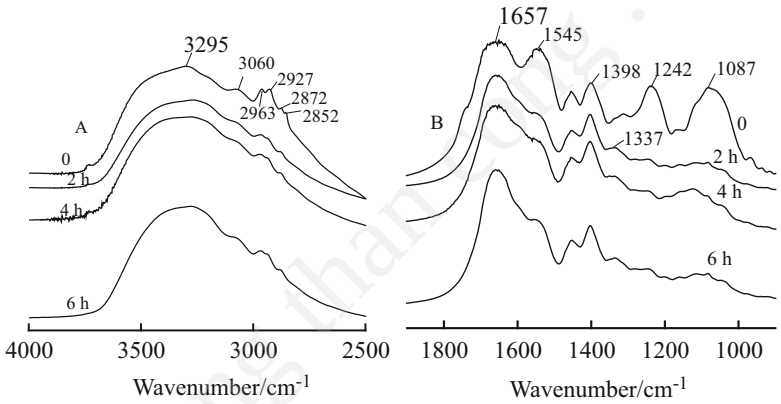

Fig. 6.21 Changes of FTIR spectra of *S. aureus* during the photocatalytic inactivation of *S. aureus* (Reprinted from Ref. [14] Copyright © 2007 American Chemical Society)

amide I band near 1653 cm^{-1} and the amide II band near 1545 cm^{-1}. In parallel, an increase in absorbance in the region related to the CO bonds of aldehydes and ketones between 1690 and 1734 cm^{-1} was observed. After 120 min, the most prominent peaks were seen at 1408 and 1337 cm^{-1}, indicating an increase in the concentration of carboxylic groups. The results revealed that the formation of carboxylic acid occurred with the photocatalytic degradation of the cell membrane. Similarly, the spectral profiles of the FTIR spectra of *S. aureus* with irradiation time also showed almost the same changes as *E. coli* during AgI/TiO_2 photocatalysis under visible-light irradiation (Fig. 6.21). Some initial spectral profile of *S. aureus* disappeared or decayed with increasing irradiation time. Equally, the carboxylic groups' peak at 1337 cm^{-1} appeared after 120 min and increased with increasing irradiation time, indicating the formation of carboxylic acid. The results indicated that the cell wall and membrane were degraded by the oxidation of the reactive species, resulting in cell death.

6.3 Plasmon-Induced Inactivation of Enteric Pathogenic Microorganisms with Ag-AgI/Al_2O_3 Under Visible-Light Irradiation

6.3.1 Plasmon-Induced Photocatalytic Pathogenic Microorganism Inactivation Under Visible-Light Irradiation

Noble metal nanoparticles (NPs) exhibit strong UV-Vis absorption due to their plasmon resonance, which is produced by the collective oscillations of surface electrons [21, 22]. The plasmon resonance results in the high photosensitivity of noble metal NPs, which is potentially applicable to the development of a new class of plasmonic photocatalysts and photovoltaic fuel cells [23, 24]. Several plasmonic photocatalysts have been developed for photocatalytic degradation in the visible or UV region of different organic pollutants. In particular, the plasmon-induced photocatalytic mechanism and the stability of NPs have been investigated in detail for Ag-AgI/Al_2O_3 in the photodegradation of organic contaminants [25]. Moreover, Ag-AgI/Al_2O_3 exhibited particularly good bactericidal performance compared to ordinary photocatalysts [26]. Its bactericidal efficiency was significantly enhanced by common inorganic anions in water including bicarbonate, phosphate, and sulfate [27]. The bactericidal activities of the AgI/Al_2O_3 and Ag-AgI/Al_2O_3 were evaluated by the inactivation of *Shigella dysenteriae* (*S. dysenteriae*) in water under visible-light irradiation. As shown in Fig. 6.22, visible light alone had no bactericidal effect on *S. dysenteriae*. In contrast, an approximately 8.5 log removal of *S. dysenteriae* was attained within 10 min and 15 min in Ag-AgI/Al_2O_3 suspension under $\lambda > 420$ nm and $\lambda > 450$ nm visible-light irradiation, respectively, while the same concentration of *S. dysenteriae* was completely removed after 25 min in AgI/Al_2O_3 suspension under $\lambda > 420$ nm visible-light irradiation. Furthermore, by inductively coupled plasma optical emission spectrometry analysis, the

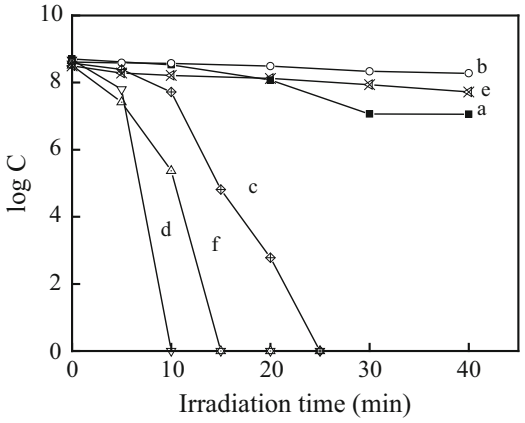

Fig. 6.22 Temporal course of the *S. dysenteriae* inactivation (pH = 7.25) in aqueous dispersions containing 0.2 g/L catalysts: (**a**) Ag-AgI/Al_2O_3 in dark, (**b**) no catalyst, (**c**) AgI/Al_2O_3 and (**d**) Ag-AgI/Al_2O_3 with $\lambda > 420$ nm, and (**e**) AgI/Al2O3 and (**f**) Ag-AgI/Al_2O_3 with $\lambda > 450$ nm (Reprinted from Ref. [27] Copyright © 2010 American Chemical Society)

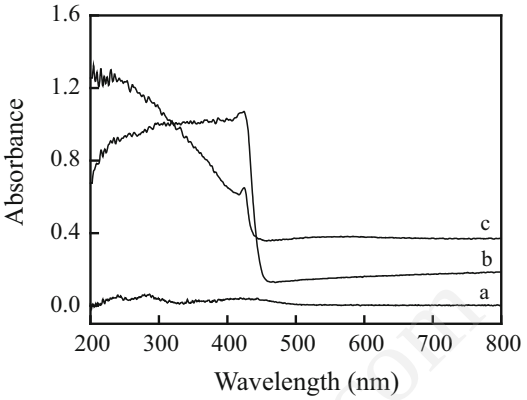

Fig. 6.23 Diffuse reflectance UV-Vis spectra of (**a**) Al_2O_3, (**b**) AgI/Al_2O_3, and (**c**) $Ag\text{-}AgI/Al_2O_3$ (Reprinted from Ref. [25] Copyright © 2010 American Chemical Society)

concentration of Ag^+ released from the $Ag\text{-}AgI/Al_2O_3$ suspension ranged from 0.17 to 0.24 ppm during the photocatalytic reaction in deionized and doubly distilled water, while in tap water, the released Ag^+ ranged from 0.01 to 0.1 ppm. An approximately 1.6 log removal of *S. dysenteriae* was attained after 40 min in the $Ag\text{-}AgI/Al_2O_3$ dark dispersion due to the released Ag^+. Obviously, AgI/Al_2O_3 showed no photocatalytic activity at visible-light irradiation under $\lambda > 450$ nm because it absorbed hardly in the wavelengths range of $\lambda > 450$ nm (Fig. 6.23). The results indicated that different photochemical processes occurred in the $Ag\text{-}AgI/Al_2O_3$ and AgI/Al_2O_3 suspensions with irradiation, which contributed to the different light absorption. As shown in Fig. 6.23, the mesoporous Al_2O_3 was transparent at wavelengths between 200 and 800 nm. AgI/Al_2O_3 exhibited two absorption bands including 200–400 nm (UV) and 400–430 nm (visible) assigned to the light absorption of AgI. Besides these, $Ag\text{-}AgI/Al_2O_3$ exhibited a band around 400–600 nm assigned to the surface plasmon absorption of Ag NPs. Therefore, the enhanced bactericidal activity of $Ag\text{-}AgI/Al_2O_3$ was due to the plasmon resonance of Ag NPs rather than the result of electron trapping by Ag NPs enhancing electron-hole separation. In particular, at wavelengths $\lambda > 450$ nm, $Ag\text{-}AgI/Al_2O_3$ photocatalytic disinfection mainly resulted from the plasmon resonance of Ag NPs. These results indicate that $Ag\text{-}AgI/Al_2O_3$ is an effective plasmon-induced photocatalyst under visible light for inactivation of enteric pathogenic bacteria.

6.3.2 *Effect of pH on Plasmon-Induced Photocatalytic Disinfection Kinetics*

Figure 6.24 shows the inactivation of *E. coli* in the irradiated $Ag\text{-}AgI/Al_2O_3$ suspension with varying initial pHs. Clearly, the bactericidal activity of $Ag\text{-}AgI/Al_2O_3$ increased significantly as the pH increased from 4.5 to 8.5. At pH 8.5, an

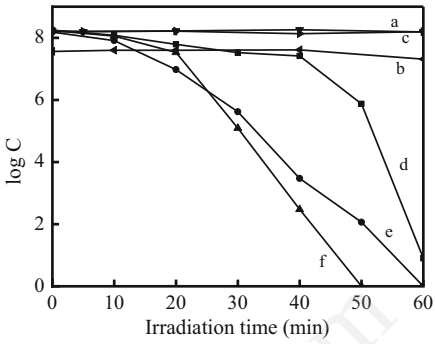

Fig. 6.24 The inactivation of *E. coli* at different starting pH in visible-light-irradiated ($\lambda > 420$ nm) Ag-AgI/Al_2O_3 suspension (0.2 g/L): (**a**) pH = 4.5 control, (**b**) pH = 7.2 control, (**c**) pH = 8.5 control, (**d**) pH = 4.5, (**e**) pH = 7.25, and (**f**) pH = 8.5 (Reprinted from Ref. [27] Copyright © 2010 American Chemical Society)

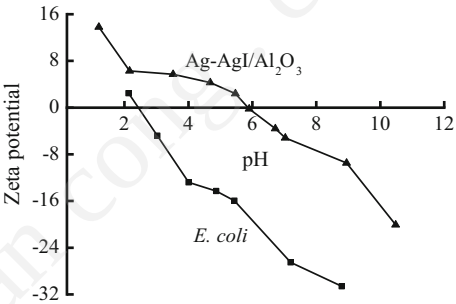

Fig. 6.25 Plots of the zeta potential as a function of pH for 0.1 g/L Ag-AgI/Al_2O_3 suspension in the presence of KNO_3 (10^{-3} M) and *E. coli* suspension in the presence of NaCl (0.1 M) (Reprinted from Ref. [27] Copyright © 2010 American Chemical Society)

8 log inactivation of *E. coli* occurred at 50 min, while at pH 7.25, the same inactivation occurred at 60 min; at pH 4.5, the same inactivation needed even more time. In addition, no significant *E. coli* inactivation was observed in the Ag-AgI/Al_2O_3-free solution with the corresponding pH, indicating that *E. coli* could live in the tested pH range. The results did not correlate with the interaction of bacteria and Ag-AgI/Al_2O_3 as a semiconductor in photocatalytic disinfection [16, 28]. As shown in Fig. 6.25, according to the charge properties of bacteria and the catalyst, electrostatic attraction existed between pH 4 and 6, leading to more *E. coli* adsorption onto the surface of the catalyst. For pH > 6, a repulsive electrostatic force occurred between them, leading to lower adsorption of *E. coli*. Based on the general photocatalytic disinfection mechanism, the former should result in higher bactericidal efficiency, while the latter should result in a lower one. In fact, the opposite results were obtained, indicating that different disinfection mechanisms existed in the reaction system.

6.3.3 *Effect of Inorganic Ions on Plasmon-Induced Photocatalytic Disinfection Kinetics*

The effects of several inorganic ions that are common in water on the bactericidal activity of Ag-AgI/Al_2O_3 were investigated under visible-light irradiation. As

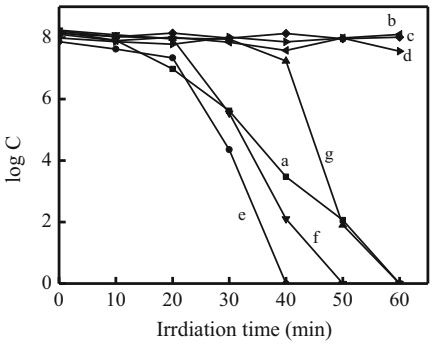

Fig. 6.26 Survival of *E. coli* with visible-light-irradiated ($\lambda > 420$ nm) Ag-AgI/Al_2O_3 (0.2 g/L) dispersions at starting pH 7.25 under otherwise different conditions: (**a**) only Ag-AgI/Al_2O_3, (**b**) $NaHCO_3$ with no catalyst, (**c**) Na_2SO_4 with no catalyst, (**d**) KH_2PO_4 with no catalyst, (**e**) $NaHCO_3$, (**f**) Na_2SO_4, and (**g**) KH_2PO_4. Anion concentration, 0.1 M (Reprinted from Ref. [27] Copyright © 2010 American Chemical Society)

shown in Fig. 6.26, both HCO_3^- and SO_4^{2-} ions significantly enhanced *E. coli* inactivation, while $H_2PO_4^-$ ions had a negative effect on the reaction at the initial stage and a positive role to cause 8 log *E. coli* inactivation at the same time with that one in the Ag-AgI/Al_2O_3 suspension without any anion. The starting pH of the suspension was adjusted to 7.25 using HCl or NaOH solution, and subsequently, the pH did not change throughout the experiments. Under visible light, the individual ion species (HCO_3^-, SO_4^{2-}, or $H_2PO_4^-$) did not exhibit any bactericidal activity, indicating that these inorganic anions themselves were not toxic to *E. coli*. These results were in contrast to those found in the photodegradation of organics with visible-illuminated Ag-AgI/Al_2O_3 suspension, whereby the degradation of 2-chlorophenol (2-CP) was markedly depressed by HCO_3^- [25]. The same system exhibited a different performance for the disinfection and elimination of organics. Moreover, inorganic anions generally suppressed the bactericidal efficiency of the photocatalyst in photocatalytic disinfection. HCO_3^-, SO_4^{2-}, and $H_2PO_4^-$ were found to have high adsorption on the surface of the catalyst. The adsorbed inorganic anions reacted with electron holes (h^+) and adsorbed $^{\bullet}OH$ on the catalyst to form $HCO_3^{\bullet}$, $SO_4^{\bullet-}$, and $H_2PO_4^{\bullet}$ [29], which were less reactive than h^+ and $^{\bullet}OH$. For the general reaction system, HCO_3^-, SO_4^{2-}, and $H_2PO_4^-$ would play a negative role [28, 30, 31]. In the Ag-AgI/Al_2O_3 suspension, the main reactive oxygen species on Ag NPs were $O_2^{\bullet-}$ and excited h^+, while the latter could be scavenged by these anions to form anion radicals, which were weaker oxidants for the degradation of organic compounds. However, since these anions could permeate the *E. coli* cell membrane and be absorbed by the cell [32], these anion radicals could lead to stronger bactericidal activity than excited h^+ on Ag NPs, which were not absorbed into the cell. Overall, these results suggest that the process of plasmon-induced photocatalytic disinfection using Ag-AgI/Al_2O_3 involves more than one mechanism.

6.3.4 Plasmon-Induced Photocatalytic Disinfection Mechanism

The increased activity of Ag-AgI/Al_2O_3 was the result of the photoexcited AgI semiconductor and plasmon-induced Ag NPs under visible-light irradiation ($\lambda > 420$ nm). However, the Ag NPs plasmon-induced photocatalysis predominated due to the stronger light absorption in the visible region. In a previous study [25], the mechanism of plasmon-induced photodegradation of organic pollutants by Ag NPs was verified by electron spin resonance and CV analyses. Two electron-transfer processes, from the excited Ag NPs to AgI and from 2-CP to the Ag NPs, occurred during the degradation of 2-CP in Ag-AgI/Al_2O_3 suspensions. Moreover, both $O_2^{\bullet-}$ and excited h^+ on Ag NPs were the main active species. However, different reaction processes occurred in the same system during the inactivation of pathogenic microorganisms. The effects of the pH and inorganic anions on the transfer of plasmon-induced charges were also investigated by CV analyses to illustrate the bactericidal mechanism of Ag-AgI/Al_2O_3. Figure 6.27 shows the changes in the photocurrent at the Ag-AgI/Al_2O_3 photoanode under different conditions. In the absence of *E. coli* under visible-light irradiation, the photocurrent increased and then decreased to zero, resulting in a peak, which contributed to the oxidation of Ag NPs. With the addition of *E. coli*, the peak gradually decreased and became indiscernible at 8×10^7 cfu/mL. The results revealed that the photocurrent was generated by the plasmon-induced Ag NPs under visible-light irradiation; this led to the photooxidation of Ag NPs, which could then be reduced by pathogenic microorganisms to obtain photostable Ag NPs. However, the same phenomena were not observed under dark but otherwise identical conditions. In the dark, the oxidation peak of Ag NPs appeared due to the oxidation of O_2 in the absence of *E. coli*, but did not disappear with the addition of *E. coli*. Thus, the plasmon induction of Ag NPs was essential for the electron transfer from *E. coli* to Ag NPs. Therefore, the plasmon-induced h^+ on Ag NPs was still one of the primary

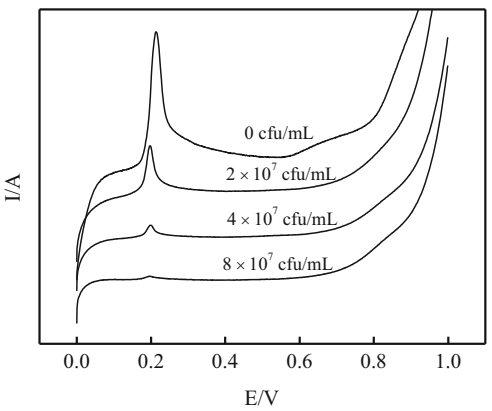

Fig. 6.27 The photocurrent changes at the Ag-AgI/Al_2O_3 photoanode under visible-light irradiation ($\lambda > 420$ nm) in air-saturated 0.1 M sodium sulfate aqueous solutions with different concentration of *E. coli* (Reprinted from Ref. [27] Copyright © 2010 American Chemical Society)

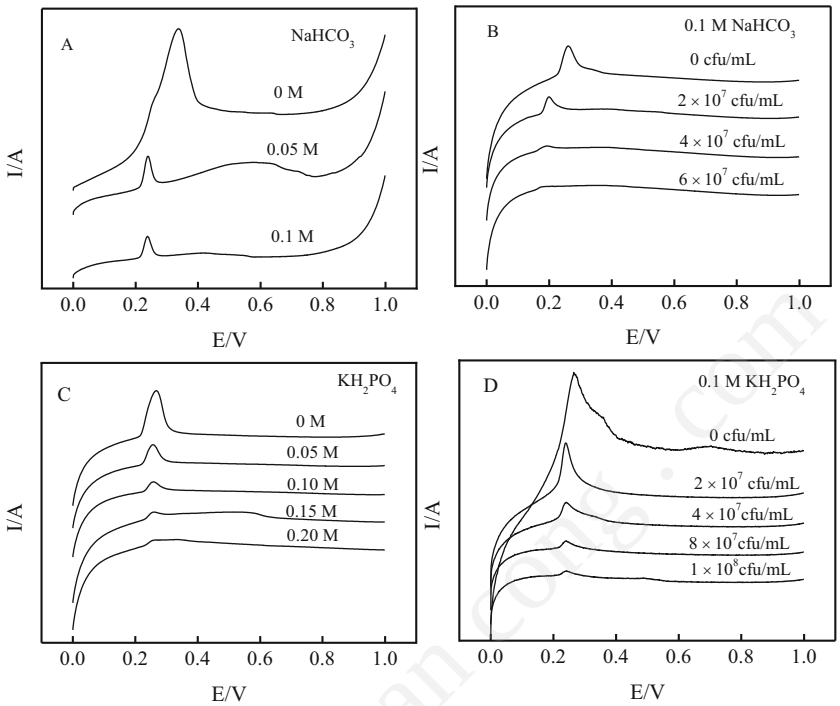

Fig. 6.28 The effects of $NaHCO_3$ and KH_2PO_4 on the photocurrent changes at the Ag-AgI/Al_2O_3 photoanode under visible-light irradiation ($\lambda > 420$ nm) in 0.1 M sodium sulfate aqueous solutions with the specified conditions (Reprinted from Ref. [27] Copyright © 2010 American Chemical Society)

active species in the photocatalytic inactivation of pathogenic microorganisms besides $O_2^{\bullet -}$.

As shown in Fig. 6.28, the peaks of Ag NPs gradually decreased and became almost indiscernible at 0.1 M HCO_3^- with the addition of HCO_3^- in the absence of *E. coli* under visible-light irradiation. In contrast, the addition of NO_3^- did not have the same influence on the oxidation of Ag NPs under otherwise identical conditions (Fig. 6.29). These results confirmed that HCO_3^- could reduce the plasmon-induced Ag^+ as electron donors to form $HCO_3^{\bullet}$; thus, electron transfer occurred from HCO_3^- to Ag NPs, but not between the plasmon-induced Ag^+ and NO_3^-. In the presence of 0.1 M HCO_3^-, with the addition of *E. coli*, the oxidation peak also gradually decreased and completely disappeared at 4×10^7 cfu/mL *E. coli*, while the peak completely disappeared at 8×10^7 cfu/mL *E. coli* without HCO_3^- (Fig. 6.28b). These results indicated that HCO_3^- enhanced electron transfer and led to higher bactericidal activity. A similar phenomenon was observed at the Ag-AgI/Al_2O_3 photoanode in the presence of $H_2PO_4^-$. With increasing $H_2PO_4^-$ concentration, the oxidation peak decreased and disappeared at 0.2 M $H_2PO_4^-$ (Fig. 6.28c), which indicated that the reductive ability of $H_2PO_4^-$ was lower than that of HCO_3^-. At 0.1 M $H_2PO_4^-$, with the addition of *E. coli*, the peak decreased as much as it did

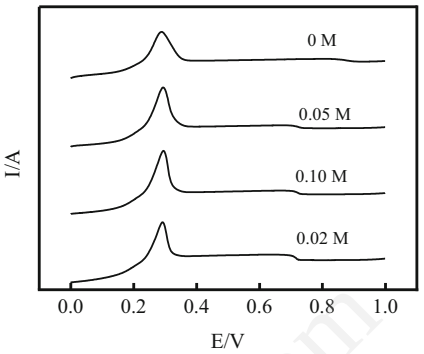

Fig. 6.29 The effect of $NaNO_3$ on the photocurrent changes at the Ag-AgI/Al_2O_3 photoanode under visible-light irradiation ($\lambda > 420$ nm) in 0.1 M sodium sulfate aqueous solutions (Reprinted from Ref. [27] Copyright © 2010 American Chemical Society)

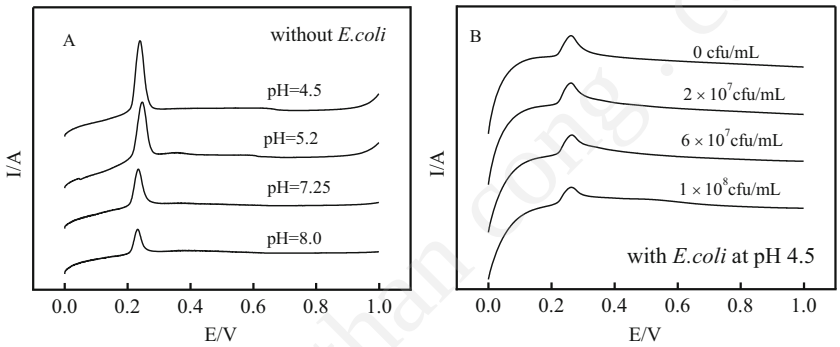

Fig. 6.30 The effect of pH on the photocurrent changes at the Ag-AgI/Al_2O_3 photoanode under visible-light irradiation in 0.1 M sodium sulfate aqueous solutions under different conditions (Reprinted from Ref. [27] Copyright © 2010 American Chemical Society)

without $H_2PO_4^-$ (Fig. 6.28d), which was parallel with the inactivation of *E. coli* under the same conditions. Since the photocurrent was determined in an air-saturated 0.1 M sodium sulfate aqueous solution, the effect of SO_4^{2-} on the electron transfer could not be observed. However, these observations verified that two electron transfers occurred from plasmon-induced h^+ on Ag NPs during the inactivation of *E. coli* in the presence of these inorganic anions. One was from *E. coli* to Ag NPs, and the other was from inorganic anions to Ag NPs to form inorganic anion radicals. Thus, the plasmon-induced h^+, inorganic radicals, and $O_2^{\bullet -}$ were involved in the inactivation of *E. coli*. These inorganic anions not only enhanced the reduction of plasmon-induced Ag^+ by promoting two electron-transfer rates from the excited Ag NPs to AgI and from *E. coli* to the Ag NPs, but the anion radicals also exhibited higher bactericidal efficiency due to their absorbability by the pathogenic cells. Similarly, pH had a similar effect on the electron transfer from Ag NPs to donors. As shown in Fig. 6.30a, the oxidation peak of Ag NPs decreased as the pH of the initial solution increased in the absence of *E. coli*. The peak intensity at pH 4.5 was higher than that at pH 8.5, which paralleled the

bactericidal activity at different pHs. Moreover, the oxidation peak at pH 4.5 decreased slightly with increasing *E. coli* (as shown in Fig. 6.30b), which was similar to the bactericidal efficiency under the same conditions. These results indicated that the plasmon-induced Ag^+ was reduced by the adsorbed hydroxyl ions (OH^-) on the catalyst. Thus, $^{\bullet}OH$ was very possibly formed with the reaction of OH^- and plasmon-induced h^+ on Ag NPs. OH^- ions also enhanced the electron transfer, leading to the higher bactericidal activity of Ag-AgI/Al_2O_3. Therefore, the Ag-AgI/Al_2O_3 photocatalytic disinfection mainly depended on the transfer of plasmon-induced charges, which resulted in the formation of ROS. The presence of these ubiquitous anions in water benefited the electron transfer, and their anionic radicals resulted in higher bactericidal activity. Plasmonic photocatalysis is a very promising method of water disinfection.

References

1. Monma H (1982) Catalytic behavior of calcium phosphates for decompositions of 2-propanol and ethanol. J Catal 75:200–203
2. Miyake M, Ishigaki K, Suzuki T (1986) Structure refinements of Pb^{2+} ion-exchanged apatites by x-ray powder pattern-fitting. J Solid State Chem 61:230–235
3. Tanizawa Y, Sawamura K, Suzuki T (1990) Reaction characteristics of dental and synthetic apatites with Fe^{2+} and Fe^{3+} ions. J Chem Soc Faraday Trans 86:1071–1075
4. Hu C, Guo J, Qu J, Hu X (2007) Efficient destruction of bacteria with Ti(IV) and antibacterial ions in co-substituted hydroxyapatite films. Appl Catal B: Environ 73:345–353
5. Matsumura Y, Kanai H, Moffat JB (1997) Catalytic oxidation of carbon monoxide over stoichiometric and non-stoichiometric hydroxyapatites. J Chem Soc Faraday Trans 93:4383–4387
6. Nishikawa H (2003) Surface changes and radical formation on hydroxyapatite by UV irradiation for inducing photocatalytic activation. J Mol Catal A: Chem 206:331–338
7. Joo SH, Feitz AJ, Waite TD (2004) Oxidative degradation of the carbothioate herbicide, molinate, using nanoscale zero-valent iron. Environ Sci Technol 38:2242–2247
8. Saito T, Iwase T, Horie J, Morioka T (1992) Mode of photocatalytic bactericidal action of powdered semiconductor TiO_2 on mutans streptococci. J Photochem Photobiol 14:369–379
9. Hu C, Hu XX, Wang LS et al (2006) Visible-light-induced photocatalytic degradation of azodyes in aqueous AgI/TiO_2 dispersion. Environ Sci Technol 40:7903–7907
10. Hu C, Lan Y, Qu J et al (2006) Ag/AgBr/TiO_2 visible light photocatalyst for destruction of azodyes and bacteria. J Phys Chem B 110:4066–4072
11. Kakuta N, Goto N, Ohkita H et al (1999) Silver bromide as a photocatalyst for hydrogen generation from CH_3OH/H_2O solution. J Phys Chem B 103:5917–5919
12. Rodrigues S, Uma S, Martyanov IN et al (2005) AgBr/Al-MCM-41 visible-light photocatalyst for gas-phase decomposition of CH_3CHO. J Catal 233:405–410
13. Lan Y, Hu C, Hu X et al (2007) Efficient destruction of pathogenic bacteria with AgBr/TiO_2 under visible light irradiation. Appl Catal B Environ 73:354–360
14. Hu C, Guo J, Qu J (2007) Photocatalytic degradation of pathogenic bacteria with AgI/TiO_2 under visible light irradiation. Langmuir 23:4982–4987
15. Tortora G, Funke RB, Case LC (2001) Microbiology: an introduction. Addison-Wesley Longman, InC., New York
16. Hamouda T, Baker JR (2000) Antimicrobial mechanism of action of surfactant lipid preparations in enteric Gram-negative bacilli. J Appl Microbiol 89:397–403

17. Maness PC, Smolinski S, Blake DM et al (1999) Bactericidal activity of photocatalytic TiO_2 reaction: toward an understanding of its killing mechanism. Appl Environ Microbiol 65:4094–4098
18. Kiwi J, Nadtochenko V (2004) New evidence for TiO_2 photocatalysis during bilayer lipid peroxidation. J Phys Chem B 108:17675–17684
19. Siegel G, Malmsten M (2002) Lipoprotein–proteoglycan interactions at a silica surface membrane. Sep Purif Technol 28:1–11
20. Naumann D (2000) Infrared spectroscopy. Wiley, Chichester
21. Jin R, Cao Y, Mirkin CA et al (2001) Photoinduced conversion of silver nanospheres to nanoprisms. Science 294:1901–1903
22. Link S, El-Sayed MA (1999) Spectral properties and relaxation dynamics of surface plasmon electronic oscillations in gold and silver nanodots and nanorods. J Phys Chem B 103:8410–8426
23. Awazu K, Fujimaki M, Rockstuhl C (2008) A plasmonic photocatalyst consisting of silver nanoparticles embedded in titanium dioxide. J Am Chem Soc 130:1676–1680
24. Wang P, Huang B, Qin X et al (2008) Ag@AgCl: a highly efficient and stable photocatalyst active under visible light. Angew Chem Int Ed 47:7931–7933
25. Hu C, Peng T, Hu X et al (2010) Plasmon-induced photodegradation of toxic pollutants with Ag-Agl/Al_2O_3 under visible-light irradiation. J Am Chem Soc 132:857–862
26. Yu JC, Ho W, Yu J et al (2005) Efficient visible-light-induced photocatalytic disinfection on sulfur-doped nanocrystalline titania. Environ Sci Technol 39:1175–1179
27. Hu X, Hu C, Peng T et al (2010) Plasmon-induced inactivation of enteric pathogenic micro-organisms with Ag–AgI/Al_2O_3 under visible-light irradiation. Environ Sci Technol 44:7058–7062
28. Rincón AG, Pulgarin C (2004) Effect of pH, inorganic ions, organic matter and H_2O_2 on *E. coli* K12 photocatalytic inactivation by TiO_2: implications in solar water disinfection. Appl Catal B: Environ 51:283–302
29. Ross AB, Neta P (1979) Rate constants for reactions of inorganic radicals in aqueous solution. National Bureau of Standards, U.S. Department of Commerce, Washington, DC
30. Marugán J, Grieken R, Sordo C et al (2008) Kinetics of the photocatalytic disinfection of Escherichia coli suspensions. Appl Catal B: Environ 82:27–36
31. Alrousan DMA, Dunlop PSM, McMurray TA et al (2009) Photocatalytic inactivation of *E. coli* in surface water using immobilised nanoparticle TiO_2 films. Water Res 43:47–54
32. Criado S, Marioli JM, Allegretti PE et al (2001) Oxidation of di- and tripeptides of tyrosine and valine mediated by singlet molecular oxygen, phosphate radicals and sulfate radicals. J Photochem Photobiol B 65:74–84

Chapter 7
Photocatalytic Disinfection by Metal-Free Materials

Wanjun Wang, Dehua Xia, and Po Keung Wong

Abstract Recent years have seen a surge of interest in the application of solar energy for water disinfection by using semiconductor photocatalysts. Seeking visible-light-driven (VLD) photocatalysts for efficient solar energy conversion for bacterial disinfection has become an intensifying endeavor in this field. While overwhelming attention has been given to metal-based semiconductors, researchers have turned their focus on metal-free materials for photocatalysis in recent years. Metal-free photocatalysts have unique advantages of earth abundance, low cost, simple structure, simple synthesis, and environmental friendliness. This chapter presents an overview of current research activities that center on the preparation, characterization, and application of metal-free photocatalysts for water disinfection under visible-light irradiation. It is organized into three major parts, according to the classification of the metal-free photocatalysts. One is graphitic carbon nitride ($g\text{-}C_3N_4$)-based photocatalysts. The other is graphene-based photocatalysts, and the third is elemental photocatalysts that are made of only one single element. The material preparation and modification, photocatalytic mechanism, and bacterial disinfection mechanism are also reviewed in detail. Finally, it is concluded with a discussion about research opportunities and challenges facing the development of metal-free photocatalysts for bacterial disinfection using solar energy.

Keywords Photocatalysis • Bacterial disinfection • Metal-free • Graphitic carbon nitride • Elemental photocatalyst

7.1 Introduction

Inadequate access to clean water and sanitation has been one of the most pervasive problems affecting people throughout the world. It has been estimated by the United Nations that 11 % of the global population (approx. 783 million people) remains without access to safe drinking water [1]. Consumption of poor-quality

W. Wang • D. Xia • P.K. Wong (✉)
School of Life Sciences, The Chinese University of Hong Kong, Shatin, N.T., Hong Kong SAR, China
e-mail: pkwong@cuhk.edu.hk

T. An et al. (eds.), *Advances in Photocatalytic Disinfection*, Green Chemistry and Sustainable Technology, DOI 10.1007/978-3-662-53496-0_7

drinking water contaminated with pathogens and chemical pollutants is associated with a number of both short- and long-term adverse health outcomes. For example, diarrhea, often resulting from ingesting pathogens with contaminated drinking water, was the cause of about 1.5 million human deaths in 2012 alone [1]. Problems with waterborne diseases are expected to grow worse in future, both in developing and industrialized nations. Therefore, effective and lower-cost methods to disinfect microorganisms contaminated waters are urgently needed, without further stressing the environment or endangering human health by the treatment itself [2].

Traditional methods of water disinfection, such as chlorination, ozonation, and UV disinfection, are often chemically, energetically, and operationally intensive [3–5]. Among potential solutions, semiconductor-based photocatalysis has emerged with inestimable superiority because it is considered as an economic, renewable, clean, and safe technology [6–8], which requires only the inexhaustible solar light as a driving force, and a suitable semiconductor as a photocatalyst to conduct catalytic reactions for microbial disinfection. Heterogeneous photocatalysis has been shown to be effective for the inactivation of a wide range of pathogenic microorganisms, including some which are resistant to other methods of disinfection. Since Matsunaga et al. first reported the inactivation of bacteria using TiO_2 photocatalysis in 1985 [9], there have been more than 1000 research papers published in this area. The effectiveness of photocatalysis against a wide range of microorganisms, including bacteria (cells [10, 11], spores [12], and biofilms [11]), viruses [13], protozoa [14], fungi [15], and algae [16], has been reported in the past few decades.

The most important task for constructing photocatalytic systems for water disinfection is the development of efficient photocatalysts. Over the past few decades, many semiconductors have been identified as potential photocatalysts under UV or visible light, such as TiO_2 [17, 18], ZnO [19, 20], SnO_2 [21], Fe_2O_3 [22], $BiVO_4$ [23], Cu_2O [24], $CdIn_2S_4$ [25], Ag_3PO_4 [26], etc. Each photocatalytic reaction basically involves three processes: photon absorption, electron-hole pair generation and separation, and catalytic reactions for bacterial inactivation. Thus, any improvement of the photocatalytic performance requires enhancement of the three aforementioned processes. So far, researchers have made numerous efforts to develop novel visible-light-active photocatalysts because visible light is abundant in the solar spectrum. For example, Liang et al. [27] reported AgI/AgBr/$BiOBr_{0.75}I_{0.25}$ nanocomposites as novel visible-light photocatalysts for inactivation of *Escherichia coli* (*E. coli*) cells. Our group also found that the magnetic Fe_2O_3-AgBr was able to inactivate both Gram-negative (*E. coli*) and Gram-positive (*Staphylococcus aureus*) bacteria under visible light [28]. On the other hand, doping of existing semiconductors (especially TiO_2) has been shown to be an effective way of extending their light absorption to visible region [29]. However, a serious drawback of existing photocatalysts is usually their low photocatalytic efficiency due to the fast recombination of charge carriers. To improve the charge carrier separation, an option is to develop suitable semiconductor composites that assure the opposite migration of electrons and holes by conduction band (CB) and valence band (VB) offsets [30]. Another choice is the immobilization of cocatalysts (such as

Pt, Au, and Ag) onto the surface of photocatalysts, which can improve the charge separation by capturing photo-generated electrons or holes. For instance, Liu et al. [31] developed Ag/TiO_2 nanofiber membrane which achieved 99.9 % *E. coli* inactivation under solar irradiation within 30 min.

Recently, metal-free materials have emerged out as a novel kind of photocatalyst for various applications including H_2 production, organic pollutant degradation, and bacterial disinfection. It has unique advantages of earth abundance, low cost, and environmental friendliness. Metal-free photocatalysts have been widely investigated in H_2 evolution from water and organic pollutant degradation, but are still in its infancy for bacterial disinfection. Based on the structure and composition, they can be classified as graphitic carbon nitride (g-C_3N_4), graphene, and elemental photocatalysts. In this chapter, we present an overview of current research activities that center on the preparation, characterization, and application of highly efficient metal-free photocatalysts for water disinfection under visible-light irradiation.

7.2 g-C_3N_4-Based Photocatalysts

Polymeric g-C_3N_4 has attracted increasing attention for photocatalytic reactions in recent years [32–37]. The heptazine ring structure and the high condensation degree enable the metal-free g-C_3N_4 to possess many advantages such as good physicochemical stability, as well as an appealing electronic structure combined with a medium bandgap (2.7 eV) [38]. These unique properties make g-C_3N_4 a promising candidate for visible-light-driven (VLD) photocatalytic applications utilizing solar energy. Unlike the traditional metal-based photocatalysts that need expensive metal salts for preparation, g-C_3N_4 photocatalyst can be facilely prepared by thermal polycondensation of the low-cost N-rich precursors, such as cyanamide [32, 39], urea [40, 41], thiourea [42, 43], melamine [44], and dicyandiamide [45]. These excellent properties make g-C_3N_4 to be used in water splitting, CO_2 reduction, organic pollutant degradation, as well as bacterial disinfection [46–49].

The photocatalytic bactericidal effects of g-C_3N_4 against *E. coli* was firstly revealed by Huang et al. [50], who synthesized mesoporous g-C_3N_4 photocatalysts by the self-condensation of cyanamide in the presence of a silica template. As shown in Fig. 7.1, *E. coli* K-12 can be efficiently killed in the presence of g-C_3N_4 under visible-light irradiation, while no disinfection occurs in light (without photocatalysts) and dark controls (without light irradiation). It was also found that the inactivation efficiency was significantly influenced by the surface properties of g-C_3N_4. For the CN230 sample (with surface area of 230 m^2/g), 4 h is required to completely inactivate *E. coli* K-12, while in the case of bulk g-C_3N_4 (CN12), the inactivation efficiency of *E. coli* is only 90 % even with an extended irradiation time of 6 h, indicating surface area is crucial for photocatalytic antibacterial property of g-C_3N_4.

Pristine g-C_3N_4 suffers from shortcomings such as rapid recombination of photo-generated electron-hole pairs, a small specific surface area, and a low

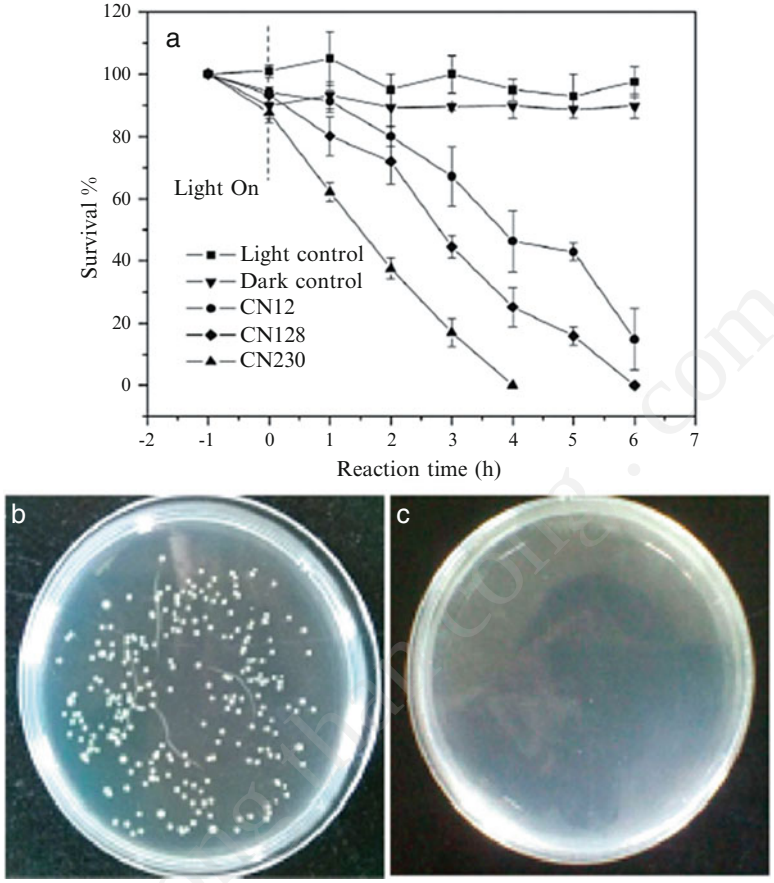

Fig. 7.1 (**a**) Photocatalytic inactivation efficiency against *E. coli* K-12 (2.5×10^6 cfu/mL, 100 mL) in the presence of g-C_3N_4 (1 mg/mL) under visible-light irradiation; (**b**) and (**c**) images of *E. coli* K-12 colonies on an agar plate before and after visible-light irradiation for 4 h using CN230 (Reprinted with permission from Ref. [50]. Copyright 2014, the Royal Society of Chemistry)

visible-light utilization efficiency [51]. In this regard, researchers have focused on the exfoliation of the layered bulk g-C_3N_4 into nanosheets to increase its photocatalytic activity. A variety of studies have confirmed that the photocatalytic activity of g-C_3N_4 can be significantly enhanced after exfoliating into a few layers or single-layer nanosheets [52, 53]. Zhao et al. [54] have fabricated an atomic single-layer g-C_3N_4(SL g-C_3N_4) by a two-step approach including thermal etching of bulk g-C_3N_4 into g-C_3N_4 nanosheets and followed by an ultrasonic exfoliation of the obtained g-C_3N_4 nanosheets. The as-prepared SL g-C_3N_4 had a thickness of only 0.5 nm (Fig. 7.2). Under the visible-light irradiation, 2×10^7 cfu/mL of *E. coli* could be inactivated completely over the SL g-C_3N_4 within 4 h, whereas only about 3 log and 5 log of *E. coli* could be inactivated on bulk g-C_3N_4 and g-C_3N_4

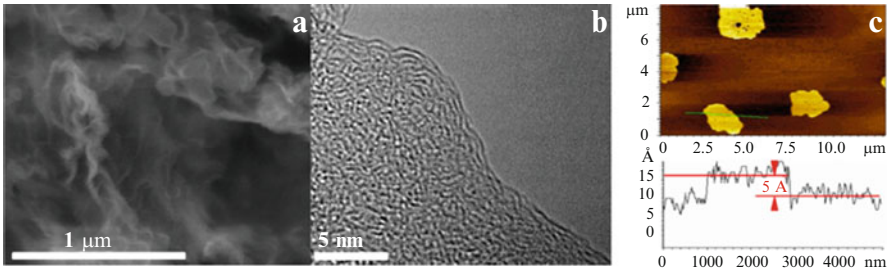

Fig. 7.2 Morphology of the SL g-C_3N_4: (**a**) SEM image, (**b**) TEM image, (**c**) AFM image (Reprinted with permission from Ref. [54]. Copyright 2014, Elsevier)

nanosheets under the same condition, respectively. The enhancement of photocatalytic efficiency of SL g-C_3N_4 was attributed to the low charge transfer resistance and efficient charge separation. This result indicates decreasing the dimension of the bulk g-C_3N_4 is an efficient pathway to improve its photocatalytic performance for bacterial disinfection.

Because of the unique two-dimensional (2D) layered structure, g-C_3N_4 is favorable for hybridizing with other components. Formation of heterostructures demonstrates a great potential to promote the photocatalytic performance of g-C_3N_4 because the electron-hole pairs can be efficiently separated, and charge carriers could transfer across the interface of the heterostructure to restrain the recombination. Recently, numerous research studies have been carried out to couple g-C_3N_4 with various semiconductors to enhance the photocatalytic activities [55, 56]. For bacterial disinfection, Ag represents the most popular substance for enhancing disinfection activity because of the antimicrobial property of Ag compounds and Ag^+ ions [57, 58]. Besides significantly promoting the photocatalytic disinfection efficiency, Ag surface deposition also leads to enhanced VLD photocatalytic activity. For instance, Bing et al. [59] have synthesized g-C_3N_4 nanosheets with embedded Ag nanoparticles (Ag/g-C_3N_4) by a facile route. Under visible-light irradiation, the reactive oxygen species (ROS) production of Ag/g-C_3N_4 nanohybrids was greatly improved compared with pristine g-C_3N_4 nanosheets. Moreover, the nanohybrids showed enhanced antibacterial efficiency and stability to disperse bacterial biofilms. Ma et al. [60] have synthesized Ag/g-C_3N_4 composite photocatalyst by thermal polymerization of melamine precursor combined with the photo-assisted reduction method. The photocatalytic activity was evaluated by inactivation of *E. coli* cells under visible-light irradiation. As shown in Fig. 7.3a, the g-C_3N_4 had no cytotoxicity to *E. coli* in the dark, while Ag/g-C_3N_4 composites exhibited almost negligible disinfection efficiencies. With light irradiation, the g-C_3N_4 displayed limited disinfection efficiency, and only about 0.4 log of *E. coli* cells could be inactivated within 90 min of visible-light irradiation. After deposition with Ag nanoparticles, the Ag/g-C_3N_4 composites exhibited obviously enhanced photocatalytic activity compared with that of g-C_3N_4 (Fig. 7.3b). The

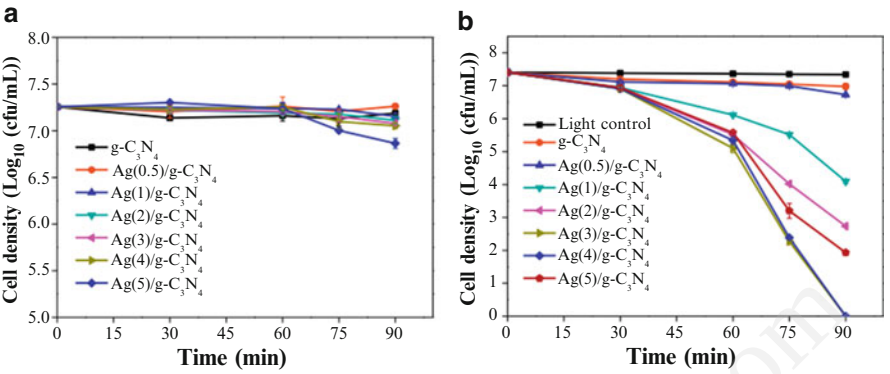

Fig. 7.3 (**a**) Inactivation efficiency toward *E. coli* (10^7 cfu/mL) with as-prepared samples (100 g/mL) in the dark and (**b**) photocatalytic inactivation efficiency toward *E. coli* (10^7 cfu/mL) with the as-prepared samples (100 g/mL) under visible-light irradiation (Reprinted with permission from Ref. [60]. Copyright 2016, Elsevier)

photocatalytic disinfection activity of Ag/g-C_3N_4 increased with Ag doping from 0.5 to 3 wt%.

Further increasing Ag doping to 5 %, the disinfection efficiency would be decreased, probably due to the excess Ag nanoparticles would occupy the reactive sites of g-C_3N_4, resulting in the decreased efficiency of charge separation. In addition, the localized surface plasmon resonance (LSPR) effects of Ag nanoparticles are also believed to contribute to the enhanced light absorption and photocatalytic disinfection efficiencies. In another study, the photocatalytic disinfection activity of Ag/g-C_3N_4 composites against *E. coli* was evaluated as a function of the Ag content of the material upon UV and visible-light excitation. In both cases, the bactericidal action takes place through a complex mechanism with key involvement of both hole and electron related charge species. Other potential contributions coming from lixiviation or silver alone are excluded to have a significant impact in the bactericidal activity of Ag/g-C_3N_4 composites [61].

Besides Ag nanoparticle combination, the g-C_3N_4 coupled with other materials for photocatalytic disinfection has also been investigated. Li et al. [62] have synthesized g-C_3N_4/TiO_2 hybrid photocatalyst with high photocatalytic bacterial inactivation activity by a facile hydrothermal-calcination method. An interesting hybrid structure composed of micron-sized TiO_2 spheres wrapped with lamellar g-C_3N_4 nanosheets was obtained, which showed significantly improved photocatalytic activity under visible-light irradiation. Using this hybrid photocatalyst, 10^7 cfu/mL of *E. coli* K-12 could be completely inactivated within 180 min of visible-light irradiation. The enhancement was attributed to the increased visible-light absorption and effective separation of photo-generated electron-hole pairs. Evidenced by the SEM images, the bacterial cells were greatly damaged, leading to severe leakage of intracellular components during photocatalytic inactivation processes.

7.3 Graphene-Based Photocatalysts

Graphene is a flat monolayer of carbon atoms tightly packed into a two-dimensional (2D) honeycomb lattice and is the basic building block for graphitic materials of all other dimensionalities, including 0D fullerenes, 1D carbon nanotubes, and 3D graphite. Graphene possesses a high thermal conductivity (5000 $W\ m^{-1}\ K^{-1}$), offers an excellent mobility of charge carriers at room temperature (20,0000 $cm^2\ V^{-1}\ s^{-1}$), and exhibits an extremely high theoretical specific surface area (2600 $m^2\ g^{-1}$). The long-range π-conjugation in graphene yields these extraordinary thermal, mechanical, and electrical properties, which is favorable for transportation of charge carriers in photocatalytic reactions. Utilization of graphene as photocatalyst support to enhance the photocatalytic activity has been extensively investigated. The pioneering work was conducted by Kamat et al., who produced graphene oxide (GO)-TiO_2 nanocrystalline composites by sonicating dispersed TiO_2 nanoparticles and GO in ethanol and demonstrated the feasibility of using graphene as an electron-transfer medium in the graphene/TiO_2 composite photocatalysts [63–66]. This work has stimulated intense research on the development of graphene-based materials as next-generation photocatalysts [67, 68]. As a metal-free material, graphene alone has antimicrobial activities, which is related to the physicochemical properties of graphene, such as morphology, size, and surface functionality [69–71]. Akhavan et al. have employed the aggregated graphene nanosheets to capture *E. coli* cells in the melatonin-bacterial suspension. The melatonin was served as a biocompatible antioxidant to reduce single-layer graphene oxide nanosheets. The bacteria trapped within the aggregated sheets were biologically disconnected from their environment, exhibiting a kind of inactivation. Importantly, the graphene-trapped bacterial cells could be reactivated by sonication or, if desired, photothermally killed by near-infrared irradiation at 808 nm. This work indicated the potential application of graphene nanosheets as an encapsulating material for delivery of desired microorganisms or as an effective photothermal agent for inactivation of the graphene-wrapped microorganisms [72].

The most important utilization of graphene in photocatalytic disinfection is combination with other materials to accelerate the photocatalytic efficiency. For instance, the well-known UV-driven TiO_2 nanoparticles have been embedded on graphene sheets by a direct redox reaction. The as-prepared graphene/TiO_2 photocatalysts exhibited visible-light absorption and also showed enhanced photocatalytic inactivation toward *E. coli* under visible-light irradiation, whereas pure TiO_2 showed negligible activity [73]. Sun and co-workers have integrated 2D graphene oxide (GO) sheets, 1D TiO_2 nanorods, and 0D Ag nanoparticles to construct a multifunctional nanocomposite (GO-TiO_2-Ag) by a facile two-phase method [74]. The obtained GO-TiO_2-Ag exhibited excellent intrinsic inactivation toward *E. coli* cells, as well as significantly enhanced photo-biocidal capability over GO-TiO_2 and GO-Ag. As shown in Fig. 7.4, the TiO_2 could be excited by UV/near-UV light from solar light, and the photo-generated electron-hole pairs were produced. Since the potential of the conduction band (CB) of TiO_2 (−4.2 eV)

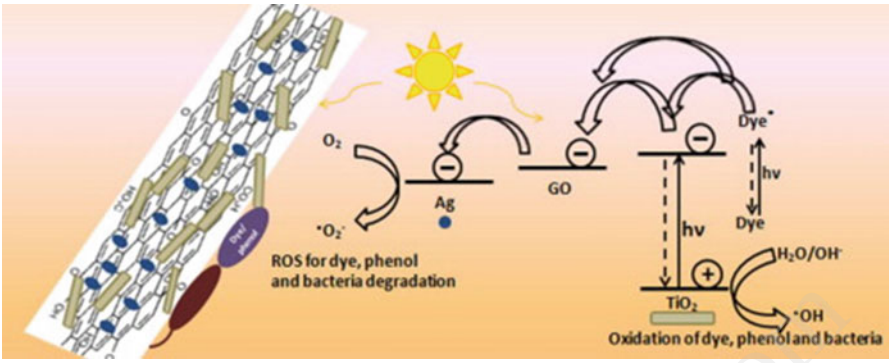

Fig. 7.4 Schematic diagram of the enhanced photocatalytic mechanisms of GO-TiO_2-Ag nanocomposites (Reprinted with permission from Ref. [74]. Copyright 2013, Elsevier)

vs. vacuum and the work function of GO (−4.42 eV), photo-generated electrons could easily transfer from TiO_2 to GO sheets [75]. Meanwhile, the work function of surface-deposited Ag nanoparticles locates at −4.74 eV, which is lower than that of GO [76]. Therefore, the photo-generated electron could further transfer from GO to Ag nanoparticles. This transfer mechanism is believed to significantly suppress the recombination of photo-generated electron-hole pairs; thus the high photocatalytic activity of GO-TiO_2-Ag nanocomposites is achieved. The positive effect of graphene as electron mediator in TiO_2-based photocatalysis for bacterial disinfection has also been repeatedly confirmed by many other studies [77–80]

In non-TiO_2-based systems, graphene has also been reported to enhance the photocatalytic activity. Among all the non-TiO_2 photocatalysts, ZnO has been once regarded as the most suitable alternatives to TiO_2 for photocatalytic applications. To grow ZnO nanorods on GO sheets, Gao et al. [81] have converted the GO sheets to sulfonated GO (SGO) sheets through sulfonation since the SGO can be dispersed uniformly in hexamethylenetetramine solution, which is a necessary environment to grow ZnO nanorods. After further depositing Ag nanoparticles on SGO-ZnO by a poly-reduction process, the obtained SGO-ZnO-Ag exhibited much higher inactivation activity toward *E. coli* cells than those of ZnO, SGO-ZnO, and ZnO-Ag. CdS is one of the most well-recognized high-efficient photocatalysts working under visible light. In this regard, attempts to synthesize graphene-CdS composites were conducted and were achieved by a novel two-phase mixing method [82]. The CdS nanoparticles were uniformly self-assembled on GO sheets at water/toluene interface. The photocatalytic activity was evaluated by inactivation of both Gram-negative *E. coli* and Gram-positive *B. subtilis* under visible-light irradiation. Figure 7.5a shows the time course of antibacterial activity by GO, CdS, and GO-CdS toward *E. coli* under visible-light irradiation for 30 min. GO has limited activity in inactivating *E. coli*, probably due to their large sheets and different oxygen-containing group. It was found that GO-CdS composites show enhanced antibacterial activity than CdS nanoparticles with inactivating 100 % of *E. coli* in 25 min, while only 55 % of *E. coli* is inactivated by CdS alone. In addition, about

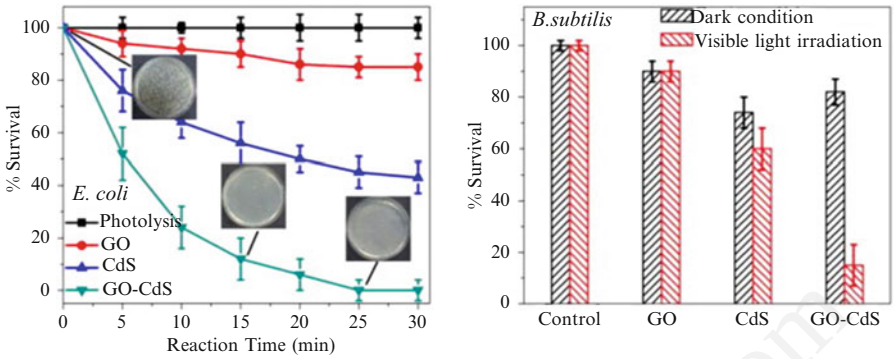

Fig. 7.5 (**a**) Time course for antibacterial activity toward *E. coli* in the presence of GO, CdS, and GO-CdS under visible-light irradiation for 30 min and (**b**) *B. subtilis* inactivation without any catalysts and after being treated with GO, CdS, and GO-CdS with/without visible light for 10 min (Reprinted with permission from Ref. [82]. Copyright 2013, Elsevier)

90 % of *B. subtilis* could be inactivated by GO-CdS in 10 min, while 60 % of *B. subtilis* was survived after being treated with pure CdS (Fig. 7.5b). These results also showed that the inactivation efficiency of GO-CdS composites against Gram-positive *B. subtilis* is a little higher than that of Gram-negative *E. coli*, which is attributed to the different structure of Gram-positive and Gram-negative bacteria. Gram-negative bacteria possess an additional outer membrane, which can protect the inner layer from attacking by radicals and other reactive species [83]. In another case, reduced graphene oxide (RGO)-Bi_2MoO_6 composite nanoplates with good uniformity and highly oriented growth of the active lattice were synthesized by a simple hydrothermal process with the assistance of GO nanosheets [84]. The RGO was observed to be formed on the surface of the Bi_2MoO_6 nanoplates after the hydrothermal treatment. The presence of graphene led to the growth of Bi_2MoO_6 along the plenary direction of graphene, forming a crystal with a highly ordered orientation. The photocatalytic bacterial disinfection activity was evaluated by inactivation of *E. coli* cells under visible-light irradiation. As shown in Fig. 7.6, the pure Bi_2MoO_6 only showed low bactericidal activity, and only 2.1 log reduction in the viable cell count was obtained after 4 h of irradiation. In the case of Bi_2MoO_6-RGO nanocomposite as the photocatalyst, 5×10^5 cfu/mL of *E. coli* cells could be completely inactivated within 3 h of visible-light irradiation. This result indicated the VLD photocatalytic inactivation performance against *E. coli* cells by the Bi_2MoO_6 could be significantly improved by combination with graphene. The enhancement was attributed to effective charge transfer from Bi_2MoO_6 to graphene.

Recently, silver orthophosphate (Ag_3PO_4) as a new visible-light photocatalyst has attracted enormous attention because of its extremely high activity for photocatalytic oxidation applications, such as water oxidation to produce O_2 and decomposition of organic compounds [85, 86]. The use of graphene to enhance the photocatalytic activity of Ag_3PO_4 has been reported by Liu et al. [26], who

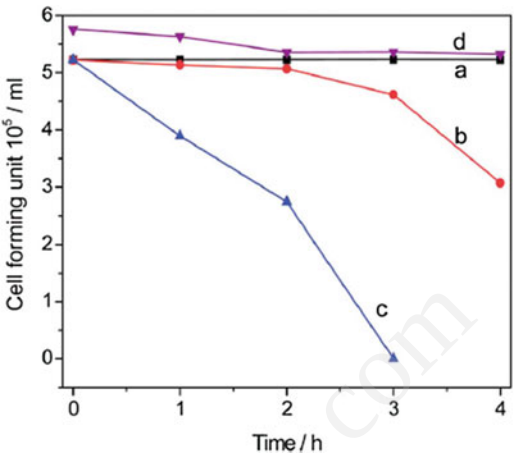

Fig. 7.6 The photocatalytic inactivation efficiencies of *E. coli* K-12 without the catalyst (**a**), with the phase pure Bi_2MoO_6 photocatalyst (**b**), with Bi_2MoO_6-RGO under visible-light irradiation (**c**), and in the dark (**d**) (Reprinted with permission from Ref. [84]. Copyright 2013, The Royal Society of Chemistry)

synthesized a novel GO-enwrapped Ag_3PO_4 (GO/Ag_3PO_4) composite as a visible-light-induced photocatalyst by an ion-exchange method of CH_3COOAg and Na_2HPO_4 in the presence of GO sheets. Photocatalytic experiments about degradation of AO7 and phenol indicated that this novel GO/Ag_3PO_4 composite exhibited significantly higher photocatalytic activities and improved stability than that of bare Ag_3PO_4. Moreover, the GO/Ag_3PO_4 composite also exhibited both excellent intrinsic antibacterial and photocatalytic disinfection activities against *E. coli* cells under visible-light irradiation. Besides graphene, similar metal-free carbon materials were also used as electron mediator to improve the photocatalytic disinfection efficiency. For example, nonwoven carbon nanofiber (CNF) was used to construct a new hierarchical nanostructured photocatalyst by anchoring flower-like nanostructures of In_2S_3 [87]. The optimized hierarchical CNF/In_2S_3 photocatalyst exhibited much higher photocatalytic activity for *E. coli* inactivation than that of pure In_2S_3 under visible-light irradiation. The enhancement was attributed to the excellent properties of enhanced light absorption, large surface area, and efficient charge separation, which were derived from the special three-dimensional hierarchical nanostructures.

7.4 Elemental Photocatalysts

Up to now, for the development of efficient photocatalysts that operate efficiently under solar light, overwhelming attention has been given to compound photocatalyst, which is made up of more than one element and usually has complicated structures. In contrast, recent efforts in searching for new visible-light-active photocatalysts have paid attention to elemental semiconductors, such as crystalline silicon (Si) [88, 89], selenium (Se) [90], red phosphorus (P) [91], α-sulfur (S) [92], β-rhombohedral boron (B) [93], and tellurium (Te) [94].

Among them, Si is the first case of a single-element metal-free photocatalyst, which was reported as early as in the late 1970s [95]. Promoted by the emergence of various nanostructures, silicon-based photocatalysts have been greatly developed in recent years. However, nanostructured Si suffers from instability in aqueous solutions, and surface modification is used to improve the activity and stability of nanostructured Si photocatalysts. For example, the HF treatment was used to modify the Si nanowires [96]. It was found that surface electron-deficient H atoms serve as an electron sink, leading to the improved photocatalytic activity and stability. The HF-treated Si nanowires even show better performance than noble metal-modified (Pd, Au, Ru, Ag) nanowires. However, the major photocatalytic applications of Si photocatalysts are water splitting, CO_2 reduction, and dye degradation [97, 98], and the application for bacterial disinfection has never been reported. Among all these elemental photocatalysts, sulfur and phosphorus represent the most promising single-element metal-free photocatalyst for bacterial disinfection under visible-light irradiation.

7.4.1 Sulfur Photocatalysts

The elemental sulfur has more than 30 allotropes, and the S_8 cyclic molecules are the most stable configuration at standard temperature and pressure (STP). It can crystallize to form three solid allotropes: orthorhombic α-sulfur, monoclinic β-sulfur, and γ-sulfur. Bulk α-sulfur crystals with a bandgap of 2.79 eV have suitable edges of valence and conduction bands for photocatalysis reactions. The photocatalytic activity of α-sulfur was firstly demonstrated by Liu et al. [92], who suggested that α-sulfur crystals have the ability to generate •OH radicals under both UV/Vis and visible light. It was found that decreasing the particle size of α-sulfur crystals by ball-milling leads to a remarkably improved photocatalytic activity in decomposing rhodamine B. The most apparent drawback of α-sulfur as a photocatalyst is its poor hydrophilicity, which makes it difficult to produce good suspensions in aqueous solutions and thus substantially weakens its photocatalytic activity. In addition, the photocatalytic activity of α-sulfur for bacterial disinfection has not been investigated until recently [99].

To improve the hydrophilicity and photocatalytic activity of α-sulfur, Wang et al. have modified the elemental crystals of cyclo-octasulfur (α-S_8) with graphene and g-C_3N_4 [99]. Two distinctive structures were fabricated by wrapping RGO and g-C_3N_4 sheets on α-S_8 in different orders through wet chemical methods. The first was RGO sheets sandwiched in heterojunction of g-C_3N_4 sheets and α-S_8 (i.e., $CNRGOS_8$), while the second structure was the other way around (i.e., $RGOCNS_8$). Both structures exhibited antibacterial activity under visible-light irradiation. $CNRGOS_8$ showed stronger bacterial inactivation than $RGOCNS_8$ in aerobic conditions. However, $RGOCNS_8$ was more active than $CNRGOS_8$ under anaerobic condition. As shown in Fig. 7.7, in the case of $CNRGOS_8$ under aerobic condition, the photo-generated e^- in the conduction band (CB) of g-C_3N_4 sheets could

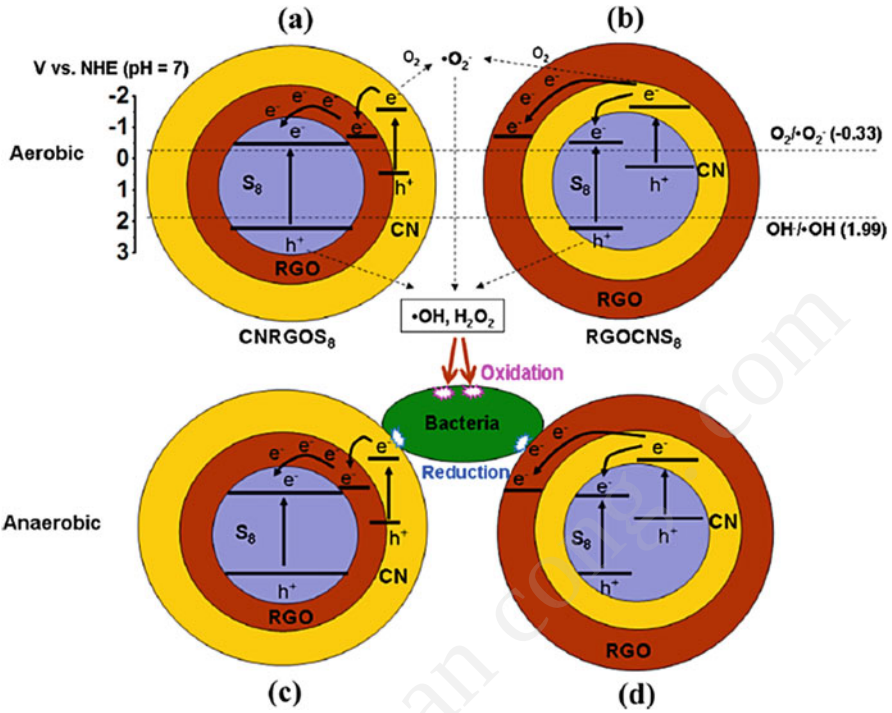

Fig. 7.7 Schematic illustration of the VLD photocatalytic bacterial inactivation mechanisms of (**a**) CNRGOS8 and (**b**) RGOCNS8 in aerobic condition and (**c**) CNRGOS8 and (**d**) RGOCNS8 in anaerobic condition (Reprinted with permission from Ref. [99]. Copyright 2013, American Chemical Society)

promptly flow to the CB of α-S_8 via RGO sheets, while the photo-generated h^+ in the valence band (VB) of α-S_8 could migrate to the VB of g-C_3N_4 via RGO sheets. The RGO sheets as the interlayer of this metal-free heterojunction photocatalyst efficiently mediated the charge transportation between α-S_8 and g-C_3N_4 sheets, leading to the high photocatalytic disinfection activity. In contrast, in the case of $RGOCNS_8$, the RGO sheets were the outer layer, which could not mediate the charge transportation effectively, because e^- excited from the CB of g-C_3N_4 could flow to RGO sheets which however could not transfer e^- to the CB of α-S_8, resulting in undesired recombination of photo-generated charge pairs. Therefore, the photocatalytic disinfection activity of $CNRGOS_8$ is much higher than that of $RGOCNS_8$. However, the case is different under anaerobic condition without O_2 participation, in which photo-generated e^- plays the major role in inactivation of bacterial cells [23, 100]. In the case of $RGOCNS_8$, the RGO sheets were the outer layer which could facilitate the injection of e^- into bacterial cells, more efficiently than the g-C_3N_4 sheets in the case of $CNRGOS_8$, because of the high electron mobility of photo-generated e^- on graphene. The quick electron trapping by bacterial cells could in turn prevent the e^--h^+ recombination of $RGOCNS_8$, leading

to a higher photocatalytic disinfection activity than that of CNRGOS$_8$. This work not only provided a metal-free heterojunction photocatalyst based on elemental α-S$_8$ for bacterial disinfection but also highlighted the different photocatalytic bacterial disinfection mechanisms under aerobic and anaerobic conditions.

7.4.2 Phosphorus Photocatalysts

Solid phosphorus mainly exists in three forms: white phosphorus, red phosphorus, and black phosphorus. Compared with the high reactivity and toxicity of white phosphorus, red phosphorus has a satisfactory stability up to around 250 °C in air and much lower toxicity. It consists of random agglomerates of P atoms and is typically considered to be polymeric or amorphous. Crystalline red phosphorus can be achieved by heat treatment in an inert atmosphere. It was found that both amorphous and crystalline red phosphorus have a wide visible-light absorption range up to 700 nm, which is very attractive for photocatalytic solar energy conversion. Wang et al. [91] have firstly reported the photocatalytic activity of red phosphorus. They found that crystalline monoclinic red phosphorus not only has the ability to photocatalytically produce hydrogen with methanol as the sacrificial agent but also able to split pure water for the nearly stoichiometric evolution of H_2 and O_2 under visible-light irradiation. Moreover, red phosphorus is also photocatalytically active for generating •OH radicals. Compared with crystalline red phosphorus, amorphous phosphorus has even a wider light absorption range of 20 nm, but only shows half the photocatalytic hydrogen evolution activity, which is attributed to its small surface area and large number of electron-hole trapping sites. To enhance the photocatalytic activity of red phosphorus, a subsequent study was conducted on red phosphorus-based composites. The hierarchical hollow microspheres of a P/YPO_4 composite were prepared by the reaction between amorphous red P and a YCl_3 aqueous solution via a hydrothermal process [101]. The as-prepared P/YPO_4 composite showed six times higher activity in photocatalytic hydrogen production than red P under visible-light irradiation. The enhancement is attributed to the promoted photo-generated carrier separation by transferring the photo-generated holes from red P to the VB of YPO_4.

Recently, the photocatalytic application of red phosphorus has also been extended to bacterial disinfection. Xia et al. [102] investigated amorphous red phosphorus as a metal-free photocatalyst for bacterial disinfection. It was found that the red phosphorus exhibited remarkable efficiency to inactivate *E. coli* K-12 cells under the full spectrum of visible light and even sunlight. The reactive oxygen species (ROSs), such as •OH, $•O_2^-$, and H_2O_2, were measured and identified to derive mainly from photo-generated e^- in the conduction band, which collectively contributed to the high efficiency of red phosphorus. *E. coli* cells with concentration of 2×10^7 cfu/mL could be inactivated within 90 min of visible-light irradiation. The cell membrane was found to be a vital first target for the reactive oxygen species oxidation. As shown in Fig. 7.8, the fluorescence microscope was used to

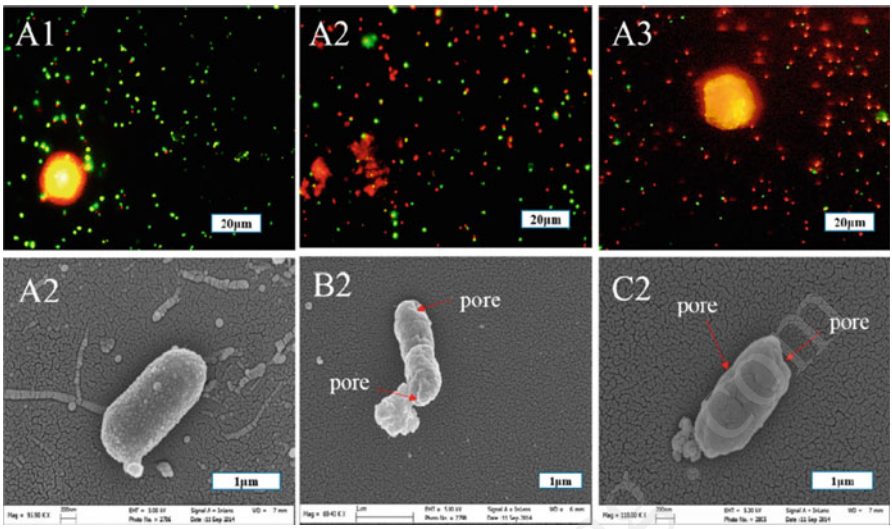

Fig. 7.8 Fluorescence microscopic images of *E. coli* K-12 (2×10^7 cfu/mL, 50 mL) and SEM images after photocatalytically treated with red phosphorus at (**a**) 0, (**b**) 60, and (**c**) 90 min (Reprinted with permission from Ref. [102]. Copyright 2015, American Chemical Society)

investigate the bacterial membrane integrity [103]. After staining with dye mixture, the number of red fluorescent cells was increased with the decrease of the green fluorescent cells after prolonged visible-light photocatalytic treatment, indicating the cell membrane was ruptured (Fig. 7.8a). In addition, SEM was also used to further confirm the damage of cell envelope. As shown in Fig. 7.8b, the untreated *E. coli* cells displayed plump rod shapes with an intact cell envelope. After 30 min of treatment, the cell surface started to wrinkle and become rougher. Finally, large amounts of hollows and holes were found almost the entire cell surface after 90 min of visible-light irradiation, indicating the severe damage of the cell envelope. Therefore, the possible photocatalytic disinfection mechanism by such metal-free elemental photocatalyst is suggested in Fig. 7.9. The photo-generated ROSs would initially oxidize cell membrane-associated proteins, such as enzymes of the respiratory chain and ATPase, resulting in the bacterial energy metabolism becomes insufficient to maintain the cell membrane potential. Thus, the loss of the cell membrane potential leads to an increase in cell membrane permeability, which would cause the leakage and rapid decay of cytoplasmic contents, such as proteins and DNA, finally resulting in cell death with no regrowth [104].

7.5 Conclusion and Outlook

Metal-free semiconductors have emerged as a new class of visible-light-driven photocatalysts. The metal-free photocatalysts investigated so far consist of earth-abundant elements, such as C, N, P, S, etc., and can be mainly classified into

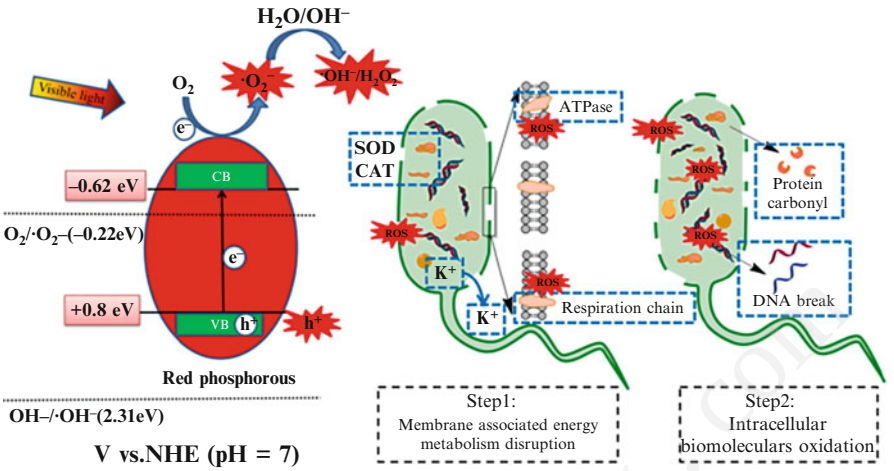

Fig. 7.9 Illustration summarizing the proposed bactericidal mechanism of red phosphorus under visible light: Red phosphorus quickly generate ROSs; ROSs subsequently inhibits bacterial surface metabolism and oxidize intracellular components (Reprinted with permission from Ref. [102]. Copyright 2015, American Chemical Society)

g-C_3N_4-based photocatalysts, graphene-based photocatalysts, and elemental photocatalysts. They share the apparent merit of low costs, environmentally friendly, and a small bandgap so that visible light can be fully absorbed. Among these metal-free photocatalysts, g-C_3N_4-based photocatalysts have been intensively investigated, because of its easy calcination synthetic method and high activity for photocatalytic H_2 production under visible-light irradiation. Therefore, it is the most promising metal-free photocatalyst for bacterial disinfection, which has attracted increasing attention in recent years. As a famous carbon material, the major function of graphene in photocatalysis is its ability to transfer photo-generated electrons efficiently, so that the charge recombination can be suppressed. When graphene is applied to construct composite photocatalyst for bacterial disinfection, the disinfection efficiency can be significantly enhanced both by the intrinsic antimicrobial property of graphene and the improved photocatalytic activity by suppressing the photo-generated e^--h^+ recombination. Therefore, the multifunctional graphene-based metal-free materials show great potential to be used in water disinfection by sunlight.

On the other hand, metal-free elemental photocatalyst has become another alternative to achieve cost-effective photocatalytic applications, as these photocatalysts consist of only one element. Although encouraging progress has been achieved for photocatalytic H_2 production and dye degradation, the application for bacterial disinfection is still in its infancy. Immediate research opportunity lies in the modification of these elemental photocatalysts to enhance the photocatalytic disinfection activity. The known strategies such as heterostructuring, doping heteroatoms, nanoscaling, and faceting [105–107], which are widely used in

compound-based photocatalysts, can also be applied to effectively optimize elemental photocatalysts. Moreover, due to elemental S and P have many crystalline forms, it should be an important strategy to increase their photocatalytic disinfection activities by constructing hetero-phase junctions of elemental photocatalysts, because of the more effective charge carrier transfer between isotype phases. Exploring other element-based photocatalysts also deserves increasing effort. For example, the elements B and Te have shown photocatalytic activity for producing ROSs, but their activity for bacterial disinfection has not been investigated. In addition, the photostability of these emerging metal-free materials needs to be taken into consideration for practical use. While these issues still pose challenges, it is expected that the next few years will bring major advancements in both basic and applied research on solar-induced photocatalytic water disinfection by using metal-free materials.

References

1. United Nation, The Millennium Development Goals Report 2012, ISBN 978-92-1-101258-3, (2012)
2. Shannon MA, Bohn PW, Elimelech M, Georgiadis JG, Marinas BJ, Mayes AM (2008) Science and technology for water purification in the coming decades. Nature 452:301–310
3. Nieuwenhuijsen MJ, Toledano MB, Eaton NE, Fawell J, Elliott P (2000) Chlorination disinfection byproducts in water and their association with adverse reproductive outcomes: a review. Occup Environ Med 57:73–85
4. Sichel C, Blanco J, Malato S, Fernández-Ibáñez P (2007) Effects of experimental condition on *E. coli* survival during solar photocatalytic water disinfection. J Photochem Photobiol A Chem 189:239–246
5. Kühn KP, Chaberny IF, Massholder K, Stickler M, Benz VW, Sonntag HG, Erdinger L (2003) Disinfection of surfaces by photocatalytic oxidation with titanium dioxide and UVA light. Chemosphere 53:71–77
6. Bard AJ (1980) Photoelectrochemistry. Science 207:139–144
7. Hoffmann MR, Martin ST, Choi W, Bahnemann DW (1995) Environmental applications of semiconductor photocatalysis. Chem Rev 95:69–96
8. Kudo A, Miseki Y (2009) Heterogeneous photocatalyst materials for water splitting. Chem Soc Rev 38:253–278
9. Matsunaga T, Tomoda R, Nakajima T, Wake H (1985) Photoelectrochemical sterilization of microbial cells by semiconductor powders. FEMS Microbiol Lett 29:211–214
10. Dunlop PSM, Byrne JA, Manga N, Eggins BR (2002) The photocatalytic removal of bacterial pollutants from drinking water. J Photochem Photobiol A Chem 148:355–363
11. Dunlop PSM, Sheeran CP, Byrne JA, McMahon MAS, Boyle MA, McGuigan KG (2010) Inactivation of clinically relevant pathogens by photocatalytic coatings. J Photochem Photobiol A Chem 216:303–310
12. Dunlop PSM, McMurray TA, Hamilton JWJ, Byrne JA (2008) Photocatalytic inactivation of Clostridium perfringens spores on TiO_2 electrodes. J Photochem Photobiol A Chem 196:113–119
13. Watts RJ, Kong S, Orr MP, Miller GC, Henry BE (1995) Photocatalytic inactivation of coliform bacteria and viruses in secondary wastewater effluent. Water Res 29:95–100

14. Sunnotel O, Verdoold R, Dunlop PSM, Snelling WJ, Lowery CJ, Dooley JSG, Moore JE, Byrne JA (2010) Photocatalytic inactivation of *Cryptosporidium parvum* on nanostructured titanium dioxide films. J Water Health 8:83–91
15. Sichel C, de Cara M, Tello J, Blanco J, Fernández-Ibánez P (2007) Solar photocatalytic disinfection of agricultural pathogenic fungi: *Fusarium* species. Appl Catal B Environ 74:152–160
16. Linkous CA, Carter GJ, Locuson DB, Ouellette AJ, Slattery DK, Smith LA (2000) Photocatalytic inhibition of algae growth using TiO_2, WO_3, and cocatalyst modifications. Environ Sci Technol 34:4754–4758
17. Scuderi V, Impellizzeri G, Zimbone M, Sanz R, Di Mauro A, Buccheri MA, Miritello M, Terrasi A, Rappazzo G, Nicotra G (2016) Rapid synthesis of photoactive hydrogenated TiO_2 nanoplumes. Appl Catal B Environ 183:328–334
18. Blake DM, Maness PC, Huang Z, Wolfrum EJ, Huang J, Jacoby WA (1999) Application of the photocatalytic chemistry of titanium dioxide to disinfection and the killing of cancer cells. Sep Purif Methods 28:1–50
19. Raju K, Navadeepthy D, Kaliyan H, Tata NR, Srinivasan A (2015) Visible-light-induced photocatalytic disinfection of E. coli pathogens with Fe^{3+}-grafted ZnO nanoparticles. Energy Environ Focus 4:232–238
20. Sanchez L, Guz L, Garcia P, Ponce S, Goyanes S, Marchi MC, Candal R, Rodriguez J (2015) Synthesis and characterization of ZnO nanorod films on PET for photocatalytic disinfection of water. J Adv Oxid Technol 18:246–252
21. Liu SW, Huang GC, Yu JG, Ng TW, Yip HY, Wong PK (2014) Porous fluorinated SnO_2 hollow nanospheres: transformative self-assembly and photocatalytic inactivation of bacteria. ACS Appl Mater Interf 6:2407–2414
22. Basnet P, Larsen GK, Jadeja RP, Hung YC, Zhao YP (2013) alpha-Fe_2O_3 nanocolumns and nanorods fabricated by electron beam evaporation for visible light photocatalytic and antimicrobial applications. ACS Appl Mater Interf 5:2085–2095
23. Wang WJ, Yu Y, An TC, Li GY, Yip HY, Yu JC, Wong PK (2012) Visible-light-driven photocatalytic inactivation of *E. coli* K-12 by bismuth vanadate nanotubes: bactericidal performance and mechanism. Environ Sci Technol 46:4599–4606
24. Xiong LB, Ng TW, Yu Y, Xia DH, Yip HY, Li GY, An TC, Zhao HJ, Wong PK (2015) N-type Cu_2O film for photocatalytic and photoelectrocatalytic processes: its stability and inactivation of *E. coli*. Electrochim Acta 153:583–593
25. Wang WJ, Ng TW, Ho WK, Huang JH, Liang SJ, An TC, Li GY, Yu JC, Wong PK (2013) $CdIn_2S_4$ microsphere as an efficient visible-light-driven photocatalyst for bacterial inactivation: synthesis, characterizations and photocatalytic inactivation mechanisms. Appl Catal B Environ 129:482–490
26. Liu L, Liu JC, Sun DD (2012) Graphene oxide enwrapped Ag_3PO_4 composite: towards a highly efficient and stable visible-light-induced photocatalyst for water purification. Catal Sci Technol 2:2525–2532
27. Liang JL, Deng J, Li M, Tong MP (2016) Bactericidal activity and mechanism of AgI/AgBr/$BiOBr_{0.75}I_{0.25}$ under visible light irradiation. Colloids Surf B 138:102–109
28. Ng TW, Zhang LS, Liu JS, Huang GC, Wang W, Wong PK (2016) Visible-light-driven photocatalytic inactivation of *Escherichia coli* by magnetic Fe_2O_3-AgBr. Water Res 90:111–118
29. Ananpattarachai J, Boonto Y, Kajitvichyanukul P (2016) Visible light photocatalytic antibacterial activity of Ni-doped and N-doped TiO_2 on *Staphylococcus aureus* and *Escherichia coli* bacteria. Environ Sci Pollut Res 23:4111–4119
30. Karunakaran C, Abiramasundari G, Gomathisankar P, Manikandan G, Anandi V (2011) Preparation and characterization of ZnO-TiO_2 nanocomposite for photocatalytic disinfection of bacteria and detoxification of cyanide under visible light. Mater Res Bull 46:1586–1592
31. Liu L, Liu ZY, Bai HW, Sun DD (2012) Concurrent filtration and solar photocatalytic disinfection/degradation using high-performance Ag/TiO_2 nanofiber membrane. Water Res 46:1101–1112

32. Wang XC, Maeda K, Thomas A, Takanabe K, Xin G, Carlsson JM, Domen K, Antonietti M (2009) A metal-free polymeric photocatalyst for hydrogen production from water under visible light. Nat Mater 8:76–80
33. Chang F, Xie YC, Li CL, Chen J, Luo JR, Hu XF, Shen JW (2012) A facile modification of g-C_3N_4 with enhanced photocatalytic activity for degradation of methylene blue. Appl Surf Sci 280:967–974
34. Wang Y, Wang XC, Antonietti M (2012) Polymeric graphitic carbon nitride as a heterogeneous organocatalyst: from photochemistry to multipurpose catalysis to sustainable chemistry. Angew Chem Int Ed 51:68–89
35. Cao SW, Yu JG (2014) g-C_3N_4-based photocatalysts for hydrogen generation. J Phys Chem Lett 5:2101–2107
36. Gong YG, Li MM, Wang Y (2015) Carbon nitride in energy conversion and storage: recent advances and future prospects. ChemSusChem 8:931–946
37. Cao SW, Low JX, Yu JG, Jaroniec M (2015) Polymeric photocatalysts based on graphitic carbon nitride. Adv Mater 1:2150–2176
38. Wang K, Li Q, Liu BS, Cheng B, Ho WK, Yu JG (2015) Sulfur-doped g-C_3N_4 with enhanced photocatalytic CO_2-reduction performance. Appl Catal B Environ 176:44–52
39. Lei JY, Chen Y, Shen F, Wang LZ, Liu YD, Zhang JL (2015) Surface modification of TiO_2 with g-C_3N_4 for enhanced UV and visible photocatalytic activity. J Alloy Comp 631:328–334
40. Shi L, Liang L, Wang FX, Liu MS, Chen KL, Sun KN, Zhang NQ, Sun JM (2015) Higher yield urea-derived polymeric graphitic carbon nitride with mesoporous structure and superior visible-light-responsive activity. ACS Sustain Chem Eng 3:3412–3419
41. Chai B, Peng TY, Mao J, Li K, Zan L (2012) Graphitic carbon nitride (g-C_3N_4)-Pt-TiO_2 nanocomposite as an efficient photocatalyst for hydrogen production under visible light irradiation. Phys Chem Chem Phys 14:16745–16752
42. Dong F, Zhao ZW, Xiong T, Ni ZL, Zhang WD, Sun YJ, Ho WK (2013) In Situ construction of g-C_3N_4/g-C_3N_4 metal-free heterojunction for enhanced visible-light photocatalysis. ACS Appl Mater Interf 5:11392–11401
43. Zhao ZW, Sun YJ, Luo Q, Dong F, Li H, Ho WK (2015) Mass-controlled direct synthesis of graphene-like carbon nitride nanosheets with exceptional high visible light activity. Sci Rep 5:14643
44. Shan WJ, Hu Y, Bai ZG, Zheng MM, Wei CH (2016) *In situ* preparation of g-C_3N_4/bismuth-based oxide nanocomposites with enhanced photocatalytic activity. Appl Catal B Environ 188:1–12
45. Chen XF, Wei J, Hou RJ, Liang Y, Xie ZL, Zhu YG, Zhang XW, Wang HT (2016) Growth of g-C_3N_4 on mesoporous TiO_2 spheres with high photocatalytic activity under visible light irradiation. Appl Catal B Environ 188:342–350
46. Hu B, Cai FP, Chen TJ, Fan MS, Song CJ, Yan X, Shi WD (2015) Hydrothermal synthesis g-C_3N_4/Nano-$InVO_4$ nanocomposites and enhanced photocatalytic activity for hydrogen production under visible light irradiation. ACS Appl Mater Interf 7:18247–18256
47. He YM, Wang Y, Zhang LH, Teng BT, Fan MH (2015) High-efficiency conversion of CO_2 to fuel over ZnO/g-C_3N_4 photocatalyst. Appl Catal B Environ 168:1–8
48. Xu H, Yan J, Xu YG, Song YH, Li HM, Xia JX, Huang CJ, Wan HL (2013) Novel visible-light-driven AgX/graphite-like C_3N_4 (X = Br, I) hybrid materials with synergistic photocatalytic activity. Appl Catal B Environ 129:182–193
49. Zhao ZW, Sun YJ, Dong F (2015) Graphitic carbon nitride based nanocomposites: a review. Nanoscale 7:15–37
50. Huang JH, Ho WK, Wang XC (2014) Metal-free disinfection effects induced by graphitic carbon nitride polymers under visible light illumination. Chem Commun 50:4338–4340
51. Liu JH, Zhang YW, Lu LH, Wu G, Chen W (2012) Self-regenerated solar-driven photocatalytic water-splitting by urea derived graphitic carbon nitride with platinum nanoparticles. Chem Commun 48:8826–8828
52. Niu P, Zhang L, Liu G, Cheng HM (2012) Graphene-like carbon nitride nanosheets for improved photocatalytic activities. Adv Funct Mater 22:4763–4770

53. Yang S, Gong Y, Zhang J, Zhan L, Ma L, Fang Z, Vajtai R, Wang X, Ajayan PM (2013) Exfoliated graphitic carbon nitride nanosheets as efficient catalysts for hydrogen evolution under visible light. Adv Mater 25:2452–2456
54. Zhao HX, Yu HT, Quan X, Chen S, Zhang YB, Zhao HM, Wang H (2014) Fabrication of atomic single layer graphitic-C_3N_4 and its high performance of photocatalytic disinfection under visible light irradiation. Appl Catal B Environ 152:46–50
55. Wang XC, Mi WB, Jiang EY, Bai HL (2009) Structure and mechanical properties of titanium nitride/carbon nitride multilayers. Appl Surf Sci 255:4005–4010
56. Yan SC, Lv SB, Li ZS, Zou ZG (2010) Organic-inorganic composite photocatalyst of g-C3N4 and TaON with improved visible light photocatalytic activities. Dalton Trans 39:1488–1491
57. Bosetti M, Masse A, Tobin E, Cannas M (2002) Silver coated materials for external fixation devices: in vitro biocompatibility and genotoxicity. Biomaterials 23:887–892
58. Chou WL, Yu DG, Yang MC (2005) The preparation and characterization of silver-loading cellulose acetate hollow fiber membrane for water treatment. Polymer Adv Technol 16:600–607
59. Bing W, Chen ZW, Sun HJ, Shi P, Gao N, Ren JS, Qu XG (2015) Visible-light-driven enhanced antibacterial and biofilm elimination activity of graphitic carbon nitride by embedded Ag nanoparticles. Nano Res 8:1648–1658
60. Ma SL, Zhan SH, Jia YN, Shi Q, Zhou QX (2016) Enhanced disinfection application of Ag-modified g-C_3N_4 composite under visible light. Appl Catal B Environ 186:77–87
61. Munoz-Batista MJ, Fontelles-Carceller O, Ferrer M, Fernandez-Garcia M, Kubacka A (2016) Disinfection capability of Ag/g-C_3N_4 composite photocatalysts under UV and visible light illumination. Appl Catal B Environ 183:86–95
62. Li GY, Nie X, Chen JY, Jiang Q, An TC, Wong PK, Zhang HM, Zhao HJ, Yamashita H (2015) Enhanced visible-light-driven photocatalytic inactivation of *Escherichia coli* using g-C_3N_4/TiO_2 hybrid photocatalyst synthesized using a hydrothermal-calcination approach. Water Res 86:17–24
63. Lightcap IV, Kosel TH, Kamat PV (2010) Anchoring semiconductor and metal nanoparticles on a two-dimensional catalyst mat. storing and shuttling electrons with reduced graphene oxide. Nano Lett 10:577–583
64. Williams G, Seger B, Kamat PV (2008) TiO_2-graphene nanocomposites. UV-assisted photocatalytic reduction of graphene oxide. ACS Nano 2:1487–1491
65. Prezhdo OV, Kamat PV, Schatz GC (2011) Virtual issue: graphene and functionalized graphene. J Phys Chem C 115:3195–3197
66. Kamat PV (2011) Graphene-based nanoassemblies for energy conversion. J Phys Chem Lett 2:242–251
67. Xiang Q, Yu J, Jaroniec M (2012) Graphene-based semiconductor photocatalysts. Chem Soc Rev 41:782–796
68. An X, Yu JC (2011) Graphene-based photocatalytic composites. RSC Adv 1:1426–1434
69. Pham VT, Truong VK, Quinn MD, Notley SM, Guo Y, Baulin VA, Al Kobaisi M, Crawford RJ, Ivanova EP (2015) Graphene induces formation of pores that kill spherical and rod-shaped bacteria. ACS Nano 9:8458–8467
70. Li J, Wang G, Zhu H, Zhang M, Zheng X, Di Z, Liu X, Wang X (2014) Antibacterial activity of large-area monolayer graphene film manipulated by charge transfer. Sci Rep 4:4359
71. Zou XF, Zhang L, Wang ZJ, Luo Y (2016) Mechanisms of the antimicrobial activities of graphene materials. J Am Chem Soc 138:2064–2077
72. Akhavan O, Ghaderi E, Esfandiar A (2011) Wrapping bacteria by graphene nanosheets for isolation from environment, reactivation by sonication, and inactivation by near-infrared irradiation. J Phys Chem B 115:6279–6288
73. Cao BC, Cao S, Dong PY, Gao J, Wang J (2013) High antibacterial activity of ultrafine TiO_2/graphene sheets nanocomposites under visible light irradiation. Mater Lett 93:349–352

74. Liu L, Bai HW, Liu JC, Sun DD (2013) Multifunctional graphene oxide-TiO_2–Ag nanocomposites for high performance water disinfection and decontamination under solar irradiation. J Hazard Mater 261:214–223
75. Yang N, Zhai J, Wang D, Chen Y, Jiang L (2010) Two-dimensional graphene bridges enhanced photoinduced charge transport in dye-sensitized solar cells. ACS Nano 4:887–894
76. Yoo DH, Cuong TV, Luan VH, Khoa NT, Kim EJ, Hur SH, Hahn SH (2012) Photocatalytic performance of a Ag/ZnO/CCG multidimensional heterostructure prepared by a solution-based method. J Phys Chem C 116:7180–7184
77. Rahimi R, Zargari S, Yousefi A, Berijani MY, Ghaffarinejad A, Morsali A (2015) Visible light photocatalytic disinfection of *E. coli* with TiO_2-graphene nanocomposite sensitized with tetrakis(4-carboxyphenyl)porphyry. Appl Surf Sci 355:1098–1106
78. Chang YN, Ou XM, Zeng GM, Gong JL, Deng CH, Jiang Y, Liang J, Yuan GQ, Liu HY, He X (2015) Synthesis of magnetic graphene oxide-TiO_2 and their antibacterial properties under solar irradiation. Appl Surf Sci 343:1–10
79. Fernandez-Ibanez P, Polo-Lopez MI, Malato S, Wadhwa S, Hamilton JWJ, Dunlop PSM, D'Sa R, Magee E, O'Shea K, Dionysiou DD (2015) Solar photocatalytic disinfection of water using titanium dioxide graphene composites. Chem Eng J 261:36–44
80. Gao P, Li AR, Sun DD (2014) Effects of various TiO_2 nanostructures and graphene oxide on photocatalytic activity of TiO_2. J Hazard Mater 279:96–104
81. Gao P, Ng K, Sun DD (2013) Sulfonated graphene oxide-ZnO–Ag photocatalyst for fast photodegradation and disinfection under visible light. J Hazard Mater 262:826–835
82. Gao P, Liu JC, Sun DD, Ng W (2013) Graphene oxide-CdS composite with high photocatalytic degradation and disinfection activities under visible light irradiation. J Hazard Mater 250:412–420
83. Liu S, Wei L, Hao L, Fang N, Chang MW, Xu R, Yang Y, Chen Y (2009) Sharper and faster "nano darts" kill more bacteria: a study of antibacterial activity of individually dispersed pristine single-walled carbon nanotube. ACS Nano 3:3891–3902
84. Zhang Y, Zhu YK, Yu JQ, Yang DJ, Ng TW, Wong PK, Yu JC (2013) Enhanced photocatalytic water disinfection properties of Bi_2MoO_6-RGO nanocomposites under visible light irradiation. Nanoscale 5:6307–6310
85. Yi ZG, Ye JH, Kikugawa N, Kako T, Ouyang SX, Stuart-Williams H, Yang H, Cao JY, Luo WJ, Li ZS, Liu Y, Withers RL (2010) An orthophosphate semiconductor with photooxidation properties under visible-light irradiation. Nat Mater 9:559–564
86. Bi Y, Ouyang S, Umezawa N, Cao J, Ye J (2011) Facet effect of single-crystalline Ag_3PO_4 sub-microcrystals on photocatalytic properties. J Am Chem Soc 133:6490–6492
87. Gao P, Li AR, Tai MH, Liu ZY, Sun DD (2014) A hierarchical nanostructured carbon nanofiber-In_2S_3 photocatalyst with high photodegradation and disinfection abilities under visible light. Chem Asian J 9:1663–1670
88. Kang ZH, Liu Y, Tsang CHA, Ma DDD, Fan X, Wong NB, Lee ST (2009) Water-soluble silicon quantum dots with wavelength-tunable photoluminescence. Adv Mater 21:661–664
89. Kang ZH, Tsang CHA, Wong NB, Zhang ZD, Lee ST (2007) Silicon quantum dots: a general photocatalyst for reduction, decomposition, and selective oxidation reactions. J Am Chem Soc 129:12090–12091
90. Chiou YD, Hsu YJ (2011) Room-temperature synthesis of single-crystalline Se nanorods with remarkable photocatalytic properties. Appl Catal B Environ 105:211–219
91. Wang F, Ng WKH, Yu JC, Zhu HJ, Li CH, Zhang L, Liu ZF, Li Q (2012) Red phosphorus: an elemental photocatalyst for hydrogen formation from water. Appl Catal B Environ 111–112:409–414
92. Liu G, Niu P, Yin LC, Cheng HM (2012) α-sulfur crystals as a visible-light-active photocatalyst. J Am Chem Soc 134:9070–9073
93. Liu G, Yin LC, Niu P, Jiao W, Cheng HM (2013) Visible-light-responsive β-rhombohedral boron photocatalysts. Angew Chem Int Ed 52:6242–6245
94. Yan CZ, Raghavan CM, Kang DJ (2014) Photocatalytic properties of shape-controlled ultra-long elemental Te nanowires synthesized via a facile hydrothermal method. Mater Lett 116:341–344

95. Bookbinder DC, Lewis NS, Bradley MG, Bocarsly AB, Wrighton MS (1979) Photoelectrochemical reduction of N, N′-dimethyl-4,4′-bipyridinium in aqueous media at p-type silicon: sustained photogeneration of a species capable of evolving hydrogen. J Am Chem Soc 101:7721–7723
96. Shao MW, Cheng L, Zhang XH, Ma DDD, Lee ST (2009) Excellent photocatalysis of HF-treated silicon nanowires. J Am Chem Soc 131:17738–17739
97. Kang ZH, Tsang CHA, Zhang ZD, Zhang ML, Wong N, Antonio Zapien J, Shan Y, Lee ST (2007) A polyoxometalate-assisted electrochemical method for silicon nanostructures preparation: from quantum dots to nanowires. J Am Chem Soc 129:5326–5327
98. Zhang RQ, Liu XM, Wen Z, Jiang Q (2011) Prediction of silicon nanowires as photocatalysts for water splitting: band structures calculated using density functional theory. J Phys Chem C 115:3425–3428
99. Wang WJ, Yu JC, Xia DH, Wong PK, Li YC (2013) Graphene and g-C_3N_4 nanosheets cowrapped elemental alpha-sulfur as a novel metal-free heterojunction photocatalyst for bacterial inactivation under visible-light. Environ Sci Technol 47:8724–8732
100. Chen YM, Lu AH, Li Y, Zhang LS, Yip HY, Zhao HJ, An TC, Wong PK (2011) Naturally occurring sphalerite as a novel cost-effective photocatalyst for bacterial disinfection under visible light. Environ Sci Technol 45:5689–5695
101. Wang F, Li CH, Li YC, Yu JC (2012) Hierarchical P/YPO_4 microsphere for photocatalytic hydrogen production from water under visible light. Appl Catal B Environ 119–120:267–272
102. Xia DH, Shen ZR, Huang GC, Wang WJ, Yu JC, Wong PK (2015) Red phosphorus: an earth-abundant elemental photocatalyst for “green” bacterial inactivation under visible light. Environ Sci Technol 49:6264–6273
103. Sun HW, Li GY, Nie X, Shi HX, Wong PK, Zhao HJ, An TC (2014) Systematic approach to in-depth understanding of photoelectrocatalytic bacterial inactivation mechanisms by tracking the decomposed building blocks. Environ Sci Technol 48:9412–9419
104. Maness PC, Smolinski S, Blake DM, Huang Z, Wolfrum EJ, Jacoby WA (1999) Bactericidal activity of photocatalytic TiO_2 reaction: toward an understanding of its killing mechanism. Appl Environ Microbiol 9:4094–4098
105. Wang WJ, Zhang LZ, An TC, Li GY, Yip HY, Wong PK (2011) Comparative study of visible-light-driven photocatalytic mechanisms of dye decolorization and bacterial disinfection by B-Ni-codoped TiO_2 microspheres: the role of different reactive species. Appl Catal B Environ 108:108–116
106. Chen HM, Chen CK, Liu RS, Zhang L, Zhang JJ, Wilkinson DP (2012) Nano-architecture and material designs for water splitting photoelectrodes. Chem Soc Chem 41:5654–5671
107. Liu G, Yu JC, Lu GQ, Cheng HM (2011) Crystal facet engineering of semiconductor photocatalysts: motivations, advances and unique properties. Chem Commun 47:6763–6783

Chapter 8
Disinfection of Waters/Wastewaters by Solar Photocatalysis

Danae Venieri and Dionissios Mantzavinos

Abstract A light source and a semiconducting material comprise a powerful duo that may offer several photocatalytic applications for environmental remediation; in recent years, photocatalytic disinfection based on sunlight has gained considerable attention as an efficient and sustainable technology to control the population of various microorganisms in several aqueous matrices. This chapter highlights recent developments in the field both from an engineering and a microbiological point of view. Advances in photocatalytic materials include the modification of all-time classic titania to perform better in the visible part of the electromagnetic spectrum, as well as synthesize novel catalysts such as silver phosphate or robust Fenton-like materials. Measuring disinfection efficiency correctly is critical in designing proper treatment systems. Disinfection kinetics are affected by several factors including reactor configuration, the water matrix, possible synergy with other oxidation processes, the selection of the test microorganism, and, most importantly, the way the population of microorganisms is measured; the latter is crucial since disinfection efficiency can easily be overestimated. All these, alongside the mechanisms of microbial structure destruction upon photocatalytic illumination and the perspectives and constraints of process scale-up, are dealt with in this chapter.

Keywords Sunlight photocatalysis • Photocatalysts • Waterborne pathogens • Disinfection kinetics and mechanisms • Public health • Test microorganism • Culture techniques • DNA-based techniques

D. Venieri
School of Environmental Engineering, Technical University of Crete, GR-73100 Chania, Greece

D. Mantzavinos (✉)
Department of Chemical Engineering, University of Patras, Caratheodory 1, GR-26504 Patras, Greece
e-mail: mantzavinos@chemeng.upatras.gr

T. An et al. (eds.), *Advances in Photocatalytic Disinfection*, Green Chemistry and Sustainable Technology, DOI 10.1007/978-3-662-53496-0_8

8.1 Introduction

The constantly growing demand for clean water of high hygiene standards has led to the exploration and the development of effective disinfection techniques. Disinfection is referred to a physical or chemical process that inactivates pathogenic or other virulent microorganisms, without necessarily reaching the point of killing them. In this context, it should be discriminated from sterilization that involves extreme conditions, under which the complete destruction of all organisms is achieved. The primary "target" of disinfection is the disease-causing microorganisms contained in water/wastewater and their concentration control to tolerable and safe limits for public health protection [1]. Waterborne diseases documented worldwide, and their rapid transmission through the consumption of contaminated water, illustrate the importance of effective inactivation of pathogens, including bacteria, viruses, and protozoa [2].

Well-known methods for the inactivation and the growth prevention of microorganisms involve the use of chemicals, radiation, or even filtration that removes the organisms physically by size exclusion [3]. Generally, water and wastewater disinfection is most commonly accomplished by chlorination, and its compounds, which are considered strong oxidizing agents and capable of inactivating a quite extended variety of microorganisms. The modes of action include interference with membrane permeability and substantial functions, enzyme impairment, or even nucleic acid denaturation [4, 5]. Despite the efficacy of those chemicals, considerable health hazards and destructive properties are associated with them. Many by-products of chlorination have already been documented as toxic and carcinogenic, depending on the water matrix and its chemical composition [6]. Moreover, it should not be overlooked the fact that certain pathogens, like bacterial spores, protozoan cysts, and viruses, exhibit considerable tolerance to chlorine, which imposes their more stringent control [7].

Such hardy pathogens may be confronted by other established disinfection methods such as ozonation and UV irradiation, both of which lead to satisfactory inactivation rates of microbes upon application. However, certain disadvantages, like high operational cost of ozonation, limited action depending on source water turbidity when UV irradiation is used, and the absence of any disinfectant residual to inhibit bacterial regrowth, restrict their widespread applications [8, 9]. In this sense, ongoing research focuses on the exploration and development of alternative disinfection methods, especially when human contact occurs or sensitive equipment and materials are present.

Advanced oxidation processes (AOPs) have been recognized as an emerging group of techniques with high oxidation potential and biocidal effect on various microorganisms in aqueous samples. The beneficial action of AOPs relies primarily on the in situ generation of highly reactive transitory species, like hydroxyl radicals, which induce oxidative stress to microorganisms and their ultimate inactivation. Moreover, their potential to mineralize various organic compounds and disinfection by-products has been highly recognized and adds to their overall value as disinfection processes [3]. Heterogeneous photocatalysis stands out among AOPs as a

promising and an effective biocidal technique, with titanium dioxide (TiO_2) being the most common catalyst employed for the purification of aqueous matrices. Upon irradiation, the massive production of reactive oxygen species (ROS) causes a gradual chain reaction beginning with a first oxidative stress when in contact with microbial cells, proceeding with deleterious alterations in cellular structure, and ending with microbial inactivation and possible destruction [10]. What makes this method even more attractive is the prospect of using the solar spectral range after specific modifications of titania, involving doping with nonmetals and/or noble and transition metals and modification of the substrates of the catalyst. In this way, the absorption spectrum of titania is expanded toward the visible light region, extending the applications of photocatalysis as a purification process [11, 12].

In this perspective, this chapter comprises a detailed presentation of the photocatalytic processes, in terms of their disinfection potential and mode of action for the inactivation of various microorganisms. Several issues are discussed, including common applications and type of catalysts, disinfection kinetics, and appropriate assessment, as well as the possibility of large-scale applications. Moreover, this report underlines the difficulty to standardize operational parameters of such techniques, due to the diverse microbial populations found in the aquatic environment and their varied behavior when exposed to the stressed conditions of disinfection.

8.2 Photocatalytic Processes for Disinfection

8.2.1 TiO_2 Photocatalysis

Titanium dioxide is one of the most widely recognized semiconductor photocatalysts, triggering off the oxidative destruction and mineralization of a wide range of organic substrates and microorganisms [13]. Heterogeneous semiconductor photocatalysis using TiO_2 as photocatalyst exhibits several advantages including operation at ambient conditions, as well as the fact that the catalyst itself is inexpensive, commercially available at various crystalline forms and particle characteristics, nontoxic, and photochemically stable. From a mechanistic point of view, illumination of TiO_2 with irradiation with energy greater than the bandgap energy of the semiconductor generates valence-band holes and conduction-band electrons. Holes and electrons may either undesirably recombine liberating heat or make their separate ways to the surface of TiO_2, where they can react with species adsorbed on the catalyst surface. Valence-band holes can react with water and the hydroxide ion (i.e., under alkaline conditions) to generate hydroxyl radicals, while electrons can react with adsorbed molecular oxygen reducing it to superoxide radical anion which, in turn, reacts with protons to form peroxide radicals [14].

On the contrary, the widespread technological use of TiO_2 photocatalyst has been hampered by its wide bandgap (~3.2 eV), which means that only UV radiation can be used for its photoactivation. Since solar irradiation reaching the surface of the earth contains only about 3–5 % UV radiation, it is of great interest to find ways to extend the adsorption wavelength range of TiO_2 to the visible region without the

decrease of photocatalytic activity. Another major drawback is the fast recombination of photogenerated electrons and holes. During the last years, studies have focused on the improvement of TiO_2 photocatalytic efficiency by several methods such as generating defect structures, doping with metallic or nonmetallic elements or modifying the TiO_2 surface with noble metals or other semiconductors [12].

Venieri et al. synthesized and tested novel Mn-, Co-, and binary Mn/Co-doped TiO_2 catalysts for the inactivation of *Escherichia coli* and *Klebsiella pneumoniae* under solar irradiation [15]. Doped catalysts could inactivate both bacteria 2–3 times faster than the pristine P25 TiO_2 with the pseudo-first-order rate expression depending on the type and concentration of dopant, concentration of catalyst, and the type and initial population of the tested bacteria. The improved activity of metal-doped titania was accredited to the optical absorption shifts toward the visible region and to the recombination delay of the electron–hole pair, since metals did not exhibit any bactericidal properties and catalysts were considerably sensitized in the absence of UV light. In further studies, the same catalysts were successfully employed for the inactivation of MS2 bacteriophages in sewage samples, achieving 99.9 % removal in less than 60 min of reaction [16]. Interestingly, inactivation of *K. pneumoniae* in sewage with Mn/Co-doped TiO_2 under simulated solar irradiation was faster than chlorination or UVC irradiation, highlighting the competitive nature of the proposed process against more conventional disinfection systems [17].

8.2.2 Slurry Versus Immobilized Catalysts

From an engineering point of view, the use of catalyst in the form of slurry requires an additional treatment step to remove it from the treated effluent. Alternatively, the catalyst may be immobilized on suitable support matrices, thus eliminating the need for post-treatment removal. The downside of this approach is that catalyst immobilization unavoidably leads to a decrease of the surface area available for reactions compared to suspended systems [18]. Ede et al. highlighted the kinetic and mechanistic differences between suspended and immobilized TiO_2 samples for the inactivation of *E. coli* and *Enterobacter cloacae*; in general, inactivation in suspended systems was faster than with immobilized catalysts [19].

The loss of photocatalytic activity when TiO_2 films are employed may be counterbalanced by applying an external electric bias in the so-called electrochemically assisted photocatalytic or photoeletrocatalytic process. The concept has been proven by Dunlop et al., who studied the inactivation of *Clostridium perfringens* spores on TiO_2/Ti films (working electrode) applying an external bias of 1 V, leading to 60–70 % higher inactivation rates compared to the case where no bias was applied [7]. The simultaneous application of a bias positive to the flat-band potential produces a bending of the conduction and valence bands which, in turn, causes a more effective separation of the photogenerated carriers within the space charge layer. In other words, the potential gradient forces the electrons toward the cathode (platinum in this case), thus minimizing the rate of electron–hole

recombination. In further studies, a TiO_2/Ti film anode and a zirconium cathode were employed for the photoelectrocatalytic disinfection of *Enterococcus faecalis* [20]. A 6.2 log reduction in *E. faecalis* population was achieved after 15 min at 10 V of applied potential and an initial concentration of 10^7 CFU/mL; photocatalysis alone under solar irradiation led to just 4.3 log reduction.

8.2.3 Photocatalysts Other Than TiO_2

Although TiO_2 is a benchmark catalyst for several photocatalytic applications, other semiconductors may also be employed for water disinfection. Zinc oxide, with a bandgap similar to titania's, has been tested for the inactivation of a wide spectrum of Gram-positive and Gram-negative bacteria, fungi, and viruses [21]. However, ZnO may suffer, unlike TiO_2, limited stability as a result of photo-corrosion and/or chemical corrosion. Cadmium sulfide (CdS) has also been reported as an efficient photocatalyst for the inactivation of *E. coli* and *Staphylococcus aureus* under visible light [22].

Silver orthophosphate (Ag_3PO_4) is a low bandgap photocatalyst that has attracted enormous attention in the past few years due to its great potential in harvesting solar energy for environmental purification and oxygen evolution. More importantly, this novel photocatalyst can achieve a quantum efficiency of up to 90 % at wavelengths >420 nm, thus implying a very low electron–hole recombination rate [23]. A drawback of silver orthophosphate is its insufficient long-term stability since it is photochemically decomposed in the absence of a sacrificial agent. This can be overcome covering the surface of Ag_3PO_4 with metallic silver nanoparticles which create localized surface plasmon resonance effects and/or synthesizing various Ag_3PO_4-based composites. Ag_3PO_4 and Ag_3PO_4/TiO_2 composites have been tested for the inactivation of *E. coli* under solar irradiation [24], while Ag_3PO_4 and $Ag_3PO_4/TiO_2/Fe_3O_4$ composites have been tested for *E. coli* under visible light [25]. In other studies [26], the bactericidal effect of several Ag_3PO_4/TiO_2/graphene composites was assessed against *E. coli*, *S. aureus*, *Salmonella typhi*, *Pseudomonas aeruginosa*, *Bacillus subtilis*, and *Bacillus pumilus*. Recently, Ag_3PO_4/TiO_2 catalysts have shown satisfactory performance under simulated solar irradiation, eliminating the coliphage MS2 in real wastewater samples (Fig. 8.1). These results broaden the application of such catalysts toward the inactivation of more persistent microorganisms like phages (viruses) in the complex matrices of sewage.

8.2.4 Heterogeneous Photo-Fenton Systems

Homogeneous Fenton reactions have extensively been tested for wastewater treatment. The process, which involves the presence of ferrous or ferric salts and hydrogen peroxide in acidic media, relies on the Fe^{2+}/Fe^{3+} redox cycle to generate

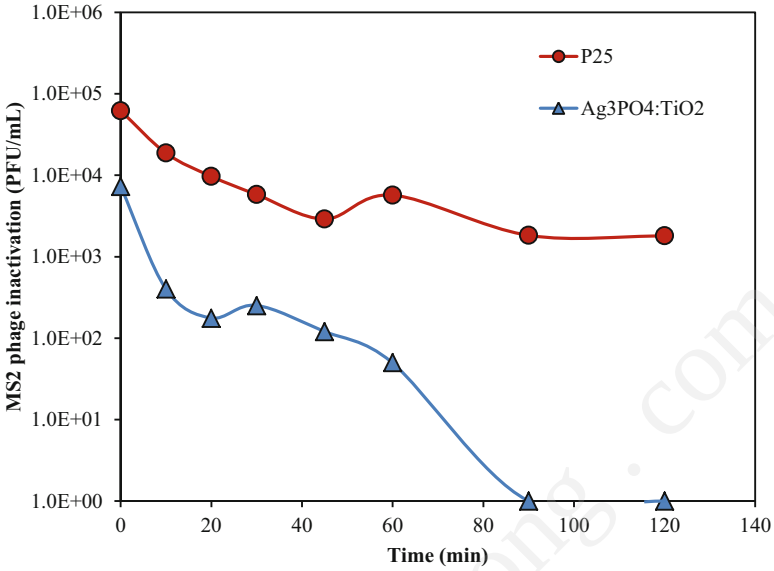

Fig. 8.1 Bacteriophage MS2 inactivation in real municipal wastewater under simulated solar irradiation in the presence of TiO_2 (P25) and Ag_3PO_4/TiO_2 (75:25) catalysts with concentration of 50 mg/L. Photocatalysis was performed in a batch-type, laboratory-scale photoreactor with a solar radiation simulator system (Newport, model 96000)

hydroxyl radicals and can further be enhanced by UV–vis irradiation; the latter promotes the transformation of Fe^{3+} to Fe^{2+} generating more radicals. The major drawback is the need to operate at pH values between 2 and 3 since higher pH values lead to iron precipitation in the form of insoluble hydroxides; this is impractical for wastewater treatment applications since (1) the treated stream has to be neutralized, and (2) iron must be removed prior to disposal.

In this view, research efforts have been directed toward heterogeneous Fenton-like systems capable of operating at neutral or near-neutral conditions. Barreca et al. prepared iron-enriched montmorillonite–alginate beads for the inactivation of *E. coli* with initial concentration of 10^7 CFU/mL at pH 7 under solar irradiation, reporting complete removal after 60 min with 10 mg/L H_2O_2 [27]. Catalyst stability issues were also investigated and partial iron dissolution was reported. Hematite (α-Fe_2O_3), goethite (α-FeOOH), and magnetite (Fe_3O_4) were found to be excellent iron-bearing oxides for the adsorption and solar-Fenton inactivation of MS2 coliphage at neutral conditions [28]. The role of irradiation was critical since inactivation in the dark did not occur with the exception of magnetite. All materials were stable leading to inconsiderable iron leaching. The same iron oxides, as well as FeO (wustite) were tested for *E. coli* inactivation under solar irradiation at neutral pH [29]. The authors reported two complementary mechanisms for inactivation, i.e., (1) Fenton-like reactions, where the oxides serve as a source of iron to decompose H_2O_2 to hydroxyl radicals, and (2) semiconductor photocatalysis-like reactions

(in the absence of H_2O_2), where iron oxides generate holes and electrons and eventually various ROS.

8.2.5 *Disinfection of Airborne Microorganisms*

Although outside the scope of this chapter, it is worth mentioning that photocatalytic disinfection has been researched to control indoor air quality, an issue of major public health concern. Some examples include filters from heating, ventilation, and air conditioning systems coated with TiO_2 to inactivate aerosolized *E. coli* [30], lamps emitting visible or UV light coated with TiO_2 to inactivate *Staphylococcus epidermidis* and *Aspergillus niger* spores in flow chambers [31], and a photocatalytic scrubber to control *E. faecalis* and infectious bursal disease virus associated with livestock houses [32].

8.3 Destruction of Microbial Structure During Photocatalysis

The remarkably extensive variety of microorganisms includes many groups with diverse structures and components, which, inevitably, affects their response during photocatalysis and the overall disinfection mode of action. Many studies have been undertaken in an attempt to elucidate the mechanisms of microbial inactivation, whose detailed procedure is yet to be shown. Although there is much information regarding bacteria and spores, research on protozoan cysts and viruses is still in an early stage.

The general observation attributes the detrimental effect of photocatalysis to the generation of ROS, which finally attack microorganisms present in the aqueous matrix of reaction. The primary species responsible for microbial destruction is hydroxyl radical ($HO^{\bullet}$) followed by superoxide radical anion ($O_2^{\bullet-}$), hydroperoxyl radical ($HO_2^{\bullet}$) and hydrogen peroxide (H_2O_2) [11]. The progressive inactivation process begins with the interaction between the microorganism and the catalyst nanoparticles, which results in the first induced oxidative stress toward outer cell wall components. The biocidal effect is expanded toward the cytoplasmic membrane, increasing cell permeability and allowing the outlet of intracellular components, which finally causes loss of viability [10, 33]. The smooth cellular surface areas are turned into rough ones, with considerable changes in the overall shape and size of the cell, as can be seen in Fig. 8.2 and in the SEM images of *E. coli*, *K. pneumoniae*, and *S. aureus* cells after solar photocatalysis with metal-doped titania. The change in cell permeability is confirmed by increased ion leakage, like that of potassium (K^+) into the external environment of the cell [15, 34]. Moreover, it has also been reported that cell death is achieved by the photooxidation of

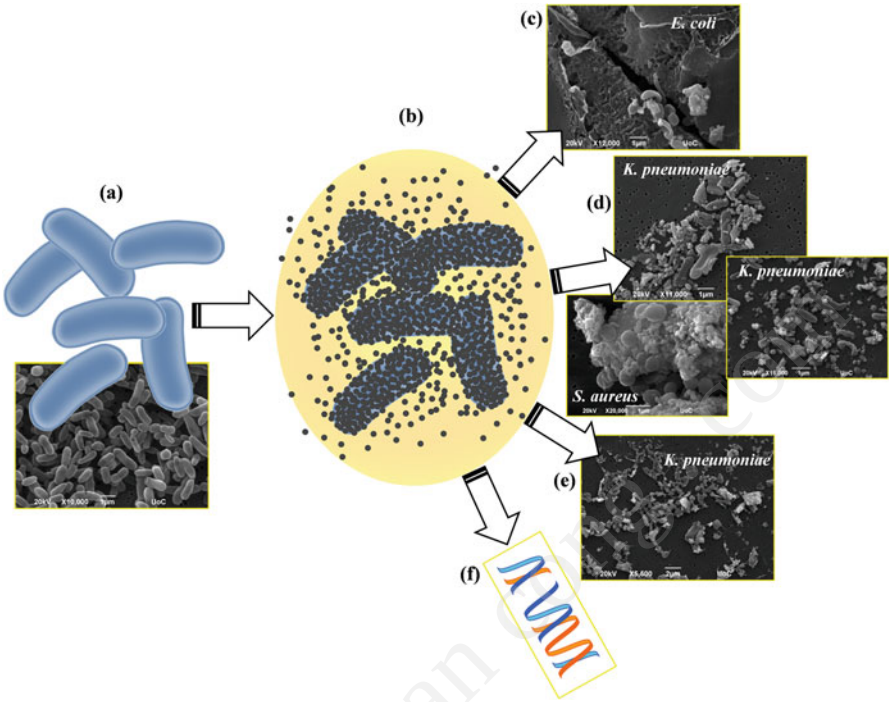

Fig. 8.2 The gradual process of bacterial inactivation through photocatalysis: (**a**) intact bacterial cells; (**b**) interaction between the catalyst nanoparticles and the bacterial surface; (**c**) and (**d**) morphological changes and deformation of *E. coli*, *K. pneumoniae*, and *S. aureus* cells after solar photocatalytic treatment with metal-doped titania; (**e**) leakage of intracellular components – *K. pneumoniae* remnants of polysaccharide capsules combined with material released from the cell after solar photocatalysis with Co-doped TiO_2; (**f**) lesions in DNA structure

coenzyme A (CoA), which inhibits the process of respiration [35]. The massive production of hydroxyl radicals in the course of photocatalysis overcomes any protection mechanism of bacterial cells, whose density in reaction mixture decreases with increasing time. The inactivation may become slow if the remaining active cells reach the protection "shields" provided by metabolites excreted from the destructed ones or if they have the potential to express cell surface structures and enzymes [9, 10]. Differences in fatty acid profiles and levels of intracellular enzymes, such as superoxide dismutase (SOD) and catalase (CAT), seem to play a role in protecting bacteria from oxidative stress.

The extent up to which cell permeability occurs varies among bacterial groups and is affected by the thickness of the cell wall. Gram-positive species possess a thick cell wall containing many layers of peptidoglycan and teichoic acids, providing them the potential of preserving their viability during photocatalytic treatment, possibly due to obstructed penetration of free radicals [36]. Nevertheless, not all studies confirm the higher tolerance of Gram-positive bacteria compared to the Gram-negative ones, as this precedence order may be reversed, depending on the

operational conditions and the bacterial indicators employed in each case [37, 38]. In this sense, Gram-negative bacteria require high catalyst concentrations up to 300 mg/L for complete elimination [39]. The actual comparison which should be under consideration is between the thick wall of Gram-positive and the outer membrane of Gram-negative, as each one represents the first line of defense [40]. Cell wall complexity still remains a nebulous parameter, and conclusions regarding its role in resistance during disinfection are still difficult to be definitive.

Another factor which defines the resistance level of bacteria is their cellular form. The endospores (spores) which may be produced by some pathogenic bacterial species may withstand the unfavorable conditions of photocatalysis. The thick spore protein coating that they possess provides resistance and requires prolonged treatment. Specifically, the coat of *Bacillus* spores may be damaged under UV-A irradiation only in the case of induced lethal mutations [35]. Also, *C. perfringens* spores tolerate oxidative stressed conditions due to a dipicolinic acid–calcium–peptidoglycan complex within the outer spore coating. The robustness of spores is only partly surpassed with the action of hydroxyl radical. The less reactive hydrogen peroxide can enter the bacterial structure and be activated by ferrous iron, which is normally incorporated into the spore coating, generating an in vivo Fenton reaction [7].

Protozoa follow almost the same trend line in terms of resistance during photocatalytic processes. Their virulence factors combined with their tough nature and difficult control have drawn special attention, as their transmittance through contaminated water may cause severe diseases of significant importance. Nonetheless, they have been merely reported in disinfection studies. Among them, *Cryptosporidium parvum* and *Giardia lamblia* are considered the most important waterborne protozoan pathogens which may be found in the aquatic environment in the form of oocysts and cysts, respectively. Treatment with a catalyst during exposure to solar irradiation causes cleavage at the suture line of oocyst cell walls with many remaining empty (ghost) cells after an extended period of time [18]. The deterioration of (oo)cysts surface, which may also occur in elevated water temperature, facilitates the transport of ROS in the inner cellular environment with subsequent biocidal results [41]. What is important is the fact that although residual oocysts of *C. parvum* make their appearance even after prolonged exposure to solar irradiation, they show no infectivity, as excystation produces sporozoites with no virulence function.

Viruses are traditionally known to be tolerant under stressed environmental conditions imposed by sunlight and temperature fluctuations and to chemical and physical treatments [16, 42]. They lack enzymes and cellular structure, and the only structure available for attack is the protein of the capsid they possess, which is simple and rigid, requiring more oxidizing power. Viral inactivation in photocatalytic processes is initiated by their adsorption onto the catalyst nanoparticles and proceeds with the attack on the protein capsid and the binding sites of the viruses [8, 43]. Adherence of viruses and phages to the catalysts accelerates the effects of short-lived radical species [2]. Conversely, other studies suggest that the interaction between the catalyst and the phage MS2 is not favored.

The predominantly negatively charged TiO_2 and the presence of both hydrophobic and hydrophilic regions within MS2 surface cause an electrostatic repulsion between them [44]. The inactivation behavior of MS2 phage is supposed to be mediated by free hydroxyl radicals in the bulk phase and not by those bound on the catalyst surface [45]. Electrostatic attraction between the negatively charged viral capsid and catalyst surface may be achieved by applying a positive potential up to 2 V to an immobilized TiO_2 electrode, leading to a better usage of bound hydroxyl radicals and increased ROS production [46]. Also, Fenton's reagent seems to show satisfactory elimination of MS2 coliphage within two distinct stages; the first is caused by oxidants generated from the oxidation of the initial Fe(II) on the outer and inner surfaces of the virus, and the second involves the Fenton cycle [47].

The ultimate target of ROS is the genetic material of microorganisms. DNA has been found to be susceptible to the oxidative conditions of photocatalytic systems, and multiple attacks may occur either at the sugar or at the base [40, 48]. The rising pyrimidine dimer products and the formation of general lesions, if unrepaired, may distort DNA helix, interfere with DNA transcription and replication, and can lead to mutations and cell death [49]. Pigeot-Rémy et al. observed a gradual degradation of nucleic acids and random damages in DNA molecules, which were attributed to the massive attack of superoxide anion and hydroxyl radicals, produced at the surface of titania during a photocatalytic process. Furthermore, they recorded the higher sensitivity of RNAs, as less stable macromolecules, with extensive damages, which correspond to the total loss of cultivability of the bacteria [50]. Other researchers observed that in Fenton systems, the DNA lesions may occur by the attack of either direct hydrogen peroxide or superoxide or by Fenton reaction-generated radicals [51].

The aforementioned structural damages induced in stressed conditions are subject to restoration, according to the potential and properties of each microorganism. Given that photocatalytic processes have no residual action, it is of great importance to verify the disinfection durability, as generated oxidative species have short half-life, and microbial reactivation may occur. The current literature confirms that this is among the main disadvantages of those treatments and is based on the so-called photoreactivation. It is an enzymatic reaction where light energy (300–500 nm) is used to split the dimers which are formed as a consequence of irradiation [52]. This way, proliferation of pathogens after treatment is possible, but it is strongly dependent on the type of microorganism and the operational conditions employed in each case. Usually, the mechanism of repair, whenever is present, is activated after treatment of bacteria with UV-C irradiation [53]. Nevertheless, it has also been documented after exposure to UV-A irradiation, involving not only bacteria but other microbes like protozoan cysts [54]. UV-exposed oocysts are able to perform DNA repair functions, restoring thymine dimers under both light and dark incubation conditions. On the contrary, other reports highlight the disability of microorganisms to recover after sufficient photocatalytic treatments. Bacteria like *E. coli* may not be reactivated or grow after photocatalytic semiconducting and heterogeneous photo-Fenton action [29]. Despite that findings obtained from current studies are quite contradictory about this issue, the possibility of microbial reactivation remains and raises certain concerns regarding the durability of

photocatalytic disinfection. Public health protection requires permanent elimination of pathogens, which may be accomplished by standardizing technical properties and applying the appropriate technique, according to the load and composition of microbial population.

8.4 Kinetics of Disinfection

8.4.1 General Considerations

To design a photocatalytic system, disinfection kinetics must be elucidated. The simplest way to address kinetics is to consider a power law, first-order expression also known as the Chick model, i.e.,

$$-\frac{dN}{dt} = k_{app}N \tag{8.1}$$

where N is the population of microorganisms and k_{app} is an apparent kinetic constant.

It is obvious that Eq. (8.1) can describe the region of logarithmic inactivation, while possible lag (i.e., at the beginning of the process) or slow-down phases (i.e., after a certain degree of inactivation has been achieved) cannot be modeled. In this respect, several other models have been developed capable of describing the various process phases such as the Hom model or the model developed by Marugán et al. [55]. From a design engineer's point of view though, simplicity is of utmost importance; therefore, a modified Chick model can be applied as follows [56]:

$$\frac{N}{N_o} = \begin{cases} 1 & \text{for } t \le t_1 \\ e^{-k_{app}(t-t_1)} & \text{for } t > t_1 \end{cases} \tag{8.2}$$

where t_1 is the time that corresponds to the initial lag phase.

Yet, Eq. (8.2) does not take into account the slow-down phase (tailing curve), where deviations from logarithmic inactivation may occur; for modeling purposes, it is advisable to select those data points between t_1 and t_2 where t_2 corresponds to the time needed to achieve a certain inactivation degree (i.e., one- or two-log reduction).

Assuming that the simplicity of Eq. (8.1) does not compromise accuracy, there are a number of points that still need to be addressed, as follows.

8.4.2 Pseudo- or True First-Order Kinetics?

Simple rate expressions like Eq. (8.1) can be prone to several misconceptions. For batch processes operating at fixed conditions of, e.g., photocatalyst concentration

and irradiance, the quantitative effect of these parameters on the kinetics is incorporated into apparent rate constants; this is erroneously reported by several researchers in the field as "pseudo-first"-order kinetics. As a matter of fact, the term "pseudo-first" should declare that experimental data fitting to Eq. (8.1) is acceptable regardless of the initial population, N_o. To confirm the actual order of reaction, experiments at different N_o are needed to compute the respective k_{app}; if k_{app} does not change with N_o, then the reaction is, indeed, true first order.

Another misconception has to do with the fact that the order is exclusively determined by N_o; this is not correct since it is the ratio of ROS concentration over N_o that eventually dictates kinetics and not the absolute value of N_o. If ROS are in excess, then the reaction is more likely first order, but if ROS is the limiting reactant, lower-order kinetics are expected. Since the concentration of ROS available to react with N depends on the concentration of photocatalyst, irradiance, and the water matrix complexity, the latter are the dominant factors in determining the actual kinetics. In simple terms, the very same reaction of a fixed N_o population with ROS can be anything between zeroth and first order with respect to N depending on how mild or harsh the employed photocatalytic conditions are.

Finally and since most processes operate at constant, batchwise conditions, there is no doubt that the order may change during the course of the reaction since N progressively decreases.

8.4.3 How Is Disinfection Efficiency Assessed?

Although most researchers in the field are aware of the advantages/drawbacks associated with the various kinetic models and the way the experimental results are treated, far fewer realize the importance of population measurement techniques on the disinfection rates. Culture techniques have traditionally been employed to count populations of microorganisms since they are relatively simple to operate and inexpensive and do not require highly specialized personnel. The culturability of bacteria represents their viability and therefore their potential to express their virulence and act as carriers of diseases. On the other hand, DNA-based techniques such as qPCR are more laborious and expensive and require specialized personnel. However, the former do not say the whole truth regarding the level of disinfection as this has recently been demonstrated by our group [57, 58]. Photocatalytic and photoelectrocatalytic tests for the inactivation of *E. coli* and *E. faecalis* were performed, and disinfection efficiency was evaluated by both plate counting and qPCR techniques; interestingly, the time needed for complete inactivation was always shorter with plate counting than qPCR, and this was attributed to the viable but not culturable (VBNC) state of microorganisms which could be captured by qPCR but not plate counting (Fig. 8.3). Bacteria in this state retain their metabolic activity and pathogenic features, posing danger for public health, while they are not recoverable in standard culture media. Also, under appropriate stimulation, they are capable of obtaining renascent metabolic activity. VBNC state is induced under

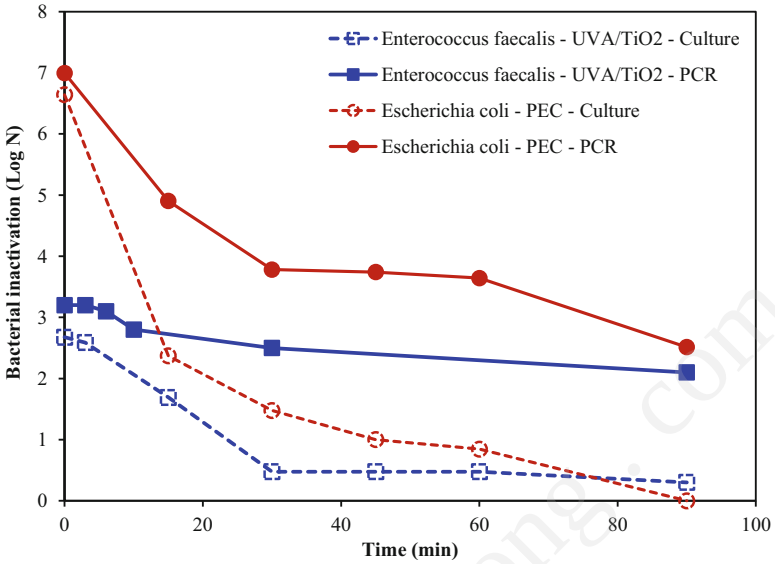

Fig. 8.3 *E. coli* and *E. faecalis* inactivation in real wastewater assessed by the culture technique and real-time PCR (qPCR). The applied methods were photoelectrocatalysis – PEC (5 V potential) – and UV-A/TiO_2 (catalyst concentration: 1000 mg/L) for *E. coli* and *E. faecalis* inactivation, respectively

environmental stresses, like those imposed during disinfection, and many waterborne pathogens reportedly enter it, like *Legionella pneumophila*, *P. aeruginosa*, and *Vibrio* sp., underestimating plate counts and increasing health risks [59]. On the contrary, molecular techniques surpass the major drawbacks of culture methods and are capable of detecting these strains contributing in a more reliable microbial evaluation of environmental samples. Yet, substantial limitations should be under consideration, such as the generation of false positives, reaction inhibitors in environmental samples, and difficulty in the quantification and determination of viable cells. However, viability PCR has already been recorded as a technique that detects solely the living cells [60]. According to Kacem et al. and based on the membrane integrity of viable bacterial cells, the treatment of samples with propidium monoazide (PMA) before DNA extraction ensures the detection of living microorganisms [60]. Nonetheless, the design of PCR and interpretation of its results demands extra caution in order for the DNA to be used as a reliable and valuable parameter for the quantification of viable organisms exposed to stressed conditions.

The framework of proper efficiency assessment of a disinfection process also includes the selection of a suitable testing microorganism. The quality of aquatic environment, in terms of public health protection and monitoring of waterborne diseases, is evaluated determining and quantifying microbes of fecal origin. Accordingly, the current legislation has established specific bacterial indicators, which reflect the level of fecal pollution, as well as the safety of water consumption

and treated wastewater disposal. Among them, the most prominent is *E. coli*, a Gram-negative bacterium that serves as the most common used microorganism in studies dealing with water/wastewater microbial quality. The same trend is being followed in cases of photocatalytic processes when their disinfection limits are estimated. Indeed, screening the relevant literature, it may be observed that the vast majority of reports employ *E. coli* as the testing bacterium for the study of solar photocatalysis under variable conditions [19, 39, 60–65]. However, the list of microbial parameters is extremely extensive with considerable variance in cell structure and virulent factors, which ultimately may lead to different photocatalytic inactivation efficiency [9, 38]. Moreover, in order to evaluate the disinfection action limits of a method in a reliable way, it is essential to test members of the microbial community with high resistance and persistence in water like enteric viruses, phages, protozoa, or even opportunistic bacterial pathogens like *K. pneumoniae* or *P. aeruginosa*. There is evidence that all those microorganisms, especially the viruses, have been detected in waters, which are compliant with the limits of traditional bacterial indicators like *E. coli* [66]. Hence, the monitoring of their die-off during water treatment is becoming of high priority, and they should be included in studies dealing with the assessment of a disinfection technique. As may be observed in Table 8.1, there are a variety of bacteria applied as target organisms in photocatalytic disinfection studies; however, protozoa have been merely mentioned only in few cases, and enteric viruses have not been employed for solar photocatalytic purposes. The main arguments of such misuse are technical issues, difficult analysis protocols, increased danger for the personnel performing the

Table 8.1 Microorganisms used in solar photocatalytic disinfection studies

Target microorganism	Solar photocatalytic process
Bacteria	
Escherichia coli	TiO_2; metal/nonmetal-doped TiO_2; immobilized catalysts; Ag_3PO_4/TiO_2 nanocomposite fibers; photoelectrocatalysis; heterogeneous photo-Fenton systems
Enterococci	TiO_2; metal/nonmetal-doped TiO_2; reactive plasma processed nanocrystalline TiO_2 powder
Clostridium perfringens	TiO_2; immobilized TiO_2; TiO_2 electrodes
Bacillus sp.	TiO_2; torularhodin-modified TiO_2/Ti surface
Staphylococcus aureus	TiO_2; metal/nonmetal-doped TiO_2; Ag_3PO_4/TiO_2 nanocomposite fibers; torularhodin-modified TiO_2/Ti surface
Pseudomonas aeruginosa	Modified TiO_2; graphene composites; torularhodin-modified TiO_2/Ti surface
Klebsiella sp.	TiO_2; metal-doped TiO_2; reactive plasma processed nanocrystalline TiO_2 powder
Protozoa	
Cryptosporidium parvum	TiO_2
Viruses	
Bacteriophages (MS2, ΦX174 and PR772)	TiO_2, doped titania, Fenton system, iron oxide coating

investigation, and, undoubtedly, the high cost of identifying and quantifying this kind of microbes. Nevertheless, the extraction of trustworthy outcomes and conclusions demands accurate and adequate design with suitable microbial indicators, taking into account resistant members, which have demonstrated a significant impact on human health. The possible suggestions range from Gram-positive bacteria like Enterococci, *Bacillus* sp., and *S. aureus* to Gram-negative opportunistic species like *Klebsiella* sp. and *P. aeruginosa* [9, 17, 22, 67–70]. Furthermore, other choices of more hardy organisms are viruses (adenoviruses and bacteriophages) and protozoa such as *C. parvum*, which have the potential to contribute in defining the assets and deficiencies of a disinfection procedure and its ability to remove a microbial load [8, 28, 45, 71].

8.4.4 The Role of the Water Matrix

Disinfection studies extend over a wide range of aqueous matrices from ultrapure water to surface/groundwaters (for potable water production) to municipal effluents that have already been subject to biological (secondary) treatment. The composition of the matrix is expected to affect the kinetics (predominantly) and mechanisms of photocatalytic disinfection due to the presence of inorganic ions (e.g., bicarbonates, chlorides, nitrates, sulfates, various cations), organics (e.g., natural organic matter (NOM) and effluent organic matter (EfOM)), and suspended solids.

As a rule of thumb, photocatalytic performance decreases with increasing matrix complexity due to the fact that the generated ROS are generally nonselective, and, therefore, they are wasted in reactions with the non-target water constituents. The detrimental effect of ammonia and nitrites on the photocatalytic disinfection of *E. coli* has been demonstrated by Zuo et al., and this was ascribed to the partial consumption of hydroxyl radicals to convert inorganic nitrogen to nitrates [72]. Marugán et al. reported the adverse effect of carbonates, phosphates, humic acid, and a municipal effluent-simulating matrix on the photocatalytic inactivation of *E. coli* [73]. On the contrary, they reported the beneficial effect of chlorides on disinfection, although they also act as radical scavengers; nonetheless, the photocatalytic formation of toxic organochlorinated by-products may offset the loss of hydroxyl radicals, thus enhancing the disinfection capacity. Interestingly, the authors performed identical experiments for the photocatalytic degradation of a dye, reporting that all inorganic and organic water constituents, including chlorides, retarded degradation.

This highlights the argument that the effect of water matrix on photocatalytic disinfection/degradation is case specific, and the net result is a function of the type of pollutant/contaminant tested, the photocatalyst used, and the experimental conditions under consideration. For instance, the consumption of hydroxyl radicals by bicarbonates leads to the generation of carbonate radicals, which are less powerful but more selective than hydroxyl radicals; the net effect of these two opposing phenomena (i.e., selectivity versus oxidizing capacity) will depend on the specific

application in question. Another example has to do with the effect of NOM on photocatalytic performance. Humic and fulvic acids are substances naturally occurring in waters, and their presence (in the order of mg/L) typically impedes photodegradation due to the scavenging of ROS and/or blockage of the photocatalyst active sites. Nevertheless and depending on the photocatalyst employed, humic acid may photosensitize the catalyst leading to enhanced reaction rates.

8.5 Large-Scale Applications

Although photocatalytic disinfection has successfully been tested in the laboratory, information regarding pilot- or large-scale applications is scarce. From a conceptual point of view, solar photocatalysis could serve as a tertiary wastewater treatment stage to (1) eliminate pathogens and (2) remove persistent micro-contaminants of emerging concern; this approach could be considered as a post-secondary treatment in conventional wastewater treatment plants (WWTPs).

The idea has recently been demonstrated by Philippe et al., who constructed a photoreactor comprising a compound parabolic collector and a novel, customized solar simulator to treat a synthetic secondary wastewater treatment plant effluent [74]. The authors reported that the process was capable of simultaneously eliminating 80 % of the nine pharmaceuticals tested and achieving a 5-log reduction of *E. coli* population at 3 kJ/L of accumulated energy with P25 TiO_2 as the photocatalyst. Along these lines is the work of Barwal and Chaudhari, who designed and tested a hybrid bio-solar system comprising a moving bed biofilm reactor followed by a parabolic trough photocatalytic reactor for the complete decontamination and disinfection of municipal wastewaters [75]. The biofilm reactor was capable of eliminating over 90 % of COD, while the remaining was removed photocatalytically under natural sunlight and TiO_2, alongside a 6-log reduction in fecal and total coliform populations.

Another interesting reactor configuration for photocatalytic tertiary wastewater treatment is the raceway pond proposed by Carra et al. [76]. Originally developed for microalgal mass culture, the raceway pond reactor was tested for the homogeneous photo-Fenton degradation of pesticide micro-contaminants. Efficient degradation of pesticides in synthetic secondary effluent could be achieved after about 30 min at 5–10 mg/L iron and pH = 2.8. Although the authors did not perform any disinfection studies, there is no reason why this set-up cannot be employed for killing pathogens. As a matter of fact, if conventional, homogeneous photo-Fenton is chosen for tertiary treatment, disinfection is likely to occur readily due to the low pH (i.e., 2–3) of the process. This has been demonstrated in a report where the simultaneous *E. coli* inactivation and estrogen degradation under solar-Fenton conditions were investigated; complete inactivation could be achieved after a couple of minutes of irradiation at acidic media [77].

Based on the above considerations, one could envisage large-scale applications of solar photocatalysis (semiconductor, photo-Fenton, and photo-Fenton alike) with

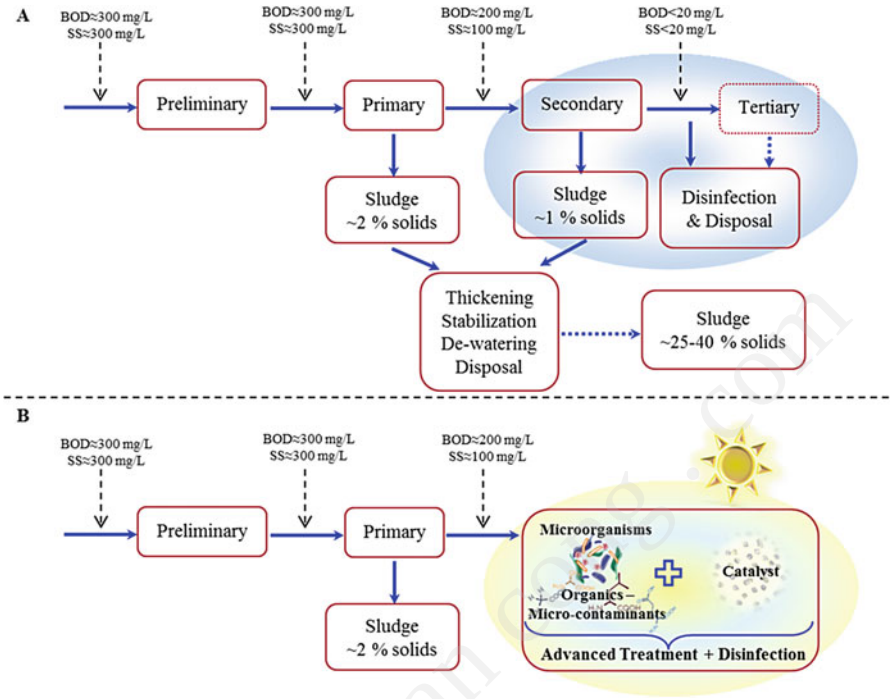

Fig. 8.4 Conventional municipal WWTP (**a**) versus an innovative, conceptual approach (**b**)

beneficial effects on public health, green economy, and the environment [11]. These could include (1) disinfection and degradation of emerging micro-contaminants in the drinking water industry and/or WWTPs and (2) possible replacement of biological treatment in WWTPs, thus offering a combined secondary and tertiary treatment. The polluting load of municipal effluents, typically in the order of a few hundred mg/L, is ideally suited for photocatalytic treatment removing organics, micro-contaminants, and pathogens. To take things a step further, the organic matter can even serve as sacrificial agent for photocatalytic water splitting to generate hydrogen. The concept is schematically illustrated in Fig. 8.4.

8.6 Perspectives, Constraints, and Recommendations

Although the environmental applications of photocatalysis, as well as several other AOPs, have been researched for about three decades now, its potential use for water disinfection is a relatively new topic for R&D. There is little doubt that economic cost is a key factor that will eventually dictate process viability, and several challenges have to be faced and overcome. In this respect, one must consider the following points:

1. Solar processes have an obvious head start in the quest of efficient disinfection/decontamination treatment technologies since they exploit a renewable energy source, avoiding capital and operational costs associated with artificial illumination.
2. The synthesis of new solar-active and stable photocatalysts can boost the technology but also increase treatment cost compared to traditional titania (for semiconductor photocatalysis) or iron-containing materials (for photo-Fenton and alike processes).
3. From an engineering point of view, process scale-up is a challenging task as specific reactor configurations and construction materials may be needed.
4. There is no such thing like "zero-cost" technology; therefore, the best thing one can opt for is "low-tech, low-cost" technologies.

A typical example of such technology is the "SODIS" process where 2 L PET bottles are simply filled with polluted water and left under sunlight for 6–48 h.

The aforementioned points of concern pinpoint the dependence of treatment efficacy (both in terms of economic cost and disinfection performance) on the level of treatment needed; the latter is a function of the (1) type of microorganisms under consideration, (2) final destination of the treated stream (e.g., disposal to watercourses, reuse for irrigation, reuse for other purposes), (3) increasingly more stringent environmental legislations, and (4) public awareness and perceptions.

In a nutshell, water disinfection is a topic lying at the interface of science and engineering, and different disciplines must join forces to tackle it in a successful way. Likewise, solar photocatalysis may benefit from the synergy with other processes to maximize performance.

References

1. Pepper IL, Gerba CP, Gentry TJ (2015) Environmental microbiology, 3rd edn. Academic, San Diego
2. Fisher MB, Keane DA, Fernández-Ibáñez P, Colreavy J, Hinder SJ, McGuigan KG, Pillai SC (2013) Nitrogen and copper doped solar light active TiO_2 photocatalysts for water decontamination. Appl Catal B Environ 130–131:8–13
3. Malato S, Fernández-Ibáñez P, Maldonado MI, Blanco J, Gernjak W (2009) Decontamination and disinfection of water by solar photocatalysis: recent overview and trends. Catal Today 147:1–59
4. Koivunen J, Heinonen-Tanski H (2005) Inactivation of enteric microorganisms with chemical disinfectants, UV irradiation and combined chemical/UV treatments. Water Res 39:1519–1526
5. Hu L, Page MA, Sigstam T, Kohn T, Mariñas BJ, Strathmann TJ (2012) Inactivation of bacteriophage MS2 with potassium ferrate(VI). Environ Sci Technol 46:12079–12087
6. Pablos C, Marugán J, van Grieken R, Serrano E (2013) Emerging micropollutant oxidation during disinfection processes using UV-C, UV-C/H_2O_2, UV-A/TiO_2 and UV-A/TiO_2/H_2O_2. Water Res 47:1237–1245
7. Dunlop PSM, McMurray TA, Hamilton JWJ, Byrne JA (2008) Photocatalytic inactivation of Clostridium perfringens spores on TiO_2 electrodes. J Photochem Photobiol A Chem 196:113–119

8. Gerrity D, Ryu H, Crittenden J, Abbaszadegan M (2008) Photocatalytic inactivation of viruses using titanium dioxide nanoparticles and low-pressure UV light. J Environ Sci Health A Tox Hazard Subst Environ Eng 43:1261–1270
9. Vijay M, Ramachandran K, Ananthapadmanabhan PV, Nalini B, Pillai BC, Bondioli F, Manivannan A, Narendhirakannan RT (2013) Photocatalytic inactivation of Gram-positive and Gram-negative bacteria by reactive plasma processed nanocrystalline TiO_2 powder. Curr Appl Phys 13:510–516
10. Robertson PKJ, Robertson JMC, Bahnemann DW (2012) Removal of microorganisms and their chemical metabolites from water using semiconductor photocatalysis. J Hazard Mater 211–212:161–171
11. Malato S, Maldonado MI, Fernández-Ibáñez P, Oller I, Polo I, Sánchez-Moreno R (2016) Decontamination and disinfection of water by solar photocatalysis: the pilot plants of the Plataforma Solar de Almeria. Mater Sci Semicond Process 42:15–23
12. Pelaez M, Nolan NT, Pillai SC et al (2012) A review on the visible light active titanium dioxide photocatalysts for environmental applications. Appl Catal B Environ 125:331–349
13. Carp O, Huisman CL, Reller A (2004) Photoinduced reactivity of titanium dioxide. Prog Solid State Chem 32:33–177
14. Klavarioti M, Mantzavinos D, Kassinos D (2009) Removal of residual pharmaceuticals from aqueous systems by advanced oxidation processes. Environ Int 35:402–417
15. Venieri D, Fraggedaki A, Kostadima M, Chatzisymeon E, Binas V, Zachopoulos A, Kiriakidis G, Mantzavinos D (2014) Solar light and metal-doped TiO_2 to eliminate water-transmitted bacterial pathogens: photocatalyst characterization and disinfection performance. Appl Catal B Environ 154–155:93–101
16. Venieri D, Gounaki I, Binas V, Zachopoulos A, Kiriakidis G, Mantzavinos D (2014) Inactivation of MS2 coliphage in sewage by solar photocatalysis using metal-doped TiO_2. Appl Catal B Environ 178:54–64
17. Venieri D, Gounaki I, Bikouvaraki M, Binas V, Zachopoulos A, Kiriakidis G, Mantzavinos D (2016) Solar photocatalysis as disinfection technique: Inactivation of *Klebsiella pneumoniae* in sewage and investigation of changes in antibiotic resistance profile. J Environ Manage 1–8
18. Byrne JA, Fernandez-Ibáñez PA, Dunlop PSM, Alrousan DMA, Hamilton JWJ (2011) Photocatalytic enhancement for solar disinfection of water: a review. Int J Photoenergy. doi:10.1155/2011/798051
19. Ede S, Hafner L, Dunlop P, Byrne J, Will G (2012) Photocatalytic disinfection of bacterial pollutants using suspended and immobilized TiO_2 powders. Photochem Photobiol 88:728–735
20. Venieri D, Chatzisymeon E, Sofianos SS, Politi E, Xekoukoulotakis NP, Katsaounis A, Mantzavinos D (2012) Removal of faecal indicator pathogens from waters and wastewaters by photoelectrocatalytic oxidation on TiO_2/Ti films under simulated solar radiation. Environ Sci Pollut Res 19:3782–3790
21. Bogdan J, Zarzyńska J, Pławińska-Czarnak J (2015) Comparison of infectious agents susceptibility to photocatalytic effects of nanosized titanium and zinc oxides: a practical approach. Nanoscale Res Lett 10:309
22. Chandran P, Kumari P, Sudheer Khan S (2014) Photocatalytic activation of CdS NPs under visible light for environmental cleanup and disinfection. Sol Energy 105:542–547
23. Yi Z, Ye J, Kikugawa N et al (2010) An orthophosphate semiconductor with photooxidation properties under visible-light irradiation. Nat Mater 9:559–564
24. Eswar NK, Ramamurthy PC, Madras G (2015) Enhanced sunlight photocatalytic activity of Ag_3PO_4 decorated novel combustion synthesis derived TiO_2 nanobelts for dye and bacterial degradation. Photochem Photobiol Sci 14:1227–1237
25. Xu JW, Gao ZD, Han K, Liu Y, Song YY (2014) Synthesis of magnetically separable Ag_3PO_4/TiO_2/Fe_3O_4 heterostructure with enhanced photocatalytic performance under visible light for photoinactivation of bacteria. Appl Mater Interfaces 6:15122–15131
26. Yang X, Qin J, Jiang Y, Li R, Li Y, Tang H (2014) Bifunctional TiO_2/Ag_3PO_4/graphene composites with superior visible light photocatalytic performance and synergistic inactivation of bacteria. RSC Adv 4:18627

27. Barreca S, Velez Colmenares JJ, Pace A, Orecchio S, Pulgarin C (2015) Escherichia coli inactivation by neutral solar heterogeneous photo-Fenton (HPF) over hybrid iron/montmorillonite/alginate beads. J Environ Chem Eng 3:317–324
28. Nieto-Juarez JI, Kohn T (2013) Virus removal and inactivation by iron (hydr)oxide-mediated Fenton-like processes under sunlight and in the dark. Photochem Photobiol Sci 12:1596–1605
29. Ruales-Lonfat C, Barona JF, Sienkiewicz A, Bensimon M, Vélez-Colmenares J, Benítez N, Pulgarín C (2015) Iron oxides semiconductors are efficients for solar water disinfection: a comparison with photo-Fenton processes at neutral pH. Appl Catal B Environ 166–167:497–508
30. Pigeot-Rémy S, Lazzaroni JC, Simonet F, Petinga P, Vallet C, Petit P, Vialle PJ, Guillard C (2014) Survival of bioaerosols in HVAC system photocatalytic filters. Appl Catal B Environ 144:654–664
31. Chuaybamroong P, Thunyasirinon C, Supothina S, Sribenjalux P, Wu CY (2011) Performance of photocatalytic lamps on reduction of culturable airborne microorganism concentration. Chemosphere 83:730–735
32. Zhao Y, Aarnink AJA, Xin H (2014) Inactivation of airborne Enterococcus faecalis and infectious bursal disease virus using a pilot-scale ultraviolet photocatalytic oxidation scrubber. J Air Waste Manage Assoc 64:38–46
33. Karunakaran C, Vijayabalan A, Manikandan G, Gomathisankar P (2011) Visible light photocatalytic disinfection of bacteria by Cd–TiO_2. Catal Commun 12:826–829
34. Lu Z-X, Zhou L, Zhang Z-L, Shi W-L, Xie Z-X, Xie H-Y, Pang D-W, Shen P (2003) Cell damage induced by photocatalysis of TiO_2 thin films. Langmuir 19:8765–8768
35. Vohra A, Goswami DY, Deshpande DA, Block SS (2005) Enhanced photocatalytic inactivation of bacterial spores on surfaces in air. J Ind Microbiol Biotechnol 32:364–370
36. Yoo S, Ghafoor K, Kim S, Sun YW, Kim JU, Yang K, Lee DU, Shahbaz HM, Park J (2015) Inactivation of pathogenic bacteria inoculated onto a Bacto™ agar model surface using TiO_2-UVC photocatalysis, UVC and chlorine treatments. J Appl Microbiol 119:688–696
37. Markowska-Szczupak A, Ulfig K, Morawski AW (2011) The application of titanium dioxide for deactivation of bioparticulates: an overview. Catal Today 169:249–257
38. Yadav HM, Otari SV, Bohara RA, Mali SS, Pawar SH, Delekar SD (2014) Synthesis and visible light photocatalytic antibacterial activity of nickel-doped TiO_2 nanoparticles against Gram-positive and Gram-negative bacteria. J Photochem Photobiol A Chem 294:130–136
39. Xiao G, Zhang X, Zhang W, Zhang S, Su H, Tan T (2015) Visible-light-mediated synergistic photocatalytic antimicrobial effects and mechanism of Ag-nanoparticles@chitosan-TiO_2 organic-inorganic composites for water disinfection. Appl Catal B Environ 170–171:255–262
40. Dalrymple OK, Stefanakos E, Trotz MA, Goswami DY (2010) A review of the mechanisms and modeling of photocatalytic disinfection. Appl Catal B Environ 98:27–38
41. McGuigan KG, Méndez-Hermida F, Castro-Hermida JA et al (2006) Batch solar disinfection inactivates oocysts of Cryptosporidium parvum and cysts of Giardia muris in drinking water. J Appl Microbiol 101:453–463
42. Jebri S, Hmaied F, Jofre J, MariemYahya MJ, Barkallah I, Hamdi M (2013) Effect of gamma irradiation on bacteriophages used as viral indicators. Water Res 47:3673–3678
43. Ditta IB, Steele A, Liptrot C, Tobin J, Tyler H, Yates HM, Sheel DW, Foster HA (2008) Photocatalytic antimicrobial activity of thin surface films of TiO_2, CuO and TiO_2/CuO dual layers on Escherichia coli and bacteriophage T4. Appl Microbiol Biotechnol 79:127–133
44. Cho M, Chung H, Choi W, Yoon J (2005) Different inactivation behaviors of MS-2 phage and Escherichia coli in TiO_2 photocatalytic disinfection. Appl Environ Microbiol 71:270–275
45. Misstear DB, Gill LW (2012) The inactivation of phages MS2, ΦX174 and PR772 using UV and solar photocatalysis. J Photochem Photobiol B Biol 107:1–8
46. Cho M, Cates EL, Kim JH (2011) Inactivation and surface interactions of MS-2 bacteriophage in a TiO_2 photoelectrocatalytic reactor. Water Res 45:2104–2110
47. Kim JY, Lee C, Sedlak DL, Yoon J, Nelson KL (2010) Inactivation of MS2 coliphage by Fenton's reagent. Water Res 44:2647–2653

48. Wong MS, Chu WC, Sun DS et al (2006) Visible-light-induced bactericidal activity of a nitrogen-doped titanium photocatalyst against human pathogens. Appl Environ Microbiol 72:6111–6116
49. Sinha RP, Häder D-P (2002) UV-induced DNA damage and repair: a review. Photochem Photobiol Sci 1:225–236
50. Pigeot-Rémy S, Simonet F, Errazuriz-Cerda E, Lazzaroni JC, Atlan D, Guillard C (2011) Photocatalysis and disinfection of water: identification of potential bacterial targets. Appl Catal B Environ 104:390–398
51. Gogniat G, Dukan S (2007) TiO_2 photocatalysis causes DNA damage via fenton reaction-generated hydroxyl radicals during the recovery period. Appl Environ Microbiol 73:7740–7743
52. Süß J, Volz S, Obst U, Schwartz T (2009) Application of a molecular biology concept for the detection of DNA damage and repair during UV disinfection. Water Res 43:3705–3716
53. Chatzisymeon E, Droumpali A, Mantzavinos D, Venieri D (2011) Disinfection of water and wastewater by UV-A and UV-C irradiation: application of real-time PCR method. Photochem Photobiol Sci 10:389–395
54. Rochelle PA, Upton SJ, Montelone BA, Woods K (2005) The response of Cryptosporidium parvum to UV light. Trends Parasitol 21:81–87
55. Marugán J, van Grieken R, Sordo C, Cruz C (2008) Kinetics of the photocatalytic disinfection of Escherichia coli suspensions. Appl Catal B Environ 82:27–36
56. Rennecker JL, Mariñas BJ, Owens JH, Rice EW (1999) Inactivation of Cryptosporidium parvum oocysts with ozone. Water Res 33:2481–2488
57. Venieri D, Chatzisymeon E, Gonzalo MS, Rosal R, Mantzavinos D (2011) Inactivation of Enterococcus faecalis by TiO_2-mediated UV and solar irradiation in water and wastewater: culture techniques never say the whole truth. Photochem Photobiol Sci 10:1744
58. Venieri D, Chatzisymeon E, Politi E, Sofianos SS, Katsaounis A, Mantzavinos D (2013) Photoelectrocatalytic disinfection of water and wastewater: performance evaluation by qPCR and culture techniques. J Water Health 11:21–29
59. Zhang S, Ye C, Lin H, Lv L, Yu X (2015) UV Disinfection induces a VBNC state in Escherichia coli and Pseudomonas aeruginosa. Environ Sci Technol 49:1721–1728
60. Kacem M, Bru-Adan V, Goetz V, Steyer JP, Plantard G, Sacco D, Wery N (2016) Inactivation of Escherichia coli by TiO_2-mediated photocatalysis evaluated by a culture method and viability-qPCR. J Photochem Photobiol A Chem. doi:10.1016/j.jphotochem.2015.11.020
61. Pratap Reddy M, Venugopal A, Subrahmanyam M (2007) Hydroxyapatite-supported Ag-TiO_2 as Escherichia coli disinfection photocatalyst. Water Res 41:379–386
62. Rizzo L, Della Sala A, Fiorentino A, Li Puma G (2014) Disinfection of urban wastewater by solar driven and UV lamp – TiO_2 photocatalysis: effect on a multi drug resistant Escherichia coli strain. Water Res 53:145–152
63. Veréb G, Manczinger L, Bozsó G, Sienkiewicz A, Forró L, Mogyorósi K, Hernádi K, Dombi A (2013) Comparison of the photocatalytic efficiencies of bare and doped rutile and anatase TiO_2 photocatalysts under visible light for phenol degradation and E. coli inactivation. Appl Catal B Environ 129:566–574
64. Nadtochenko VA, Rincon AG, Stanca SE, Kiwi J (2005) Dynamics of E. coli membrane cell peroxidation during TiO_2 photocatalysis studied by ATR-FTIR spectroscopy and AFM microscopy. J Photochem Photobiol A Chem 169:131–137
65. Helali S, Polo-López MI, Fernández-Ibáñez P, Ohtani B, Amano F, Malato S, Guillard C (2013) Solar photocatalysis: a green technology for E. coli contaminated water disinfection. Effect of concentration and different types of suspended catalyst. J Photochem Photobiol A Chem 276:31–40
66. Rames E, Roiko A, Stratton H, Macdonald J (2016) Technical aspects of using human adenovirus as a viral water quality indicator. Water Res 96:308–326
67. Zielińska A, Kowalska E, Sobczak JW, Łącka I, Gazda M, Ohtani B, Hupka J, Zaleska A (2010) Silver-doped TiO_2 prepared by microemulsion method: Surface properties, bio- and photoactivity. Sep Purif Technol 72:309–318

68. Cheng CL, Sun DS, Chu WC et al (2009) The effects of the bacterial interaction with visible-light responsive titania photocatalyst on the bactericidal performance. J Biomed Sci 16:7
69. Swetha S, Santhosh SM, Balakrishna RG (2010) Enhanced bactericidal activity of modified titania in sunlight against Pseudomonas aeruginosa, a water-borne pathogen. Photochem Photobiol 86:1127–1134
70. Fagan R, McCormack DE, Dionysiou DD, Pillai SC (2016) A review of solar and visible light active TiO_2 photocatalysis for treating bacteria, cyanotoxins and contaminants of emerging concern. Mater Sci Semicond Process 42:2–14
71. Pecson BM, Decrey L, Kohn T (2012) Photoinactivation of virus on iron-oxide coated sand: Enhancing inactivation in sunlit waters. Water Res 46:1763–1770
72. Zuo X, Hu J, Chen M (2015) The role and fate of inorganic nitrogen species during UVA/TiO_2 disinfection. Water Res 80:12–19
73. Marugán J, van Grieken R, Pablos C (2010) Kinetics and influence of water composition on photocatalytic disinfection and photocatalytic oxidation of pollutants. Environ Technol 31:1435–1440
74. Philippe KK, Timmers R, van Grieken R, Marugan J (2016) Photocatalytic disinfection and removal of emerging pollutants from effluents of biological wastewater treatments, using a newly developed large-scale solar simulator. Ind Eng Chem Res 55:2952–2958
75. Barwal A, Chaudhary R (2016) Feasibility study for the treatment of municipal wastewater by using a hybrid bio-solar process. J Environ Manag 177:271–277
76. Carra I, Santos-Juanes L, Acién Fernández FG, Malato S, Sánchez Pérez JA (2014) New approach to solar photo-Fenton operation. Raceway ponds as tertiary treatment technology. J Hazard Mater 279:322–329
77. Frontistis Z, Xekoukoulotakis NP, Hapeshi E, Venieri D, Fatta-Kassinos D, Mantzavinos D (2011) Fast degradation of estrogen hormones in environmental matrices by photo-Fenton oxidation under simulated solar radiation. Chem Eng J 178:175–182

Chapter 9
Photoelectrocatalytic Materials for Water Disinfection

Huijun Zhao and Haimin Zhang

Abstract This chapter summarizes recent progress on semiconductor-based photoelectrocatalytic materials with UV and visible light activities that are applicable to bactericidal purpose. Semiconductor photocatalysis (e.g., TiO_2, ZnO, WO_3, SnO_2, and C_3N_4) under UV/visible light irradiation has been extensively investigated in environmental remediation during the past 40 years because the developed photocatalysts are powerful toward the decomposition of organic pollutants and inactivation of biohazards. However, low photocatalytic efficiency of photocatalysts has been a general issue limiting photocatalysis technology for practical application owing to rapid recombination of photogenerated electrons and holes. To date, considerable efforts have been made to suppress the recombination of photogenerated carriers (e.g., photoelectrons and holes), thus effectively improving the photocatalytic efficiency of photocatalyst, such as surface modification (e.g., noble metal, graphene modification) of photocatalyst and coupling of several semiconductor photocatalysts with matched electronic band structures. Among all investigated approaches, photoelectrochemical technology has been a general means to effectively suppress the recombination of photogenerated carries by an applied potential bias serving as external motive force to rapidly remove the photocatalytically generated electrons to the external circuit then to the counter electrode where forced reduction reactions occur. The rapid removal of the photoelectrons from the conduction band of photocatalyst effectively suppresses the recombination of the photogenerated carries and prolongs the lifetime of photoholes to facilitate the direct photohole oxidation reactions. However, the photoelectrocatalytic performance is highly dependent on its key component – photoelectrode material, such as structure, crystal phase, chemical composition, and exposed crystal facets. Herein, we summarize the recent development of

H. Zhao (✉)
Centre for Clean Environment and Energy, Griffith University, Gold Coast Campus, Gold Coast, QLD 4222, Australia
e-mail: h.zhao@griffith.edu.au

H. Zhang
Key Laboratory of Materials Physics, Centre for Environmental and Energy Nanomaterials, Anhui Key Laboratory of Nanomaterials and Nanotechnology, Institute of Solid State Physics, Chinese Academy of Sciences, Hefei 230031, China
e-mail: zhanghm@issp.ac.cn

T. An et al. (eds.), *Advances in Photocatalytic Disinfection*, Green Chemistry and Sustainable Technology, DOI 10.1007/978-3-662-53496-0_9

semiconductor-based photoelectrocatalytic materials for bactericidal application in this chapter, which would be helpful to design and fabricate high-efficiency photoelectrodes for photoelectrocatalytic water disinfection. Further, the challenges and opportunities of photoelectrocatalytic materials for bactericidal application are also discussed and prospected in this chapter.

Keywords Photoelectrocatalysis • Photoelectrocatalytic materials • Photoelectrodes • Bactericidal applications • Water disinfection

9.1 Introduction

Since Honda and Fujishima's pioneering work in 1972, intensive research efforts have been made to develop UV and visible light active photocatalytic materials for environmental remediation and clean fuel production [1–6]. For environmental remediation, most studies on these photocatalytic materials are mainly focused on photocatalytic degradation of organic pollutants under UV or visible light irradiation [2, 7–9]. It is well known that biohazards (e.g., waterborne pathogens) have been major concerns for managers of water resources, as they can directly or indirectly cause diseases or major disorder and even death in humans or animals when they are ingested or got in touch with [10]. Therefore, development of simple and effective bactericidal technologies for water disinfection application is critically important to safeguard the use of water. Among all developed water disinfection technologies, photocatalysis (PC) has been an effective and environmentally friendly means to rapidly inactivate and decompose microorganisms in water and wastewater [11–15]. Photocatalytic bactericidal study using TiO_2 particles under UV irradiation was first reported by Matsunaga and co-workers [11]. Since then a considerable effort has been made to demonstrate the bactericidal effects of illuminated TiO_2 and other photoactive semiconductor photocatalysts toward a variety of pathogens such as *E. coli*, *Lactobacillus acidophilus*, *Saccharomyces cerevisiae*, *phage MS2, phage PL-1, bacteriophage Qβ, bacteriophage T4 poliovirus I, hepatitis B virus, rotavirus, astrovirus*, and *feline calicivirus* [14, 16–19]. Despite the noticeable progress, the reported PC bactericidal methods (e.g., TiO_2) are almost exclusively carried out in particle suspension system. Such bactericidal methods generally require long reaction time (e.g., 1–6 h) to achieve total inactivation of a sample with a bacteria population greater than 10^6 CFU/mL owing to low photocatalytic efficiency [12]. This is because for such reaction systems, the oxidation and reduction half-reactions simultaneously occur at different locations on the same photocatalyst particle (regarding as a microintegrated photoelectrocatalytic cell), and overall rate of reaction is often limited by the reduction half-reaction, due to the insufficient electron acceptor concentration (dissolved O_2 is used as the electron acceptor for most cases, but it is poorly soluble in aqueous media) in solution that causes severe recombination of photoelectrons/holes [20, 21]. Studies demonstrated that such issues can be effectively overcome by photoelectrocatalytic approach [20–22]. The photocatalytic efficiency of a

photoelectrocatalysis (PEC) system is independent of the availability of electron acceptor because the applied potential bias can serve as an external motive force to rapidly remove the photocatalytically generated electrons to the external circuit then to the counter electrode where reduction reactions occur [20–22]. The rapid removal of the photoelectrons from the conduction band can effectively suppress the recombination of photogenerated electrons and holes and prolong the lifetime of photoholes to facilitate the direct photohole oxidation reactions, thus significantly improving photocatalytic bactericidal performance [20–22].

To date, the studies on photocatalysis bactericidal application for water disinfection purpose have been widely reported and reviewed by some research groups [14–16, 23–26]. However, the reports on bactericidal applications using photoelectrocatalysis (PEC) technique are relatively few owing to the limitation of photoelectrocatalytic materials. As a key component of PEC technique, photoelectrocatalytic materials are critically important to fabricate high-performance photoelectrodes for bactericidal applications. The developed PEC materials must possess these advantages of high chemical/photochemical/electrochemical stability as photoelectrode utilization, suitable band structures with UV or visible light activity, and easy fabrication. So far, TiO_2 is still an overwhelming photocatalytic material for PEC bactericidal application owing to its superior photocatalytic activity and high chemical/photochemical/electrochemical stability. In this respect, our group mainly investigated the effect of different TiO_2 nanostructure photoelectrodes including nanoparticle film, nanotube film, and {111} faceted TiO_2 nanostructure film on bactericidal performance [27–30]. The results demonstrated that vertically aligned TiO_2 nanostructures (e.g., TiO_2 nanotubes) can provide superior photoelectron transport pathways, thus effectively improving photocatalytic efficiency and bactericidal performance [29]. Additionally, carbon nanotube-modified TiO_2, Ag/AgBr (AgCl)-modified TiO_2, Cu_2O and $ZnIn_2S_4$photoelectrocatalytic materials have also been developed by other groups for visible light active bactericidal applications, exhibiting promising performance [17–19, 31, 32]. However, these PEC bactericidal materials are far from being enough for practical bactericidal application in water disinfection. Therefore, development of more high-performance PEC bactericidal materials is highly desired for practical water disinfection application of PEC technology.

In this chapter, a recent progress on semiconductor-based photoelectrocatalytic materials for bactericidal application in water disinfection is summarized and discussed on the basis of our and others' studies in recent years. The related information should be helpful to design and develop high-efficiency UV and visible light active photoelectrocatalytic bactericidal materials for water disinfection application.

9.2 Fundamentals of Photocatalysis (PC) and Photoelectrocatalysis (PEC) Processes

For traditional semiconductor-based photocatalysis (PC) suspension solution system, the redox reactions including photooxidation and photoreduction half-reactions occur on the same photocatalyst particle that can be regarded as a microintegrated

photoelectrocatalytic cell (Fig. 9.1a) [2, 3, 22, 33, 34]. Such approach readily results in a fast recombination of photogenerated carriers (e.g., photoelectrons and holes) to release heat or light, thus significantly decreasing the photocatalytic efficiency. Some review papers have summarized possibly used procedures during a semiconductor photocatalysis process [2, 33]:

1. The formation of photogenerated carriers (e.g., electrons and holes) under light excitation
2. The recombination of photogenerated electrons and holes.
3. Reduction half-reaction at conduction band.
4. Oxidation half-reaction at valence band.
5. Hydrolysis or reaction with active oxygen species or mineralization.
6. The trapping of a conduction band electron in a dangling surface bond
7. The trapping of a valence band hole at the photocatalyst surface.

The occurrence of processes (2), (6), and (7) is very unfavourable for high photocatalytic efficiency, especially for process (2), which is closely related to the photocatalytic materials. Additionally, powder-formed photocatalyst in suspension solution needs to be recycled by other techniques such as membrane filtration, which undoubtedly enhances the cost of practical applications.

The abovementioned issues on rapid recombination of photogenerated carriers and photocatalyst recycling of traditional PC system can be solved very well by photoelectrocatalysis (PEC) technique (Fig. 9.1B) with many advantages [35–39]:

1. One is that powder-formed photocatalyst can be immobilized on conductive substrate to form photocatalyst film, thus solving the recycling issue of powder-formed photocatalyst after reaction.
2. Another is that an applied potential bias in PEC technique is utilized to force the photogenerated electrons to external circuit, and then to auxiliary electrode, which effectively inhibits the recombination of photogenerated electrons and holes, thus significantly improving the photocatalytic efficiency.
3. More importantly, the oxidation half-reaction (at the working electrode) is physically separated from the reduction half-reaction (at the auxiliary electrode) by this PEC technique (Fig. 9.1B), allowing the reaction of interest (e.g., the photocatalytic oxidation of water and organics) to be quantitatively studied in isolation [22, 40–46]. These distinct advantages make PEC method a very promising technique for bactericidal application in water disinfection.

Compared to conventional semiconductor-based photocatalysis technique, one important advantage of PEC technique is that the photogenerated electrons and holes can be effectively and efficiently separated by an applied potential bias, thus significantly inhibiting the recombination of photogenerated electrons and holes and improving the photocatalytic efficiency [22, 40–46]. In the process of the photoelectrocatalytic reaction, the directly formed photogenerated holes (h^+) by light excitation and indirectly formed radicals (e.g., OH•, HO_2•, O_2•$^-$) can participate in the oxidation reactions for inactivation and decomposition of biohazards in water [27, 47–51]. Owing to greatly inhibited recombination of photogenerated

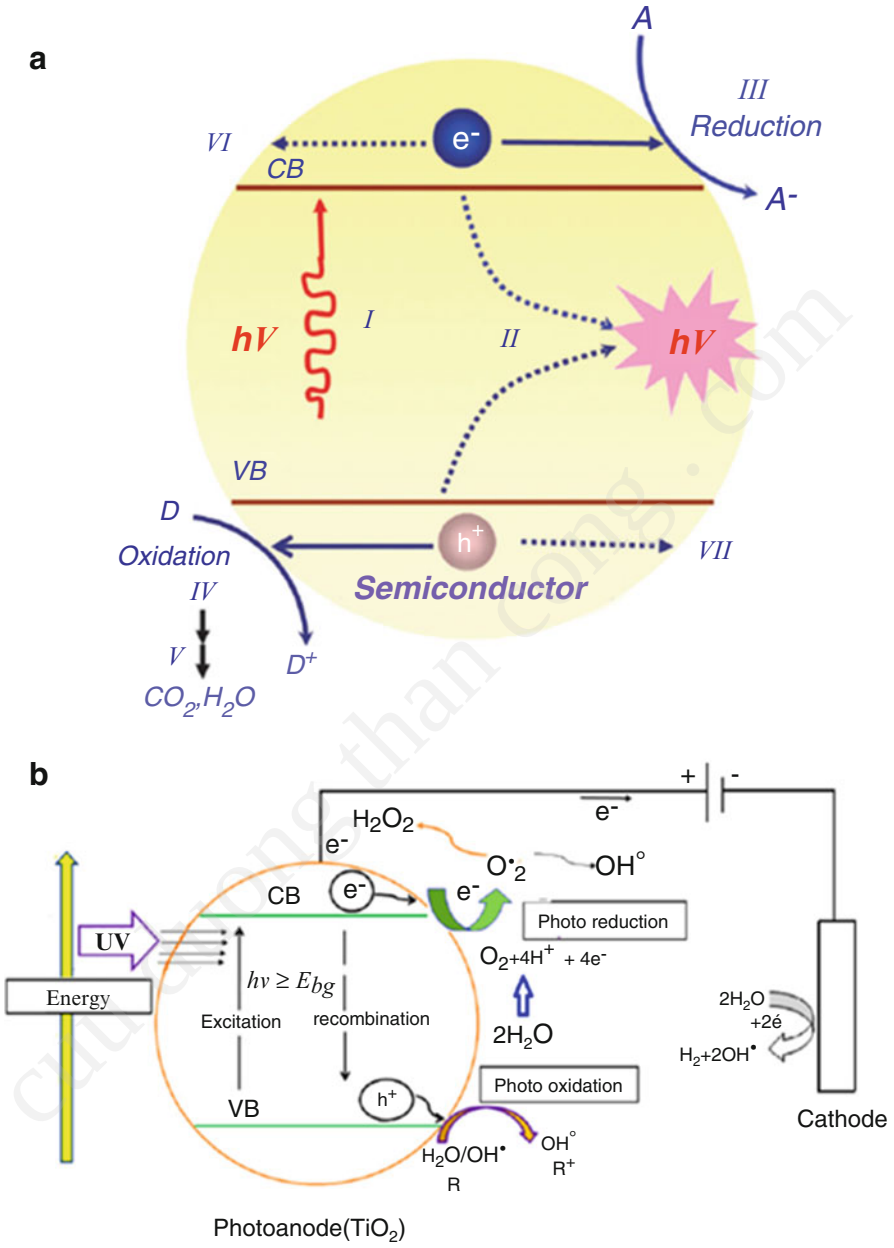

Fig. 9.1 Fundamentals of photocatalysis and photoelectrocatalysis processes ((**a**) Reprinted from Ref. [33] Copyright©2014 The Royal Society of Chemistry and (**b**) Ref. [35] Copyright©2012 Elsevier)

Table 9.1 The redox potentials of some typical oxidants

Oxidants	Redox potential (V) vs. SHE	References
h^+	3.1 (Anatase TiO_2)	[2]
$H_2O/OH•$	2.81	[52]
O_2/O_3	2.07	[53]
$SO_4^{2-}/S_2O_8^{2-}$	2.05	[54]
MnO_2/MnO_4^{2-}	1.77	[55]
H_2O/H_2O_2	1.77	[56]
Cl^-/ClO_2^-	1.57	[56]
Ag^+/Ag^{2+}	1.50	[55]
Cl^-/Cl_2	1.36	[57]
H_2O/O_2	1.23	[58]

electrons and holes by PEC technique, the lifetimes of the generated photoholes (h^+) and radicals (e.g., OH•, HO_2•, O_2•$^-$) can be effectively prolonged, thus significantly improving PEC water disinfection efficiency. Table 9.1 shows the redox potential of some typical oxidants.

9.3 Photoelectrocatalytic Materials and Photoelectrodes

As a key component of photoelectrocatalytic reaction system, photoelectrode material is critically important to determine the inactivation efficiency of biohazards in aqueous solutions, which has been intensively reviewed in recent reported papers [35, 38, 39, 59–61]. Figure 9.2 shows the conduction band (*CB*) and valence band (*VB*) energy levels of some typical semiconductor-based photocatalytic materials [62]. To date, varieties of photoelectrode materials with UV and visible light activities have been developed and investigated for application in photoelectrocatalytic water disinfection, such as TiO_2, Ag/AgBr/TiO_2, $ZnIn_2S_4$, Cu_2O, and their composites [17–19, 27, 31, 63–66]. The PEC inactivation efficiency is highly dependent on the properties of photoelectrode materials, e.g., structure, light activity, surface area, photoelectron transport property, exposed crystal facets, and stability.

9.3.1 TiO_2-Based Photoelectrocatalytic Bactericidal Materials

Owing to superior physical and chemical properties, TiO_2-based photocatalysts have been the most widely investigated photoelectrode materials for photoelectrocatalysis (PEC) water disinfection [11, 27, 67–71]. A PEC process permits the use of a potential bias as external driving force to rapidly remove the

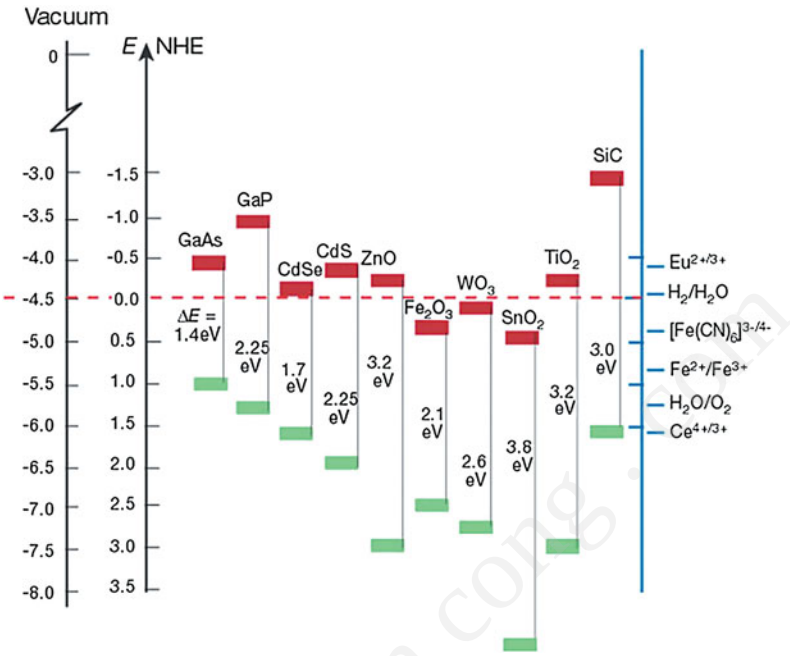

Fig. 9.2 CB and VB energy levels of some typical semiconductor-based photocatalytic materials (Reprinted from Ref. [62] Copyright©2001 Nature Publishing Group)

photoelectrons from TiO_2 conduction band to the external circuit then to the counter electrode where the electrons are consumed by forced reduction reactions [22, 40–46]. Consequently, a high concentration of reactive oxygen species (ROSs) such as $^{\bullet}OH$, $O_2^{\bullet-}$, $HOO^{\bullet}$, and H_2O_2 can be sustained due to the effectively suppressed photoelectrons/holes recombination [27, 29, 30, 68]. The photohole can be a more effective bactericide than that of ROSs due to its strong oxidative power (+3.1 V for anatase TiO_2) (Table 9.1). However, a photocatalysis process solely relies on ROSs to achieve disinfection because the direct photohole reaction could barely occur. In contrast, the ability of a PEC process to rapidly remove photoelectrons and physically separate the reduction half-reactions (at the counter electrode) from the oxidation half-reactions (at the TiO_2 photoanode) prolongs the lifetime of photoholes to enable direct photohole reactions, thus effectively improving bactericidal performance [27, 29, 30, 68].

To date, UV and visible light active TiO_2-based photoelectrodes with different structures have been investigated for water disinfection application [19, 27–30, 63–66, 68, 69, 71, 75, 77–81]. Table 9.2 shows some reported UV and visible light active TiO_2-based materials for PEC water disinfection including photoelectrode fabrication method, type of biohazards, and inactivation performance. In the early days, Matsunaga and co-workers innovatively applied photoelectrochemical approach to inactivate biohazards such as *Lactobacillus acidophilus*, *Saccharomyces cerevisiae*, and *Escherichia coli* (10^3 cells/mL) using TiO_2/Pt photocatalytic

Table 9.2 A brief summarization on some reported UV and visible light active TiO_2-based photoelectrocatalytic bactericidal materials for water disinfection

Photoelectrode	Fabrication method	Type of biohazards	Inactivation performance and light source	References
TiO_2 nanoparticle film	Sol–gel method	*E. coli*	1.57 s, 100 % inactivation, UV	[27]
TiO_2 nanotube array film	Anodization	*E. coli*	97 s, 100 % inactivation, UV	[29]
TiO_2/Ti film	Thermal treatment	*E. coli*	1 h, 100 % inactivation, UV	[72]
TiO_2 nanotube array film	Anodization	*Mycobacteria -contained water*	3 min, 100 % inactivation, UV	[64]
Ti/TiO_2-Ag nanotube film	Anodization and immersion method	*Mycobacterium smegmatis*	3 min, 100 % inactivation, UV	[69]
TiO_2 nanotube array film	Anodization	*E. coli*	0.3 s, 100 % inactivation, UV	[73]
Ag/TiO_2 nanotube array film	Anodization and immersion method	*E. coli and S. aureus*	82.5 and 82.9 % inactivation for E. coli and S. aureus	[74]
TiO_2 film with exposed (111) surface	Hydrothermal method	*E. coli*	10 min, 99.97 % inactivation, UV; 180 min, 100 % inactivation, visible light	[30]
Ag/AgBr/TiO_2 nanotube film	Anodization and photoassisted deposition	*E. coli*	80 min, 100 % inactivation, visible light	[31]
CdS/Pt-TiO_2 nanotube array film	Anodization, electrodeposition, chemical reaction	*E. coli*	60 min, 99.2 % at 0.6 V inactivation, visible light	[65]
Ag/AgCl/TiO_2 nanotube film	Anodization and electrodeposition	*Microcystin-LR*	5 h, 92 % inactivation, visible light	[75]
Self-doped TiO_2 nanotube array film	Anodization and chemical reduction process	*E. coli*	40 min, 100 % inactivation, visible light	[76]
N-doped carbonaceous/TiO_2 composite film	Hydrothermal method	*E. coli*	30 min, 100 % inactivation, visible light	[77]

material, indicating 100 % inactivation performance under metal halide lamp irradiation for 60–120 min [11]. Since then, much efforts have been made to fabricate high-performance TiO_2-based photoelectrodes for photoelectrocatalysis (PEC) water disinfection, such as TiO_2 particle film, TiO_2 nanotube array film, and modified TiO_2 nanostructured film (Table 9.2) [19, 27–30, 63–66, 68, 69, 71, 75, 77–81]. In this respect, our group developed some high-performance TiO_2

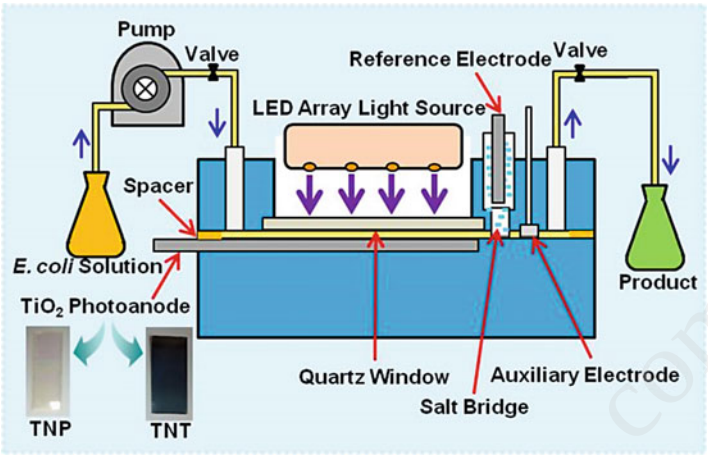

Fig. 9.3 Home-made thin-layer photoelectrochemical flow reactor for photoelectrocatalysis water disinfection (Reprinted from Ref. [29] Copyright©2013 The Royal Society of Chemistry)

photoelectrodes and innovatively used thin-layer photoelectrochemical flow reactor (Fig. 9.3) for PEC water disinfection, exhibiting superior inactivation efficiencies of biohazards [27–30, 68]. This thin-layer photoelectrochemical flow reactor is portable and favorable for improving bactericidal performance and quantitatively studying bactericidal mechanisms. Using anatase TiO_2 nanoparticle film photoelectrode, we developed a PEC-Br bactericidal technique to in situ photoelectrocatalytically generate photoholes (h^+), long-lived dibromide radical anions ($Br_2^{\cdot-}$) and active oxygen species (AOS) under UV irradiation for instant inactivation and rapid decomposition of Gram-negative bacteria such as *Escherichia coli* (*E. coli*) [27]. The results demonstrated that this PEC-Br technique is capable of inactivating 99.90 and 100 % of 9×10^6 CFU/mL *E. coli* within 0.40 and 1.57 s, respectively [27]. To achieve the same inactivation effect, the proposed method is 358 and 199 times faster than that of the photoelectrocatalytic method in the absence of Br^- and 2250 and 764 times faster than that of the photocatalytic method in the absence of Br^-[27]. More importantly, it was found that *E. coli* can be effectively and efficiently decomposed on TiO_2 photoanode film by this PEC-Br technique (Fig. 9.4), further verifying superior PEC activity of the fabricated TiO_2 photoelectrode [27]. The decomposition experimental results obtained from 600 s PEC–Br-treated samples demonstrated that over 90 % of *E. Coli* body mass was decomposed and 42 % biological carbon contents in the sample was completely mineralized and converted into CO_2 [27]. The inactivation/decomposition mechanisms of *E. coli* can be due to a collective contribution of the generated photoholes (h^+), long-lived dibromide radical anions ($Br_2^{\cdot-}$), and active oxygen species (AOS) [27].

Owing to superior photoelectron transport capability of vertically aligned nanotube array structure, TiO_2 nanotube array film photoelectrodes have exhibited high photoelectrocatalytic performance of water disinfection [29, 64, 73–75]. Using

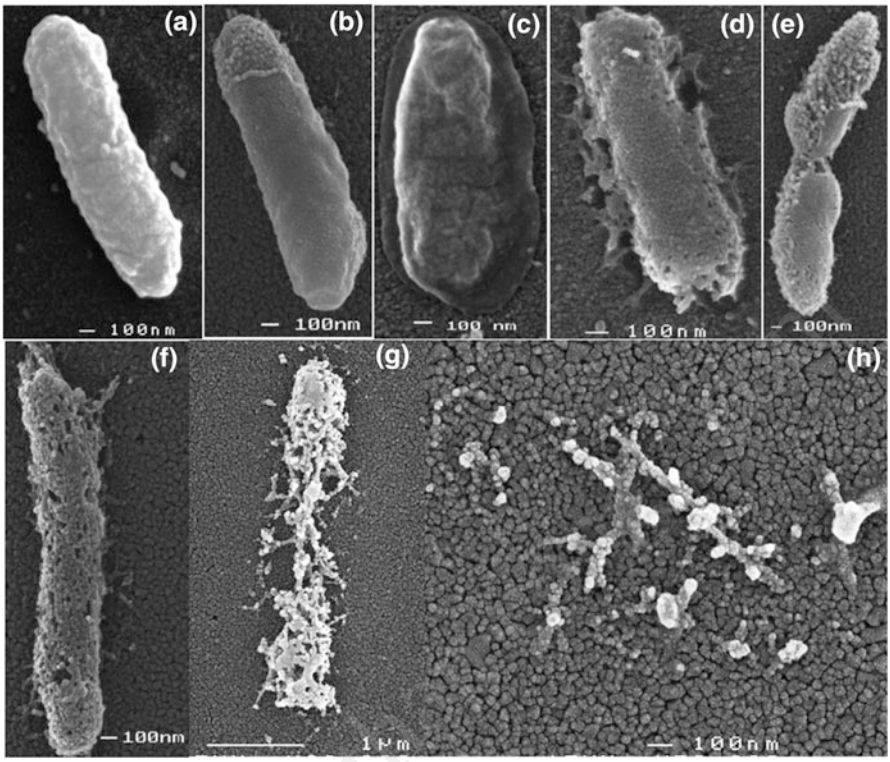

Fig. 9.4 SEM images of *E. coli* cell attached to the TiO_2 photoanode under UV irradiation. (**a**) Without treatment; (**b**) after 900 s of photocatalysis treatment; (**c**) after 60 s of PEC treatment; (**d**) after 300 s of PEC treatment; and (**e**) after 60 s of PEC–Br treatment; (**f**) after 120 s of PEC–Br treatment; (**g**) after 300 s of PEC–Br treatment; (**h**) after 600 s of PEC–Br treatment (Reprinted from Ref. [27] Copyright© 2011 Elsevier)

homemade thin-layer photoelectrochemical flow reactor, we also compared the inactivation performance of *E. coli* using vertically aligned anatase TiO_2 nanotube array film and anatase TiO_2 nanoparticle film photoelectrodes with similar thickness [29]. The experimental results demonstrated that 100 % inactivation of *E. coli* (1.0×10^7 CFU/mL) can be achieved within 97 s using vertically aligned TiO_2 nanotube array film photoelectrode under UV irradiation, which is almost 2.2 times faster than using TiO_2 nanoparticle film photoelectrode with a similar film thickness, as shown in Fig. 9.5 [29]. The excellent bactericidal performance of vertically aligned TiO_2 nanotube array film photoelectrode can be due to the highly photoelectrocatalytic capability of the nanotube structure owing to superior photoelectron transport property to effectively generate active oxygen species (AOS) such as $^{\cdot}OH$, $H_2O^{\cdot}$, $O_2^{\cdot -}$, $HOO^{\cdot}$, and H_2O_2 for *E. coli* inactivation under UV irradiation [29].

TiO_2 nanostructures with exposed high-energy reactive facets have aroused great research interest because of their excellent performance for environmental

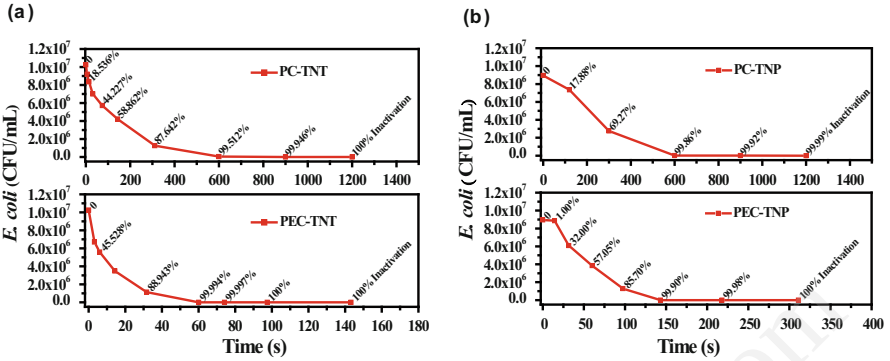

Fig. 9.5 Surviving *E. coli* treated by photocatalysis (PC) and photoelectrocatalysis (PEC) processes against resident time at TiO_2 nanotube film photoelectrode (**a**) and TiO_2 nanoparticle film photoelectrode (**b**) under UV illumination with a light intensity of 8.0 mW/cm^2 and an applied potential bias of +0.7 V (Reprinted from Ref. [29] Copyright©2013 The Royal Society of Chemistry)

remediation and energy applications [82–88]. However, the reports on using high-energy faceted TiO_2 nanostructure photoelectrode for bactericidal applications are few to date. In this respect, we developed a facile hydrothermal method to synthesize 100 % {111} faceted rutile TiO_2 nanostructure photoelectrode for water disinfection (Fig. 9.6A–D) [30]. Importantly, it was found that the fabricated 100 % {111} faceted rutile TiO_2 nanostructure photoelectrode possesses suitable band structure with concurrent UV and visible light photocatalytic activities [30, 46, 89]. The visible light activity of the fabricated rutile TiO_2 photoelectrode with 100 % exposed {111} facets can be due to the presence of Ti^{3+} in the bulk of the rutile TiO_2 film [89–91]. In this work, the first-principle DFT calculations was employed to study the surface energy of the {110} and {111} faceted rutile TiO_2 [46]. The atomic structure of (111) surface used for the calculation was established according to the rutile TiO_2 crystal structure. The calculated surface energies are 0.35 and 1.46 J/m^2 for (110) and (111) surfaces, respectively (Fig. 9.6E) [46]. Our calculation results suggest that the surface energy for {111} faceted rutile TiO_2 is four times greater than that of a commonly obtained {110} faceted rutile TiO_2, which could be an important attribute for the high photocatalytic activity, favorable for improving bactericidal efficiency [46]. For bactericidal application, the experimental results demonstrated that under the UV irradiation, 99.97 % inactivation of 45 mL of 1.0×10^7 CFU/mL *E. coli* cells can be achieved within 10 min for photoelectrocatalysis treatment, while only 96.40 % inactivation can be obtained within 30 min for photocatalysis treatment [30]. Under the visible light irritation, 88.46 % inactivation can be achieved with 180 min photocatalytic treatment, while 100 % inactivation by photoelectrocatalytic treatment can be achieved over the same period [30]. The high bactericidal performance of 100 % {111} faceted rutile TiO_2 nanostructure photoelectrode under UV and visible light irradiation can be due to the highly arrayed structures providing superior photoelectron transport pathways and exposed {111} facets with high reactive energy.

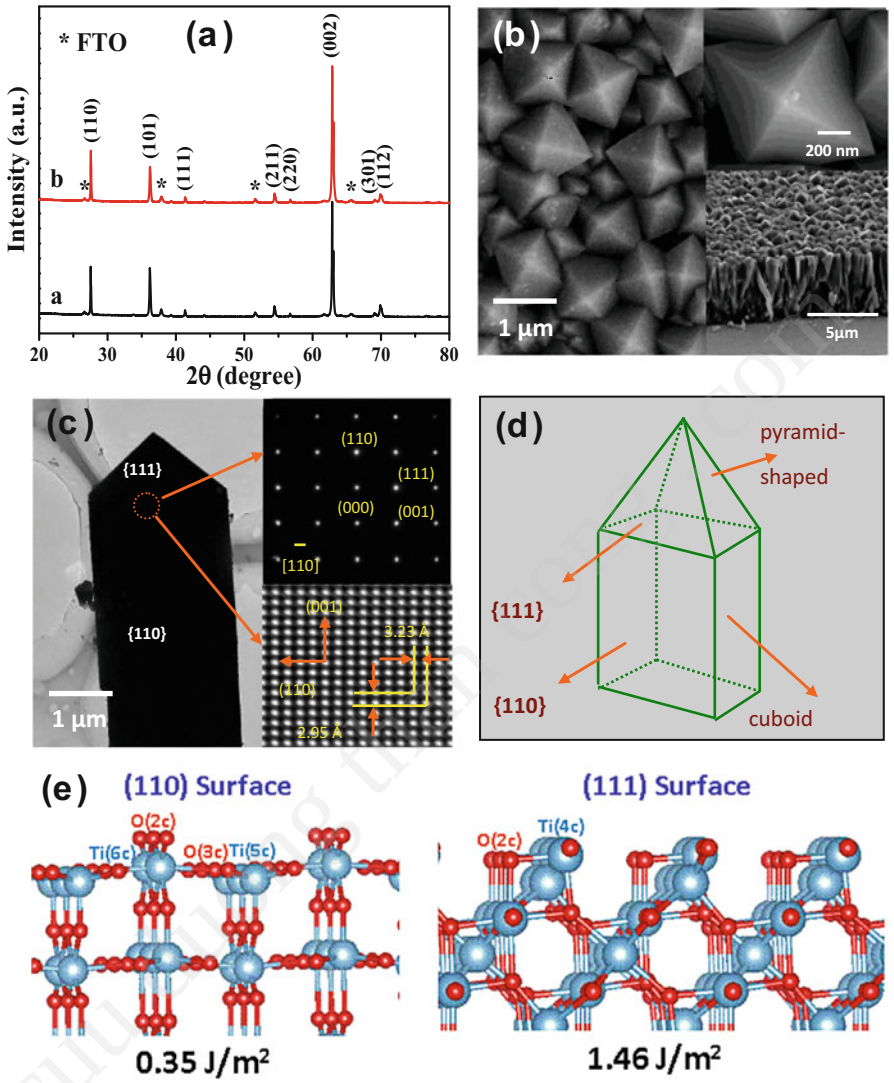

Fig. 9.6 (**a**) XRD patterns of the as-synthesized and calcined product in Ar. (**b**) SEM image of the calcined TiO_2 sample in Ar_2; insets of high-magnification SEM image (*top*) and cross-sectional SEM image (*bottom*). (**c**) TEM image of an individual rod-like structure; insets of SAED pattern (*top*) and HRTEM image (*bottom*). (**d**) Schematic diagram of an individual rod-like structure. (**e**) Atomic structures of rutile TiO_2 (110) and (111) surfaces (Reprinted from Ref. [46] Copyright©2014 The Royal Society of Chemistry)

Although TiO_2 materials possess high photocatalytic/photoelectrocatalytic activities in environmental remediation, its wide bandgap makes TiO_2 only able to use UV light. This greatly limits its practical application using solar energy because UV portion only accounts for ~5 % of the sunlight full spectrum [65].

Therefore, development of visible light active TiO_2 photoelectrode materials is more significant for practical water disinfection application. To date, varieties of visible light active TiO_2-based photoelectrocatalytic materials have been developed for water disinfection applications, such as Ag/AgBr (AgCl)-modified TiO_2 nanotubes, carbon nanotube-modified TiO_2 thin film, and N-doped carbonaceous TiO_2 composite film (Table 9.2). Azimirad and co-workers prepared carbon nanotube (CNT)-modified TiO_2 films with various CNT contents by sol–gel method [19]. The fabricated CNT-modified TiO_2 films exhibited decreased optical bandgap energy from 3.2 to 3.3 to less than ~2.8 eV with increasing CNT content from zero to 40 wt %, and the best visible light inactivation performance of *E. coli* was achieved by using CNT-modified TiO_2 film with 20 wt % CNT content. Also, Oh et al. demonstrated that silver-treated carbon nanotube-modified TiO_2 composite showed high photoelectrocatalytic antibacterial activity against Escherichia coli K-12 under sunlight irradiation [66]. Zhang and co-workers fabricated visible light active Ti^{3+} self-doped TiO_2 nanotube array film by a combination approach of anodization and electrochemical reduction route [76]. Under visible light irradiation, the resulting Ti^{3+} self-doped TiO_2 nanotube array film as photoanode obtained a 100 % inactivation performance toward *E. coli* K-12 within 40 min. In this respect, a visible light active N-doped carbonaceous/TiO_2 composite photoanode was developed by our group through a facile hydrothermal calcination approach using melamine as an N-doped carbonaceous source [77]. The results demonstrated that 10^7 cfu/mL of *E. coli* can be completely inactivated within 30 min by using the composite photoanode obtained from 120 °C hydrothermal treatment at an applied potential bias of +1.0 V and a light intensity of 15 mW/cm^2 under visible light irradiation. The high photoelectrocatalytic bactericidal activity of composite photoanodes under visible light irradiation can be mainly ascribed to the synergistic effect between N-doped carbonaceous and TiO_2 components, benefiting the light adsorption and the effective charge separation. Cai et al. fabricated a ternary hybrid CdS/Pt-TiO_2 nanotube photoelectrode by dipping and deposition technique as well as successive ionic layer adsorption and reaction [65]. Compared with Pt-TiO_2 nanotubes and pure TiO_2 nanotubes, the ternary nanotube photoelectrode displayed higher photoelectrocatalytic bactericidal performance toward *Escherichia coli* under simulated solar light irradiation. Li and co-workers reported the synthesis of a ternary Ag/AgBr/TiO_2 nanotube array photoelectrode with enhanced visible-light activity by a two-step approach including electrochemical process of anodization and an in situ photoassisted deposition strategy [31]. The results revealed that the fabricated TiO_2 nanotubes possessed an average diameter of about 90 nm and the nanotube length around 550 nm (Fig. 9.7A and B). After the photoassisted deposition process, Ag/AgBr nanoparticles with a diameter of *ca.* 20 nm were observed on the nanotube film surface (Fig. 9.7C and D). The fabricated Ag/AgBr/TiO_2 nanotube array photoelectrode possessed superior visible light photoelectrocatalytic activity and exhibited 100 % inactivation of *E. coli* within 80 min under visible light irradiation. Their study suggested oxidative attack from the exterior to the interior of the *Escherichia coli* by $OH^{\cdot}$, $O_2^{\cdot-}$, photoholes, and Br^0, causing the bacterial cell to die as the primary mechanism of photoelectrocatalytic

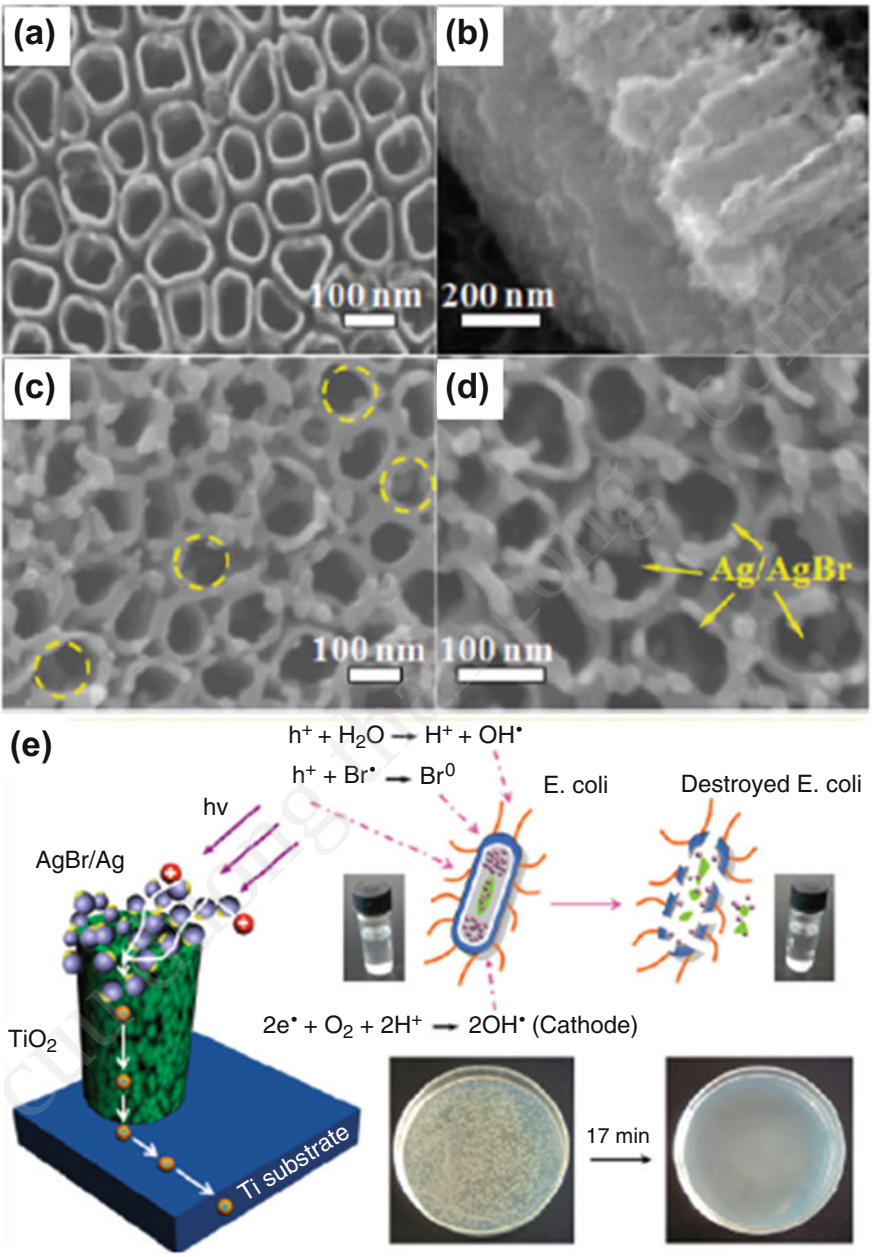

Fig. 9.7 (**a**) Top surface view and (**b**) cross-section view of TiO_2 nanotube array films. (**c**) Top surface view and (**d**) high-magnification top surface view of $Ag/AgBr/TiO_2$ nanotube array films. (**e**) A schematic illustration of photoelectrocatalytically bactericidal mechanism of $Ag/AgBr/TiO_2$ nanotube array photoelectrode (Reprinted from Ref. [31] Copyright©2012 American Chemical Society)

inactivation (Fig. 9.7E). Similarly, Zhang et al. used almost the same fabrication method to synthesize visible light active Ag/AgCl/TiO_2 nanotube array photoelectrode for photoelectrocatalytic degradation of microcystin-LR under visible light irradiation [75], exhibiting excellent photoelectrocatalytic performance. They suggested that the generated photoholes, $OH^{\cdot}$, and $O_2^{\cdot -}$ in the photoelectrocatalytic reaction were responsible for the degradation of microcystin-LR.

9.4 Other Semiconductor-Based Photoelectrocatalytic Materials

To date, most studies on photoelectrocatalytic water disinfection are almost exclusively employed TiO_2-based photocatalytic materials with UV and visible light activities [19, 27–30, 63–66, 68, 69, 71, 75, 77–81], while the reports on using other semiconductor-based photoelectrocatalytic materials are few [17, 18]. In this respect, we firstly reported photoelectrocatalytic inactivation of *Escherichia coli* K-12 by cuprous oxidation (Cu_2O) film photoelectrode under visible light irradiation [18]. Figure 9.8 shows the schematic diagrams of experimental reactors with about 100 mL of volume glass container for photocatalysis (PC) and photoelectrocatalysis (PEC) regulation of *E. coli*. In this work, it was found that the bacterial inactivation efficiency was significantly improved by photoelectrocatalytic technique, in which seven logs of *E. coli* could be completely inactivated within 2 h by using visible light active Cu_2O film photoelectrode at an applied potential bias of 0.1 V. The high bactericidal performance can be due to H_2O_2, photoholes, and toxicity of Cu_2O film responsible for the inactivation of *E. coli*. Although the Cu_2O film photoelectrode exhibited high photoelectrocatalysis inactivation performance, the low photochemical/electrochemical stability of Cu_2O film during bactericidal reaction may be the biggest limitation of this photoelectrocatalytic material for practical water disinfection application. Quan and co-workers synthesized visible light active $ZnIn_2S_4$ nanostructure film onto metal titanium substrate by a two-step approach including electrodeposition and annealing [17]. Their experimental results demonstrated that more than three logs of *E. coli* was inactivated by photocatalytic process within 60 min with the $ZnIn_2S_4$ film under visible light irradiation, while almost 100 % inactivation of *E. coli* was achieved by photoelectrocatalytic process at an applied potential bias of +0.6 V within 60 min of visible light irradiation.

9.5 Conclusions and Outlook

Photoelectrocatalytic technique has been regarded as a good alternative to conventional photocatalysis for effectively improving the photocatalytic efficiency for applications in environmental and energy fields. A key issue is to develop

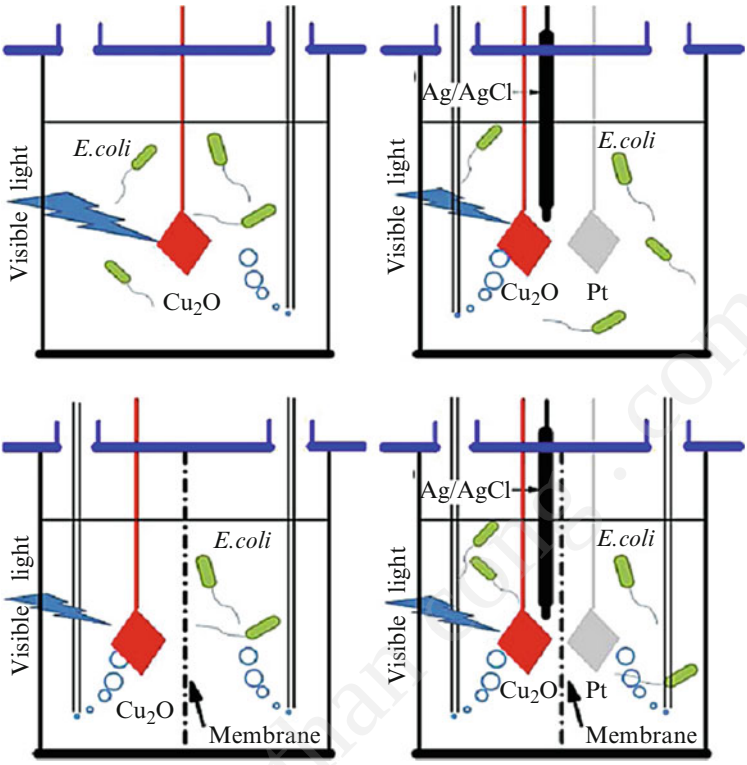

Fig. 9.8 Schematic diagrams of experimental reactors with about 100 mL of volume glass container for photocatalysis (PC) and photoelectrocatalysis (PEC) regulation of *E. coli* (Reprinted from Ref. [18] Copyright©2015 Elsevier)

high-performance photoelectrocatalytic materials for these applications. Although the application of photoelectrocatalytic technique has currently shown successful results at the laboratory scale, the photoelectrocatalytic technique also displays some shortcomings: (1) limited illumination area owing to current electrode fabrication technique or light source dimension, resulting in limited utilization of photocatalyst; (2) introduction of electrochemical technique possibly leading to the instability of photoelectrode materials (some electrochemical reactions may happen); (3) most of photoelectrode materials with UV light activity greatly decreasing sunlight utilization efficiency – thus development of visible light active photoelectrode materials is highly desired. These drawbacks of photoelectrocatalytic technique limit its practical large-scale water disinfection applications. However, the photoelectrocatalytic technique has been demonstrated to be a very effective and reliable means for fundamental study (e.g., photoelectron transport property, dynamic and thermodynamic behaviors in photocatalytic reaction process) [21, 22, 40, 92, 93]. Therefore, photoelectrocatalysis technique can not only effectively improve bactericidal efficiency for water disinfection but also

quantitatively study the bactericidal mechanisms in the process of bacteria inactivation and decomposition. To obtain these purposes, several key scientific issues still remain as a huge challenge and need to be addressed:

1. Developing visible light active photoelectrode materials with high chemical/photochemical/electrochemical stability for improving sunlight utilization efficiency
2. Developing highly ordered nanostructure photoelectrodes, such as nanotubes, nanorods, and nanowires, capable of providing superior electron transport pathways to offset the shortcoming of limited illumination area
3. Coupling photoelectrocatalytic technique with other techniques such as fuel cell and membrane separation to effectively improve water disinfection efficiency
4. Modifying photoelectrode surface by some methods such as molecular imprinting technique to achieve artificially generated functionalized recognition sites for qualitative and quantitative investigation of bactericidal mechanisms
5. Combining theoretical calculations such as frontier electron densities calculations and density functional theory calculations to understand in depth the photoelectrocatalytic inactivation mechanism and guide photoelectrode synthesis
6. Designing suitable photoelectrochemical reactors to meet the needs of high-efficiency and large-scale bactericidal applications

In summary, photoelectrocatalytic techniques have shown great potential for applications in environmental and energy fields (e.g., photoelectrocatalytic water disinfection, photocatalytic generation of hydrogen, and CO_2 reduction to generate fuels). In this chapter, we mainly concentrated on recent progress of semiconductor-based photoelectrocatalytic materials in these aspects of structure, composition, synthetic method, and bactericidal performance. We believe that the related information in this chapter including our perspectives on future opportunities and challenges would be helpful to design and synthesize high-performance photoelectrocatalytic materials and promote a further development of photoelectrocatalytic technique to thus realize its real applications in water disinfection.

References

1. Fujishima A, Honda K (1972) Electrochemical photolysis of water at a semiconductor electrode. Nature 238(5358):37–38
2. Hoffmann MR, Martin ST, Choi W et al (1995) Environmental applications of semiconductor photocatalysis. Chem Rev 95(1):69–96
3. Linsebigler AL, Lu G, Yates JT Jr (1995) Photocatalysis on TiO_2 surfaces: principles, mechanisms, and selected results. Chem Rev 95(3):735–758
4. Wang G, Ling Y, Wang H et al (2014) Chemically modified nanostructures for photoelectrochemical water splitting. J Photochem Photobiol C 19:35–51
5. Neau S, Macia-Agullo Juan A, Garcia H (2014) Solar light photocatalytic CO_2 reduction: general considerations and selected bench-mark photocatalysts. Int J Mol Sci 15(4):5246–5262

6. Habisreutinger SN, Schmidt-Mende L, Stolarczyk JK (2013) Photocatalytic reduction of CO_2 on TiO_2 and other semiconductors. Angew Chem Int Ed 52(29):7372–7408
7. Bingham S, Daoud WA (2011) Recent advances in making nano-sized TiO_2 visible-light active through rare-earth metal doping. J Mater Chem 21(7):2041–2050
8. Xu Y, Langford CH (2001) UV- or visible-light-induced degradation of X3B on TiO_2 nanoparticles: the influence of adsorption. Langmuir 17(3):897–902
9. Pelaez M, Nolan NT, Pillai SC et al (2012) A review on the visible light active titanium dioxide photocatalysts for environmental applications. Appl Catal B Environ 125:331–349
10. Ryan JN, Harvey RW, Metge D et al (2002) Field and laboratory investigations of inactivation of viruses (PRD1 and MS2) attached to iron oxide-coated quartz sand. Environ Sci Technol 36 (11):2403–2413
11. Matsunaga T, Tomoda R, Nakajima T et al (1985) Photoelectrochemical sterilization of microbial cells by semiconductor powders. FEMS Microbiol Lett 29(1–2):211–214
12. Benabbou AK, Derriche Z, Felix C et al (2007) Photocatalytic inactivation of Escherichia coli. Effect of concentration of TiO_2 and microorganism, nature and intensity of UV irradiation. Appl Catal B Environ 76(3–4):257–263
13. Christensen PA, Curtis TP, Egerton TA et al (2003) Photoelectrocatalytic and photocatalytic disinfection of E. coli suspensions by titanium dioxide. Appl Catal B Environ 41(4):371–386
14. Dalrymple OK, Stefanakos E, Trotz MA et al (2010) A review of the mechanisms and modeling of photocatalytic disinfection. Appl Catal B Environ 98(1–2):27–38
15. Malato S, Blanco J, Alarcon DC et al (2007) Photocatalytic decontamination and disinfection of water with solar collectors. Catal Today 122(1–2):137–149
16. Foster HA, Ditta IB, Varghese S et al (2011) Photocatalytic disinfection using titanium dioxide: spectrum and mechanism of antimicrobial activity. Appl Microbiol Biotechnol 90 (6):1847–1868
17. Yu HT, Quan X, Zhang YN et al (2008) Electrochemically assisted photocatalytic inactivation of Escherichia coli under visible light using a ZnIn(2)S(4) film electrode. Langmuir 24 (14):7599–7604
18. Xiong LB, Ng TW, Yu Y et al (2015) N-type Cu_2O film for photocatalytic and photoelectrocatalytic processes: its stability and inactivation of E-coli. Electrochim Acta 153:583–593
19. Akhavan O, Azimirad R, Safa S et al (2010) Visible light photo-induced antibacterial activity of CNT-doped TiO_2 thin films with various CNT contents. J Mater Chem 20(35):7386–7392
20. Zhao H, Jiang D, Zhang S et al (2004) Development of a direct photoelectrochemical method for determination of chemical oxygen demand. Anal Chem 76(1):155–160
21. Zhao H, Jiang D, Zhang S et al (2007) Photoelectrocatalytic oxidation of organic compounds at nanoporous TiO_2 electrodes in a thin-layer photoelectrochemical cell. J Catal 250(1):102–109
22. Jiang D, Zhao H, Zhang S et al (2003) Characterization of photoelectrocatalytic processes at nanoporous TiO_2 film electrodes: photocatalytic oxidation of glucose. J Phys Chem B 107 (46):12774–12780
23. Chong MN, Jin B, Chow CWK et al (2010) Recent developments in photocatalytic water treatment technology. A review. Water Res 44(10):2997–3027
24. Okpara CG, Oparaku NF, Ibeto CN (2011) An overview of water disinfection in developing countries and potentials of renewable energy. J Environ Sci Technol 4(1):18–30
25. Anthony Byrne J, Fernandez-Ibanez PA, Dunlop PSM et al (2011) Photocatalytic enhancement for solar disinfection of water: a review. Int J Photoenergy 798051:1–12
26. Ibhadon AO, Fitzpatrick P (2013) Heterogeneous photocatalysis: recent advances and applications. Catalysts 3(1):189–218
27. Li G, Liu X, Zhang H et al (2011) In situ photoelectrocatalytic generation of bactericide for instant inactivation and rapid decomposition of Gram-negative bacteria. J Catal 277(1):88–94
28. Li G, Liu X, Zhang H et al (2014) Adenovirus inactivation by in situ photocatalytically and photoelectrocatalytically generated halogen viricides. Chem Eng J 253:538–543
29. Liu X, Han Y, Li G et al (2013) Instant inactivation and rapid decomposition of Escherichia coli using a high efficiency TiO_2 nanotube array photoelectrode. RSC Adv 3(43):20824–20828

30. Liu X, Zhang H, Liu C et al (2014) UV and visible light photoelectrocatalytic bactericidal performance of 100% {111} faceted rutile TiO_2 photoanode. Catal Today 224:77–82
31. Hou Y, Li X, Zhao Q et al (2012) Role of hydroxyl radicals and mechanism of Escherichia coli inactivation on Ag/AgBr/TiO_2 nanotube array electrode under visible light irradiation. Environ Sci Technol 46(7):4042–4050
32. Shi H, Li G, Sun H et al (2014) Visible-light-driven photocatalytic inactivation of E. coli by Ag/AgX-CNTs (X = Cl, Br, I) plasmonic photocatalysts: bacterial performance and deactivation mechanism. Appl Catal B Environ 158–159:301–307
33. Wang H, Zhang L, Chen Z et al (2014) Semiconductor heterojunction photocatalysts: design, construction, and photocatalytic performances. Chem Soc Rev 43(15):5234–5244
34. Yang J, Wang D, Han H et al (2013) Roles of cocatalysts in photocatalysis and photoelectrocatalysis. Acc Chem Res 46(8):1900–1909
35. Daghrir R, Drogui P, Robert D (2012) Photoelectrocatalytic technologies for environmental applications. J Photochem Photobiol A 238:41–52
36. Ochiai T, Fujishima A (2012) Photoelectrochemical properties of TiO_2 photocatalyst and its applications for environmental purification. J Photochem Photobiol C 13(4):247–262
37. Sires I, Brillas E (2012) Remediation of water pollution caused by pharmaceutical residues based on electrochemical separation and degradation technologies- a review. Environ Int 40:212–229
38. Zhang H, Chen G, Bahnemann DW (2009) Photoelectrocatalytic materials for environmental applications. J Mater Chem 19(29):5089–5121
39. Zhang Y, Xiong X, Han Y et al (2012) Photoelectrocatalytic degradation of recalcitrant organic pollutants using TiO_2 film electrodes: an overview. Chemosphere 88(2):145–154
40. Jiang D, Zhao H, Zhang S et al (2004) Kinetic study of photocatalytic oxidation of adsorbed carboxylic acids at TiO_2 porous films by photoelectrolysis. J Catal 223(1):212–220
41. Jiang D, Zhao H, Zhang S et al (2003) Photoelectrochemical measurement of phthalic acid adsorption on porous TiO2 film electrodes. J Photochem Photobiol A 156(1–3):201–206
42. Jiang D, Zhao H, Zhang S et al (2006) Comparison of photocatalytic degradation kinetic characteristics of different organic compounds at anatase TiO_2 nanoporous film electrodes. J Photochem Photobiol A 177(2–3):253–260
43. Jiang D, Zhang S, Zhao H (2007) Photocatalytic degradation characteristics of different organic compounds at TiO_2 nanoporous film electrodes with mixed anatase/rutile phases. Environ Sci Technol 41(1):303–308
44. Zhang S, Jiang D, Zhao H (2006) Development of chemical oxygen demand on-line monitoring system based on a photoelectrochemical degradation principle. Environ Sci Technol 40 (7):2363–2368
45. Zhang H, Zhao H, Zhang S et al (2008) Photoelectrochemical manifestation of photoelectron transport properties of vertically aligned nanotubular TiO_2 photoanodes. ChemPhysChem 9 (1):117–123
46. Zhang H, Liu X, Wang Y et al (2013) Rutile TiO_2 films with 100% exposed pyramid-shaped (111) surface: photoelectron transport properties under UV and visible light irradiation. J Mater Chem A 1(7):2646–2652
47. Elahifard MR, Rahimnejad S, Haghighi S et al (2007) Apatite-coated Ag/AgBr/TiO_2 visible-light photocatalyst for destruction of bacteria. J Am Chem Soc 129(31):9552–9553
48. Lu Z-X, Zhou L, Zhang Z-L et al (2003) Cell damage induced by photocatalysis of TiO_2 thin films. Langmuir 19(21):8765–8768
49. Cho M, Chung H, Choi W et al (2004) Linear correlation between inactivation of E. coli and OH radical concentration in TiO_2 photocatalytic disinfection. Water Res 38(4):1069–1077
50. Sunada K, Watanabe T, Hashimoto K (2003) Bactericidal activity of copper-deposited TiO_2 thin film under weak UV light illumination. Environ Sci Technol 37(20):4785–4789
51. Maness P-C, Smolinski S, Blake DM et al (1999) Bactericidal activity of photocatalytic TiO_2 reaction: toward an understanding of its killing mechanism. Appl Environ Microbiol 65 (9):4094–4098

52. Colmenares JC, Luque R (2014) Heterogeneous photocatalytic nanomaterials: prospects and challenges in selective transformations of biomass-derived compounds. Chem Soc Rev 43 (3):765–778
53. Kerc A, Bekbolet M, Saatci AM (2003) Effect of partial oxidation by ozonation on the photocatalytic degradation of humic acids. Int J Photoenergy 5(2):75–80
54. Peternel I, Grcic I, Koprivanac N (2010) Degradation of reactive azo dye by UV/peroxodisulfate system: an experimental design approach. React Kinet Mech Catal 100 (1):33–44
55. Chen G (2004) Electrochemical technologies in wastewater treatment. Sep Purif Technol 38 (1):11–41
56. Martinez-Huitle CA, Andrade LS (2011) Electrocatalysis in wastewater treatment: recent mechanism advances. Quim Nova 34(5):850–858
57. Jiang Y, Luo Y, Lu Z et al (2014) Influence of inorganic ions and pH on the photodegradation of 1-methylimidazole-2- thiol with TiO2 photocatalyst based on magnetic multi-walled carbon nanotubes. Bull Kor Chem Soc 35(1):76–82
58. Lu X, Xie S, Yang H et al (2014) Photoelectrochemical hydrogen production from biomass derivatives and water. Chem Soc Rev 43(22):7581–7593
59. Egerton TA, Christensen PA, Kosa SAM et al (2006) Photoelectrocatalysis by titanium dioxide for water treatment. Int J Environ Pollut 27(1-3):2–19
60. Zhang Q, Xu H, Yan W (2012) Highly ordered TiO_2 nanotube arrays: recent advances in fabrication and environmental applications-a review. Nanosci Nanotechnol Lett 4(5):505–519
61. Lewerenz HJ, Heine C, Skorupska K et al (2010) Photoelectrocatalysis: principles, nanoemitter applications and routes to bio-inspired systems. Energy Environ Sci 3(6):748–760
62. Gratzel M (2001) Photoelectrochemical cells. Nature 414(6861):338–344
63. Philippidis N, Nikolakaki E, Sotiropoulos S et al (2009) Photoelectrocatalytic inactivation of E. coli XL-1 blue colonies in water. J Chem Technol Biotechnol 85(8):1054–1060
64. Brugnera MF, Miyata M, Zocolo GJ et al (2014) Ti/TiO_2 nanotubes enhance Mycobacterium fortuitum, Mycobacterium chelonae and Mycobacterium abscessus inactivation in water. J Chem Technol Biotechnol 89(11):1686–1696
65. Kang Q, Lu QZ, Liu SH et al (2010) A ternary hybrid CdS/Pt-TiO_2 nanotube structure for photoelectrocatalytic bactericidal effects on Escherichia Coli. Biomaterials 31(12):3317–3326
66. Zhang F-J, Chen M-L, Oh W-C (2011) Photoelectrocatalytic properties and bactericidal activities of silver-treated carbon nanotube/titania composites. Compos Sci Technol 71 (5):658–665
67. Egerton TA, Christensen PA (2004) Photoelectrocatalysis processes. In: Advanced oxidation processes for water wastewater treatment. IWA, London, pp 167–184
68. Li G, Liu X, Zhang H et al (2013) Comparative studies of photocatalytic and photoelectrocatalytic inactivation of E. coli in presence of halides. Appl Catal B Environ 140–141:225–232
69. Brugnera MF, Miyata M, Zocolo GJ et al (2012) Inactivation and disposal of by-products from Mycobacterium smegmatis by photoelectrocatalytic oxidation using Ti/TiO_2-Ag nanotube electrodes. Electrochim Acta 85:33–41
70. Venieri D, Chatzisymeon E, Politi E et al (2013) Photoelectrocatalytic disinfection of water and wastewater: performance evaluation by qPCR and culture techniques. J Water Health 11 (1):21–29
71. Baram N, Starosvetsky D, Starosvetsky J et al (2009) Enhanced inactivation of E. coli bacteria using immobilized porous TiO_2 photoelectrocatalysis. Electrochim Acta 54(12):3381–3386
72. Philippidis N, Nikolakaki E, Sotiropoulos S et al (2010) Photoelectrocatalytic inactivation of E. coli XL-1 blue colonies in water. J Chem Technol Biotechnol 85(8):1054–1060
73. Nie X, Li G, Gao M et al (2014) Comparative study on the photoelectrocatalytic inactivation of Escherichia coli K-12 and its mutant Escherichia coli BW25113 using TiO_2 nanotubes as a photoanode. Appl Catal B Environ 147:562–570
74. Zhao C, Feng B, Li Y et al (2013) Preparation and antibacterial activity of titanium nanotubes loaded with Ag nanoparticles in the dark and under the UV light. Appl Surf Sci 280:8–14

75. Liao W, Zhang Y, Zhang M et al (2013) Photoelectrocatalytic degradation of microcystin-LR using Ag/AgCl/TiO_2 nanotube arrays electrode under visible light irradiation. Chem Eng J 231:455–463
76. Liao W, Yang J, Zhou H et al (2014) Electrochemically self-doped TiO_2 nanotube arrays for efficient visible light photoelectrocatalytic degradation of contaminants. Electrochim Acta 136:310–317
77. Nie X, Li G, Wong P-K et al (2014) Synthesis and characterization of N-doped carbonaceous/TiO_2 composite photoanodes for visible-light photoelectrocatalytic inactivation of Escherichia coli K-12. Catal Today 230:67–73
78. Brugnera MF, Miyata M, Zocolo GJ et al (2013) A photoelectrocatalytic process that disinfects water contaminated with Mycobacterium kansasii and Mycobacterium avium. Water Res 47 (17):6596–6605
79. Cho M, Cates EL, Kim J-H (2011) Inactivation and surface interactions of MS-2 bacteriophage in a TiO_2 photoelectrocatalytic reactor. Water Res 45(5):2104–2110
80. Li GY, An TC, Nie XP et al (2007) Mutagenicity assessment of produced water during photoelectrocatalytic degradation. Environ Toxicol Chem 26(3):416–423
81. Rahmawati F, Kusumaningsih T, Hastuti A (2011) Photo- and electro-catalysis for solar disinfection of Escherichia coli-contaminated water using Ag-TiO_2/graphite. Toxicol Environ Chem 93(8):1602–1612
82. Yang HG, Sun CH, Qiao SZ et al (2008) Anatase TiO_2 single crystals with a large percentage of reactive facets. Nature 453(7195):638–641
83. Yang HG, Liu G, Qiao SZ et al (2009) Solvothermal synthesis and photoreactivity of anatase TiO_2 nanosheets with dominant {001} facets. J Am Chem Soc 131(11):4078–4083
84. Liu G, Yang HG, Pan J et al (2014) Titanium dioxide crystals with tailored facets. Chem Rev 114(19):9559–9612
85. Liu B, Aydil ES (2011) Anatase TiO_2 films with reactive {001} facets on transparent conductive substrate. Chem Commun 47(33):9507–9509
86. Zhang H, Han Y, Liu X et al (2010) Anatase TiO(2) microspheres with exposed mirror-like plane {001} facets for high performance dye-sensitized solar cells (DSSCs). Chem Commun (Camb) 46(44):8395–8397
87. Zhang H, Liu P, Li F et al (2011) Facile fabrication of anatase TiO_2 microspheres on solid substrates and surface crystal facet transformation from 001 to 101. Chem Eur J 17 (21):5949–5957
88. Zhang H, Wang Y, Liu P et al (2011) Anatase TiO_2 crystal facet growth: mechanistic role of hydrofluoric acid and photoelectrocatalytic activity. ACS Appl Mater Interfaces 3 (7):2472–2478
89. Liu X, Zhang H, Yao X et al (2012) Visible light active pure rutile TiO_2 photoanode with 100% exposed pyramid-shaped (111) surface. Nano Res 5(11):762–769
90. Zuo F, Bozhilov K, Dillon RJ et al (2012) Active facets on Titanium(III)-doped TiO_2: an effective strategy to improve the visible-light photocatalytic activity. Angew Chem Int Ed 124 (25):6327–6330
91. Zuo F, Wang L, Wu T et al (2010) Self-doped Ti^{3+} enhanced photocatalyst for hydrogen production under visible light. J Am Chem Soc 132(34):11856–11857
92. Wen W, Zhao H, Zhang S et al (2008) Rapid photoelectrochemical method for in situ determination of effective diffusion coefficient of organic compounds. J Phys Chem C 112 (10):3875–3880
93. Zhang S, Wen W, Zhang H et al (2009) In situ photoelectrochemical measurement of phthalic acid on titania. J Photochem Photobiol A 208(2–3):97–103

Chapter 10
Photocatalytic and Photoelectrocatalytic Inactivation Mechanism of Biohazards

Guiying Li, Huijun Zhao, and Taicheng An

Abstract Biohazards are widely present in wastewater, and contaminated water can lead to disease. Consequently, effectively removing biohazards from water is a worldwide need. Advanced oxidation processes (AOPs), based on TiO_2 photocatalysis, have effectively degraded a wide spectrum of organics and inactivated biohazards. Photoelectrochemical technology with an anode bias has recently emerged in the research as an alternative tool for photocatalytic inactivation of biohazards. The applied cell voltage can greatly accelerate separation and suppresses the recombination of photogenerated electrons and holes, enabling direct holes attack reactions. This chapter provides an overview of current research activities that focus on using TiO_2 photocatalysis and photoelectrocatalysis AOPs to remove biohazards and inactivate microorganisms. To understand the full spectrum of inactivation mechanisms of living microorganisms, the chapter uses a bottom-up strategy to review the decomposition of a series of biological contaminants, ranging from small biological compounds, to large biological compounds, to living biohazards. The chapter concludes by discussing the advancements needed to advance our understanding of the photocatalytic and photoelectrocatalytic decomposition of biohazards and the inactivation mechanism of microorganisms.

G. Li
Institute of Environmental Health and Pollution Control, School of Environmental Science and Engineering, Guangdong University of Technology, Guangzhou 510006, Guangdong, China

Centre for Clean Environment and Energy, Griffith University, Gold Coast Campus, Gold Coast QLD 4222, Australia
e-mail: ligy1999@gdut.edu.cn

H. Zhao
Centre for Clean Environment and Energy, Griffith University, Gold Coast Campus, Gold Coast QLD 4222, Australia
e-mail: h.zhao@griffith.edu.au

T. An (✉)
Institute of Environmental Health and Pollution Control, School of Environmental Science and Engineering, Guangdong University of Technology, Guangzhou 510006, Guangdong, China

State Key Laboratory of Organic Geochemistry, Guangzhou Institute of Geochemistry, Chinese Academy of Sciences, Guangzhou 510640, China
e-mail: antc99@gdut.edu.cn; antc99@gig.ac.cn

T. An et al. (eds.), *Advances in Photocatalytic Disinfection*, Green Chemistry and Sustainable Technology, DOI 10.1007/978-3-662-53496-0_10

Keywords Photocatalysis • Photoelectrocatalysis • Biohazards • Inactivation • Mechanism • Kinetics

10.1 Introduction

Biohazards, such as bacteria and viruses, are widely present in wastewater; contaminated water can lead to diseases [1–3]. Proper treatment and delivery of safe water is one of the best ways to reduce infections caused by waterborne biohazards. Disinfecting water and wastewater is a prime method to prevent waterborne diseases from spreading and to make the water safe for human beings and the environment. However, many conventional disinfection methods have limitations. For example, potential carcinogenic by-products may be produced by the chlorination process [4–6], and some pathogens, particularly some viruses, are naturally resistant to ultraviolet (UV) and chlorination treatment [7, 8]. As such, novel technologies like advanced oxidation processes (AOPs) can provide a new method to solve these problems.

AOPs based on TiO_2 photocatalysis are highly effective in inactivating bacteria [9–14]. Therefore, this chapter focuses on the photocatalytic (PC) inactivation of biohazards on the TiO_2 photocatalyst surface. Although the mechanisms leading to the degradation or killing are debated, it is generally accepted that the attack on the target is done by the photocatalytically generated superior oxidative power holes and other resulting reactive oxygen species (ROSs), such as $^{\bullet}OH$, $O_2^{\bullet -}$, $HOO^{\bullet}$, and H_2O_2 (Fig. 10.1) [15–17]. However, the current photocatalytic bactericidal method using TiO_2 normally requires 1–6 h to fully inactivate a bacteria population greater than 10^6 colony-forming units per mL (cfu mL^{-1}) [10, 18–20].

The slow bacteria inactivation may be attributed to the rapid recombination of photocatalytically generated holes and electrons, resulting in insufficient ROS's in situ production concentrations. Two possible approaches may enhance TiO_2-based bactericidal efficiency. One approach is to remove the photogenerated electrons and

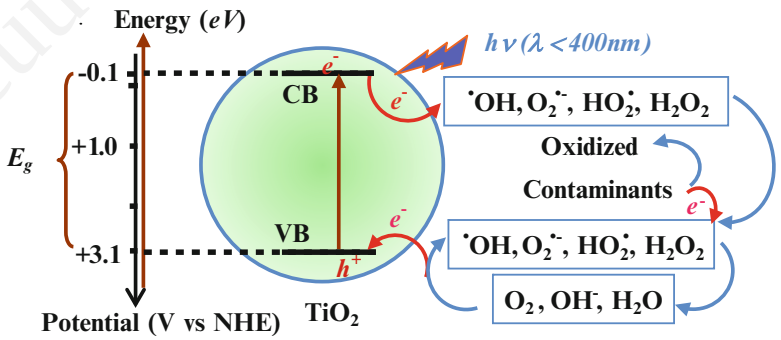

Fig. 10.1 Schematic representation of the photocatalytic processes taking place at a TiO_2 photocatalyst surface (*CB* conduction band, *VB* valence band)

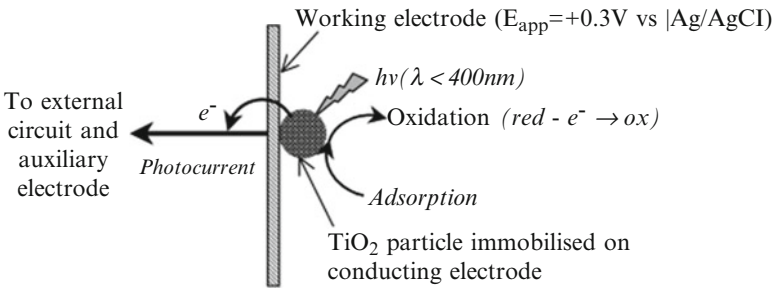

Fig. 10.2 Schematic representation of the photoelectrocatalytic processes taking place at a TiO_2 thin-film electrode [21] (Reprinted with permission from *Analytical Chemistry*, 2004, 76: 155–160. Copyright © 2004 American Chemical Society)

physical separation of holes (h^+) and electrons using an applied potential bias (photoelectrocatalytic (PEC) process) (Fig. 10.2) [21–23]. This bias prolongs the lifetime of h^+, enabling direct h^+ attack reactions [23, 24]. Previous studies have successfully used the PEC method to inactivate bacteria and viruses [25–30]. Another way is to use the photocatalytic oxidation power of the illuminated TiO_2 to generate different types of highly stable bactericidal species that can sustain high concentrations. Studies show that halogen radicals are effective bactericides and can be readily produced by the photocatalytic oxidation of halide ions with illuminated TiO_2 [31]. The photocatalytic production of high concentrations of halogen radicals is possible because these radicals can form stable dihalide radical anions ($X_2^{\bullet -}$) in the presence of X^- (X: Br, Cl) [32, 33].

Living biohazards are composed of various large biological compounds (building blocks of biohazards), and these large biological compounds are composed of small biological compounds (basic building blocks of large biological compounds). Inactivating and decomposing biohazards may involve multiple steps: biohazards may be broken into large biological compounds, then into small biological compounds, and then mineralized into CO_2 and H_2O. Therefore, this chapter uses a bottom-up strategy to describe the inactivation mechanisms of biohazards, including the PC and PEC inactivation of biohazards and the PC and PEC degradation of the associated biological compounds.

10.2 Photocatalysis and Photoelectrocatalysis

10.2.1 Degradation of Small Biological Compounds

Small biological compounds are the basic building blocks of large biological compounds. For example, nucleosides (adenosine, thymidine, cytidine, guanosine, and uridine) make up nucleic acids, such as deoxyribonucleic acid (DNA) and

ribonucleic acid (RNA). Nucleosides consist of nucleotide bases and a 5-carbon sugar (either ribose or deoxyribose). Purine and pyrimidine are two essential classes of nucleotide bases. Alongside nucleic acids, proteins (including enzymes) are another important building block of living microorganisms. The basic building blocks of proteins are amino acids with combining the acidic (–COOH) and basic ($–NH_2$) functional groups together.

These basic building blocks exist in natural biological species and as environmental pollutants. For example, uridine is a versatile therapeutic agent for patients with diseases such as hereditary orotic aciduria, liver dysfunction, and cystic fibrosis [34, 35]. Nucleotide bases may result from the degradation of insecticides, biological species, and antibiotics [36–39]. Amino acids are also present in industrial effluents, such as cosmetics, pharmaceuticals, and foods [40, 41]. As such, studying the PC and PEC degradation of small biomolecules can help us simplify and better understand the PC and PEC inactivation of biohazards and also understand their fate and degradation patterns in aquatic environments.

For these small biological compounds with known chemical formulas, the extent of mineralization is determined by measuring the charge originating from their photocatalytic oxidation using the PeCOD^{TM} technique [21, 42]. Figure 10.3a, b illustrates the quantification methods of the net charges (Q_{net} or $Q_{\Delta net}$), originating from the PEC and PC degradation of small biological compounds, respectively [43]. In PC or PEC degradation processes, the nitrogen atoms in organics are converted to NH_3/NH_4^+ or NO_3^- or both [44]. Mineralization percentages are calculated by assigning the measured charge transfer to the mineralization products, with organic nitrogen being fully converted to NH_3/NH_4^+ or NO_3^-. The number of electron transfers required to mineralize the organic nitrogen to NH_3/NH_4^+ (n_{NH_3/NH_4^+}) for the following four representative nucleotide bases is 10 for uracil, 16 for

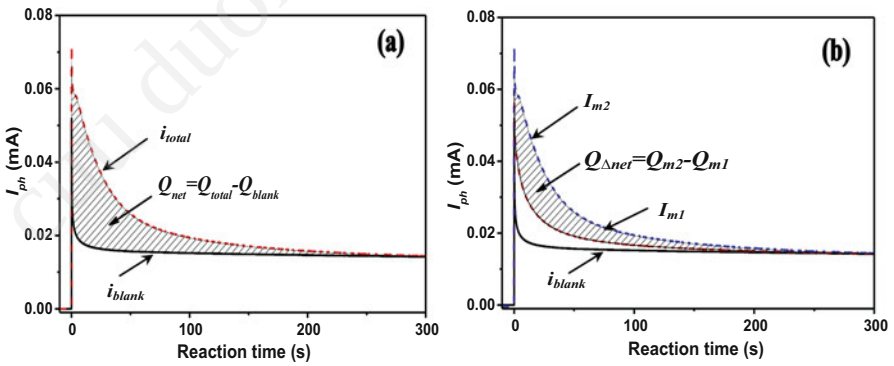

Fig. 10.3 Schematic illustration of charge quantification using a set of typical photocurrent profiles of the TiO_2 photoanode in the photoelectrochemical reactor of PEC (**a**) and PC (**b**) degradation of organics [43]. (i_{blank}, photocurrent is attributed to PEC or PC oxidation of water; i_{total}, photocurrent is attributed to PEC oxidation of both water and organics; i_{m1} and i_{m2}, represent the photocurrent profiles of the same sample solution before and after PC treatment) (Reprinted with permission from *Catalysis Today*, 2015, 245: 46–53. Copyright © 2014 Elsevier B.V)

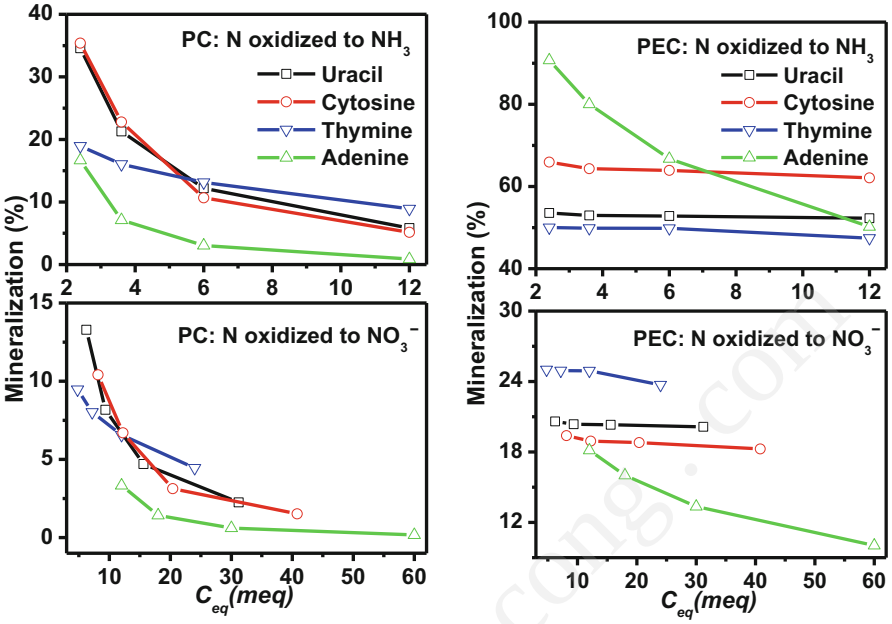

Fig. 10.4 Photocatalytic (PC) and photoelectrocatalytic (PEC) degradation of uracil, cytosine, thymine, and adenine [45] (Reprinted with permission from *Catalysis Today*, 2015, 242: 363–371. Copyright © 2014 Elsevier B.V)

thymine, 10 for cytosine, and 10 for adenine; the number of transfers required to mineralize the nitrogen of nucleotide bases to NO_3^- ($n_{NO_3^-}$) is 26 for uracil, 32 for thymine, 34 for cytosine, and 50 for adenine. These numbers demonstrate that the mineralization extent of nucleotide bases is strongly affected by the final mineralization products of organic nitrogen. This is because the electron transfer numbers required to convert the organic nitrogen to NH_3/NH_4^+ and NO_3^- are different for different nucleotide bases [44].

For the PC degradation of all four representative nucleotide bases (Fig. 10.4), an increase in C_{eq} (electron concentration: $C_{eq} = n_{NH_3/HN_4^+} \cdot C_M$; $C_{eq} = n_{NO_3^-} \cdot C_M$, where C_M is the molar concentration of nucleotide bases) leads to a decrease in the mineralization percentage for the conversion to both NH_3/NH_4^+ and NO_3^-. Furthermore, except for thymine, mineralization decreases rapidly as C_{eq} increases within the low concentration range of all bases. Thymine exhibits a lower extent of PC mineralization (conversion to NH_3/NH_4^+ and NO_3^-) at lower concentrations but higher mineralization at higher concentrations than the other two pyrimidines. The effects of C_{eq} on the mineralization of cytosine and uracil are very similar. In addition, the mineralization percentages of the double-ringed purine (adenine) are lower than the single-ringed pyrimidine (uracil, cytosine, and thymine) within the concentration range tested.

In comparison to PC, the extent of PEC mineralization of pyrimidine is not greatly affected by concentration (Fig. 10.4), while the mineralization of purine

decreases as C_{eq} increases. The mineralization of PEC-treated samples is much higher than that of PC, indicating a higher PEC capability. The mineralization of the organic nitrogen of adenine is higher than that with pyrimidine, when converted to NH_3/NH_4^+ within the lower concentration range. The mineralization of organic nitrogen of thymine to NH_3/NH_4^+ is lower than that of adenine within the entire concentration range tested. When converting to NH_3/NH_4^+ at lower concentration, the mineralization percentages are, from highest to lowest, adenine, cytosine, uracil, and thymine. However, when converting to NO_3^-, the order is reversed. Herewith, the percentages are highest for thymine, then uracil, then cytosine, and then adenine within the investigated concentration range. Furthermore, the electron transfer number ratio ($n_{NH_3/NH_4^+}/n_{NO_3}-$) follows this order: thymine (0.500) is greater than uracil (0.385), which is greater than cytosine (0.294), which is greater than adenine (0.200). This is in the same order for mineralization during NO_3^- conversion but is in the reverse order for NH_3/NH_4^+ conversion. This means that the ratio of carbon to nitrogen and their oxidation states in bases determines the extent of PEC mineralization. These characteristics are distinctively different from those of PC-treated samples.

The different degradation efficiencies between PC and PEC processes may be attributed to differences in the degradation mechanism. The high-performance liquid chromatography chromatograms of PC- and PEC-treated single-ringed pyrimidine (thymine) and double-ringed purine (adenine) samples show the difference (Fig. 10.5). With PC treatment, there are more hydrophilic intermediates than original bases in the mixture of samples for all pyrimidines tested (thymine, cytosine, and uracil); hydrophilic and hydrophobic intermediates are the major intermediates for the double-ringed purine (adenine) base. The results are completely different during the PEC process. That is, there are more hydrophobic products than original single-ringed pyrimidine in the sample mixture; more hydrophilic intermediates dominate the PEC-treated purine samples [45].

These differences can be explained as followed that when TiO_2 nanoparticles are illuminated by UV light, the photoinduced e^- and h^+ could be created. These h^+ can further react with hydroxyl ions or water to form active oxidative radicals, including $^{\bullet}OH$ [15]. During the PC degradation process, active $^{\bullet}OH$ are mainly involved in indirect addition/substitution reactions [46]; the direct h^+ attack is more likely to occur during PEC rather than PC degradation processes [21]. According to frontier electron densities (FEDs) calculations, the predicted favorable initial reaction sites induced by h^+ and $^{\bullet}OH$ differ from each other [45]. This may point to a mechanistic pathway difference between PC and PEC processes.

The PC and PEC degradation of amino acids, another group of small biological compounds, are also systematically investigated. Similar to the nucleotide bases, amino acids are photocatalytically and photoelectrocatalytically degradable. PEC degradation efficiencies were higher than PC degradation efficiencies for all studied amino acids, with PEC superiority more obvious at higher concentrations. For PC or PEC treatment, the hydrophilic characteristics of the produced intermediates depend on the type of amino acids involved; for a given amino acid, the intermediates are differently hydrophilic during PC and PEC treatments. Theoretical

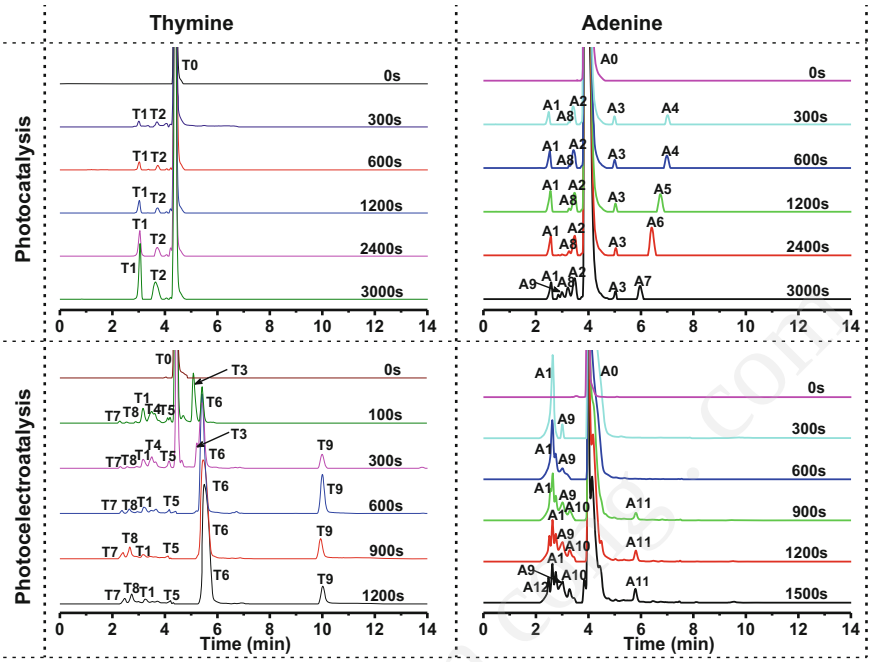

Fig. 10.5 The chromatograms obtained for PC- and PEC-treated thymine and adenine samples at different reaction intervals under 8.0 mW/cm^2 UV intensity. Initial concentration, 12 meq (N oxidized to NH_3); applied potential bias for PEC, +0.40 V *vs*. Ag/AgCl [45] (Reprinted with permission from *Catalysis Today*, 2015, 242: 363–371. Copyright © 2014 Elsevier B.V)

calculations reveal that the initial attack reaction sites may differ for the direct h^+ attack in the PEC process, compared with the $^{\bullet}OH$ attack in the PC process. For tyrosine and phenylalanine, which are single-ringed amino acids, the initial reaction likely occurs on the atoms within the 6-membered ring structure during both treatment processes. For tryptophan, which is a double-ringed amino acid, the initial reaction site likely occurs at the 6-membered ring structure (PC process) or 5-membered ring structure (PEC process). Theoretical calculations and experimental results align, suggesting that the mechanism of the PEC process differs from the PC process [43].

10.2.2 Degradation of Large Biological Compounds

Large biological compounds are the building blocks of living microorganisms. Studying the PC and PEC degradation of these large biomolecules informs the inactivation mechanisms of biohazards. Some of these biological compounds are also environmental pollutants, with detrimental effects during water disinfection

[47, 48]. For example, antibiotic resistance genes may be driving the evolution of multidrug-resistant bacteria [49, 50], which cause serious diseases that are more virulent, more transmissible, and harder to treat [51, 52]. This has led to great interest in the degradation and mineralization of large biomolecules in water environments [53, 54]. Current quantification methods use initial and final mass concentrations to calculate the mineralization extent of the target biological compounds, without considering the differences in chemical structures between organics.

As such, a new method was developed by us to estimate the PC and PEC mineralization of large molecule biological compounds with unknown chemical formulas. This method is experimentally validated by examining the PC and PEC mineralization of representative large biomolecules, such as proteins, DNA, and lipids. The method uses standard dichromate chemical oxygen demand (COD) values to obtain Q_{chem} (the equivalent amount of transferred electrons) values of model compounds with unknown chemical formulas. Assuming the obtained Q_{chem} values are the theoretical charge required to mineralize organic pollutants, the mineralization efficiencies can be derived. Total organic carbon (TOC) is also used as a reference to confirm the mineralization capacity of dichromate chemical oxidation.

This method allows the determination of mineralization of large biological compounds, such as bovine serum albumin (BSA), lecithin, and bacterial DNA, during PC and PEC processes. All large biological compounds investigated can be photocatalytically and photoelectrocatalytically degraded. Incomplete PC mineralization is seen for all large biological compounds, particular for BSA; the PEC degradation method is more effective across all investigated large biological compounds. The PEC mineralization of DNA is highest for lecithin and BSA; the lowest PEC mineralization percentage is obtained for lecithin. PEC/PC mineralization ratios are highest for BSA, followed by lecithin and DNA [55].

10.2.3 Inactivation of Biohazards

Living biohazards, such as bacteria and viruses, are composed of various large biological compounds. This section focuses on *Escherichia coli* (*E. coli*) and replication-deficient recombinant adenovirus (RDRADS) as representative bacteria and viruses, respectively, to better understand the PC and PEC inactivation of biohazards. *E. coli* is an effective representative bacteria because of the extensive data available about it [56] and because it is often used as an indicator of fecal contamination (and by extension pathogenic microorganisms) in water [57]. RDRADS is selected to represent viruses, because it is found in water throughout the world and is on the Drinking Water Contaminant Candidate List [58]. Furthermore, adenoviruses like RDRADS are more resistant to common treatment than other biohazards of concern in drinking water [59, 60], and

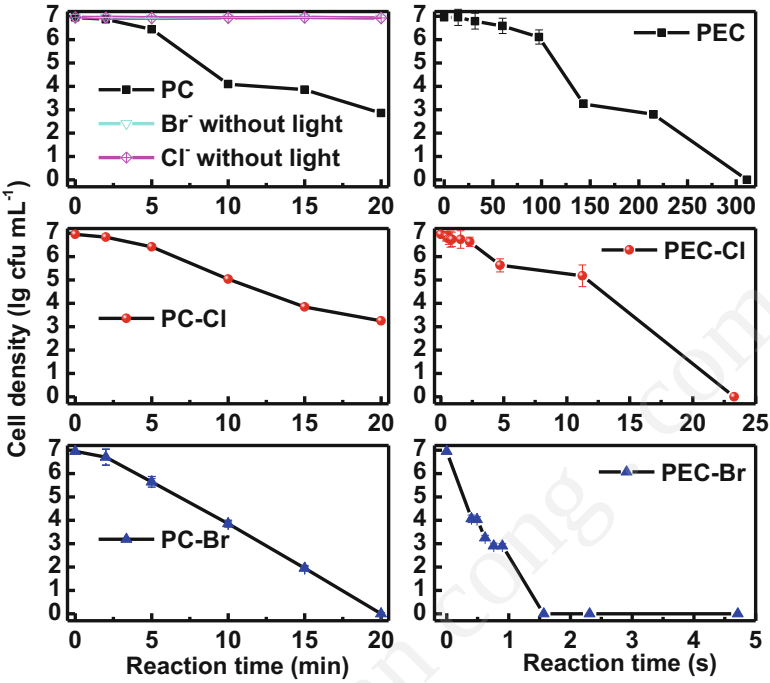

Fig. 10.6 Survived *E. coli* after different photocatalytic and photoelectrocatalytic treatment plot against resident time [62] (Reprinted with permission from *Applied Catalysis B: Environmental*, 2013, 140–141: 225–232. Copyright © 2013 Elsevier B.V)

RDRADS is a safe experimental model that causes no secondary infection due to its replication deficiency [61].

As *E. coli* was subjected to PC inactivation (Fig. 10.6), the bacterial population is almost stable for the first 2 min. This may be because the bacteria are already attacked by various ROSs but are protected by bacterial defenses against oxidative stress [14]. As reaction time continued, the cell population decreases gradually. Approximately 4-log of *E. coli* is inactivated within 20 min in PC system (without halides Cl^- or Br^-). The results are similar when Cl^- is present (PC–Cl). When Br^- is present (PC–Br), there is a linear decrease in cell density after 2 min, and all bacteria are inactivated within 20 min. The PC–Br inactivation efficiency (95.1 % at 5 min) is much higher than PC and PC–Cl treatment, suggesting that low levels of Br^- significantly enhance PC inactivation efficiency [62].

As *E. coli* was subjected to PEC treatment, the PEC bactericidal efficiencies are much higher than that of PC treatment, because the photogenerated e^- is removed quickly and the lifetime of h^+ is prolonged [24, 63]. The bactericidal capability of PEC treatment is ten times faster than PC treatment within 143 s; all bacterial cells are inactivated within 311 s. PEC inactivation efficiency was significantly enhanced by the presence of halides, especially Br^-. It took only 23.3 and 1.57 s to fully inactivate *E. coli* with PEC–Cl and PEC–Br treatments, respectively. Higher PEC

inactivation efficiencies in the presence of halides were found not only using a nanoparticulate TiO_2 thin-film photoanode [64] but also using a TiO_2 nanotubular photoanode [65].

The superior inactivation efficiency of PEC–Br and PEC–Cl method can be attributed to the effectiveness of the generated reactive species (RSs), such as $X^{\bullet}$ and $X_2^{\bullet -}$, in these processes [31, 62]. However, it takes longer for PEC–Cl to achieve the same inactivation effects as PEC–Br. This is surprising, because the thermodynamic nature of $Cl^{\bullet}$ should make it a more effective bactericide, due to its higher oxidation potential ($E^0[Cl^{\bullet}/Cl^-] = +2.41$ V) [66] than $Br^{\bullet}$ ($E^0[Br^{\bullet}/Br^-] = +1.96$ V) [33]. Higher effectiveness of the PEC–Br treatment may be driven by the fact that the reaction equilibrium constant for the formation of $Br_2^{\bullet -}$ ($K = 3.9 \times 10^5$ M^{-1}) is higher than $Cl_2^{\bullet -}$ ($K = 1.4 \times 10^5$ M^{-1}) during the photocatalytic process [67]. In addition, compared with PC–X method, PEC–X method is extremely effective in fully inactivating *E. coli*, although the main bactericides are the same [64]. As noted above, the PEC process can effectively prolong the lifetime of h^+ [23, 24], where X^- is oxidized to higher concentrations of $X^{\bullet}$ and $X_2^{\bullet -}$.

Field-emission scanning electron microscopy (FESEM) images of treated *E. coli* validate the results above. As shown from Fig. 10.7, an untreated *E. coli* cell has a well-preserved rodlike shape and intact membrane surface. During the PC process without halides, damage occurs first to the cell membrane, as the cell shows an abnormal wavy surface. Further treatment leads to further morphological change and the release of more intracellular content, finally leading to the peeling off of the outer cell membrane. Comparatively, while similar damage is observed during the shorter PC–Cl treatment time, the damage is mainly at the outer membrane with the prolonged reaction time. This clearly differs from PC-treated cells. This may be because the cell was attacked by different RSs. FESEM images of *E. coli* treated by PC–Br method demonstrate a similar damage pattern as seen with the PC–Cl method. Nevertheless, the observed damage is less substantial for PC–Cl- than PC–Br-treated cells at a corresponding treatment time; this may support the high inactivation efficiency of PC–Br method [62].

During the PEC process (Fig. 10.8), the cell first shrank and was depressed, with silklike cell contents released within a short treatment time. The silklike contents may be the nuclear acids [68], released from severely broken bacterial cells. The bacterial genomic DNA leakage and damage were also seen during the PEC processes reported in a previous study [14]. Further treatment time leads to severely decomposed released cell contents and the cell body contact with the catalyst, with slight damage to other cell parts. During the PEC–Cl process, little shrinkage depression was initially found on the *E. coli* surface. Then, the cell membrane became porous; this is similar to the results of PC–Cl treatment, except for longer treatment time is needed for PC–Cl. This indicates that the bacteria were attacked by similar RSs, such as $Cl^{\bullet}/Cl_2^{\bullet -}$. A longer treatment time damages large parts of the cell body. Compared with PEC–Cl treatment, the damage forms were almost the same as with the PEC–Br treatment, except that the cell damage extent by PEC–Br treatment was more significant with the same comparable treatment time [62].

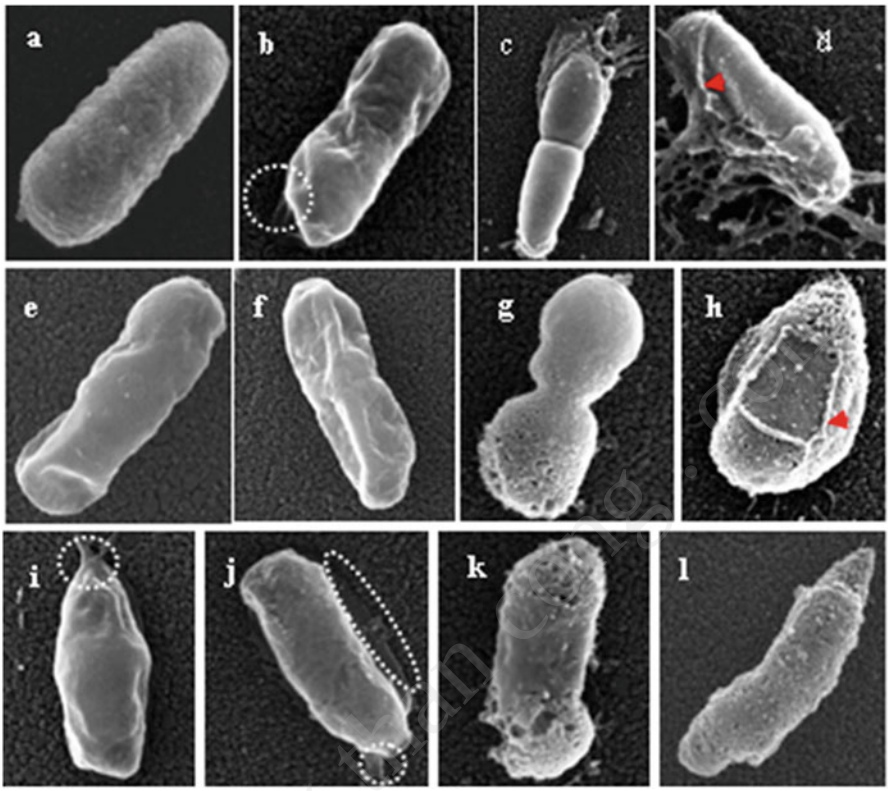

Fig. 10.7 FESEM images of *E. coli* cell. (**a**) Without treatment, (**b**) after PC 300 s, (**c**) PC 600 s, (**d**) PC 900 s, (**e**) PC–Cl 150 s, (**f**) PC–Cl 300 s, (**g**) PC–Cl 600 s, (**h**) PC–Cl 900 s, (**i**) PC–Br 150 s, (**j**) PC–Br 300 s, (**k**) PC–Br 600 s, and (**l**) PC–Br 900 s [62] (Reprinted with permission from *Applied Catalysis B: Environmental*, 2013, 140–141: 225–232. Copyright © 2013 Elsevier B.V)

The trends are different for virus (RDRADS) inactivation (Fig. 10.9). During the PC inactivation process, an initial rapid inactivation was achieved for RDRADS, but prolonged treatment time does not dramatically increase inactivation efficiency. In contrast, when Cl^- is included, the inactivation efficiencies increase rapidly during initial stage and then increase gradually to above 95 % at PC–Cl 97.5 s [69]; this is more than 2.5 times higher than with PC treatment alone at identical treatment times.

These results differ from the bacterial inactivation, where the observed change in cell density with Cl^- was very similar to that of PC inactivation without it [62]. The difference is due to different outer structures. The adenovirus is a nonenveloped virus, with a capsid protein coat; in contrast, *E. coli* contains phospholipids in the inner membrane and lipopolysaccharide in its outer membrane. X^- can be photocatalytically oxidized to $X^{\bullet}/X_2^{\bullet -}$, X_2, and HOX/XO^-. The $X^{\bullet}/X_2^{\bullet -}$ were the main RSs for bacteria inactivation, while HOX/XO^- may also play important role in virus inactivation system (in addition to $X^{\bullet}/X_2^{\bullet -}$). This is because HOX prefers to

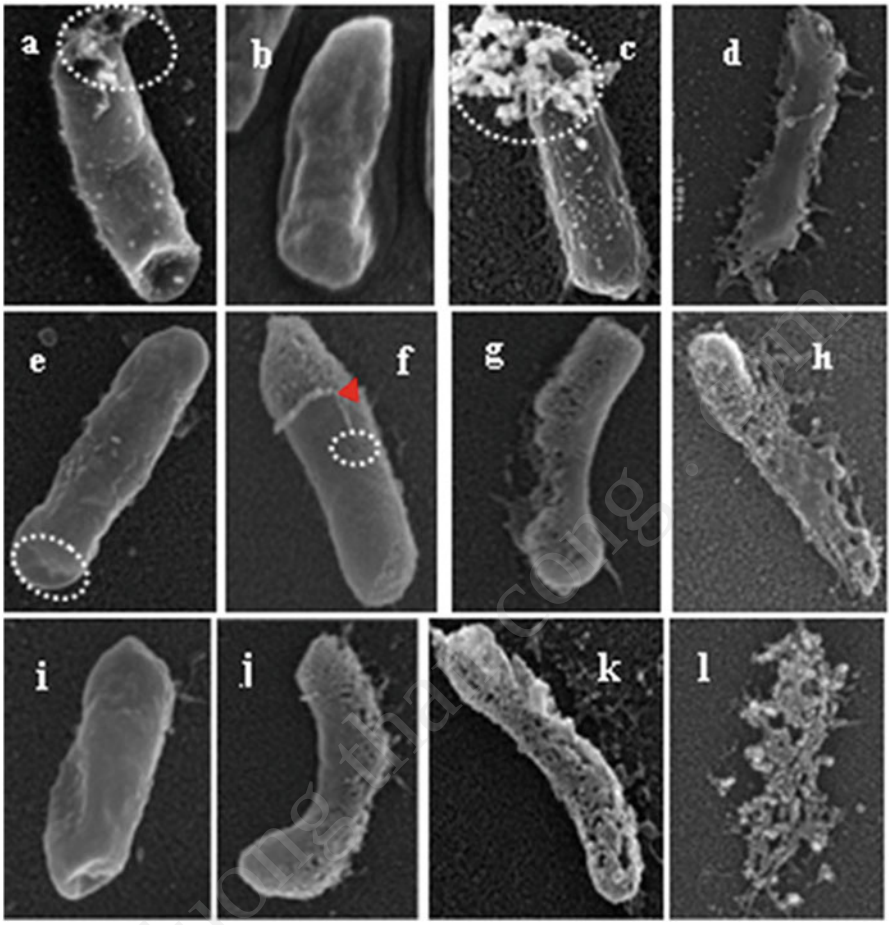

Fig. 10.8 FESEM images of *E. coli* cell. (**a**) After PEC 30 s, (**b**) PEC 60 s, (**c**) PEC 150 s, (**d**) PEC 300 s, (**e**) PEC–Cl 30 s, (**f**) PEC–Cl 60 s, (**g**) PEC–Cl 150 s, (**h**) PEC–Cl 300 s, (**i**) PEC–Br 30 s, (**j**) PEC–Br 60 s, (**k**) PEC–Br 150 s, and (**l**) PEC–Br 300 s [62] (Reprinted with permission from *Applied Catalysis B: Environmental*, 2013, 140–141: 225–232. Copyright © 2013 Elsevier B.V)

react with amino acids that have amino group side chains [70] and is particularly effective in inactivating proteins containing sulfhydryl groups [71]. PC–Br treatment showed a slower inactivation rate than PC–Cl treatment within initial 30 s. Once 60 s was reached, however, the inactivation efficiencies of PC–Br surpassed PC–Cl, inactivating 100 % of RDRADS at 97.5 s.

As the potential bias was applied, inactivation was significantly enhanced compared with PC treatment, although slightly less than half of the RDRADS were inactivated as the treatment time lengthened beyond 15 s. The presence of halide ions further improves the inactivation efficiency of viruses in the PEC system; the RDRADS was fully inactivated at the PEC–Br point of 31.7 s.

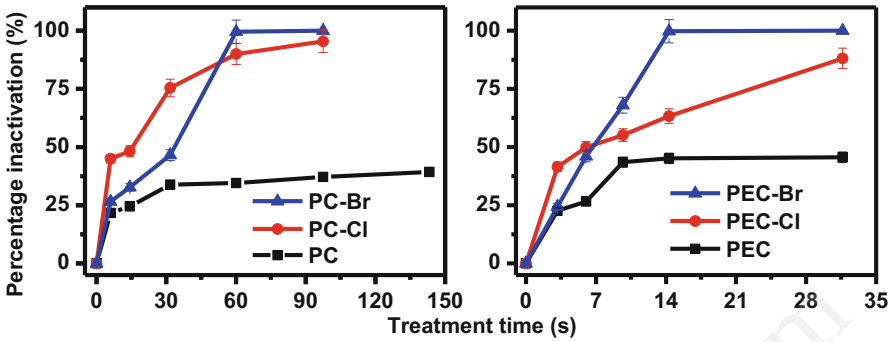

Fig. 10.9 PC and PEC inactivation efficiencies for RDRADS at nanoparticulate TiO_2 film photoanode in the absence of halide ions (PC) and in the presence of 1.0 mM NaCl (PC–Cl) and 1.0 mM NaBr (PC–Br) [69] (Reprinted with permission from *Chemical Engineering Journal*, 253: 538–543. Copyright © 2014 Elsevier B.V)

All these results demonstrate that low concentration halides can improve the inactivation efficiency of viruses with PC treatment; applying potential bias further enhances this process. RDRADS is more difficult to photocatalytically inactivate than *E. coli*; RDRADS is a double-stranded DNA virus and can be rapidly repaired by a host cell enzyme if its DNA is damaged [72]. Also, unlike complex bacterial cell membrane structures, viruses lack enzymes and other sensitive systems. This helps the viruses prolong survival outside the body [73].

10.3 Conclusions and Outlook

Biohazards in different water environments affect human health and economic development. Using PC and PEC technologies with illuminated nanostructured TiO_2 has been proved to be an excellent tool for the inactivation of biohazards and the mineralization of organics in water. To better understand how biohazards are killed using PC and PEC technologies, this chapter used a bottom-up strategy to study the mechanistic pathways of bacteria and virus inactivation, as well as biological compound decomposition. Despite many studies, however, knowledge gaps remain. The precise chemical structures of the photocatalytically and photoelectrocatalytically produced intermediates of small and large biological compounds must be correctly identified. To further improve the inactivation efficiency of biohazards, PEC and PEC-X inactivation mechanistic aspects of different types of bacteria, fungi, and viruses should investigated with a bottom-up strategy, because the effectiveness of inactivation depends on the killing mechanism. Additional work should focus on describing the relationships between the inactivation mechanisms of biohazards with the decomposition of their building blocks.

Acknowledgments This work was financially supported by National Natural Science Funds for Distinguished Young Scholars (41425015), National Natural Science Foundation of China (41573086 and 21077104), Australian Research Council (ARC) Discovery Project, and Research Grant Council, Hong Kong SAR Government (GRF476811).

References

1. Soller JA, Schoen ME, Varghese A, Ichida AM, Boehm AB, Eftim S, Ashbolt NJ, Ravenscroft JE (2014) Human health risk implications of multiple sources of faecal indicator bacteria in a recreational waterbody. Water Res 66:254–264
2. Dobrowsky PH, De Kwaadsteniet M, Cloete TE, Khan W (2014) Distribution of indigenous bacterial pathogens and potential pathogens associated with roof-harvested rainwater. Appl Environ Microbiol 80(7):2307–2316
3. de Man H, van den Berg HHJL, Leenen EJTM, Schijven JF, Schets FM, van der Vliet JC, van Knapen F, de Roda Husman AM (2014) Quantitative assessment of infection risk from exposure to waterborne pathogens in urban floodwater. Water Res 48:90–99
4. Liviac D, Wagner ED, Mitch WA, Altonji MJ, Plewa MJ (2010) Genotoxicity of water concentrates from recreational pools after various disinfection methods. Environ Sci Technol 44(9):3527–3532
5. Zhang XR, Li WG, Blatchley ER, Wang XJ, Ren PF (2015) UV/chlorine process for ammonia removal and disinfection by-product reduction: comparison with chlorination. Water Res 68:804–811
6. Qin F, Zhao YY, Zhao YL, Boyd JM, Zhou WJ, Li XF (2010) A toxic disinfection by-product, 2,6-dichloro-1,4-benzoquinone, identified in drinking water. Angew Chem Int Ed 49 (4):790–792
7. Eischeid AC, Thurston JA, Linden KG (2011) UV disinfection of adenovirus: present state of the research and future directions. Crit Rev Environ Sci Technol 41(15):1375–1396
8. Gayan E, Serrano MJ, Pagan R, Alvarez I, Condon S (2015) Environmental and biological factors influencing the UV-C resistance of *Listeria monocytogenes*. Food Microbiol 46:246–253
9. Carre G, Hamon E, Ennahar S, Estner M, Lett MC, Horvatovich P, Gies JP, Keller V, Keller N, Andre P (2014) TiO_2 photocatalysis damages lipids and proteins in *Escherichia coli*. Appl Environ Microbiol 80(8):2573–2581
10. Rizzo L, Della Sala A, Fiorentino A, Puma GL (2014) Disinfection of urban wastewater by solar driven and UV lamp – TiO_2 photocatalysis: effect on a multi drug resistant *Escherichia coli* strain. Water Res 53:145–152
11. Zhang W, Zhang XZ (2015) Adsorption of MS2 on oxide nanoparticles affects chlorine disinfection and solar inactivation. Water Res 69:59–67
12. Kubacka A, Diez MS, Rojo D, Bargiela R, Ciordia S, Zapico I, Albar JP, Barbas C, dos Santos VAPM, Fernandez-Garcia M, Ferrer M (2014) Understanding the antimicrobial mechanism of TiO_2-based nanocomposite films in a pathogenic bacterium. Sci Rep 4:4134. doi:10.1038/srep04134
13. Fanourgiakis S, Frontistis Z, Chatzisymeon E, Venieri D, Mantzavinos D (2014) Simultaneous removal of estrogens and pathogens from secondary treated wastewater by solar photocatalytic treatment. Glob Nest J 16(3):543–552
14. Sun HW, Li GY, Nie X, Shi HX, Wong PK, Zhao HJ, An TC (2014) Systematic approach to in-depth understanding of photoelectrocatalytic bacterial inactivation mechanisms by tracking the decomposed building blocks. Environ Sci Technol 48(16):9412–9419
15. Hoffmann MR, Martin ST, Choi WY, Bahnemann DW (1995) Environmental applications of semiconductor photocatalysis. Chem Rev 95(1):69–96

16. Malato S, Fernandez-Ibanez P, Maldonado MI, Blanco J, Gernjak W (2009) Decontamination and disinfection of water by solar photocatalysis: recent overview and trends. Catal Today 147 (1):1–59
17. Rincon AG, Pulgarin C (2010) Solar disinfection of water by TiO_2 photoassisted processes: physicochemical, biological, and engineering aspects. In: Electrochemistry for the environment. Springer, New York, pp 443–472
18. Kiwi J, Rtimi S, Sanjines R, Pulgarin C (2014) TiO_2 and TiO_2-doped films able to kill bacteria by contact: new evidence for the dynamics of bacterial inactivation in the dark and under light irradiation. Int J Photoenergy. doi:10.1155/2014/785037
19. Venieri D, Fraggedaki A, Kostadima M, Chatzisymeon E, Binas V, Zachopoulos A, Kiriakidis G, Mantzavinos D (2014) Solar light and metal-doped TiO_2 to eliminate water-transmitted bacterial pathogens: photocatalyst characterization and disinfection performance. Appl Catal B Environ 154–155:93–101
20. Sun DD, Wu Y, Gao P (2014) Effects of TiO_2 nanostructure and operating parameters on optimized water disinfection processes: a comparative study. Chem Eng J 249:160–166
21. Zhao HJ, Jiang DL, Zhang SQ, Catterall K, John R (2004) Development of a direct photoelectrochemical method for determination of chemical oxygen demand. Anal Chem 76 (1):155–160
22. Mandelbaum PA, Regazzoni AE, Blesa MA, Bilmes SA (1999) Photo-electro-oxidation of alcohols on titanium dioxide thin film electrodes. J Phys Chem B 103(26):5505–5511
23. Jiang DL, Zhao HJ, Zhang SQ, John R (2003) Characterization of photoelectrocatalytic processes at nanoporous TiO_2 film electrodes: photocatalytic oxidation of glucose. J Phys Chem B 107(46):12774–12780
24. Jiang DL, Zhang SQ, Zhao HJ (2007) Photocatalytic degradation characteristics of different organic compounds at TiO_2 nanoporous film electrodes with mixed anatase/rutile phases. Environ Sci Technol 41(1):303–308
25. Brugnera MF, Miyata M, Zocolo GJ, Fujimura Leite CQ, Boldrin Zanoni MV (2013) A photoelectrocatalytic process that disinfects water contaminated with *Mycobacterium kansasii* and *Mycobacterium avium*. Water Res 47(17):6596–6605
26. Brugnera MF, Miyata M, Zocolo GJ, Leite CQF, Zanoni MVB (2012) Inactivation and disposal of by-products from *Mycobacterium smegmatis* by photoelectrocatalytic oxidation using Ti/TiO_2-Ag nanotube electrodes. Electrochim Acta 85:33–41
27. Baram N, Starosvetsky D, Starosvetsky J, Epshtein M, Armon R, Ein-Eli Y (2009) Enhanced inactivation of *E-coli* bacteria using immobilized porous TiO_2 photoelectrocatalysis. Electrochim Acta 54(12):3381–3386
28. Cho M, Cates EL, Kim J (2011) Inactivation and surface interactions of MS-2 bacteriophage in a TiO_2 photoelectrocatalytic reactor. Water Res 45(5):2104–2110
29. Christensen PA, Curtis TP, Egerton TA, Kosa SAM, Tinlin JR (2003) Photoelectrocatalytic and photocatalytic disinfection of *E-coli* suspensions by titanium dioxide. Appl Catal B Environ 41(4):371–386
30. Zhang FJ, Chen ML, Oh WC (2011) Photoelectrocatalytic properties and bactericidal activities of silver-treated carbon nanotube/titania composites. Compos Sci Technol 71(5):658–665
31. Selcuk H, Sarikaya HZ, Bekbolet M, Anderson MA (2006) Bromate formation on the non-porous TiO_2 photoanode in the photoelectrocatalytic system. Chemosphere 62 (5):715–721
32. Cheng MM, Bakac A (2008) Photochemical oxidation of halide ions by a nitratochromium(III) complex. Kinetics, mechanism, and intermediates. J Am Chem Soc 130(16):5600–5605
33. Merenyi G, Lind J (1994) Reaction-mechanism of hydrogen abstraction by the bromine atom in water. J Am Chem Soc 116(17):7872–7876
34. Weinberg ME, Roman MC, Jacob P, Wen M, Cheung P, Walker UA, Mulligan K, Schambelan M (2011) Enhanced uridine bioavailability following administration of a triacetyluridine-rich nutritional supplement. Plos One 6(2):e14709. doi:10.1371/journal.pone.0014709

35. Williams MG, Palandra J, Shobe EM (2003) Rapid determination of rat plasma uridine levels by HPLC-ESI-MS utilizing the Captiva (TM) filter plates for sample preparation. Biomed Chromatogr 17(4):215–218
36. Singh HK, Saquib M, Haque MM, Muneer M (2007) Heterogeneous photocatalyzed degradation of uracil and 5-bromouracil in aqueous suspensions of titanium dioxide. J Hazard Mater 142(1-2):425–430
37. Jaussaud C, Paisse O, Faure R (2000) Photocatalysed degradation of uracil in aqueous titanium dioxide suspensions: mechanisms, pH and cadmium chloride effects. J Photochem Photobiol A Chem 130(2-3):157–162
38. Saltzman S, Acher AJ, Brates N, Horowitz M, Gevelberg A (1982) Removal of the phytotoxicity of uracil herbicides in water by photo-decomposition. Pestic Sci 13(2):211–217
39. Pozharskii AF, Soldatenkov AT, Katritzky AR (1997) Heterocycles in life and society: an introduction to heterocyclic chemistry and biochemistry and the role of heterocycles in science, technology, medicine, and agriculture. Wiley, New York First published
40. Elsellami L, Pigeot-Remy S, Dappozze F, Vocanson F, Houas A, Guillard C (2010) Comparison of initial photocatalytic degradation pathway of aromatic and linear amino acids. Environ Technol 31(13):1417–1422
41. Lachheb H, Dappozze F, Houas A, Guillard C (2012) Adsorption and photocatalytic degradation of cysteine in presence of TiO_2. J Photochem Photobiol A 246:1–7
42. Zhang SQ, Jiang DL, Zhao HJ (2006) Development of chemical oxygen demand on-line monitoring system based on a photoelectrochemical degradation principle. Environ Sci Technol 40(7):2363–2368
43. Li GY, Liu XL, An JB, Yang H, Zhang SQ, Wong PK, An TC, Zhao HJ (2015) Photocatalytic and photoelectrocatalytic degradation and mineralization of small biological compounds amino acids at TiO_2 photoanodes. Catal Today 245:46–53
44. Li GY, Zhang YL, Sun HW, An JB, Nie X, Zhao HJ, Wong PK, An TC (2013) Photocatalytic and photoelectrocatalytic degradation of small biological compounds: a case study of uridine. Catal Today 201:167–174
45. Li GY, Liu XL, An TC, Yang H, Zhang SQ, Zhao HJ (2015) Photocatalytic and photoelectrocatalytic degradation of small biological compounds at TiO_2 photoanode: a case study of nucleotide bases. Catal Today 242(Part B):363–371
46. Zhu XL, Yuan CW, Bao YC, Yang JH, Wu YZ (2005) Photocatalytic degradation of pesticide pyridaben on TiO_2 particles. J Mol Catal A Chem 229(1–2):95–105
47. Westgatet PJ, Park C (2010) Evaluation of proteins and organic nitrogen in wastewater treatment effluents. Environ Sci Technol 44(14):5352–5357
48. Chuang YH, Lin AYC, Wang XH, Tung HH (2013) The contribution of dissolved organic nitrogen and chloramines to nitrogenous disinfection byproduct formation from natural organic matter. Water Res 47(3):1308–1316
49. Martinez JL (2008) Antibiotics and antibiotic resistance genes in natural environments. Science 321(5887):365–367
50. Mao DQ, Luo Y, Mathieu J, Wang Q, Feng L, Mu QH, Feng CY, Alvarez PJJ (2014) Persistence of extracellular DNA in river sediment facilitates antibiotic resistance gene propagation. Environ Sci Technol 48(1):71–78
51. Kessler R (2012) Superbug hideout finding MRSA in US wastewater treatment plants. Environ Health Perspect 120(11):A437
52. Ferber D (2010) Infectious disease from pigs to people: the emergence of a new superbug. Science 329(5995):1010–1011
53. Cadet J, Wagner JR (2013) DNA base damage by reactive oxygen species, oxidizing agents, and UV radiation. Csh Perspect Biol 5(2). doi:10.1101/cshperspect.a012559
54. Nowicka AM, Kowalczyk A, Sek S, Stojek Z (2013) Oxidation of DNA followed by conformational change after OH radical attack. Anal Chem 85(1):355–361

55. Li GY, Liu XL, An TC, Wong PK, Zhao HJ (2016) A novel method developed for estimating mineralization efficiencies and its application in PC and PEC degradations of large molecule biological compounds with unknown chemical formula. Water Res 95:150–158
56. Hayashi K, Morooka N, Yamamoto Y, Fujita K, Isono K, Choi S, Ohtsubo E, Baba T, Wanner BL, Mori H, Horiuchi T (2006) Highly accurate genome sequences of *Escherichia coli* K-12 strains MG1655 and W3110. Mol Syst Biol 2. doi:10.1038/msb4100049
57. Blaustein RA, Pachepsky Y, Hill RL, Shelton DR, Whelan G (2013) *Escherichia coli* survival in waters: temperature dependence. Water Res 47(2):569–578
58. USEPA (2005) the drinking water candidate contaminant list
59. Ballester NA, Malley JP (2004) Sequential disinfection of adenovirus type 2 with UV-chlorine-chloramine. J Am Water Works Assoc 96(10):97–103
60. Thurston-Enriquez JA, Haas CN, Jacangelo J, Riley K, Gerba CP (2003) Inactivation of feline calicivirus and adenovirus type 40 by UV radiation. Appl Environ Microbiol 69(1):577–582
61. Li XY, Liu QC, Bi XH, Sheng GY, Fu JM, Ran PX, Li B (2008) An in vitro model to evaluate virus aerosol characteristics using a GFP-expressing adenovirus. J Med Microbiol 57 (11):1335–1339
62. Li GY, Liu XL, Zhang HM, Wong PK, An TC, Zhao HJ (2013) Comparative studies of photocatalytic and photoelectrocatalytic inactivation of *E. coli* in presence of halides. Appl Catal B Environ 140–141:225–232
63. Zhao HJ, Jiang DL, Zhang SQ, Wen W (2007) Photoelectrocatalytic oxidation of organic compounds at nanoporous TiO_2 electrodes in a thin-layer photoelectrochemical cell. J Catal 250(1):102–109
64. Li GY, Liu XL, Zhang HM, An TC, Zhang SQ, Carroll AR, Zhao HJ (2011) In situ photoelectrocatalytic generation of bactericide for instant inactivation and rapid decomposition of Gram-negative bacteria. J Catal 277(1):88–94
65. Nie X, Li GY, Gao MH, Sun HW, Liu XL, Zhao HJ, Wong PK, An TC (2014) Comparative study on the photoelectrocatalytic inactivation of *Escherichia coli* K-12 and its mutant *Escherichia coli* BW25113 using TiO_2 nanotubes as a photoanode. Appl Catal B Environ 147:562–570
66. Rogers JE, Abraham B, Rostkowski A, Kelly LA (2001) Mechanisms of photoinitiated cleavage of DNA by 1,8-naphthalimide derivatives. Photochem Photobiol 74(4):521–531
67. Liu Y, Pimentel AS, Antoku Y, Giles BJ, Barker JR (2002) Temperature-dependent rate and equilibrium constants for $Br^{\bullet}$ (aq) + Br^{-}(aq)↔ $Br_2^{-\bullet}$ (aq). J Phys Chem A 106 (46):11075–11082
68. Campbell NA, Reece JB, Meyers N (eds) (2004) Biology, 7th edn. Benjamin Cummings, San Francisco
69. Li GY, Liu XL, Zhang HM, Wong PK, An TC, Zhou WQ, Li B, Zhao HJ (2014) Adenovirus inactivation by in situ photocatalytically and photoelectrocatalytically generated halogen viricides. Chem Eng J 253:538–543
70. Dychdala GR (1991) Chlorine and chlorine compounds. In: Disinfection, sterilization and preservation. Lea & Febiger, Philadelphia, pp 131–151
71. Knox WE, Stumpf PK, Green DE, Auerbach VH (1948) The inhibition of sulfhydryl enzymes as the basis of the bactericidal action of chlorine. J Bacteriol 55:451–458
72. Gerba CP, Gramos DM, Nwachuku N (2002) Comparative inactivation of enteroviruses and adenovirus 2 by UV light. Appl Environ Microbiol 68(10):5167–5169
73. Montgomery JM (1985) Water treatment principles and design. Wiley, New York, pp 262–283

Chapter 11
Photoelectrocatalytic Inactivation Mechanism of Bacteria

Taicheng An, Hongwei Sun, and Guiying Li

Abstract This chapter reviews literature about the mechanisms associated with the photocatalytic (PC) and photoelectrocatalytic (PEC) inactivation of bacteria. It introduces PEC system configuration, reviews bactericide identification (mainly the reactive species (RSs) generated in situ), and identifies the RSs attacking bacterial cell targets. The review concludes that the major cellular component first attacked by RSs is the cell envelope, particularly the membrane lipid contents, resulting in the increase of membrane permeability and the leakage of the bacterial cytoplasmic substances such as K^+, proteins, and DNA. In addition, intracellular enzymes (such as superoxide dismutase (SOD) and catalase), the proteins, and the DNA might also be attacked by the RSs generated inside the cell. This induces enzyme inactivation and oxidative damage to proteins and DNA. Any of these cellular disruptions may be responsible for bacterial inactivation.

Keywords Photoelectrocatalysis • Bacterial inactivation mechanism • Reactive oxygen species • Membrane permeability • Protein • DNA • Antioxidative enzymes

T. An (✉)
The State Key Laboratory of Organic Geochemistry, Guangzhou Institute of Geochemistry, Chinese Academy of Sciences, Guangzhou 510640, China

Institute of Environmental Health and Pollution Control, School of Environmental Science and Engineering, Guangdong University of Technology, Guangzhou 510006, Guangdong, China
e-mail: antc99@gdut.edu.cn; antc99@gig.ac.cn

H. Sun
The State Key Laboratory of Organic Geochemistry, Guangzhou Institute of Geochemistry, Chinese Academy of Sciences, Guangzhou 510640, China

Key Laboratory of Aquatic Botany and Watershed Ecology, Wuhan Botanical Garden, Chinese Academy of Sciences, Wuhan 430074, China
e-mail: sunhw@wbgcas.cn

G. Li
Institute of Environmental Health and Pollution Control, School of Environmental Science and Engineering, Guangdong University of Technology, Guangzhou 510006, Guangdong, China
e-mail: ligy1999@gdut.edu.cn

T. An et al. (eds.), *Advances in Photocatalytic Disinfection*, Green Chemistry and Sustainable Technology, DOI 10.1007/978-3-662-53496-0_11

11.1 Introduction

Microbes present in drinking water can cause illnesses, such as gastrointestinal disease and diarrhea, or even death [1]. According to the World Health Organization (WHO), approximately 80 % of human diseases are either directly or indirectly related to drinking water [2, 3], making disinfection treatments particularly critical for drinking water supplies. Chlorination has been widely adopted worldwide to disinfect drinking water, due to its low cost and high disinfection efficiency, and because free chlorine residuals left after disinfection may suppress microbe regrowth during water distribution. However, this residual chlorine also leaves a bad taste to the water. Other problems with chlorination have also been revealed, such as insufficient disinfection capacity, which was responsible for the waterborne disease bursts [4, 5], and the production of carcinogenic by-products, including haloacetic acids (HAAs) and trihalomethanes (THMs) from reactions between dissolved natural organic matters and chlorine [6]. These shortcomings have highlighted the need for safer and more effective technologies for drinking water disinfection [7, 8].

Photocatalytic (PC) disinfection using semiconductors has been explored extensively since the pioneering work done by Matsunaga et al. in 1985 [9–15]. The PC disinfection technique is promising because of the solar-driven potential and self-cleaning capacity [11, 16–18], as well as the absence of carcinogenic disinfection by-products [8].

Photoelectrocatalytic (PEC) disinfection technique is another alternative. Different from the PC system, PEC uses the immobilized catalyst as a photoanode and applies a potential bias to enhance disinfection performance [19–21]. As Fig. 11.1 shows, the photoanode is activated by photons to produce the hole and electron pairs (h^+/e^-). Unlike the fast recombination of h^+ and e^- in the PC system, the e^- is immediately removed to the counter electrode to achieve real-time separation of the h^+/e^- pairs and enhanced photon utilization ratios [22, 23]. The h^+ and e^- then react with the water and oxygen molecules, respectively, to produce reactive species (RSs), which were believed to be responsible for organics degradation and bacteria inactivation [20, 24, 25]. PEC also avoids the problem of catalyst separation in PC systems, making the successive operation and catalyst recycle possible [26].

Commonly used photoanodes in PEC systems include immobilized TiO_2 films, TiO_2 nanotubes, graphene-based materials, and some others. Immobilized TiO_2 films have been extensively investigated and prepared using methods such as powder loading, sol-gel, vapor deposition, and electrochemical deposition [27–32]. However, the PEC efficiency of TiO_2 nanoparticle films is limited by poor connectivity among TiO_2 particles. Comparatively, TiO_2 nanotube array photoanodes have been shown to be more effective, with highly ordered structure, larger specific area, and excellent orientation and conductivity [21, 33]. Baram et al. compared the PEC disinfection efficiencies of a TiO_2 nanotube with mesoporous TiO_2, finding that the TiO_2 nanotube anode was more effective, inactivating 10^6

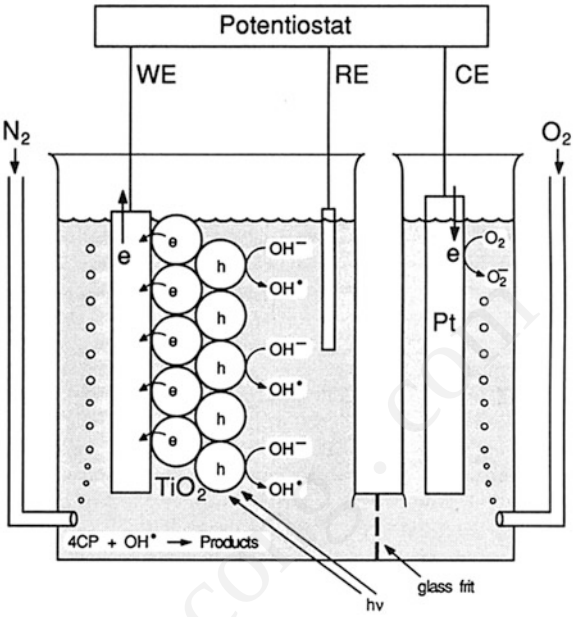

Fig. 11.1 The schematic diagram of photoelectrocatalytic (PEC) system (*WE* working electrode, *RE* reference electrode, *CE* counter electrode. Reprinted from Ref. [22] Copyright © 1994 American Chemistry Society)

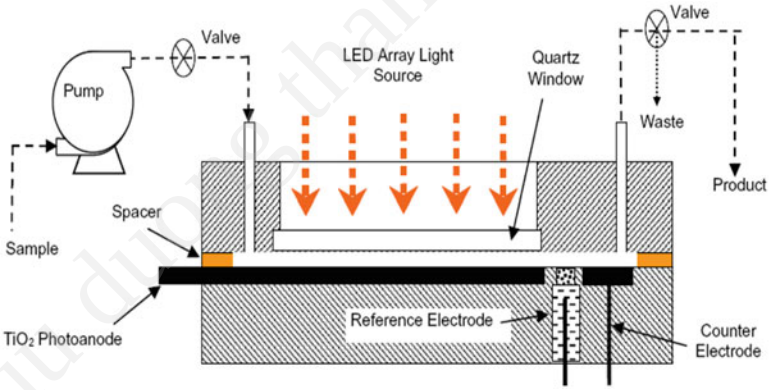

Fig. 11.2 The thin-layer cell for PEC disinfection (Reprinted from Ref. [20] Copyright © 2011 Elsevier)

colony-forming units per milliliter (CFU mL^{-1}) of *E. coli* within 10 min [34]. Furthermore, the TiO_2 nanotube anode also demonstrated high recycling capacity [35].

PEC apparatus setup greatly affects disinfection performance; there are two main types of reactors reported for lab tests. The first type is a microreactor, with very tiny reaction volumes. For instance, Li et al. used a thin-layer PEC reactor with a volume of approximately 40 μL (Fig. 11.2) [20], pumping the bacterial suspension through the PEC reactor at constant flow. A bacterial inactivation efficiency of 99.90 % (*E. coli*, 9×10^6 CFU mL^{-1}) was achieved at a residence time of 0.4 s. The

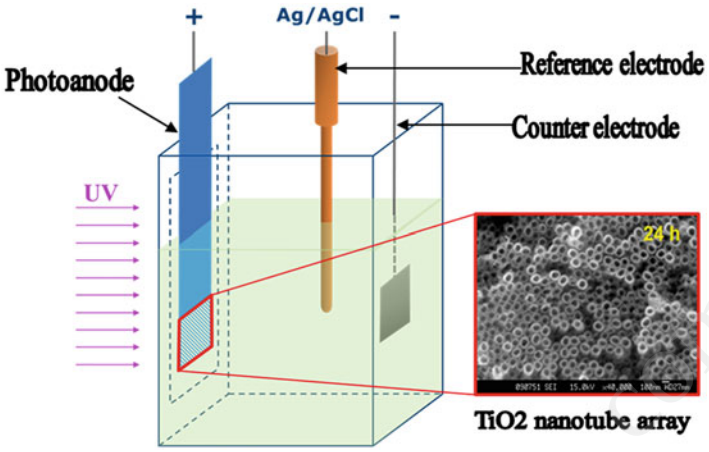

Fig. 11.3 Schematic diagrams of the bulk apparatus for PEC experiments (Reprinted from Ref. [36] Copyright © 2014 American Chemistry Society)

microreactor was generally designed to characterize photoanodes and conduct disinfection kinetic research. When larger sample volumes have been required, researchers have adopted bulk reactors with volumes at tens or hundreds of milliliters. Figure 11.3 shows the typical configuration of the bulk reactor with three electrodes adopted for PEC disinfection, where all bacterial cells (50 mL, 1.1×10^7 CFU mL^{-1}) can be inactivated within 45 min [36].

11.2 Bactericide in PEC System

When considering PEC disinfection mechanisms, it is commonly accepted that the in situ generated RSs such as h^+, e^-, $^{\bullet}OH$, H_2O_2, and $^{\bullet}O_2^-$ are responsible for microorganism inactivation. In PC systems using a suspended catalyst, $^{\bullet}OH$ has been reported to be the dominant bactericide, because of its high redox potential (+2.27 V vs. standard hydrogen electrode (SHE)). For example, Zhang et al. investigated the contribution of various RSs to *E. coli* inactivation in an AgBr-Ag-Bi_2WO_6 suspension system. The $^{\bullet}OH$, h^+, e^-, and H_2O_2 were scavenged with isopropanol, oxalate, Cr(VI), and Fe(II)-EDTA, respectively, and the results showed that the dominant bactericidal RS was the free $^{\bullet}OH$ [37].

Cho et al. [38] determined the steady-state $^{\bullet}OH$ concentrations ($[^{\bullet}OH]_{ss}$) in a PC disinfection system with TiO_2 P25 powder and revealed a linear relationship between $[^{\bullet}OH]_{ss}$ and the *E. coli* inactivation efficiencies, confirming that $^{\bullet}OH$ was the dominant inactivating RSs [39]. However, e^- was also found to be the predominant bactericide, instead of $^{\bullet}OH$, in a PC inactivation system using natural sphalerite as the photocatalyst [40]. This was attributed to the lower redox potential of the conduction band of natural sphalerite (−1.4 V vs. Saturated calomel electrode

(SCE)) compared with TiO_2 (0.765 V vs. SCE) [41], and the *E. coli* cells were inactivated by the reduction stress. H_2O_2 was also demonstrated to be an essential bactericide in a separate study using *E. coli* isogenic mutants and sphalerite under visible light irradiation [42]. These studies highlight that the dominant RSs for bacteria inactivation vary when using different catalysts for PC treatment.

When immobilized photocatalysts are adopted, the dominant bactericidal RSs may vary from the powdered catalyst suspension PC systems. Kikuchi et al. [43] used a hydrophilic polytetrafluoroethylene (PTFE) membrane to separate an *E. coli* suspension from the TiO_2 thin film. The bacteria were inactivated under UV irradiation, adding mannitol (scavenger of $^{\bullet}OH$) did not suppress PC inactivation efficiency. Given this, the authors argued that the major bactericidal species was not $^{\bullet}OH$ but H_2O_2, as the diffusion length of $^{\bullet}OH$ was insufficient to traverse the PTFE membrane and attack the *E. coli*. Wang et al. [44] also confirmed this conclusion through RS scavenger experiments, using B-Ni-co-doped TiO_2 (BNT) microspheres as the photocatalyst in a modified partition system (shown in Fig. 11.4). These findings suggest that the contact between the photocatalyst and the bacterial cells is an essential factor in determining the bactericide.

Other studies also indicate that the bactericide may vary significantly when halide ions (Cl^-, Br^-) are present [10, 45]. Both PC and PEC inactivation efficiencies were elevated significantly when low concentrations of halides were supplied, especially Br^-. Bactericidal performance is dominated by the photoelectrocatalytically generated $Br^{\bullet}/Br_2^{\bullet-}$ for PEC inactivation in the presence of Br^-. In these cases, halide ions act as an electron mediator, with an unchanged chemical form before and after bactericidal processes [10]. The optimal concentration of Br^- was found to be 1 mM for PEC inactivation of *E. coli* K-12 [45].

The microorganism species also affects the major bactericide. Cho et al. investigated the dominant inactivating RSs using MS-2 phage and *E. coli* as the target microorganisms, respectively. Scavenging experiments determined the inactivation contribution of diffused $^{\bullet}OH$ in the bulk solution, as well as the adsorbed $^{\bullet}OH$ on the

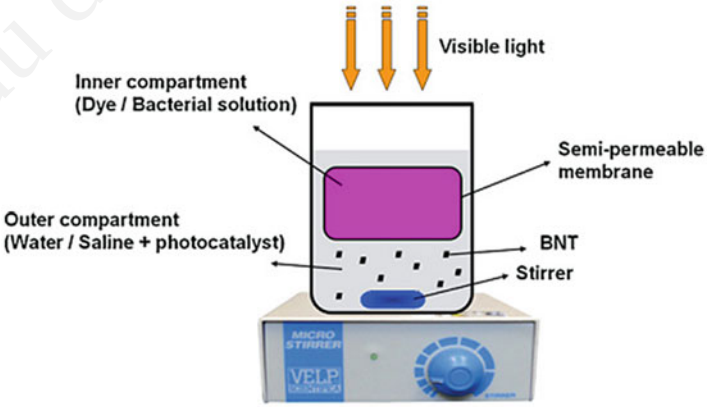

Fig. 11.4 Schematic illustration of partition system setup used in the photocatalytic bacterial disinfection (Reprinted from Ref. [44] Copyright © 2011 Elsevier)

catalyst surface. The results showed that the MS-2 phage was mainly inactivated by diffused $^{\bullet}OH$, whereas *E. coli* was inactivated by both types of $^{\bullet}OH$ [39].

Most studies to date have focused on the RSs outside bacterial cells; few studies investigate RS levels inside the bacterial cells. Measuring intracellular RS levels are also important, because this activity may drive the inactivation of enzymes [46] and oxidative damages of both proteins and DNA [47]. Thus, our group measured the intracellular RS levels during PEC inactivating *E. coli*, using 2′,7-′-dichlorodihydrofluorescein diacetate (DCFH-DA) as the fluorescent probe [36]. DCFH-DA (nonfluorescent) penetrates the bacterial membrane and is hydrolyzed by the esterase and oxidized by intracellular RSs to result in fluorescent products. Intracellular RS levels increase as soon as the PEC inactivation treatment starts. Although H_2O_2 was found to be the major bactericidal RSs in this PEC system, H_2O_2 was much less reactive than $^{\bullet}OH$ and can be eliminated by catalase. This finding was inconsistent with the high inactivating efficiency of the PEC process. Therefore, it was inferred that the increase of intracellular RS levels was due to the movement of H_2O_2 across the bacterial membrane. The much more reactive $^{\bullet}OH$ was generated in situ inside the cytomembrane through a Fenton reaction [48] or Haber-Weiss reaction [43] to inactivate the cells directly:

$$Fe^{2+} + H_2O_2 + H^+ \rightarrow Fe^{3+} + {}^{\bullet}OH + H_2O \quad (11.1)$$

$$^{\bullet}O_2^- + H_2O_2 \rightarrow {}^{\bullet}OH + OH^- + O_2 \quad (11.2)$$

Where $^{\bullet}O_2^-$ is consistently generated as a by-product of the aerobic respiration process [49]. Approximately 20 μM of the iron available for the Fenton reaction in vivo was contained in the *E. coli* cells [50]. The shortcoming of this probing method is that it can only determine the levels of total RSs, leaving individual species concentrations unknown. The mechanisms driving the intracellular inactivation of bacteria are far from well established, but this study provided new information about these mechanisms.

11.3 Cellular Targets of RS Attack

It is generally accepted that PC or PEC disinfection works when RSs attack and damage microorganism cellular components. Matsunaga et al. first proposed that PC treatment causes the dimerization of coenzyme A, subsequently suppressing cellular respiration [16]. Additional evidence indicated that the PC or PEC inactivation of a microorganism was related to the damaged cell wall and membrane [51, 52]. It was also reported that intracellular micromolecules, such as DNA, were also damaged by oxidation, leading to inactivation [48]. Figure 11.5 points to the possible cellular targets of RS attack when there are specific bacteria involved, such as *E. coli*. In this example, *E. coli* cells were 2–4 μm long and 0.5–1.0 μm in diameter; the volume of a single bacterium was approximately 0.83 μm^3. Cellular component proportions are protein, 50–60 %; RNA, 13–25 %; polysaccharide,

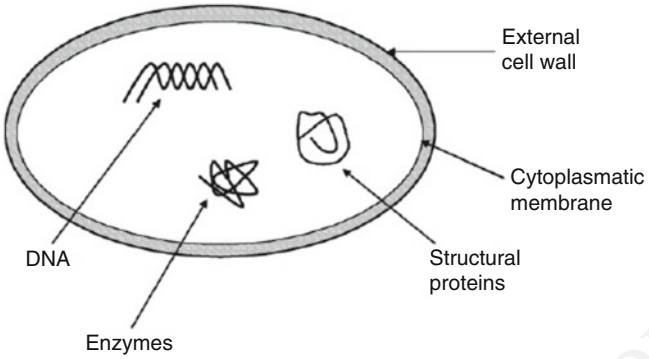

Fig. 11.5 The possible bacterial cellular components attacked by RSs during PC or PEC disinfection (Reprinted from Ref. [58] Copyright © 2009 Elsevier)

9–17 %; lipid, 8–9 %; and DNA, 2–4 % [1]. The potential RSs attacking targets included the cell wall, membrane, enzymes, proteins, and DNA.

11.3.1 Extracellular Polymeric Substance (EPS, Capsule)

The EPS, also known as the bacterial capsule, is located outside the cell wall and mainly consists of polysaccharide and polypeptide. The EPS helps bacteria attach to surfaces, maintain moisture, and store nutrients [53]. EPS layers protect bacterial cells during PEC disinfection by scavenging the RSs. Liu et al. compared the PC inactivation efficiencies of bacteria with and without the EPS layer, and the latter was shown to be more sensitive [54]. Utilizing the wild-type *Pseudomonas aeruginosa* and its mutant strains deficient in EPS synthesis, Christopher et al. discovered that EPS could facilitate contact between the catalyst and bacteria and protect the bacterial cells from RS attack [55]. The dual roles of capsular EPS in PC inactivation of bacteria were also demonstrated by comparing *E. coli* BW25113 and its isogenic mutants with upregulated and regulated production of EPS. In a partition system with inhibited direct contact between bacteria and TiO_2, an increased EPS fraction strengthened bacterial resistance to PC treatment. In contrast, with direct contact, capsular EPS increased bacterial susceptibility to PC inactivation [56]. However, Gong et al. compared the sensitivity to $^{\bullet}OH$ attack of four *E. coli* strains with different EPS levels and found no significant variance [57]. These conflicting findings suggest that additional research is needed to clarify the role of EPS during PEC or PC disinfection processes.

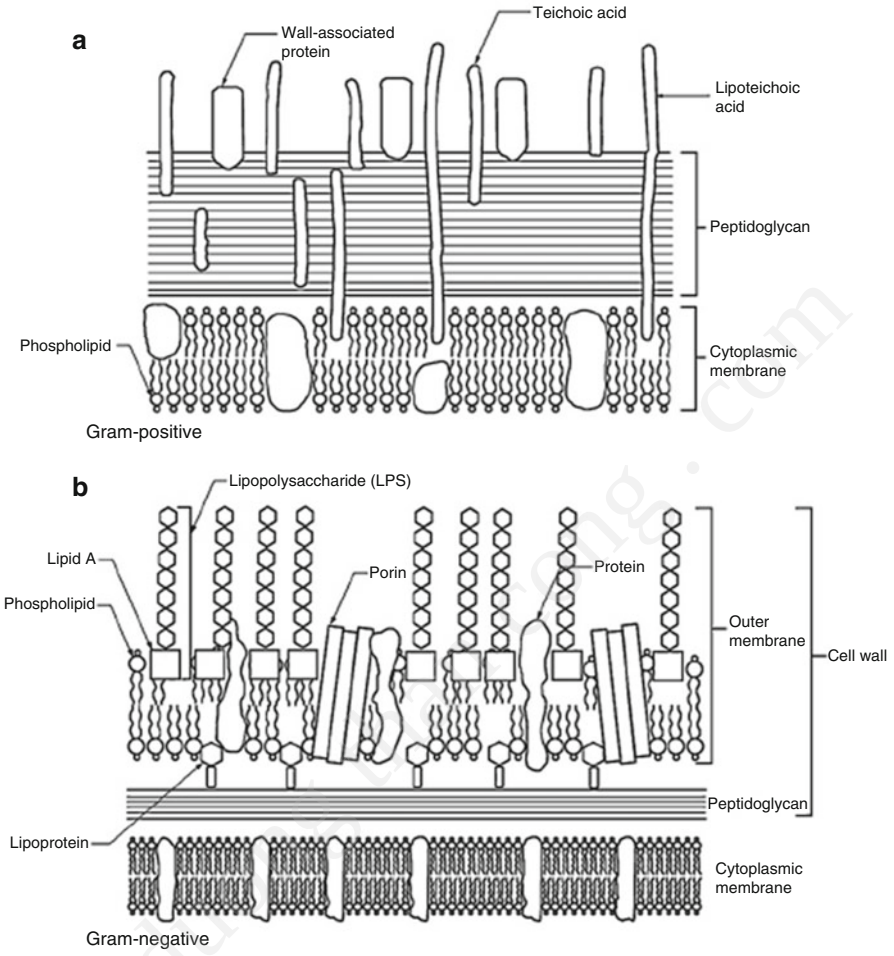

Fig. 11.6 The envelope structure of (**a**) Gram-positive bacteria and (**b**) Gram-negative bacteria (Reprinted from Ref. [60] Copyright © 2010 Elsevier)

11.3.2 Cell Wall and Membrane (Envelope)

Bacterial envelope structure differs between Gram-positive and Gram-negative bacteria. As Fig. 11.6 shows, Gram-positive bacteria have thicker peptidoglycan layers; the Gram-negative bacteria have the outer membrane outside the peptidoglycan layers.

Damaged bacterial envelopes have been frequently observed during PC and PEC disinfection. The leakage of intracellular substances, such as K^+, is the most compelling proof [52] because K^+ is an important element for bacterial cells, maintaining membrane potential, osmotic pressure, and conducting signals. A

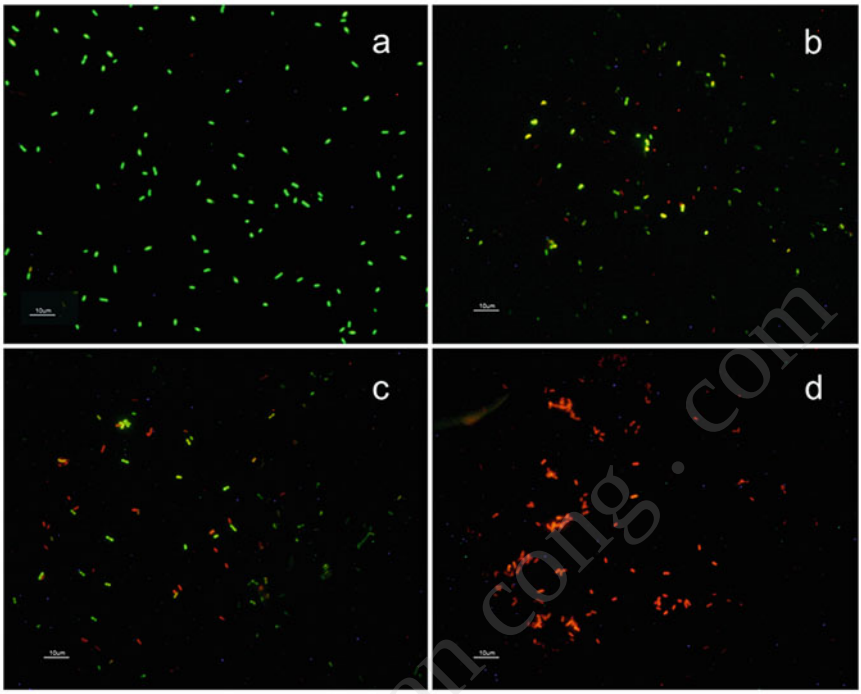

Fig. 11.7 Fluorescent microscope images of PEC-inactivated K-12 suspension stained with Live/Dead BacLight Bacteria Viability Kit. (**a**) 0 min; (**b**) 10 min; (**c**) 30 min; (**d**) 60 min (Reprinted from Ref. [36] Copyright © 2014 American Chemistry Society)

Na^+-K^+ pump in intact bacterial cells can maintain high levels of intracellular K^+ [59]. K^+ leakage during the PEC inactivation was observed at the early stage of PEC treatment in a previous study [36], and this leakage pointed to the damaged bacterial envelope and the elevated permeability of the cell membrane.

The fluorescent staining method using a Live/Dead BacLight Bacterial Viability Kit is commonly used to monitor bacterial membrane integrity during PEC inactivation [20]. Figure 11.7 shows the typical microscopic images of stained bacteria. The intact cells are stained green and the cells with compromised membranes are stained red. The PEC treatment appears to have increased the proportion of the red cells, suggesting that the PEC treatment disrupted bacterial membrane integrity.

β-D-galactosidase activity assay is another method used to assess membrane permeability changes. This enzyme is located in the cytoplasm and catalyzes the hydrolysis of o-nitrophenyl-β-D-galactopyranoside (ONPG, colorless) to o-nitrophenol (ONP, yellow). For intact cells, ONPG entry into the bacterial cytoplasm is limited by the cytoplasmic membrane and the lactose permease [61]. When an RS attack permeates the membrane, ONPG enters the cell more freely, inducing an increased ONPG hydrolysis rate [61]. The total enzymatic

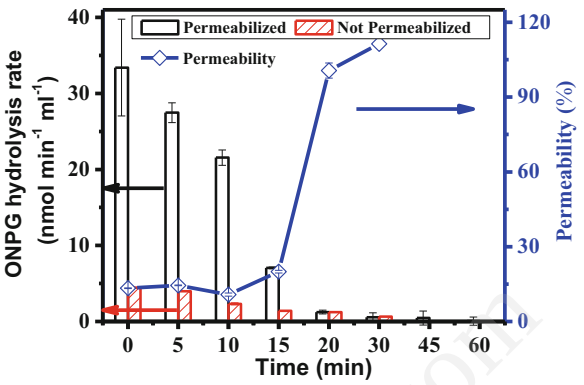

Fig. 11.8 β-D-galactosidase activity and membrane permeability of PEC-treated bacteria determined by ONPG hydrolyzation assay (Reprinted from Ref. [36] Copyright © 2014 American Chemistry Society)

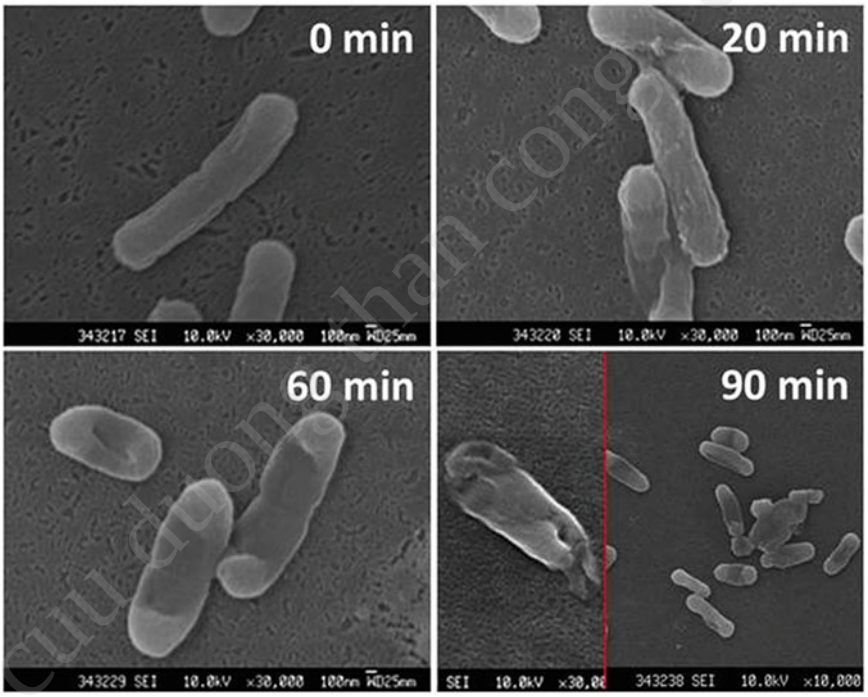

Fig. 11.9 SEM images of bacteria inactivated by PEC process for 0, 20, 60, and 90 min (Reprinted from Ref. [36] Copyright © 2014 American Chemistry Society)

activity can be determined after permeating the bacteria with sodium dodecyl sulfate (SDS)/chloroform; the cellular permeability is reflected in the ratio of ONPG hydrolysis rate to total enzyme activity. As showed from Fig. 11.8, PEC treatment causes a dramatic rise of cell permeability. Lu et al. observed that quantum dots of ~5 nm penetrated the *E. coli* cells after PC treatment with TiO_2

for 20 min, suggesting cell envelope destruction and intracellular macromolecule leakage [32].

Cell envelope damage can also be directly observed using scanning electron microscope (SEM) or transmission electron microscopy (TEM). Figure 11.9 shows typical SEM images of PEC-inactivated *E. coli* cells. The untreated *E. coli* cells have a plump rod shape with intact cell envelopes. After PEC treatment, the bacterial surfaces become rougher with wrinkle sand and then collapse; then the cells shrivel, indicating cell envelope decomposition and cytoplasm leakage [36]. Sunada et al. reported the release of endotoxin (lipid A, the components of outer membrane for Gram-negative bacteria) along with PC inactivation of *E. coli*, suggesting the damage of outer membrane components during PC treatment [62].

Bacterial membrane permeability changes after PC or PEC disinfection may be due to the functional disruption of membrane-associated proteins. In an earlier report about the solar disinfection process by Bosshard et al. [63], membrane-associated proteins, such as enzymes involved in cellular respiration and the ATPase, were found to be inactivated quickly, and there was insufficient energy to maintain bacterial membrane potential. The loss of membrane potential subsequently caused increased membrane permeability, as it is important for substrate transport processes across the bacterial membrane. The decreased respiration rate and adenosine triphosphate (ATP) generation potential have also been observed for bacteria inactivated by PEC treatment, suggesting a similar mechanism for deactivating bacteria compared with solar disinfection [67].

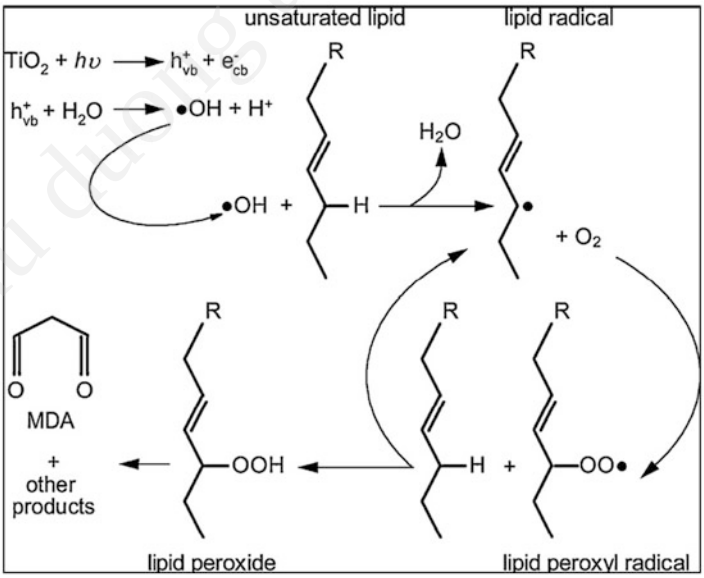

Fig. 11.10 Schematic diagram of the lipid peroxidation induced by RS attack (Reprinted from Ref. [65] Copyright © 2011 Elsevier)

The oxidative stress-induced lipid peroxidation of the membrane may be responsible for bacteria envelope damage during PC or PEC inactivation [60, 64]. Figure 11.10 illustrates the lipid peroxidation process, where RSs attack the unsaturated fatty acid contents of the bacterial membrane forming the lipid radical, which subsequently reacts with oxygen molecules forming lipid peroxyl radical. This radical reacts with another lipid molecule in a chain reaction mode [65]. The lipid peroxide or malonaldehyde (MDA) produced during this process has been generally used as an indicator of lipid peroxidation.

Dalrymple et al. synthesized a lipid vessel to simulate an *E. coli* membrane and used PC to treat both the vessel and *E. coli* cells by PC. The production of MDA and lipid peroxide was found to be similar, suggesting that the bacterial membrane was damaged at the lipid content, through lipid peroxidation caused by RS attack [65]. Leung et al. compared the inactivation performances of two marine bacteria strains. They discovered that the bacteria with more short-chained and branch-chained fatty acids were more sensitive to inactivation, because the lipid bilayer with the short-chained and branch-chained fatty acids was looser and more fluid and more sensitive to RS attack [66]. Similarly, another research compared the PEC disinfection performances of parental *E. coli* BW25113 with its isogenic mutants. The mutants have a higher proportion of unsaturated fatty acids in the membrane and were found to be more vulnerable. Additionally, the unsaturated fatty acid proportion decreased during PEC treatment, suggesting that the unsaturated fatty acid content of the membrane lipid is an important target of RS attack [67].

11.3.3 Enzymes

Increased RSs, such as $^{\bullet}O_2^-$ and H_2O_2, both outside and inside bacterial cells create oxidative stress to the bacteria. In response to this stress, antioxidative enzymes such as superoxide dismutase (SOD) and catalase (CAT) catalyze $^{\bullet}O_2^-$ and H_2O_2 conversion and detoxification, respectively [49, 68, 69]. During PEC bactericidal treatment, both SOD and CAT activities decrease, suggesting that rapidly elevated intracellular RS levels during PEC inactivation may overwhelm the antioxidative capacity of these two enzymes [36]. SOD and CAT may have been damaged by the free radicals attack through oxidation, resulting in the fragmentation of proteins and the generation of protein carbonyl derivatives [70]. The loss of SOD and CAT activities would in turn accelerate the accumulation of both extracellular and intracellular RSs, as well as bacterial inactivation.

11.3.4 Proteins and Nucleic Acids

SEM images (Fig. 11.9) imply the leakage of intracellular substances, such as proteins and nucleic acids. A previous study recorded a reduction in the protein

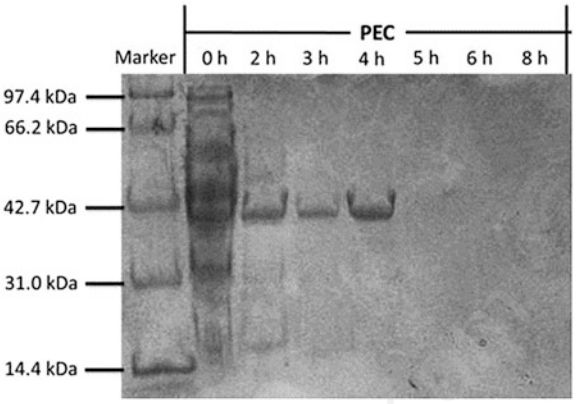

Fig. 11.11 Protein SDS-PAGE assay of the bacterial samples treated by PEC inactivation (Reprinted from Ref. [36] Copyright © 2014 American Chemistry Society)

content of the bacterial cells (10^7 CFU mL^{-1}) from 182.0 to 4.5 μgmL^{-1} after 90 min of PEC treatment [36]. The protein SDS-PAGE assay, shown in Fig. 11.11, was conducted to provide more details about the protein leakage. Protein bands with molecular weights from 14.4 to 97.4 kDa showed time-dependent weakening during PEC inactivation. Carre et al. also discovered the loss of membrane-associated proteins when PC was applied to inactivate *E. coli* [71].

It was previously believed that the RSs generated during PC or PEC treatment were mainly associated with the catalysts' surfaces. These RSs were difficult to diffuse and tended be scavenged before they encountered the bacterial membrane [43]. Given this assumption, the damage of intracellular bacterial components, such as proteins and DNA, caused by RS attack during PC or PEC disinfection had not been extensively investigated. However, it has since been found that PEC raised the bacterial intracellular RS levels, suggesting that the intracellular macromolecules were probably exposed to RS attack as well.

The in situ generated RSs during PC or PEC inactivation may cause protein oxidization at the side chains, especially lysine, arginine, and threonine, generating carbonyl groups [72]. A previous report found the protein carbonyl level rise during PEC inactivation, especially after the inactivation of CAT and SOD [46], supporting this hypothesis. Further, bacterial protein contents can be aggregated after solar disinfection treatment by RS attack [73]. Thus, it may be inferred that the proteins are likely undergoing similar changes during PC or PEC processes. This is because they are also RS-mediated reactions and the aggregation is the direct consequence of protein oxidation. Nevertheless, this inference needs further investigations in the near future.

Oxidative-damaged proteins may be repaired under certain conditions and inactivated bacteria regrowth is possible [66]. Conversely, DNA damage or loss, especially chromosomal DNA, is a lethal factor in bacterial inactivation. This is because DNA is more sensitive to oxidative stress, compared with other macromolecules. This results in DNA lesions, such as base loss, breaks of single strand and both strands [74]. In a previous report, the genomic DNA in PEC-treated

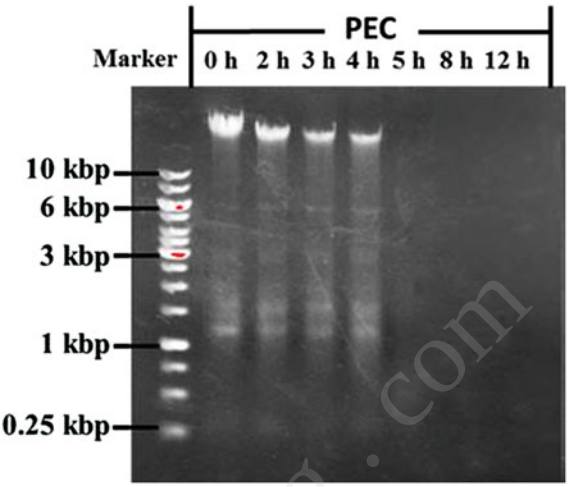

Fig. 11.12 The leakage and damage of bacterial genomic DNA during PEC disinfection process determined by agarose gel electrophoresis (Reprinted from Ref. [36] Copyright © 2014 American Chemistry Society)

bacteria samples was measured using DNA agarose gel electrophoresis (AGE). As Fig. 11.12 shows, the band intensities of genomic DNA decreased and disappeared after PEC inactivation. The electrophoretic mobility of the genomic DNA increased slightly over a prolonged PEC time, possibly due to genomic DNA leakage and segmentation [36]. Gogniat et al. discovered that a *E. coli* mutant deficient in iron intake regulation was more fragile to PC treatment, suggesting that DNA was attacked by $^{\bullet}OH$ generated through an intracellular Fenton reaction [48], as shown in Eq. 11.1.

11.4 Mineralization of Bacteria

The cytoplasmic substances, including the proteins and DNA, that have leaked from bacterial cells are attacked directly by the extracellular RSs, damaged through oxidation or segmentation, or completely mineralized [46, 47]. Leung et al. investigated the total organic carbon (TOC) concentrations of the suspended catalyst PC disinfection system. The solid and the dissolved phases were separated with a centrifuge to determine TOC. The TOC in the solid phase decreased after PC disinfection; the dissolved TOC increased into a peak and then fell. This suggests the release of bacterial components into the dissolved phase, followed by further degradation [66]. Li et al. achieved a decrease in TOC by 42 % within 600 s using PEC treatment in a thin-layer cell [20]. In the bulk reactor (50 mL, 10^7 CFU mL^{-1} *E. coli*), PEC reduced the TOC by ~50 % within 5 h [36].

11.5 Conclusions

Many researchers have systematically investigated the mechanisms driving PC and PEC inactivation of bacteria, resulting in the following proposed disinfection mechanism. The RSs produced in situ are responsible for the bacterial inactivation; the dominant RSs may vary between different systems. For PEC systems, H_2O_2 has emerged as the major disinfectant, crossing the bacterial membrane and generating $^{\bullet}OH$ through a Fenton reaction inside the cytoplasm. RSs inside and outside the cells can be quenched by bacterial SOD and CAT, but when the RS generation potential overwhelms the antioxidation capacity of these enzymes, CAT and SOD are gradually inactivated. Thus, in turn, it causes further intracellular RS accumulation. The RSs then attack the bacterial membrane and cell wall, inducing the peroxidation of the membrane lipid and increasing membrane permeability. This results in cytoplasmic substance leakage of K^+ ions, proteins, and DNA. The macromolecules may be attacked directly by the intracellular RSs, as well as the extracellular RSs, leading to oxidative damage to proteins and DNA. With prolonged PC or PEC treatment, the leaked substances and the cell debris are further degraded and mineralized into CO_2 and water.

Acknowledgments This work was financially supported by the National Natural Science Funds for Distinguished Young Scholars (41425015), National Natural Science Foundation of China (41573086 and 21077104), and Research Grant Council, Hong Kong SAR Government (GRF476811).

References

1. Sucher NJ, Carles MC, Nowotny J, Bak T (2012) Photocatalytic water disinfection on oxide semiconductors: part 2-structure, functional properties and reactivity of microbial agents. Adv Appl Ceram 111(1–2):16–33
2. WHO (2005) The world health report 2005 – make every mother and child count. World Health Organization, Geneva
3. Fenwick A (2006) Waterborne infectious diseases – could they be consigned to history? Science 313(5790):1077–1081
4. Leclerc H, Schwartzbrod L, Dei-Cas E (2002) Microbial agents associated with waterborne diseases. Crit Rev Microbiol 28(4):371–409
5. Mac Kenzie WR, Hoxie NJ, Proctor ME, Gradus MS, Blair KA, Peterson DE, Kazmierczak JJ, Addiss DG, Fox KR, Rose JB, Davis JP (1994) A massive outbreak in milwaukee of *Cryptosporidium* infection transmitted through the public water supply. New Engl J Med 331(3):161–167
6. Li QL, Mahendra S, Lyon DY, Brunet L, Liga MV, Li D, Alvarez PJJ (2008) Antimicrobial nanomaterials for water disinfection and microbial control: potential applications and implications. Water Res 42(18):4591–4602
7. Sketchell J, Peterson HG, Christofi N (1995) Disinfection by-product formation after biologically assisted Gac treatment of water-supplies with different bromide and DOC content. Water Res 29(12):2635–2642

8. Kulkarni P, Chellam S (2010) Disinfection by-product formation following chlorination of drinking water: artificial neural network models and changes in speciation with treatment. Sci Total Environ 408(19):4202–4210
9. Matsunaga T, Tomoda R, Nakajima T, Wake H (1985) Photoelectrochemical sterilization of microbial-cells by semiconductor powders. FEMS Microbiol Lett 29(1–2):211–214
10. Xia DH, Ng TW, An TC, Li GY, Li Y, Yip HY, Zhao HJ, Lu AH, Wong PK (2013) A recyclable mineral catalyst for visible-light-driven photocatalytic inactivation of bacteria: natural magnetic sphalerite. Environ Sci Technol 47(19):11166–11173
11. Wang WJ, Yu Y, An TC, Li GY, Yip HY, Yu JC, Wong PK (2012) Visible-light-driven photocatalytic inactivation of *E. coli* K-12 by bismuth vanadate nanotubes: bactericidal performance and mechanism. Environ Sci Technol 46(8):4599–4606
12. Li Q, Xie RC, Ll YW, Mintz EA, Shang JK (2007) Enhanced visible-light-induced photocatalytic disinfection of *E. coli* by carbon-sensitized nitrogen-doped titanium oxide. Environ Sci Technol 41(14):5050–5056
13. Cheng YW, Chan RC, Wong PK (2007) Disinfection of *Legionella pneumophila* by photocatalytic oxidation. Water Res 41(4):842–852
14. Shi HX, Chen JY, Li GY, Nie X, Zhao HJ, Wong PK, An TC (2013) Synthesis and characterization of novel plasmonic Ag/AgX-CNTs (X = Cl, Br, I) nanocomposite photocatalysts and synergetic degradation of organic pollutant under visible light. ACS Appl Mater Interfaces 5(15):6959–6967
15. Kozlova EA, Safatov AS, Kiselev SA, Marchenko VY, Sergeev AA, Skarnovich MO, Emelyanova EK, Smetannikova MA, Buryak GA, Vorontsov AV (2010) Inactivation and mineralization of aerosol deposited model pathogenic microorganisms over TiO_2 and Pt/TiO_2. Environ Sci Technol 44(13):5121–5126
16. Matsunaga T, Tomoda R, Nakajima T, Wake H (1985) Photoelectrochemical sterilization of microbial cells by semiconductor powders. FEMS Microbiol Lett 29(1–2):211–214
17. Rincon AG, Pulgarin C (2007) Fe^{3+} and TiO_2 solar-light-assisted inactivation of *E-coli* at field scale – Implications in solar disinfection at low temperature of large quantities of water. Catal Today 122(1–2):128–136
18. Gao P, Liu J, Sun DD, Ng W (2013) Graphene oxide-CdS composite with high photocatalytic degradation and disinfection activities under visible light irradiation. J Hazard Mater 250:412–420
19. Li GY, Liu XL, An TC, Yang H, Zhang SQ, Zhao HJ (2015) Photocatalytic and photoelectrocatalytic degradation of small biological compounds at TiO_2 photoanode: a case study of nucleotide bases. Catal Today 242:363–371
20. Li GY, Liu XL, Zhang HM, An TC, Zhang SQ, Carroll AR, Zhao HJ (2011) In situ photoelectrocatalytic generation of bactericide for instant inactivation and rapid decomposition of Gram-negative bacteria. J Catal 277(1):88–94
21. Baram N, Starosvetsky D, Starosvetsky J, Epshtein M, Armon R, Ein-Eli Y (2007) Enhanced photo-efficiency of immobilized TiO_2 catalyst via intense anodic bias. Electrochem Commun 9(7):1684–1688
22. Vinodgopal K, Stafford U, Gray KA, Kamat PV (1994) Electrochemically assisted photocatalysis. 2. The role of oxygen and reaction intermediates in the degradation of 4-chlorophenol on immobilized TiO2 particulate films. J Phys Chem 98(27):6797–6803
23. Sun LZ, Bolton JR (1996) Determination of the quantum yield for the photochemical generation of hydroxyl radicals in TiO_2 suspensions. J Phys Chem 100(10):4127–4134
24. Zhang FJ, Chen ML, Oh WC (2011) Photoelectrocatalytic properties and bactericidal activities of silver-treated carbon nanotube/titania composites. Compos Sci Technol 71(5):658–665
25. Kang Q, Lu QZ, Liu SH, Yang LX, Wen LF, Luo SL, Cai QY (2010) A ternary hybrid CdS/Pt-TiO_2 nanotube structure for photoelectrocatalytic bactericidal effects on *Escherichia Coli*. Biomaterials 31(12):3317–3326
26. Gan WY, Zhao H, Amal R (2009) Photoelectrocatalytic activity of mesoporous TiO_2 thin film electrodes. Appl Catal A Gen 354(1–2):8–16

27. Zhang SQ, Zhao HJ, Jiang DL, John R (2004) Photoelectrochemical determination of chemical oxygen demand based on an exhaustive degradation model in a thin-layer cell. Anal Chim Acta 514(1):89–97
28. Jiang D, Zhao H, Zhang S, John R, Will GD (2003) Photoelectrochemical measurement of phthalic acid adsorption on porous TiO_2 film electrodes. J Photochem Photobiol A 156 (1–3):201–206
29. Kim DS, Kwak SY (2008) Photocatalytic inactivation of *E. coli* with a mesoporous TiO_2 coated film using the film adhesion method. Environ Sci Technol 43(1):148–151
30. Nolan MG, Pemble ME, Sheel DW, Yates HM, Yates HM (2006) One step process for chemical vapour deposition of titanium dioxide thin films incorporating controlled structure nanoparticles. Thin Solid Films 515(4):1956–1962
31. Sun L, An TC, Wan SG, Li GY, Bao NZ, Hu XH, Fu JM, Sheng GY (2009) Effect of synthesis conditions on photocatalytic activities of nanoparticulate TiO2 thin films. Sep Purif Technol 68(1):83–89
32. Lu ZX, Zhou L, Zhang ZL, Shi WL, Xie ZX, Xie HY, Pang DW, Shen P (2003) Cell damage induced by photocatalysis of TiO_2 thin films. Langmuir 19(21):8765–8768
33. Shankar K, Basham JI, Allam NK, Varghese OK, Mor GK, Feng XJ, Paulose M, Seabold JA, Choi KS, Grimes CA (2009) Recent advances in the use of TiO_2 nanotube and nanowire arrays for oxidative photoelectrochemistry. J Phys Chem C 113(16):6327–6359
34. Baram N, Starosvetsky D, Starosvetsky J, Epshtein M, Armon R, Ein-Eli Y (2009) Enhanced inactivation of *E-coli* bacteria using immobilized porous TiO_2 photoelectrocatalysis. Electrochim Acta 54(12):3381–3386
35. Baram N, Starosvetsky D, Starosvetsky J, Epshtein M, Armon R, Ein-Eli Y (2011) Photocatalytic inactivation of microorganisms using nanotubular TiO_2. Appl Catal B Environ 101(3–4):212–219
36. Sun HW, Li GY, Nie X, Shi HX, Wong PK, Zhao HJ, An TC (2014) Systematic approach to in-depth understanding of photoelectrocatalytic bacterial inactivation mechanisms by tracking the decomposed building blocks. Environ Sci Technol 48(16):9412–9419
37. Zhang LS, Wong KH, Yip HY, Hu C, Yu JC, Chan CY, Wong PK (2010) Effective photocatalytic disinfection of *E. coli* K-12 using AgBr-Ag-Bi_2WO_6 nanojunction system irradiated by visible light: the role of diffusing hydroxyl radicals. Environ Sci Technol 44 (4):1392–1398
38. Cho M, Chung H, Choi W, Yoon J (2004) Linear correlation between inactivation of *E. coli* and OH radical concentration in TiO_2 photocatalytic disinfection. Water Res 38(4):1069–1077
39. Cho M, Chung HM, Choi WY, Yoon JY (2005) Different inactivation Behaviors of MS-2 phage and *Escherichia coli* in TiO_2 photocatalytic disinfection. Appl Environ Microbiol 71 (1):270–275
40. Chen YM, Lu AH, Li Y, Zhang LS, Yip HY, Zhao HJ, An TC, Wong PK (2011) Naturally occurring sphalerite as a novel cost-effective photocatalyst for bacterial disinfection under visible light. Environ Sci Technol 45(13):5689–5695
41. Fujishima A, Rao TN, Tryk DA (2000) Titanium dioxide photocatalysis. J Photochem Photobiol C: Photochem Rev 1(1):1–21
42. Shi HX, Huang GC, Xia DH, Ng TW, Yip HY, Li GY, An TC, Zhao HJ, Wong PK (2015) Role of in situ resultant H_2O_2 in the visible-light-driven photocatalytic inactivation of *E. coli* using natural sphalerite: a genetic study. J Phys Chem B 119(7):3104–3111
43. Kikuchi Y, Sunada K, Iyoda T, Hashimoto K, Fujishima A (1997) Photocatalytic bactericidal effect of TiO_2 thin films: dynamic view of the active oxygen species responsible for the effect. J Photochem Photobiol A 106(1–3):51–56
44. Wang WJ, Zhang LS, An TC, Li GY, Yip HY, Wong PK (2011) Comparative study of visible-light-driven photocatalytic mechanisms of dye decolorization and bacterial disinfection by B–Ni-codoped TiO_2 microspheres: the role of different reactive species. Appl Catal B Environ 108–109:108–116

45. Nie X, Li GY, Gao MH, Sun HW, Liu XL, Zhao HJ, Wong PK, An TC (2014) Comparative study on the photoelectrocatalytic inactivation of *Escherichia coli* K-12 and its mutant *Escherichia coli* BW25113 using TiO_2 nanotubes as a photoanode. Appl Catal B Environ 147:562–570
46. Suryo Rahmanto A, Pattison DI, Davies MJ (2012) Photo-oxidation-induced inactivation of the selenium-containing protective enzymes thioredoxin reductase and glutathione peroxidase. Free Radic Biol Med 53(6):1308–1316
47. Hirakawa K, Mori M, Yoshida M, Oikawa S, Kawanishi S (2004) Photo-irradiated titanium dioxide catalyzes site specific DNA damage via generation of hydrogen peroxide. Free Radic Res 38(5):439–447
48. Gogniat G, Dukan S (2007) TiO_2 photocatalysis causes DNA damage via Fenton reaction-generated hydroxyl radicals during the recovery period. Appl Environ Microbiol 73 (23):7740–7743
49. Vatansever F, de Melo WC, Avci P, Vecchio D, Sadasivam M, Gupta A, Chandran R, Karimi M, Parizotto NA, Yin R, Tegos GP, Hamblin MR (2013) Antimicrobial strategies centered around reactive oxygen species – bactericidal antibiotics, photodynamic therapy, and beyond. FEMS Microbiol Rev 37(6):955–989
50. Park S, Imlay JA (2003) High levels of intracellular cysteine promote oxidative DNA damage by driving the Fenton reaction. J Bacteriol 185(6):1942–1950
51. Kiwi J, Nadtochenko V (2005) Evidence for the mechanism of photocatalytic degradation of the bacterial wall membrane at the TiO_2 interface by ATR-FTIR and laser kinetic spectroscopy. Langmuir 21(10):4631–4641
52. Hu C, Guo J, Qu JH, Hu XX (2007) Photocatalytic degradation of pathogenic bacteria with AgI/TiO_2 under visible light irradiation. Langmuir 23(9):4982–4987
53. Eboigbodin KE, Biggs CA (2008) Characterization of the extracellular polymeric substances produced by Escherichia coli using infrared spectroscopic, proteomic, and aggregation studies. Biomacromolecules 9(2):686–695
54. Liu Y, Li J, Qiu XF, Burda C (2007) Bactericidal activity of nitrogen-doped metal oxide nanocatalysts and the influence of bacterial extracellular polymeric substances (EPS). J Photochem Photobiol A 190(1):94–100
55. Hessler CM, Wu MY, Xue Z, Choi H, Seo Y (2012) The influence of capsular extracellular polymeric substances on the interaction between TiO_2 nanoparticles and planktonic bacteria. Water Res 46(15):4687–4696
56. Huang GC, Xia DH, An TC, Ng TW, Yip HY, Li GY, Zhao HJ, Wong PK (2015) Dual roles of capsular extracellular polymeric substances in the photocatalytic inactivation of *Escherichia coli*: comparison of *E. coli* BW25113 with its isogenic mutants. Appl Environ Microbiol 81 (15):5174–5183
57. Gong AS, Lanzl CA, Cwiertny DM, Walker SL (2012) Lack of influence of extracellular polymeric substances (EPS) level on hydroxyl radical mediated disinfection of *Escherichia coli*. Environ Sci Technol 46(1):241–249
58. Malato S, Fernández-Ibáñez P, Maldonado MI, Blanco J, Gernjak W (2009) Decontamination and disinfection of water by solar photocatalysis: recent overview and trends. Catal Today 147 (1):1–59
59. Wang H-YL, O'Doherty GA (2012) Modulators of Na/K-ATPase: a patent review. Expert Opin Ther Pat 22(6):587–605
60. Dalrymple OK, Stefanakos E, Trotz MA, Goswami DY (2010) A review of the mechanisms and modeling of photocatalytic disinfection. Appl Catal B Environ 98(1–2):27–38
61. Zheng H, Maness PC, Blake DM, Wolfrum EJ, Smolinski SL, Jacoby WA (2000) Bactericidal mode of titanium dioxide photocatalysis. J Photochem Photobiol A 130(2–3):163–170
62. Sunada K, Kikuchi Y, Hashimoto K, Fujishima A (1998) Bactericidal and detoxification effects of TiO_2 thin film photocatalysts. Environ Sci Technol 32(5):726–728
63. Bosshard F, Bucheli M, Meur Y, Egli T (2010) The respiratory chain is the cell's Achilles' heel during UVA inactivation in *Escherichia coli*. Microbiology 156(7):2006–2015

64. Singh S, Brocker C, Koppaka V, Chen Y, Jackson BC, Matsumoto A, Thompson DC, Vasiliou V (2013) Aldehyde dehydrogenases in cellular responses to oxidative/electrophilic stress. Free Radic Biol Med 56:89–101
65. Dalrymple O, Isaacs W, Stefanakos E, Trotz M, Goswami D (2011) Lipid vesicles as model membranes in photocatalytic disinfection studies. J Photochem Photobiol A 221(1):64–70
66. Leung TY, Chan CY, Hu C, Yu JC, Wong PK (2008) Photocatalytic disinfection of marine bacteria using fluorescent light. Water Res 42(19):4827–4837
67. An TC, Sun HW, Li GY, Zhao HJ, Wong PK (2016) Differences in photoelectrocatalytic inactivation processes between *E. coli* and its isogenic single gene knockoff mutants: destruction of membrane framework or associated proteins? Appl Catal B Environ 188:360–366
68. Farr SB, Kogoma T (1991) Oxidative stress responses in *Escherichia Coli* and *Salmonella Typhimurium*. Microbiol Rev 55(4):561–585
69. Storz G, Tartaglia LA, Farr SB, Ames BN (1990) Bacterial defenses against oxidative stress. Trends Genet 6(11):363–368
70. Kwon HY, Choi SY, Won MH, Kang TC, Kang JH (2000) Oxidative modification and inactivation of Cu, Zn-superoxide dismutase by 2,2′-azobis(2-amidinopropane) dihydrochloride. Biochim Biophys Acta 543(1):69–76
71. Carre G, Hamon E, Ennahar S, Estner M, Lett MC, Horvatovich P, Gies JP, Keller V, Keller N, Andre P (2014) TiO_2 photocatalysis damages lipids and proteins in *Escherichia coli*. Appl Environ Microbiol 80(8):2573–2581
72. Dalle-Donne I, Rossi R, Giustarini D, Milzani A, Colombo R (2003) Protein carbonyl groups as biomarkers of oxidative stress. Clin Chim Acta 329(1–2):23–38
73. Bosshard F, Riedel K, Schneider T, Geiser C, Bucheli M, Egli T (2010) Protein oxidation and aggregation in UVA-irradiated Escherichia coli cells as signs of accelerated cellular senescence. Environ Microbiol 12(11):2931–2945
74. Hidaka H, Horikoshi S, Serpone N, Knowland J (1997) In vitro photochemical damage to DNA, RNA and their bases by an inorganic sunscreen agent on exposure to UVA and UVB radiation. J Photochem Photobiol A 111(1–3):205–213

Chapter 12
Bacterial Oxidative Stress Responses and Cellular Damage Caused by Photocatalytic and Photoelectrocatalytic Inactivation

Hongwei Sun, Guiying Li, and Taicheng An

Abstract This chapter review's recent research works about the bacterial oxidative stress responses and cellular damage during the photocatalytic (PC) and photoelectrocatalytic (PEC) bacterial inactivation processes. In the PC or PEC systems, high levels of reactive oxygen species (ROSs) would be generated, causing oxidative stress to bacterial cells. Bacterial anti-oxidative responses regulated by *oxyR* and *soxRS* can be induced by elevated ROS level. However, the oxidative stress responses, producing catalase and superoxide dismutase (SOD), failed to occur during PEC inactivation process, indicating that the ROS levels increased too sharply and overwhelmed the bacterial tolerance. Nevertheless, both catalase and SOD were proved to contribute greatly to the bacterial resistance to PEC inactivation, demonstrated by the different inactivation performance of parental *E. coli* BW25113 and its *katG* or *sodA* single-gene knockout mutants. More proofs were supplied by the growing bacterial catalase level together with their tolerance to PEC treatment as the bacteria were preincubated by low concentrations of hydrogen peroxide. Another aspect to understand the disinfection mechanism is

H. Sun
The State Key Laboratory of Organic Geochemistry, Guangzhou Institute of Geochemistry, Chinese Academy of Sciences, Guangzhou 510640, China

Key Laboratory of Aquatic Botany and Watershed Ecology, Wuhan Botanical Garden and Sino-Africa Joint Research Center, Chinese Academy of Sciences, Wuhan 430074, China
e-mail: sunhw@wbgcas.cn

G. Li
Institute of Environmental Health and Pollution Control, School of Environmental Science and Engineering, Guangdong University of Technology, Guangzhou 510006, Guangdong, China
e-mail: ligy1999@gdut.edu.cn

T. An (✉)
The State Key Laboratory of Organic Geochemistry, Guangzhou Institute of Geochemistry, Chinese Academy of Sciences, Guangzhou 510640, China

Institute of Environmental Health and Pollution Control, School of Environmental Science and Engineering, Guangdong University of Technology, Guangzhou 510006, Guangdong, China
e-mail: antc99@gdut.edu.cn; antc99@gig.ac.cn

T. An et al. (eds.), *Advances in Photocatalytic Disinfection*, Green Chemistry and Sustainable Technology, DOI 10.1007/978-3-662-53496-0_12

the bacterial oxidative damage, especially the lethal disruption step of PC or PEC inactivation, which is essential for the development of mechanism-based PC or PEC disinfection kinetic models. Recent reports revealed that the oxidative damage of bacterial membrane structure (lipid bilayers), which is commonly recognized as the most important attack target of ROSs, however, was probably not the mortal injury to cells during PEC treatment because it happened later as compared with the inactivation behavior. It was the disruption of adenosine triphosphate (ATP) generation potential that directly causes bacterial death, because relative ATP generation rate and bacterial survival ratio coincided with each other, and ATP metabolism is crucial for cellular survival. The membrane structure destruction, represented by the oxidative damage of unsaturated fatty acids, was supposed to cause increasing membrane permeability and exposure of ATP metabolism complex to ROSs, thus promoted the bacterial inactivation.

Keywords Photocatalysis (PC) • *E. coli* • Oxidative stress • Catalase • Superoxide dismutase (SOD) • Reactive oxygen species (ROSs) • Membrane • Fatty acid • Respiration chain • Adenosine triphosphate (ATP)

12.1 Introduction

Photocatalytic (PC) technology has shown to be a promising candidate for water disinfection [1–6]. The mostly used catalyst for PC disinfection was metal oxide like TiO_2. When illuminated by UV light, TiO_2 can absorb the energy of photons to generate hole (h^+) and electron (e^-) pairs. The holes and electrons may subsequently react with water molecules or dissolved oxygen molecules through complex reactions, forming various derivatives so-called reactive oxygen species (ROSs), such as hydroxyl radical ($^{\bullet}OH$), superoxide anion ($^{\bullet}O_2^-$), singlet oxygen ($^1O_2$), and hydrogen peroxide (H_2O_2). These ROSs are highly reactive (oxidative or reductive) and therefore were believed to attack the bacterial cellular components such as the membrane, causing cellular damage and even death [7]. However, due to the highly frequent recombination of h^+ and e^- pairs, the quantum yield of traditional PC reaction was not high enough. Alternatively, photoelectrocatalytic (PEC) applies a potential bias between immobilized catalyst photoanode and counter electrode, to separate h^+/e^- pairs and suppress their recombination. As such, the bacterial inactivation performance was greatly improved by using PEC system compared with PC system [8–10].

Nevertheless, the application of PC or PEC technology in practical water disinfection is limited, and one possible reason is that the mechanisms of PC or PEC inactivation have not been well established. For instance, the contribution of various bactericides in PC and PEC inactivation systems was still controversial [11, 12]. In particular, it is important to better understand how PEC inactivation impacts the bacterial responses against oxidative stress posed by the ROSs during PC or PEC inactivation process. ROSs are inevitably by-produced through bacterial

oxygen utilization. For example, $\cdot O_2^-$ and H_2O_2 are produced by a reduced form of nicotinamide adenine dinucleotide (NADH) dehydrogenase II of the respiratory chain (Eq. 12.1), and ·OH can be formed in the presence of unincorporated ferrous iron and H_2O_2 through intracellular Fenton chemistry (Eq. 12.2) [13]. ROSs can cause oxidative stress to bacterial cells and damage several cellular sites, such as iron-sulfur clusters, protein cysteine and methionine residues, and DNA [14, 15]. In PC or PEC inactivation systems, ROSs with much higher concentration than the background level can be generated [16]. Therefore, the bacterial responses against the oxidative stress during PC or PEC treatment might be quite different. Another important aspect to understand the PC and PEC inactivation mechanism is to reveal the cellular oxidative damages caused by ROSs attack, such as the membrane disruption, cytoplasm leakage, and protein damage [17, 18]. Nevertheless, the lethal steps of PC or PEC inactivation are still not clear, which limit the development of mechanism-based PC or PEC disinfection kinetic model and subsequently the application of this disinfection technology:

$$O_2 + e^- \xrightarrow{\text{FAD}} \cdot O_2^- \tag{12.1}$$

$$\text{Fe(II)} + H_2O_2 \rightarrow \text{Fe(III)} + \cdot OH + OH^- \tag{12.2}$$

12.2 Bacterial Oxidative Stress Responses

As indicated above, the ROSs are the inevitable by-products during bacterial aerobic metabolism. Therefore, oxidative stress response systems have been necessarily developed to ensure survival under aerobic conditions [15], including a variety of antioxidant enzymes and repair enzymes, most of which are expressed at low levels during normal growth. Among which are two important bacterial antioxidative enzymes: superoxide dismutase (SOD) and catalase. SOD catalyzes the dismutation reaction of $^{\bullet}O_2^-$, forming H_2O_2 and O_2, while catalase subsequently catalyzes the further decomposition of H_2O_2 to nontoxic H_2O and O_2 [13].

There are three types of SOD available in typical Gram-negative bacteria *E. coli*, with different metal cationic centers, namely, Mn-SOD, Fe-SOD, and Cu Zn-SOD. They are encoded by different genes, namely, *sodA*, *sodB*, and *sodC*, respectively. The expression of *sodA* (Mn-SOD) is regulated by the *soxRS* transcription factor. In response to elevated $^{\bullet}O_2^-$levels, the [2Fe–2S] cluster of the dimeric transcription factor SoxR is oxidized, which activates the transcription of *soxS*. The resultant SoxS protein further activates the expression of more than 100 genes involved in oxidative stress response, including *sodA* [19]. Gene *sodC* expression is controlled by *RpoS* regulon which is related with stationary phase and general stress, but the regulation of *sodB* expression is not yet elucidated till now [13, 20]. *E. coli* also contains two kinds of catalase: hydroperoxidase I (HPI) and hydroperoxidase II (HPII), encoded by *katG* and *katE*, respectively. Elevated H_2O_2 concentration

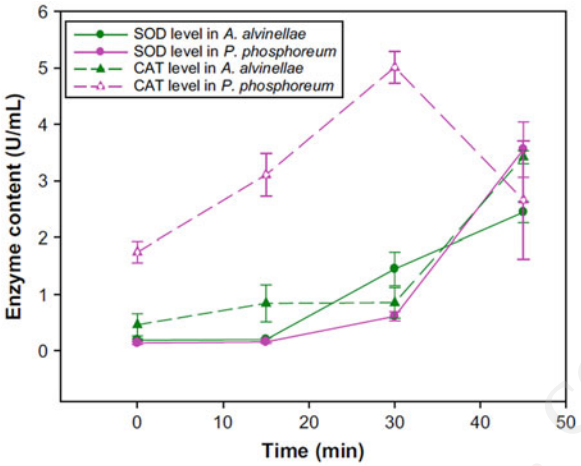

Fig. 12.1 Induction of SOD and catalase levels under PC inactivation of *A. alvinellae* and *P. phosphoreum*. Experimental conditions: TiO_2 concentration = 100 mg L^{-1}, light source (intensity) = fluorescent lamp (visible light intensity = 5.295 mW cm^{-2}), irradiation time = 45 min, agitation rate = 200 rpm, initial cell density = 3×10^7 colony-forming unit per milliliter (CFU mL^{-1}). Each data point and error bar represents means and the standard deviations, respectively, of independent triplicates (Reprinted from Ref. [22], Copyright 2008, with permission from Elsevier)

would reversibly oxidize the transcription factor OxyR protein to its active form, and oxidized OxyR activates the transcription of many genes including *katG*. Similar with *sodC*, *katE* is also regulated by *RpoS* [13, 21].

As mentioned above, SOD and catalase are inducible by ROSs such as $^{\bullet}O_2^-$ and H_2O_2. Therefore, considering the elevated ROSs levels in the PEC or PC systems, both enzymes may be important for bacterial oxidative stress responses during PEC or PC disinfection. For instance, Leung et al. reported increasing catalase and SOD activities in marine bacteria during PC inactivation (Fig. 12.1), probably indicating that the bacterial oxidative stress responses were induced by the rising ROSs levels [22].

In our recent study, the oxidative stress responses and their impact on PEC inactivation mechanism were investigated in detail, using *E. coli* BW25113 and its single-gene knockout mutants (Δ*katG* and Δ*sodA*) [23]. As Fig. 12.2 shows, compared with the parental strain BW25113, both mutants were found to be more sensitive toward PEC inactivation. For instance, after 30 min of PEC treatment, (3.43 ± 0.49) and (4.34 ± 0.34) log value of mutant Δ*katG* and Δ*sodA* survived, respectively, whereas the survived bacteria were (5.72 ± 0.24) log for the parental strain. The PEC-resistant capacity exhibited BW25113 > Δ*sodA* > Δ*katG* ($P < 0.05$, one-way ANOVA). Given that the dominant bactericide in this exact PEC inactivation system was hydrogen peroxide [16], it thus infers that catalase

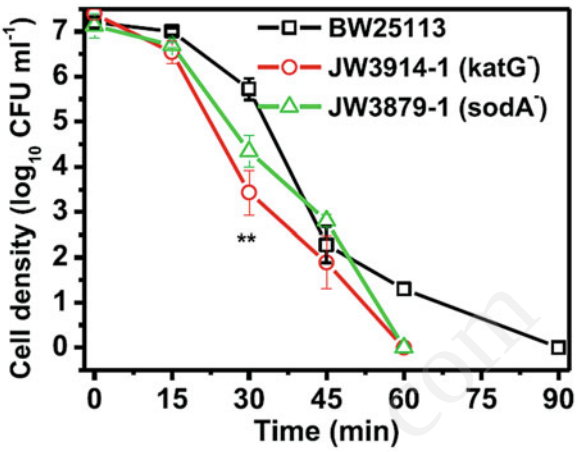

Fig. 12.2 PEC inactivation efficiency of *E. coli* BW25113 and isogenic mutants Δ*katG* and Δ*sodA* in mid-log phase. Data expressed as mean ± standard deviation (SD); bars, SD; $n = 3$. ** ($P < 0.01$) indicates the significant level determined by one-way ANOVA (Reprinted from Ref. [23], Copyright 2016, with permission from Elsevier)

activity plays an important role in the bacterial oxidative stress responses against PEC inactivation.

To collect more information of bacterial anti-oxidative enzymes defending PEC inactivation, the enzymatic activities and PEC inactivation susceptibility of bacteria in different growing stages were further investigated. It was found that bacteria in mid-log phase possessed the highest catalase as well as SOD activity and correspondingly the lowest susceptibility toward PEC inactivation (Ref. [23], data not shown here). Given that the bacterial catalase activity can be induced by rising H_2O_2 concentration, the H_2O_2 pretreatment was conducted before the bacteria samples were subjected to PEC inactivation, and the catalase levels and PEC inactivation efficiencies before and after pretreatment with various doses of hydrogen peroxide were monitored. As shown in Fig. 12.3a, the catalase level of *E. coli* BW25113 raised steadily with H_2O_2 concentration used for preincubation, but Δ*katG* mutant did not show any increase of catalase, demonstrating that *katG* was H_2O_2 inducible and *katE* was H_2O_2 independent. For the PEC inactivation performance after preincubation, the resistance to PEC inactivation increased for BW25113 (Fig. 12.3b) but was not the case for Δ*katG* mutant (Fig. 12.3c). It was found that the shoulder length of the inactivation curves after fitted with GInaFIT disinfection models was positively correlated with the catalase level (Ref. [23], data not shown). Therefore, low doses of hydrogen peroxide could induce the elevated catalase activity and subsequently the enhanced bacterial resistance to PEC inactivation.

The intracellular ROS level and catalase activity changes during the PEC inactivation process were also monitored to find the internal oxidative stress and bacterial responses, and the results are shown in Fig. 12.4. As the figure shows, the intracellular ROS level (monitored by the fluorescent intensity of the probe DCFH-

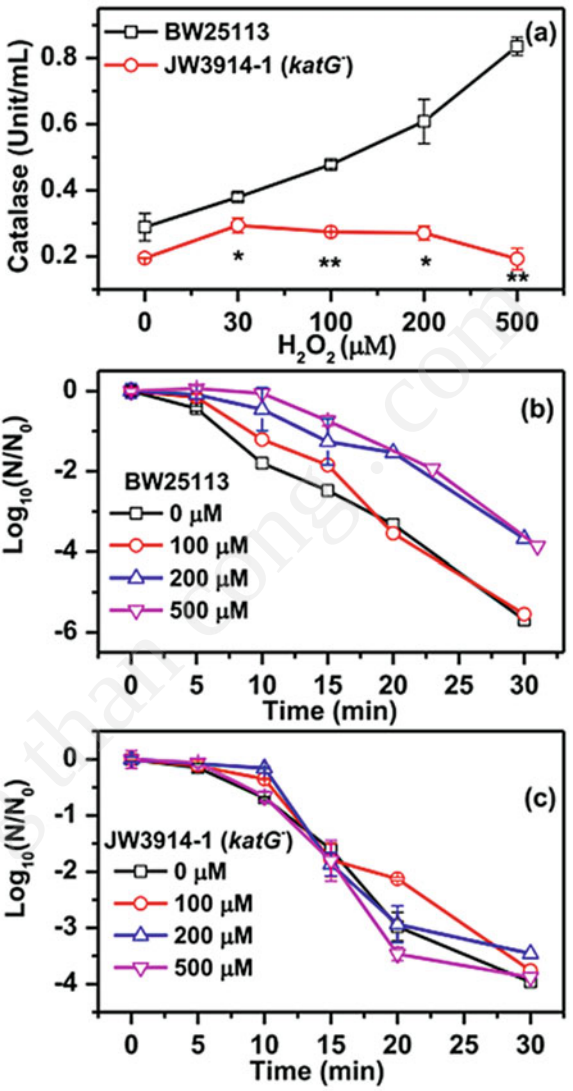

Fig. 12.3 (**a**) Catalase activity of *E. coli* after preincubation with various H_2O_2 levels; PEC inactivation performance with H_2O_2 preincubated (**b**) BW25113 strain and (**c**) Δ*katG* strain. Data expressed as mean ± standard deviation (SD); bars, SD; $n = 3$. *($P < 0.05$) and **($P < 0.01$) indicate the significant levels determined by Student's *t* test (Reprinted from Ref. [23], Copyright 2016, with permission from Elsevier)

DA) quickly rose up in the initial 30 min and fell down thereafter. The initial increase trend was similar with the extracellular H_2O_2 concentration, indicating that the intracellular ROSs originated from the diffuse of outer ROSs [24]. The fluorescent decrease after PEC 30 min treatment may be explained by the leakage of endogenous fluorescence due to the damaged membrane [25]. However, the bacterial catalase and SOD activities were found to decrease gradually, and no increase

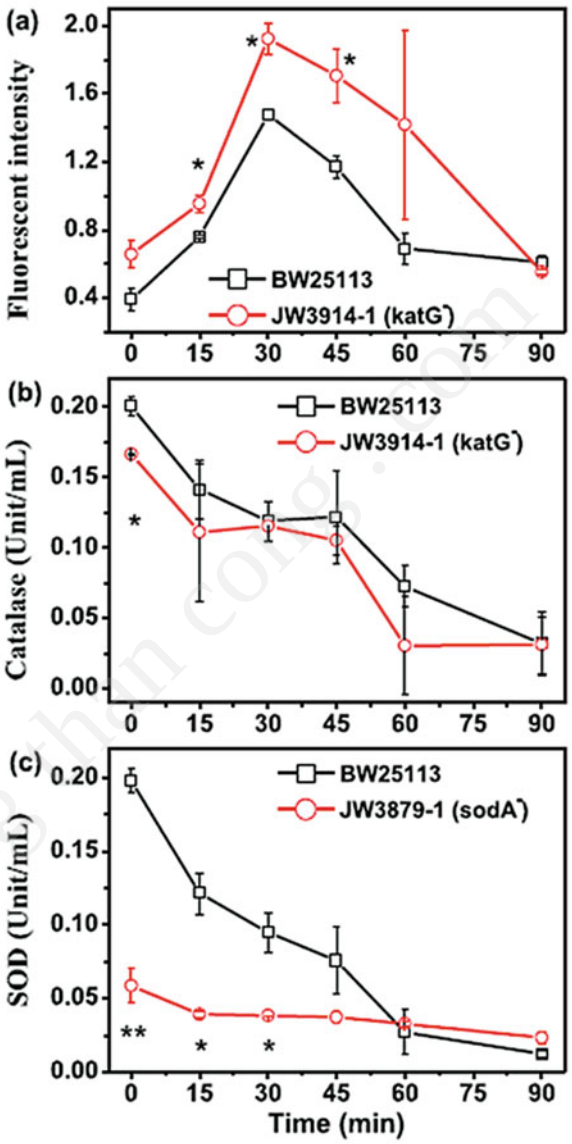

Fig. 12.4 (**a**) Intracellular ROS level tested by DCFH-DA, (**b**) catalase activity, and (**c**) SOD activity of three *E. coli* strains during PEC inactivation process. Data expressed as mean ± standard deviation (SD); bars, SD; $n = 3$. * ($P < 0.05$) and ** ($P < 0.01$) indicate the significant levels determined by Student's *t* test (Reprinted from Ref. [23], Copyright 2016, with permission from Elsevier)

was observed during the whole PEC inactivation process (Fig. 12.4b, c), suggesting that these anti-oxidative enzymes were not induced. The reason causing this may be that the ROS level in the PEC system elevated too quickly, and it would be too stressed for bacterial anti-oxidative responses.

12.3 Bacterial Oxidative Damage and Lethal Step During PC or PEC Inactivation

The above discussion showed that the ROS level in PC or PEC inactivation systems can increase very quickly, which would generally cause oxidative damages to bacterial cells, especially in the case of PEC inactivation where bacterial oxidative stress responses fail to be induced [23]. Various cellular components including the membrane [26], cell wall [27], proteins [18], and DNA [28] can be attacked by ROSs. Among these sites, the membrane was considered to be the most easily attacked component because it was located at the outer layer of bacterial cells (especially the Gram-negative bacteria) and thus was exposed to ROSs more directly than other sites. Furthermore, the membrane itself is more sensitive to oxidative stress than other sites such as the cell wall through pathways such as lipid peroxidation [29].

To investigate the bacterial membrane oxidative damage during PEC inactivation process, *E. coli* BW25113 and its single-gene knockout mutants Δ*fabR* and Δ*fabH* were used in our recent published study [30]. Both *fabR* and *fabH* genes are important in bacterial fatty acid biosynthesis, and both mutants were reported to possess higher proportions of unsaturated fatty acid content as compared with their parental strain [31–33]. Two concentration levels of bacterial suspension, namely, 2×10^7 and 2×10^8 CFU mL^{-1}, were subjected to PEC inactivation, and the bacterial inactivation performance of three strains is shown in Fig. 12.5. For bacterial suspension of 2×10^7 CFU mL^{-1} (Fig. 12.5a), the parental strain BW25113 showed lower inactivation efficiency as compared with the two mutants, with a shoulder region at the initial stage. Inactivation performance of the three strains showed similar trends when using bacterial suspension of 2×10^8 CFU mL^{-1}, apart from that it consumed longer time to achieve complete inactivation (~45 min for lower concentration and ~1.5 h for higher concentration). The bacterial fatty acid profiles before and after PEC inactivation were also analyzed, and the results shown in Table 12.1. In the intact BW25113 cells, palmitic acid (16:0) was the dominant congener (45.6 %), followed by hexadecenoic acid (16:1, 12.1 %) and octadecenoic acid (18:1, 22.9 %), which was a typical fatty acid profile of *E. coli* [29, 33]. As expected, the mutants displayed decreased proportions of saturated fatty acid and elevated unsaturated fractions, consistent with the gene function of *fabR* and *fabH*. As known, fatty acid is the major composite of phospholipid bilayer and lipopolysaccharide in the bacterial membrane. The phospholipid buildup with saturated fatty acids was less fluid and more viscous than those consisted of unsaturated fatty acids and therefore showed stronger tolerance to oxidative stress [34]. Therefore, it is reasonable that BW25113 with higher saturated fatty acid fractions was more recalcitrant to PEC treatment. Such phenomenon was also observed by other reports of PC inactivation investigations [22, 35]. This can also be further confirmed by the fatty acid profile changes after PEC inactivation (Table 12.1). As seen, the bacterial unsaturated fatty acid proportions decreased for all three strains after PEC inactivation, especially for the

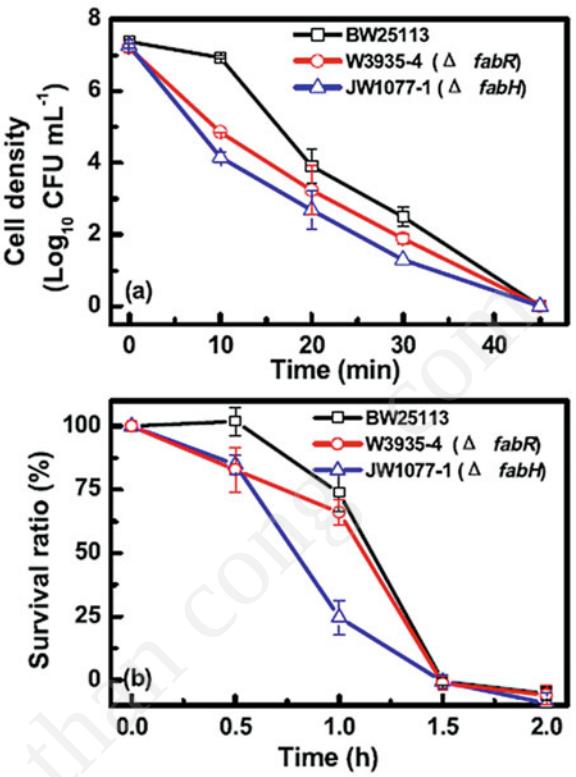

Fig. 12.5 The PEC inactivation performances of parental strain *E. coli* BW25113 and isogenic mutants deficient in fatty acid biosynthesis (*E. coli* JW3935-4 and *E. coli* JW1077-1). (**a**) The initial bacterial density of the suspension is ~2×10^7 CFU mL^{-1}, and the survived bacteria determined by the colony counting method. (**b**) The initial bacterial density of the suspension is ~2×10^8 CFU mL^{-1}, and the cell viability determined by Live/Dead fluorescent kit (Reprinted from Ref. [30], Copyright 2016, with permission from Elsevier)

Table 12.1 The bacterial fatty acid profile of parental strain *E. coli* BW25113 and isogenic single-gene deleted mutants deficient in fatty acid biosynthesis (*E. coli* JW3935-4 and *E. coli* JW1077-1) before and after PEC inactivation (2×10^8 CFU mL^{-1})

	Percentage (%)								
	BW25113			JW3935-4 (Δ*fabR*)			JW1077-1 (Δ*fabH*)		
Fatty acid	0 h	1 h	2 h	0 h	1 h	2 h	0 h	1 h	2 h
12:0	2.8 ± 0.3	2.2	2.2	3.2 ± 0.03	1.9	2.6	3.3 ± 0.5	1.9	2.6
14:0	9.3 ± 1.0	7.9	7.9	10.4 ± 0.5	7.4	8.5	9.7 ± 0.7	7.6	8.0
16:0	45.6 ± 0.6	54.0	56.1	37.6 ± 3.2	48.5	54.3	38.5 ± 2.0	46.6	48.8
18:0	7.3 ± 5.4	6.4	6.8	2.9 ± 0.3	6.2	5.9	2.9 ± 0.3	5.2	5.7
16:1[a]	12.1 ± 1.6	8.1	7.6	18.3 ± 1.5	7.6	7.6	19.1 ± 1.6	13.4	10.6
18:1[b]	22.9 ± 3.0	21.3	19.3	27.6 ± 2.5	28.5	21.1	26.6 ± 1.8	25.4	24.3
Saturated	65.0 ± 4.6	70.7	73.1	54.1 ± 4.0	63.9	71.3	54.3 ± 3.4	61.2	65.1
Unsaturated	35.0 ± 4.6	29.3	26.9	45.9 ± 4.0	36.1	28.7	45.7 ± 3.4	38.8	34.9

Reprinted from Ref. [30], Copyright 2016, with permission from Elsevier
[a]The sum of monounsaturated fatty acid with 16 carbons
[b]the sum of monounsaturated fatty acid with 18 carbons

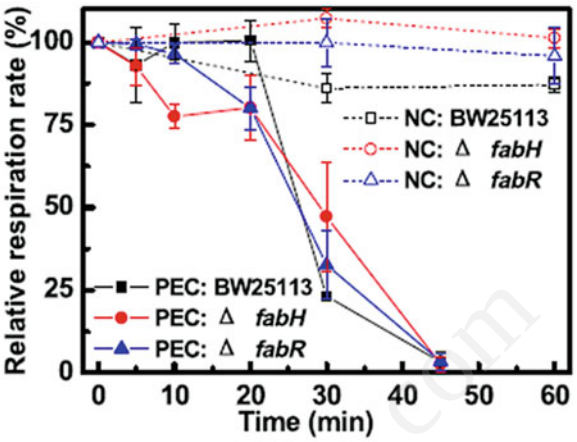

Fig. 12.6 The bacterial respiration rate assays of parental strain *E. coli* BW25113 and two isogenic mutants (Δ*fabR* and Δ*fabH*) during PEC inactivation (~2×10^8 CFU mL^{-1}). NC: negative control (Reprinted from Ref. [30], Copyright 2016, with permission from Elsevier)

mutants with higher initial unsaturated fatty acid fraction. Meanwhile, the mutants also showed faster loss of membrane integrity than the parental strain, as demonstrated by the cytoplasmic K^+ leakage assay, the Live/Dead BacLight™ fluorescent staining test, and the SEM images of bacterial cells during PEC processes [30] (data not shown). In addition, this observation may also indicate that fatty acid was an important target for ROS attack during PC and PEC inactivation process.

However, the oxidative damage of membrane structure generally occurred much later compared with the bacterial inactivation. This might imply that the membrane structural damage is not the lethal step of PEC inactivation. Apart from the membrane framework such as the phospholipid bilayer, various membrane-associated proteins are also exposed to ROS attack during PEC inactivation process [36, 37]. Important among them is the bacterial respiratory chain, which is consisted of various enzymes, flavoproteins, iron-sulfur proteins, and cytochromes [38]. Respiration is an essential pathway of energy production especially for aerobic bacteria, and the energy released during this process is finally stored in the form of adenosine triphosphate (ATP). Therefore, the bacterial respiration rates were monitored during PEC treatment process (Fig. 12.6). As illustrated, the respiration rate of all three strains (parental BW25113; two mutants: Δ*fabR* and Δ*fabH*) showed a shoulder stage within the initial 20 min and decreased sharply thereafter, which fully faded out after 45 min of PEC inactivation. When comparing the respiration rate decrease with the bacterial inactivation rate under identical bacterial concentration (~2×10^8 CFU mL^{-1}, Fig. 12.5b), it was obvious that the respiration rate decreased far more quickly than bacterial inactivation, which is similar with Bosshard's observation in the case of solar disinfection [39]. This suggested that the loss of respiration activity caused injury but not inactivation to the bacteria. Therefore, the damage of bacterial respiratory chain was not the mortal step either, perhaps because *E. coli* can produce energy through other pathways than aerobic respiration, such as the fermentation via substrate level phosphorylation [40].

Table 12.2 The ATP generation rate of parental strain *E. coli* BW25113 and its isogenic mutants after PEC inactivation with different treatment times

	$\Delta ATP/\Delta t$ (10^{-7}pmol min^{-1} per cell)			Percentage (%)		
PEC time (min)	BW25113	JW3935-4	JW1077-1	BW25113	JW3935-4	JW1077-1
0	0.62	0.92	0.74	100.0	100.00	100.00
2.5	–	0.88	0.75	–	95.56	100.38
5	0.54	0.81	0.04	87.3	87.81	4.82
7.5	–	0.35	0.00	–	38.21	0.00
10	0.20	0.04	0.00	32.7	4.40	0.00
15	−0.01	0.00	0.00	−1.4	0.00	0.00
20	0.00	0.00	0.00	0.6	0.00	0.00
25	0.01	–	–	1.5	–	–
30	0.01	–	–	1.9	–	–

Reprinted from Ref. [30], Copyright 2016, with permission from Elsevier

To elucidate the lethal damage to bacterial cells by PEC treatment, the bacterial ATP generation potential changes were further investigated, and the results are listed in Table 12.2. Obviously, the cellular ATP generation rates for all three strains were found to decrease rather quickly during PEC inactivation. Interestingly, the loss of ATP generation potential coincided with the bacterial survival ratio (Fig. 12.5a). For instance, in terms of BW25113, the relative ATP generation rate was 32.7 % at 10 min and 0 % at 15 min, and the survival ratio was 35.3 % and ~1 % correspondingly. Similar trends were also observed for the mutants of Δ*fabR* and Δ*fabH*. Thus, it was sensible to infer that the loss of ATP generation capacity was the direct cause of the bacterial inactivation. Complete loss of ATP synthesis capacity would mean that all the energy metabolism pathways were completely blocked, which was necessary for the repair of cellular damages and bacterial growth. For example, ATP was necessary to maintain the membrane potential and Na^+-K^+ ATPase activity, but the lack of ATP would cause the leakage of cytoplasmic K^+ [16, 37]. On the other hand, membrane lipid bilayer damage was supposed to increase the cell permeability and subsequently higher exposure probability of ATP synthesis complex to ROS attack, as proved by the different performance of the mutants and the parental strain.

12.4 Conclusions

ROSs generated during PC or PEC inactivation were able to cause oxidative stress and damage to bacterial cells. Correspondingly, bacterial oxidative stress responses can be induced, such as elevated catalase or SOD activity. Particularly, in PEC inactivation process where H_2O_2 was identified as the dominant bactericide, catalase level was found to contribute greatly to bacterial PEC tolerance. However, both catalase and SOD failed to be induced by the elevated ROS concentrations in PEC

inactivation process, but showed a quick decrease in enzymatic activity. This may be attributed to the ROS level in PEC system overwhelmed by the bacterial anti-oxidative response capacity. Among all the oxidative damage of bacterial cells caused by ROSs, the disruption of bacterial energy metabolism system was the lethal step for bacteria during PEC inactivation, particularly the loss of ATP generation potential. Other damages caused by PEC treatment including the loss of membrane integrity and increased permeability and unsaturated fatty acids were demonstrated to be an important target of ROS attack.

Acknowledgments This work was financially supported by the National Natural Science Funds for Distinguished Young Scholars (41425015), National Natural Science Foundation of China (41573086 and 21077104), Australian Research Council (ARC) Discovery Project, and Research Grant Council, Hong Kong SAR Government (GRF476811).

References

1. Shi H, Huang G, Xia D, Ng TW, Yip HY, Li G, An T, Zhao H, Wong P (2015) Role of in situ resultant H_2O_2 in the visible-light-driven photocatalytic inactivation of *E. coli* using natural sphalerite: a genetic study. J Phys Chem B 119(7):3104–3111
2. Foster HA, Ditta IB, Varghese S, Steele A (2011) Photocatalytic disinfection using titanium dioxide: spectrum and mechanism of antimicrobial activity. Appl Microbiol Biotechnol 90 (6):1847–1868
3. Rincon AG, Pulgarin C (2007) Fe^{3+} and TiO_2 solar-light-assisted inactivation of *E-coli* at field scale – Implications in solar disinfection at low temperature of large quantities of water. Catal Today 122(1–2):128–136
4. Wang WJ, Yu Y, An TC, Li GY, Yip HY, Yu JC, Wong PK (2012) Visible-light-driven photocatalytic inactivation of *E. coli* K-12 by bismuth vanadate nanotubes: bactericidal performance and mechanism. Environ Sci Technol 46(8):4599–4606
5. Dalrymple OK, Stefanakos E, Trotz MA, Goswami DY (2010) A review of the mechanisms and modeling of photocatalytic disinfection. Appl Catal B Environ 98(1–2):27–38
6. Gao P, Liu J, Sun DD, Ng W (2013) Graphene oxide-CdS composite with high photocatalytic degradation and disinfection activities under visible light irradiation. J Hazard Mater 250:412–420
7. Robertson PKJ, Robertson JMC, Bahnemann DW (2012) Removal of microorganisms and their chemical metabolites from water using semiconductor photocatalysis. J Hazard Mater 211:161–171
8. Li GY, Liu XL, An TC, Yang H, Zhang SQ, Zhao HJ (2015) Photocatalytic and photoelectrocatalytic degradation of small biological compounds at TiO_2 photoanode: a case study of nucleotide bases. Catal Today 242:363–371
9. Li GY, Liu XL, Zhang HM, An TC, Zhang SQ, Carroll AR, Zhao HJ (2011) In situ photoelectrocatalytic generation of bactericide for instant inactivation and rapid decomposition of Gram-negative bacteria. J Catal 277(1):88–94
10. Baram N, Starosvetsky D, Starosvetsky J, Epshtein M, Armon R, Ein-Eli Y (2007) Enhanced photo-efficiency of immobilized TiO_2 catalyst via intense anodic bias. Electrochem Commun 9(7):1684–1688
11. Cho M, Chung HM, Choi WY, Yoon JY (2005) Different inactivation behaviors of MS-2 phage and *Escherichia coli* in TiO_2 photocatalytic disinfection. Appl Environ Microbiol 71 (1):270–275

12. Kikuchi Y, Sunada K, Iyoda T, Hashimoto K, Fujishima A (1997) Photocatalytic bactericidal effect of TiO_2 thin films: dynamic view of the active oxygen species responsible for the effect. J Photochem Photobiol A Chem 106(1–3):51–56
13. Chiang SM, Schellhorn HE (2012) Regulators of oxidative stress response genes in *Escherichia coli* and their functional conservation in bacteria. Arch Biochem Biophys 525 (2):161–169
14. Dalle-Donne I, Rossi R, Giustarini D, Milzani A, Colombo R (2003) Protein carbonyl groups as biomarkers of oxidative stress. Clin Chim Acta 329(1–2):23–38
15. Storz G, Imlayt JA (1999) Oxidative stress. Curr Opin Microbiol 2(2):188–194
16. Sun HW, Li GY, Nie X, Shi HX, Wong PK, Zhao HJ, An TC (2014) Systematic approach to in-depth understanding of photoelectrocatalytic bacterial inactivation mechanisms by tracking the decomposed building blocks. Environ Sci Technol 48(16):9412–9419
17. Nie X, Li GY, Gao MH, Sun HW, Liu XL, Zhao HJ, Wong PK, An TC (2014) Comparative study on the photoelectrocatalytic inactivation of *Escherichia coli* K-12 and its mutant *Escherichia coli* BW25113 using TiO_2 nanotubes as a photoanode. Appl Catal B Environ 147:562–570
18. Carre G, Hamon E, Ennahar S, Estner M, Lett MC, Horvatovich P, Gies JP, Keller V, Keller N, Andre P (2014) TiO_2 photocatalysis damages lipids and proteins in *Escherichia coli*. Appl Environ Microbiol 80(8):2573–2581
19. Gu MZ, Imlay JA (2011) The SoxRS response of *Escherichia coli* is directly activated by redox-cycling drugs rather than by superoxide. Mol Microbiol 79(5):1136–1150
20. Storz G, Tartaglia LA, Farr SB, Ames BN (1990) Bacterial defenses against oxidative stress. Trends Genet 6(11):363–368
21. Mukhopadhyay S, Schellhorn HE (1994) Induction of *Escherichia-coli* hydroperoxidase-i by acetate and other weak acids. J Bacteriol 176(8):2300–2307
22. Leung TY, Chan CY, Hu C, Yu JC, Wong PK (2008) Photocatalytic disinfection of marine bacteria using fluorescent light. Water Res 42(19):4827–4837
23. Sun HW, Li GY, An TC, Zhao HJ, Wong PK (2016) Unveiling the photoelectrocatalytic inactivation mechanism of *Escherichia coli*: Convincing evidence from responses of parent and anti-oxidation single gene knockout mutants. Water Res 88:135–143
24. Vatansever F, de Melo WC, Avci P, Vecchio D, Sadasivam M, Gupta A, Chandran R, Karimi M, Parizotto NA, Yin R, Tegos GP, Hamblin MR (2013) Antimicrobial strategies centered around reactive oxygen species – bactericidal antibiotics, photodynamic therapy, and beyond. FEMS Microbiol Rev 37(6):955–989
25. Rohnstock A, Lehmann L (2007) Evaluation of the probe dihydrocalcein acetoxymethylester as an indicator of reactive oxygen species formation and comparison with oxidative DNA base modification determined by modified alkaline elution technique. Toxicol in Vitro 21 (8):1552–1562
26. Shi HX, Li GY, Sun HW, An TC, Zhao HJ, Wong PK (2014) Visible-light-driven photocatalytic inactivation of *E. coli* by Ag/AgX-CNTs (X = Cl, Br, I) plasmonic photocatalysts: bacterial performance and deactivation mechanism. Appl Catal B Environ 158–159:301–307
27. Malato S, Fernandez-Ibanez P, Maldonado MI, Blanco J, Gernjak W (2009) Decontamination and disinfection of water by solar photocatalysis: recent overview and trends. Catal Today 147 (1):1–59
28. Gogniat G, Dukan S (2007) TiO_2 photocatalysis causes DNA damage via fenton reaction-generated hydroxyl radicals during the recovery period. Appl Environ Microbiol 73 (23):7740–7743
29. Dalrymple OK, Isaacs W, Stefanakos E, Trotz MA, Goswami DY (2011) Lipid vesicles as model membranes in photocatalytic disinfection studies. J Photochem Photobiol A Chem 221 (1):64–70

30. An TC, Sun HW, Li GY, Zhao HJ, Wong PK (2016) Differences in photoelectrocatalytic inactivation processes between *E. coli* and its isogenic single gene knockoff mutants: destruction of membrane framework or associated proteins? Appl Catal B Environ 188:360–366
31. Zhang Y-M, Marrakchi H, Rock CO (2002) The FabR (YijC) transcription factor regulates unsaturated fatty acid biosynthesis in *Escherichia coli*. J Biol Chem 277(18):15558–15565
32. Lai CY, Cronan JE (2003) Beta-ketoacyl-acyl carrier protein synthase III (FabH) is essential for bacterial fatty acid synthesis. J Biol Chem 278(51):51494–51503
33. Tsay JT, Oh W, Larson TJ, Jackowski S, Rock CO (1992) Isolation and characterization of the beta-ketoacyl-acyl carrier protein synthase III gene (fabH) from *Escherichia coli* K-12. J Biol Chem 267(10):6807–6814
34. Trauble H, Overath P (1973) The structure of *Escherichia coli* membranes studied by fluorescence measurements of lipid phase transitions. Biochim Biophys Acta 307(3):491–512
35. Gao MH, An TC, Li GY, Nie X, Yip HY, Zhao H, Wong PK (2012) Genetic studies of the role of fatty acid and coenzyme A in photocatalytic inactivation of *Escherichia coli*. Water Res 46 (13):3951–3957
36. Berney M, Weilenmann HU, Egli T (2006) Flow-cytometric study of vital cellular functions in *Escherichia coli* during solar disinfection (SODIS). Microbiology 152(6):1719–1729
37. Bosshard F, Berney M, Scheifele M, Weilenmann HU, Egli T (2009) Solar disinfection (SODIS) and subsequent dark storage of *Salmonella typhimurium* and *Shigella flexneri* monitored by flow cytometry. Microbiol-Sgm 155:1310–1317
38. Stansfield WD (ed) (1996) Schaum's outline of theory and problems of molecular and cell biology. McGraw-Hill Companies, Inc., New York
39. Bosshard F, Bucheli M, Meur Y, Egli T (2010) The respiratory chain is the cell's Achilles' heel during UVA inactivation in *Escherichia coli*. Microbiology 156(7):2006–2015
40. Clark DP (1989) The fermentation pathways of *Escherichia coli*. FEMS Microbiol Rev 5 (3):223–234

Chapter 13
Mechanistic Modeling of Photocatalytic Water Disinfection

O. Kofi Dalrymple and D. Yogi Goswami

Abstract In this chapter, conceptual and mechanistic models for water disinfection are discussed. The goal is to describe fundamental interactions between microbial cells and TiO_2 catalyst suspensions, and the light-induced chemical species that ultimately lead to cell inactivation. A number of disinfection models have been developed to address the kinetics of these interactions and they are examined here. In general, photocatalytic disinfection data has been fitted to many empirical models. However, frequent deviations from such models have been widely reported. Although empirical models can be very useful, they do not allow designers to explicitly determine the overall influence of important parameters such as catalyst concentration, light intensity, ionic strength, and pH on the disinfection process. It is difficult to account for many of the complex interactions that occur during photocatalytic inactivation without over-fitting data with numerous parameters. A major benefit of a mechanistic model is the significant cost reduction associated with performing fewer preliminary experiments to determine the effectiveness of various factors. These may include, for example, catalyst concentration and light intensity for a given organism.

In our own work, we have proposed a model that is consistent with processes involving the attachment of titanium dioxide (TiO_2) nanoparticles to the bacterial cell surface, the adsorption of inorganic salts to the TiO_2 surface (inhibition phenomena), light propagation through the suspension, the quantum yield of hydroxyl radical generation, and cell surface oxidation. Unknown inactivation kinetic parameters were derived from the fits of experimental data. The good fit of the model to the experimental results indicates that high levels of inactivation can be achieved by maintaining a relatively low catalyst-to-microbe ratio while maximizing the light intensity at low to moderate ionic strength. These results and others from literature suggest that mechanistic modeling of photocatalytic disinfection should allow for predictive capability of this important process.

O.K. Dalrymple
Algenol Biotech, Fort Myers, FL, USA

D.Y. Goswami (✉)
Clean Energy Research Center, University of South Florida, Tampa, FL, USA
e-mail: goswami@usf.edu

T. An et al. (eds.), *Advances in Photocatalytic Disinfection*, Green Chemistry and Sustainable Technology, DOI 10.1007/978-3-662-53496-0_13

Keywords DLVO • Colloid stability • Electrophoresis • Photocatalysis • Zeta potential

13.1 Introduction

It is well known that illuminated suspensions of titanium dioxide (TiO_2) particles produce hydroxyl radicals and other reactive oxygen species capable of degrading cellular biomolecules. In these suspensions, the size of TiO_2 can range from a few nanometers to hundreds of nanometers, particularly when aggregated [1–3]. On the other hand, cells may be a few microns large and assume a variety of shapes. These size relationships tend to make modeling photocatalytic disinfection particularly challenging. Overall, it involves a complex set of processes including light absorption and scattering by semiconductor particles, electrochemical surface reactions, microbe-semiconductor particle interactions, and the oxidation of biomolecules. The modeling of these processes is important to establish the process kinetics for photocatalytic disinfection. Current models, based largely on chemical reacting systems, do not adequately account for most of these mechanisms [4]. Even the Langmuir model developed for heterogeneous systems cannot describe the interactions of such large colloidal particles [5–7]. As a result, it is difficult to assess the combined effects of many important factors, which go into the design of a photocatalytic disinfection system. In this chapter we will describe these processes and associated models.

13.2 Microbe-Catalyst Interactions

For photocatalytic disinfection to occur, microbes must be in close proximity or make contact with the surface of the semiconductor to allow for the exchange of electrons (or light-induced oxidants) and subsequent chemical reactions. Although TiO_2 has been studied extensively to disinfect microorganisms, most of what is known about microbe-catalyst interactions in aqueous suspensions is qualitative. No study has quantitatively assessed the significance of these interactions on the disinfection process. The important concepts related to microbe-catalyst interactions are discussed in this section. While *E. coli* is used as the model organism in this discussion, similar principles still apply to other microbes of similar size.

13.2.1 Catalyst Surface Electrochemistry

The surface of a metal oxide particle in an electrolyte solution is almost always electrically charged. Upon exposure to water, there is a spontaneous formation of an

adsorbed water layer of oriented water dipoles [8, 9]. The terminal oxygen atoms at the surface react with water to produce hydroxylated sites (Fig. 13.1), which are involved in proton exchange reactions imparting a pH-dependent surface charge [10–12]. In the case of TiO_2, the hydroxyl groups on the surface are known to undergo the following acid-base reactions [13]:

$$\equiv \mathrm{TiOH}_2^+ \overset{K_{a1}^S}{\leftrightarrow} \equiv \mathrm{TiOH} + \mathrm{H}^+ \tag{13.1}$$

$$\equiv \mathrm{TiOH} \overset{K_{a2}^S}{\leftrightarrow} \equiv \mathrm{TiO}^- + \mathrm{H}^+ \tag{13.2}$$

where K_{a1}^S and K_{a2}^S are the surface acidity constants, which are related to the acidity constant in the bulk solution as [13, 14]

$$K_{a1}^S = K_{a1}^{\mathrm{bulk}} \left(\frac{e\psi_0}{k_B T} \right) \tag{13.3}$$

$$K_{a2}^S = K_{a2}^{\mathrm{bulk}} \left(\frac{e\psi_0}{k_B T} \right) \tag{13.4}$$

where ψ_0 is the surface potential, e is the electron charge, k_B is the Boltzmann constant, and T is the absolute temperature. The pH dependence of the dominant surface species for TiO_2 is shown in Fig. 13.2. The surface is known to have a net surface charge of zero close to pH 6 when the neutral TiOH species covers most of the surface sites [15–17].

The adsorption of organic molecules or surface-active ions may also occur at the surface. The distribution of the electrolyte ions at the interface and the electric potential play a key role in the stability of catalyst suspensions during photocatalysis [1, 19–21], as well as their post-treatment recovery [3, 22].

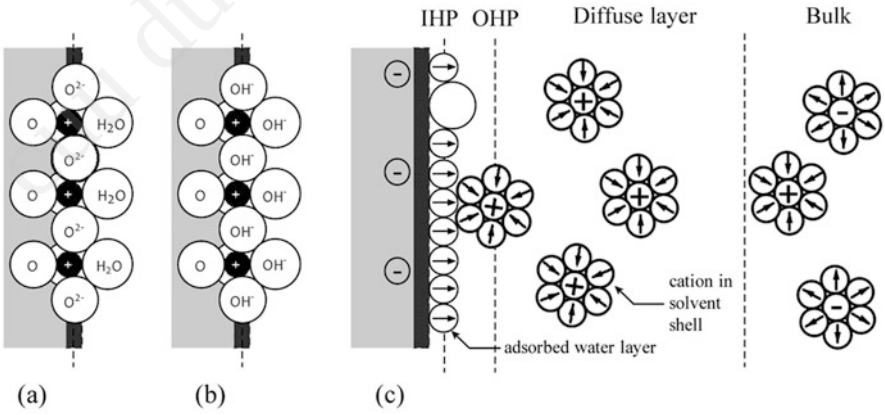

Fig. 13.1 TiO_2 surface in water: (**a**) water layer [10]; (**b**) hydroxylated surface [10]; and (**c**) schematic of double layer according to Stern-Grahame model [18]

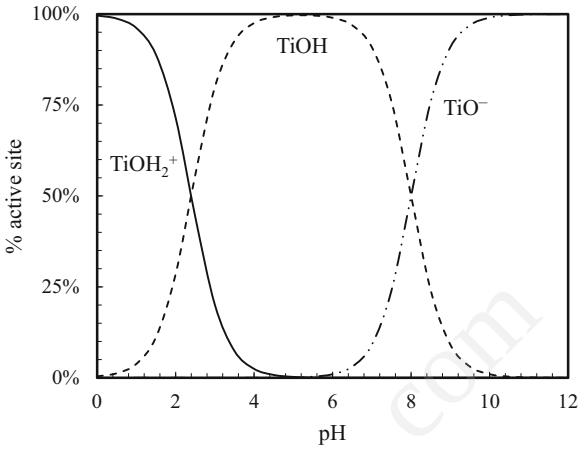

Fig. 13.2 Surface hydroxylated species of TiO_2 a function of pH calculated according to Eqs. (13.1) and (13.2) using $pK_{a1}^{S} = 2.4$ and $pK_{a2}^{S} = 8$ as determined by Korman et al. [17] for Degussa P25 at 25 °C

Figure 13.1 schematically shows the electric double layer at the TiO_2 surface in contact with a solution according to the Stern-Grahame model [23, 24]. Species are attracted to localized surface sites via electrostatic or hydrophobic effects and displace the primary adsorbed water layer, becoming specifically adsorbed on the oxide surface [25–27]. This type of short-range interaction is generally called specific adsorption, and the ions lose a portion of their hydration shell to become part of the monolayer at the surface. This is particularly the case for anions, since the hydration energies are generally higher for cations [28]. The specific adsorption of chloride, sulfate, and phosphate ions has been observed on the surface of TiO_2 [29, 30]. The plane of mean charge of the specifically adsorbed ions defines the inner Helmholtz layer (IHL). The amount of specifically adsorbed charge per unit area σ_{ads} can be expressed using a modified Langmuir isotherm [13]:

$$\sigma_{ads} = \frac{zeCN_{ads}\exp\left(-\frac{\Delta G_{ads}}{k_B T}\right)}{1+\exp\left(-\frac{\Delta G_{ads}}{k_B T}\right)} \tag{13.5}$$

in which ΔG_{ads} is the Gibbs energy of adsorption per molecule according to

$$\Delta G_{ads} = ze\psi_0 + \Delta G_{spec} \tag{13.6}$$

where $ze\psi_0$ represents the electrostatic interaction energy and ΔG_{spec} is the Gibbs energy of specific interaction. N_{ads} is the number of adsorption sites per unit area. C and z are the bulk concentration and the valence of specifically adsorbing ions, respectively.

Some ions are adsorbed to the surface through long-range Coulombic interactions. They tend to retain their hydration layer and are therefore restricted in their

approach to the surface. The mean geometric location of their charge centers defines the outer Helmholtz layer (OHL). The IHL and OHL together constitute the Stern layer. Beyond this region lies the so-called diffuse layer in which ions are fully mobile, and whose spacing from one another is a function of the total ionic concentration in bulk solution. The concentration of ions in this layer is governed by the need to maintain overall charge neutrality, including those species adsorbed at the surface of the metal oxide. The concentration of ions (C_i) in the diffuse layer is described by the Boltzmann distribution:

$$C_i(x) = C_i^{\text{bulk}} \exp\left(-\frac{z_i e\psi(x)}{kT}\right) \tag{13.7}$$

where C_i^{bulk} is the concentration in the bulk solution. The Poisson distribution gives the electrostatic potential of the double layer as

$$\nabla^2\psi = -\frac{\rho_e}{\varepsilon} \tag{13.8}$$

where ρ_e is the charge density given as

$$\rho_e = \sum_{i=1}^{N} C_i z_i e \tag{13.9}$$

and ε is the dielectric permittivity of the solution. Using Eqs. (13.8) and (13.9), the Poisson-Boltzmann equation for the electric potential profile is derived as

$$\nabla^2\psi = -\frac{e}{\varepsilon}\sum_{i=1}^{N} C_i^{\text{bulk}} z_i \exp\left(-\frac{z_i e\psi}{kT}\right) \tag{13.10}$$

Equation (13.10) is restricted to low electrolyte solutions because the ions are treated as point charges. Using the Debye-Huckel approximation for low potential, i.e., $ze\psi \ll kT$, the electric potential profile is given as

$$\nabla^2\psi = \kappa^2\psi \tag{13.11}$$

where κ is the Debye-Huckel parameter and is given by

$$\kappa = \sqrt{\frac{e^2}{\varepsilon kT}\sum_{i=1}^{N} C_i^{\text{bulk}} z_i{}^2}. \tag{13.12}$$

The solution for Eq. (13.11) for a double layer around a spherical particle of radius a is given as [5]

$$\psi = \psi_d \frac{a}{x} \exp(-\kappa(x - a)) \tag{13.13}$$

in which the potential ψ_d is the potential difference across the diffuse part of the double layer, which is related to the charge density σ_d in the double layer through

$$\sigma_d = \varepsilon \frac{1 + \kappa a}{a} \psi_d \tag{13.14}$$

The total surface charge Q_e is given as

$$Q_e = 4\pi\varepsilon a(1 + \kappa a)\psi_d \tag{13.15}$$

The total surface charge and electrostatic potential of the surface are determining factors for behavior of the colloids in suspension. Particles of similar charge tend to be stabilized as they repel each other. If particles have no charge, there is usually no force to prevent their agglomeration.

13.2.2 Bacterial Cell Surface Electrochemistry

The surface of a bacterium is much more complex than the surface of impenetrable solid colloids. A bacterial surface is a heterogeneous three-dimensional arrangement of various biomolecules. The surface properties may vary at specific locations as a result of the presence of certain structures. Some cells also have structures that protrude from the surface such as fimbriae, pili, and flagella. Fimbriae and pili are thought to be involved in cell attachment to environmental surfaces, while flagella are special structures used for cell locomotion [31]. To understand cell electrochemistry, a brief description of the cell surface is necessary.

13.2.2.1 Structural Composition of Bacterial Surface

The outer surface of a bacterial cell is made up of a cell wall and cytoplasmic membrane that encircles the fluid cytoplasm (Fig. 13.3). The cytoplasm is a complex mixture of substances and structures including deoxyribonucleic acid (DNA), ribonucleic acid (RNA), ribosomes, and other dissolved and suspended materials. The cell wall and cell membrane act as barriers to prevent unwanted materials from entering the cell, while also holding the internal contents together. Only water and a few other small, uncharged molecules like oxygen and carbon dioxide diffuse freely across the membrane. All other substances enter through active transport or diffuse through transmembrane proteins, whose channels open and close according to the needs of the cell.

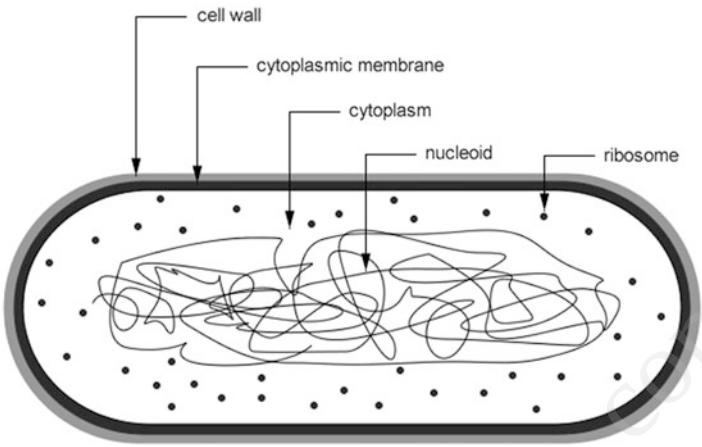

Fig. 13.3 Typical bacterial cell structure (not to scale) [31]

These outer layers are the primary means through which an organism interacts with the environment. Most species of bacteria can be divided into two broad groups based on their cell wall by the Gram-staining method simply as Gram-positive and Gram-negative [31]. Figure 13.4 shows the structure of bacterial cell surfaces. The cell wall of both groups is composed of peptidoglycan, a peptide cross-linked polysaccharide matrix layer. The peptidoglycan layer is made up sheets formed from individual strands of peptidoglycan lying adjacent to one another. It accounts for as much as 90 % of the Gram-positive cell wall with several (up to 25) sheets stacked upon each other to height of 15–80 nm. In Gram-negative bacteria, it makes up only about 10 % of the cell wall (1–2 nm) and is located between the two layers of phospholipids, the outer membrane and the cytoplasmic membrane. Peptidoglycan confers rigidity to maintain shape and internal pressure. In both Gram-negative and Gram-positive bacteria, peptidoglycan is very porous and allows particles of approximately 2 nm to pass through [32].

Approximately 45 % of the surface of Gram-negative bacteria may be covered with lipopolysaccharide (LPS), which are anchored in the lipids of the outer membrane. It is made up of three distinct regions covalently linked together, a hydrophobic lipid component (lipid A), a core polysaccharide, and *O*-antigen. Some bacterial strains may not possess the *O*-antigen side chain. The LPS core polysaccharide consists of five to ten negatively charged sugar units, which often carry phosphate and carboxylic acid groups. The *O*-antigen consists of 20–70 repeating units of three to five sugars, which protrude up to 30 nm or more from the cell surface. It is very likely that the *O*-antigen plays a major role in polymer interactions with surfaces reported for Gram-negative bacteria [33].

Similar to the LPS in Gram-negative bacteria, the cell wall of Gram-positive bacteria may contain teichoic acids which are attached, directly or indirectly by way of phosphodiester bonds, to carbon 6 of *N*-acetylmuramic residues of the peptidoglycan or anchored in the underlying lipid bilayer. In the latter case, these

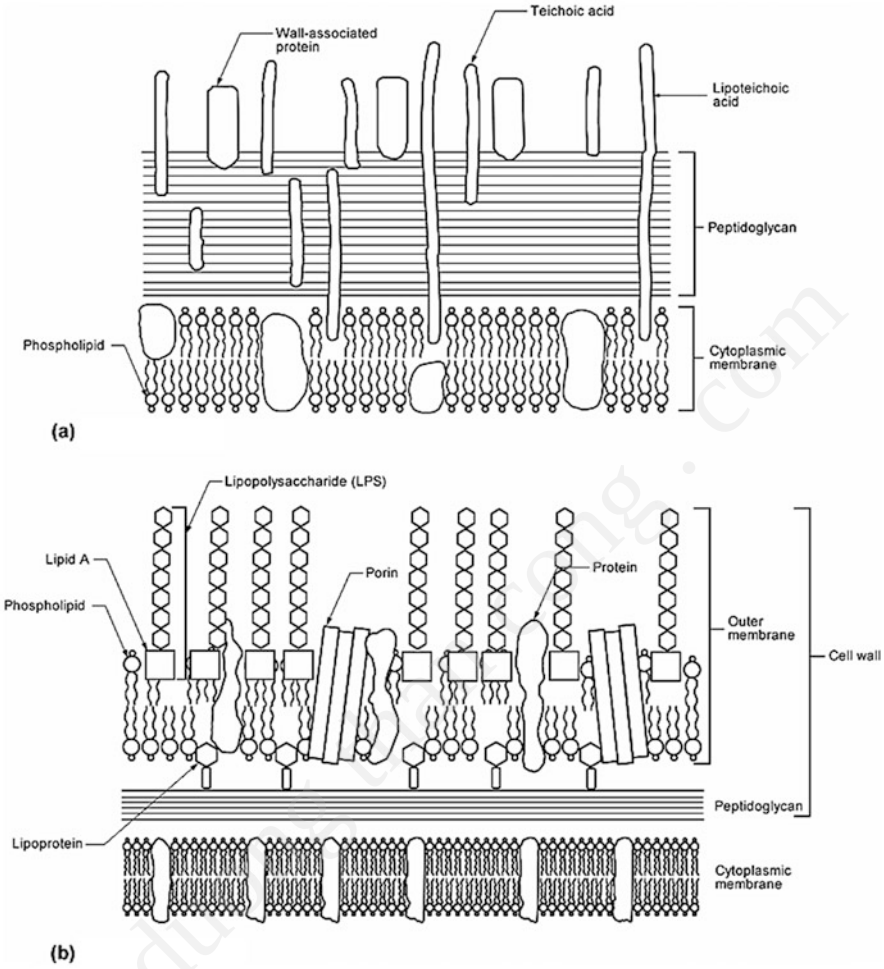

Fig. 13.4 Outer layers of bacteria [31]. (**a**) Gram-positive. (**b**) Gram-negative

are called lipoteichoic acids and are covalently bound to the lipid bilayer via a glyceride. In general, teichoic acids include all wall, membrane, or capsular polymers of either ribitol phosphate or glycerophosphate residues. They are connected via phosphodiester bonds and usually have other sugars and D-alanine attached.

Both Gram-negative and Gram-positive bacteria have a cytoplasmic membrane composed almost entirely of lipids and proteins. In Gram-negative bacteria, a second phospholipid bilayer is present in the outer cell membrane. Phospholipid bilayers are composed of conventional glycerol phospholipids, mainly phosphatidylethanolamine (PE), phosphatidylglycerol (PG), and cardiolipin [34–36]. Phospholipids have a hydrophobic head and two hydrophobic tails and are arranged in a two-layer sheet with the tails pointing toward the center of the layer. The head of

the lipid is generally made up of a negatively charged phosphate group and glycerol. The tail is usually a long chain of fatty acid hydrocarbons.

Finally, the cell wall and cytoplasmic membrane are populated with proteins, which are either firmly embedded (integral proteins) or associated firmly with one of the membrane structures (peripheral proteins). Some proteins bind substrates or process large molecules for transport into the cell, while lipoproteins are involved in energy metabolism and other important cellular functions.

13.2.2.2 Surface Charges and Ionizable Functional Groups

Much of the charge on a bacterial cell surface is derived from functional groups associated with the surface structures. Bioassay studies suggest that the charge on the cell wall results predominantly from proton exchange reactions involving carboxylic, phosphate, and amino moieties [37–40]. The reactions for the dominant functional groups in *E. coli* and the range of their associated acidity constants (pK_a) are shown in Table 13.1.

Considering that the site density of carboxyl and phosphate groups is generally greater than amines, the cell surface of *E. coli*, like most bacterial cells, is negatively charged at neutral pH [38, 41]. In the absence of other ions, the surface charge density resulting from the ionizable functional groups at the bacterial surface may be derived by considering the generic proton exchange reactions:

$$\mathrm{LH} \overset{K_a^{\text{acid}}}{\longleftrightarrow} \mathrm{L}^- + \mathrm{H}^+ \tag{13.16}$$

$$\mathrm{LH}^+ \overset{K_a^{\text{base}}}{\longleftrightarrow} \mathrm{L} + \mathrm{H}^+ \tag{13.17}$$

where L is the proton-binding site on the cell surface for acidic and basic moieties, respectively. The apparent equilibrium constants (K_a) for Eqs. (13.16) and (13.17) are defined as

$$K_a^{\text{acid}} = \frac{[\mathrm{H}^+][\mathrm{L}^-]}{[\mathrm{LH}]} \tag{13.18}$$

Table 13.1 Ionizable functional groups located on the surface of *E. coli* and the associated acidity constants (pK_a) for zero salt effects at 25 °C

Reaction	Location	pK_a
$\mathrm{R-COOH} \leftrightarrow \mathrm{R-COO^- + H^+}$	Proteins, sugars, and LPS	2.0–6.0
$\mathrm{R-NH_3^+} \leftrightarrow \mathrm{R-NH_2 + H^+}$	Proteins and phospholipids	9.0–11.0
$\mathrm{R-HPO_4} \leftrightarrow \mathrm{R-PO_4^- + H^+}$	Phospholipids	3.2–3.5
$\mathrm{R-H_2PO_4} \leftrightarrow \mathrm{R-HPO_4^- + H^+}$	LPS	3.2–3.5
$\mathrm{R-HPO_4^-} \leftrightarrow \mathrm{R-PO_4^{2-} + H^+}$	LPS	5.6–7.2

Data compiled from Martinez et al. [38] and Jiang et al. [40]

$$K_a^{\text{base}} = \frac{[\text{H}^+][\text{L}]}{[\text{LH}^+]} \tag{13.19}$$

The fixed surface charge ρ_{fix} associated with the various sites is given by

$$\rho_{\text{fix}} = e\sum_{i=1}^{m}\left(\frac{L_{TB,i}[\text{H}^+]}{K_{a,i}^{\text{base}} + [\text{H}^+]}\right) - e\sum_{j=1}^{n}\left(\frac{L_{TA,i}K_{a,j}}{K_{a,j}^{\text{acid}} + [\text{H}^+]}\right) \tag{13.20}$$

where L_{TB} and L_{TA} are the total concentrations of basic and acidic sites, respectively. The acidity constants associated with each site must be adjusted according to Eqs. (13.3) and (13.4) to account for the electrostatic influence of the surface.

13.2.2.3 Electric Double Layer at Bacterial Surface

Since a bacterial surface has a three-dimensional configuration into which ions and solvent molecules are able to penetrate, the bacteria-water interface may best be described as an ion-penetrable layer with volume spread electric charge [42–46]. Figure 13.5 schematically shows the distribution of ions at the bacterial surface according to the ion-penetrable model. The charges associated with the ionizable functional groups attract counter ions, but there is no definite boundary at the molecular level. Polymers and surface appendages may also change conformation depending on the ionic character of the microscopic local environment [41, 47]. Unlike a hard colloidal particle, the bacterial surface has a finite thickness, which restricts the charges within the ion-penetrable layer. Surface charge density may be deduced from proton titration experiments [39]. However, since it is difficult to determine the spatial distribution of the charge through the cell membrane, it is usually assumed to be uniform.

The electric potential of the ion-penetrable layer is made up of the fixed charges associated with functional groups, as well as the charge density of the ions which have diffused into the layer [46]. To derive the electric potential within the layer, Eq. (13.8) may be adjusted appropriately as follows:

$$\nabla^2\psi = -\frac{\rho_{\text{fix}}(x) + \rho_{el}(x)}{\varepsilon_m} \tag{13.21}$$

where ρ_{el} is the charge density contribution of the ions in the ion-penetrable layer and ε_m is the dielectric constant within the membrane layer. The ions in the membrane have an energy, which is equal to $ze\psi$ and follow the Boltzman distribution. Therefore, the concentration of ions in the ion-penetrable membrane is given by Eq. (13.7). The semi-permeable cytoplasmic membrane maintains an unequal distribution of ions on either side of the membrane. At equilibrium, the electrostatic potential across the membrane is called the Donnan potential, ψ_{DON}. Equation (13.7) may therefore be rewritten as

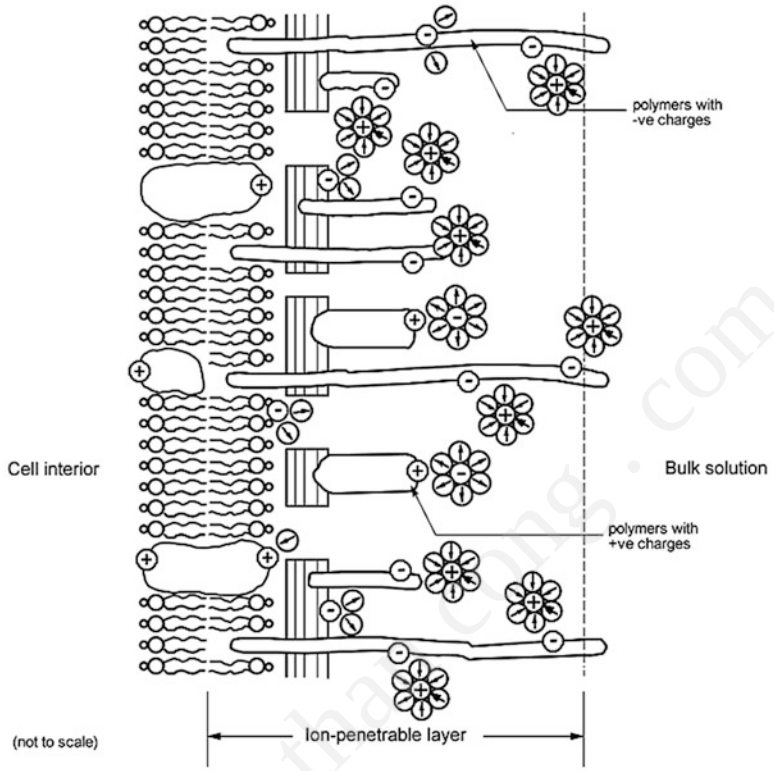

Fig. 13.5 Schematic of bacteria-water interface [42]

$$C_i^{\text{mem}} = C_i^{\text{bulk}} \exp\left(-\frac{z_i e \psi_{DON}}{kT}\right) \tag{13.22}$$

To satisfy conditions of charge neutrality in the membrane, the following is true:

$$\rho_{\text{fix}} + eN_A \sum_{i=1}^{N} C_i^{\text{bulk}} z_i \exp\left(-\frac{z_i e \psi_{DON}}{kT}\right) = 0 \tag{13.23}$$

A particular solution for Eq. (13.23) gives the Donnan potential for a membrane in contact with a 1–1 electrolytic solution as [45]

$$\psi_{DON} = \frac{kT}{e} \operatorname{arcsinh}\left(\frac{\rho_{\text{fix}}}{2n^{\text{bulk}} F}\right) \tag{13.24}$$

where F is the Faraday constant.

Various approaches have been taken to derive the electric potential across the cell membrane. A useful approach is to assume infinite thickness of the membrane,

even though the solution indicates that the electric field only exists within a finite thickness of the membrane [48]. However, the origin $(x = 0)$ is located at a hypothetical boundary between the membrane and the electrolyte solution such that $x < 0$ represents the membrane, and $x > 0$ is the electrolyte solution. The Poisson-Boltzmann equation for this model is given as

$$\frac{d^2\psi}{dx^2} = -\frac{1}{\varepsilon_s \varepsilon_o}\left\{\rho_{\text{fix}} + eN_A \sum_{i=1}^{N} n_i^{\text{bulk}} z_i \exp\left(-\frac{z_i e\psi}{kT}\right)\right\} \text{for} x < 0 \tag{13.25}$$

$$\frac{d^2\psi}{dx^2} = -\frac{1}{\varepsilon_s \varepsilon_o}\left\{eN_A \sum_{i=1}^{N} n_i^{\text{bulk}} z_i \exp\left(-\frac{z_i e\psi}{kT}\right)\right\} \text{for} x > 0 \tag{13.26}$$

where ε_m and ε_s are the relative dielectric constants of the membrane and the solution, respectively. Equations (13.25) and (13.26) can be solved numerically after applying the appropriate boundary conditions [46, 48, 49] to yield the electric potential profile across a cell membrane.

13.2.3 Microbe-Catalyst Electrical Doublelayer Interactions

Since contact between the catalyst and the microbe is a prerequisite for photocatalysis, interactions which enhance contact without destabilizing the suspension should result in more effective disinfection. The interaction between the two colloids, as described by classical DLVO theory [50], is governed by the balance of repulsive and attractive forces, usually summed up in electrostatic and van der Waals forces. Electrostatic forces can be both repulsive and attractive depending on the overall charge of the colloids, while van der Waals interactions are usually attractive. Bacterial surface polymers may also play a major role during the interaction [41, 42, 51–53].

For simplicity, it may be assumed that both catalyst and microbes are spherical particles (even though *E. coli* is rod-shaped). It is likely that given the relative size of a bacterium to an individual TiO_2 particle that the system may best be described as a hard spherical particle interacting with an ion-penetrable plate. However, for generality, both particles will be considered spheres (Fig. 13.6). Taguchi et al. [54] calculated the potential energy for the interaction between a sphere covered with an ion-penetrable membrane and a solid spherical particle. Many other cases can be found in the literature which describes specific interactions [55–58], particularly the interaction of a spherical particle covered with an ion-penetrable layer and a flat solid plate [58]. The latter may be applicable to thin film photocatalysis systems.

The total potential energy V_T of two spherical particles is given by the sum of their van der Waals and electrostatic interaction energies [54, 56],

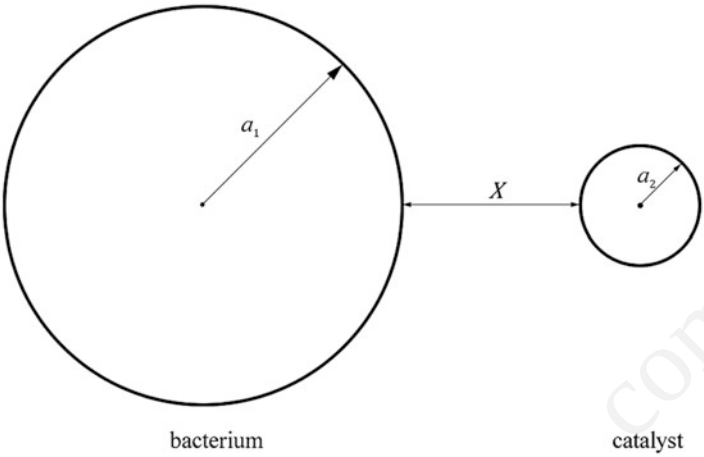

Fig. 13.6 Proposed model for the interaction between a bacterium and a catalyst particle of radii a_1 and a_2, respectively, separated by X between their surfaces

$$V_T(X) = V_v(X) + V_e(X) \tag{13.27}$$

Consider two spheres of radii a_1 and a_2 separated at a distance X (Fig. 13.6). The potential energy for van der Waal interaction between the two particles is given as

$$V_v(X) = \frac{a_1 a_2}{a_1 + a_2}\frac{A}{6X} \tag{13.28}$$

where A is the Hammaker constant. The potential energy of double layer interaction between the two spheres is

$$V_e(X) = \frac{2\pi a_1 a_2}{a_1 + a_2}\int_X^\infty V_{pl}(x)\,dx \tag{13.29}$$

where $V_{pl}(x)$ is the potential energy of the electrostatic interactions per unit area between two plates at separation x. During the interaction of the double layers, two cases are introduced for the solid particle [54, 56, 58]: (1) constant surface potential and (2) constant surface charge. The potential inside the organism may be assumed to remain constant at the Donnan potential. Terui et al. [55] derived V_{pl} for solid particles under assumptions (1) and (2) above interacting with an ion-penetrable particle, respectively,

$$V_{pl}(x) = 2\varepsilon_r\varepsilon_o\kappa\left[\psi_1 e^{-\kappa x}\psi_2 - \frac{1}{2}(\psi_1)^2 e^{-2\kappa x}\right] \tag{13.30}$$

$$V_{pl}(x) = 2\varepsilon_r \varepsilon_o \kappa \left[\psi_1 e^{-\kappa x} \psi_2 + \frac{1}{2}(\psi_1)^2 e^{-2\kappa x} \right] \tag{13.31}$$

By substituting Eqs. (13.30) and (13.31) into (13.29), the potential energy of double layer interaction for a bacterium with TiO_2 particle under the constant potential assumption is

$$V_e(X) = \frac{4\pi a_1 a_2}{a_1 + a_2} \varepsilon_r \varepsilon_o \left[\psi_1 e^{-\kappa x} \psi_2 - \frac{1}{4}(\psi_1)^2 e^{-2\kappa x} \right] \tag{13.32}$$

and under the constant surface charge assumption is

$$V_e(X) = \frac{4\pi a_1 a_2}{a_1 + a_2} \varepsilon_r \varepsilon_o \left[\psi_1 e^{-\kappa x} \psi_2 + \frac{1}{4}(\psi_1)^2 e^{-2\kappa x} \right]. \tag{13.33}$$

These reactions are important as they define the potential energy of interaction between the suspended colloids. The net interaction energy gives an indication of the colloidal suspension. If van der Waals dominates the interaction, then overwhelming attractive forces can lead to irreversible coagulation. If the electrostatic forces dominate, then the particles should be stabilized.

13.3 Conceptual Model

Consider a reaction suspension containing catalyst particles and bacterial cells. The catalyst is assumed to be Degussa P25 TiO_2 with an average particle diameter of 25 nm. On the other hand, the bacterial cells are much larger having a length of 1000 nm and diameter of 500 nm. Due to the relative size relationship, it is expected that multiple catalyst particles will adsorb to a cell. Equation 13.13 defines the electrostatic surface potential of the catalyst. In like manner, the surface potential profile of the cells is defined by Eqs. (13.25) and (13.26). Under the pH conditions of interest (6–8, i.e., mostly neutral) and low electrolyte concentration, the TiO_2 surface is dominated by non-charged surface-hydroxylated species, while the cell surface is mostly negative. The potential energy of interaction between the particles can be described mathematically according to Eqs. (13.27, 13.28, 13.29, 13.30, 13.31, 13.32, and 13.33). However, it is easy to see that under the given conditions, TiO_2 particles would not experience significant repulsion from the bacterial surface because the particles are close to the point of zero charge. Therefore, short-range van der Waals, hydrophilic, and hydrophobic forces will mostly govern adsorption of TiO_2 to the bacterial cells.

For simplicity, it is assumed that the bacterial cell can be represented as a sphere of diameter 1000 nm. Therefore, imagine a situation where the small spherical catalyst particles surround the much larger bacterial cell as shown in Fig. 13.7.

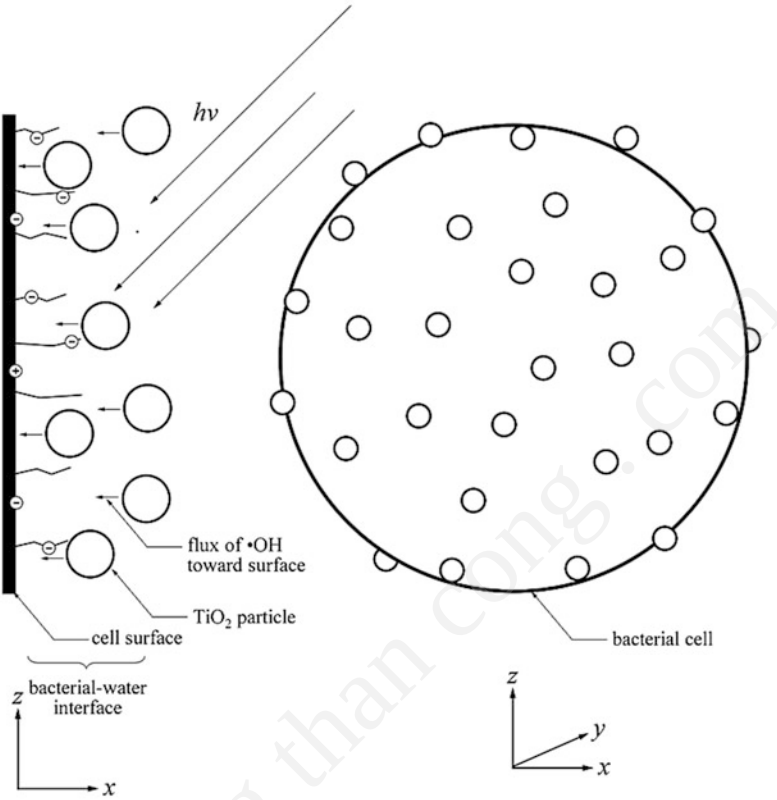

Fig. 13.7 Schematic representation of surface coverage of catalyst particles on bacterial cell

However, it should be noted that catalyst particles in suspension can agglomerate to sizes comparable with cells [59]. Since the repulsive forces are low, the catalyst particles are able to approach the cell at very close separation distances (possibly on the order of angstroms). In some cases, specific bonding may occur with bacterial surface appendages and polymers.

Hence, with time, TiO_2 particles are immobilized at the cell surface. Under illuminated conditions, free radicals, mostly hydroxyl radicals, are formed on the surface of the TiO_2 and begin to react with bacterial surface sites. The reaction produces by-products that diffuse away from the interface toward the bulk, but in the process they also react with radicals within the interface. With sufficient time, the cell would have experienced significant radical attack, which eventually results in the inactivation of the bacterium.

13.3.1 Adsorption Kinetics of Catalysts and Cells

It is important to analyze the amount of TiO_2 particles reaching the bacterial surface since only these particles are really involved in the photocatalytic process. The analysis would also provide insight into the expected dependence of the process on catalyst concentration. The transport of catalyst particles from the bulk solution to the bacterial surface can be described by the general continuity equation

$$\frac{\partial n_p}{\partial t} + \nabla \cdot j = s \tag{13.34}$$

where n_p is the number concentration of catalyst particles, t is time, j is a vector function describing the flows (flux) of n_p, and s is the sink function describing, for example, bulk aggregation of the particles. The flux function involves particle diffusion and convection functions and may be defined as

$$j = -D \cdot \nabla n_p + U n_p \tag{13.35}$$

where D is the particle diffusivity tensor, U the particle translation velocity vector. The terms described in Eqs. (13.34) and (13.35) can be determined by considering the specific particle-particle interactions as presented in the previous chapter.

However, if the system shown previously in Fig. 13.6 is considered in which catalyst particles are approaching the bacterial surface in a dilute colloidal suspension (i.e., $n \ll 10^{12}$ mL^{-1}), then the initial adsorption flux can be considered independent of the concentration of particles at the interface [60]. The particle concentration varies only along coordinate axis indicated by X, i.e., perpendicular to the bacterial surface. Assuming that there is no bulk aggregation of particles, Eq. (34) may then be adopted in a one-dimensional form as

$$\frac{\partial n_p}{\partial t} - D_b \frac{\partial^2 n_p}{\partial x^2} + v_x(x) \frac{\partial n_p}{\partial x} = 0 \tag{13.36}$$

where D_b is the diffusion coefficient in the bulk and $v_x(x)$ is the fluid velocity component directly perpendicular to the interface. If it is assumed that there is a primary minimum distance x_m at the interface at which particles approach and are irreversibly adsorbed [5], then the boundary condition at the bacterial interface is given as

$$n_p = 0 \ \ at \ \ x = x_m \tag{13.37}$$

and away from the surface

$$n_p \rightarrow n_b \tag{13.38}$$

where n_b is the concentration of particles away from the surface (i.e., in the bulk solution). After applying the boundary conditions, the uniform flux of particles toward the bacterial surface can be obtained as [60]

$$j_0 = \left(D_b \frac{\partial n_p}{\partial x}\right)_{x=x_m} = \frac{D_b}{x_d} n_b \tag{13.39}$$

where x_d is the thickness of the organism's diffusive boundary layer (which for small organisms is of a similar magnitude with the characteristic length, a_1 in this case, the organism's radius).

13.3.2 Adsorption in the Absence of Mechanical Mixing

It is not uncommon during experiments to have a standing suspension of catalyst and bacteria in which the colloids are neutrally buoyant. The one-dimensional transport equation for this condition in which $v_x(x) = 0$ is given as [60]

$$\frac{\partial n_p}{\partial t} - \mathrm{D_{rel}} \frac{1}{r^2} \frac{\partial}{\partial \mathrm{r}} \left(r^2 \frac{\partial n_p}{\partial r}\right) = 0 \tag{13.40}$$

where $r = X + a_1 + a_2$ and $D_{\mathrm{rel}} = D_{\mathrm{bac}} + D_{\mathrm{cat}}$ is the relative diffusion coefficient (D_{bac} is the diffusion coefficient of the bacteria and D_{cat} is the catalyst particle diffusion coefficient; when $a_2 \ll a_1$, the bacterial diffusion can be neglected). After applying the same boundary conditions as before, the uniform adsorption flux of particles toward the bacterial surface under these conditions is given by [60]

$$j_0(t) = \frac{D_{\mathrm{rel}} n_b}{a_1} \left(\frac{1}{\sqrt{\pi \tau_d}} + \frac{1}{1 + A_r}\right) \tag{13.41}$$

where $A_r = a_2/a_1$ and the dimensionless parameter $\tau_d = t/t_r$. Here $t_r = {a_1}^2/D_{\mathrm{rel}}$ and is the time required for the catalyst particle to get across the organism's diffusive boundary layer. Therefore, the first term in the parentheses describes the transient adsorption flux which becomes negligible when $\tau_d \gg 1$ (i.e., when $t \gg t_r$). It is then clear to see that a constant flux is achieved for times exceeding the relaxation time; hence

$$j_0 = \frac{D_{\mathrm{rel}} n_b}{a_1} \left(\frac{1}{1 + A_r}\right) \tag{13.42}$$

The relaxation time for a catalyst particle with $D_{\mathrm{cat}} = 10^{-12}\ \mathrm{m^2\ s^{-1}}$ diffusing across a layer of 500 nm thickness would be 0.25 s which is a negligible time compared to the exposure time required for disinfection (on the order of minutes).

13.3.3 Adsorption in the Presence of Mechanical Mixing

Mechanical mixing of the suspension introduces hydrodynamic shearing forces, which, while maintaining suspension uniformity, reduce mass transfer for colloids. The quantitative analysis for the effects of hydrodynamic forces can be complicated, but approximations are available for simplified scenarios, including colloids in uniform flow in the absence of electrostatic forces. The flux of spherical particles toward a spherical surface can be approximated by [60]

$$j_0 = 0.89 \frac{{D_b}^{2/3} {v_b}^{1/3}}{a_1} n_b \tag{13.43}$$

where v_b is the velocity of the fluid flow in the bulk phase.

13.3.4 Surface Coverage of Catalyst on Bacteria

13.3.4.1 Surface Coverage with Low Catalyst Concentration

The dimensionless surface coverage is denoted by θ and is the ratio of the area covered by particles to the total surface area of the collector (in this case the bacterial surface). Mathematically, this may be expressed as

$$\theta = \frac{n_s \pi {a_2}^2}{\Delta S} \tag{13.44}$$

where n_s is the number of particles with diameter a_2 collected on an element of area ΔS. If the elemental area is defined by vector r_s, then the rate of change of surface coverage with time is [60]

$$\frac{\mathrm{d}\theta}{\mathrm{d}t} = \pi {a_2}^2 n_b \bar{j}(r_s, t) \tag{13.45}$$

where $\bar{j}(r_s, t)$ is the normalized flux given by $j(r_s, t)/n_b$. By integrating Eq. (13.45), the expression for $\theta(t)$ is obtained as

$$\theta(t) = \theta_t + \pi {a_2}^2 n_b \bar{j}_0(r_s) t \tag{13.46}$$

where θ_t is the surface concentration of particles adsorbed during the transient conditions and $\bar{j}_0$ is the normalized stationary adsorption flux previously defined. Equation (13.46) is only valid when the initial surface concentration is low so that already adsorbed particles do not have a significant influence (blocking) on the adsorption of new particles. This condition is true when $\theta_t \ll 1$ and can be determined from [60]

$$\theta_t = \pi a_2{}^2 n_b \bar{j}_0 \tau_d \tag{13.47}$$

For a suspension of spheres not subject to mechanical agitation, θ_t can be approximated as

$$\theta_t = \pi a_2{}^2 a_1 n_b \tag{13.48}$$

Similarly, for spherical particles in a uniform flow,

$$\theta_t = 0.55\pi a_2{}^2 a_1{}^{2/3} n_b v_x{}^{-1/3} D_b{}^{1/3}. \tag{13.49}$$

13.3.4.2 Surface Coverage with High Catalyst Concentrations

The kinetics of adsorption differs for systems with high colloid concentrations [60, 61]. Catalyst particles already adsorbed at the surface of the bacteria essentially preclude or block other particles from adsorbing within an exclusion zone. Therefore, the time evolution of the surface coverage is affected by existing coverage. A number of other models can be employed to model these systems (e.g., see reference [60]). One of the simplest, but powerful, approaches is the random sequential adsorption (RSA) model [62]. In an RSA simulation, particles are randomly placed at the surface at a constant rate. Once the particle is placed, it is permanently affixed to the surface. Particles are not allowed to overlap, so a surface saturation is eventually reached when there are no more available spaces to fit particles. With this model, the surface is never completely covered. Even though spaces remain, they are not large enough to allow the positioning of other particles. Hence, the saturation level is commonly referred to as the "jamming" limit and has a value of 54.7 % for monodispersed spheres when only steric effects are considered [62]. RSA models have been developed to incorporate short-range interactions between particles [61]. Even though these assumptions are straightforward, the RSA configuration for high surface concentration, especially in three dimensions, can usually only be predicted by numerical simulation [61, 63].

However, the kinetic curves describing the dependence of surface coverage θ on the adsorption time have been extensively calculated for hard and soft spheres by other authors under many different scenarios including no mixing conditions, electrostatic interactions, and hydrodynamic flows [60, 63, 64]. Adamczyk et al. [60] provide approximations which can be used in place of complex numerical simulations. The RSA derived expression for the time evolution of surface coverage can be approximated by

$$\theta(\tau) = \frac{\theta_\infty}{\left(1 + H^*\right)^2}\left[1 - 0.432\left(\frac{1}{\sqrt{\pi a_2{}^2 j_0 n_b t}}\right)\right] \tag{13.50}$$

where H^* is a dimensionless parameter that defines the effective interaction range and depends on the energy of interaction and the double layer thickness as indicated by κa^{-1}. H^* may be approximated from

$$H^* = L_e \ln\xi - L_e \ln\left(1 + \frac{1}{2} L_e \ln\xi\right) \tag{13.51}$$

where L_e is the dimensionless double layer thickness give by κa^{-1} and ξ is the dimensionless interaction energy [60].

For colloidal particles affected by hydrodynamic shear forces, the surface coverage can be approximated by

$$\theta(t) = \frac{1}{\theta_h}\left[1 - \exp\left(-\frac{\theta}{\theta_h}\tau\right)\right] \tag{13.52}$$

where θ_h is given as

$$\theta_h = \frac{1}{\left[4\left(1 + H^*\right)^2 + C_h \overline{G}\right]} \tag{13.53}$$

and

$$\overline{G} = \frac{G a_2{}^2}{D_b} \gg 1 \tag{13.54}$$

where G is the shear rate at a given point on the interface and C_h is a dimensionless fitting parameter which must be determined by simulations.

13.3.5 Kinetics of Hydroxyl Radicals at Interface

13.3.5.1 Generation Rate

The generation of the radicals is central to the overall photocatalytic process. At steady-state conditions, it is the difference between the rate of light absorption and the recombination rate. As can be imagined, the latter process would be nearly impractical to measure in a real system. The rate of light absorption is more amenable to experimentation, but intense light scattering effects still makes this a difficult task. However, the incident photon flux I_0 in a solution can be determined by use of actinometry [65–68], and the absorbed flux I_a can be estimated for a sample by determining its integrated absorption fraction F_s from spectrophotometric methods. Hence,

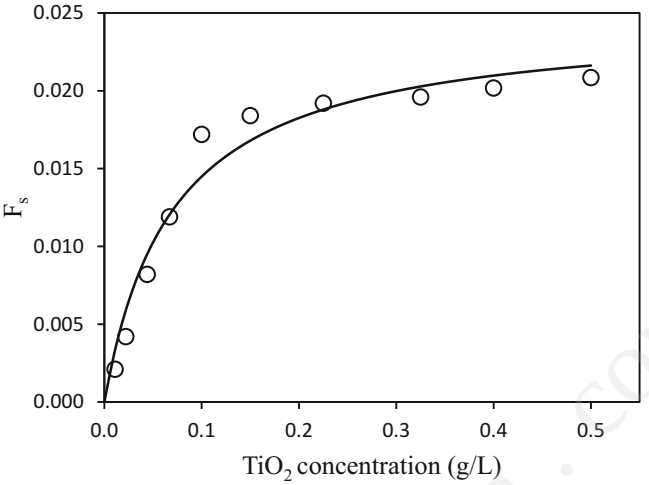

Fig. 13.8 Plot of integrated absorption fraction F_s for TiO_2 concentration

$$I_a = I_0 F_s \tag{13.55}$$

F_s has been previously determined for a range of TiO_2 concentrations [69]. The chart in Fig. 13.8 has been reconstructed based on interpolation and extrapolation of the literature data.

Once the rate of adsorbed photon flux is determined, the rate of OH radical generation can be estimated by [70]

$$G_{\cdot \mathrm{OH}} = I_{\mathrm{a}} \varphi_{\cdot \mathrm{OH}} \tag{13.56}$$

where $\varphi_{\cdot \mathrm{OH}}$ is the quantum yield of radical generation. The rate of generation of OH radicals and quantum yields for TiO_2 in chemical photocatalytic reaction systems were determined by Sun and Bolton [69] according to the method described above. The radical generation rate is a function of catalyst concentration, the physical and chemical properties of the catalyst, light intensity, and dissolved oxygen concentration. Also important to note is that the addition of hydrogen peroxide has a positive effect on the generation rate [69, 71–74].

13.3.5.2 Nature of OH Radicals at the Bacterial Membrane

In general, there are two theories concerning the nature of radicals at the catalyst surface; (1) radicals remain surface-bound to the catalyst during reaction with adsorbed species [75–77]; and (2) radicals diffuse away from the surface to react with compounds in solution or on the catalyst surface [77–80]. It would be very difficult to distinguish between these two possibilities in the overall kinetics of the process. However, in the latter case, it is recognized that hydroxyl radicals, in

particular, are diffusion limited owing to their high reactivity. Depending on the concentration of oxidizable species, hydroxyl radicals have been found to diffuse up to a distance of 10 nm away from the site of generation [81, 82]. Therefore, it is possible that radicals can diffuse into a bacterial membrane during very close approach with a catalyst surface. The diffusion coefficient of hydroxyl radicals in water has been estimated to be on the order of 10^{-9} m^2s^{-1} at 25 °C [83–85]. If the nearest substrate were 10–100 nm away from the site of generation, it would take a radical much less than a fraction of a second to move across this range of distance. However, a number of factors may hinder diffusion near the vicinity of the cell membrane, including electrolyte ions, hydrophobic zones, and the solvation shell around the radical [83, 86, 87].

13.3.6 Microbial Survival

The model presented by Haas [88] may be adopted for the reaction of hydroxyl radicals with cells in a simple bimolecular reaction

$$m[\cdot\mathrm{OH}] + [\mathrm{cell}]_l \xrightarrow{k_{dis}} [\mathrm{cell}]_d + m\mathrm{OH}^- \tag{13.57}$$

where the subscripts l and d denote live and dead cells, respectively, and k_{dis} is the observed rate constant for disinfection. The overall disinfection reaction rate for this bimolecular reaction is given as

$$R_d = -k_{\mathrm{dis}}[\cdot\mathrm{OH}]^n[\mathrm{cell}]_l^y \tag{13.58}$$

where n and y are the reaction orders related to radicals and cells, respectively. The concentration units for hydroxyl radicals are moles per liter, but for the cell they are given as cell number density (cells per liter). The observed disinfection rate k_{dis} has contributions from (1) the diffusion-controlled rate constant k_d at which the cell-radical complex $[\mathrm{cell}\cdot\mathrm{OH}]_d$ is formed

$$m[\cdot\mathrm{OH}] + [\mathrm{cell}]_l \underset{k'_d}{\overset{k_d}{\rightleftarrows}} \left[\mathrm{cell}\cdot(\mathrm{OH})_m\right]_d \tag{13.59}$$

(2) the rate constant for dissociation (or radical quenching and repair) $k_{d'}$, and (3) the rate constant k_{inv} at which the cell is eventually inactivated after being exposed to the radical.

$$\left[\mathrm{cell}\cdot(\mathrm{OH})_m\right] \xrightarrow{k_{\mathrm{inv}}} [\mathrm{cell}]_d + m\mathrm{OH}^- \tag{13.60}$$

It can be shown that the observed disinfection rate has the form

$$k_{\text{dis}} = \frac{k_d k_{\text{inv}}}{k_{\text{inv}} + k'_d} \tag{13.61}$$

If the inactivation rate constant is much faster than the repair/radical quenching, that is, $k_{inv} \gg k'_d$, then as radicals encounter the cell, it is rapidly inactivated without time for repair or quenching. In this case, the observed rate is equal to the diffusion rate constant ($k_{\text{dis}} = k_d$), and the reaction depends on how fast radicals can encounter the cells. However, if the inactivation rate is much slower than the repair and quenching mechanisms, then the observed rate is given by

$$k_{\text{dis}} = \frac{k_d}{k'_d} k_{\text{inv}} = K_{\left[\text{cell} \cdot (\text{OH})_m\right]} k_{\text{inv}} \tag{13.62}$$

where $K_{\left[\text{cell} \cdot (\text{OH})_m\right]}$ is the equilibrium constant for the formation of the cell-radical complex.

13.3.7 Kinetics of By-Product Evolution

The effect of free radicals on cellular molecules has long been reported (e.g., see [89, 90]). In particular, the hydroxyl radical is very reactive and is capable of injuring virtually all biological macromolecules. Free radicals associated with the photocatalytic process can react with macromolecules on the bacterial surface, including proteins, polysaccharides, and lipids. Of these, lipids are known to be the most prone to oxidative damage, particularly lipids with unsaturated fatty acids. Proteins are also very susceptible to radical oxidation. The extent of the damage to particular targets depends on a number of factors, including the concentration of the target, the reaction rate constants, the relative locations of the target and oxidant, the occurrence of secondary damaging events, the occurrence of transfer reactions, and the repair and scavenging reactions [91–93]. In addition, the oxidation of intracellular constituents can occur through the generation of secondary oxidants, such as lipid radicals, hydrogen peroxide, and superoxide [94–96]. Superoxide and hydrogen peroxide can also produce hydroxyl radicals in the intracellular environment through the Fenton reaction involving "free" iron [97, 98].

For *E. coli*, most of the outer membrane is made up of phospholipids. In addition to their abundance, their ease of oxidizability makes this group of biomolecules prime targets for hydroxyl radical attack. Lipid peroxidation has been identified as a leading reaction mechanism during photocatalysis [94, 99–102]. The peroxidation of lipids involves three distinct steps: initiation, propagation, and termination. Figure 13.9 illustrates these processes schematically. The initiation reaction occurs when ·OH abstracts an H atom from the unsaturated fatty acid forming a carbon-centered radical. In the propagation reactions, the carbon-centered radical reacts with oxygen and yields a peroxyl radical. The peroxyl radical then abstracts an H

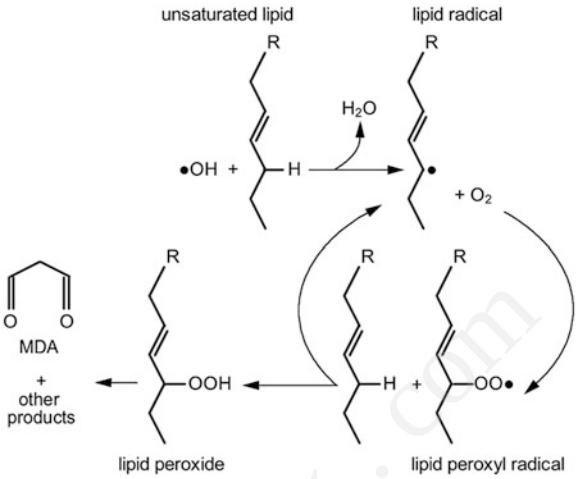

Fig. 13.9 Schematic of lipid peroxidation

atom from a second fatty acid forming a lipid hydroperoxide (LOOH) and leaving another carbon-centered free radical [89, 90]. The lipid hydroperoxide eventually degrades into malondialdehyde (MDA) and other unsaturated aldehydes. Termination occurs when two radicals react together forming neutral products (Fig. 13.9). The peroxidation of lipids can often result in damage to biomolecules at sites considerably distant from where the initial free radical reaction occurred [103]. Lipid peroxidation can be monitored by assessing the rate of oxygen uptake or the production of by-products including MDA and lipid hydroperoxides [104, 105].

Most of the by-products are formed within the interface where the hydroxyl radicals react with the cell surface. Since by-products can be considered molecular fragments of disinfection, they diffuse throughout the solution and absorb to the catalyst surface. For simplicity, it is assumed that the Langmuir model can describe adsorption kinetics. Hence, in the absence of other adsorbing molecules, the rate of by-product oxidation is given as

$$R_{BP} = -k_{BP}\frac{K_{BP}^{\text{ads}} C_{BP}}{1 + K_{BP}^{\text{ads}} C_{BP}} \tag{13.63}$$

where $-k_{BP}$ is the reaction rate constant, K_{BP}^{ads} is the Langmuir adsorption rate constant, and C_{BP} is the concentration of all by-products. The OH radical is known to react very efficiently with biomolecules at diffusion-controlled rate with a reaction rate constant on the order of 10^9 M^{-1} s^{-1} in homogeneous solutions [106–108].

13.3.8 Adsorption and Inhibition Kinetics of Inorganic Ions

Inorganic electrolyte ions, particularly anions, such as chloride (Cl^-), sulfate (SO_4^{2-}), phosphate (HPO_4^{2-}), bicarbonate (HCO_3^-), and nitrate (NO_3^-), are known to adsorb to the surface of TiO_2 [29, 30] and inhibit the photocatalytic process [109–113]. However, there has never been any model to quantify the effect of these ions on photocatalytic disinfection efficiency. To include these effects in the current model, the formation of surface complexes is analyzed. The adsorption of inorganic ions to the surface of TiO_2 can be described in terms of ligand exchange reactions with surface hydroxyl groups. This process is similar to complex formation in homogeneous solution, but the apparent equilibrium constants are adjusted to account for the electrostatic effects of the double layer [17]. The adsorption kinetics is governed by the properties of the adsorbing ion and the properties of the surface. The primary parameters for a quantitative description of ion adsorption are the acidity constants (K_a) of the ionic species and the surface hydroxyl groups, and the constants for the formation of the complexes (K_A^s). With these constants the surface speciation can be computed as a function of pH and concentration of ionic species.

However, for a given pH and low surface coverage, anion adsorption on metal oxide surfaces can be described by the Langmuir equation [30, 114]

$$K_{\mathrm{An}}^s = \frac{[\mathrm{Ti}-\mathrm{An}]}{[\mathrm{Ti}-\mathrm{OH}][C_{\mathrm{An}}][\mathrm{H}^+]} \tag{13.64}$$

where $[\mathrm{Ti}-\mathrm{An}]$ is the concentration of an adsorbed anion, $[\mathrm{Ti}-\mathrm{OH}]$ is the activity of all protonated surface moieties that can be displaced by the anion, and $[\mathrm{C_{An}}]$ is the concentration of the anion in solution. Constants for the formation of complexes by common anions on the surface of TiO_2 have been reported in the literature [13, 17, 115] and are given in Table 13.2. In the absence of other absorbing molecules, Eq. (13.64) can be rearranged to give the Langmuir equation.

$$\theta_{\mathrm{An},i} = \frac{K_{\mathrm{An},i}C_{\mathrm{An},i}[\mathrm{H}^+]}{1+\sum_{i=1}^{N} K_{\mathrm{An},i}C_{\mathrm{An},i}[\mathrm{H}^+]} \tag{13.65}$$

Table 13.2 Adsorption equilibrium constants for some common anions on the surface of TiO_2

Anion	Equilibrium constant M^{-1}
Cl^-	1×10^5 [17]
CO_3^{2-}	6×10^4 [116]
SO_4^{2-}	2×10^8 [117]
$H_2PO_4^-$	8×10^6 [118]

where $\theta_{An,i}$ is the surface coverage of the ith anion species and $C_{An,i}$ is the concentration of the specific anion species in solution.

In homogenous solutions inorganic ions react with hydroxyl radicals at diffusion-controlled rates. The rate constants and mechanisms for these interactions have been reported [119, 120]. However, since the rate of generation (and by extension, the concentration) of hydroxyl radicals in TiO_2 suspensions is significantly lower than the homogeneous diffusion-controlled rates, the overall reaction between the ions and the radicals is likely to be limited by the generation rate of radicals. The concentration of radicals during photocatalysis $\left(\ll 1 \times 10^{-8}\mathrm{M}\right)$ is usually much lower than the electrolyte concentration [121]. If it assumed that the generation of radicals is uniformed across the entire catalyst surface, then the rate of the inhibition reactions is directly proportional to the extent of coverage. The latter may be determined from the specific adsorption isotherms of the various ions in solution [111, 112]. Therefore, it is only important to determine the surface coverage of ions to understand the extent of inhibition on the disinfection process.

Guillard et al. [112] found that electrolyte ions form a salt layer at the surface of TiO_2 which prevented the adsorption of organic substrate. In the same way, inorganic ions, due to their molecular size, can approach the catalyst surface and specifically adsorb in a much more efficient way that large micron-sized bacterial cells. However, at low salt concentration, there is low screening of the cells and enough available hydroxyl sites to generate radicals. Under these conditions, the efficiency of disinfection is optimal. Conversely, at higher concentrations the opposite is true; that is, most of the radicals are consumed by inorganic ions and the cells are screened to a larger extent. Therefore, it can be argued that disinfection must occur as a result of the residual hydroxyl radicals, which are able to escape the catalyst surface or interact directly through surface-to-surface contact. The residual hydroxyl radical generation is the difference between the photo-generation rate of radicals and the rate of inhibition. As before in the absence of other absorbing molecules, the rate of inhibition or radical quenching can be expressed as a factor of the ·OH generation rate $G_{\cdot OH}$ as

$$R_{q,i} = -\theta_T \times G_{\cdot OH} = \sum_{i=1}^{N} \frac{K_{An,i} C_{An,i}[H^+]}{1 + \sum_{i=1}^{N} K_{An,i} C_{An,i}[H^+]} G_{\cdot OH} \tag{13.66}$$

As $C \to \infty$, $\theta_T \to 1$, which represents the maximum theoretical inhibition, θ_T is the total surface coverage found by summing the individual coverage of all ionic species. When all active sites for hydroxyl radical generation are blocked, then the rate of disinfection is at its lowest.

13.3.9 Model for Overall Inactivation Kinetics

13.3.9.1 Mass Balance of Live Cells

The survival of cells is given by Eq. (13.58). The differential form of the equation can be written as

$$\frac{\mathrm{d}[\mathrm{cell}]_l}{\mathrm{d}t} = -k_{\mathrm{dis}}[\cdot\mathrm{OH}]^n[\mathrm{cell}]_l^y \tag{13.67}$$

The disinfection reaction is peculiar in that it involves the reaction of molecules (usually given in mol L^{-1}) and cells (given in CFU L^{-1}). Therefore, it is important to recognize that Eq. (13.58) can be expressed in two ways with respect to the reactants: (1) the rate of disinfection (CFU L^{-1} s^{-1}) as given in Eq. (13.67), where the units of the disinfection rate constant k_{dis} are M^{-n} s^{-1}, and (2) the rate of consumption of hydroxyl radicals given in concentration per time (M s^{-1}). To reconcile this irregularity, Eq. (13.67) can also be expressed in terms of radical consumption,

$$\frac{\mathrm{d}[\cdot\mathrm{OH}]}{\mathrm{d}t} = -k_{\cdot\mathrm{OH}}[\cdot\mathrm{OH}]^n[\mathrm{cell}]_l^y \tag{13.68}$$

where $k_{\cdot\mathrm{OH}}$ is the reaction rate constant given in units of L^n M^{n-1} CFU^{-1} s^{-1}.

This reaction rate constant is dependent on the light intensity and TiO_2 concentration. Most studies show that disinfection is most effective with relatively lower concentration of catalyst and increases with light intensity. For the disinfection of *E. coli*, we estimated the reaction rate constant between 1 and $3.5 \times 10^{-12} L^n$ M^{n-1} CFU^{-1} s^{-1}, where n ranged from 1.2 to 1.5.

13.3.9.2 Mass Balance of By-Products

In order to account for the accumulation of by-product, Eq. (13.59) is rewritten as

$$m[\cdot\mathrm{OH}] + [\mathrm{cell}]_l \rightarrow [\mathrm{cell}]_d + \gamma[\mathrm{BP}] \tag{13.69}$$

One of the inherent difficulties of Eq. (13.69) is that one radical can set off a chain of reactions resulting in numerous by-products being formed. However, if it is assumed that most of the by-products result from oxidation of lipids, then the reaction kinetics in the membrane would be very similar to OH radicals reacting with lipids in solution (i.e., outside of a bilayer formation) [122–125]. Therefore, if $\gamma = m$, the accumulation of by-products is given by

$$\frac{\mathrm{d}C_{BP}}{\mathrm{d}t} = k_{\cdot\mathrm{OH}}[\cdot\mathrm{OH}]^x[\mathrm{cell}]_l^y - k_{BP}\frac{K_{BP}^{\mathrm{ads}}C_{BP}}{1 + K_{BP}^{\mathrm{ads}}C_{BP} + \sum_{i=1}^{N} K_{\mathrm{An},i}C_{\mathrm{An},i}[\mathrm{H}^+]} \tag{13.70}$$

.

The rate of phospholipid membrane degradation was determined in the work of Dalrymple et al. (2011) using model membranes and comparing it to disinfection of actual *E. coli* cells. They measured the malondialdehyde (MDA) and lipid hydroperoxide (LOOH) production and lipid peroxidation by-products. Thiobarbituric acid reactive species (TBARS) and ferrous oxidation of xylenol (FOX) assays were used to assess each by-product. The results showed that the oxidation kinetics of lipid vesicles closely matched the oxidation of *E. coli* cells in photocatalytic systems. In addition to other studies, their findings further validated membrane peroxidation as an important process in the mechanism of photocatalytic disinfection. However, the overall inactivation process is likely much more complex, involving a collection of other processes.

13.3.9.3 Mass Balance of OH Radicals

The mass balance for OH radicals in the interface between a catalyst and the cell surface is given as

$$\frac{\mathrm{d}[\cdot\mathrm{OH}]}{\mathrm{d}t} = G_{\cdot\mathrm{OH}}(1 - \theta_{\mathrm{An}} - \theta_{BP}) - k_{\cdot\mathrm{OH}}[\cdot\mathrm{OH}]^{x}[\mathrm{cell}]_{l}^{y} \tag{13.71}$$

where θ_{An} and θ_{BP} are the surface coverage of anions and by-products, respectively. It is customary for researchers to assume that the concentration of OH radicals is constant during the reaction. However, that assumption is not applied here.

While specific mechanisms may be applied to different systems, it is also possible to solve these series of equations for a complete system by numerical integration. A fifth-order Runge-Kutta method in MATLAB, for example, coupled with a least-square solver to obtain three unknown parameters (k_{dis}, n, and k_{OH}) can be performed.

13.4 Results

13.4.1 Effect of Light Intensity

Figure 13.10 shows the variation in survival for the three different light intensity levels at the lowest TiO_2 concentration. The trend is typical for other concentrations, except that the variation is greatest at concentration value shown. Many workers have found that the disinfection rate is usually proportional to the square root of light intensity at relatively high photon fluxes and linear at low flux [69, 71, 126–129]. The mechanistic model is able to predict this relationship. However, compared to most literature values, the intensity levels used in this research would be classified as low fluxes. The results indicate that disinfection response is linearly proportional to light intensity as illustrated in Fig. 13.11.

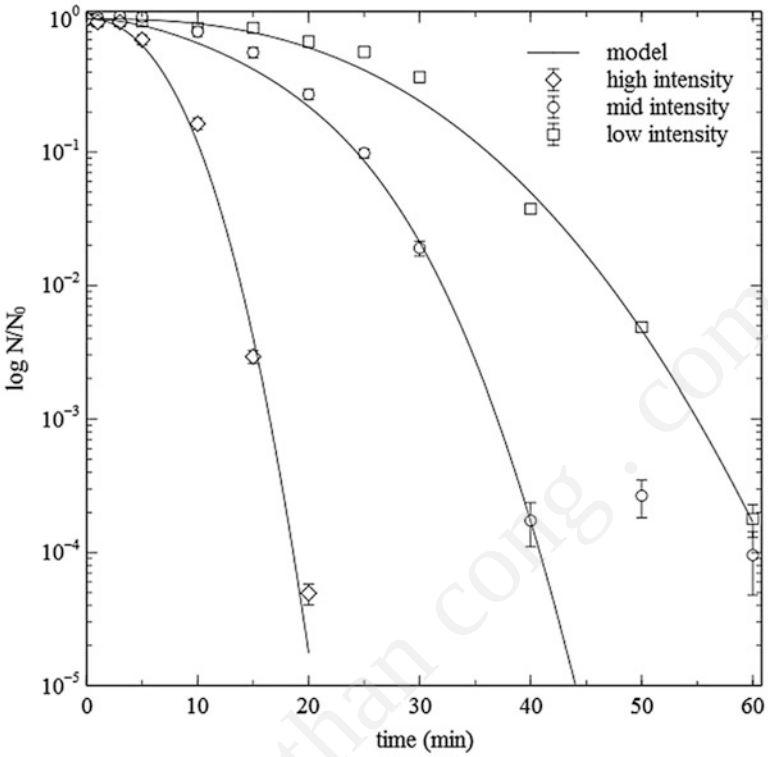

Fig. 13.10 Effect of light intensity on disinfection for control organisms at 0.01 g L^{-1}Degussa P25 TiO_2

Fig. 13.11 Relationship between intensity and average survival at 20 min

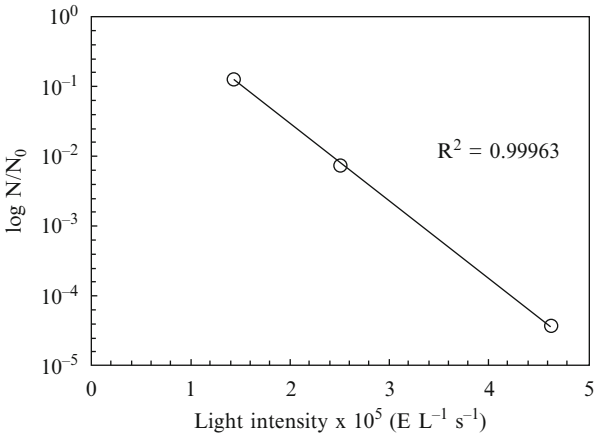

This behavior is directly related to the generation of hydroxyl radicals that occurs as a result of the interaction of the catalyst and light energy. At high light intensity, the recombination of the electron-hole pair is enhanced, while at low fluxes OH radical formation can compete with recombination [130–132]. Further, the rate becomes independent of light intensity at higher fluxes and the expected rate-limiting factor becomes the mass transfer [133].

13.4.2 Effect of TiO_2 Concentration

A log-linear relationship with catalyst concentration from 0.10 to 0.50 g L^{-1} of TiO_2 is predicted by the model (Fig. 13.12). Disinfection is much lower on average for 0.01 g L^{-1}. However, it must be kept in mind that these are main effects. Specific interactions are discussed in the next section. The interaction between light intensity and catalyst concentration produced completely different results.

Without reference to the specific interactions, the general trend for increased disinfection is to reduce catalyst concentration. Block et al. [134] made this observation for a similar range of catalyst concentrations. This behavior is a direct result of colloidal absorption phenomena and light distribution in the reactor. The surface coverage of catalyst particles on the cells is expected to be relatively lower at low concentrations of TiO_2. Very high catalyst concentrations (>0.5 g L^{-1}) actually result in destabilization of the colloidal suspension. As the catalyst concentration is increased without a change in pH, the condition for heterocoagulation is met as the total interaction energy V_T of the colloidal system approaches zero according to Eq. (13.27) [54]. The result is that the catalyst and microbes particles co-flocculate and rapidly settle out of solution.

Since the process is synergistic, that is, it depends on the interaction of light and TiO_2, the level of disinfection is significantly reduced due to the increase shading

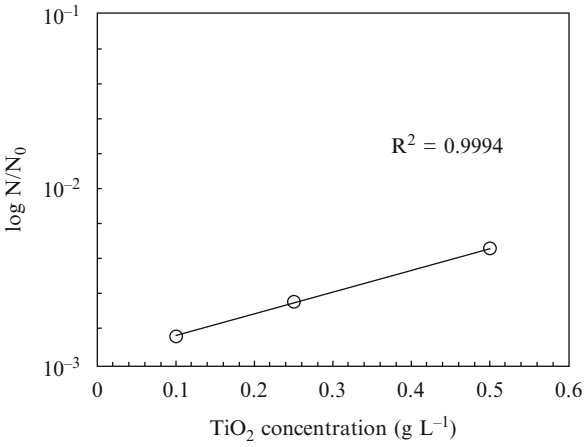

Fig. 13.12 Log-linear relationship between relatively high catalyst concentration (0.10–0.50 g L^{-1}) and *E. coli* survival

and scattering of light in high TiO_2 suspensions. It indicates that the effectiveness of the process is determined by some optimum surface coverage and a maximum penetration of light. Beyond these values, increased catalyst concentration retards the disinfection process.

13.4.3 *Interaction Effects: Light Intensity and TiO_2 Concentration*

Light intensity and catalyst concentration are evidently the two most important factors to be considered for photocatalysis. By analyzing the main effects, it can be seen that disinfection efficiency increases as light intensity increases and catalyst concentration decreases. Even though there is some minor sensitivity to high light intensity (result not shown), disinfection was always greater in the presence of the catalyst. At low and mid light intensity, there is much less variation in effectiveness for concentrations from 0.10 to 0.50 g L^{-1} TiO_2. Also, the effectiveness at the same light intensity for 0.01 g L^{-1} is much less at the chosen time interval when compared to all other concentration values.

At high light intensity, the interaction effects change dramatically. The lowest concentration of TiO_2 becomes the most effective and the effectiveness decreases with catalyst concentration across two orders of magnitude (Fig. 13.13). By doubling the light intensity from the mid to high position, an increase of 5 log units of disinfection was achieved within the same 20 min. Whereas, the same increase in light intensity for other concentrations produced much less disinfection.

The interaction between light intensity and catalyst concentration is the most important interaction because the main oxidants in the disinfection process are produced as result of the absorption of light by the catalyst. However, with increasing catalyst concentrations, the reaction solution becomes saturated and

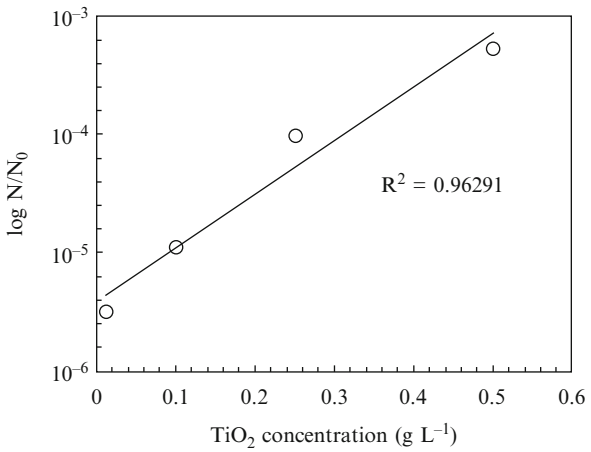

Fig. 13.13 Relationship between survival and TiO_2 concentration at high light intensity

only a portion of the particles receive irradiation. Although more surface area may be available for reaction, the additional catalyst particles do not participate in the reaction and the reaction rate does not increase with growing catalyst load beyond the optimum level [135].

Three main factors are responsible for these observations: colloidal adsorption and interaction, light transmission through the solution, and OH generation. The interaction of these phenomena is illustrated in the simple model of Fig. 13.14.

Firstly, the effects of absorption of TiO_2 unto a bacterial surface can be theoretically illustrated based on colloidal absorption theory. From TEM analysis it appears that there is very strong specific adsorption between the TiO_2 particles and microbial cells at neutral pH. According to Fig. 13.15, the catalyst particles (dark spots) are bound to the cells (rod-shaped features). They also form secondary layers or clusters with each other in some areas. It is interesting to note that the TiO_2 particles are not found in isolated areas with themselves, but predominantly occur with the cells.

Further, when the theoretical adsorption kinetics of TiO_2 to the cell surface is analyzed, it reveals that there is a transition from linear to nonlinear adsorption for the range of TiO_2 concentration used in the research. Linear adsorption occurs when the existing adsorption of particles at the bacterial surface does not significantly prevent other particles from adsorbing [60]. This occurs mostly at low particle concentrations ($<10^{12}$ mL^{-1}).

However, at higher particle concentrations, the existing coverage blocks other particles and prevents access to the surface. Under these circumstances, if TiO_2

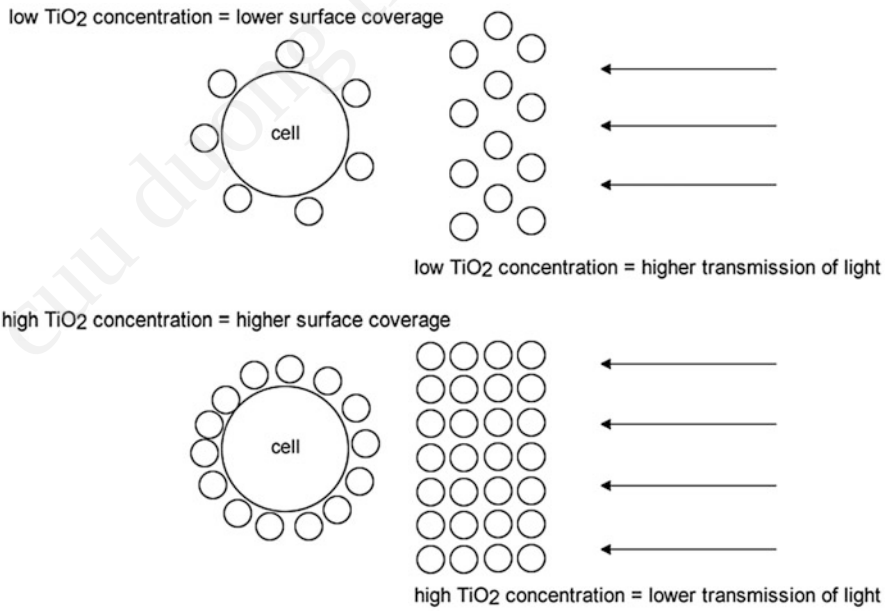

Fig. 13.14 Particle interaction and light transmission in TiO_2 suspensions

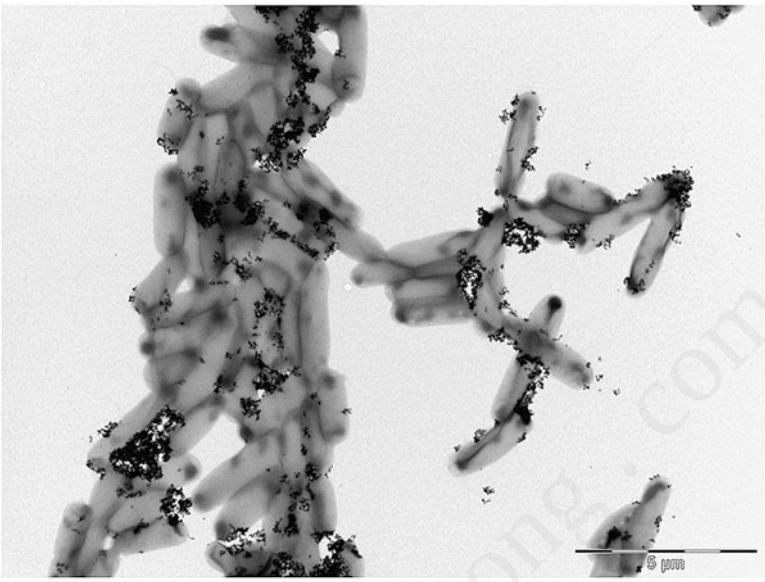

Fig. 13.15 TEM image of TiO_2 particles (*dark spots*) attached to *E. coli*

particles could be viewed as carriers of hydroxyl radicals, then it is easy to see that the access of radicals to the surface is also reduced under high concentration. However, for concentrations ranging from 0.10 to 0.50 g L^{-1}, this effect does not vary significantly.

13.4.4 Survival Curve Predictions

The model was used to predict the disinfection behavior of *E. coli* with different concentrations of TiO_2 and light intensity. The simulations show good agreement with the experimental data for stable colloidal suspensions, that is, suspensions in which rapid aggregation of cells and TiO_2 do not occur. Increased disinfection rates and high levels of inactivation can be achieved by maintaining a relatively low catalyst-to-microbe ratio while maximizing the light intensity. The influence of pH and ionic strength on the disinfection process have been included in the model, but these are only expected to be accurately predicted when the solution remains stable.

For the inactivation of *E. coli*, a typical sigmoidal survival curve is produced when plotted on the linear axes (Fig. 13.16). The initial lag and the onset of the log-linear phase for most of the disinfection data are well defined by the model (Fig. 13.17). However, the greatest challenge seems to be replicating the latter end of the disinfection curves close to the limit of detection. There are a number of factors responsible for this deviation.

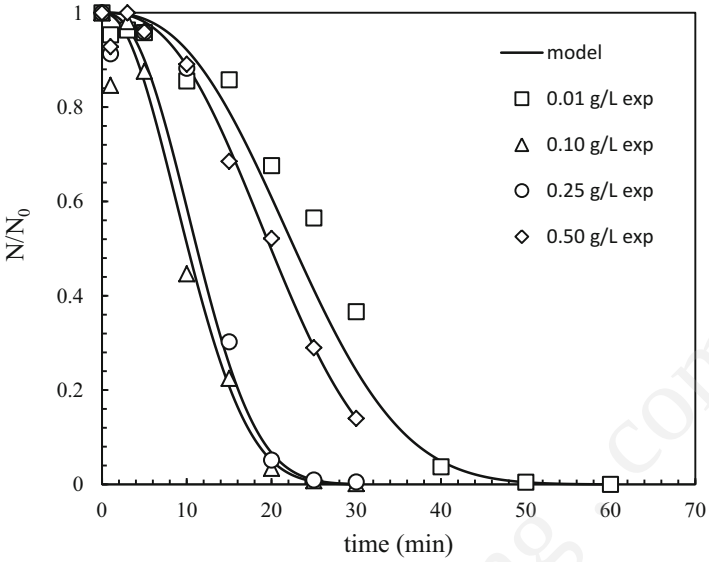

Fig. 13.16 Typical sigmoidal survival of *E. coli* at low intensity illumination ($1.51 \times 10^{-5} \pm 8.53 \times 10^{-6}$ E L^{-1} s^{-1}), $N_0 = 1 \times 10^6$ CFU L^{-1}

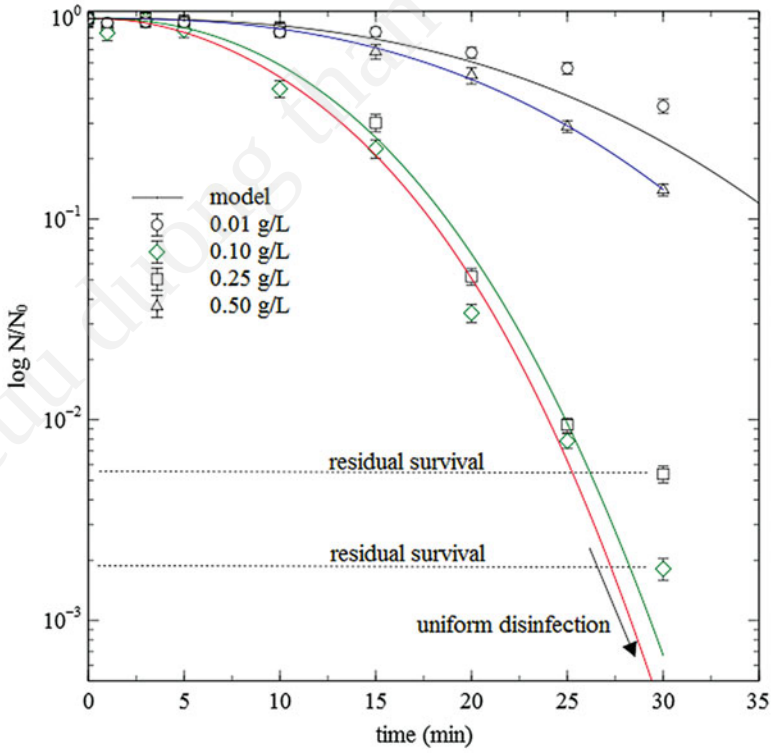

Fig. 13.17 Survival curve for *E. coli* treated at low light intensity ($1.51 \times 10^{-5} \pm 8.53 \times 10^{-9}$ E L^{-1} s^{-1})

Firstly, an implicit assumption in the development of the model is that the disinfection process is deterministic. This assumption works well for molecules because their numbers are so incredibly high. However, it can be argued that disinfection begins as a deterministic process when the number of microbes in solution is high (10^9 L^{-1}). This means that each microbe has about the same chance of being inactivated. However, as the microbial numbers drop significantly, it transitions to a stochastic process where the probability of inactivation varies from one organism to the next. The stochastic approach to model this behavior would be to define a function which accounts for the changing survival probabilities of individual cells [136]. The challenge, however, is that stochastic models are mostly empirical and cannot be obtained from deterministic formulations. Even though there may be mechanistic contributions to the probability function, such as uneven distribution of light, particularly in high concentration suspensions of TiO_2, it is still very difficult to formulate such a function and determine the influence of many other parameters as in the current model.

A second challenge, which occurs toward the end of the survival curve, is the determination of cell numbers close to the limit of detection. At very low concentrations, there is an inherent restriction on the number of cells that can appear on agar plates with sufficient accuracy to allow a resolution of the true cell count. In general, the lowest count that could be determined is 1 CFU per 100 μL (i.e., 10 CFU mL^{-1}). This corresponds to 1 CFU on an agar plate with an associated relative error of 100 %. The results indicate that there are significant fluctuations when determining cells at low concentration. The challenge for the model is that close to limit of detection, it predicts a uniform rate of disinfection. It is unlikely that this level of disinfection can be realized in a real population of cells or replicated in the lab.

Lastly, the existence of a finite residual survival, particularly for high catalyst concentration, was observed. The residual survival is characterized by a sudden tailing off of the disinfection curve following the exponential decay (Fig. 13.18). This was determined to be a real phenomenon because the cell count was usually to the right of the limit of detection. As previously explained, it is believed that the uneven distribution of light in the high concentration suspensions reduces the exposure of cells in the irradiated fraction of the reactor. This is accompanied by a sharp reduction in the disinfection rate. Recall that for suspensions with less catalyst loading, the irradiation zone is much wider, that is, the light distribution is more uniformed. As the cells are disinfected, the probability of entering the irradiated zone also drops, but not as much as in the case of high catalyst concentration. The consequence of this phenomenon is that disinfection is more "complete" in the case of lower concentrations, even if the overall process is slower.

13.4.4.1 Influence of Light Intensity and Catalyst Concentration

The model captures the effect of light intensity and catalyst concentration on the disinfection very well. Without much change in the rate constants, it shows that the

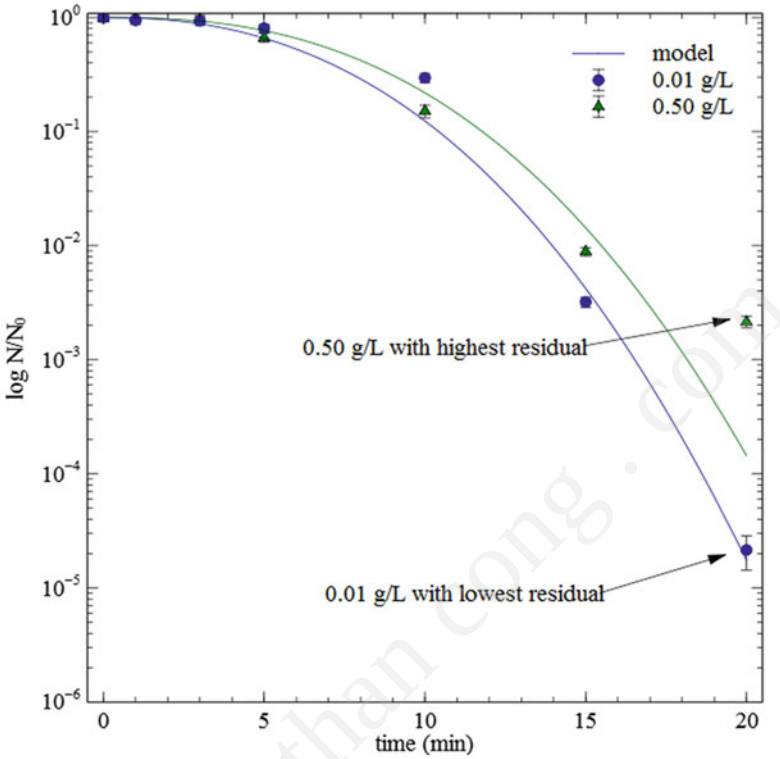

Fig. 13.18 Effect of concentration loading on residual survival of *E. coli* at high light intensity ($4.37 \times 10^{-5} \pm 5.19 \times 10^{-6}$ E L^{-1} s^{-1})

main effects are dominated by the interaction of these variables as determined previously. The processes involved in this interaction include light transmission, OH radical generation, and the absorption effects between colloids. Most of the variations from one survival curve to another are related to changes in light intensity and catalyst concentration, since other parameters were held constant.

13.5 Conclusions

The photocatalytic disinfection of *E. coli* with suspended catalyst particles is a complex process that involves the interplay of many phenomena. These include light absorption and scattering, semiconductor photoexcitation and charge carrier generation, electrochemical surface reactions (including electron transfer reactions, adsorption, and acid-base reactions), and heterogeneous colloidal interactions. All these processes play a significant role in the overall inactivation efficiency. For a given solution composition, light intensity and catalyst concentration are the most

significant operational factors in the entire process. The combination of light intensity and catalyst concentration determine the light absorption and scattering effects and the OH radical generation rate. Low catalyst concentration and high light intensity favor higher log inactivation. At low TiO_2 concentrations, the colloidal suspension is more stable, the distribution of light is fairly uniform, and there is a higher radical generation rate per mass of catalyst.

The mechanistic model is flexible and has good validity for predicting the disinfection behavior of *E. coli*. However, there is an inherent challenge to replicate residual survival, especially at low cell concentration because of the deterministic nature of the model. The model predicts uniform inactivation close to and beyond the limit of detection, which is not always the case. The high fluctuations of bacteria at low concentrations make this challenge very difficult to solve. One technique would be to utilize stochastic models that can define the probability of disinfecting an individual organism based on the reaction composition.

Despite the shortcomings of the current model, the simulations show good agreement with the experimental data for stable colloidal suspensions, that is, suspensions in which rapid aggregation of cells and TiO_2 do not occur. Increased disinfection rates and high levels of inactivation can be achieved by maintaining a relatively low catalyst-to-microbe ratio while maximizing the light intensity. The influence of pH and ionic strength on the disinfection process can be included in the model, but these are only expected to be accurately predicted when the solution remains stable.

References

1. Allouni ZE et al (2009) Agglomeration and sedimentation of TiO_2 nanoparticles in cell culture medium. Colloids Surf B: Biointerfaces 68(1):83–87
2. Gumy D et al (2006) Catalytic activity of commercial of TiO_2 powders for the abatement of the bacteria (E. coli) under solar simulated light: influence of the isoelectric point. Appl Catal B Environ 63(1–2):76–84
3. Sentein C et al (2009) Dispersion and stability of TiO_2 nanoparticles synthesized by laser pyrolysis in aqueous suspensions. J Phys Conf Ser 170(1):012013
4. Dalrymple OK et al (2010) A review of the mechanisms and modeling of photocatalytic disinfection. Appl Catal B Environ 98(1–2):27–38
5. Boström M et al (2006) Extended DLVO theory: electrostatic and non-electrostatic forces in oxide suspensions. Adv Colloid Interf Sci 123–126:5–15
6. Boström M, Williams DRM, Ninham BW (2001) Specific ion effects: why DLVO theory fails for biology and colloid systems. Phys Rev Lett 87(16):168103
7. Lyklema J, van Leeuwen HP, Minor M (1999) DLVO-theory, a dynamic re-interpretation. Adv Colloid Interf Sci 83(1–3):33–69
8. Al-Abadleh HA, Grassian VH (2003) Oxide surfaces as environmental interfaces. Surf Sci Rep 52(3–4):63–161
9. Brown GE Jr (2001) Surface science: how minerals react with water. Science 294 (5540):67–69
10. Boehm HP (1971) Acidic and basic properties of hydroxylated metal oxide surfaces. Discuss Faraday Soc 52:264–275

11. Stefanovich EV, Truong TN (1999) Ab initio study of water adsorption on TiO_2(110): molecular adsorption versus dissociative chemisorption. Chem Phys Lett 299(6):623–629
12. William HC, Marcus AC (1993) Brønsted reactions on oxide mineral surfaces and the temperature-dependence of their dissolution rates. Aquat Sci 55(4):304–313
13. Hoffmann MR et al (1995) Environmental applications of semiconductor photocatalysis. Chem Rev 95(1):69–96
14. Davis James A, Leckie James O (1979) Speciation of adsorbed ions at the oxide/water interface. In: Chemical modeling in aqueous systems. American Chemical Society, Washington, DC, pp 299–317
15. Yurdakal S et al (2007) Optical properties of TiO_2 suspensions: influence of pH and powder concentration on mean particle size. Ind Eng Chem Res 46(23):7620–7626
16. Predota M et al (2004) Electric double layer at the rutile (110) surface. 2. Adsorption of ions from molecular dynamics and X-ray experiments. J Phys Chem B 108(32):12061–12072
17. Kormann C, Bahnemann DW, Hoffmann MR (1991) Photolysis of chloroform and other organic molecules in aqueous titanium dioxide suspensions. Environ Sci Technol 25 (3):494–500
18. Gonzalez-Caballero F, Shilov VN (2006) Electrical double-layer at a colloid particle. In: Encyclopedia of surface and colloid science, 2nd edn. Taylor & Francis, New York, pp 1932–1936
19. Imae T, Muto K, Ikeda S (1991) The pH dependence of dispersion of TiO_2 particles in aqueous surfactant solutions. Colloid Polym Sci 269(1):43–48
20. Cabuil V et al (2004) Stability of TiO_2 suspensions in reactors for degradation of toxic pollutants. In: Cabuil V, Leviz P, Treiner C (eds) Trends in colloid and interface science XVII. Springer, Berlin/Heidelberg, pp 117–120
21. French RA et al (2009) Influence of ionic strength, pH, and cation valence on aggregation kinetics of titanium dioxide nanoparticles. Environ Sci Technol 43(5):1354–1359
22. Watts RJ, Kong S, Lee W (1995) Sedimentation and reuse of titanium dioxide: application to suspended-photocatalyst reactors. J Environ Eng 121(10):730–735
23. Grahame DC (1947) The electrical double layer and the theory of electrocapillarity. Chem Rev 41(3):441–501
24. Stern O (1924) The theory of the electric double layer. Z Elektrochem 30:508
25. Rodriguez R, Blesa MA, Regazzoni AE (1996) Surface complexation at the TiO_2(anatase)/aqueous solution interface: chemisorption of catechol. J Colloid Interface Sci 177 (1):122–131
26. Lausmaa J, Löfgren P, Kasemo B (1999) Adsorption and coadsorption of water and glycine on TiO_2. J Biomed Mater Res 44(3):227–242
27. Weng Y-X et al (2003) Surface-binding forms of carboxylic groups on nanoparticulate TiO_2 surface studied by the interface-sensitive transient triplet-state molecular probe. J Phys Chem B 107(18):4356–4363
28. Olivera P, Patrito M, Sellers H et al (1999) Electronic structure calculations of polyatomic oxyanions adsorbed on metal surfaces. In: Interfacial electrochemistry: theory, experiment, and applications. Marcel Dekker, Inc, New York
29. Kazarinov VE, Andreev VN, Mayorov AP (1981) Investigation of the adsorption properties of the TiO_2 electrode by the radioactive tracer method. J Electroanal Chem Interfacial Electrochem 130:277–285
30. Horányi G (2003) Investigation of the specific adsorption of sulfate ions on powdered TiO_2. J Colloid Interface Sci 261(2):580–583
31. Magdigan MT, Martinko JM (2006) Brock biology of microorganisms, 11th edn. Pearson Education, Inc, Upper Saddle River, p 992
32. Demchick P, Koch AL (1996) The permeability of the wall fabric of Escherichia coli and Bacillus subtilis. J Bacteriol 178(3):768–773
33. van Loosdrecht MCM et al (1989) Bacterial adhesion: a physicochemical approach. Microb Ecol 17(1):1–15

34. Oleary WM (1962) Fatty acids of bacteria. Bacteriol Rev 26(4):421–447
35. Cronan JE Jr, Gelmann EP (1973) An estimate of the minimum amount of unsaturated fatty acid required for growth of Escherichia coli. J Biol Chem 248(4):1188–1195
36. Magnuson K et al (1993) Regulation of fatty acid biosynthesis in Escherichia coli. Microbiol Mol Biol Rev 57(3):522–542
37. Cox JS et al (1999) Characterizing heterogeneous bacterial surface functional groups using discrete affinity spectra for proton binding. Environ Sci Technol 33(24):4514–4521
38. Martinez RE et al (2002) Determination of intrinsic bacterial surface acidity constants using a Donnan shell model and a continuous pK_a distribution method. J Colloid Interface Sci 253 (1):130–139
39. van der Wal A et al (1997) Determination of the total charge in the cell walls of Gram-positive bacteria. Colloids Surf B: Biointerfaces 9(1–2):81–100
40. Jiang W et al (2004) Elucidation of functional groups on Gram-positive and Gram-negative bacterial surfaces using infrared spectroscopy. Langmuir 20(26):11433–11442
41. Neu TR (1996) Significance of bacterial surface-active compounds in interaction of bacteria with interfaces. Microbiol Rev 60(1):151–166
42. Poortinga AT et al (2002) Electric double layer interactions in bacterial adhesion to surfaces. Surf Sci Rep 47(1):1–32
43. Poortinga AT (2001) Electric double layer interactions in bacterial adhesion and detachment. In: Institute of biomedical materials science and applications. University of Groningen, Groningen, p 170
44. Sonohara R et al (1995) Difference in surface properties between Escherichia coli and Staphylococcus aureus as revealed by electrophoretic mobility measurements. Biophys Chem 55(3):273–277
45. Ohshima H, Kondo T (1990) Relationship among the surface potential, Donnan potential and charge density of ion-penetrable membranes. Biophys Chem 38(1–2):117–122
46. Ohshima H (1995) Electrophoresis of soft particles. Adv Colloid Interf Sci 62(2–3):189–235
47. Busscher HJ, Weerkamp AH (1987) Specific and non-specific interactions in bacterial adhesion to solid substrata. FEMS Microbiol Lett 46(2):165–173
48. Wasserman E, Felmy AR (1998) Computation of the electrical double layer properties of semipermeable membranes in multicomponent electrolytes. Appl Environ Microbiol 64 (6):2295–2300
49. Makino K, Ohshima H, Kondo T (1987) Surface potential of an ion-penetrable charged membrane. J Theor Biol 125(3):367–368
50. Van Oss CJ (1994) Interfacial forces in aqueous media. M. Dekker, New York
51. Luttge A, Zhang L, Nealson KH (2005) Mineral surfaces and their implications for microbial attachment: results from Monte Carlo simulations and direct surface observations. Am J Sci 305(6–8):766–790
52. Jucker BA et al (1997) Adsorption of bacterial surface polysaccharides on mineral oxides is mediated by hydrogen bonds. Colloids Surf B: Biointerfaces 9(6):331–343
53. Landini P, Zehnder AJB (2002) The global regulatory hns gene negatively affects adhesion to solid surfaces by anaerobically grown Escherichia coli by modulating expression of flagellar genes and lipopolysaccharide production. J Bacteriol 184(6):1522–1529
54. Taguchi T et al (1990) Interaction between an ion-penetrable particle and a solid particle. II. Criteria for heterocoagulation. Colloid Polym Sci 268(1):83–87
55. Terui H et al (1990) Interaction between an ion-penetrable particle and a solid particle. 1. Electrical double-layer interaction. Colloid Polym Sci 268(1):76–82
56. Ohshima H, Kondo T (1993) Electrostatic interaction of an ion-penetrable sphere with a hard plate: contribution of image interaction. J Colloid Interface Sci 157(2):504–508
57. Hsu J-P, Liu B-T (1998) Electrical interaction between two spherical particles covered by an ion-penetrable charged membrane. Chem Phys 236(1–3):63–76

58. Kuo Y-C, Hsieh M-Y, Hsu J-P (2002) Interactions between a particle covered by an ion-penetrable charged membrane and a charged surface: a modified Gouy-Chapman theory. Langmuir 18(7):2789–2794
59. Fernandez-Ibanez P et al (2003) Application of the colloidal stability of TiO2 particles for recovery and reuse in solar photocatalysis. Water Res 37(13):3180–3188
60. Adamczyk Z et al (1994) Kinetics of localized adsorption of colloid particles. Adv Colloid Interf Sci 48:151–280
61. Oberholzer MR et al (1997) 2-D and 3-D interactions in random sequential adsorption of charged particles. J Colloid Interface Sci 194(1):138–153
62. Widom B (1966) Random sequential addition of hard spheres to a volume. J Chem Phys 44 (10):3888–3894
63. Adamczyk Z et al (1990) Structure and ordering in localized adsorption of particles. J Colloid Interface Sci 140(1):123–137
64. Adamczyk Z (2000) Kinetics of diffusion-controlled adsorption of colloid particles and proteins. J Colloid Interface Sci 229(2):477–489
65. Yang Q et al (2005) Light distribution field in catalyst suspensions within an annular photoreactor. Chem Eng Sci 60(19):5255–5268
66. Hatchard CG, Parker CA (1956) A new sensitive chemical actinometer. II. Potassium ferrioxalate as a standard chemical actinometer. Proc R Soc Lond A Math Phys Sci 235 (1203):518–536
67. Kuhn HJ, Braslavsky SE, Schmidt R (2004) Chemical actinometry. Pure Appl Chem 76 (12):2105–2146
68. Bunce NJ, LaMarre J, Vaish SP (1984) Photorearrangement of azoxybenzene to 2-hydroxyazobenzene: a convenient chemical actinometer. Photochem Photobiol 39 (4):531–533
69. Sun L, Bolton JR (1996) Determination of the quantum yield for the photochemical generation of hydroxyl radicals in TiO_2 suspensions. J Phys Chem 100(10):4127–4134
70. Zhang H, Chen G, Bahnemann DW (2010) Environmental photo(electro)catalysis: fundamental principles and applied catalysts. In: Comninellis C, Chen G (eds) Electrochemistry for the environment. Springer, New York
71. Rincon A-G, Pulgarin C (2004) Effect of pH, inorganic ions, organic matter and H_2O_2 on E. coli K12 photocatalytic inactivation by TiO_2: implications in solar water disinfection. Appl Catal B Environ 51(4):283–302
72. Chu W, Wong CC (2004) The photocatalytic degradation of dicamba in TiO2 suspensions with the help of hydrogen peroxide by different near UV irradiations. Water Res 38 (4):1037–1043
73. Wong CC, Chu W (2003) The hydrogen peroxide-assisted photocatalytic degradation of alachlor in TiO_2 suspensions. Environ Sci Technol 37(10):2310–2316
74. Wang Y, Hong C-s (1999) Effect of hydrogen peroxide, periodate and persulfate on photocatalysis of 2-chlorobiphenyl in aqueous TiO_2 suspensions. Water Res 33 (9):2031–2036
75. Mills A, Le Hunte S (1997) An overview of semiconductor photocatalysis. J Photochem Photobiol A Chem 108(1):1–35
76. Matsunaga T et al (1985) Photoelectrochemical sterilization of microbial cells by semiconductor powders. FEMS Microbiol Lett 29(1–2):211–214
77. Turchi CS, Ollis DF (1990) Photocatalytic degradation of organic water contaminants: mechanisms involving hydroxyl radical attack. J Catal 122(1):178
78. Thiebaud J, Thevent F, Fittschen C (2010) OH radicals and H_2O_2 molecules in the gas phase near to TiO_2 surfaces. J Phys Chem C 114(7):3082–3088
79. Lee MC, Choi W (2002) Solid phase photocatalytic reaction on the soot/TiO_2 interface: the role of migrating OH radicals. J Phys Chem B 106(45):11818–11822

80. Murakami Y et al (2006) Direct detection of OH radicals diffused to the gas phase from the UV-irradiated photocatalytic TiO_2 surfaces by means of laser-induced fluorescence spectroscopy. J Phys Chem B 110(34):16808–16811
81. Roots R, Okada S (1975) Estimation of life times and diffusion distances of radicals involved in x-ray-induced DNA strand breaks or killing of mammalian cells. Radiat Res 64 (2):306–320
82. Murakami Y et al (2007) Can OH radicals diffuse from the UV-irradiated photocatalytic TiO_2 surfaces? Laser-induced-fluorescence study. J Phys Chem C 111(30):11339–11346
83. Svishchev IM, Plugatyr AY (2005) Hydroxyl radical in aqueous solution: computer simulation. J Phys Chem B 109(9):4123–4128
84. Campo MG, Grigera JR (2005) Classical molecular-dynamics simulation of the hydroxyl radical in water. J Chem Phys 123(8):084507
85. Kupperman A (1967) Diffusion model of the radiation chemistry of aqueous solutions. In: Silini G (ed) Radiation Research: proceedings of the Third International Congress of Radiation Research. Wiley, New York, pp 212–234
86. Vassilev P, Louwerse MJ, Baerends EJ (2004) Ab initio molecular dynamics simulation of the OH radical in liquid water. Chem Phys Lett 398(1–3):212–216
87. Campo MG, Grigera JR (2005) Classical molecular-dynamics simulation of the hydroxyl radical in water. J Chem Phys 123(8):084507–6
88. Haas CN (1980) A mechanistic kinetic model for chlorine disinfection. Environ Sci Technol 14(3):339–340
89. Halliwell B, Gutteridge J (1989) Free radicals in biology and medicine, 2nd edn. Clarendon Press, Oxford
90. Pryor WA (ed) (1976) Free radicals in biology. Vol. 1. Academic Press, Inc, New York, p 287
91. Dean RT et al (1997) Biochemistry and pathology of radical-mediated protein oxidation. Biochem J 324(1):1–18
92. Hawkins CL, Davies MJ (2001) Generation and propagation of radical reactions on proteins. Biochim Biophys Acta Bioenergetics 1504(2–3):196–219
93. Gutteridge JMC (1984) Lipid peroxidation initiated by superoxide-dependent hydroxyl radicals using complexed iron and hydrogen peroxide. FEBS Lett 172(2):245–249
94. Cheng YW, Chan RCY, Wong PK (2007) Disinfection of Legionella pneumophila by photocatalytic oxidation. Water Res 41(4):842–852
95. Lu Z-X et al (2003) Cell damage induced by photocatalysis of TiO_2 thin films. Langmuir 19 (21):8765–8768
96. Huang N-P et al (1997) The study of the photokilling effect and mechanism of ultrafine TiO_2 particles on U937 cells. J Photochem Photobiol A Chem 108(2–3):229–233
97. Stefan IL, Irwin F (1999) Superoxide and iron: partners in crime. IUBMB Life 48(2):157–161
98. Carlioz A, Touati D (1986) Isolation of superoxide-dismutase mutants in *Escherichia coli* – Is superoxide-dismutase necessary for aerobic life. EMBO J 5(3):623–630
99. Kiwi J, Nadtochenko V (2005) Evidence for the mechanism of photocatalytic degradation of the bacterial wall membrane at the TiO_2 interface by ATR-FTIR and laser kinetic spectroscopy. Langmuir 21(10):4631–4641
100. Kiwi J, Nadtochenko V (2004) New evidence for TiO_2 photocatalysis during bilayer lipid peroxidation. J Phys Chem B 108(45):17675–17684
101. Maness P et al (1999) Bactericidal activity of photocatalytic TiO_2 reaction: toward an understanding of its killing mechanism. Appl Environ Microbiol 65(9):4094–4098
102. Nadtochenko VA et al (2005) Dynamics of E. coli membrane cell peroxidation during TiO_2 photocatalysis studied by ATR-FTIR spectroscopy and AFM microscopy. J Photochem Photobiol A Chem 169(2):131–137
103. Porter N, Caldwell S, Mills K (1995) Mechanisms of free radical oxidation of unsaturated lipids. Lipids 30(4):277–290
104. Janero DR (1990) Malondialdehyde and thiobarbituric acid-reactivity as diagnostic indices of lipid peroxidation and peroxidative tissue injury. Free Radic Biol Med 9(6):515–540

105. Jiang Z-Y, Woollard A, Wolff S (1991) Lipid hydroperoxide measurement by oxidation of Fe_2^+ in the presence of xylenol orange. Comparison with the TBA assay and an iodometric method. Lipids 26(10):853–856
106. Barber DJW, Thomas JK (1978) Reactions of radicals with lecithin bilayers. Radiat Res 74 (1):51–65
107. Joseph JM, Aravindakumar CT (2000) Determination of rate constants for the reaction of hydroxyl radicals with some purines and pyrimidines using sunlight. J Biochem Biophys Methods 42(3):115–124
108. Buxton GV et al (1988) Critical review of rate constants for reactions of hydrated electron, hydrogen atom and hydroxyl radicals (OH/O^-) in aqueous solution. J Phys Chem Ref Data 17:513–817
109. Minero C et al (2000) Photocatalytic transformation of organic compounds in the presence of inorganic ions. 2. Competitive reactions of phenol and alcohols on a titanium dioxide-fluoride system. Langmuir 16(23):8964–8972
110. Calza P, Pelizzetti E (2001) Photocatalytic transformation of organic compounds in the presence of inorganic ions. Pure Appl Chem 73(12):1839–1848
111. Chen HY, Zahraa O, Bouchy M (1997) Inhibition of the adsorption and photocatalytic degradation of an organic contaminant in an aqueous suspension of TiO_2 by inorganic ions. J Photochem Photobiol A Chem 108(1):37–44
112. Guillard C et al (2005) Why inorganic salts decrease the TiO_2 photocatalytic efficiency. Int J Photoenergy 7(1):1–9
113. Abdullah M, Low GKC, Matthews RW (1990) Effects of common inorganic anions on rates of photocatalytic oxidation of organic carbon over illuminated titanium dioxide. J Phys Chem 94(17):6820–6825
114. McBride MB (1994) Environmental chemistry of soils. Oxford University Press, New York
115. Dzombak DA, Morel F (1990) Surface complexation modeling: hydrous ferric oxide. Wiley, New York
116. Ku Y, Lee W-H, Wang W-Y (2004) Photocatalytic reduction of carbonate in aqueous solution by UV/TiO_2 process. J Mol Catal A Chem 212(1–2):191–196
117. Hug SJ, Sulzberger B (1994) In situ Fourier transform infrared spectroscopic evidence for the formation of several different surface complexes of oxalate on TiO_2 in the aqueous phase. Langmuir 10(10):3587–3597
118. Connor PA, McQuillan AJ (1999) Phosphate adsorption onto TiO_2 from aqueous solutions: an in situ internal reflection infrared spectroscopic study. Langmuir 15(8):2916–2921
119. Kochany J, Lipczynska-Kochany E (1992) Application of the EPR spin-trapping technique for the investigation of the reactions of carbonate, bicarbonate, and phosphate anions with hydroxyl radicals generated by the photolysis of H_2O_2. Chemosphere 25(12):1769–1782
120. Matthews RW, Mahlman HA, Sworski TJ (1972) Elementary processes in the radiolysis of aqueous sulfuric acid solutions. Determinations of both GOH and GSO4. J Phys Chem 76 (9):1265–1272
121. Chang CY et al (2007) Formation and calculation of hydroxyl radical in the optimal photocatalytic process using the Taguchi method. Environ Informatics 5:655–663
122. Tejero I et al (2007) Theoretical modeling of hydroxyl-radical-induced lipid peroxidation reactions. J Phys Chem B 111(20):5684–5693
123. Cubillos MA, Lissi EA, Abuin EB (2000) Kinetics of lipid peroxidation in compartmentalized systems initiated by a water-soluble free radical source. Chem Phys Lipids 104(1):49–56
124. Wagner BA, Buettner GR, Burns CP (2002) Free radical-mediated lipid peroxidation in cells: oxidizability is a function of cell lipid bis-allylic hydrogen content. Biochemistry 33 (15):4449–4453
125. Li Q-T, Yeo MH, Tan BK (2000) Lipid peroxidation in small and large phospholipid unilamellar vesicles induced by water-soluble free radical sources. Biochem Biophys Res Commun 273(1):72–76

126. McLoughlin OA et al (2004) Photocatalytic disinfection of water using low cost compound parabolic collectors. Sol Energy 77(5):625–633
127. Rincon AG, Pulgarin C (2003) Photocatalytical inactivation of E. coli: effect of (continuous-intermittent) light intensity and of (suspended-fixed) TiO_2 concentration. Appl Catal B Environ 44(3):263–284
128. Pal A et al (2007) Photocatalytic inactivation of Gram-positive and Gram-negative bacteria using fluorescent light. J Photochem Photobiol A Chem 186(2–3):335–341
129. Horie Y et al (1996) Effects of light intensity and titanium dioxide concentration on photocatalytic sterilization rates of microbial cells. Ind Eng Chem Res 35(11):3920–3926
130. Kaneko M, Kaneko M, Okura I (eds) (2002) Photocatalysis: science and technology. Biological and Medical Physics Series, ed. Greenbaum E. Springer, New York, p. 356
131. Turchi CS (1991) Effect of light intensity on photocatalytic reaction. In: Potential applications of concentrated solar energy: proceedings of a workshop. Commission on Engineering and Technical Systems (CETS), Washington, DC
132. Egerton TA, King CJ (1979) Influence of light intensity on photoactivity in titanium dioxide pigmented systems. J Oil Col Chem Assoc 62(10):386–391
133. Coleman HM et al (2005) Photocatalytic degradation of 17[beta]-oestradiol, oestriol and 17 [alpha]-ethynyloestradiol in water monitored using fluorescence spectroscopy. Appl Catal B Environ 55(1):23–30
134. Block SS, Seng VP, Goswami DW (1997) Chemically enhanced sunlight for killing bacteria. J Sol Energy Eng 119(1):85–91
135. Parra S, Olivero J, Pulgarin C (2002) Relationships between physicochemical properties and photoreactivity of four biorecalcitrant phenylurea herbicides in aqueous TiO_2 suspension. Appl Catal B Environ 36(1):75–84
136. Corradini MG, Normand MD, Peleg M (2010) Stochastic and deterministic model of microbial heat inactivation. J Food Sci 75(2):R59–R70